

Quantifying the probability of light damage to masonry structures

An exploration of crack initiation and progression due to seismic vibrations on masonry buildings with existing damage

Korswagen, Paul A.

DOI

[10.4233/uuid:e56827d2-c821-4547-922e-ea24bd748e68](https://doi.org/10.4233/uuid:e56827d2-c821-4547-922e-ea24bd748e68)

Publication date

2024

Document Version

Final published version

Citation (APA)

Korswagen, P. A. (2024). *Quantifying the probability of light damage to masonry structures: An exploration of crack initiation and progression due to seismic vibrations on masonry buildings with existing damage*. [Dissertation (TU Delft), Delft University of Technology]. <https://doi.org/10.4233/uuid:e56827d2-c821-4547-922e-ea24bd748e68>

Important note

To cite this publication, please use the final published version (if applicable).
Please check the document version above.

Copyright

Other than for strictly personal use, it is not permitted to download, forward or distribute the text or part of it, without the consent of the author(s) and/or copyright holder(s), unless the work is under an open content license such as Creative Commons.

Takedown policy

Please contact us and provide details if you believe this document breaches copyrights.
We will remove access to the work immediately and investigate your claim.

QUANTIFYING THE PROBABILITY OF LIGHT DAMAGE TO MASONRY STRUCTURES

**AN EXPLORATION OF CRACK INITIATION AND
PROGRESSION DUE TO SEISMIC VIBRATIONS ON
MASONRY BUILDINGS WITH EXISTING DAMAGE**

QUANTIFYING THE PROBABILITY OF LIGHT DAMAGE TO MASONRY STRUCTURES

**AN EXPLORATION OF CRACK INITIATION AND
PROGRESSION DUE TO SEISMIC VIBRATIONS ON
MASONRY BUILDINGS WITH EXISTING DAMAGE**

Dissertation

for the purpose of obtaining the degree of doctor
at Delft University of Technology,
by the authority of the Rector Magnificus, Prof.dr.ir. T.H.J.J. van der Hagen,
chair of the Board for Doctorates,
to be defended publicly on
16 October 2024 at 12:30

by

Paul Alexander KORSWAGEN EGUREN

Master of Science in Civil Engineering,
Delft University of Technology, The Netherlands
born in Lima, Perú

This dissertation has been approved by the promotor:

Prof.dr.ir. J.G. Rots

Dr.ir. K.C. Terwel

Composition of the doctoral committee:

Rector Magnificus

Chairman

Prof.dr.ir. J.G. Rots

Promotor, Delft University of Technology, NL

Dr.ir.

K.C. Terwel

Co-promotor, Delft University of Technology, NL

Independent members:

Prof.dr.ir. S.N. Jonkman

Delft University of Technology, NL

Prof.dr.ir. M.A.N. Hendriks

Delft University of Technology, NL

Prof.dr.ir. S.N.M. Wijte

Eindhoven University of Technology, NL

Prof.dr. P.B. Lourenço

University of Minho, PT

Assoc.Prof.dr. K. Beyer

École Polytechnique Fédérale de Lausanne, CH



Parts of this research were performed within the scope of the projects:

Damage sensitivity of Groningen Masonry Structures, funded by *Nederlandse Aardolie Maatschappij B.V. (NAM)*;

Advies Schadebeoordeling IMG [WP2.3, 2.4, 3.2, 3.3, 5.1], funded by the *Instituut Mijnbouwschade Groningen (IMG)*;

Onderzoek naar de oorzaken van bouwkundige schade in Groningen, funded by *Nationaal Coördinator Groningen (NCG)*.

Keywords: Unreinforced Masonry (URM), Light Damage, Probabilistic Quantification, DIC

Printed by: IPSKAMP

Cover design: Author

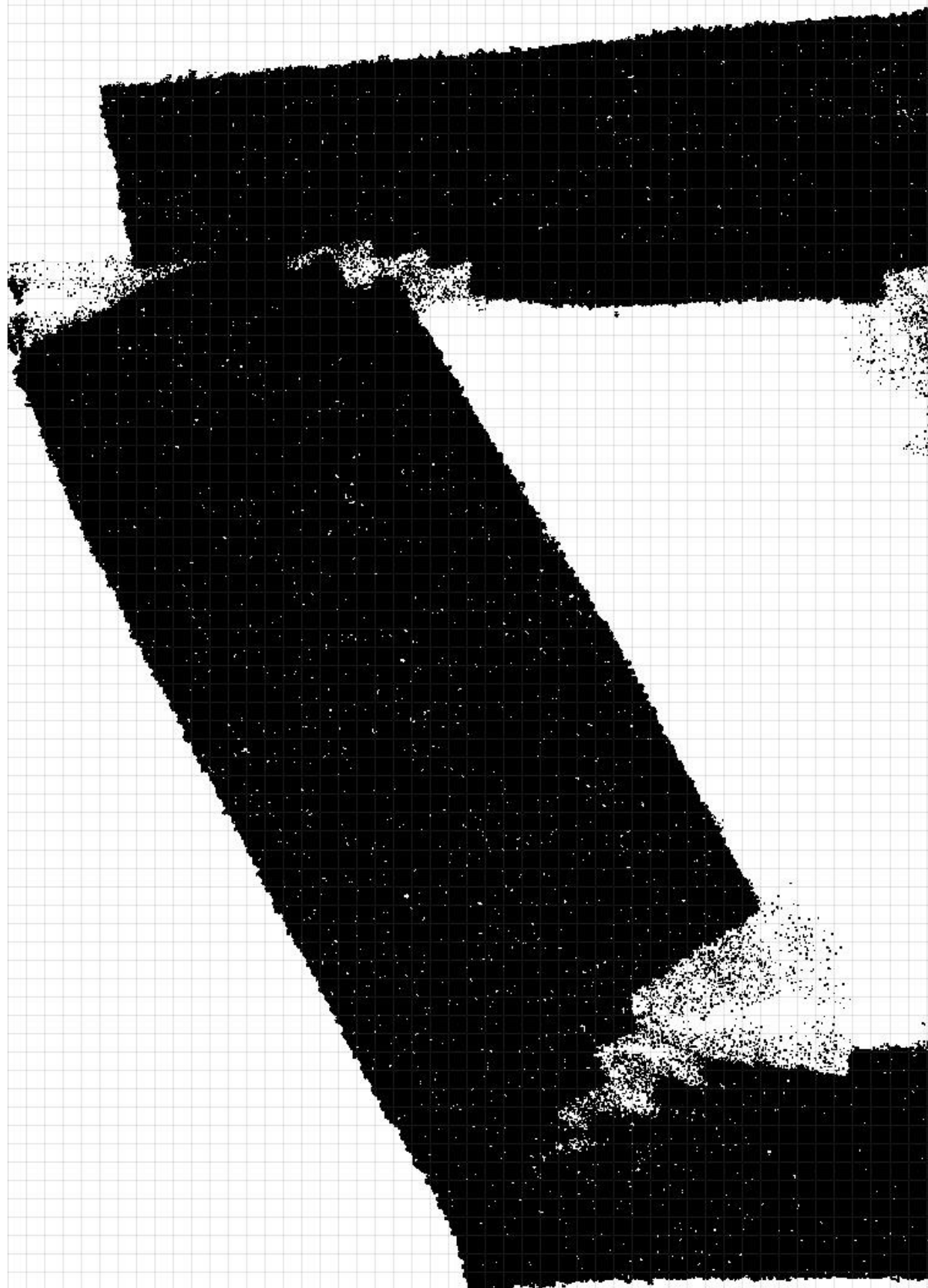
Copyright © 2024 by P. Korswagen. All rights reserved.

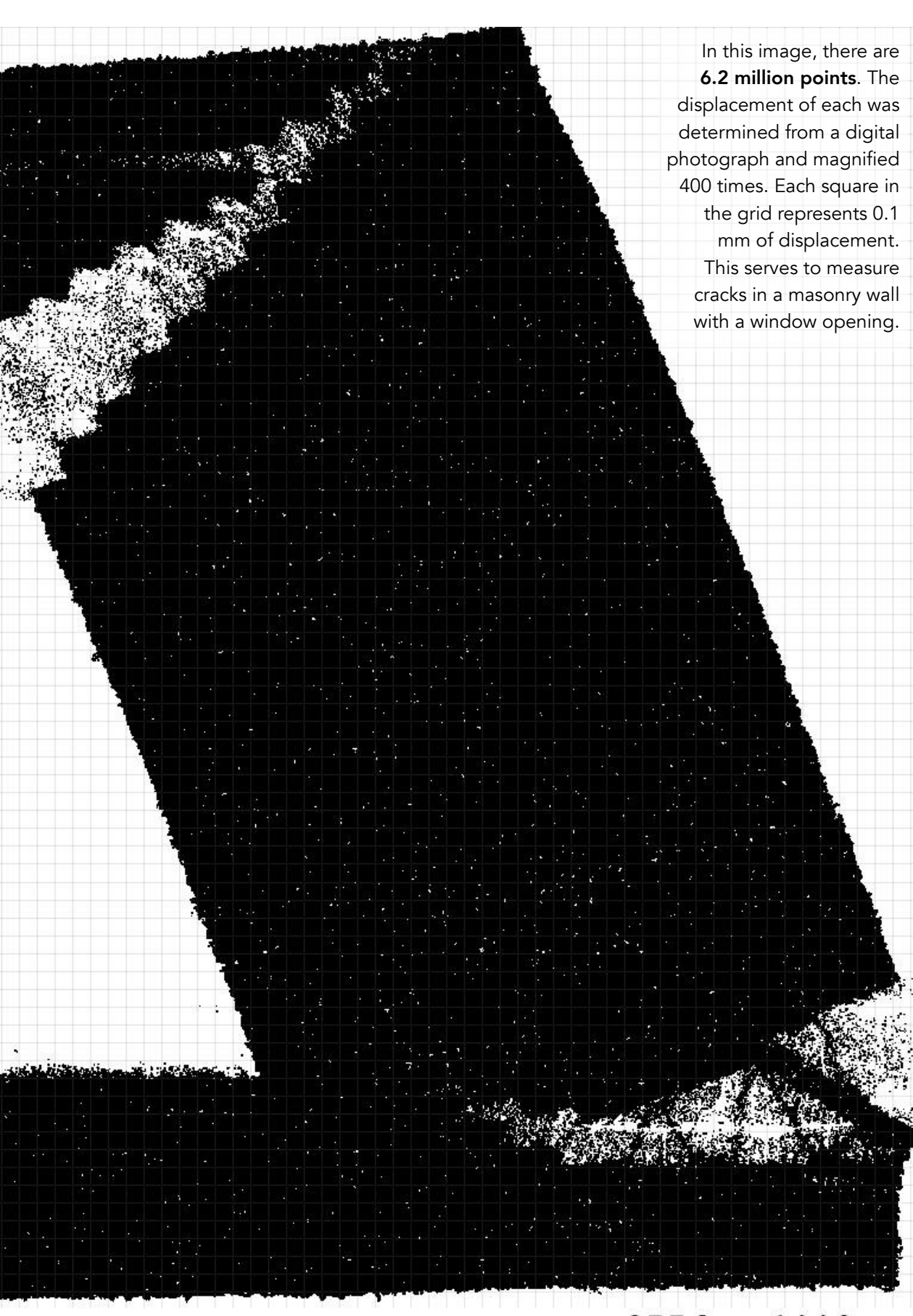
ISBN 978-94-6384-648-6

An electronic version of this dissertation is available at:

<http://repository.tudelft.nl/>

to my mother...





In this image, there are **6.2 million points**. The displacement of each was determined from a digital photograph and magnified 400 times. Each square in the grid represents 0.1 mm of displacement.

This serves to measure cracks in a masonry wall with a window opening.

Abstract

This book in one page

To quantify damage to unreinforced masonry structures, sensitive to tensile stresses and thus to vibrations caused by induced earthquakes in the north of the Netherlands, a bottom-up or physical approach has been followed. First, the crack-based damage expected on these common structures, was defined on a continuous scale (Ψ) based on width, length and number of cracks, so that it could also be quantified. Then, the initiation of cracks was investigated on full-scale masonry walls, single-wythe and of fired-clay bricks, using high resolution Digital Image Correlation; at 0.1 mm in width, cracks become visible. Further, the propagation of cracks, as they widen and lengthen, was monitored during repeated and cyclic testing. At repeated, identical in-plane drift, cracks still propagate and damage increases, though the increase is minor.

The experiments on walls and spandrels, displaying horizontal, diagonal, and vertical cracks, were used to calibrate numerical, finite-element-method models. These reproduced the behaviour of the tests also in terms of crack patterns and propagation, besides stiffness, strength, and hysteresis. Then, the models were adapted to explore the effect of earthquake vibrations, also in combination with existing damage caused by settlement-like actions. In this manner, the effect of initial damage could be quantified. Several other parameters were varied, such as the material strength, the geometry of the masonry walls, the soil properties in a soil-structure interaction interface, the record, PGV, and repetition of the vibrations, and the intensity of initial damage.

Relationships between these parameters and damage were captured into a surrogate model, which was used in a MonteCarlo simulation to determine the probability of damage. The fragility curves reveal, for instance, that fired-clay brick walls with no visible pre-damage ($\Psi_0=0$) have a 5% chance of visible damage ($\Psi \geq 1$) at a PGV of, for example, 10 mm/s, a probability that rose to 20% if the walls had undetectable pre-existing damage ($\Psi_0=0.5$). The probability of exceeding aesthetic damage ($\Psi \approx 2.5$) at this PGV is less than 1%. A lower PGV is associated with a smaller probability of damage.

Furthermore, it was concluded that repeated events lead to an increase in damage of about 10% for five similar events. This increase is not noticeable. In a sequence of events, similar events accumulate little damage and increases appear when larger events are experienced by a masonry structure.

Table of Contents

An extended table of contents is provided in the last pages of this work. In the digital version of this book, links help navigation.

Abstract	I
Table of Contents	II
Summary English	VII
Samenvatting Dutch	XXI
Chapter 1 Introduction	1
1.1. Relevance.....	2
1.2. State of the Art and Knowledge Gaps.....	4
1.3. Research Objective.....	8
1.4. Research Methodology.....	9
Chapter 2 Damage Metric for Masonry Cracking	13
2.1. Background and Introduction	15
2.2. The Ψ Damage Parameter.....	28
2.3. Utilisation: Examples of Application of Ψ	41
2.4. Discussion	47
2.5. Conclusions about Ψ , $\Delta\Psi$, Ψ_0	51
Chapter 3 Experiments to Characterise Cracks	53
3.1. Definition of Experiments to Investigate Light Damage.....	55
3.2. Results from Experiments on Walls and Spandrels.....	73

3.3. Crack-Based Drift Limits from Experimental Results.....	93
3.4. Conclusions: Experiments to Understand Crack Behaviour.....	105
Chapter 4	107
Damaging (Multi)Hazards and Modelling their Effects	
4.1. Hazards and Multi-hazards.....	109
4.2. Overview of Actions causing Damage to Masonry Buildings.....	113
4.3. Calibrating Crack Behaviour from Experiments into FEM Models	117
4.4. Modelling Damage: Shrinkage, Settlements, and Vibrations.....	139
4.5. Conclusions: Modelling and Calibration.....	147
Chapter 5	149
Fragility	
5.1. Introduction	150
5.2. Extrapolation to Non-Linear Dynamic Analyses	152
5.3. Regression of Damage Function from FEM Results.....	167
5.4. Fragility Curves for Seismic Vibrations.....	178
5.5. Fragility Curves for Settlements from Soil Curvatures	191
5.6. Conclusions: Probability of Damage and Aggravation.....	206
Chapter 6	209
Hastening: Damage Accumulation Function	
6.1. Analysis of Repetition Effect in Experiments	212
6.2. Damage Accumulation due to Repetition in FEM Models	218
6.3. Damage Accumulation Function (DAF)	229
6.4. Concept of Damage Hastening	248
Chapter 7	257
Conclusions and Outlook	
7.1. Answers and Conclusions	258
7.2. Relevance and Contributions.....	265
7.3. Limitations - Restrictions of the Scope	268

Summary	IV	Table of Contents
Chapter 1	7.4. Recommendations for Further Study	271
	7.5. Outlook.....	275
Chapter 2	List of Publications	277
	Bibliography	281
Chapter 3	Appendix A	i
	Overview of Related Work	
Chapter 4	Appendix B	xxix
	Ψ Damage Parameter	
Chapter 5	Appendix C	xxxv
	Supervised MSc Projects	
Chapter 6	Appendix D	xxxix
	Glossary	
Chapter 7	Appendix E	xliii
	Loppersum Visit	
Appendices	Appendix F	xlix
	Dataset	
Appendices	Appendix G	li
	Tool for Crack Tracking	
Appendices	Curriculum Vitæ	lxvii
	Propositions	lxix
Appendices	Acknowledgements	lxxi
	Extended Table of Contents	lxxvi

Appendices	Chapter 7	Chapter 6	Chapter 5	Chapter 4	Chapter 3	Chapter 2	Chapter 1	Summary
------------	-----------	-----------	-----------	-----------	-----------	-----------	-----------	---------

Summary

English

Unreinforced masonry is ubiquitous in the Netherlands. Much of both housing and historical infrastructure sport a variety of masonry patterns with units of fired-clay brick and lime-based or cementitious mortars. In modern housing, structural walls and outer veneers, typically forming a cavity wall, are masonry, with calcium-silicate units supporting reinforced concrete floors. Older buildings, with double-wythe walls, are even founded on plain masonry footings. Unreinforced masonry, however, with limited tensile strength, is susceptible to damage induced by vibrations. Moreover, soft soils and shallow footings combined, are likely to result in building settlements also leading to tensile stresses.

In the north of the Netherlands, gas extraction has led to induced seismicity and deep subsidence. These induced earthquakes in turn, have produced vibrations with the potential to damage buildings, especially those of unreinforced masonry, while subsidence could (indirectly) have lead to settlements. The earthquakes, considered light by international standards, have been occurring repeatedly since the early nineties. Towards the centre of the affected regions, peak-ground-velocities of 5 mm/s have been exceeded several times per year.

How much damage to masonry can be expected from a light earthquake vibration? And, do the repeated events lead to an accumulation of damage? Older structures have been subjected to other causes of damage over the years and might display pre-existing damage. Does this initial condition affect the earthquake-induced damage to be expected? From a probabilistic perspective, how far away from the epicentres is this vibration-induced damage unlikely?

Five Steps within a Physical Approach

This work strived to answer these questions in an objective manner. For that purpose, a physical approach was followed to investigate the effect of earthquakes on masonry. Such an approach comprises understanding the

processes that cause damage and the factors that affect it. In this work, it includes five steps: first, the objective definition of damage; second, the analysis of experiments to investigate the initiation and propagation of cracks in masonry; third, numerical models to replicate the cracking behaviour and (fourth) to evaluate the effects of the vibrations. Finally, the fifth step derives relationships between damage and parameters that affect its appearance and development; it includes the probabilistic aspects of damage (progression) and the effect of repetition.

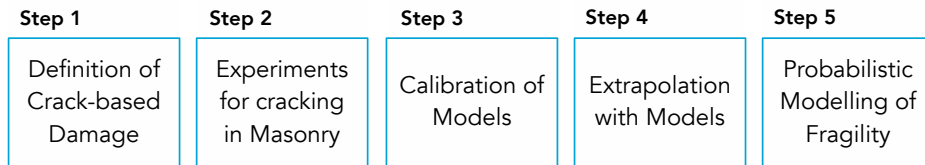


Figure 1.3. Steps in the methodology of this work.

Step 1: Define how to Measure Crack-Based Damage

First, it was paramount to define 'damage' in the relevant context of masonry and (light) earthquakes. When the tensile strength of masonry is exceeded, a fracture or crack will appear. As this crack widens, it becomes visible. A wide crack will upset the aesthetic quality of the masonry; it can also affect the perception of safety of the building's users and can compromise the watertightness of a structure leading to potentially more damage. Hence, to quantify damage, a measure was devised which included the width and length of the cracks and the number of cracks present.

This continuous damage parameter, called Ψ , was tuned against existing damage scales, the visibility of the damage, and its cost of repair. Unlike existing scales, the mathematical formulation for Ψ guarantees that evaluating damage leads objectively to the same value regardless of the inspector or measuring method. Moreover, a single number makes it easy to evaluate an increase in damage $\Delta\Psi$, or the effect of an initial condition, Ψ_0 . The thresholds set for Ψ mean that a value of $\Psi \geq 1$ represents visible damage (with a crack width of 0.1 mm) while an increase in damage of $\Delta\Psi \geq 0.2$ depicts a noticeable increase. Furthermore, the probability of damage, $p(\Psi \geq 1)$, or of noticeable increases in damage $p(\Delta\Psi \geq 0.2)$, for various thresholds, can be represented. This continuous scale becomes widely applicable to evaluate the effect of earthquake vibrations in existing masonry structures, laboratory experiments, and numerical models.

Step 2: Look at Cracking in Experiments with Masonry

The experiments to evaluate crack development focused on fired-clay brick masonry and consisted, in addition to companion tests to obtain the mechanical properties of masonry, of two types of tests: spandrels (1.5x0.5m) and walls (3x2.7m), both at full scale. Tests on calcium-silicate masonry were also conducted. To assess the initiation and propagation of cracks in these tests, two important aspects were developed. First, a testing protocol which would actually allow observing crack formation and crack development. Second, a measuring system which could detect and monitor the progression of cracks in brick masonry.

Protocols to trigger Light Damage

For the former, three protocols were formulated, two for the wall and one for the spandrels. The spandrel tests mimic a four-point bending test with counterweights located opposite to two hydraulic jacks. These allow for repetition, or one-way cyclic loading. Bending causes a vertical crack in the centre of most specimens. Consequently, the tests were controlled on the width at the mouth of this crack. The crack width was monotonically increased until about 2 millimetres when most specimens had failed. Failure, however, depended on the type of crack that formed. The notion of a vertical crack actually represents a toothed crack zigzagging through head and bed joints; opening of the head joints and sliding at the bed joints allows for a large deformation capacity. Based on these monotonic tests, a repetitive protocol was conceived. An initial step consisted of a crack width of 0.05 mm which was repeated several times, followed by steps with increments of 0.05 mm. The number of repetitions in each step was varied among tests to find a certain convergence. The force required to enforce a specific crack width decreased with each repetition and stabilised asymptotically after about 30 repetitions. Hence, most tests were conducted with a protocol of 3 steps, of 30 repetitions each, at 0.05, 0.1 and 0.15 mm followed by a monotonic increase until failure. This allowed to evaluate the propagation of the cracks and the degradation of the force.

For the walls, which were tested in-plane with an enforced horizontal drift, the protocols also applied a cyclic behaviour derived from a monotonic test. In this case, the first test was stopped when a crack of 0.1 mm was observed. The corresponding drift was then repeated in a one-way cyclic step with 30 repetitions. Subsequently, this drift was increased by 25% for the following step. Five steps, followed by at least six steps with a two-way cyclic drift, were enforced. The values of drift varied between 0.1‰ and 1‰. This was denoted as the light-damage protocol. The various cycles, enforced at identical

displacements, were viewed as several repeated earthquake records. A second loading protocol, called the asymmetric light damage protocol, consisted of cycles where the drift achieved in one direction was twice as large as in the other direction. This mimicked the fact that earthquake records are seldom symmetric. Walls, for which shear-based failure was expected, were tested with this protocol.

Photogrammetry to Capture Cracks

To observe cracks, a photogrammetry-based solution was employed. Digital image correlation (DIC) was improved by maximising the resolution at which displacements could be precisely measured. This consisted of a custom speckle pattern painted on the masonry with random shapes of 2-4 pixels spaced a similar distance and a high-resolution camera of 51 Mpx. A sharp lens, stopped down to f/8 and paired with a flash firing at 1/63000 of a second, produced crisp and high-contrast images. Additionally, a correlation algorithm was formulated, focused on determining the displacements of each virtual node individually. This allowed a more precise measurement of displacement discontinuities, or cracks, on the walls and spandrels, as traditionally, software is optimised to measure strains. The program developed could thus detect cracks on walls already at 0.02 mm in width and track their progression over the various steps and repetitions.

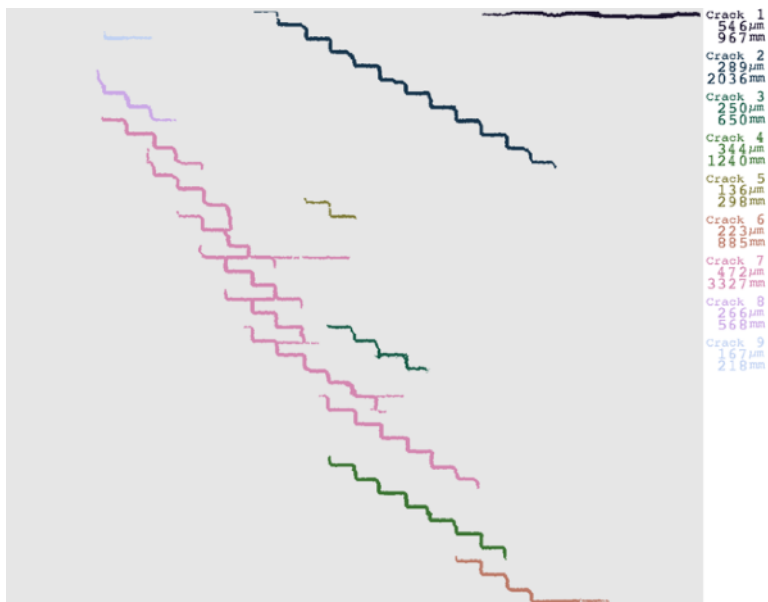


Figure I.1. Automatically identified cracks from the displacement field captured by DIC of a fired-clay brick wall without opening. $\psi=2.1$. Most cracks follow the bed and head joints of the masonry.

Drift Limits for Light Damage

Results interpreted from the masonry wall experiments relate crack metrics from DIC to in-plane wall drift at each measurement instance. High correlations were identified between drift and damage, alongside influences from other relevant parameters in the experiments such as wall type, material, boundary conditions, and test progression.

Repeated drift instances led to slightly increased damage. Cantilever-bound walls tolerated more drift before similar crack damage compared to double-clamped ones. Shear walls and calcium-silicate (CaSi) walls exhibited more damage than walls with openings and fired-clay brick walls, respectively. Simplified models showed CaSi's upper drift limit for light damage was 40% lower than fired-clay's 0.5%. Noticeable light damage begins at 0.5‰ and 0.6‰ drift for CaSi and clay, with corresponding crack widths of 1 mm. These thresholds help in designing for limited significant damage. For older or repeatedly loaded structures and shear walls, a 10% reduced drift value is recommended.

Cracks Propagate from Corners

It was observed that cracks mostly initiate from the corners of openings or at the lateral edges of walls. In the case of walls without openings, body cracks may also manifest. Most observed cracks were either horizontal or step-wise diagonal, coalescing into a single crack from being spread over multiple joints initially. The experiments show how the width and length of cracks grow simultaneously, with a notable observation that cracks appear (in DIC) even before they become visible to the eye, suggesting the presence of 'invisible' cracks that could potentially propagate if conditions vary. Different types of cracks, whether horizontal, diagonal, vertical, tapered, or uniform, exhibit similar aggravation under increased loading. Some invisible cracks unload as other cracks appear and ultimately never become visible.

Calcium-silicate brick masonry seems more brittle than fired-clay brick, especially when looking at vertical cracks developing in the spandrels. In this case, the cracks, which zigzag around head and bed joints of fired-bricks, split the calcium-silicate units vertically.

Repetition affects Propagation

Moreover, repetition affects crack propagation, where identical loading conditions lead to measurable but consistent increases in crack width and length. Also, the force required to obtain identical drifts would degrade by about 10% between the first and the last repetition of a step.

Step 3: Calibrate Models to Experiments

In collaboration with other authors, computational models were developed to reproduce the behaviour observed in the experiments. In contrast to typical calibration strategies that focus on reproducing the stiffness, strength and ultimate capacity of the specimens, the objective was to include crack patterns and propagation. Finite-element-method models with plane-stress elements using the Engineering Masonry Model in Diana FEA, were successful in replicating the experimental behaviour once the material parameters were tuned. Parameters such as the Young's moduli, tensile strength and fracture energy were highlighted as most influential in guaranteeing a successful calibration.

The EMM is orthotropic and includes both horizontal and vertical tensile softening, with shear softening, too. In addition, unloading is secant for tension, while elastic for shear. The crack orientations are pre-fixed, unlike a rotating total strain model. These characteristics make it ideally suited to model masonry which consists of units, bed- and head-joints in a homogenised model. Other issues like mesh objectivity and convergence were explored.

While the wall models were sufficiently accurate, computational constraints made it difficult to model as many cycles as were tested experimentally. Instead, only three cycles in every step were included. This was enough to observe some degradation as seen experimentally and the effect stabilised after three cycles. In future studies, the material model could be further refined to include the cyclic degradation observed.

Moreover, micro-models, where the bricks and mortar joints are modelled independently, were also considered. These produced more accurate results in terms of crack patterns, but were computationally expensive. Ultimately, for the large number of models required, the continuum model using the EEM, was selected.

Step 4: Extrapolate Models to Initial Condition + Seismic Vibrations

The boundary of the models that include accurate crack initiation and propagation behaviour, validated against the experiments on masonry walls and spandrels, are adjusted to analyse the effect of settlements and of earthquake vibrations. These are the extrapolated models. At the top of the model of the walls, a mass representing the dynamic effect of the floor and roof, is attached. At the bottom of the model, an interface to account for the soil-structure interaction at the foundation is included. Finally, at the walls' sides, vertical springs are positioned to consider the influence of the walls transversal to the main wall studied. As a first load, a vertical displacement is

applied at the bottom of the interface representing a loss of support consistent with a settlement shape. This causes the wall to settle and develop cracks compatible with those found in buildings affected by settlement damage. The intensity of the settlement is adjusted so as to generate various initial values of Ψ , denoted as Ψ_0 ; a case without settlement damage, $\Psi_0=0$, is also contemplated. As second load, an acceleration time history is applied at the bottom of the wall after locking the tangential stiffness of the soil-interface.

Record-to-record Variability

Multiple acceleration signals were investigated. Two correspond to the earthquake of Zeerijp of 2018 and two were recorded during the earthquake of Westerwijrtwerd in 2019. One record of each event was registered nearby the epicentre ($\approx 3\text{km}$) and the other farther away ($\approx 8\text{km}$). The goal was to investigate the influence of near and far events which differ in their frequency content, effective cycles and relationship between horizontal and vertical components. Additionally, the records were scaled to various levels of PGV varying from 2 mm/s until 100 mm/s. Also, identical records were repeated in the same analysis to investigate the influence of repeated events.

Many Variations in Parameters

The parameters related to initial damage Ψ_0 and to the earthquake load applied (PGV, repetition, record type) were not the only ones varied to investigate their relationship to damage. Two geometries for the wall were analysed, one with an opening for a window and one without. Similarly, two soil types, reflected in the soil-structure interface, were observed. Additionally, three sets of material parameters were included. These correspond to a weak masonry, standard, and strong masonry and vary the Young's moduli, tensile and shear strengths and fracture energies.

Relationship between Parameters and Damage

Key observations about the influence on damage by each of these parameters based on thousands of the extrapolated wall models is described next:

For the two **wall geometries**, flexible walls, referred to as façade A with a window opening, typically sustain more damage compared to the more rigid façade B, especially under near-type earthquake conditions. This is attributed to the flexible wall's vulnerability to stress concentrations at window corners, which facilitate the initiation of cracks.

Soil type also plays a pivotal role in the extent of damage a structure undergoes during an earthquake. Buildings on softer soil (type B) require larger deformations to reach the same level of damage as those on stiffer soil (type

A). This difference is due to the stiffer soil causing sharper wall curvatures and higher stress levels, resulting in more concentrated and severe damage.

The **distance** to the earthquake's epicentre to the structure significantly influences damage outcomes as well. Near-field motions tend to propagate existing cracks, while far-field motions primarily widen them, which makes damage more visible. This difference is particularly notable between the two wall types under similar seismic conditions, highlighting the nuanced interactions between structural features and earthquake dynamics.

Additionally, the **initial state of damage**, or pre-damage, within a structure before an earthquake critically affects the severity of damage from subsequent seismic events. Structures with higher levels of pre-damage tend to show more significant overall damage after an earthquake, although the incremental damage decreases with increased pre-damage levels.

Material properties of the façade also influence the damage patterns. Weaker materials are less capable of resisting tensile and shear stresses, resulting in more extensive damage under identical seismic conditions compared to stronger materials. This is evident in the varied crack patterns and damage distributions observed across different material configurations.

The aggravating effect of **multiple earthquakes** is another important factor. Structures subjected to repeated seismic events show progressively higher damage levels, though the rate of increase is relatively modest with each additional event. This finding underscores the importance of considering the repetition of earthquakes when assessing structural resilience.

Lastly, the **intensity of the earthquake**, measured by PGV, directly correlates with the degree of damage. Higher PGVs consistently result in more severe damage, demonstrating a clear relationship between earthquake intensity and structural impact. While this relationship was expected, it has now been quantified.

Capturing these Relationships into a Model

The influence of each parameter can be captured in a surrogate model. Two types of models were explored. First, a 'reasoned' model where the observed trends are coded into specific functions such as power laws or logistic relationships. Then, a fitting procedure is used to obtain the coefficients in the functions. Second, a supervised machine learning model was trained on the data. The best-performing machine learning model was a neural network. However, the machine learning models were found to generalise poorly and failed to capture physical relationships. The reasoned model, which enforces

such relationships, like higher damage for higher PGV, was ultimately selected as the surrogate model to use for the next step. An uncertainty parameter was included to account for the model error and for other uncertainties in the FE modelling strategy.

Step 5: Assign Distributions to the Parameters and Determine the Probability of Damage

The various parameters listed can be represented with a probabilistic distribution. For example, experiments on the tensile strength of masonry, one of the most influential parameters in the calibration of the models, show that it is normally distributed with a deviation of 30%. For the models, the same distribution is assigned. The distance to the epicentre is correlated to the PGV; higher PGVs are more likely to originate from a nearby epicentre. The soil type followed a uniform distributions according to statistics about the soils found in the Groningen region. In this manner, all the parameters except PGV and Ψ_0 , which were independently assessed, could be sampled from distributions.

Then, using the surrogate model, a Monte Carlo simulation was run. For a given PGV and initial damage, the probability of exceeding certain values of Ψ were computed. These fragility curves reveal for instance that fired-clay brick walls with no visible pre-damage ($\Psi_0=0$) had a 5% chance of light damage ($\Psi \geq 1$) at a PGV of 10 mm/s, a probability that rose to 20% if the walls had undetectable pre-existing damage ($\Psi_0=0.5$); at a lower PGV, the probability of damage is also lower.

Fragility Curves can become Maps

The fragility curves can be convoluted with a distribution of PGV for any given location resulting in a probability of damage for a given event. Moreover, if at a specific location the maximum PGV from various events is determined, one can obtain the maximum probability of damage for masonry buildings at that location. This is put together into a map, depicted in Figure 5.4.5. In this case, an initial damage of $\Psi_0=1$ is assumed, corresponding to just visible cracks of 0.1mm; and, an increase in damage of $\Delta\Psi=0.5$, representing a noticeable increase in damage, is considered. The map shows that for a relatively large region in the north of the buffer zone of the Groningen gas field, the probability of this noticeable increase in light damage is 1 in 100 (or 1%). The entirety of the buffer zone, six kilometres from the edges of the gas fields, and a large portion outside it, is subjected to a probability of 1%. This is a very small probability when discussing cracks pertaining to light damage. If ten thousand buildings are considered, 10 buildings would be expected ($p=50\%$) to show this damage aggravation of $\Delta\Psi=0.5$. The probability of exceeding

Damage State 1 ($\Psi > 2.5$), however, is about 0.1‰ for the entirety of the buffer zone.

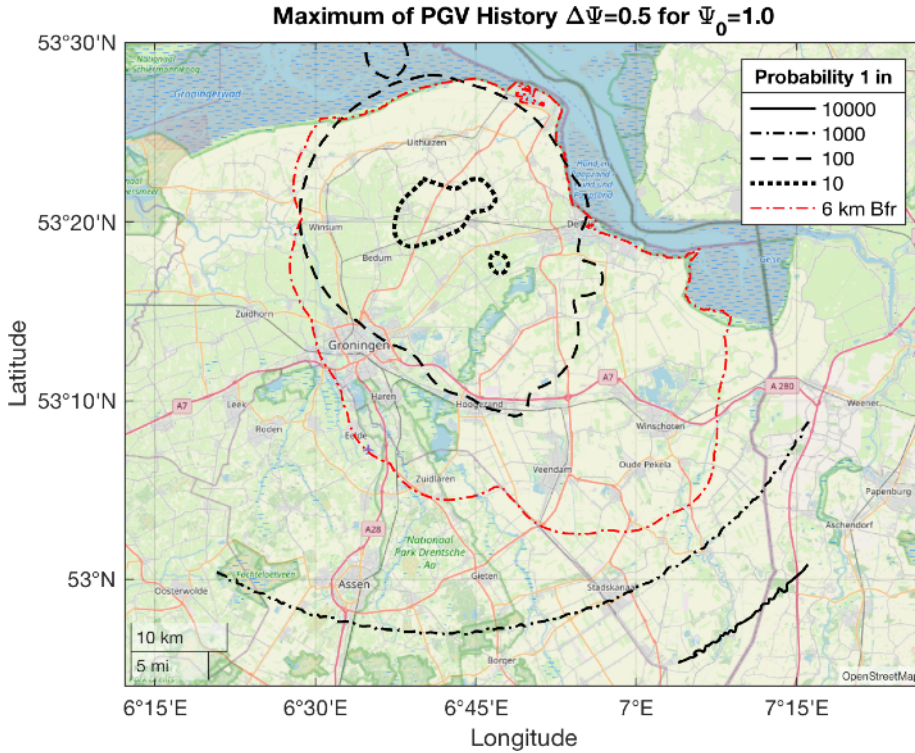


Figure 5.4.5. Probability map for the historical maximum PGV convoluted with masonry wall fragility. The case of a $\Delta\Psi$ of 0.5 for an initial condition of just visible damage is exemplified. See "Limitations" for the applicability of this map. The contours are constrained by the domain of the model.

The Effect of Repetition in the Experiments

The experiments were conducted with repeated, identical cycles. It was observed that repeated displacements lead to a reduction in the force required to achieve the same displacement, a phenomenon termed "force degradation". This was observed both in walls and spandrels. It was found that after about thirty repetitions, the amount of force degradation stabilised. Different testing protocols, including one-way and two-way cyclic displacements, showed that the effect of force degradation was consistent, especially after thirty repetitions. If a direction was damaged before, negligible degradation occurred when testing that displacement again. The findings suggest that both the magnitude and direction of the load affect the degradation behaviour. Moreover, along with force degradation, repeated displacements also caused observable increases in damage, notably in the

form of crack propagation. This indicates that not only does the force required to move the walls and spandrels decrease, but also that cracks grow in width and length with each repetition.

The Effect of Repetition in the Models

The FE models were also subjected to repeated records. In most cases, records with identical PGVs were applied (homogeneous sequences); in other cases, a heterogeneous sequence was evaluated. The assessment of Ψ from these time-history analyses revealed that repeated events do lead to an accumulation in damage, albeit in small quantities. Moreover, vibrations of lower intensity than previous vibrations increase damage negligibly, while vibrations of similar or larger intensity than previous vibrations may increase damage by 10%, though this is dependent on the intensity of the vibrations and the number of repetitions. For a second vibration of 10 mm/s for example, damage is expected to increase by 6%. The limited number of models and variations, and lack of comparison field data, should be further expanded to validate these model-based observations.

Damage Accumulation Function (DAF)

The observations drawn from experiments and models evaluating repetition were incorporated into a function to evaluate any sequence of PGV so as is expected from a real history of earthquake events. The DAF was built on top of the surrogate model to predict Ψ . In this manner, the DAF outputs a probabilistic distribution for Ψ for every PGV in the sequence and computes the final damage aggravation for an initial Ψ_0 . The function uses two components, one for events with a similar PGV as previous events, and another for events with a PGV that is larger than earlier events. The latter leads to a larger increase in damage. The DAF was then validated against the model results and the experimental observations. Ultimately, the DAF is used to determine the expected damage and its probability for masonry buildings in the region of Groningen subjected to decades of repeated earthquakes.

Using the DAF in contrast to Single Fragility Curves

To evaluate the contribution of considering the accumulation of damage with the DAF, a comparison is drawn against the maps produced with the maximum PGV. First, the shape of the contours from a single event is mostly circular as the propagation in the Ground Motion Prediction Equations (GMPEs) depends on the distance to the epicentre. For the DAF, multiple events are considered with their own epicentres which leads to an irregular shape. Second, the outer probability contours from the single event encircle slightly smaller regions. This

means that considering the accumulated effect of multiple events leads to higher probabilities. Third, the contours towards the centre of the region are much larger for the DAF case. This is because of the larger number of events and the fact that their epicentres are spread out thus modifying the shape of the contours.

For a specific location, the DAF can lead to a significant influence. This is the case for places close to the centre of the Groningen region but relatively far from the specific event of Huizinge (largest recorded magnitude). In Delfzijl, for instance, the probability of displaying visible damage is less than 1% in the case of Huizinge, but considering the entire history of events, this probability rises to 10%. However, the probability of exceeding $\Psi \geq 2.5$ is virtually unaffected regardless of the initial damage condition. For this case, the single, large event plays a more important role than the accumulated effect of multiple smaller events. The repeated smaller events, regardless of how many are accumulated, don't have the capacity to cause a structure to exceed light damage ($\Psi \geq 2.5$).

Contributions in Comparison to Literature

In comparison to literature, this bottom-up approach presents several contributions. Three types of reference studies can be identified: First, empirical analyses, which have difficulty isolating the origin of the reported damage and thus cannot draw quantitative conclusions about the effects of earthquake or repetition. Second, extrapolative curves, which, on the basis of ULS or a pushover curve, infer the behaviour or limits for light damage. These cannot express clear limits for visible damage or its propagation. Nonetheless, many of these fragility curves fall within the thresholds established in this work. Third, studies which do look at crack formation but where damage is insufficiently quantified; these rarely take the step to calibrate models and employ them to investigate the effect of earthquakes. In this context, the present work adds upon these shortages.

Concluding Remarks

Indeed, this project was embarked on to quantify the probability of light damage to masonry structures due to repeated seismic vibrations while considering an initial damage condition. The methodology proposed, considering experiments to validate numerical models, and models to assess the influence of the loads on crack-based damage, has been successful in providing an approach with which to quantify damage.

Additionally, important observations have been made about the effect of earthquakes. For example, repeated events will increase damage by about

10% depending on the intensity of the PGV. Moreover, existing damage will be aggravated, though for the majority of events, PGVs larger than 10 mm/s are usually required to produce a noticeable increase in damage. In general, most fired-clay brick masonry structures in the epicentre of the Groningen seismic region will have developed visible damage, with cracks of at least 0.1 mm in width, over the period of 2000-2020. For the rest of the buffer zone of the gas field, the probability of such damage is at least 1%; however, if some initial, yet invisible, damage was present, this probability increases ten fold. Only a compact area reaches a small probability of 1% of exceeding serviceability damage with DS1, even if the structures begun with visible initial damage.

Limitations

While the methodology comprised experiments and models, a third aspect should be added: that of monitoring. The findings should be validated against field data. However, reliable monitoring over such an extensive time frame is difficult and expensive and cannot guarantee that all intertwined damage causes are disentangled. Other alternatives should be contemplated to validate these results in the future.

Other limitations of the approach must also be highlighted. First, walls are used as proxy for masonry buildings. The effect of 3D buildings and more complex façades must still be further studied; preliminary results show good agreement. Secondly, damage is considered for in-plane effects and single-wythe walls. Out-of-plane effects are predicted to be less relevant for light damage, but the progression of cracks in double-wythe walls could be different. Thirdly, the conclusions presented here are valid for fired-clay brick masonry. Other materials will behave differently. Calcium-silicate brick has also been explored in experiments but its fragility is yet to be thoroughly evaluated. Fourthly, the quasi-static experiments have been used to validate models extrapolated to dynamic loading. Additional experiments with dynamic loading should be studied barring the increased complexity of loading, boundaries and crack monitoring possibilities during dynamic testing. Finally, the degradation observed at the masonry material level is not fully represented in the current numerical models; a cyclic degradation effect for the EMM would make these models more accurate.

Outlook: Relevance of Light Damage in the Future

Understanding light damage will become even more relevant in the future as climate change leads to more extreme weather events, to changes in the soil and new energy requirements like geothermal energy.

Extreme weather events like stronger storms, droughts, heavy rainfall, and heatwaves can cause structural damages—from roof and wall damages to soil-induced settlements. Additionally, the risk of floods and necessary underground interventions for climate mitigation, such as carbon storage, pose new challenges to building resilience.

The shift from fossil fuels to renewables affects buildings, too. Geothermal drilling and underground energy storage may induce subsidence similar to (gas) mining. Also, as homeowners adopt new energy technologies and retrofit buildings, the structural integrity could be compromised if not managed properly, leading to damage.

In the Netherlands, poor communication and late policy implementation on the effects of gas extraction-induced seismicity led to a strong public backlash and risk aversion. The perceived risks, although minor, are magnified by uncertainty and lack of clear policies, similar to the opposition seen with nuclear energy.

The future requires building a society that accepts and manages these risks effectively. With climate change posing increased threats, clear policies are necessary to ensure fair and proactive handling of building-related issues and other climate-related risks. This is only possible with a clear understanding of the relationship between hazards and damage.

Samenvatting

Dutch

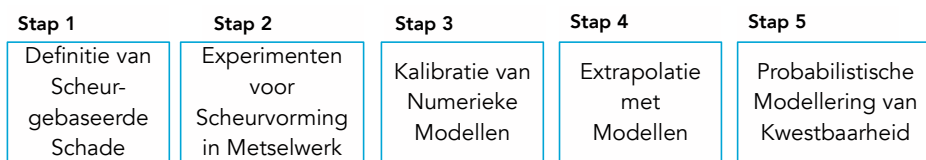
In Nederland en wereldwijd komt ongewapend metselwerk veelvuldig voor, zowel in woonhuizen als in historische bouwwerken. Deze constructies bestaan uit baksteen verbonden door kalkhoudende of cement-mortels in een verscheidenheid aan metselwerkverbanden. Moderne woningen zijn vaak uitgerust met dragende muren en gevelbekledingen die samen een spouwmuur vormen. Dragende muren bestaan vaak uit kalkzandsteen-metselwerk op betonnen funderingen en ondersteunen gewapende betonnen vloeren. Oudere gebouwen hebben vaak steensmuren op metselwerk-funderingen. Ongewapend metselwerk, met beperkte treksterkte, blijkt bijzonder gevoelig voor schade veroorzaakt door trillingen. Daarnaast zijn de zachte bodem en de ondiepe funderingen op staal, gevoelig voor ongelijkmatige zetting die op hun beurt trek- en buigspanningen en daarmee schade veroorzaken in het metselwerk.

Sinds begin jaren negentig heeft de gaswinning in het noorden van Nederland geleid tot geïnduceerde seismiteit en significante bodemdalingen. Deze door menselijke activiteit veroorzaakte aardbevingen, met vanuit internationaal perspectief relatief beperkte intensiteit, veroorzaken trillingen die potentieel schadelijk zijn voor gebouwen, vooral voor die van ongewapend metselwerk. In het centrum van de getroffen regio's zijn piek grondsnelheden (PGV) van 5 mm/s meerdere keren per jaar overschreden.

Dit roept belangrijke vragen op: Hoeveel schade aan metselwerk door een lichte aardbeving kan men verwachten? En leiden herhaalde trillingen tot een cumulatie van schade? Vooral oudere constructies die mogelijk al schade hebben opgelopen door andere oorzaken, kunnen vatbaarder zijn voor nieuwe schade. Hoe beïnvloedt een initieel, reeds aanwezige voorschade de verdere schade die door aardbevingen wordt veroorzaakt? Daarnaast is het vanuit een probabilistisch perspectief ook belangrijk om te bepalen op welke afstand deze door trillingen geïnduceerde schade onwaarschijnlijk wordt.

Vijf Stappen binnen een Fysisch-Gebaseerde Aanpak

Dit onderzoek heeft als doel gesteld om op een objectieve manier de effecten van aardbevingen op metselwerk te evalueren. Daartoe is een systematische fysisch gebaseerde aanpak gehanteerd die zowel de processen die schade veroorzaken als de beïnvloedende factoren meeneemt. Deze aanpak bestaat uit vijf gedetailleerde stappen. Ten eerste, het is essentieel om te beginnen met een heldere en objectieve definitie van het begrip schade binnen de context van metselwerk en lichte aardbevingen. Wanneer de treksterkte van metselwerk wordt overschreden, leidt dit tot het ontstaan van scheuren. Deze scheuren worden wijder en langer en daarmee zichtbaarder naarmate de schade toeneemt, wat de esthetische kwaliteit en constructieve integriteit van het metselwerk kan aantasten. De tweede stap omvat het onderzoeken van de initiatie en de voortplanting van scheuren in metselwerk door middel van gecontroleerde laboratorium experimenten. Het doel is om een diepgaand inzicht te krijgen in hoe scheuren ontstaan en zich uitbreiden in verschillende proefstukken onder verschillende belastingsomstandigheden. Deze proeven valideren numerieke modellen die het mogelijk maken om het gedrag van scheuren na te bootsen en te analyseren hoe trillingen invloed hebben op metselwerk. Deze modellen helpen bij het voorspellen van schade onder variërende omstandigheden die in de praktijk kunnen voorkomen. In de vierde stap worden de numerieke modellen gebruikt om de effecten van trillingen veroorzaakt door aardbevingen op het metselwerk te evalueren. Dit helpt bij het vaststellen van de kwetsbaarheid van metselwerk-gebouwen onder seismische belasting. De laatste stap leidt tot het vaststellen van relaties tussen de waargenomen schade en verschillende invloedsfactoren. Deze stap omvat ook het onderzoeken van probabilistische aspecten van schadevoortgang inclusief het effect van herhaalde aardbevingen en de cumulatie van bevingen met voorschade.



Figuur 1.3. Stappen in de methodologie van dit werk.

Stap 1: Definitie van Scheur-gebaseerde Schadeschaal

Bij het beoordelen van de impact van lichte aardbevingen op metselwerk is een nauwkeurige definitie van 'schade' cruciaal. Scheuren ontstaat wanneer de treksterkte overschreden wordt, resulterend in de vorming van schade.

Naarmate deze scheuren wijder worden, worden ze zichtbaar en beginnen ze invloed uit te oefenen op zowel de esthetische kwaliteit als de constructieve samenhang van het gebouw. Wijde scheuren kunnen de veiligheidsperceptie van gebruikers ondermijnen en de waterdichtheid van de constructie aantasten, wat leidt tot verdere schade.

Om schade kwantitatief te beoordelen, is een continue schadeparameter ontwikkeld, aangeduid als Ψ . Deze parameter representeert het aantal scheuren, de breedte en de lengte ervan in één getal. De parameter is afgestemd op bestaande schadeschalen en neemt zichtbaarheid van de schade en reparatiekosten in overweging. In tegenstelling tot andere schadeschalen, zorgt de wiskundige formulering van Ψ voor een objectieve schadebeoordeling die consistent is ongeacht de inspecteur of meetmethode. Ψ maakt het mogelijk om zowel de aanwezige schade als de verandering of verergering van schade ($\Delta\Psi$) ten opzichte van een initiële schade (Ψ_0) te kwantificeren. De drempelwaarden zijn ingesteld zodat een Ψ -waarde van $\Psi \geq 1$ net voor het blote oog zichtbare schade vertegenwoordigt (scheurbreedte van 0,1 mm) als drempel geldt. Een verergering van schade met een waarde van $\Delta\Psi \geq 0,2$ duidt op een waarneembare toename. Daarnaast kan de kans op schade, $p(\Psi \geq 1)$, voor verschillende drempels worden berekend. Deze schaal aanpak maakt het mogelijk om de effecten van belastingen zoals trillingen en zettingen op metselwerk in bestaande gebouwen, laboratoriumexperimenten en numerieke modellen systematisch te evalueren.

Stap 2: Blik op Scheurvorming in Experimenten op Metselwerk

Deze stap van het onderzoek richtte zich op het evalueren van scheurvorming in baksteenmetselwerk door middel van experimenten. Deze experimenten omvatten twee hoofdtypen: buigproeven op borstweringen (spandrels), met een afmeting van 1,5 bij 0,5 meter, en schuifproeven op wanden van 3 bij 2,7 meter. Daarnaast werden begeleidende proeven op kleinere monsters uitgevoerd om de mechanische eigenschappen van het metselwerk vast te stellen. Om de initiatie en voortplanting van scheuren effectief te kunnen beoordelen, zijn twee cruciale aspecten ontwikkeld binnen het experimentele protocol:

Ten eerste, het testprotocol is specifiek ontworpen om de observatie van zowel de initiële scheurvorming als de verdere ontwikkeling van deze scheuren te faciliteren. Dit protocol speelt een essentiële rol in het nauwkeurig documenteren van hoe scheuren ontstaan en hoe ze zich uitbreiden onder verschillende belastingen. Ten tweede, een geavanceerd meetsysteem werd ingezet om de progressie van scheuren in het baksteenmetselwerk te

detecteren en te monitoren. Dit systeem stelt onderzoekers in staat om nauwkeurige en continue data te verzamelen over het verloop van de scheurvorming in de tijd, wat cruciaal is voor het analyseren van de respons van het metselwerk op seismische belastingen. Deze gecombineerde benadering van zowel een gestructureerd testprotocol als een geavanceerd meetsysteem zorgt ervoor dat de experimentele analyse van scheurvorming in metselwerk gedetailleerd en betrouwbaar is.

Protocollen om Lichte Schade te Genereren

De methodiek om lichte schade in metselwerk te genereren voor dit onderzoek bestond uit het toepassen van diverse specifiek ontworpen protocollen voor zowel de wanden als de borstweringen.

Borstweringen werden onderworpen aan een vierpunts buigproef met behulp van contragewichten en twee hydraulische krikken om eenzijdige cyclische belasting te realiseren. Deze configuratie induceerde verticale scheuren in het midden van de meeste proefstukken, waarbij tijdens de test het verloop in scheurwijdte nauwkeurig werd gevolgd. De wijdte aan de mond van de scheur werd geleidelijk verhoogd tot ongeveer 2 millimeter, het punt waarop de meeste proefstukken faalden. Dit falen was afhankelijk van de verbindingvorm van de scheur die meestal vertand- en zigzaggend door stoot- en lintvoegen liep, en soms diagonal getrapt. Dit resulteerde in aanzienlijke vervormingscapaciteit door het openen van de stootvoegen en het afschuiven langs de lintvoegen. Op basis van deze initiële proeven werd een repeterend testprotocol ontwikkeld waarbij een initiële scheurwijdte van 0,05 mm meerdere keren werd herhaald, met incrementele stappen van 0,05 mm. Het aantal herhalingen per stap varieerde om een bepaalde convergentie in de resultaten te bereiken. De benodigde kracht om een specifieke scheurwijdte te induceren nam af bij elke herhaling en stabiliseerde na ongeveer 30 cycli. De meeste tests volgden een drie-staps protocol van 30 herhalingen bij 0,05, 0,1 en 0,15 mm, gevolgd door een continue toename tot falen, waardoor de voortplanting van scheuren en degradatie van de krachtcapaciteit kon worden beoordeeld.

De muren werden vertical voorbelast en vervolgens in het vlak getest met een opgelegde horizontale verplaatsing. Hier werden protocollen toegepast waarbij het cyclisch deel werd bepaald na een monotone aanloophase. De aanloop-test werd gestopt zodra een scheur van 0,1 mm werd waargenomen, waarna de bijbehorende verplaatsing cyclisch werd herhaald met 30 herhalingen. Deze 'drift' (de verhouding tussen de horizontale verplaatsing en de wandhoogte) werd vervolgens met 25% verhoogd voor de volgende

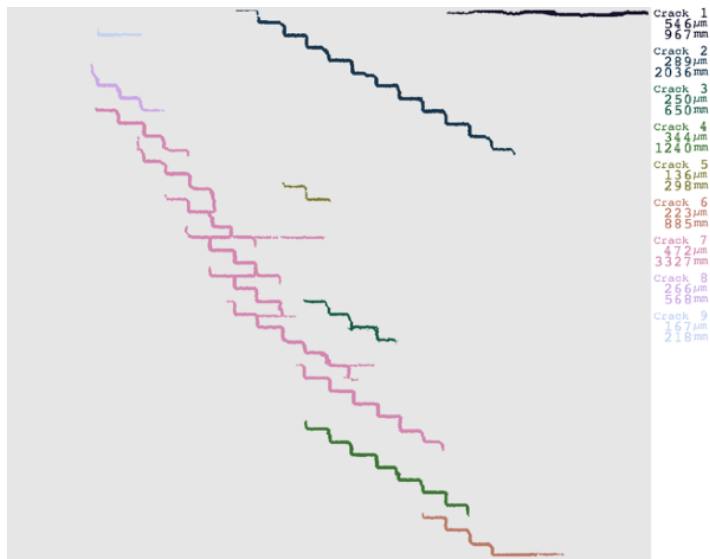
stappen. In totaal werden vijf stappen gevolgd door ten minste zes stappen van tweezijdige cyclische drift toegepast, met driftwaarden variërend tussen 0,1‰ en 1‰, aangeduid als het lichte-schadeprotocol. Deze cycli, consistent toegepast bij identieke verplaatsingen, simuleerden herhaalde aardbevingen. Een alternatief belastingsprotocol, het asymmetrische lichte-schadeprotocol, bestond uit cycli waarbij de drift in één richting dubbel zo groot was als in de andere, wat de asymmetrie in daadwerkelijke aardbevingen nabootste. Muren die naar verwachting zouden bezwijken op afschuiving werden getest volgens dit protocol.

Fotogrammetrie om Scheuren Vast-te-leggen

Voor het observeren en vastleggen van scheuren in metselwerk werd in dit onderzoek gebruik gemaakt van een geavanceerde fotogrammetrische techniek genaamd Digital Image Correlation (DIC). Deze methode is geoptimaliseerd om de resolutie te maximaliseren en verplaatsingen met hoge nauwkeurigheid te meten. Het proces begon met het aanbrengen van een speciaal ontworpen spikkelpatroon op het metselwerk. Dit patroon bestond uit willekeurige vormen van 2 tot 4 pixels groot, die op gelijke afstanden van elkaar werden geschilderd.

Voor de opname van beelden werd gebruik gemaakt van een camera met een hoge resolutie van 51 megapixels. Een scherpe lens, ingesteld op een diafragma van $f/8$, in combinatie met een flitser die afgaat op $1/63000$ van een seconde, zorgde voor scherpe en contrastrijke beelden die essentieel zijn voor nauwkeurige beeldanalyse.

Verder werd een specifiek correlatiealgoritme ontwikkeld, gericht op het nauwkeurig bepalen van de verplaatsingen van elk virtueel knooppunt op de beelden. Dit algoritme stelde de onderzoekers in staat om met grote precisie de discontinuïteiten in verplaatsing, oftewel de scheuren, te detecteren en te analyseren. In tegenstelling tot traditionele software, die voornamelijk is geoptimaliseerd voor het meten van vervormingen, kon het ontwikkelde programma scheuren detecteren bij een minimale breedte van 0,02 mm. Het vermogen om deze fijne scheuren en hun voortgang gedurende verschillende teststappen en herhalingen te volgen, biedt een ongekend inzicht in de dynamiek en het verloop van scheurontwikkeling in metselwerk onder cyclische belasting.



Figuur 1.1. Automatisch geïdentificeerde scheuren uit het verplaatsingsveld vastgelegd door DIC van een bakstenen wand zonder opening. $\Psi=2.1$. De meeste scheuren volgen de voegen van het metselwerk.

Drift-limieten voor Lichte Schade

De analyse van de experimentele resultaten voor metselwerkmuren heeft significante inzichten opgeleverd over de relatie tussen verplaatsing in het vlak van de wand en de ontwikkeling van scheuren, zoals gemeten via DIC. Er is een sterke correlatie vastgesteld tussen de mate van drift en de omvang van schade, naast de invloeden van andere relevante parameters zoals het type wand, het gebruikte materiaal, de randvoorwaarden en de voortgang van de test.

Uit de resultaten blijkt dat herhaalde verplaatsing leidt tot een lichte toename van schade. Dragende muren die alleen aan de onderzijde waren ingeklemd (cantilever) vertoonden een hogere tolerantie voor drift voordat vergelijkbare schade optrad, in vergelijking met muren die zowel onder als boven waren ingeklemd. Verder bleek dat massieve wanden gevoeliger waren voor schade dan muren met openingen of traditionele bakstenen muren.

De experimenten hebben geleid tot het vaststellen van specifieke driftgrenzen waarbij lichte schade begint op te treden. Voor kalkzandsteen muren ligt de bovengrens 40% lager dan de grens van 0,5% die voor baksteen is vastgesteld. Concreet begint waarneembare lichte schade bij een drift van 0,5‰ voor baksteen en 0,6‰ voor CaSi, waarbij de scheurwijdte van 1mm wordt bereikt. Deze vastgestelde limieten zijn essentieel voor het ontwerpen van wanden waarvoor slechts beperkte significante schade wordt geaccepteerd.

Voor oudere constructies die herhaaldelijk aan belasting zijn blootgesteld, evenals voor massieve muren belast op afschuiving, wordt een 10% lagere driftwaarde aanbevolen om de kans op significante schade te minimaliseren.

Scheuren Propageren vanuit Hoeken

De meest voorkomende scheuren verliepen horizontaal en trapsgewijs diagonaal. In muren met openingen ontstonden de scheuren vaak vanuit de hoeken van de openingen. In muren zonder openingen ontstonden vaak meerdere diagonal trapsgewijze scheuren die uiteindelijk samenvloeiden tot een enkele, gelokaliseerde scheur. Deze observaties onderstrepen dat zowel de breedte als de lengte van scheuren tegelijkertijd toenemen.

Een opvallende observatie uit DIC is dat scheuren detecteerbaar waren nog voordat ze met het blote oog zichtbaar werden. Dit wijst op de aanwezigheid van 'onzichtbare' scheuren die potentieel kunnen propageren onder veranderende omstandigheden. Onder verhoogde belasting vertoonden alle typen scheuren—horizontaal, diagonaal, verticaal, taps of uniform—vergelijkbare verergeringen. Interessant is dat sommige van deze onzichtbare scheuren zichzelf ontlasten en mogelijk nooit zichtbaar worden terwijl er ook nieuwe scheuren ontstaan die alle aandacht naar zich toe trekken.

Verder bleek uit de experimenten dat kalkzandsteen metselwerk brosser lijkt dan baksteen metselwerk, vooral in het geval van verticale scheuren die zich ontwikkelen in de spandrels. In situaties waarbij de scheuren zigzaggen rond de stoot- en lintvoegen, werd waargenomen dat deze scheuren de kalkzandstenen verticaal splijten. Dit geeft aan dat het verband en de samenstellende materialen van het metselwerk aanzienlijke invloed hebben op de manier waarop schade zich manifesteert en ontwikkelt onder cyclische belastingen.

Bovendien beïnvloedt herhaling de scheurpropagatie, waarbij identieke belastingen leiden tot meetbare, maar consistente toenames in scheurbreedte en -lengte. Omgekeerd geldt dat de kracht die nodig is om identieke drifts te verkrijgen, met ongeveer 10% afneemt tussen de eerste en de laatste herhaling van een stap.

Stap 3: Kalibratie van Modellen aan Experimenten

In deze fase van het onderzoek is samengewerkt aan de ontwikkeling van numerieke modellen die het gedrag, waargenomen tijdens de experimenten, nauwkeurig nabootsen. Naast het reproduceren van de stijfheid, (piek-) sterkte, taaiheid, en na-piek capaciteit van de proefstukken, lag de focus op het repliceren van scheurpatronen en hun propagatie.

We gebruikten de niet-lineaire eindige-elementenmethode (EEM) met vlakspanningselementen in combinatie met het constitutieve Engineering Masonry Model (EMM) binnen Diana FEA software, wat succesvol bleek in het repliceren van het experimentele gedrag na correcte afstelling van de materiaalparameters. Belangrijke parameters zoals de elasticiteitsmodulus, treksterkte, en breukenergie speelden een cruciale rol in de kalibratie. Het EMM, dat orthotroop is en zowel trek-softening in horizontale als verticale richting omvat, alsook wrijving en afschuif-softening, bleek bijzonder geschikt voor deze taken. Het model gebruikt een secant ontlasting/herbelasting voor trek en elastisch voor afschuiving. In dit uitgesmeerde continuum scheurmodel zijn de scheuroriëntaties vooraf vastgesteld (gefixeerd), hetgeen aanmerkelijk betere resultaten geeft dan een roterend scheurmodel. Andere aspecten zoals mesh objectiviteit en convergentie zijn ook zorgvuldig onderzocht.

Hoewel de wandmodellen voldoende nauwkeurig waren, was het rekenintensief om evenveel cycli te modelleren als in de experimenten. Daarom werden in elke stap slechts drie cycli opgenomen, wat voldoende was om een vergelijkbare degradatie waar te nemen die na drie cycli stabiliseerde. In toekomstige studies zou het model verder verfijnd kunnen worden om de cyclische degradatie die waargenomen werd tijdens de experimenten nauwkeuriger te kunnen repliceren.

Daarnaast werden micro-modellen overwogen, met afzonderlijke modellering van de stenen en mortelvoegen. Deze modellen leverden nauwkeurigere resultaten op wat betreft de scheurpatronen, maar waren zeer rekenintensief. Voor het omvangrijke aantal benodigde modellen werd uiteindelijk gekozen voor het gebruik van het EMM continuümmodel, dat een goede balans bood tussen nauwkeurigheid en computationele haalbaarheid.

Stap 4: Extrapoleren naar de Initiële Condities + Seismische Trillingen

In de vierde stap van het onderzoek zijn de modellen, die nauwkeurig scheurinitiatie en -propagatie gedrag weergeven en die gevalideerd zijn aan statisch-cyclische experimenten op muren en spandrels, verder ontwikkeld om het effect van zettingen en aardbevingstrillingen te analyseren. Deze extrapolatie-modellen zijn uitgebreid met dynamische tijdsnormen (NLTHA) en bevatten meerdere essentiële aanpassingen om realistische gebouw-omstandigheden na te bootsen.

Aan de bovenkant van het wandmodel is een massa toegevoegd die de dynamische effecten van de vloer en het dak simuleert, wat essentieel is om het daadwerkelijke gedrag van constructies tijdens seismische activiteiten te begrijpen. Onderaan het model is een interface opgenomen die de interactie

tussen de bodem en de constructie bij de fundering weergeeft. Verder zijn aan de zijkanten van de muren veren aangebracht om de invloed van aangrenzende dwarsmuren te simuleren. Bij de berekeningen met voorschade wordt eerst aan de onderzijde van deze interface een ongelijkmatige zetting aangebracht. Deze opgelegde verplaatsing simuleert het verlies van ondersteuning zoals dat zou gebeuren bij zettingsschade, waardoor de muur zakt en scheuren ontwikkelt die overeenkomen met schades waargenomen in daadwerkelijk aangetaste gebouwen.

De intensiteit van deze opgelegde zetting is gevarieerd teneinde verschillende initiële condities van schade, aangeduid als Ψ_0 , te genereren. Daarbij is ook een scenario zonder zettingsschade ($\Psi_0=0$) onderzocht. Vervolgens wordt als tweede belasting een versnelling over de tijd aan de onderkant van de muur opgelegd, nadat de tangentiële stijfheid van de grond-constructie interface is vergrendeld, om zo de reactie van het metselwerk op seismische trillingen na zetting te beoordelen.

Record-to-record Variabiliteit

In het onderzoek is record-to-record variabiliteit onderzocht door meerdere versnellingssignalen te analyseren. Specifiek is gekeken naar vier signalen van twee recente aardbevingen: twee van de aardbeving bij Zeerijp in 2018 en twee van de aardbeving bij Westerwijtwerd in 2019. Voor elk van deze gebeurtenissen zijn gegevens verzameld van opnames die zowel dichtbij het epicentrum (ongeveer 3 km afstand) als verder weg (ongeveer 8 km afstand) gemaakt zijn.

Het doel van deze analyse was om inzicht te krijgen in hoe de nabijheid van een seismische gebeurtenis de impact op gebouwen kan beïnvloeden. Dit omvatte het bestuderen van verschillen in frequentie-inhoud, de effectieve cycli van de aardbevingen, en de interactie tussen horizontale en verticale componenten van de seismische golven. Bovendien zijn de signalen geschaald naar verschillende niveaus van PGV, variërend van 2 mm/s tot 100 mm/s, om een breed scala aan seismische intensiteiten te simuleren. Voor de studie van het repetitie-effect zijn de signalen herhaald toegepast in eenzelfde analyse, al dan niet geschaald.

Veel Variaties in Parameters

Naast de initiële schade, aangeduid als Ψ_0 , en de aardbevingsbelasting zoals PGV en herhalingsfrequentie, zijn twee wand-geometrieën gemodelleerd: een met en een zonder raamopening. Ook zijn twee bodemtypes onderzocht en drie sets materiaalparameters, die verschillen qua elasticiteitsmodulus, treksterkte, schuifsterkte en breukenergie. Dit leidde tot duizenden

geëxtrapoleerde wandmodellen. De analyses daarvan hebben belangrijke inzichten opgeleverd over hoe de complexe interactie tussen bouwkundige en materiaalkundige parameters de schade aan metselwerk beïnvloeden tijdens aardbevingen:

Wand geometrieën: Muren met een raamopening (Gevel A) krijgen doorgaans meer schade dan stijvere muren zonder openingen (Gevel B), vooral bij aardbevingen die dichtbij plaatsvinden. De grotere schade bij Gevel A kan toegeschreven worden aan spanningsconcentraties rond de raamhoeken, die het ontstaan van scheuren vergemakkelijken.

Bodemtype: De aard van de ondergrond speelt een belangrijke rol in de mate van schade tijdens aardbevingen. Gebouwen op zachtere bodem (type B) ondergaan grotere vervormingen voordat ze vergelijkbare schade krijgen als gebouwen op stijvere bodem (type A), waarbij de laatste scherpere muurkrommingen en hogere spanningsniveaus veroorzaakt, wat resulteert in ernstigere schade.

Afstand tot het epicentrum: De nabijheid van het epicentrum heeft een significante impact op de schade. Bewegingen dichtbij het epicentrum hebben de neiging om bestaande scheuren te propageren, terwijl bewegingen verder weg de scheuren voornamelijk wijder maken, waardoor de schade zichtbaarder wordt.

Initiële Schade: De aanwezigheid van initiële schade van een constructie heeft een bepalende invloed op de ernst van de uiteindelijke schade wanneer naderhand een beving optreedt. Constructies met een hoger niveau van initiële schade tonen meer totaalschade na een aardbeving, hoewel de incrementele schade afneemt bij hogere niveaus van voorschade.

Materiaaleigenschappen: Ook de eigenschappen van de gebruikte bouwmaterialen beïnvloeden het schadepatroon. Zwakkere materialen zijn minder bestand tegen trek- en afschuifspanningen, wat leidt tot meer omvangrijke schade onder identieke seismische condities vergeleken met sterkere materialen.

Piek Grondsnelheid (PGV): Er is een directe correlatie tussen de intensiteit van een aardbeving, gemeten door PGV, en de mate van schade. Hogere PGV's leiden consequent tot ernstigere schade, wat een duidelijke relatie tussen PGV en schade bevestigt.

Herhaling van aardbevingen: De invloed van herhaalde seismische gebeurtenissen toont aan dat constructies die aan herhaalde bevingen worden blootgesteld telkens een toename van schade laten zien, hoewel de toename relatief kleiner wordt bij elke extra gebeurtenis. Kwalitatieve trends zijn

getoond voor verschillende scenarios van herhalingsreeksen met oplopende of afnemende intensiteit per beving.

Vastleggen van Relaties in een Model

Vervolgens is de invloed van elk van bovenstaande parameters vastgelegd in een surrogaatmodel. Hierbij zijn twee verschillende technieken verkend om te bepalen welke het beste de complexe interacties tussen aardbevingen en schade kan simuleren.

De eerste benadering is een 'beredeneerd' model, dat waargenomen trends omzet in specifieke wiskundige functies zoals machtsfuncties of logistieke relaties. De coëfficiënten binnen deze functies worden vervolgens gekalibreerd en ge-fit op de verzamelde data. Dit model stelt onderzoekers in staat om fysische relaties rechtstreeks af te leiden, zoals het verband tussen hogere schade en hogere piek grondsnelheid.

De tweede benadering betreft een supervised machine learning model, waarbij een neurale netwerk wordt getraind met de verzamelde gegevens. Hoewel dit model uitstekend presteert op bepaalde datasets, blijkt het lastig te generaliseren over verschillende soorten gegevens en faalt het in het nauwkeurig vastleggen van de onderliggende fysische relaties.

Gezien deze bevindingen werd uiteindelijk gekozen voor het beredeneerde model als het surrogaatmodel voor verdere analyses. Dit model biedt een robuust raamwerk (framework) voor het simuleren van seismische responsen, met expliciete formuleringen die de realiteit van bouwkundige variaties nabootsen. Om rekening te houden met mogelijke onzekerheden in het model en de strategie van de eindige-elementen-modellering (FE-modellering), is een onzekerheids-parameter geïntegreerd. Deze parameter helpt bij het inschatten van de invloed van mogelijke fouten in het model en andere onzekerheden binnen de modelleringsstrategie, wat essentieel is voor het naderhand verfijnen van de voorspellingen en aanbevelingen.

Stap 5: Toewijzen van Verdelingen aan de Parameters en Bepalen van de Schadekans

In deze fase van het onderzoek worden de verschillende parameters, die invloed hebben op schade tijdens bevingen, gerepresenteerd door probabilistische verdelingen. Dit helpt bij het kwantificeren van de onzekerheden en variabiliteiten in de eigenschappen die worden gebruikt om de modellen te kalibreren. Bijvoorbeeld, uit experimenten blijkt dat de treksterkte van metselwerk normaal verdeeld is met een standaardafwijking van 30%. Deze verdeling wordt vervolgens toegepast in de wegging van de model resultaten om consistentie te waarborgen.

De afstand tot het epicentrum wordt eveneens probabilistisch gemodelleerd. Hogere piek grondsnelheden worden waarschijnlijker geacht naarmate het epicentrum dichterbij ligt. Daarnaast is het type ondiepe bodem, essentieel voor het bepalen van de interactie tussen de constructie en de grond tijdens een aardbeving, uniform verdeeld verondersteld op basis van statistieken van de bodems gevonden in de regio Groningen. Hierdoor kan een realistisch beeld worden geschetst van de bodeminvloeden op de constructieve respons.

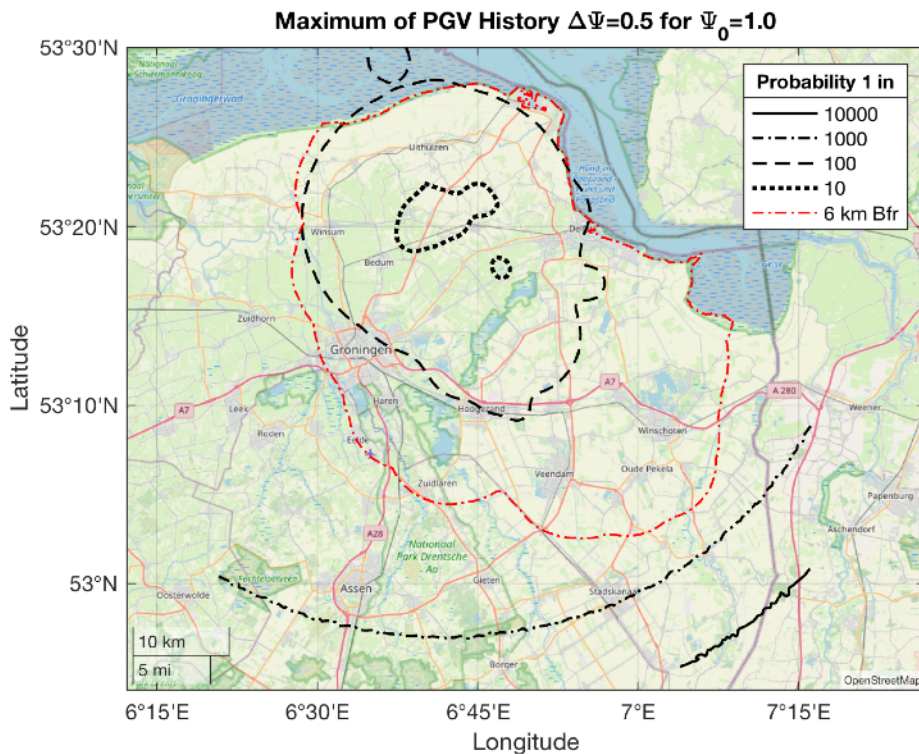
Met deze probabilistisch bepaalde parameters wordt een MonteCarlo simulatie uitgevoerd met behulp van het surrogaatmodel. Deze simulatie berekent de waarschijnlijkheid dat bepaalde waarden van de schadeparameter Ψ worden overschreden voor gegeven piek-grondsnelheden en gegeven initiële schadecondities. Dit resulteert in zogenaamde kwetsbaarheidscurven. Zo wordt bijvoorbeeld onthuld dat muren van baksteen zonder zichtbare voorschade ($\Psi_0=0$) een kans van 5% hebben op het ervaren van zichtbare schade ($\Psi \geq 1$) bij een PGV van 10 mm/s. Deze kans neemt toe naar 20% wanneer de muren zeer lichte, voor het blote oog nog onzichtbare voorschade vertonen ($\Psi_0=0.5$).

Kwetsbaarheidscurven omgezet in Kaarten

Kwetsbaarheidscurven bieden een waardevol instrument om de kans op schade te voorspellen en kunnen worden gecombineerd met een verdeling van piek grondsnelheden voor specifieke locaties. Dit resulteert in een gedetailleerd beeld van de kans op schade door seismische gebeurtenissen op die locaties. Voor een nog nauwkeuriger beeld kan de maximale piek grondsnelheid van verschillende gebeurtenissen per locatie worden vastgesteld, wat helpt om de maximale kans op schade voor metselwerk-gebouwen in dat gebied te bepalen.

Deze informatie wordt vervolgens gevisualiseerd in een kaart. Figuur 5.4.5 toont een voorbeeld van de kans op een schadetoename van $\Delta\Psi=0.5$ voor een initiële schade van $\Psi_0=1$, hetgeen overeenkomt met een juist merkbare

toename van initieel net zichtbare scheuren. Uit de kaart blijkt dat voor een relatief groot gebied in het noorden van de bufferzone van het Groningse gasveld, de kans op deze merkbare toename in lichte schade ongeveer 1 op 100 (of 1%) is. Over de gehele bufferzone en een groot deel daarbuiten ligt de kans op lichte schade op 1‰. Dit suggereert een zeer kleine kans op het ontstaan van scheuren die betrekking hebben op lichte schade. Als men bijvoorbeeld tienduizend gebouwen in dit gebied beschouwt, zouden statistisch gezien 10 gebouwen een verergering van schade van $\Delta\Psi=0.5$ kunnen vertonen, met een kans van 50%. De kans op het overschrijden van DS1 ($\Psi>2.5$) blijft echter ongeveer 0.1‰ voor de gehele bufferzone.



Figuur 5.4.5. Waarschijnlijkheidskaart voor de historische maximale PGV geconvolueerd met de kwetsbaarheid van metselwerk. De figuur geeft de situatie weer met een $\Delta\Psi$ van 0.5, voor een initiële conditie van net zichtbare schade, $\Psi_0=0.1$.

Het Effect van Herhaling in Experimenten

In de experimenten die uitgevoerd werden op wanden en spandrels, zijn herhaalde, identieke cycli gebruikt om de impact van herhaalde belastingen te observeren. Ontdekt werd dat herhaalde verplaatsingen leiden tot een fenomeen bekend als "krachtdegradatie", waarbij de kracht die nodig is om dezelfde verplaatsing te bereiken afneemt. Dit effect stabiliseerde na ongeveer

dertig herhalingen. Verschillende testprotocollen, inclusief eenrichtings- en tweerichtings-cyclische verplaatsingen, toonden consistentie in het effect van krachtdegradatie. Opvallend was dat, indien een richting vooraf beschadigd was, bij herhaald testen in diezelfde richting nauwelijks verdere degradatie optrad. Bovendien leidden deze herhaalde verplaatsingen tot zichtbare toenames in schade, vooral in de vorm van scheurpropagatie, wat suggereert dat niet alleen de vereiste kracht afneemt, maar ook dat scheuren in breedte en lengte toenemen bij elke herhaling.

Het Effect van Herhaling in Modellen

De FE-modellen werden ook onderworpen aan herhaalde signalen, waarbij vaak signalen met identieke piek grondsnelheden werden gebruikt, en soms werd een heterogene sequentie geëvalueerd. Tijd-historieanalyses toonden aan dat herhaalde gebeurtenissen inderdaad leiden tot een accumulatie van schade, al waren de toenames klein. Interessant is dat trillingen van lagere intensiteit dan de voorgaande de schade nauwelijks verhoogden, terwijl trillingen van dezelfde of grotere intensiteit dan eerdere trillingen de schade met ongeveer 10% konden verhogen. Zo wordt bijvoorbeeld een tweede trilling van 10 mm/s verwacht de schade te doen verergeren met 6%. Echter, de beperkingen in het aantal modellen en variaties, samen met een gebrek aan vergelijkende veldgegevens, benadrukken de noodzaak om deze modelgebaseerde observaties verder te verifiëren en uit te breiden.

Schade Accumulatie Functie (DAF)

De resultaten van experimenten en modellen die het effect van herhaling onderzoeken, zijn geïntegreerd in een geavanceerde functie, bekend als de Schade Accumulatie Functie (DAF). Deze functie is ontworpen om de reeks van PGV's te evalueren, zoals die zou voorkomen in een werkelijke geschiedenis van aardbevingen. De DAF bouwt voort op het bestaande surrogaatmodel en wordt gebruikt om de waarde van de schadeparameter Ψ voor elke PGV in de reeks te voorspellen.

De DAF genereert een probabilistische verdeling voor Ψ en berekent de uiteindelijke schadeverergering vanuit een initiële schadestaat Ψ_0 . De functie onderscheidt twee belangrijke componenten: één voor gebeurtenissen met een PGV vergelijkbaar met eerdere gebeurtenissen, en een andere voor gebeurtenissen waarbij de PGV groter is dan bij eerdere gebeurtenissen. Deze laatste component resulteert in een grotere schadetoename. De DAF is uitvoerig gevalideerd tegen zowel de resultaten van de modellen als tegen de experimentele waarnemingen. De functie wordt uiteindelijk gebruikt om zowel de verwachte schade als de waarschijnlijkheid van schade te schatten voor

metselwerkwanden in de regio Groningen, die al decennialang worden blootgesteld aan herhaalde aardbevingen.

Het Gebruik van de DAF in Vergelijking met Enkele Kwetsbaarheidscurven

Om de meerwaarde van het overwegen van schadeaccumulatie met de Schade Accumulatie Functie (DAF) te bepalen, wordt een vergelijking gemaakt met kaarten die zijn gegenereerd op basis van de maximale piek grondsnelheid voor enkele gebeurtenissen. Bij deze enkele gebeurtenissen zijn de contouren van schade meestal cirkelvormig, wat voortkomt uit de manier waarop de Ground Motion Prediction Equations (GMPEs) de voortplanting van beweging baseren op de afstand tot het epicentrum. In tegenstelling tot deze enkele gebeurtenissen, houdt de DAF rekening met meerdere gebeurtenissen die elk hun eigen epicentra hebben, wat resulteert in onregelmatige vormen van schadecontouren.

Bovendien blijken de buitenste waarschijnlijkheidscontouren van de enkele gebeurtenis kleiner te zijn dan die gegenereerd door de DAF. Dit toont aan dat het overwegen van het cumulatieve effect van meerdere gebeurtenissen leidt tot hogere kansen op schade. Verder zijn de contouren volgens de DAF in het centrum van de regio aanzienlijk groter dan buiten het centrum, hetgeen wijst op de invloed van meerdere verspreide epicentra en een groter aantal gebeurtenissen.

De DAF heeft significant invloed op specifieke locaties, vooral in gebieden die dicht bij het centrum van de regio liggen maar relatief ver van een specifieke grote gebeurtenis, zoals de aardbeving bij Huizinge. Bijvoorbeeld in Delfzijl, waar de kans op zichtbare schade minder dan 1% is in het geval van de aardbeving bij Huizinge, stijgt deze kans naar 10% wanneer rekening wordt gehouden met de volledige geschiedenis van gebeurtenissen. Echter, de kans op het overschrijden van een schadestaat van $\Psi \geq 2.5$ wordt nauwelijks beïnvloed, ook niet door de initiële schadeconditie. Dit illustreert dat een enkele, grote gebeurtenis hier een belangrijkere rol speelt dan het cumulatieve effect van meerdere kleinere gebeurtenissen, die, ondanks hun aantal, niet genoeg zijn om lichte schade significant te doen toenemen.

Deze analyses benadrukken het belang van het integreren van de geschiedenis van seismische activiteit in het beoordelen van bestaande schade en het voorspellen van toekomstige schade, en tonen de noodzaak aan om zowel individuele grote gebeurtenissen als opeenvolgende kleinere trillingen in overweging te nemen bij het beoordelen van schade risico's.

Bijdragen in Vergelijking met de Literatuur

Deze studie hanteert een bottom-up fysische en probabilistische benadering die zich onderscheidt van de bestaande literatuur die vaak empirisch, deterministisch en 'benaderend terugschalend' van bezwijksgrenstoestanden naar lagere schadegrenstoestanden zijn. Diverse substantiële bijdragen, met name op het gebied van seismische schadebeoordeling en modelvalidatie zijn geleverd. Er zijn drie soorten referentiestudies geïdentificeerd die elk specifieke uitdagingen (of onderwerpen) vertegenwoordigen waaraan deze studie heeft gewerkt.

Ten eerste, empirische analyses, die vaak worstelen met het isoleren van de oorsprong van gerapporteerde schade. Deze analyses bieden beperkt inzicht omdat ze geen kwantitatieve conclusies kunnen trekken over de specifieke effecten van aardbevingen of het effect van herhaling van dergelijke gebeurtenissen. De aanpak in deze studie decomponeert de effecten en maakt gebruik van gedetailleerde data en simulaties om directe correlaties en causale relaties te identificeren, die helpen bij het nauwkeuriger voorspellen van schade.

Ten tweede worden extrapolatie methoden behandeld. Deze worden gewoonlijk gebruikt om het gedrag en de schadelimieten van constructies onder seismische belasting te voorspellen, zoals gebaseerd op Ultimate Limit State (ULS) of pushover analyses. Hoewel deze extrapolerende methoden nuttig zijn, missen ze vaak de precisie om duidelijke grenzen voor zichtbare schade en de voortplanting ervan uit te drukken. De in dit onderzoek ontwikkelde modellen en schadeaccumulatiefuncties (DAF) bieden meer gedetailleerde en fysisch-onderbouwde toepasbare inzichten binnen de vastgestelde grenzen.

Ten derde zijn er studies die scheurvorming onderzoeken, maar vaak falen in het kwantificeren van de schade of het gebruiken van deze data om modellen te kalibreren. Deze studies bieden zelden een praktische benadering voor het gebruik van voorspellingsmodellen in echte scenario's. In tegenstelling tot deze studies, heeft de hier ontwikkelde benadering niet alleen de modelkalibratie verbeterd maar ook de toepasbaarheid van de modellen in het voorspellen van het effect van aardbevingen op schade verhoogd.

Slotopmerkingen

Dit onderzoek was gericht op het kwantificeren van de kans op lichte schade aan metselwerk door herhaalde seismische trillingen, met speciale aandacht voor de aanwezigheid van voorschade. De toegepaste methodologie, waarin experimentele data gebruikt worden om numerieke modellen te valideren en

deze modellen vervolgens gebruikt worden om de impact van belastingen op scheur-schade te voorspellen, heeft effectief aan de doelstelling voldaan.

De studie heeft belangrijke inzichten opgeleverd over het effect van aardbevingen. Herhaalde seismische gebeurtenissen verhogen de (kans op) schade met ongeveer 10%, afhankelijk van de intensiteit van de PGV. Aanzienlijke schadeverschillen ontstaan vooral wanneer PGV's de 10 mm/s overstijgen, wat leidt tot een waarneembare toename in schade. Specifiek in de seismische regio Groningen hebben bakstenen muren aanzienlijke zichtbare schade opgelopen, met scheuren van minimaal 0,1 mm breedte in de periode van 2000 tot 2020. In de bufferzone van het Groningse gasveld is de kans op dergelijke schade over het algemeen minstens 1%. Deze kans verhoogt echter aanzienlijk—tot wel tien keer—indien er reeds enige initiële, zij het onzichtbare, schade aanwezig was. Enkel in een beperkt gebied bereikt de kans op het overschrijden van de serviceability limit state (DS1/DS2) een percentage van 1%, zelfs als de constructies aanvankelijk zichtbare schade vertoonden.

De bevindingen benadrukken het belang van rekening houden met historische seismische activiteiten en de initiële staat van bouwconstructies bij het voorspellen van toekomstige schaderisico's, en onderstrepen de noodzaak van geavanceerde monitoring en preventieve strategieën om de aardbevingsbestendigheid van bouwwerken in seismisch actieve regio's te verbeteren.

Beperkingen van de Studie

De methodologie van deze studie, hoewel uitgebreid, omvat enkele beperkingen die de interpretatie en toepasbaarheid van de resultaten beïnvloeden. Eén primair aandachtspunt is het toevoegen van monitoring in het veld. De huidige benadering gaat vooral uit van gecontroleerde of gedecomposeerde lab-experiments, maar de bevindingen, hoewel veelbelovend, vereisen validatie met (lange termijn) veldgegevens. Betrouwbare monitoring gedurende een lange periode is echter complex en kostbaar, en biedt geen garantie dat alle onderliggende schadeoorzaken volledig worden ontrafeld. Daarnaast zijn er ook andere beperkingen verbonden aan de methodologische aanpak:

In deze studies dienen wanden als een vereenvoudigde representatie voor volledige metselwerkgebouwen. Het effect van driedimensionale constructies en meer complexe gevels dient verder onderzocht te worden, ondanks dat voorlopige resultaten een goede overeenstemming tonen. Verder, de studie heeft zich voornamelijk gericht op in-het-vlak schade-effecten in halfsteen muren. Uit-het-vlak effecten, hoewel minder relevant voor lichte schade,

evenals de progressie van scheuren in steensmuren en ter plaatse van bouwkundige aansluiting met kozijnen, vereisen verder onderzoek.

De conclusies zijn primair geldig voor metselwerk van baksteen. Andere bouwmaterialen, zoals kalkzandsteen, gedragen zich mogelijk anders. Hoewel kalkzandsteen in sommige experimenten is opgenomen, moet de kwetsbaarheid ervan nog grondig worden beoordeeld. De waargenomen degradatie op materiaalniveau wordt niet volledig weergegeven in de huidige numerieke modellen. Het ontwikkelen van een cyclisch degradatie-effect voor het gebruikte Engineering Masonry Model (EMM) zou de nauwkeurigheid van deze modellen verbeteren.

De validatie van modellen is uitgevoerd met behulp van quasi-statische experimenten, die zijn geëxtrapoleerd naar scenario's met dynamische belasting. Verdere experimenten onder deze dynamisch belaste omstandigheden zijn noodzakelijk om de complexiteit van seismische belasting en scheurmonitoring adequaat te begrijpen.

Deze beperkingen benadrukken de noodzaak voor aanvullende studies en alternatieve benaderingen om de robuustheid van de onderzoeksresultaten te verhogen en de realiteit van seismische impact op gebouwen nauwkeuriger te modelleren.

Toekomstperspectief: Relevantie van Lichte Schade in de Toekomst

In de toekomst zal het begrip van lichte schade nog belangrijker worden, vanwege de toenemende impact van klimaatverandering, veranderingen in de bodem en de overstap naar hernieuwbare energiebronnen.

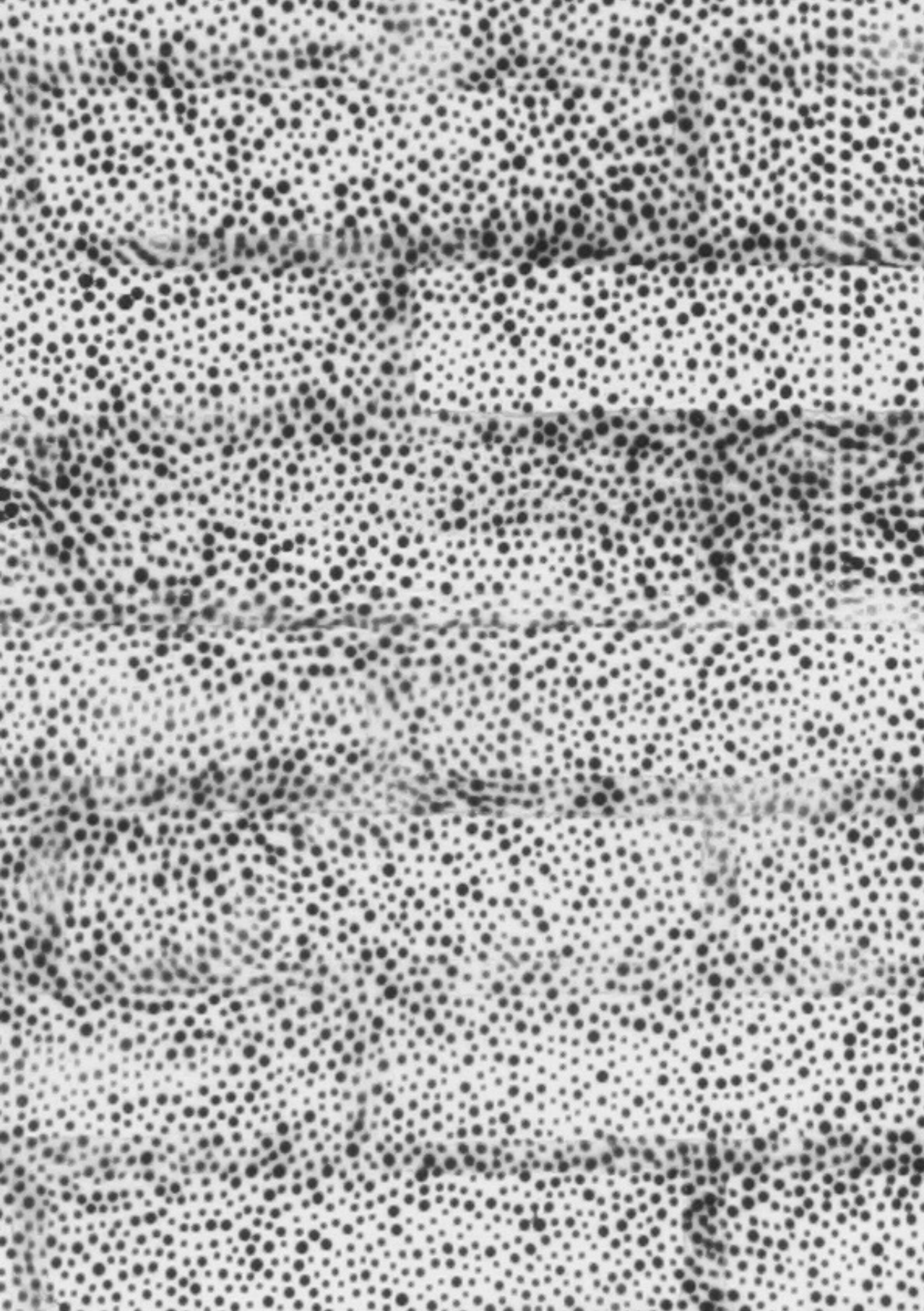
Extreme weersomstandigheden zoals stormen, droogtes en overstromingen zullen naar verwachting toenemen, wat kan leiden tot schade aan gebouwen en toenemende geïndiceerde zettingen. Dit zal het incasseringsvermogen van gebouwen op de proef stellen en nieuwe uitdagingen met zich meebrengen voor bouwprojecten.

De overgang van fossiele brandstoffen naar hernieuwbare energie zal eveneens invloed hebben op gebouwen. Geothermie en ondergrondse energieopslag kunnen, net als gaswinning, leiden tot bodembeweging en daarmee tot schade aan constructies. Slecht beheerde renovaties en de overgang naar nieuwe energietechnologieën kunnen constructies tot schade leiden.

Nederland heeft de uitdagingen van door gaswinning veroorzaakte seismiciteit ervaren met tekortschietende communicatie en trage beleidsimplementatie, wat heeft geresulteerd in publieke weerstand. Duidelijke beleidsmaatregelen

zijn nodig om bouwgerelateerde kwesties en klimaat- en mijnbouwrisico's effectief aan te pakken.

De toekomst vereist het bouwen aan een samenleving die deze risico's accepteert en weet te managen, met een duidelijk begrip van de relatie tussen gevaren en schade. Dit kan alleen worden bereikt door proactieve beleidsmaatregelen en een nauwe samenwerking tussen overheden, wetenschappers en de gemeenschap.





How to Read this Dissertation

The reader will notice certain peculiarities in this work. First, references may be cited using square brackets or author names. References in numbered square brackets [1 - 33] are my own publications or collaborations; see the List of Publications. Other references are cited with authors' names; see the Bibliography. This approach makes it easier to identify works with which the reader may be familiar, while keeping citations brief and avoiding the repetition of this author's name. Similarly, the literature list includes two lines for each work, the first line exactly as it is referenced in the text. Finally, references in curly brackets {5.3} indicate sections within this text.

Second, figures and tables are referred to not merely as names but as addresses. For example, Figure 3.3.2, with its full address (not name), is Figure 2 in Section 3.3. Within the same section, it may be referred to simply as Figure 2, while from within Chapter 3, it can be identified as Figure 3.2. This is similar to how telephone landlines used to work, allowing users to skip country and area codes when calling within the same region. Similarly, this method is employed to refer to neighbouring sections within the same chapter. Moreover, some figures may appear out of order. Figure 2 may appear before Figure 1 if the latter is a full-page figure that allowed space for Figure 2 before it. The figures are sequential to the order in which they are referred to in the text.

Chapter 1

Introduction

Prologue

Since the earthquake of Huizinge in August of 2012, the area surrounding the Groningen gas field in the north of the Netherlands, has been the scene of social and economic unrest due to the light and frequent seismic vibrations causing damage to the existing building stock. The earthquakes began two decades earlier, but not until the Huizinge earthquake would their effect be clearly recognised.

Many studies have been carried out to determine the safety of the buildings subjected to these earthquakes. However, the appearance of small cracks on the walls, often without major structural significance, has been much more widespread than severe, safety-concerning damage. These minor cracks have led to a large number of damage claims, triggering social unease, and impacting the local and national economy. Many other actions on structures, like settlements induced by the soft Dutch soil or thermal effects, intrinsic to structures, cloud the cracks' origins. This unclear relationship between the earthquakes and the damage, together with the initial focus on safety, means that small cracks have not been studied extensively.

This crack-based damage, categorised into the so-called damage state 1 (DS1), started to receive technical attention in recent years as the (international) expertise shifted when the safety of the structures had been appraised and the inverse of proof was implemented - a ruling that declared all cracks to have been caused by earthquakes unless proven otherwise. Still, their initiation and later accumulation with existing causes, remains understudied and is thus the focus of this work.

This introductory chapter further explains the background of this study, presents a brief literature review into efforts to characterise minor damage in masonry, details the resulting research questions to fill the current knowledge gaps, and includes an outline of this work.

1.1. Relevance

1.1.1. Societal Relevance

The Groningen region has experienced significant societal and economic unrest due to the seismic activities linked to gas extraction. The frequency of minor seismic events, particularly highlighted by the notable Huizinge earthquake of 2012, has led to a proliferation of damage primarily manifesting as minor, often superficial cracks. This damage, while sometimes dismissed as merely cosmetic, has broader implications for the affected communities. Not only do these cracks reduce the aesthetic and market value of properties, but they may also compromise the structural integrity and safety of buildings, leading to concerns over watertightness, increased susceptibility to environmental damage, and reduced perception of safety.

Moreover, the identification and attribution of responsibility for these damages are critical in a societal context where legal and insurance frameworks rely heavily on clear causation. The ruling, that assumes all cracks are caused by earthquakes unless proven otherwise, has placed a significant burden on the shoulders of gas extraction companies, impacting their operational strategies and their interactions with local communities. This situation has led to a heightened demand for effective damage assessment and repair strategies that are both timely and economically viable. Understanding and addressing minor damage is thus crucial for maintaining public trust and ensuring that the social fabric of the region remains intact.

1.1.2. Scientific Relevance

From a scientific perspective, the Groningen case presents a unique opportunity to study the effects of induced seismicity on masonry structures—a subject that has been under-explored in the broader field of earthquake engineering. While substantial research has focused on the structural impacts of natural seismic events, the nuanced effects of smaller, recurrent, man-made earthquakes pose different challenges. These challenges include the assessment of damage that does not immediately compromise building safety but may affect its long-term usability and maintenance: light damage. In fact, the science looking at the Ultimate Limit State (ULS) is mature. Yet, it concerns an extremely low probability of failure associated however with large consequences of structural collapse and loss of life. In contrast, the light damage, or Serviceability Limit State (SLS), linked to more likely failures, product of repeated seismic events and with relatively small consequences (cracks), is scarcely or only superficially investigated.

The scientific relevance of studying this minor damage extends beyond the mere characterisation of damage. It involves developing predictive models that accurately reflect the cumulative effect of multiple minor seismic events on masonry structures. Traditional models often fail to address the initiation and propagation of minor cracks, particularly in the context of repeated exposure to low-intensity seismic vibrations. This gap in knowledge is critical not only for predicting future damage but also for designing buildings that are resilient to such events. Additionally, understanding the specific causes and mechanisms of minor damage can lead to innovations in building materials and construction techniques that are specifically tailored to resist such actions.

Furthermore, the shift in international expertise towards a more detailed understanding of seismic impacts, as evidenced by the inverse proof ruling, underscores the need for a scientific approach that can dissect the interplay between seismic forces and building responses. This understanding is key for developing more effective mitigation and adaptation strategies in regions similar to Groningen or others around the world facing similar issues due to induced seismicity. Studies on the effect of other potential sources of induced seismicity, like geothermal energy, will also benefit from this work.



Figure 1.1.1. An example of a narrow crack in fired-clay brick masonry with a stretcher pattern and a cementitious general-purpose mortar in 10mm bed and head joints. This photograph was obtained from an experiment on a wall (see Chapter 3).

1.2. State of the Art and Knowledge Gaps

This brief literature review provides a glimpse into the state-of-the art of the understanding of minor cracking of masonry (light damage). In particular, damage due to the effects of gas extraction to buildings. These are composed by quasi-static and dynamic soil movements. The former lead to gradual subsidence over a kilometre-scale region, which is much larger than the building scale and are thus mostly unrelated to building damage; hence, damage from deep subsidence is not considered herein (see Appendix A). The latter, dynamic movements, result in seismic vibrations which are more likely to affect structures at the building scale. The focus is placed on Dutch masonry buildings, often pre-damaged by other causes such as (local) ground settlements or temperature movements. A specific overview of literature is also included in subsequent chapters.

1.2.1. Literature and its Limitations

Earthquakes, induced by gas extraction activities in the north of the Netherlands (Pickering et al. 2015, Vlek 2018), have triggered extensive studies into the safety and damage vulnerability of unreinforced masonry structures (Crowley et al., 2019). These structures, built throughout the region and in the rest of the country, were never prepared to be exposed to seismic activity and its resulting vibrations. Consequently, the unreinforced fired-clay brick masonry, ubiquitous to masonry veneers or outer cavity wall leaves and also present in older (double-wythe) structural walls, has exhibited damage, principally, in the form of cracks opening in the plane of the walls (Van Staalkduinen et al. 2018). The earthquakes, frequent, but light in nature, with vibration levels in the order of 5 to 20 mm/s (Noorlandt et al., 2018), have led to mostly aesthetic or cosmetic damage, depicted by cracks which are considered to range between 0.1 and 5 mm in width.

While wider cracks and more severe damage have been reported in rare cases, these are outside the scope of this study, laying the focus on lighter and more common expressions of damage due to processes acting in the plane of the walls. Out-of-plane failures are more commonly associated with the ultimate limit state (ULS) or near-collapse states of the structures, while light damage is linked to in-plane actions (Van Staalkduinen et al.). The focus is thus on the minor damage states, DS1 and DS2. Damage states, as defined by the European Macroseismic Scale (Grünthal et al. 1998, de Vent et al. 2011) categorise the condition of a structure on a scale of zero to five where DS0 corresponds to no damage, DS1 to aesthetic damage and DS5 to total collapse.

To estimate the impact of seismic activity on a regional level and to predict its future consequences, it is necessary to quantify the probability of damage to buildings. Studies have sought to characterise the behaviour of masonry structures for the states DS3 to DS5 as these are relevant for quantifying the safety of the structures (Esposito et al. 2016 & 2019, Messali et al. 2018, Tomassetti et al. 2017, Graziotti et al. 2017) yet, the durability/cosmetic damage state (DS1), or light damage, more difficult to evaluate due to the increased influence of the variability in the structures and materials and the interaction of other loading processes, has proven to be especially relevant in the context of induced seismicity where an operator is responsible for the damage with associated economic losses and social unrest (Bakema et al. 2018).

The lower damage states are usually identified in various manners; four methods are highlighted:

Extrapolation from Higher Damage States

First, some studies obtain DS1 by extrapolating it from higher damage states related to building safety or its near-collapse state. Gehl et al. (2013) for instance, uses the yield displacement of a bilinear curve fit to the results of a pushover analysis to establish where the threshold for DS1 should lie. Similarly, Crowley et al. (2019), uses single degree of freedom approximations of pushover curves from a variety of Finite Element models; however, these and the consequences of lateral building deformations are tuned to the near-collapse state, with DS1 being defined as the yield point in the bilinear curve. Since DS1 represents durability, cosmetic, and/or aesthetic damage, its intensity cannot be captured with a bilinear curve that expresses the strength and deformation capacity of the structure.

Empirical Damage Claims Analysis

Second, other studies quantify DS1 empirically using data from case reports or damage claims. For example, Crowley et al. (2018), looked at the number and type of earthquake damage claims submitted in the Groningen region up to 2015 and associated it with the local seismic intensity of various earthquake events by using ground motion prediction equations (GMPEs). In this way, they determined the likelihood of damage against increasing earthquake intensity. However, the accuracy of the empirical approach is affected by the way the samples are captured, with an unknown number of undamaged cases and uncertainty of the different thresholds that motivated claims to be submitted. Moreover, the initial situation of the structure, and thus the accumulation of damage, are unknown.

Masonry Panel Cracking Studies

Third, additional studies look at cracking in masonry panels. For instance, Didier et al. (2018) quantified damage based on cracks on masonry panels subjected to in-plane actions. While the Swiss masonry of the study does offer insight into the fundamentals of masonry cracking, it differs from Dutch masonry in stiffness, strength and toughness. Furthermore, the aspect of repetition, when the masonry is subjected to identical loads, is not covered in this reference study; and, a damage scale to assess the aggravation of the damage is also not part of it.

Finite Element Models and Probability Analysis

Fourth, a few studies analyse the probability of damage initiation using finite element models. A known study is that of Waarts (1997), who adapted the FE models of Raaijmakers (1994), with probabilistic distributions of the material parameters. This allowed the estimation of the probability of when damage would appear at increasing measures of ground motion. Still, the initiation of damage was measured using the tensile strength of the masonry; this is insufficient to capture the intensity of the damage since stresses redistribute when materials crack and because exceeding the tensile strength does not necessarily lead to visible cracks.

1.2.2. Knowledge Gaps

The literature and industry practices concerning the effects of man-made seismic events, particularly in the context of minor structural damages such as narrow cracks in masonry, reveal significant knowledge gaps that this research aims to address. These gaps, as derived from the overall discussion and the specific insights into the current state of understanding, are as follows:

Quantification and Visibility of Minor Damage

There is a critical need for a robust methodology to quantify minor cosmetic damage. Current literature lacks detailed, consistent criteria for when such damage becomes visible and how it progresses under repeated seismic loads. This gap hinders effective prediction and management of the damage, clear communication about damage, setting of thresholds for reimbursements, and comparisons between cases, among other limitations.

Experimental Studies on Crack Development

There is a lack of experimental research observing the behaviour of masonry under seismic conditions with a focus on minor damage states. Most studies do not adequately explore the initiation stages of cracking and how these cracks

develop over time under various loading scenarios. The campaign that began in 2017 at TU Delft marks a significant step, but comprehensive studies are still required to establish a broad base of empirical evidence.

Modelling of Cosmetic and Durability-Related Damage

While existing studies have primarily focused on assessing structural strength and safety, there is a noticeable deficiency in models that specifically address cosmetic and durability aspects of damage, such as crack width and progression. Existing finite-element-method (FEM) models are not sufficiently detailed or validated in terms of capturing the initiation and propagation of minor cracks, especially under conditions of repeated seismic activity. This limitation calls for the development of enhanced models refined through experimental validation.

Characterisation of the Probability of Light Damage

The literature indicates a gap in characterising the probability of light damage, particularly in terms of how material properties, seismic events, and other/ existing loading actions contribute to such damage. This lack of detailed exploration makes it challenging to predict and mitigate light damage effectively. There is a need for more sophisticated probabilistic models that can incorporate the variability of materials and the complex interactions of different load types.

By addressing these knowledge gaps, this research will not only contribute to the academic field but also provide practical insights and tools that can significantly improve the management of seismic risk in regions similar to Groningen. This work is poised to enhance both the scientific understanding and the practical approaches to dealing with minor, yet significant, structural damage caused by induced seismicity.

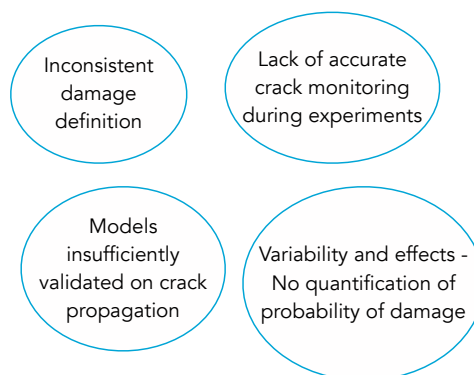


Figure 1.2.1 Main knowledge gaps highlighted.

1.3. Research Objective

Induced earthquakes may lead to damage in masonry buildings; repetition may aggravate this effect. The contribution of earthquakes to damage claims is uncertain. The stated problems, in the context of the societal and scientific relevance and within the frame of the knowledge gaps identified, lead to the goal of this work: to **objectively and probabilistically quantify the initiation and aggravation of crack-based damage in (pre-damaged) masonry for repeated seismic events** characterised by their intensity in Peak Ground Velocity (PGV).

To achieve this objective, several subquestions are formulated:

- i. What is a damage scale or measure capable of objectively characterising masonry light damage (for various relevant causes)?
- ii. How can cracking, relevant for light damage, be accurately...
 - a. surveyed from experiments? And,
 - b. modelled for masonry? (Collaboration with other authors)
- iii. How is light damage, caused by settlement or other autogenous actions in masonry buildings, aggravated by seismic vibrations, especially after multiple seismic events?
- iv. What is the probability of visible light damage for masonry structures in the region of Groningen, primarily due to seismic actions, but considering the probable current state of the buildings?
- v. How is the appearance of intrinsic light damage hastened* by seismic vibrations? *See Glossary.

This leads to a method and a strategy for the quantification of the probability of damage initiation and aggravation. To further illustrate the context and approach of this work, a few hypotheses are presented next.

Intuitively, masonry with existing cracks is more vulnerable than undamaged or virgin masonry. Yet, the additional flexibility of the cracked masonry may help the structure in dynamic situations. This emphasises the need to quantify the effect of pre-damage in terms of the increase of the probability of additional damage. Moreover, it could be expected that initial damage will also increase the probability of additional damage; and, that repeated loading will further increase this probability. Similarly, damage may accumulate with exposure to repeated earthquake events. Consequently, seismic events may hasten the intrinsic development of light damage in a masonry structure, where (existing) damage from shrinkage, thermal, or settlement phenomena is common.

Additionally, there may be a threshold below which cosmetic damage is not relevant and above which damage is no longer cosmetic.

Note that the probability of earthquake damage for a general building is a concept that differs from the attributability of attested damage having been caused by an earthquake for a particular building. In this case, the context of the building will alter the probability of damage; this is the specific vulnerability. For example, the probability of damage due to a seismic event for masonry buildings in one region may be 5%. For a specific building showing damage, it does not mean that the damage is 5% attributable to the earthquake nor is the damage 5% likely to have been caused by the earthquake. If for this particular building, other damaging causes (like settlements or recent renovations) are more or less relevant, the probability of the earthquake being the cause of the damage will differ. In this work, the general probability of damage for masonry buildings is explored.

1.4. Research Methodology

The quantification of the probability of damage initiation and aggravation has been casted into is a five step process, further exemplified herein by the assessment of masonry cracking due to settlements and vibrations. This process is presented in Figure 1.4.1 and partly related to the structure of this text.

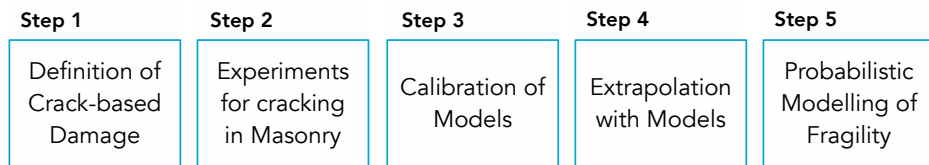


Figure 1.4.1. Five steps to physically understand light damage.

The first step is to determine a scale with which to measure the damage; this is handled in Chapter 2. The scale should be compatible and capable of measuring damage caused by all the actions considered [1, 14]. In a deterministic approach, individual cases are assessed; this does not give insight into the likelihood of observing damage in a population of buildings. For this, computing the probability of damage is needed.

Secondly, to accurately determine the probability of damage, several fundamental aspects about the masonry need to be known. Some are obtained from earlier, referenced studies; for instance, the characterisation of the material properties and their variability is procured from the extensive research of Jafari et al. (2017); here, the expected variations of, for example, the tensile

strength or the Young's Modulus of the masonry is investigated from replicated material tests based on samples from real structures in the Groningen region. Additionally, how cracks propagate in masonry must be understood; this is the basis of the second step. Several experimental campaigns, comprising a multi-scale approach with walls and spandrels, have been conducted with this goal; an overview is provided in Chapter 3. This step is thus to experimentally observe the processes that lead to in-plane, crack-based damage.

The third step comprises the calibration of models capable of replicating the damage of interest. This is included in Chapter 4 which expands on the possible damage-causing actions, how these can be modelled, and what effects are influential and should be considered. Moreover, to determine the probability of damage, numerous and accurate models of structures need to be evaluated; these models call for a representative view of reality. The experiments conducted on masonry walls, monitoring the initiation and propagation of cracks and gathered in Chapter 3, were used in various studies to develop calibrated computational models tuned to replicate the behaviour of the walls not only in terms of stiffness, strength, and hysteresis but also of the intensity and pattern of cracks [1, 2, 3, 12]. These models are partly included in this work in Chapter 4.

The fourth step comprises the investigation of damage as a result of one or several actions with the calibrated models that then become extrapolations to new situations. The models are expanded to simulate the behaviour of masonry walls within the constraints of a structure interacting with the soil and the vibrations of earthquakes; the latter component is taken from a complementary study [5]. The deformation of the soil during earthquake vibrations and in prior potentially damaging processes was seen to lead to increased light damage and earlier damage detection (Van Staalduinen et al. 2018, [4, 15]). This is also introduced in Chapter 4 and further implemented in Chapter 5.

In the exploration with these extrapolation models, the effect of initial damage is also considered. Since soft soils are predominant in the Netherlands, the majority of Dutch buildings, founded on shallow (strip) foundations, need to account for settlements. It follows that settlements are a common cause for existing damage. Therefore, settlement deformations are selected as the cause of the initial damage considered in this work.

These prior steps have dealt with the deterministic, yet vital background for the probabilistic assessment required. These are employed to further the insight into light damage. Using physical modelling to characterise probabilistic behaviour can be a powerful tool (Fiore et al. 2014, Rapone et al. 2020). The extension or extrapolation with the existing calibrated models is explored in

Chapter 5 and used to create a large pool of results where the relationships between damage and parameters such as the material strength, soil type, earthquake intensity, etc. can be explored. These relationships are then captured in a surrogate or regression model. Such a model, investigating the physical implications of the established relationships, is developed in Chapter 5 and used, on the basis of a Monte Carlo simulation, to compute the pursued fragility curves depicting the probability of damage. This represents the fifth and final step of the proposed method. Additionally, Chapter 5 includes fragility curves not only for earthquake damage and earthquake-caused aggravation of existing settlement damage, but also for settlement damage given (curvature) deformations in the soil. These serve as a further example of the methodology presented.

This project comprises therefore, three main research aspects: experiments, FE models, and analyses of the damage behaviour of masonry based on experiments and models.

Yet an additional chapter is included. While the probability of damage is characterised in Chapter 5, the effect of repetition is independently investigated in Chapter 6. This chapter comprises both analyses from the models, to estimate the damage behaviour of masonry, subjected to repeated earthquakes, and from the experiments, subjected to repeated cycles. This is used to compose a damage accumulation function (DAF) that describes how to increase the damage value for earthquakes with different intensities, or how much of an increase can be expected due to the repetition of actions. In a sense, Chapter 6 presents additional fragility curves for the repetition of events over time.

The text is concluded with Chapter 7 which includes the answer to the research questions, an analysis of the limitations of the approach presented, recommendations for future study, and an outlook on relevant topics.

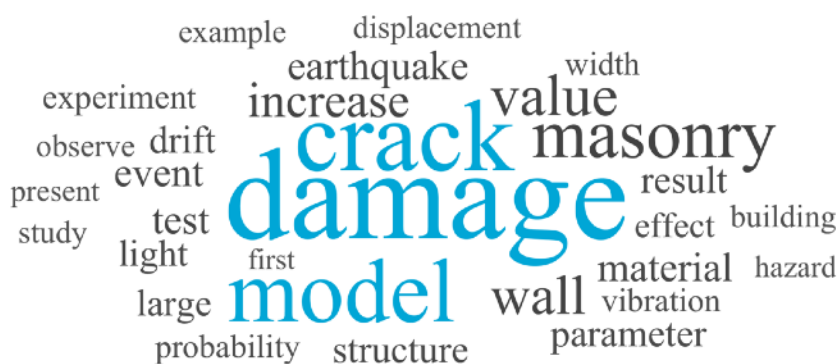


Figure 1.4.3. Word cloud of the text highlighting the 30 words most frequently used.

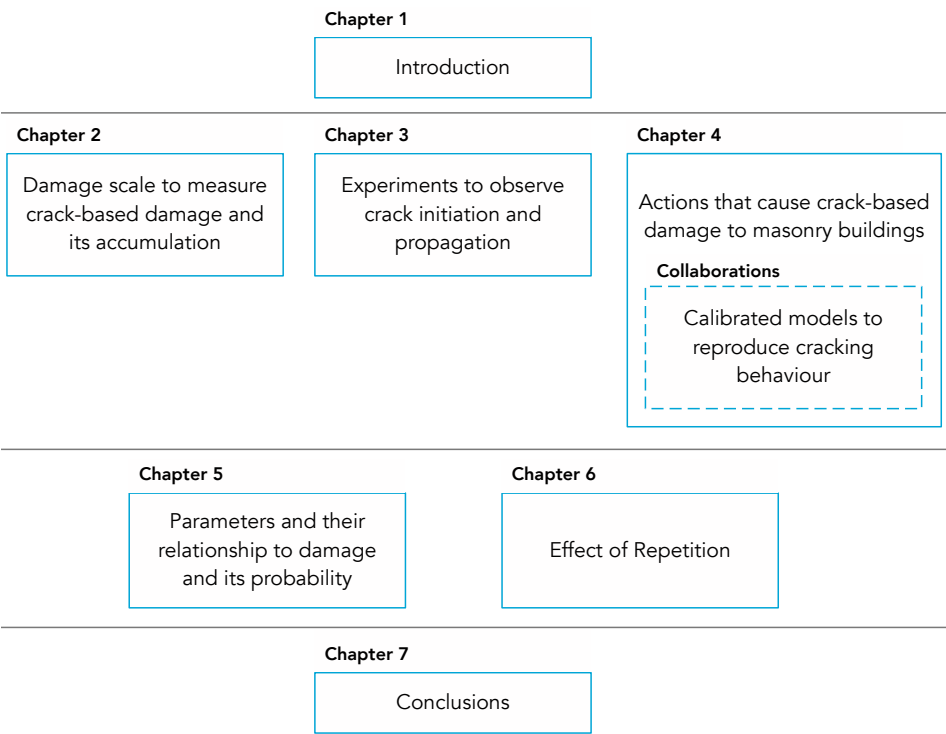


Figure 1.4.2. Outline of this work.

In addition to the outline of Figure 2, which presents the topics treated in this work, the word cloud of Figure 3 illustrates the contents of this text in a key-word based graphic. The thirty words that appear most often are presented and vary in size depending on their frequency, with ‘damage’ being the most used. Similar variations of the same word are grouped; for example, ‘earthquake’ and ‘earthquakes’. Short and common english words are not considered. Each chapter is provided with a similar word cloud further highlighting the topics discussed; however, the chapter clouds exclude the most commonly used words in the rest of the text such that only the unique topics in each chapter are highlighted. Like in several publications, where keywords are employed, these figures represent the content of the chapter; yet unlike those keywords, these are based on the words that are used the most.

Chapter 2

Damage Metric for Masonry Cracking

What is a damage scale or measure capable of objectively characterising masonry light damage (for various relevant causes)?

This chapter proposes Ψ , a crack-based damage parameter, for the objective measuring of damage and its aggravation ($\Delta\Psi$). The content is partly based on several adapted publications but is expanded to include unique insight and new work, consolidating the background of Ψ into a single chapter.

Related works are [1, 2, 14, 23]; see [List of Publications](#).

intensity present
example parameter
state base length
determine width value
repair scale threshold
measure action

Chapter 2 : Table of Contents

2.1. Background and Introduction	15
2.1.1. Necessity for Objective Measurement.....	16
2.1.2. Damage in Masonry.....	16
2.1.3. Fracture Mechanics and Cracks-based Damage	19
2.1.4. Visible Cracks and Visibly Aggravated Cracks.....	22
2.1.5. Limitations of Existing Approaches.....	24
2.2. The Ψ Damage Parameter	28
2.2.1. Damage Classification Based on Visibility and Ease of Repair	28
2.2.2. Cost of Repair	29
2.2.3. Proposal for Ψ Damage Intensity Parameter	32
2.2.4. Thresholds for Ψ , $\Delta\Psi$, and Their Meaning	35
2.2.5. Agglomeration of Ψ	39
2.2.6. Perception of Damage and Ψ	39
2.3. Utilisation: Examples of Application of Ψ	41
2.3.1. Ψ in Experiments surveyed with Digital Image Correlation.....	41
2.3.2. Damage Aggravation by $\Delta\Psi$ in Finite Element Models	44
2.3.3. Predictions with Ψ	46
2.4. Discussion	47
2.4.1. Transitory and Residual Damage	47
2.4.2. Summary of Advantages, Disadvantages and Limitations.....	48
2.4.3. Potential Future Improvements	49
2.4.4. Relevance of Ψ for Modelling and for Real Life Uses	51
2.5. Conclusions about Ψ, $\Delta\Psi$, Ψ_0	51

2.1. Background and Introduction

Prologue

To quantify damage, one must first define it and its quantification. “Damage” is any detrimental change in state, reduction in value, or loss of performance or function. The definition of damage will change depending on the perspective too, whether technical or juridical. This requires additional detail.

In the fields of damage assessment or loss prediction, a damage scale is the first step in defining what kind of damage is being considered and how its expression looks like. The simplest damage scale has two categories: undamaged and damaged. A threshold set for a measure of the damage is used to distinguish between the two states. Depending on the kind of damage being considered, a suitable measure should be selected. For example, a bent steel profile can be considered damaged if a permanent deformation is observable; or, a masonry wall may be described as frost-damaged if spalling or scaling of the bricks has occurred. Damage scales can be subdivided into additional states or grades, each linked to a range of a measurable/observable parameter or a combination of parameters. Each measure is linked to an expression of damage. If damage is defined as observable manifestations of lack of performance, then the threshold is the value where damage becomes observable.

These concepts will be further described in this chapter focusing on the definition of an objective, continuous damage scale to assess crack-based damage in masonry. Section 1 explains what damage actually is, what cracks are in masonry, when they become visible, how they have been measured into damage so far, and why these approaches are insufficient.

Section 2 presents a proposal for a continuous damage parameter linked to the visibility of the damage and its cost of repair, building upon the limitations of earlier strategies. Section 3 shows examples of the application of this parameter to further emphasise its relevance and usefulness. Next, section 4 discusses the limitations and disadvantages of this approach while drawing some comparisons to the world of concrete crack damage. Finally, section 5 presents the main conclusions of this chapter. For the reader that wishes to understand this story in a different sequence, a table of contents is provided.

2.1.1. Necessity for Objective Measurement

A damage scale is objective if a given damage is always categorised into the same damage state regardless of the measuring equipment, the experience of the assessor, or the exhaustiveness of the report. This fact is so important, that this subsection is placed before others to set the context.

The Cambridge dictionary defines objective as being “based on real facts and not influenced by personal beliefs or feelings”. For example, many damage scales, that quantify damage from soil movements, contain descriptors specifying whether doors or windows have become stuck (Grünthal et al. 1998). The degree to which doors or windows are stuck will inevitably depend on the experience of the observer. Such a damage scale could be useful to roughly assign a state to a large number of buildings following a field investigation or rapid assessment (Ademović et al. 2020), but would not be suited to accurately track the increase in damage of a single building over time, especially if several inspectors are involved.

To measure small increases in damage, a damage scale needs to be objective. The definition of the scale must be such that it employs quantifiable measures. If it can be assessable by an automatic system, then the definition is likely objective. Depending on the measure, meaningful thresholds can be set such that damage states are distinct. Empirical data can sometimes help establish meaningful thresholds (Boscardin & Cording, 1989).

2.1.2. Damage in Masonry

This work is about quantifying damage in masonry; specifically, damage that is caused or aggravated by seismic vibrations. For this purpose, one must first understand the different types of damage that can appear in masonry and relate them to different (kinds of) actions that cause them; Figure 2.1.1 and Table 2.1.1 help to provide such understanding (Gill & Malamud, 2014). There are several expressions of damage or symptoms of problems in masonry; the most commonly mentioned is cracking, where the material splits creating fissures or cracks that represent discontinuities or openings.

Cracks result in a reduction in strength (Almeida et al. 2012), allow for ingress of water or pollutants into the material or into the structure (which can result in additional damage due to other causes), and lead to a lesser perception of safety and aesthetic value (Sucuoğlu, 2013). Cracks are usually caused by actions that demand excessive strength of the structure; see next subsection. De Vent (2011) and Van Staaldin et al. (2018) also provide comprehensive strategies to relate damage patterns to actions.



Figure 2.1.1. Examples of expressions of damage in masonry. a) A crack at the corner of a structure. b) Fine vertical cracks in the masonry due to excessive compression (crushing). c) Blistering on the bricks and the mortar due to efflorescence of salts. d) Serious scaling or delamination likely due to freeze-thaw cycles.

Another expression of damage are blisters (Lubelli et al. 2004). These consist of small “bubbles” that form under the surface of the masonry and expel a portion of the material. Depending on the type of blisters, these can lead to larger portions of material delaminating from the masonry (Stryzewska & Kańka 2019). These larger pieces are a symptom called spalling, scaling or flaking and are usually caused by the freezing of moisture inside the masonry, crystallisation of salts/pollutants, or rapid temperature changes such as exposure to fire. Very high frequency vibrations can also lead to delamination. Finally, masonry can also be damaged internally. To determine internal weakening, one must use (ultrasonic) radar, x-ray or other scanning techniques. The degree of blistering or spalling can be related to a section loss at the surface of the material, for instance. Since this work focuses on actions causing cracking however, this expression will be emphasised.

Table 2.1.1. Expressions of damage commonly associated with various processes with mostly mechanically-based processes at the top of the table and chemically-based processes at the bottom. The focus of this work is placed on cracking. An empty circle indicates "a weaker relationship".

Actions / Processes	Expressions of Damage (Symptoms)			
	<u>Cracking</u>	Section Loss		Internal Weakening <i>not observable</i>
		Spalling/ Scaling	Blistering	
Overloading	●			
Earthquakes	●	○		
Vibrations (Other)	●	●		
Wind loading	●	○		
Settlements	●			○
Thermal-hygro variations	●			●
Fire	●	●	●	●
Freeze-thaw cycles	●	●	○	●
Erosion by wind or		●		
Biological (insects or animals)		●	●	●
Salt crystallisation		●	●	●
Material imperfections	○	○	●	●
Formation of expansive compounds (including pollutants, corrosion)	●	●	●	●
Dissolution and leaching		●		●
Ageing		●		●

2.1.3. Fracture Mechanics and Cracks-based Damage

Earthquake and settlements are of interest when considering crack-based damage in the Netherlands (Negulescu et al. 2014). Consequently, the focus in this work is placed on actions that lead to an excessive strength demand from the masonry (structure) and result in visible cracks. Gravity or wind overloading, vibrations, and soil deformations are usually associated with the expressions of cracks.

Masonry is a brittle or quasi-brittle material. When subjected to tensile stresses, the material quickly reaches its tensile strength and fractures. Once fractured, the tensile capacity rapidly diminishes until tension can no longer be resisted. This rapid reduction in tensile capacity after fracturing is called softening and characterises masonry as a quasi-brittle material (Rots & De Borst, 1989).

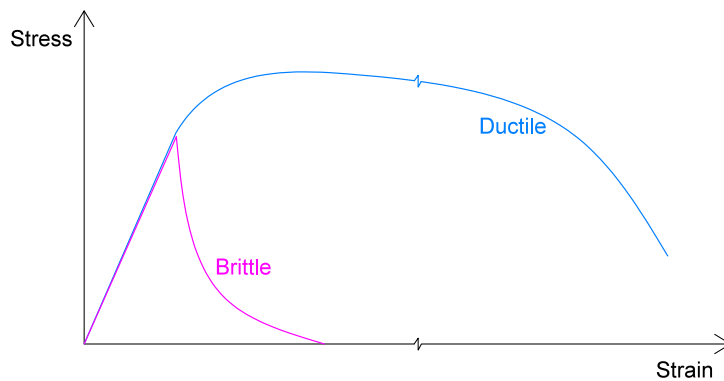


Figure 2.1.2 Tension stress-strain diagram illustrating the behaviour difference between ductile (plastic, hardening) and brittle (with softening, i.e. quasi-brittle) materials.

For (quasi-) brittle materials, such as unreinforced masonry, the maximum tensile strain is near the maximum elastic strain, meaning that shortly after reaching the maximum tensile strength, a crack will form suddenly, without warning prior to it. (Almeida et al., 2012). Additionally, because of this extremely low ductility pre-peak, cracks can also appear in shear of compressive zones, where the conjugated stress direction is in tension. In comparison to ductile materials, brittle ones exhibit no hardening in tension, that is, a stress higher than the maximum elastic stress is not possible and the material exhibits a post-peak softening in the stress-strain relation (Hillerborg, 1985). This means that cracks are unstable: If a crack initiates, the load applied to (the fracture surface of) the material needs to be reduced otherwise the crack will rapidly “snap” through the entire section (Rots et al., 1997). Figure 2.1.2 illustrates this fundamental difference between ductile and brittle materials. It is worth noting that perfectly brittle materials have a theoretical

softening region of zero, while quasi-brittle materials have a “longer” softening curve; since the point of transition between perfectly and quasi-brittle materials is subjective, the materials are here denoted as simply brittle. Masonry and concrete are also known as elastic-softening materials, implying that the strains localise into a crack, while the material at either side of the crack unloads elastically (e.g. Rots, 1985). Micro-cracks coalesce into a visible macro-crack. Cracking in masonry occurs due to fracture of mortar and/or bricks or debonding of mortar and bricks. While the parameters governing these three cases are not equal, all seem to be accurately described by a brittle fracture with softening theory (CUR, 1990; Almeida et al., 2012), such as developed for concrete brittle fracture by Hillerborg et al. (1976 and 1985). The application of this theory has been executed successfully by many authors including: Červenka et al. (1998) including a mixed-mode behaviour (that is, observing the modification of shear on the fracture), or by Schneemayer et al. (2014) who observed the influence of grooves on the fracture’s characteristics. Cracks in masonry usually follow the mortar joints unless the failure mechanism forces cracks to run through bricks, as is the case when shear effects are predominant (Rots et al., 1997).

Settlements, for instance, cause cracking in masonry and the stresses are relieved once the newly developed crack has allowed the structure to accommodate to the settlement (Simpson & Grose, 1996). Similarly, contraction and expansion due to environmental temperature changes, may also lead to cracks which relieve the stresses caused by these actions (Scherer, 2006). Other loads of a dynamic nature, such as vibrations or earthquakes, also produce transient tensile stresses which trigger cracking in masonry. Unless these loads are extreme, cracking is focused around areas where stresses are higher and the dynamic loads cease before the cracks extend.

Sufficient literature is available on the (tensile) strength of masonry and the brittle nature of cracking, but the propagation of brittle cracking under repetitive loading appears to require additional research. Vandoren et al. (2012) also explored the initiation and propagation patterns with a computational model, but did not observe the case of repetitive loading and damage. The propagation and growth of cracks due to repetitive loading (some dozens of applications) must not be confused with the phenomenon of fatigue, common to ductile materials and where the loss of strength is related to an internal weakening of the material due to thousands or millions of stress variations (e.g. traffic or wave loading).

In a masonry element, such as a wall, the loss of local stiffness due to an initiated crack, may be sufficient to accommodate the amplitude of the

repetitive load without further cracking; or, the load progresses the crack until the failure of the entire fracture surface. Figure 2.1.3 demonstrates this dichotomy.

It is important to note that the physical properties of masonry can be divided as those of the anisotropic, heterogeneous composite, or of the individual elements that compose it (bricks, mortar and bond). In the latter case, the parameters of the head (vertical) joints or of the bed (horizontal) joints, as well as the bond between bricks and mortar in these cases, may all be different. This makes reproducing, testing, and modelling masonry quite difficult and vulnerable to uncertainties.

For a comprehensive characterisation of masonry, all tension, shear, and compressive behaviour must be characterised in stiffness, strength, and toughness. The flexural behaviour, which is a mix of tension and compression, is sometimes characterised separately, too. This is because of the highly non-linear properties of the masonry composite. In shear (Mode II), Coulomb friction, consisting of friction and cohesion with softening, represents the behaviour of the joints well.

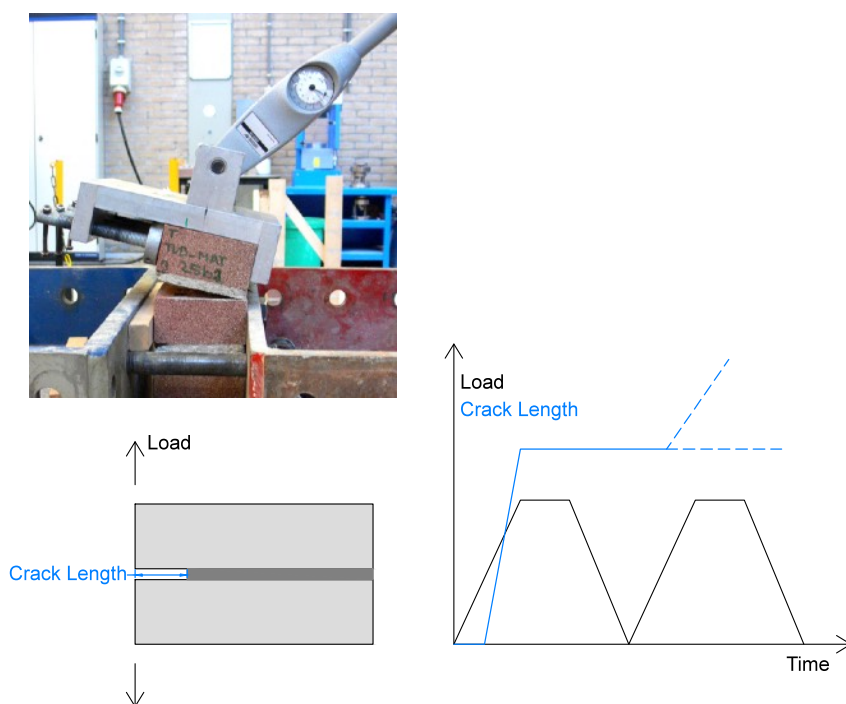


Figure 2.1.3. Behaviour possibilities for illustrative crack propagation when subjected to a load repetition of equal intensity. Top: photo of a bond-wrench test on a masonry couplet.

The compressive behaviour of masonry is more complex (Vermeltfoort, 2005). Here, failure occurs via the crushing of mortar, or of bricks, or spalling of mortar, or of bricks, or by instabilities. Since masonry is heterogeneous, it is particularly prone to buckling instabilities. Local instabilities also contribute to spalling. Here, compressive stresses result in high perpendicular tension stresses that cause fracture of the bricks (Ewing et al., 2004). Masonry in compression has a small hardening region before gradually softening (Lourenço, 1996). This can be modelled as following a bi-parabolic curve. Nonetheless, the compressive behaviour of masonry is not of much relevance when observing light damage due to cracking for low-rise masonry dwellings, and as such, won't be treated further.

Olivito et al. (2001), Grünberg et al. (2005), Reyes et al. (2008), Wang et al. (2012), and Vandoren et al. (2012) in particular, have all looked at the initiation and propagation of cracks in masonry. All of these studies agree: that the tensile capacity of masonry is low, that the bond between bricks and mortar is the most likely place for failure, and that cracks can propagate rapidly due to the brittle nature of the bond. From these and other studies, the path of the crack (or crack pattern), can be inferred based on the stress conditions. As such, the initiation and propagation of tensile cracks is a fairly certain phenomenon when the load and boundary configurations and material properties are known. However, none of these studies addresses the propagation of cracks under cyclic or repetitive loading. Here, the behaviour of a crack or of a crack pattern on a wall is still unknown. Engineering judgement predicts that for repetitive increasing loading, cracks should grow, but for repetitive constant loading this is difficult to infer.

2.1.4. Visible Cracks and Visibly Aggravated Cracks

So far, cracks have been presented as a relevant expression of damage in masonry. It follows that wide cracks correspond to more intense damage than narrow cracks. There are several ways to categorise the severity of cracks: the degree to which they compromise watertightness, the cost of repairing the masonry, or the visibility of the cracks. For the first, depending on the type of masonry, one could establish a relationship between the width of a crack and the water permeability over a unit length; setting meaningful threshold however, is not straightforward. For the second, repair or intervention techniques will differ depending on the intensity of the damage, varying from sealing or repointing to replacement. While thresholds can be set, these are not readily apparent when detecting the damage. The visibility of the damage, albeit subjective, does present an intuitive path to selecting thresholds for both

the initiation as the propagation of damage and it's directly related to the width of the cracks and thus the intensity of the damage.



Figure 2.2.0. Photographs of cracks in bare masonry walls. (a) Small crack narrower than 0.5 mm; (b) crack approximately 2 mm wide; (c) crack narrower than 2 mm; and (d), wider than 5 mm. Adapted from [SBR].

In the best of lighting and contrast conditions, the normal human eye can distinguish lines down to 30 μ m in width (see for instance, Österberg, 1935). The highest display resolutions on available mobile devices today have pixel sizes of 45 μ m, while high-resolution computer monitors have pixel sizes of approximately 0.2mm and conventional LCD monitors of 0.5mm. It follows that on a rough surface such as a wall, in particular when it has not been plastered, cracks narrower than 0.1mm are almost impossible to detect; in the context of visible damage, no damage would be apparent. Based on practical experience during testing, the limit of 0.1mm was confirmed as a sensible lower boundary to detect damage.

On a wall with one crack, when a second crack becomes visible, damage on the wall has become visibly more intense. It is more difficult, however, to determine when an existing crack has become visibly wider. Comparing two lines side-by-side or observing a line become wider, makes it easier to determine if a line is thicker. Cracks do not behave this way; the earlier state of

the crack is not available to compare directly (unless two photographs are compared) nor do cracks coincidentally widen under observation. As a rule of thumb, narrow cracks must triple before an increase can be perceived, while wider cracks of 10mm may be only 10% wider before aggravation becomes observable.

Similarly, an aggravation of damage due to an increase in length can be considered. Seldom do cracks propagate in length without increasing in width. Moreover, the noticeability of an increase in length is actually linked to a local increase in width. In other words, the tip of the crack, which was invisible before, will become wider such that it will cross the threshold of what is visible. Hence, an increase in length is a discussion of a local increase in width at the crack tip.

2.1.5. Limitations of Existing Approaches

An extensive presentation of damage definitions and quantifications will not be presented. Instead, this subsection focuses on the strategies employed by some key sources and highlights their limitations when attempting to objectively quantify crack-based damage aggravation.

Alternatively, the reader is referred to the work of De Vent (2011) who collected and contrasted a multitude of damage assessment strategies from various handbooks and sources. They identified four ways in which damage was classified: 1) based on the material where damage is present, 2) based on the type of element where damage appears, 3) based on the cause of the damage, and 4) based on the appearance or type of damage. For this work, several of these classifications are preordained: the material is masonry, the location are walls, and the appearance defines crack-based damage.

In this context, a limited field of masonry crack-based damage can be scrutinised. The European Macroseismic scale (EMS) includes a damage scale for masonry buildings subjected to earthquakes. It is discretised into five damage grades or states with the following descriptors. Sometimes, DS0 (No damage) is included.

Damage Grade 1 (DS1): Slight Damage. Hairline cracks in very few walls; fall of small pieces of plaster; cracks in a few tiles. Generally, the damage is mostly cosmetic and easily repairable, affecting non-structural elements.

Damage Grade 2 (DS2): Moderate Damage. Small cracks in many walls; fall of fairly large pieces of plaster; cracks in chimneys, often from top. Some structural elements might be slightly affected. The damage requires more

significant repair but does not typically compromise the overall structural integrity of the building.

Damage Grade 3 (DS3): Substantial to Heavy Damage. Large and extensive cracks in most walls; partial collapse of chimneys; detachment of roofs from the main structure. Structural damage is evident, and there might be a need for extensive repairs or reinforcement before the building can be considered safe for occupancy.

Damage Grade 4 (DS4): Very Heavy Damage. Serious failure of walls, with partial collapses; collapse of roofs and floors. The building has sustained serious structural damage across multiple elements, potentially requiring very extensive repair or suggesting that demolition and rebuilding might be more feasible.

Damage Grade 5 (DS5): Destruction. Total or near-total collapse of the structure. The building is destroyed to the extent that it is beyond repair, and reconstruction is necessary.

There are several issues with this scale if one wants to look at damage consisting of small cracks. First, the descriptors are not precise enough to determine an aggravation of damage. If the grades or classes are large, when considering damage aggravation, few cases would change classes, so the conclusion would be that there was no aggravation in damage. A continuous scale avoids this issue and is thus ideally suited to evaluate damage aggravation.

Many studies have been specific about the usage of crack width as the main descriptor or measure in the scale. Burland et al. (1977), Boscardin & Cording (1989), or Mair et al. (1996) all use crack width to define damage grades. However, they refrain from being specific about the crack widths linked to the threshold between grades. The number of cracks is mentioned to have some influence but is not specified. Hence, it is possible that two inspectors would assign two different damage grades to the same structure - this is not objective.

Some studies that employ a continuous scale, actually look at crack width as the only indicator; see Chen & Hutchinson (2010). The maximum crack width is the measure of damage. This is useful when observing a structure where only one crack is present or only one crack is expected, like a single beam subjected to three-point bending. With this approach, it is possible to accurately measure damage and its aggravation. The issue arises when several cracks appear. Typically, the maximum overall crack width is used, but this is not representative of damage where multiple cracks are present.

Other studies make the link directly to the probability of damage. This is the case, for instance, of Waarts (1997). Here, the flexural strength of the masonry is used as the threshold for damage. This doesn't not have a clear relationship with visible crack-based damage.

Yet other studies set the threshold on the cause of damage. This is the case of the SBR (Trillingsrichtlijn A: Schade aan bouwwerken, 2017). Here, a limit on the intensity of a vibration is set so that damage to a neighbouring building is unlikely. For 'sensitive buildings', which presumable are those with a certain degree of initial damage, the limits are reduced. Nevertheless, the type of damage that is being limited is not discussed.

Comparison vs. Classification Strategies for Concrete Damage

Like masonry, concrete can also develop cracks. Crack-based scales for concrete also exist. However, concrete is typically reinforced. The reinforcement changes the nature in which cracks appear, usually producing a greater number of fine, parallel cracks.

Farhizadeh et al. (2013) employ the maximum crack width to classify crack-based damage in concrete walls. This is consistent with the Structural Health Monitoring strategies employed for concrete where a single crack is used to assign a damage grade. Whether there are many other cracks of similar width or none at all, is not considered. However, Farhizadeh et al. propose a new damage index based on the fractal dimension formed by a net of cracks. In reinforced concrete, cracks are "smeared" due to the rebar; a denser net of cracks, and thus a higher fractal dimension, will correspond to higher strains and greater damage. According to the consulted work, this damage index offers a good representation of the damage state of a concrete component as it correlates better with the loss of lateral stiffness of the tested shear walls. However, this approach is not useful for unreinforced masonry where cracks coalesce into wider, discrete cracks instead of forming nets.

Bhowmick & Nagarajaiah (2020) work on identifying multiple cracks from a concrete element but do not elaborate on the intensity of the damage due to the multiple cracks. Soysal & Arici (2023) however, investigate cracking over the thickness of a concrete monolith. On its face, multiple parallel cracks can appear depending on the hazards intensity. To characterise the intensity of damage, they employ the sum of the multiple crack widths. In this manner, whether the crack strain localises into a single crack or is smeared over multiple openings, is considered in the damage grading.

Similarly, Younis et al. (2020) recognise that using a crack width to define the damage state of large-diameter reinforced concrete pipes is subjective during

visual inspections. Instead, they conduct destructive tests to relate the expected crack width to a deformation-based indicator, more compatible with current laser inspection tools, in order to improve the relevant ASTM standard.

In sum, literature about crack-based damage classification strategies for concrete is scarce. The focus lies on the maximum crack width to identify the damage intensity. In the case of parallel cracks, the total crack width is also used.

Summary of Knowledge Gaps

Specific gaps about existing strategies to assess damage in masonry have been recognised. First, imprecise descriptors make it difficult or subjective to classify cases into grades. These are missing precise values for the width and number of cracks. Crack length is not mentioned. Second, the coarseness of the grades doesn't allow to measure small increases in damage.

These translate into requirements for the proposal of a new damage scale.

2.2. The Ψ Damage Parameter

To measure whether damage is present or has worsened, a damage scale is useful. In this section, a damage parameter and its corresponding damage scale is proposed. The goal is to formulate a scale that is objective, quantitative, continuous, comparable between cases, related to detectability and ease of repair (cost), relatable to existing scales, and applicable to the type of damage being investigated.

Hence, the new parameter is meant to characterise crack-based masonry damage associated with “light damage”. The parameter will be used to assess damage and increases of damage in experiments, thought, it can be used to evaluate damage in numerical models, too.

2.2.1. Damage Classification Based on Visibility and Ease of Repair

Burland & Wroth (1977) first proposed a damage scale based on the width of the cracks and used it to analyse masonry damage in structures subjected to soil deformations. In the same context, Boscardin & Cording (1989) employed the same damage scale to compare empirical data on soil deformations and building damage. Table 2.2.1 summarises this scale. Heath et al. (2008) also uses a similar crack-based scale derived from the Australian Standard AS2870; the scale is based on a single crack width.

Indeed, while the scales are based on the width of cracks, the number of cracks also affect the damage state that a building would be assigned to. This is not entirely defined in the scale, leading to loss of objectivity. Additionally, other descriptors such as damage on service pipes, also partake in the scale. The thresholds are defined based on the type of repair that would be needed and thus indirectly also on the cost of the repair. Nonetheless, one should not assume that crack width is a hard measure to distinguish between repair strategies.

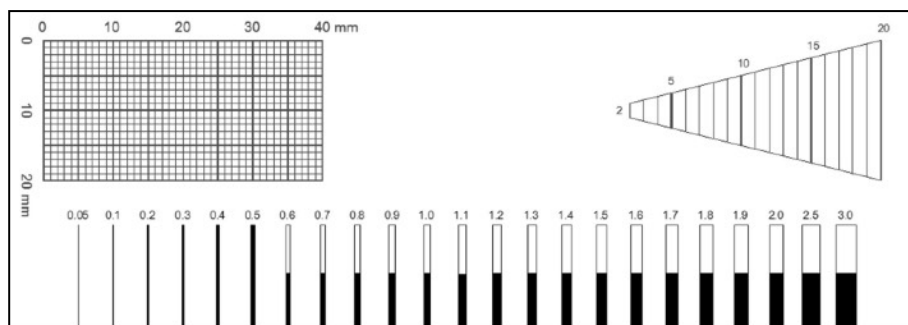


Figure 2.2.1. A transparent ruler usually used to determine crack width when held against a wall. Printed 1:1.

To formulate a more objective scale, the intensity of the damage must be related to a single expression of damage and be fully quantifiable, regardless of the number of the cracks. Furthermore, the crack width, directly related to visibility, is a good measure to quantify aesthetic damage. In most damage scales for measuring building damage, this first grade is denoted damage state 1 - DS1. In the scale initially proposed by Burland & Wroth (1974), DS1 is subdivided into 3 categories.

2.2.2. Cost of Repair

The damage scale proposed by Burland et.al.(1977) and expanded by Boscardin and Cording (1989) is roughly related to the relative cost of repair between the different strategies required for different types or intensity of crack-based damage. Consequently, the proposed parameter is also related to the cost of repair. To better explore this relationship, Table 2.2.2 has been put together enumerating the costs of common repair strategies in the Netherlands. For example, "very slight" damage would require repainting at about €40/m², while "slight" damage would need repointing at €100/m², about 2.5x as expensive. Similarly, "moderate" damage, requiring the replacement of portions of masonry, could cost €400/m², or about 10 times more than "very slight" damage. This information is used to inspire the formulation of the proposed parameter; see next.

Table 2.2.1. Adapted from Burland et.al. (1977), Boscardin & Cording (1989) and Giardina et al. (2013). Damage scale definition based on width of repair and thresholds set by ease of repair. Notice that crack length is not mentioned.

Category of damage	Damage	Description of typical damage and ease of repair	Approx. crack width (mm)
Aesthetic damage (DS1)	Negligible	Hairline cracks of less than about 0.1mm width.	up to 0.1mm
	Very slight	Fine cracks which can easily be treated during normal decoration. Perhaps isolated slight fracturing in building. Cracks in external brickwork visible on close inspection.	up to 1mm
	Slight	Cracks easily filled. Redecoration probably required. Several slight fractures showing inside of building. Cracks are visible externally and some repainting may be required externally to ensure water tightness. Doors and windows may stick slightly.	up to 5mm
Functional damage, affecting service (DS2-DS3)	Moderate	The cracks require some opening up and can be patched by a mason. Recurrent cracks can be masked by suitable linings. Repainting of external brickwork and possibly a small amount of brickwork to be replaced. Doors and windows sticking. Service pipes may fracture. Weather-tightness often impaired.	5 to 15mm or a number of cracks > 3 mm
	Severe	Extensive repair work involving breaking out and replacing sections of walls, especially over doors and windows. Windows and door frames distorted, floors sloping noticeably. Walls leaning or bulging noticeably, some loss of bearing in beams. Service pipes disrupted.	15 to 25mm but depends on number of cracks
Structural damage, affecting stability (DS3-DS4)	Very severe	This requires a major repair involving partial or complete rebuilding. Beams lose bearing, walls lean badly and require shoring. Windows broken with distortion. Danger of instability.	> 25mm but depends on number of cracks

Table 2.2.2. Approx. unitary repair cost of typical masonry damage in the Netherlands in 2020. Adapted from [IMG repair matrix, 2020].

Type	Repair Type	Unit	Lower bound.	Upper bound.	Median Unit. Cost
			> 10 m, > 10 m ²	1 m, 1 m ²	
All	Dilation joint, conversion or new	€ / m	€ 25	€ 35	€ 30
	Painting / Coating	€ / m ²	€ 35	€ 50	€ 40
Exposed brick, base masonry	Repointing	€ / m ²	€ 60	€ 190	€ 100
	Repointing with epoxy mortar	€ / m ²	€ 120	€ 440	€ 280
	Replacement of individual units	€ / unit	€ 50	€ 120	€ 100
	Replacement of masonry	€ / m ²	€ 280	€ 700	€ 400
	Reinforcement cavity: helical	€ / m	€ 90	€ 165	€ 130
Plastered masonry	Local replastering/filling of	€ / m	€ 70	€ 115	€ 100
	Replastering	€ / m ²	€ 155	€ 215	€ 190
	Repair cracks and base for interior plastering	€ / m	€ 80	€ 225	€ 150
Interior Finishing (in addition to plastering)	Decorative plastering	€ / m ²	€ 50	€ 125	€ 90
	Wallpaper	€ / m ²	€ 30	€ 85	€ 50
	Wallpaper (Fibre)	€ / m ²	€ 60	€ 200	€ 100
Lintels	Soldier lintel repair /	€ / m	€ 100	€ 500	€ 300
	Concrete lintel repair / replacement	€ / m	€ 160	€ 800	€ 500
	Steel lintel replacement	€ / m	€ 800	€ 900	€ 850

2.2.3. Proposal for Ψ Damage Intensity Parameter

The earlier scales based damage on crack width and partly on the number of cracks. However, the number of cracks and the relative importance of numerous cracks is not clear. Therefore, a new damage scale is proposed that includes this. The number of cracks, and their length, will also be related to the cost of repair.

The resulting damage scale can be used to determine the importance of various damage situations and evaluate modelling results. Furthermore, the way it is presented indicates the amount of repair costs, as will be explained later.

The damage scale shown in section 2.2.1 can be associated with a continuous parameter fit to match the most relevant thresholds between grades. This parameter is symbolised with the capital greek letter Ψ . First, the threshold between negligible and visible damage, corresponding to crack widths of 0.1mm, is matched to a value of $\Psi=1$. The next threshold, for cracks wider than 1 mm which would then require repair, is matched to a value of $\Psi = 2$. This results in the following fit (Equation 2.1), where c is the width of the crack and the factor 2 and exponent 0.3 are algebraically solved for. The trend of this power law is illustrated in Figure 2.2.2, where the link between Ψ and crack width is also shown.

$$\Psi = 2 \cdot c^{0.3} \quad \text{Equation 2.1}$$

However, the number of cracks (n) is also a relevant parameter. This is not clear from the damage scale defined in Table 2.2.1 but, section 2.2.2 treating the cost of a repair intervention, is presented to complement this definition. So as to not affect the relationship presented in Equation 2.1, another power law is presented and defined in Equation 2.2. Here the exponent of 0.15 means that one additional crack increases the measured damage by 11%, a further additional crack by 6%, the next one by 4%, etc. This influence is illustrated also in Figure 2.2.2.

$$\Psi \sim n^{0.15} \quad \text{Equation 2.2}$$

This is congruent with costs where an additional crack does not represent much additional labor nor material. It also means that the value of Ψ remains close to the definition of the Burland damage scale.

Finally, there is the matter of crack length. Longer cracks are more costly to repair. And while some contractors may charge repair costs directly proportional to the crack length, it is the crack width which defines the strategy of repair and thus the main cost; see again Tables 2.2.2 and B.1. Consequently,

the cost of repair of a wall with several cracks of different widths will be dominated by the width of the widest crack. More importantly, the visibility of the damage will be even more influenced by the widest cracks. Yet, the cost of repairing two cracks of different width should be offset towards the longer crack, even if that is the narrower crack and especially if it is the wider crack. This is achieved by weighting the average crack width by the length of each crack. Since crack width is more important, it is set squared in Equation 2.3, where the weighted average crack width is determined. The choice for the square exponent follows from Table 2.2.2 and engineering judgement; ultimately, since costs can vary, the exponent is somewhat arbitrary.

$$c_w = \frac{\sum_{i=1}^n c_i^2 \cdot L_i}{\sum_{i=1}^n c_i \cdot L_i} \quad \text{Weighted crack width: Equation 2.3}$$

$$c_i = \sqrt{c_o^2 + c_s^2} \quad \text{Squared Sum. Equation 2.3b}$$

Where c_i is the maximum crack width of crack i in millimetres, and L_i is the length in millimetres. The crack width is composed by both the opening (c_o) and sliding (c_s) components. Most visible cracking is characterised by crack opening (Mode I), but sliding at the interface (Mode II) can also be visible damage as small parts around the fracture break off. The resulting crack width is the squared sum of the opening and sliding displacements as per part b of equation 2.3. In most cases however, only the opening component is relevant.

The final equation to compute Ψ is thus as follows:

$$\Psi = 2 \cdot n^{0.15} \cdot c_w^{0.3} \quad \text{Definition of } \Psi: \text{Equation 2.4}$$

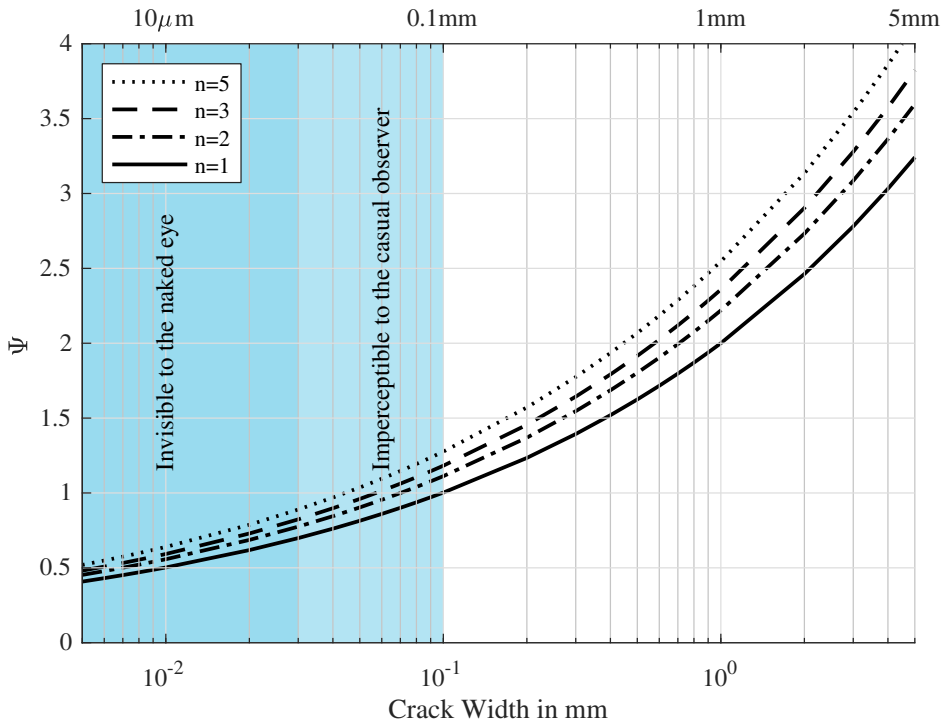


Figure 2.2.2. Relationship between the width of cracks (c), the number of cracks (n) and the damage parameter Ψ .

While the weighted average may give the impression that the intensity parameter would decrease if a second narrow crack appears, the inclusion of n and the selected exponents makes sure that additional cracks always leads to increased damage. For example, if a single crack of 1 mm width ($\Psi=2$) is joined by a second crack of 0.1 mm width that has just become visible, the resulting Ψ is 2.2. If the second crack is much longer, however, then it is theoretically possible for the value of Ψ to decrease. This situation is unlikely since the aggravation of damage is usually associated with an increase in width and length of all visible cracks. Additional discussion about the meaning and limitations of Ψ are examined in the following sections.

In Figure 2.2.3 examples of a masonry façade with various crack patterns are given. This illustrates the types of crack combinations that lead to typical Ψ values.

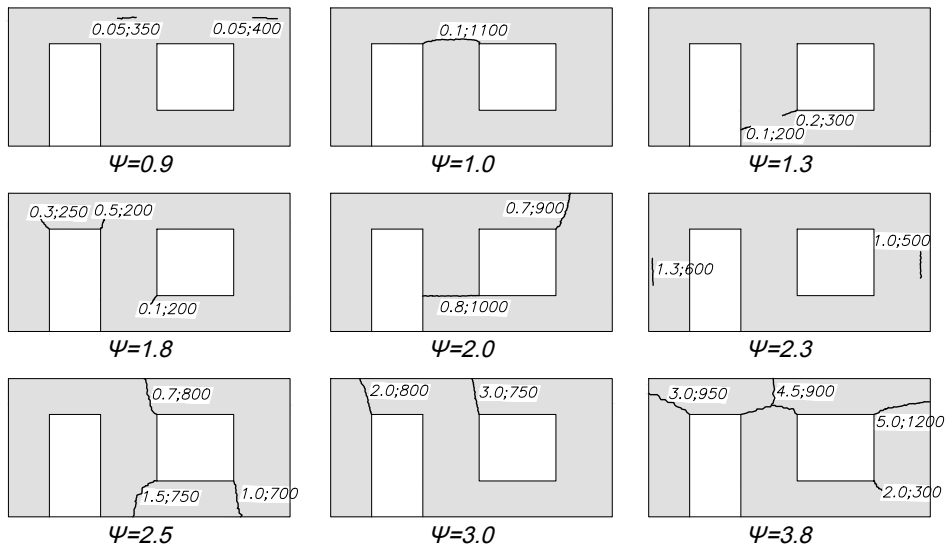


Figure 2.2.3. Examples of a masonry façade displaying cracks (width; length in millimetres) and their evaluated Ψ value.

2.2.4. Thresholds for Ψ , $\Delta\Psi$, and Their Meaning

Ψ is a continuous damage parameter, which means that any positive rational scalar or number between zero and infinite are defined. In practice, values of Ψ above 9 are meaningless as masonry structures reach the near-collapse state at $\Psi=8$ when cracks are the result of in-plane damage on structural walls. In fact, while cracks are a good measure of light damage for DS1 or DS2, as damage increases, cracks will fail to capture the level of safety of a structure, usually better associated with its remaining capacity. For lateral loads, the inter-storey drift is a good predictor of the remaining structural capacity, for example. This means that values of Ψ above 4, no longer related to light damage, are not very useful.

Despite its continuous nature, it is still convenient to set thresholds for Ψ relating it to various categories of damage. First, $\Psi=1$ is perhaps the most useful threshold. It distinguishes between invisible or visible damage. In the most strict analyses of crack-based damage on masonry, potentially-visible damage is the absolute lowest threshold. Because, multiple cracks may be involved, these thresholds can go up to a value of 1.4, as is presented in Table 2.2.2, comparing traditional damage states (EMS) and the damage categories initially set by Burland et.al. (1977). Next is the value for $\Psi=2$ which corresponds to cracks that usually require (or are) repaired. Finally, a value of $\Psi=3.5$, with cracks in the order of 5mm determine the end of light damage.

Additionally, while Ψ is meant to characterise crack-based masonry damage associated with “light damage”, experiments on masonry walls, tested until near-collapse, help link Ψ to the remaining damage states, DS3 - DS5. This is detailed in Table 2.2.2 which also presents descriptors for Ψ with the values commonly associated to them. Values of Ψ below 1 are difficult to measure in practice since cracks cannot be observed. However, strain gauges, crack meters, cameras and other sensors will be able to capture these low values. Also, Ψ can be used to evaluate damage in numerical models, too. In this context, any value of Ψ can be measured. These invisible values are useful for determining the initial condition of a pre-damaged structure where Ψ_0 is later affected by a subsequent action.

Table 2.2.2. Comparison Damage States and damage levels with approximate values of Ψ .

State	DS0		DS1		DS2
Level	DL0	DL1	DL2	DL3	DL4
Ψ	$\Psi < 1$	$1 < \Psi < 1.4$	$1.5 < \Psi < 2.4$	$2.5 < \Psi < 3.4$	$\Psi > 3.5$
Aproximate Crack Width	Imperceptible cracks	up to 0.1mm	up to 1mm	up to 5mm	5 to 15mm

The association of Ψ with the damage states (DS) from the EMS scale is fuzzy. This is because the EMS scale is not entirely crack-based. A similar issue occurs when comparing Ψ to the scale of Burland. Since the latter is not entirely objective, the separation between grades and Ψ is not always fixed. For this reason, certain values of Ψ could be linked to multiple DSs. Furthermore, DS1 and DS2 have been classified into ‘light damage’. Thus, the lower threshold for the beginning of light damage is also unclear. The strict definition is that the just-visible cracks mark the initiation of light damage ($\Psi=1$), as adopted in Table 2.2.3. However, a more practical threshold above a Ψ of 1 can also be set; see Section 3.2.

The higher damage states, linked to stability and near-collapse, are associated with sudden failures, large shear deformations, crushing and compressive failures, large amounts of debris, partial collapses, connections failures, and sudden increases in drift, for example. Some, like a reduction in a lateral or vertical force or displacement capacity, are not visible. These indicators offer a more reliable link to structural damage than Ψ .

Table 2.2.3. Overview of the scalar value of Ψ for SLS (black) and ULS (grey). ULS values are derived from experimental results, see Chapter 3.

Values of Ψ	Description	Representative Crack Width	Damage State	
$\Psi = 0$	No damage	N.A.	DS0	L
$\Psi \approx 0.5$	Invisible damage	< 0.1 mm		i
$\Psi \geq 1.0$	Just-visible light damage	> 0.1 mm		g
$\Psi \geq 2.0$	Easily-observable light damage	> 1 mm	DS1	t
$\Psi \geq 2.5$	Costly light damage	> 2 mm	DS1 or DS2	D
$\Psi \geq 3.0$	End of light damage	> 4 mm	DS2	a
	Severe.			m
$\Psi \geq 4.5$	No longer light damage, usage of a different damage metric is recommended.	> 10 mm	DS3	a
$\Psi \geq 6.0$	Very Severe	> 25 mm	DS4	b
$\Psi \geq 8.0$	Near Collapse	> 50 mm	DS4 or DS5	i
				l
				t
				y

Initial Damage: Ψ_0

The term Ψ -zero refers to a value of Ψ at the beginning of the assessment. It is used to contrast an initial condition to a later one. When considering a situation with existing yet invisible crack-based damage, a value of $\Psi_0 \approx 0.5$ can be assumed. This is typically sufficient for cracking to have developed (see 2.1.3: Fracture Mechanics) but is far from visible damage.

Increase in Damage: $\Delta\Psi$

The continuous nature of Ψ is meant to give it the ability to accurately track small increases in damage. In fact, in the study of damage aggravation, more important than measuring Ψ is the evaluation of $\Delta\Psi$ or the increase in damage. For $\Delta\Psi$, thresholds can also be set. In particular, the question of when does an increase in damage become noticeable or significantly increase the cost of repair, is paramount.

$$\Delta\Psi = \Psi - \Psi_0$$

Damage Increase: Equation 2.5.

Where Ψ_0 is the initial damage condition and $\Delta\Psi$ is the increase in damage. Because of the power law of Equation 2.4, the importance of the absolute

damage increase remains constant within the light damage range ($\Psi_0 < 3$); this means that an increase of $\Delta\Psi$ of 0.2 for instance, will be equally noticeable and affect the cost of repair in a similar manner for a case of $\Psi_0=1$ or $\Psi_0=2$. In both situations, a $\Delta\Psi$ of 0.2 represents a measurable increase in damage and is used as the lower threshold for quantifying an aggravation in crack-based damage. Note that “noticeable” is used in this work as an indication of whether a casual observer would perceive the damage or its increase.

*Table 2.2.4. Overview and thresholds for $\Delta\Psi$ when $\Psi_0 \geq 1.0$ for noticeable increases of damage. *Note: photographs and measurements are considered to include simple tools as those available to a common observer. Hence, these threshold are not applicable for monitoring.*

Values of $\Delta\Psi$	Description
$\Delta\Psi < 0.1$	Hardly noticeable
$0.2 > \Delta\Psi \geq 0.1$	Only noticeable in comparison photographs/measurements*
$0.5 > \Delta\Psi \geq 0.2$	Above 0.2 an increase in damage becomes visible for recurrent observers
$1 > \Delta\Psi \geq 0.5$	Evident damage increase, significant influence in the cost of repair
$\Delta\Psi \geq 1$	Increase in damage contributes most to repair cost and detectability; fully attributable damage

These thresholds are meant as a guide of what sort of damage increase would be noticeable to the occupants of a building. Since some building users are more careful than others and will employ photographs or even measuring rulers to monitor damage, it is clear that the thresholds must present averages or expected values from which it is sensible to consider that an aggravation of damage would be perceived.

In this light, it must be said that the thresholds were not set on the basis of an extensive survey of what building users would notice. The aspect of time would complicate such a survey besides the fact that the survey would be biased if participants were conscious about monitoring damage aggravation.

Instead, the thresholds come from three sources: 1) the increases of damage reported with the assumption that if small increases are never reported it is also because they could not be detected. The database for this, in any case, is quite limited [8]. 2) the relationships between width and length observed from the experiments. This is well documented in Chapter 3. And 3), a study of many hypothetical cases varying crack width, length and number, in combination with engineering judgement to conclude where the thresholds should lay. Some examples appear in [Appendix B](#). Note that the detectability of an increase in

length is linked to the local increase in width at the crack tip. This means that the length of the crack is determined by a lower threshold of what width can be observed.

Relative Increase in Damage: $r\Delta\Psi$

The relative increase, $\Delta\Psi/\Psi$ or $\Delta\Psi/\Psi_0$, can also be used to characterise damage aggravation. However, because Ψ is based on a power law, the importance of relative increases are dependent on the starting value of Ψ . For example, an increase of 50% when $\Psi_0=0.5$ doesn't reach visible damage; but, if $\Psi_0=2$, the increase of $\Delta\Psi=1$ is significant. For this reason, the $r\Delta\Psi$ is only sporadically used, with a preference instead to the absolute $\Delta\Psi$ as presented in Table 2.2.4.

2.2.5. Agglomeration of Ψ

The Ψ parameter has been mainly developed to assess the progression of damage on a certain specimen or between identical specimens. However, sometimes different walls or structures would like to be compared to each other to determine which presents lower or higher damage. In this case, it is convenient to express a relative version of Ψ based on the surface area of the masonry:

$$\Psi'_i = \Psi_i \cdot \frac{A_i \cdot \zeta_i}{\bar{A}} \quad \text{Equation 2.6.}$$

Where A_i is the surface area of the wall i , \bar{A} is the mean area of the walls considered and Ψ' is the relative Ψ . Additionally, if the walls are of different masonry material, the unitary cost of repair ζ can be included in the comparison.

Furthermore, if a structure where each wall is monitored separately wants to be characterised with a single value of Ψ , the damage in the N walls can be accounted as:

$$\bar{\Psi} = \frac{1}{A_T} \sum_{i=1}^N \Psi_i \cdot A_i \quad \text{Equation 2.7.}$$

Where $\bar{\Psi}$ is the mean Ψ value and A_T is the sum of the surface areas. However, Ψ can be directly determined as the sum of all cracks in the structure.

2.2.6. Perception of Damage and Ψ

Two identical masonry walls subjected to similar actions will be similarly damaged; however, if one wall is finished with a plaster that is old and stiff while the other has walls covered in flexible wallpaper, the former will display any crack prominently, while the latter will hide cracks. The first wall will be

perceived to be more damaged than the second one. This is the perceived damage state which may differ from the actual damage state. The actual damage state will determine the damage progression behaviour of the masonry and is referred to as the physical damage. This work focuses on physical damage and observes the processes that lead to it, but it is still important to acknowledge that damage can be subjective and that certain combinations of architectural building parameters will lead to more reported damage. Understanding how damage is likely to be perceived also gives insight into overall damage conditions. Furthermore, in some cases, reporting the estimated perceived damage may be closer to observations from field cases than the calculated damage, especially if the damage report did not follow an objective procedure.

The following is an empirical proposal of how and which parameters relating to the aesthetic and architectural disposition of the structure, as well as the situation in which damage was observed, may affect the way in which damage is perceived.

$$\psi = \Psi^{\frac{k}{3}} \quad \text{Equation 2.8.}$$

Where:

ψ is the perceived damage intensity (lowercase ψ)

Ψ is the damage parameter measuring physical damage (uppercase Ψ)

k is the average of the empirically-determined influence parameters (on a scale of 1 to 5 with a median of 3) for various category as shown in Table B.2. These values have been determined using expert judgment and interviews with experts in the assessment of masonry damage in the Netherlands; hence, additional, quantitative analyses need to be done to better substantiate them. They are presented here as an illustration of the approach and exemplification of the relationship between actual damage and its perception. It is possible to include as many categories as deemed relevant into the evaluation of the perception of damage. Additionally, the relation can be inverted to try to estimate the actual damage of a structure from a study case report. In the former case, an estimation of how damage will be perceived can be inferred from a numerical model, while in the latter, a more accurate estimation of damage can be registered from an uncertain field report.

The definitions for Ψ are gathered in [Appendix B](#).

2.3. Utilisation: Examples of Application of Ψ

This section is about the utilisation of Ψ in three distinct examples: one about physical experiments, another about numerical models, and a third about predictions. These illustrate different aspects about the usage of Ψ .

To determine Ψ , cracks need to be measured and identified. Work was conducted for this purpose. However, crack surveillance techniques or crack identification procedures are not the focus of this chapter. These are mentioned where necessary but are not explained in detail. The reader is referred to the cited works and related publications.

2.3.1. Ψ in Experiments surveyed with Digital Image Correlation

Photogrammetry techniques can be used to automatically detect cracks (Mojsilović et al. 2016, Dhanasekar et al. 2019, Tung et al. 2008). Digital Image Correlation (DIC) has been increasingly used in laboratories to measure displacement and strains on small samples or large surfaces where the use of multiple sensors is inconvenient (Laurin et al. 2012, Ramos et al. 2015). However, strains are not easily linked to cracks. Usually, measured strains are smoothed out over a certain surface to correct for noise and the relatively low resolution of DIC. The smooth strains are thus not representative of the discrete cracks appearing on masonry specimens.

As part of the experimental validation of the usage of the Ψ parameter, cracks had to be automatically detected to assess the progression of damage over hundreds of loading cycles [4]. The setup thus allows for the observation of the initiation and, most importantly, the progression (in width and in length) of cracks visible and invisible to the naked eye over the entire surface of a full-scale wall. In this manner, the measuring system is compatible with the definition for Ψ (Equation 2.4).

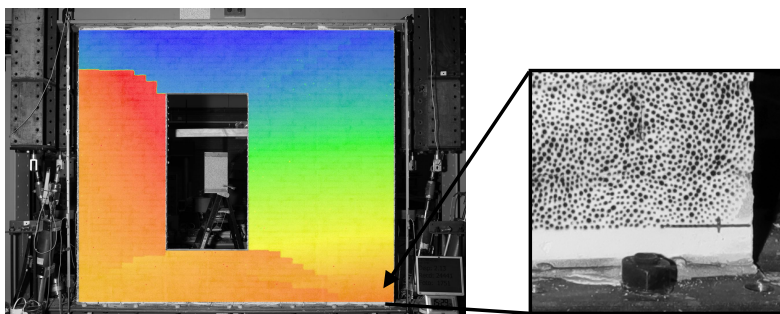


Figure 2.3.1. Laboratory wall specimen (3.1m x 2.7m) overlaid with the horizontal displacement field obtained with DIC during testing of a lateral top displacement in-plane. Right, zoomed-in corner of the wall depicting the speckle pattern used for DIC.

Brief Description of DIC Tool

Figure 2.3.1 presents an example of a 2.7m-tall masonry wall covered in a speckle pattern. In Figure 2.3.1, the displacement field reveals the presence of cracks. The DIC pattern on the wall in combination with the camera allowed for the monitoring of the full displacement field of the wall in a grid with a spacing of 2.7x2.7 mm and a precision of 20 μm , comprising over 1.2 million measurement (or grid) points. Images were taken at precise time-points throughout the test. The accuracy of the setup allows to detect displacements as small as a fifth of the threshold set for visible cracks ($\Psi=1$); this is herein considered as high-resolution.

The raw or unmodified displacement field, acquired by a DIC-algorithm using small subsets (of approximately 10 pixels) to avoid smoothing the displacement values, can be scanned for discontinuities above a certain threshold; large groups of discontinuities are likely to correspond to cracks. The relative displacement between one side of the discontinuity and the other corresponds to the width of the crack. Figure 2.3.2 presents the result of this operation where each crack is automatically characterised in width and length. Note that the wall specimens of both figures are not the same. While many authors utilise strains to map cracks, strains would need to be integrated over a crack-bandwidth to be able to output the crack width and length, and can thus only be used in an illustrative manner. The detection and characterisation of discontinuities, on the other hand, is better tailored to obtain the crack kinematics. Gehri et al. (2020) specify this approach in detail. The resulting data can provide an in-depth look at crack progression; Figure 2.3.3 presents the crack width at the centreline of the crack over multiple experimental cycles. It can be observed that the crack grows in width and in length throughout the experiment. The centreline is captured automatically by following the trend of the maximum width over the crack. It can also be seen that the DIC output is not free from noise; however, with thousands of measurement points over the crack, reasonable values can be computed.

Cracks and Ψ from Experiments

For each frame in the experiment, with crack widths and lengths determined, the Ψ value is computed as in Figure 2.3.4. This illustrates how Ψ increases throughout the experiment, even during cycles of equal amplitude.

While the algorithm employed here was custom-written to detect cracks with the highest accuracy possible, commercial DIC tools have started to implement crack-oriented solutions and it remains convenient to tailor solutions to specific

experiments (Gehri et al., 2020). These analysis tools will allow for an easier characterisation of light damage in masonry.

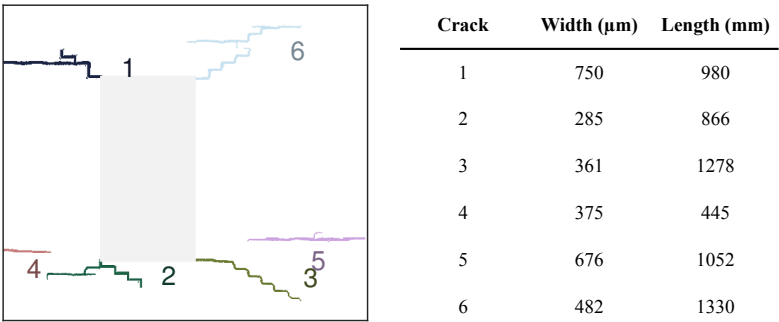


Figure 2.3.2. Detected cracks in DIC data of a laboratory masonry wall. $\Psi=2.2$.

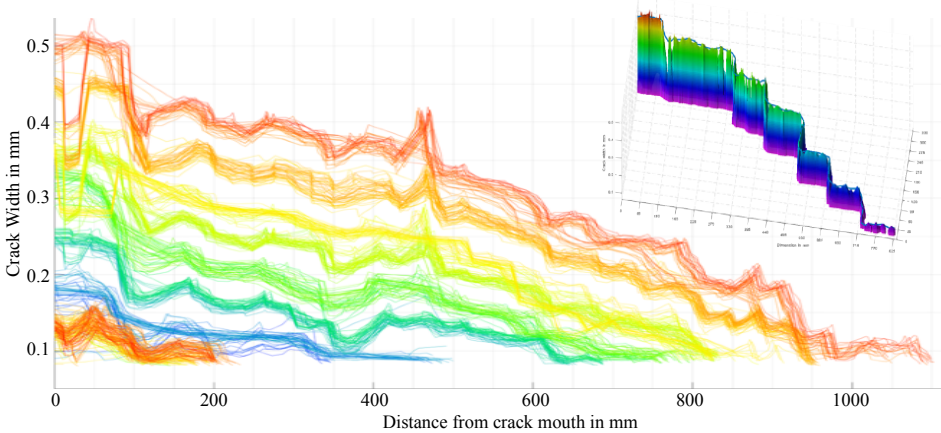


Figure 2.3.3. Crack width against crack length as measured by the centreline of the crack, for numerous test cycles. The slope of the lines is linked to the “tapered-ness” of the cracks. The length is measured over the path of the crack; together with its width, a 3D path emerges, as plotted in the top right corner.

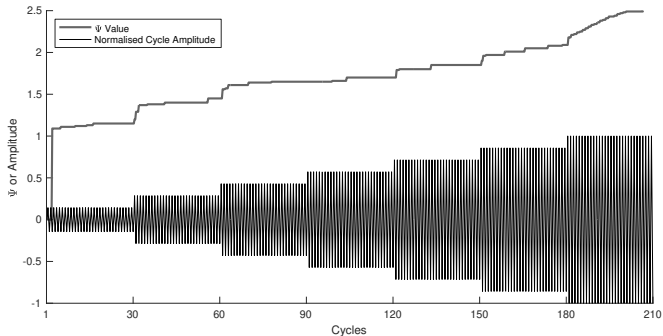


Figure 2.3.4. Development of the Ψ value throughout testing of a wall indicating also the progression of the amplitude of the applied lateral displacement.

2.3.2. Damage Aggravation by $\Delta\Psi$ in Finite Element Models

The Ψ damage parameter is not only useful in laboratory settings but can also be employed for the analysis of damage in numerical models that output crack width. Finite-element-method models are particularly well suited when a continuum material model produces crack strains or crack width at the integration point level. These types of models are explored more extensively in following chapters but a brief example is presented in this subsection.

Numerical models are capable of analysing the effect of several, subsequent actions. For example, a masonry façade can be subjected to a temperature gradient that leads to stresses due to hindered deformations; these stresses can result in cracks. Subsequently, on the cracked or pre-damaged model other actions can be analysed, for instance, deformations originating from the soil or vibrations from various sources. Then, the change in the existing cracks can be measured as $\Delta\Psi$. Since the damage of both actions leads to cracks, and damage is measured from these cracks, the damage scale is compatible with this multi-hazard analysis [multi hazards paper]. In fact, any crack-causing action (see Table 2.1.1), can be progressively evaluated in a numerical model to determine the damage contribution of each action.

Evaluating models using specific values of Ψ_0 can help quantify the effect of the existing damage on the later damage increase. For example, a certain façade displaying cracks amounting to $\Psi_0=1$ may respond differently to vibrations than the same façade with $\Psi_0=1.5$. Similarly, identical façades with equal initial damage intensity ($\Psi_0=1$ for instance) yet caused by different actions, may also lead to a different damage aggravation when subjected to the same action. Using quantifiable values of Ψ_0 and $\Delta\Psi$ helps to objectively assess the influence of initial damage.

Analogously, numerical models, where cracks can be measured and quantified with Ψ , can be used to investigate the influence of other parameters like the strength of the material. Regardless of the number or the location of cracks, if two otherwise identical models are simulated only varying the Young's moduli of the masonry for example, a difference in Ψ or $\Delta\Psi$ will serve as a measure for a sensitivity analysis. In this manner, variations in material strength, geometrical features such as wall size, thickness, or dimensions of the openings, intensity or repetition of the actions, etc. can be quantified with Ψ .

In Figure 2.3.5 an example of damage aggravation using a FEM model is presented. Here, the façade of a masonry monument is modelled and first subjected to a differential settlement that results in a Ψ value of 1.1. Then, a vibration corresponding to a Dutch earthquake with an intensity of 32 mm/s is

applied at the base and cracks are seen to propagate at the corners of the windows. The resulting value of Ψ is 2.0 thus representing an aggravation of $\Delta\Psi=0.9$. It is common to observe existing cracks becoming wider and longer, and other cracks appearing at new locations, in particular, at the corners of windows and doors where stresses localise. The model exemplified is treated in more detail in [14] where the influence of the source of the vibration is explored using Ψ . Similarly, [9, 22] investigates variations in the type and intensity of the soil deformations.

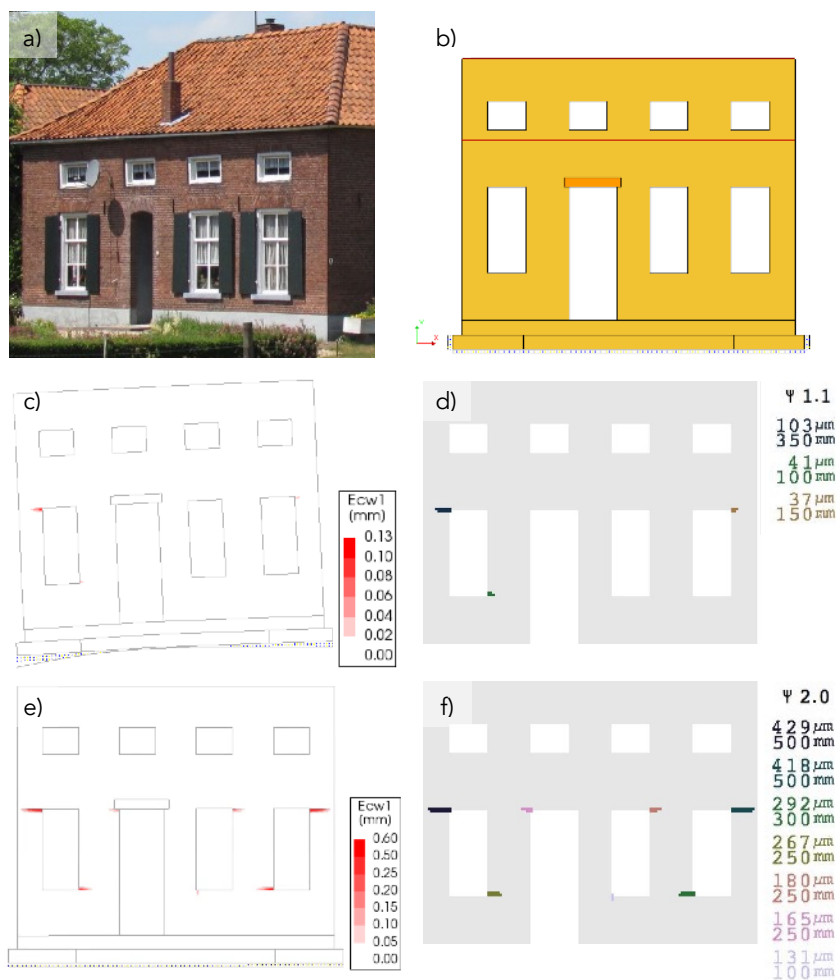


Figure 2.3.5. Example of a monumental façade (a) in the Oude IJsselstreek, the Netherlands, from 1873 modelled with FEM (b), displaying the principal crack width output E_{cw1} (c, e), and automatically interpreted to determine the individual cracks and their characteristics to calculate Ψ (d, f). In a first analysis (c), the façade model is subjected to a soil deformation underneath its foundation, which cases $\Psi=1.1$. Later, the model is subjected to vibrations that cause a $\Delta\Psi=0.9$. Images adapted from [20].

2.3.3. Predictions with Ψ

When the relationship between building features, the intensity of an action, and the resulting Ψ is known, Ψ can be used to predict the probability of damage. For the case of seismic vibrations and clay-brick walls, [7] established a function that based on a number of parameters like the wall geometry, masonry material strength, the soil type underneath the foundation, the initial damage Ψ_0 , the type of earthquake, and its intensity and repetition, would produce a continuous value of $\Delta\Psi$. Associating probabilistic distributions to each of these parameters allows for a calculation of the probability of Ψ or the building fragility in terms of Ψ in response to the earthquake intensity. If a relationship between Ψ and cost is defined, the expected cost for specific earthquake scenarios can be studied.

Other damage scales can also be used for this purpose, but the continuous nature of Ψ and the summation of damage into a single scalar where the meaning of $\Delta\Psi$ is independent of the initial intensity, makes Ψ particularly well suited, especially for light damage. Figure 2.3.6 presents such an example, where contour lines are drawn on a map of the north of the Netherlands representing the exceedance probability for $\Psi=1$ due to past earthquake vibrations on clay-brick masonry walls. This type of quantification will be treated in more detail in following chapters.

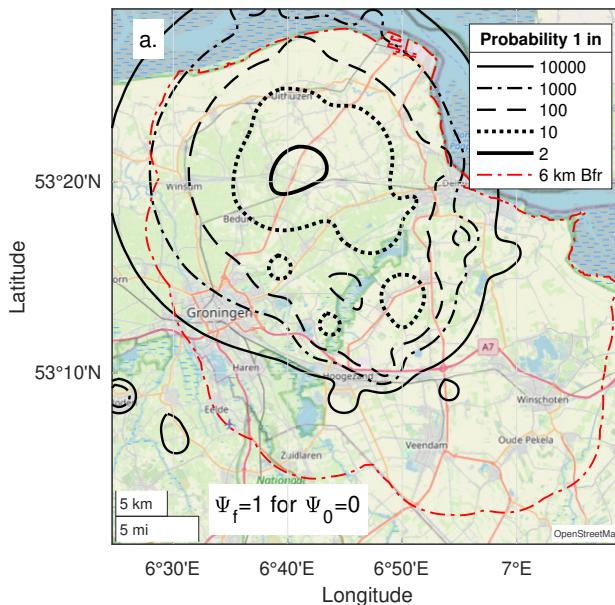


Figure 2.3.6. Example of a map where the probability of damage due to past earthquake events is quantified with Ψ . This map considers a history of multiple events; see Chapter 6.

2.4. Discussion

2.4.1. Transitory and Residual Damage

So as 'perceived damage', transitory damage, may differ from a structure's actual damage level. Transitory damage reflects a structure's state at a specific time and might not align with its state at the time of observation. For instance, during an earthquake, cracks of 1mm may appear at the moment of maximum deformation but partially close by the end of the event. The proposal in this study is that damage is analogous to transitory or transient damage, a conservative approach suitable for evaluating light damage. A few arguments are listed:

Firstly, narrower cracks (DS1) in light damage scenarios, unlike larger cracks, are less likely to close due to the roughness of the crack interface. Cracks through bricks or finished walls are irreversible and remain visible.

Secondly, unreinforced masonry, designed without considering tensile strength, usually lacks forces to keep cracks open. However, additional stresses, such as hygro-thermal expansion, can cause cracks to remain open. Unlike laboratory experiments with restitutory forces, real cases may lack such forces, keeping cracks open.

Thirdly, in real cases, transitory damage is observable and easier to detect than hardly-noticeable residual damage in lightly damaged instances. Laboratory experiments yield higher transitory than residual damage, making it challenging to determine the actual residual damage in real cases with complex interactions.

Fourthly, analysing a combination of actions or repeated actions requires considering the true damaged state revealed by the maximum transitory state. This state accurately represents the structure's loss of strength and response to subsequent excitations.

Fifthly, when assessing structural design adherence to regulations, drift limits focus on maximum displacement rather than residual displacement. Evaluating a structure's final damage state commonly involves looking at its maximum transitory state.

Therefore, this work consistently uses transitory damage to refer to damage. While it's expected that for light damage, transitory damage closely aligns with final damage, it's noted that the final damage measure employed is slightly lower than the transitory damage.

2.4.2. Summary of Advantages, Disadvantages and Limitations

Throughout this chapter, the working of Ψ has been detailed. Some advantages of using Ψ must be apparent, specifically because of its definition. First, Ψ is always objective, meaning that the value computed will be the same for a specific case. Similarly, it is quantitative, without the use of descriptions to determine damage grades. Second, consolidating damage into a single scalar makes comparisons and predictions, via surrogate models for instance, more straightforward. This is useful when crack-based damage comprises multiple cracks. Moreover, Ψ is linked to established damage scales based on crack width, which reinforces its validity. Third, Ψ is continuous which makes small changes measurable - though this is more applicable to predictions than practical measurements on masonry walls. Fourth, the values used for the scale of Ψ are intuitive, with a value of 1 being assigned to the start of visible damage. Similarly, discussing Ψ_0 , or an initial state, is clear, and, $\Delta\Psi$ can be used to express changes in damage. Finally, the relationship between Ψ and the detectability and cost of repair of the damage, makes Ψ a practical parameter.

The simplicity of Ψ , however, is a tradeoff of certain capabilities, i.e. disadvantages. First, when damage is consolidated into a single scalar, the picture of damage is lost; whether cracks appeared underneath windows or at corners cannot be retrieved from the Ψ scalar. Second, Ψ includes the length of cracks as a weighting parameter. Some changes such as the increase in length of one narrow crack while observing no changes in any other cracks, will produce an unexpected change in the value of Ψ . This is an unrealistic situation for which the parameter has not been calibrated. Such changes, however, have a small influence in the value of Ψ and will be limited to a centesimal change. This leads to a loss of precision, but helps to realise that attempting to capture aesthetic damage with a high precision is not sensible.

Moreover, a few words about the influence of crack length in the formulation of Ψ must be said. In a wall with multiple cracks, if all parameters remain the same and only the length of the cracks increase, Ψ might not change. The formulation of Ψ could be adapted to include this effect, but this would make it more complex, defeating part of its purpose. Instead, one must remember that Ψ is supposed to be a practical formulation and does not need to conform to theoretical edge cases. Indeed, in experiments of walls and analyses of field reports, cracks never only grow in length. In a tapered crack, an increase in length is also related to an increase in width. In a uniform crack, an increase in length is not possible. Furthermore, when discussing an increase in Ψ ($\Delta\Psi$), an increase in length is inevitably linked to an increase in width because the

detectability of the longer crack is based on the local increase in width at the crack tip. One could observe that the crack became longer because the tip became wider. In this light, the noticeability of a crack width increasing (as per Table 2.2.4) is governing. Note that this is applicable for cracks in masonry (or concrete) where the crack tip related to a non-zero crack strain is invisible to the naked eye. For a crack to grow in visible length without increasing in width, it must be sustaining a transition from a tapered crack to a uniform crack; that is, the slope of the crack width over the length is diminishing. This is not measured by Ψ but could be included in a different parameter; this is also discussed in the next section.

In sum, when discussing crack length, it must be realised that Ψ is a crack-width based parameter linked to the early damage scale formulations drawn from Burland et al. (1974) where crack length was not present. In this sense, the influence of length, both in damage intensity and aggravation, will be limited.

In this light, the parameter needs always to be evaluated within realistic scenarios. For example, masonry walls are subjected to a limited number of cracks: attempting to evaluate Ψ with a high number of cracks is hence unrealistic. Moreover, since the parameter is related to the ease of repair, which in turn is related to the width of the cracks and not to their length, as was shown in Table 1, an extension in crack length will not necessarily lead to an increase in Ψ ; in masonry, a significant increase in length is accompanied by a realistic increase in width, which is then reflected by a higher Ψ value.

In a structure, there are active and inactive cracks. Some cracks open and others unload; cracks often also localise into a single cracks. For seasonal temperature changes, for instance, the term of 'breathing cracks' is also employed. Transitory damage has also been discussed. Clearly, Ψ is poorly suited to capture the importance of this damage. For both experiments and numerical models, there are potential solutions such as considering the maximum cumulative crack width when evaluating Ψ . However, these become troublesome when assessing $\Delta\Psi$.

2.4.3. Potential Future Improvements

The proposed implementation of Ψ is not the only way in which to objectively measure crack-based damage in masonry. As stated in the preceding subsection, the parameter has several limitations such as the limited influence of the crack length, the lack of consideration for the crack shape or location, or the degree to which a crack is active. These specific limitations are brought to mind because they could be amended in a second version of the parameter or perhaps in a more complex cousin parameter. Indeed, considering any of these

inclusions would make assessing Ψ significantly more complex which would partly defeat its purpose; nevertheless, let us consider these potential revisions.

Firstly, to address the low effect of the length, or the fact that increases in length without increases in width may lead even to a reduction in width, or even in situations where the maximum crack width is difficult to determine, it could be useful to integrate the crack width over the length of the crack. Alternatively, the cumulative sum of crack width for each crack could be considered.

Secondly, the shape of the crack, whether it is tapered or uniform, would be implicitly included in such a width integration over the length, but could also be explicitly incorporated as a stand-alone variable in the formulation. This would emphasise the distinction between the crack shapes. Similarly, crack opening and crack sliding, so the local components of the displacement relative to the crack path, could be individually weighted or included in the formulation such that shear cracks, for example, have a higher effect on the damage intensity. This would incorporate the fact that transitory damage for shear cracks is closer to the maximum damage detected while flexural cracks with pure opening are more likely to fully close in a way that maximum damage differs from transitory damage.

Thirdly, the location of the crack could be considered. Two factors could be included in a revised formulation: the distance of the local crack width to an edge in the geometry of the wall or façade, and the location of the crack relative to the masonry (bed, or head joint, or brick). The latter would be weighted heavily as having a higher contribution to the damage intensity. Similarly, the further a crack is located from any edge, the more important it is for damage. In this way, shear or body cracks could be given a higher importance.

While these improvements could be included in a straightforward manner within an automatic detection and formulation, they would require significant more inputs in situations where such a measurement system is not available. Moreover, the precise way in which all these inputs would be put together is not simple. Extensive studies would be required to account for all the correct effects and verify that none is being considered twice. A data-driven approach, perhaps empirically determined with a machine-learning model, would be a good alternative.

With the goal of formulating an uncomplicated damage intensity parameter, the Ψ parameter neglects many of these possible effects and focuses on providing a single scalar as a summary of damage.

2.4.4. Relevance of Ψ for Modelling and for Real Life Uses

The damage parameter was conceived to measure small increases in damage objectively. Additionally, a lower threshold from which damage becomes measurable was determined. These two goals are mostly useful for modelling and laboratory cases where small damage increases can be measured, even before damage becomes visible. These small increases, perhaps imperceivable in real situations, are key in drawing relationships between modelling variations and damage.

Yet, Ψ can also be used in real life cases, though less so in individual cases. The predictive power of Ψ , to categorise the probability of damage for typologies of buildings, cannot be applied at the individual level since the precise history and context of a building, usually unknown, will affect its damage development. Moreover, from Table 2.2.4 it follows, that small increases in damage ($\Delta\Psi$) will not be measurable in the field unless sensitive sensors have been left in place.

Other practical limitations are sometimes encountered. For example, how to determine Ψ when a single crack spans multiple walls around a building corner or over different types of material can represent confusing scenarios (see section 2.2.5). Additionally, field surveys to evaluate cost of repairs should be exhaustive and summarising damage into a single value (Ψ) is usually over simplified. In these cases, Ψ could be used to give a comparison to an earlier measurement epoch.

2.5. Conclusions about Ψ , $\Delta\Psi$, Ψ_0

The following conclusions incorporate the essential aspects of the Ψ parameter and its application in damage assessment in masonry:

Objective Measurement of Damage: Ψ offers an objective way to measure damage, ensuring consistent results regardless of the observer's experience or the measurement tools used. This objectivity is crucial in fields such as damage assessment and loss prediction.

Quantitative Nature: Unlike scales that rely on descriptions or limited categories, the Ψ parameter is quantitative. It uses measurable factors such as crack width, number of cracks, and crack length, making the assessment process more precise and less subjective. Existing approaches typically employ only crack width.

Continuous Scale: Ψ operates on a continuous scale. This feature allows for the easy measurement of both absolute values and incremental changes in damage, facilitating a nuanced understanding of damage progression.

Linked to Detectability and Cost of Repair: Ψ is directly related to the detectability of damage and the ease (and cost) of repair. This connection makes it a practical tool for assessing the impact and severity of damage in masonry.

Wide Applicability: The metric is applicable to a range of damage types, including mining-induced damage from both dynamic soil movements like earthquake vibrations and static soil movements like subsidence. It is also useful in finite element and other models, laboratory tests with digital image correlation or other crack registration techniques, and real cases where cracks are monitored with the naked eye, existing crack measuring apparatus, or innovative photographic techniques.

Quantification of Damage Increase ($\Delta\Psi$) and Relative Increase ($\Delta\Psi/\Psi_0$): The Ψ parameter enables the objective quantification of damage increase, including the relative increase. For example, it can express damage increase as a percentage, such as “an increase of 10% in damage.” This aspect is particularly relevant for assessing cumulative damage (e.g., earthquake damage on top of pre-existing damage from settlements) and repetitive damage (e.g., multiple earthquakes over time), which is crucial in cases like the Groningen induced seismicity. It should be noted that the advantage of a simple parameter might underestimate some influences.

In conclusion, the Ψ parameter represents a significant advancement in the field of damage assessment, offering a reliable, quantitative, and versatile tool for measuring and understanding **crack-based damage** in masonry structures under various conditions and influences.

Chapter 3

Experiments to Characterise Cracks

What does the initiation and propagation of cracks in masonry look like?

Central to this chapter is the focus on the initiation and propagation of cracks in masonry. The experiments conducted were not only aimed at observing crack formation but also meticulously designed to track the evolution of these cracks under various test conditions. This approach provides an in-depth understanding of the mechanics behind crack formation and growth, a critical aspect in assessing the light damage of masonry structures.

The experimental campaign began in 2017 and has continued into 2024. It is not feasible to showcase every experiment in detail. These are treated on early reports [23, 24], follow-up conference papers [11, 12, 13, 15, 16, 18, 31], and journal publications [1, 3, 4]. Instead, the work presented in this chapter is summative; it collects and digests the main observations from these experiments and draws comparisons between the various tests performed.

repetition threshold
brick width limit result
value drift first
protocol test light cycle
displacement loading

Chapter 3: Table of Contents

The chapter is split into three main sections. A first 'methods' sections looks at the definition and provides an overview of the experiments included herein. Next, Section 3.2 gathers the 'results' of the tests in a summarising manner under the loupe of crack propagation. Finally, Section 3.3 concludes with a direct 'application' of the experiments: drift limits for light damage. The relationship between drift and Ψ is explored with a classification model and limits for the lower and upper thresholds of light damage are defined.

3.1. Definition of Experiments to Investigate Light Damage	55
3.1.1. Loading Protocol for Light Damage and Evaluating Repetition	56
3.1.2. DIC Monitoring System for Experimental Crack-Based Damage	63
3.1.3. Overview of the Tests Performed from 2017 to 2024	68
3.2. Results from Experiments on Walls and Spandrels	73
3.2.1. Summary of Results on Wall Tests	73
3.2.2. Summary of Results on Spandrel Tests	79
3.2.3. Lessons about Crack Propagation	84
3.2.4. Conclusions about Crack Propagation	91
3.2.5. Four Ways to Utilise the Experimental Results	92
3.3. Crack-Based Drift Limits from Experimental Results	93
3.3.1. Drift Limits for Light Damage Lacking in Literature	93
3.3.2. Repetition in the Loading Protocol of Experiments	95
3.3.3. Relationship between Crack-based Damage and in-plane Drift	96
3.3.4. Discussion and Comparison to Other Drift Limits	102
3.3.5. Summary of Drift Limits for Light Damage	104
3.4. Conclusions: Experiments to Understand Crack Behaviour	105

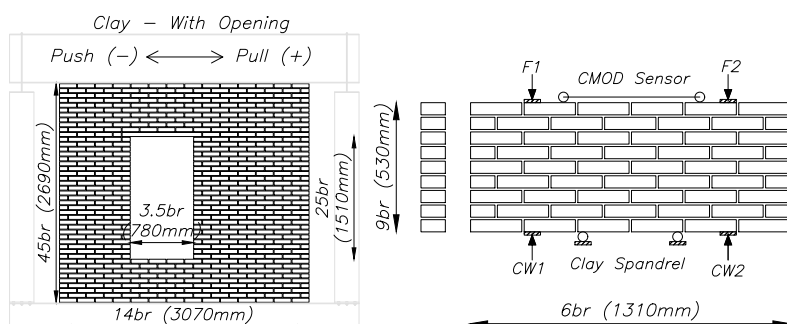


Figure 3.1.1. Left, a wall or component test; right, a spandrel or 'window bank' test which is a modified four-point-bending test with counterweights (CW) and CMOD control. In both cases, the fired-clay brick specimens are depicted.

3.1. Definition of Experiments to Investigate Light Damage

Jafari et al., Esposito et al., and Messali et al. (2018) conducted an extensive multi-scale campaign to characterise the mechanic behaviour of masonry and assess the safety of masonry structures. The campaign included small scale 'companion tests' such as bond-wrench tests to characterise the bond between masonry units, shear-triplet tests to obtain friction and cohesion values, and compression tests for stiffness, compressive strength and toughness. Larger tests like three- or four-point-bending tests in several directions also helped gather stiffness, flexural, and tensile properties of the masonry investigated. Moreover, larger masonry components such as walls were tested both in-plane and out-of-plane (Damiola et al. 2018). Finally, two assemblages representing the entire structure of a masonry house were also assayed. All tests were quasi-static and under displacement control in order to capture stiffness, strength, and toughness properties of the masonry. While cracks were observed during some of these tests, there were no specific efforts to measure them precisely. Additionally, observed cracks were noted at high values of displacement corresponding to damage states above DS2; this was sufficient to mark overall crack patterns and failure mechanisms but not to characterise light damage.

To investigate the very initiation of cracks and monitor their development, many of these tests were adapted and two vital modifications were conceived: a loading protocol that slowly started before DS1, and an instrumentation system capable of measuring and tracking any cracks throughout the tests. Moreover, the in-plane tests on walls were maintained, slightly varying their geometry to foment cracks to form around an opening, and the in-plane four-point-bending tests were modified to allow for repetition; see Figure 3.1.1 for the two types of 'light damage tests'. The adaptations are discussed here.

This section is split into three subsections. Their order is somewhat arbitrary as all three components are equally important to define the tests needed to investigate cracking in masonry. Ultimately, it is as follows:

- Section 3.1.1 presents the loading protocol for tests, aimed at generating light damage. The protocols are exemplified and were developed on the basis of (preliminary) experiments from the last bullet point.
- Section 3.1.2 details a system that can determine crack initiation and track crack propagation in experiments. Its capabilities are illustrated with the results of the experiments, too.
- Finally, section 3.1.3 presents the experiments chose to investigate cracking; their definition is based on the properties and capabilities of the first two sections.

3.1.1. Loading Protocol for Light Damage and Evaluating Repetition

The loading protocol is essential during laboratory testing. It defines, together with the boundary conditions imposed by the test setup, the stresses and strains to which the samples will be subjected. A first adaptation was to come up with a loading protocol that allowed to: 1) measure cracks at their initiation, before they become visible to the naked eye; 2) monitor the propagation of the cracks as in-plane drift increased and damage intensified; and 3) look at the effect of repetition of identical loads.

In these tests, displacement-control schemes are employed due to the non-linear behaviour of damaged specimens. In this manner, it is possible to capture not only the pre-peak but also the post-peak softening regimes. Moreover, the enforced displacement changes throughout the test. The initial stage involves one-way cyclic loading, which prevents stress reversal on crack surfaces, aiding in understanding crack progression. One-way cyclic loading is also known as unidirectional or repetitive loading.

This is succeeded by two-way cyclic loading (bi-directional loading) to mimic seismic excitation and compare crack development in both pre-cracked and uncracked loading directions, as detailed in Section 3.2. To track material degradation, cycles of equal displacement amplitude are used, identifying degradation through reduced force resistance. This results in a portion of the cycles being identical, leading to a step-wise incremental loading approach.

The cycle number and amplitudes draw partially from Mergos et al. (2014, 2015), which discusses protocols for low-seismicity regions, considering various structure types and ductility. This is supplemented by Beyer et al. (2015), who highlight the importance of cycle number in flexural versus shear failure mechanisms. Studies like Ntinalexis et al. (2022) and Spetzler et al. (2017) note that structures often endure many small earthquakes, implying the necessity of numerous small cycles. Conversely, large-amplitude cycles, typical of major earthquakes near epicentres, are less frequent in distant structures, where flexural crack propagation is more common (Bal et al., 2018).

Protocol for Walls under Horizontal Shear and Flexure

Figure 2 contrasts Beyer's function with the selected protocols for walls being tested in flexure where crack formation is mainly due to tensile stresses. Notably, more cycles are included to reflect multiple earthquake scenarios, reorganising the cycles to better observe degradation. Bal et al. (2018) mention that repetitive induced events can lead to cumulative damage, similar to tectonic earthquakes.

The initial part of the test diverges from Beyer et al. (2015)'s suggestion. Large amplitudes, being unidirectional, might cause less damage than bidirectional amplitudes. Trial tests indicated that very small amplitudes, as per Beyer et al., would remain within the elastic region of specimens, deeming them insignificant. The methodology includes an 'alpha' parameter, linked to the structure's natural period, with a value of 1.5 for periods over 0.3 seconds.

Thus, for lightly damaged, unreinforced masonry structures prone to frequent small earthquakes, and aiming to study crack mechanics and material degradation, an incrementally repetitive loading protocol with a high number of cycles is followed by bi-directional loading. This approach, as shown in Figure 2, provides a comprehensive understanding of the structural response under various loading conditions.

For this loading protocol, the very first displacement amplitude needs to be defined. The remaining steps follow from this first with a constant increase of 25% for normalised amplitudes of 1.0, 1.25, 1.5, 1.75, 2.0, 2.25, and 2.5 for up to seven steps in the two-way cyclic section of the protocol. The first amplitude was obtained by monotonically increasing the in-plane drift until a crack width of 0.1 mm was measured at one of the expected crack locations. For this purpose, the first wall was instrumented more heavily than subsequent walls since the location of the first crack was uncertain. The measured crack width would correspond to a Ψ value of approximately 1; this was later confirmed with photogrammetry. In fact, subsequent walls could rely entirely on photogrammetry as an immediate result about crack width was not needed. To ensure comparability, the drift of the first wall was applied to all other walls; in most cases this corresponded to a Ψ of 1 though in some cases Ψ would be slightly lower or higher.

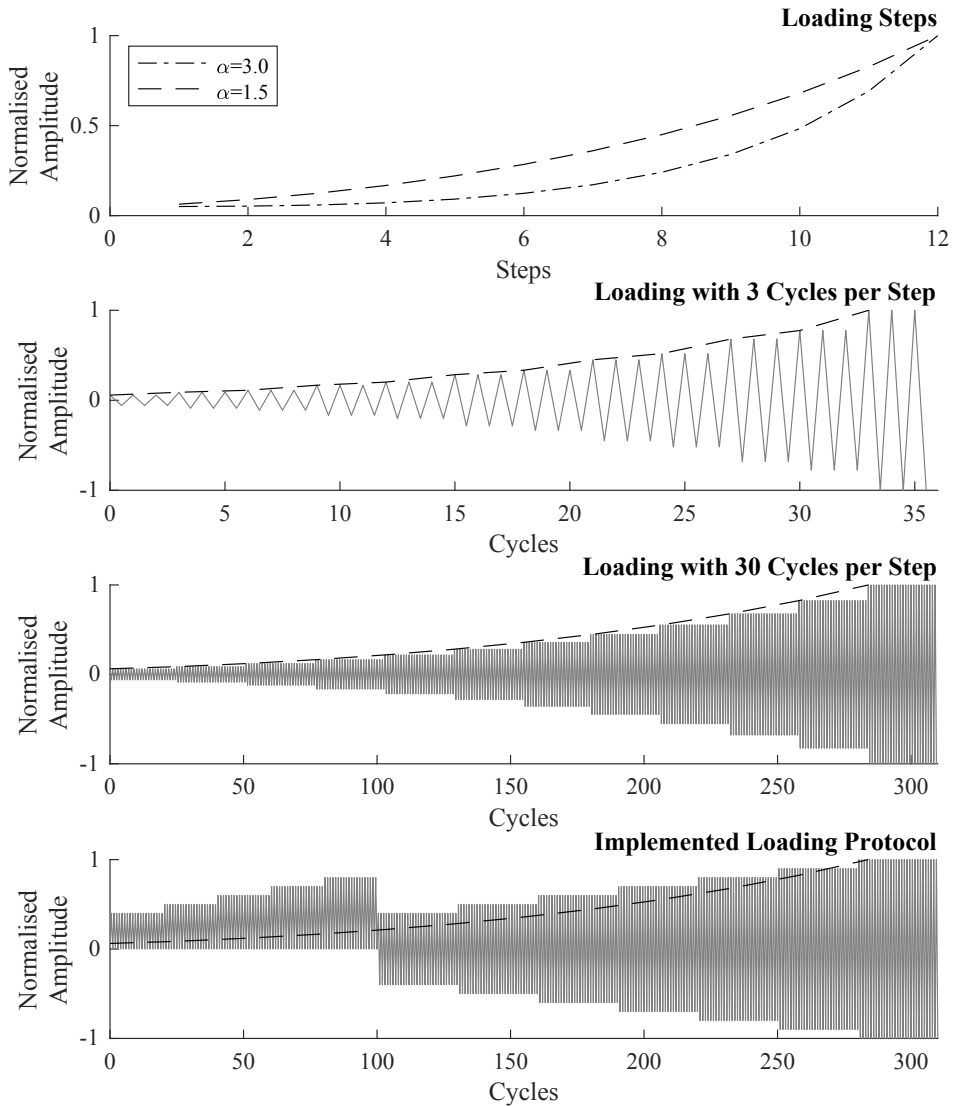


Figure 3.1.2: Comparison of loading protocols. Includes Beyer et al. (2015) methodology with 12 steps for two 'alpha' values, 12 steps with 3 cycles each at $\alpha=1.5$, adapted loading with 30 cycles per step, and this study's protocol for wall samples with a total of 310 cycles, combining repetitive (one-way cyclic) and bi-directional (two-way cyclic) parts.

Asymmetric Protocol for Walls in Horizontal Shear

For the walls tested under a double-clamped boundary condition which encourages shear failure, a different protocol was conceived. It draws on the same premises and goals as the light damage protocol (LDP). Beyer's approach suggests fewer cycles for walls loaded predominantly in shear, so the number of key cycles was reduced. At the same time, cracks in shear are characterised by sliding and opening. When sliding occurs repeatedly, a deformation tends to accumulate if displacements are not identical in both directions - earthquake displacements are rarely symmetric. Therefore, it was important to enable this accumulated sliding behaviour, or 'walking', via the loading protocol. To replicate and study this behaviour, the protocol needed to incorporate this asymmetry in its loading sequences.

To achieve this, the protocol was informed by an analysis of real earthquake data, specifically focusing on the Zeerijp earthquake of 2018. The observed ground motions from this event were asymmetric, with the amplitude in the positive drift direction being significantly larger than that in the negative direction, a detail reflected in Figure 3.1.3. This deliberate asymmetry in the loading cycles was implemented to closely mimic the natural movements of earthquakes, thereby facilitating a more accurate study of (shear) damage accumulation under such conditions. The protocol involves conducting a series of identical loading cycles at each specified drift level, enabling the detailed tracking of damage development over time. This process is detailed in Figure 3, which presents various key elements of the earthquake and the testing protocol:

Time Series and Arias Intensity Analysis (3.a) displays the maximum rotated component of the horizontal acceleration recorded during the Zeerijp earthquake, alongside the Arias intensity parameter (Arias, 1970). This visual representation helps in understanding the distribution and intensity of the earthquake's energy release. Subfigure 3.b highlights the time frame in which most of the earthquake's energy was discharged. Section 3.c shows the ground displacement that corresponded to the time span of the most intense energy release.

Part 3.d depicts the asymmetric loading profile used in the protocol, loosely representing the ground motion patterns observed during the earthquake (3.c). Incremental Loading Steps (3.e) illustrates how the asymmetric profile is applied in repeated cycles - 10 per step - across 6 incremental steps. These steps range from a starting point of 0.27‰ maximum in-plane lateral drift and increase by 0.065‰ at each step, culminating at 0.69‰. This sequence forms the Asymmetric Light Damage Protocol (ALDP).

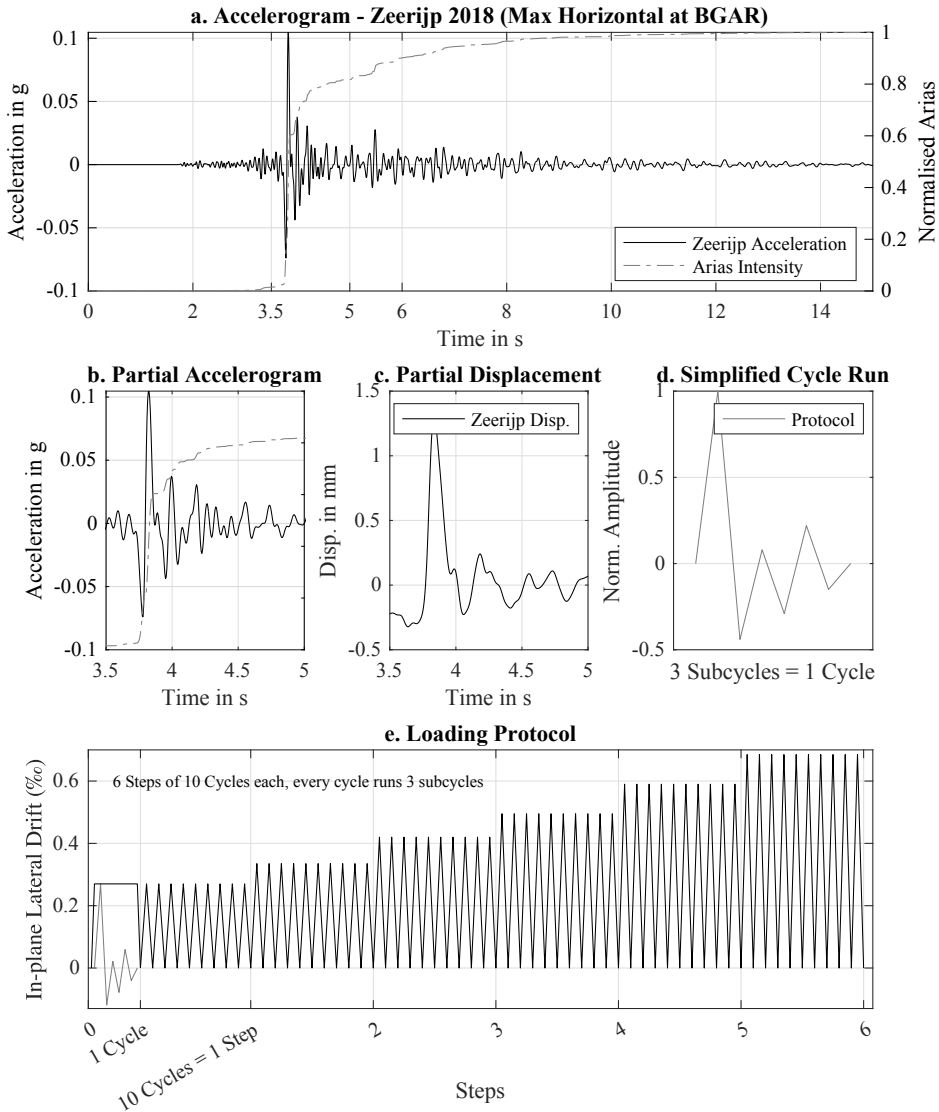


Figure 3.1.3. Overview of Shear Wall Test Protocol: (a) Representative accelerogram from a Groningen earthquake, focusing on the maximum rotated horizontal component recorded during the Zeerijp earthquake (January 2018) at the BGAR station. (b) Detailed view of section (a). (c) Displacement patterns derived from section (b). (d) Simplified cyclic test derived from displacement patterns in (c). (e) Comprehensive loading scheme, comprising a sequence of sub-cycles, full cycles, and incremental steps. Over the six steps, each consisting of ten cycles, there are three subcycles in each cycles and thus $3 \times 10 \times 6 = 180$ subcycles in total.

The flexure-focused LDP protocol set the initial drift to correspond to a crack width indicator of $\Psi=1$. However, unlike the LDP, it was impractical to instrument the entire surface of the wall to detect crack formation in the ALDP. Hence, the first wall underwent a series of stepped monotonic tests, with incremental increases of 0.025%. Images captured at each step were sent to a remote server for analysis to look at the onset of cracking. They confirmed that the first cracks were occurring at the rocking locations (see later Section 3.1.3) where sensors had been placed; later cracks would also appear in the body of the shear walls. Based on these sensors, the drift associated with a first crack of 0.1 mm width ($\Psi=1$) could be set.

Loading Protocol for Spandrels in Vertical Shear

Complementary to the wall, laboratory experiments included tests of the spandrels below window banks. These had the goal of closely monitoring the propagation of vertical cracks in bending, and were performed monotonically and repetitively. Opposite to the work of Gattesco et al. (2016), where the behaviour of a masonry spandrel located between piers on upper floors is investigated for typical spandrel behaviour during earthquake loading (double bending and predominantly shear), the window bank tests presented here are to mimic the behaviour of a spandrel on a ground floor which may have experienced bending cracks due to actions such as settlements or restrained shrinkage. It is the repetitive effect of subsequent seismic excitations, and of seasonal temperature effects, acting on these types of cracks which are of interest. Furthermore, this configuration is used to calibrate models to the behaviour of vertical cracks in masonry which were not present in the experimental full-scale walls as these exhibited mainly horizontal bed-joint cracks and diagonal stepped cracks, but might have appeared under different boundary conditions.

The standard four-point-bending test (4PBT) was modified in such a way that a repeated loading protocol could be applied. Two linked hydraulic jacks were used and opposite to their application point on the specimen, counterweights were located.; see earlier Figure 3.1.1. In this manner, there is a restitution force that helps unload the specimen for repeated cycles. To prevent the cables from the counterweights interfering with the photogrammetry, the sample was inverted such that the supports are located in the middle and the forces are applied at the extremes. A traditional 4PBT mimics a beam where the supports are at the sides. Placing the supports in the middle also helped to counteract the effect of gravity attempting to split the (damaged) specimen. Moreover, the inversion guaranteed that the controlling sensor, monitoring the Crack Mouth Opening Displacement (CMOD) over the top three vertical joints

of the sample, would not be affected if a brick dislodged due to bending nor would it be damaged if the middle of the sample collapsed downwards as in the standard 4PBT. To trigger the start of the crack in the centre of the sample, a notch was introduced by having left a piece of PVC in the central top head joint at the time of construction. However, the initiation of the crack proved to be unrelated to the existence or position of the notch, with some cracks starting on the neighbouring top head joints.

Nonetheless, while this setup allowed for cyclic loading, the loading direction could not be reversed. This meant that the loading protocol could only be one-way cyclic. Several specimens were tested monotonically first to obtain an idea about the types of displacements that could be repeated. In the initial campaign, fourteen spandrel tests were performed of which seven were monotonic and the remaining were repetitive with three sets of incremental displacements (Figure 3.4). Three specimens were tested with 10 repetitions per set, three with 30, and one with 100 repetitions. The amplitude of the steps was determined based on the results of the monotonic tests such that they occurred in the non-linear region before the peak force. These were also set around the threshold for a visible crack at 0.1 mm. The results showed that 30 repetitions were sufficient to observe the force degradation occurring at each step. Therefore, subsequent tests were conducted with 30 repetitions per step.

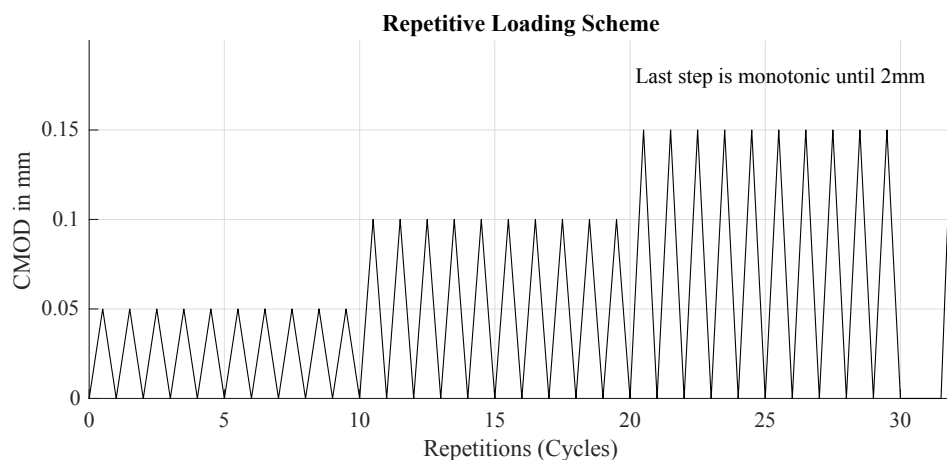


Figure 3.1.4. Loading protocol for the window bank tests with 10 repetitions: 3x10.

3.1.2. DIC Monitoring System for Experimental Crack-Based Damage

Besides the protocol designed to investigate light damage, a monitoring strategy to accurately capture the light damage is needed. This comprises the monitoring of crack width over the entire length of a crack. Displacement sensors such as Linear Variable Differential Transformers (LVDTs) can measure the relative displacement between two points with high accuracy; they would need to be installed along the entire crack path. This presents several issues: First, the sensors only measure displacement along their axis, meaning that to capture sliding as well as opening, at least two sensors are required. Second, along the crack length, a large number of sensors would need to be placed. Installing, calibrating, verifying, managing, and reading a large number of sensors quickly becomes unfeasible; thirty sensors is already a very high number of connections to be managed at a monitoring station. Third, the location of the crack is not known a priori. This means that, if all the potential crack locations are to be surveyed, hundreds of sensors would need to be used. Moreover, cracks sometimes split bricks, further increasing the number of sensors. Using traditional displacements sensors to monitor crack propagation on a full-scale wall is resolutely unmanageable.

Photogrammetry techniques can measure displacements at several points simultaneously. A digital image is analysed and specific points are tracked over several images. Before the light damage campaign, photogrammetry was used to track individual bricks using a few markers per brick. This allowed surveying the displacement and rotations of bricks. To accurately track invisible cracks however, many more measuring points are needed. For this purpose, Digital Image Correlation was used. In DIC, small portions of the image, or subsets, are used to identify measuring points. To make this process more robust, specimens are painted with a high-contrast pattern. In Figure 3.5, a wall and a spandrel specimen are presented. These are equipped with a black-and-white pattern that when zoomed-in reveals the subset size. Because of the speckle pattern, each subset of pixels is unique in comparison to its neighbours. The smaller the subset, the more points on the image can be surveyed, though the subset should remain sufficiently unique. In the image, the subset on the wall is 5x5 millimetres and only 1.5x1.5 mm for the spandrel. Subsets can also overlap. Ultimately, a mesh of 2.7x2.7 mm could be surveyed on the face of the wall. For a single brick of "Waalformaar", this translates to about 1500 points for which in-plane horizontal and vertical displacements can be tracked. Additional points are tracked on the mortar joints. This would be impossible with LVDTs.

Figure 3.1.5 presents an example of a 2.7m-tall masonry wall covered in a speckle pattern where dots are randomly positioned and randomly vary in diameter between 4 and 8 pixels. To produce such a pattern, a stencil was laser-cut from a flexible acrylic plate and was applied on the masonry by spraying black paint with a compressed-air nozzle, similar to the approach of Ghorbani et al. (2015). The random pattern is generated with a script that allowed changing the sizes and distances of the dots. Multiple patterns were tested on small specimens to determine the best set of parameters. The pattern allows a (standard) DIC-algorithm to detect the relative displacements between an initial image and a later image. In Figure 3.1.6, the displacement field reveals the presence of cracks.

A strong contribution was made in minimising the subset size. The ideal pattern was optimised such that the subset could be small and unique. This is coupled to the camera. A camera with a lower resolution requires a larger pattern; a smaller specimen with the camera closer to it, will require a finer pattern. See again Figure 3.5. A higher resolution image could be stitched together from several cameras but problems with positioning of the camera, the stitching procedure, lens distortion, illumination, etc, quickly make this alternative undesirable. A single image is preferable. For additional details on the equipment see Appendix A.1.

The size of the subset is also linked to the post-processing of the images. A custom program was written to handle small subsets and process them individually. This is important for monitoring cracks since they represent discontinuities in the displacement field. Commercial software focuses on outputting strains which smear out the cracks. Instead, the relative displacement between two neighbouring subsets can then be seen as a crack. In this manner, crack widths of 20 μm could already be detected. Since along a crack path, several measuring points are located, noisy data can be rejected; see [24.H].

In this way, post-processing was improved in several areas: the correlation procedure to obtain the displacement field; the presentation of the displacement field; the detection of cracks; and, the post-processing of crack information. The correlation procedure has been mentioned in the previous paragraph and included treating small subsets as independent to obtain clear displacement discontinuities where cracks could be identified. It also comprised several programming optimisations to run in modern multi-core processors which significantly sped up the analysis time.

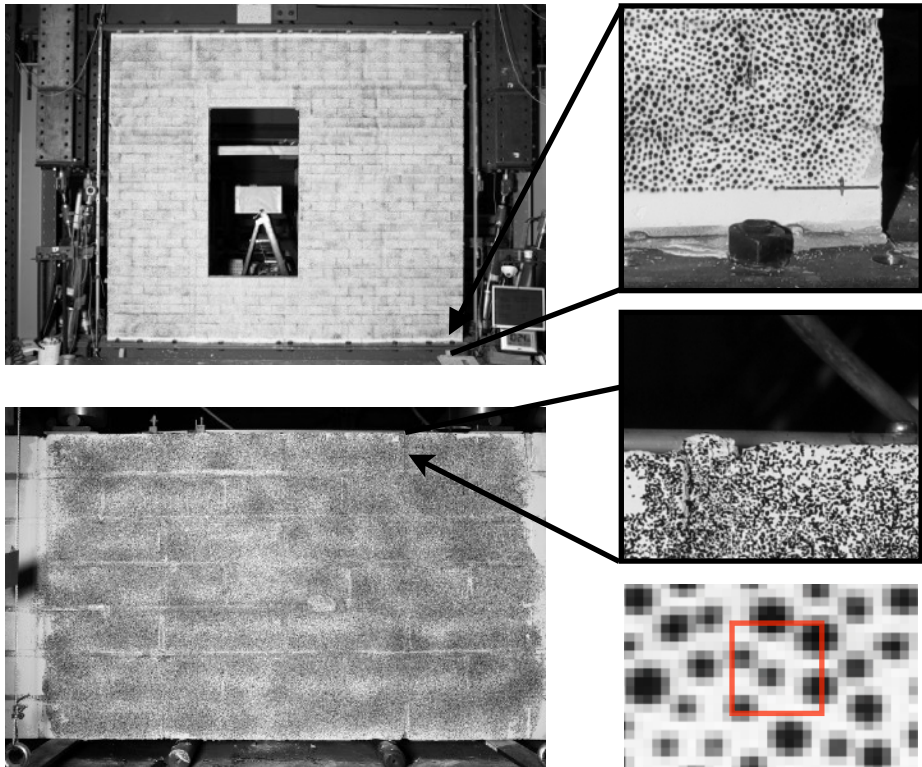


Figure 3.1.5. DIC pattern and subset. Top, wall and zoomed-in stencil speckle pattern. Bottom, spandrel and zoomed-in particle speckle pattern. And bottom right, subset of 10x10 pixels from the image.

Deformed Shapes

To present the results, a deformed shape plot was included. Unlike the current trend of software to present displacements with a range of colours, the FEM strategy of magnifying the displacements was adopted. By removing colour, the results become exceedingly clear. See Figure 6 where two examples are presented. On the left, a test on a shear wall reveals the body cracks and the rocking crack at the top right. The test has a double clamped boundary condition which must ensure that the top and bottom supports remain parallel, ideally horizontal. Since the wall is stiff and the setup is not infinitely stiff, some rotation of the boundaries is identified. In fact, the location of the several bolts anchoring the beams to the setup can be inferred from the deformations.

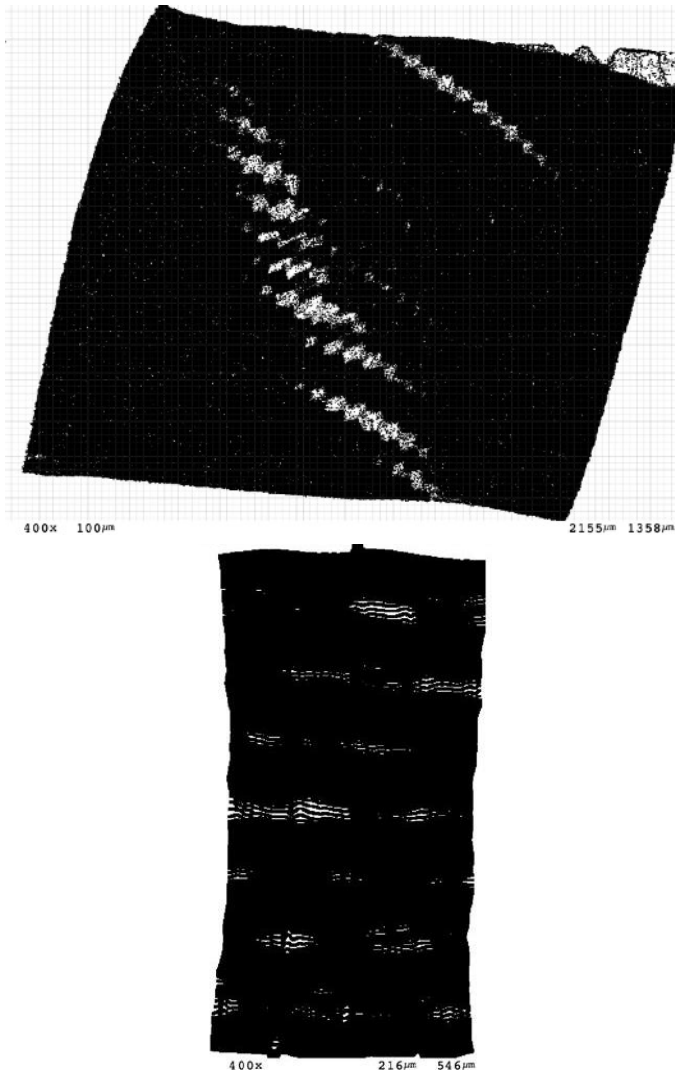


Figure 3.1.6. Deformed shapes. Left, A wall tested in-plane. Right, a compression wallet with an inverted displacement field: extension shows contraction, opening depicts crushing.

The right side of Figure 6 shows a compression wallet from the companion characterisation campaign. This small sample comprises eight courses of bricks. In the figure, the sample appears elongated. This is because the displacements have been inverted. In this manner, the crushing at the mortar joints appears as openings. The restrictive influence of the top and bottom boundaries due to friction is visible. The Poisson effect, that makes the specimen bulge out horizontally (displayed as contraction), is thus restricted by the boundaries.

Crack Detection

Two important contributions in terms of crack monitoring from the DIC data were made: characterising cracks and tracking them throughout an experiment. Crack detection follows directly from the discontinuities in the displacement field. These identify between which points relative opening or sliding has occurred. Two 'cracked' neighbouring points are assumed to belong to a single crack. In this sense, what constitutes a crack is harder to define. For people, intuitively, cracks are easy to identify; this is not as clear for a computer program. The strategy employed is simple: 'cracked' points that are closer than 10 mm, the thickness of the mortar, belong to a single crack. Once the individual cracks have been identified, they can be characterised. The width and length of the crack is computed. Together, Ψ can be calculated; see chapter 2.

Next, cracks over the entire experiment are consolidated. If two individual cracks exist where later a single crack is present, then they are the same crack. In this manner, cracks are identified retroactively and a single crack is tracked from the beginning until the end of the experiment. In this way, the width and length of individual cracks can be monitored and crack propagation can be quantified. Figure 7 demonstrates the progression of crack width and length over several cycles.

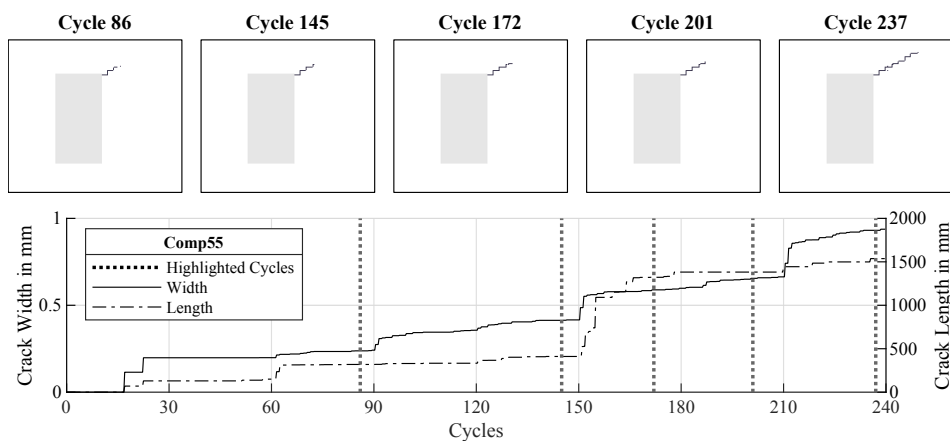


Figure 3.1.7. Example of crack monitoring over cyclic loading, extracted from the cyclic test of Comp55, observing the crack at the top right corner of the window opening.

3.1.3. Overview of the Tests Performed from 2017 to 2024

The tests gathered herein have formed part of several testing campaigns, though within the ‘light damage campaign’ started in 2017. Throughout these sub-campaigns, the loading protocol has been mostly consistent as has the crack measuring system. In addition to Figure 1, Figure 9 shows six different geometries and masonry brick material tested, namely fired-clay and calcium-silicate brick. The chief geometry difference is the inclusion of an opening for a window. Moreover, the test differ based on the boundary condition enforced in the laboratory. Two conditions are possible: cantilever, where the top is allowed to rotate freely, and fixed, where the top edge is kept parallel to the bottom edge; see Figure 8 for a scheme of the boundaries and the corresponding idealised deformation of the walls. The spandrel, or four-point bending test is also included.

The overview of twenty full-scale wall tests, or component tests, is gathered in Table 3.1. The result of each individual test will not be presented here due to brevity. Instead, a comparison of the most relevant results is digested in the next sections.

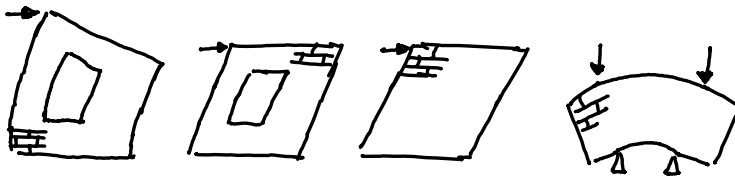


Figure 3.1.8. Schematic deformation of the walls and the spandrels. From left to right: a wall with an opening with a cantilever boundary and with a fixed or double-clamped boundary; a wall without openings under a fixed boundary; a spandrel under four-point bending.

Additional details can be found in several publications. The original five walls, Comp40 to Comp44 are presented in [1, 11, and 23]. These helped establish the light damage loading protocol and verified the potential of DIC measurements. The next two walls focused on the effect of pre-damage; Comp45 and Comp46. These were addressed in [12, 24]. Next were Comp47 and Comp48 which introduced a double-clamped boundary and shear behaviour; they are analysed in [4, 24]. Comp49 and Comp50 explored the light-damage behaviour of calcium-silicate brick masonry for the first time and are discussed in [3, 13, 24].

The subsequent walls were tested as complementary campaign to further understanding into the light damage behaviour of calcium-silicate brick masonry [30]. Additionally, new experiments with a double-clamped boundary

for fired-clay brick walls with an opening were tested. These walls, Comp52 to Comp54, are specifically discussed in [31].

In addition to the full-scale walls, spandrels or window-banks were also tested. A large set of twenty three fired-clay brick spandrels and five calcium-silicate specimens were tested, each set of nominally-identical geometry; see Figure 3.1.10. An overview of these is presented in Table 3.2. The tests were controlled using the crack-mouth-opening-displacement and included monotonic and repetitive loading protocols. Table 3.2 already gathers results from these tests. The maximum capacity is listed, with an average of 20 kN for the fired-clay tests and 31 kN for the calcium-silicate tests. Moreover, the reduction in force (or degradation) observed in each step is averaged over the various loading steps. This means, for instance, that for a loading protocol of 3x10, three values are averaged: one corresponding to the maximum reduction of the first step (between the very first and the tenth cycle), and two for the second and third steps respectively. These results are further discussed in the next section.

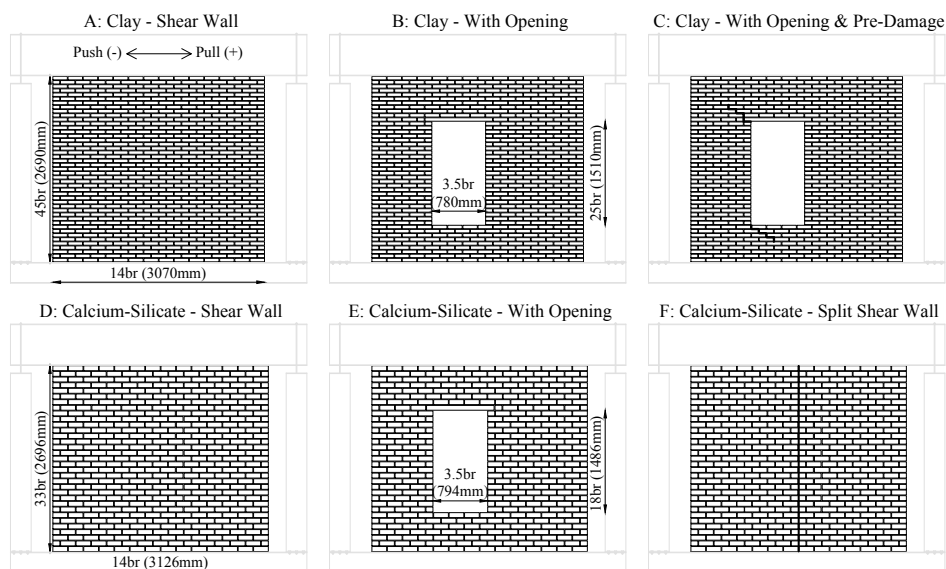


Figure 3.1.9. Scheme of various wall types tested during the light-damage campaign to characterise crack propagation in solid fired-clay (CLBR) and calcium-silicate brick (CSBR) masonry walls.

Table 3.1. Overview of full-scale walls tested and their corresponding (cyclic) protocols. See Figure 3.1.9 for wall types. Boundaries are Cantilever or Fixed.

Wall Name	Wall Type	Lab Boundary	Year Built	Protocol		
				Repetitive	Cyclic	Near Collapse
Comp40	B	C	2017	5x3	7x50	81 mm
Comp41	B	C	2017	5x10	7x30	40 mm
Comp42	B	C	2017	6x20	7x30	40 mm
Comp43	B	C	2017	NA	7x50	40 mm
Comp44	B	C	2017	6x20	NA	NA
Comp45	C	C	2018	5x30	7x30	NA
Comp46	C	C	2018	5x30	7x30	81 mm
Comp47	A	F	2018	A 7x10		27 mm
Comp48	A	F	2018	A 7x10		NA
Comp49	E	C	2018	5x30	7x30	40 mm
Comp50	E	C	2018	5x30	7x30	40 mm
Comp51	E	C	2021	5x30	7x30	81 mm
Comp52	E	C	2021	5x30	7x30	81 mm
Comp53	E	F	2021	5x30	7x30	40 mm
Comp54	B	C	2021	5x30	5x30	NA
Comp55	B	F	2021	6x30	8x30	27 mm
Comp56	B	F	2021	5x30	7x30	27 mm
Comp57	D	F	2021	A 7x10		40 mm
Comp58	F	F	2021	A 7x10		67 mm
Comp59	F	F	2021	A 7x10		54 mm

Table 3.2. Overview of full-scale spandrels over the experimental campaigns of 2017 and 2018 including the force reduction observed during repetitive testing protocols.

Test Code	Specimen Code	Year	Protocol	Maximum Force kN	CMOD at Max Force μm	Average Cyclic Force Reduction
Mat-50 Fired- Clay Brick	1B	2017	Mono- tonic	17.0	130	NA
	1D			20.0	380	
	1E			18.0	390	
	1F			25.0	510	
	1G			19.0	340	
	1H			30.0	590	
	1I			15.0	430	
	1J			17.0	310	
	1T	2017	2x10	22.0	280	18%
	1K	2017	3x10	17.0	860	20%
	1L			19.0		11%
	1N			18.0	580	16%
	1O			15.0	470	16%
	1U			25.0	430	12%
	1P	2017	3x100	25.0	450	16%
	1M	2017	3x30	18.0	270	17%
	1S			20.0	240	21%
	1C	2017	5x3	29.0	740	13%
	2A	2018	3x30	29.0	170	15%
	2C			25.0	110	17%
	2D	2018	5x30	16.0		32%
	2E			22.0	360	27%
	2G			15.0	70	32%
	2B	2018	6x15	26.0	120	11%
	2F			28.0	310	10%
	2I	2018	8x15	25.0		19%
	2J			20.0	420	19%
Mat-51 Calcium- Silicate Brick	2a	2018	3x30	31.0	190	14%
	2b			29.0	130	14%
	2c			35.0	150	13%
	2d			34.0	100	15%
	2e			31.0	90	13%

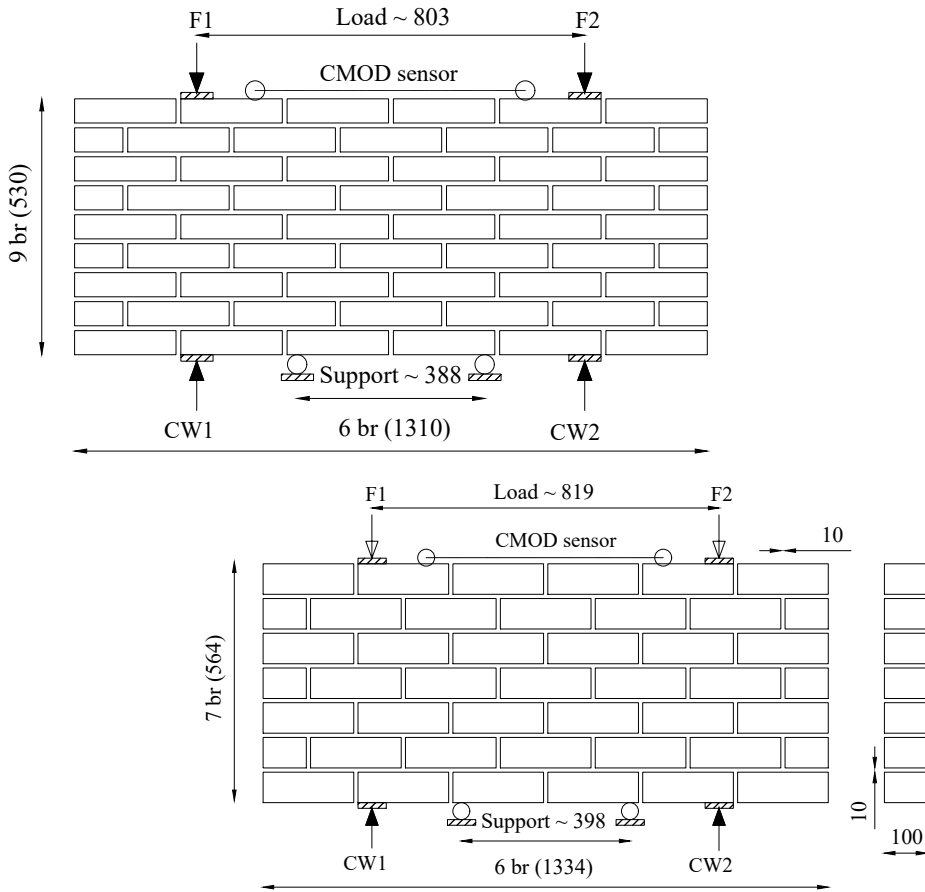


Figure 3.1.10. Geometry of fired-clay, top, and calcium-silicate, brick masonry spandrels. The exact dimension and positioning of the load actuators was measured for each specimen.

3.2. Results from Experiments on Walls and Spandrels

This section presents an overview of relevant results from the aforementioned wall and spandrel tests, monitored to observe crack propagation. Many of these tests are discussed independently in their associated publications and reports; however, this summary consolidates the results in a manner which allows more direct comparisons, establishing trends and observing general behaviour.

3.2.1. Summary of Results on Wall Tests

Several walls were tested first with the repetitive, **one-way cyclic**, loading protocol. These results are presented in terms of force and in-plane lateral displacement in Figure 1a, sorted by maximum force capacity. The displacement is divided by the height of the walls and expressed as drift. The curves reveal several aspects to the behaviour of the walls: most walls have a similar initial stiffness though the calcium-silicate brick walls (CSBR) are stiffer. Most fired-clay walls reach their maximum capacity but do not continue into softening. In contrast, the CSBR walls are more likely to display a drop in capacity at the applied drifts beyond the peak. The curves display, of course, the repetitive cycles enforced during the test with increasing drift. A reduction in force is associated with every repetition of identical drift. Similarly, the hysteresis behaviour is not negligible; a partially elastic unloading means that to return to zero displacement, the wall must be subjected to a negative force. In general, the CSBR walls show a higher hysteresis.

While most of the walls with the fixed boundary were tested with the asymmetric loading protocol, two walls were also tested repetitively, one of each material. Due to the double-clamped boundary, these last have the highest capacity in terms of force, yet the behaviour between CL and CS is distinctly different. The fired-clay displays like hysteresis and secant unloading, while the CS wall shows a larger release of energy. Over the steps, both walls develop large increases in force in contrast to the cantilever walls.

The second part of the figure shows the **two-way cyclic** test that followed (1b). The first six plots, corresponding to fired-clay walls tested under a cantilever boundary, show little hysteretic energy. Especially in the positive drift direction, the reduction in force and the hysteresis are limited. This is because the repetitive tests, in positive drift, had already damaged this direction. In the negative drift direction, the tests display similar behaviour as during the repetitive tests. The following three walls however, of calcium-silicate brick, show a large hysteresis corresponding to a lowering force capacity, with shear

behaviour and matching elastic unloading. These walls develop additional damage at these values of drift.

The walls under double-clamped (or fixed) boundary conditions develop larger lateral forces. The largest capacity corresponds to Comp57, the CSBR shear wall, which develops a sliding shear failure mechanism clearly reflected in the force-drift curve; failure was abrupt. The previous two walls, shear walls made of fired-clay (47 & 48), show nearly identical behaviour, with energy release occurring only in the positive drift direction (asymmetric).

The behaviour of the walls is further compared in Figure 2, where the envelopes of the cyclic tests are drawn together. Indeed, the CSBR walls show the largest hysteresis, followed by the CLBR shear walls. It is also interesting to observe the behaviour of Comp58 and Comp59. These were shear walls with a vertical dilation joint. Comp58, which had the vertical joint in the middle, shows lower capacity and little energy release, with failure consisting only of rocking. Comp59, which had the joint at one-third of the wall's length, experienced shear failure in the wider pier, resulting in a larger release of energy. This is associated with progressively propagating cracks (see the next subsection).

A comparison of the near-collapse envelopes is included in Figure 2. For clarity, not all walls are presented; instead, the figure includes walls of different types. Other walls are excluded because their behaviour is markedly different—these are walls that were repaired or strengthened after the light-damage (LD) tests and were tested again, including both LD and NC protocols. These studies, which are not discussed in this work, included bed-joint reinforcement with steel rebar (Licciardello et al. 2021) and structural glass in window openings (Gaggero et al. 2022).

The near-collapse tests involved much higher drift values, which led to a reduction in the lateral force capacity of most walls and resulted in much larger hysteresis envelopes. Failures included sliding, rocking, and crushing in the case of walls with double-clamped boundaries.

Finally, the results are further compared in Figure 3, where the deformed shapes of a few walls are shown for particular instances during the tests. These plots illustrate the magnified horizontal and vertical displacements of each grid point from the DIC survey. In the figure, these displacements are magnified 400 times. Additionally, the instances are linked to specific moments in the tests, automatically selected at the maximum drift in both negative and positive directions for the cyclic tests, and at the positive drift during the repetitive tests. These instances are taken from the last cycles of each test. Similarly,

residual displacements at the end of the tests, when the applied drift was returned to zero, are also plotted.

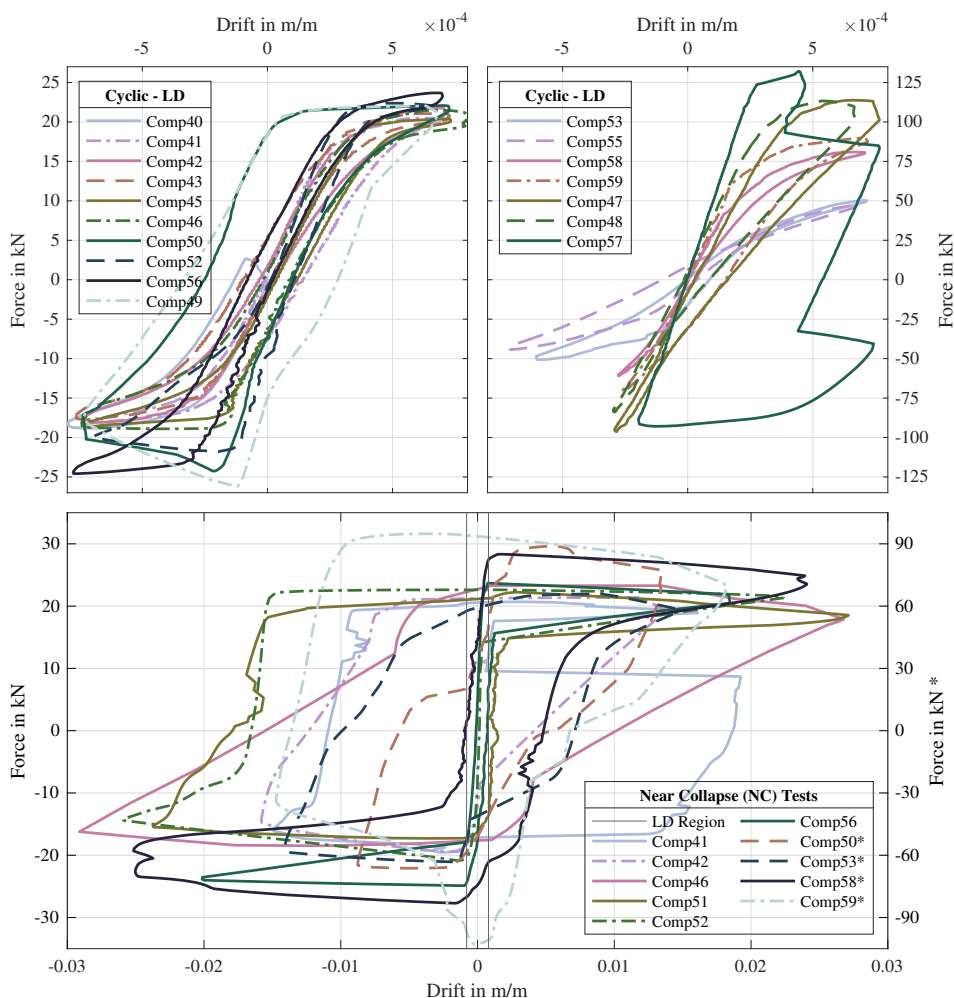


Figure 3.2.2. Envelope of the force-drift curves for the cyclic tests, top, and for the near-collapse tests, bottom. Walls with * are read on the right axis.

Despite its black-and-white nature, Figure 3 is illustrative. For instance, it shows how cracking leads to the decomposition of walls into rigid blocks in some cases, like Comp45, while in others, like Comp55 (which was tested with double-clamped boundaries), the piers are clearly deformed. The figure also shows how some walls experience cumulative shear sliding along the cracks, leaving the piers with residual lateral displacement, as in the case of Comp49. In addition, the behaviour of the shear walls with dilation joints becomes clear: at larger drifts, the piers come into contact with each other, and vertical sliding

takes place. For Comp59, the residual zero position shows that sliding at the bottom of the right pier led to an increase in the opening of the dilation joint. Of course, since the displacements are magnified, what appear to be large cracks are, in the worst cases, only about 2 mm wide. Nevertheless, the locations and configurations of the cracks along their lengths are remarkably clear. The deformed shapes can also be used for one-on-one calibration strategies for computational models, where the displacement at each node is compared against the grid points from DIC.

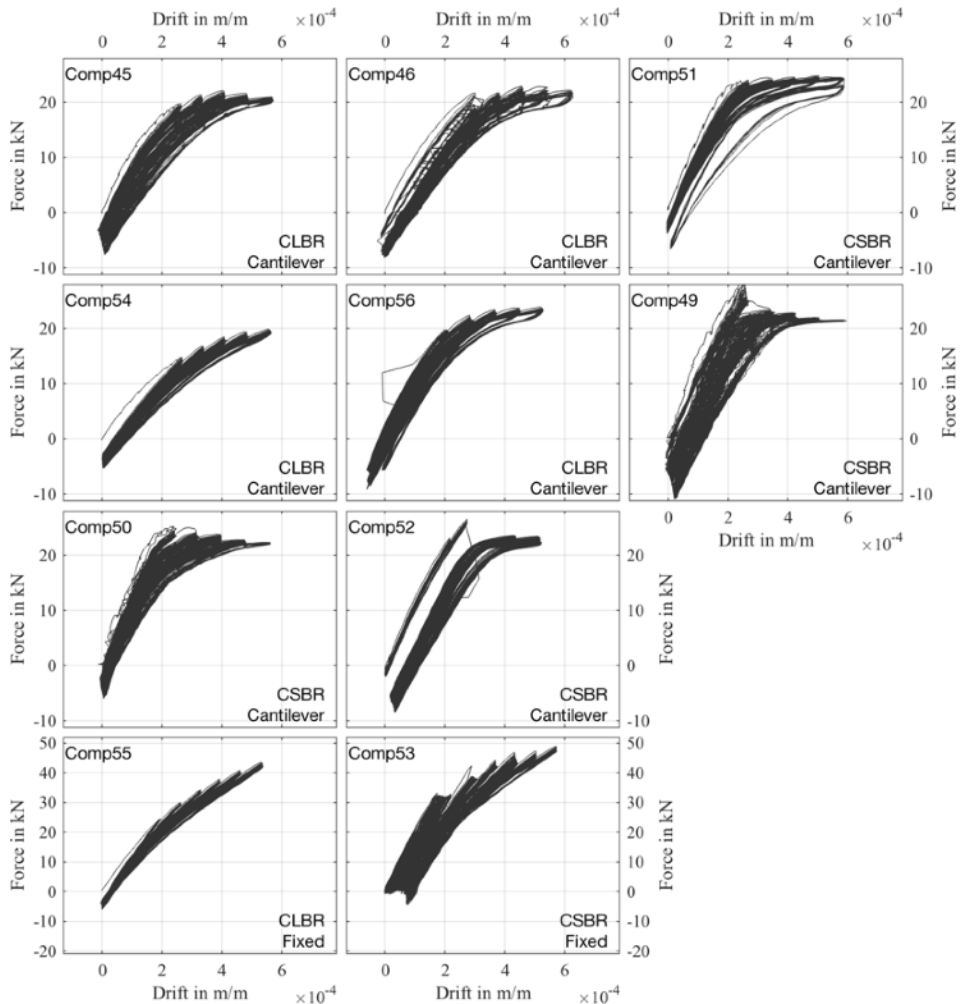


Figure 3.2.1a. Force-Drift curves for the repetitive parts of wall tests.

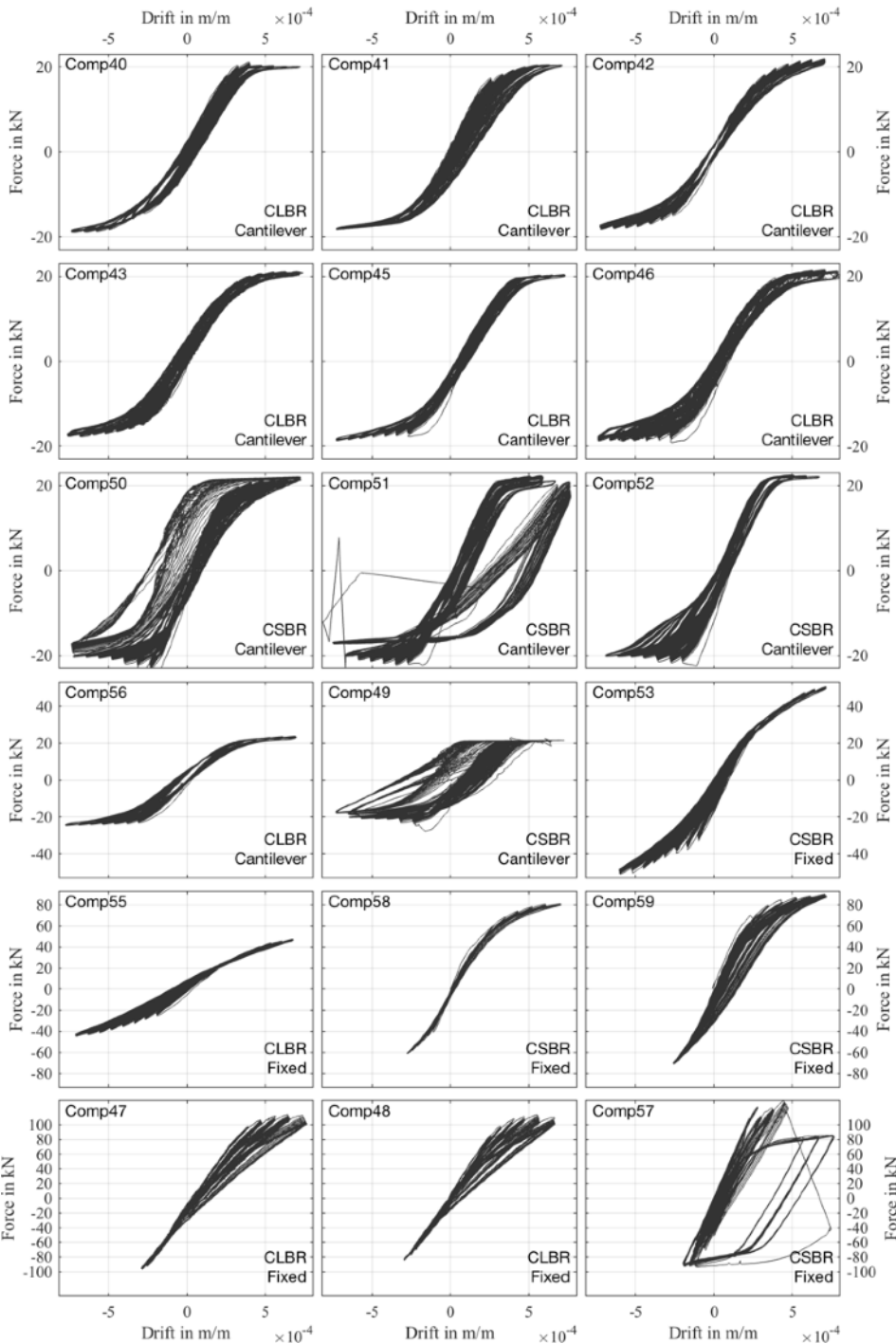


Figure 3.2.1b. Force-Drift curves for the cyclic parts of wall tests; this includes the tests with the asymmetric loading protocol.

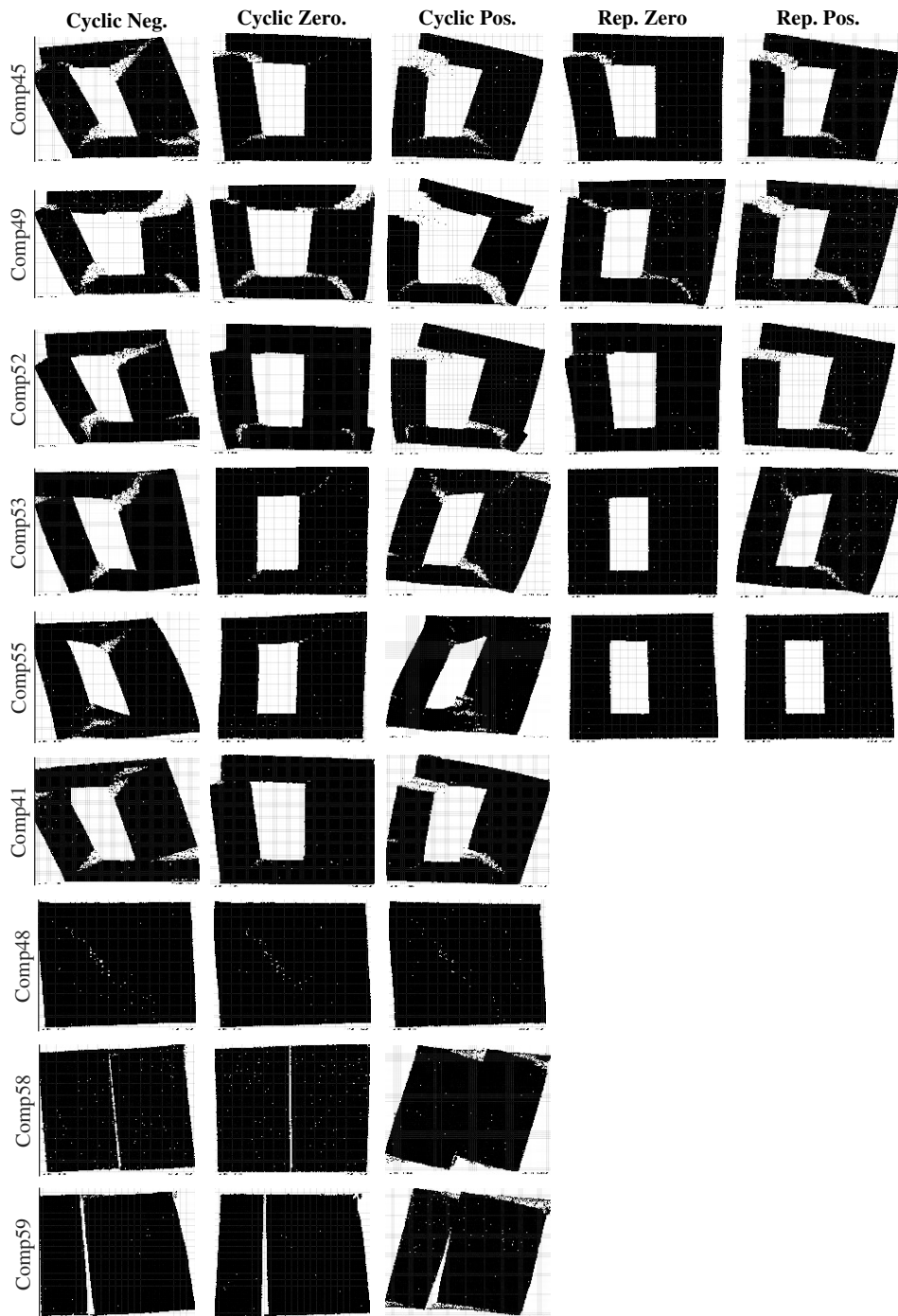


Figure 3.2.3. Magnified deformed shapes towards the end of the tests for several walls.

3.2.2. Summary of Results on Spandrel Tests

The window banks were designed to develop a single vertical crack due to bending or vertical shear. This sort of crack are common due to in-plane bending of façades because of shrinkage or settlement actions, see Chapter 4, and appear above doors or underneath openings for windows - hence the name of the test. Additionally, these cracks may occur due to Rayleigh waves propagating through the soil due to earthquakes.

Since the location of this single crack was known, it was also possible to control the test by monitoring this crack; see Figure 3.2.4. This is known as a crack-mouth-opening-displacement (CMOD) controlled experiment. The CMOD was slowly increased by controlling the force applied with the hydraulic actuators (jacks). For the repetitive tests, it was also possible to unload the samples down to a minimum load of 2 kN; the cracks would then partially close. This behaviour is illustrated in Figure 5 for every specimen tested.

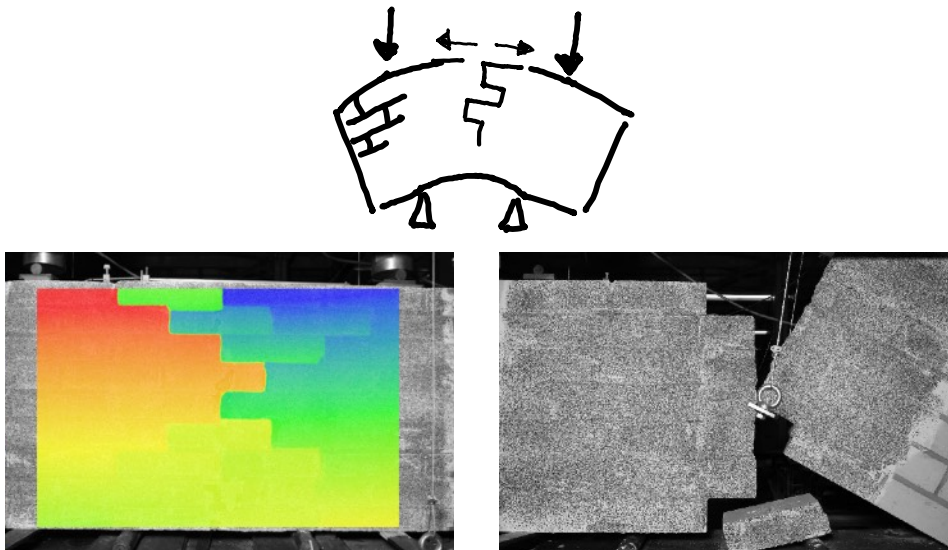


Figure 3.2.4. Spandrel specimen 2B, fired-clay with toothed crack revealed by DIC output; and sample 2a, calcium-silicate brick masonry with brittle, brick-splitting vertical crack.

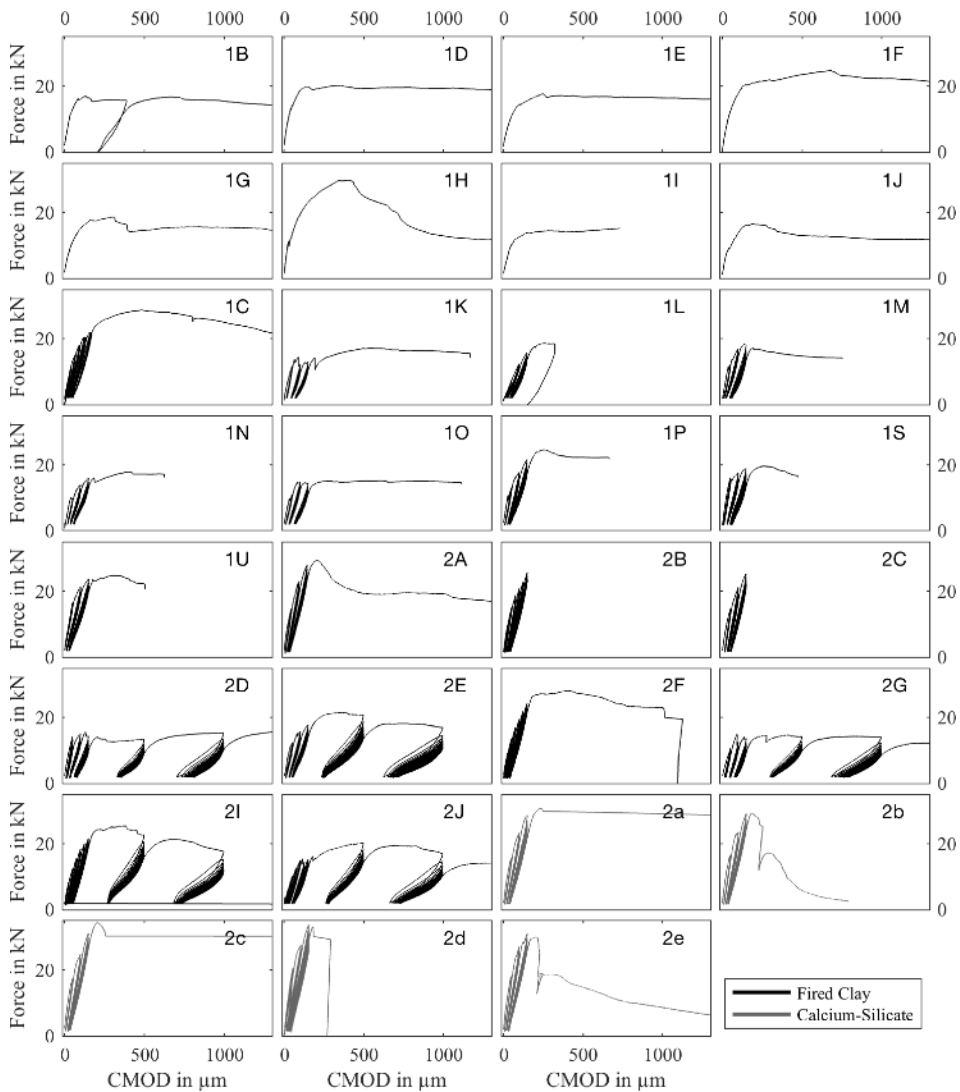


Figure 3.2.5. Force versus crack-mouth-opening-displacement for all the spandrel tests, both monotonic and repetitive. See Table 3.2 for an overview of the specimens.

Because a relatively large number of specimens could be tested, many different trials were conducted in terms of loading. For example, specimen 2D was tested with the established 3x30 repetitive protocol at 50 μm , 100 μm , and 150 μm crack opening, but two additional steps were added at 500 μm and 1000 μm . For specimen 2E, these additional steps resulted in early failure, before the monotonic phase. At 1 mm, the force degradation occurring during the repetitions was significant; up to 40% in comparison to the 10% observed during wall testing. Some specimens, like 2B, failed during the initial set of repetitions, too, while others, like 2J could sustain the planned 6x15 repetitions

and two additional sets of 15 at the higher CMOD; failure occurred later during the final monotonic stage.

The large reduction in force during the repetitive steps in comparison to the degradation observed at the walls was likely due to several reasons: First, unlike the walls, the spandrels develop a single prominent crack. Through the repetitions this toothed crack propagates but also slides over its zigzag pattern. A part of this sliding remains during elastic unloading and so every repetition requires a lower force to achieve the same overall displacement. This central crack is a Mode I crack for tension in the vertical direction; however, at the local scale, Mode II behaviour is observed at the bed-joints. For the walls, the cracks have comparatively only Mode I behaviour. Nonetheless, calcium-silicate samples did not develop the zigzag crack. Therefore, their fracture energy for tension in the horizontal direction appears drastically lower in comparison to the clay specimens [3]. Crack behaviour is further discussed in follow-up Section 3.2.3.

Secondly, the spandrels were CMOD controlled which also contributed to the large force degradation. In contrast, the walls are drift controlled; the repetitions imposed an identical drift and saw a force reduction *and* crack propagation in terms of length and width. The spandrels, in turn, enforced a constant crack width and so it follows that a larger force reduction or degradation should be observed.

Finally, the repetitions for the spandrels occur at a proportionally higher percentage of their ultimate displacement capacity. The repetitions were conducted at an applied displacement 1/100 to 1/10 of the displacement where the specimens failed. The walls, instead, were subjected to drift values from 0.2 % to 0.7 % during repetitions and the near-collapse tests were halted at drifts between 1 % to 3%. This means that the walls were tested at 1/150 to 1/50 of their ultimate drift. However, the walls were never allowed to fully fail due to safety reasons so their ultimate drift might have been much larger; the setup of the window banks, instead, could contain the samples even during total failure, see Figure 4.

The force applied during the spandrel tests can also be plotted against the displacement at the point of application of the force. This is presented in figure 3.13 for the monotonic tests and the envelope of repetitive tests. The graph is drawn with the displacement on a logarithmic scale to better illustrate the behaviour of the experiment where the initial branch appears stiff otherwise (see Figure 3.11). On this logarithmic scale, the initially linear branch appears as a rising curvature which changes to a downwards curvature as it approaches the peak of maximum force. The inflection point corresponds thus to the start

of non-linear behaviour. This means that cracks have begun much earlier than the maximum capacity. In fact, the inflection point occurs at about one third of the maximum force reached. This is also the relationship between the flexural strength of the masonry (in-plane, head-joint opening) and its tensile strength. The location of this inflection point relates to a measured CMOD of 45 μm , 52 μm , and 42 μm for the monotonic, repetitive, and calcium-silicate brick tests respectively. It seems that at this crack width, cracking displays an effect on the non-linear behaviour of the masonry.

The figure also shows that calcium-silicate tests are stiffer and stronger than their clay counterparts. However, they are also significantly less ductile. Indeed, all calcium-silicate spandrels failed in a brittle manner with a vertical crack splitting bricks. The toothed crack developed by the fired-clay specimens did not appear.

The reasons for the differing failure mechanisms are multiple. First the geometry of the samples varies. Because of the larger calcium-silicate bricks employed (70 vs 50 mm tall) the CSBR sample is slightly taller (17%). This was compensated by separating the support points slightly, however, it still results in internal forces where the CSBR samples experience comparatively more shear while the CLBR ones have more bending.

Second and probably most influential, the relative strength between brick, mortar, and brick-mortar interface result in a more detrimental combination for the CSBR material. The clay bricks are stronger in tension and the initial shear strength (cohesion) of the interface is lower. This means that the CS bricks are subjected to more horizontal tension, for which they are ill prepared.

The bottom graph of Figure 3.2.6 demonstrates that the behaviour of the monotonic tests well represented by the envelope of the repetitive tests. This means that the envelope of cyclic tests can be used to validate also models with monotonic loading.

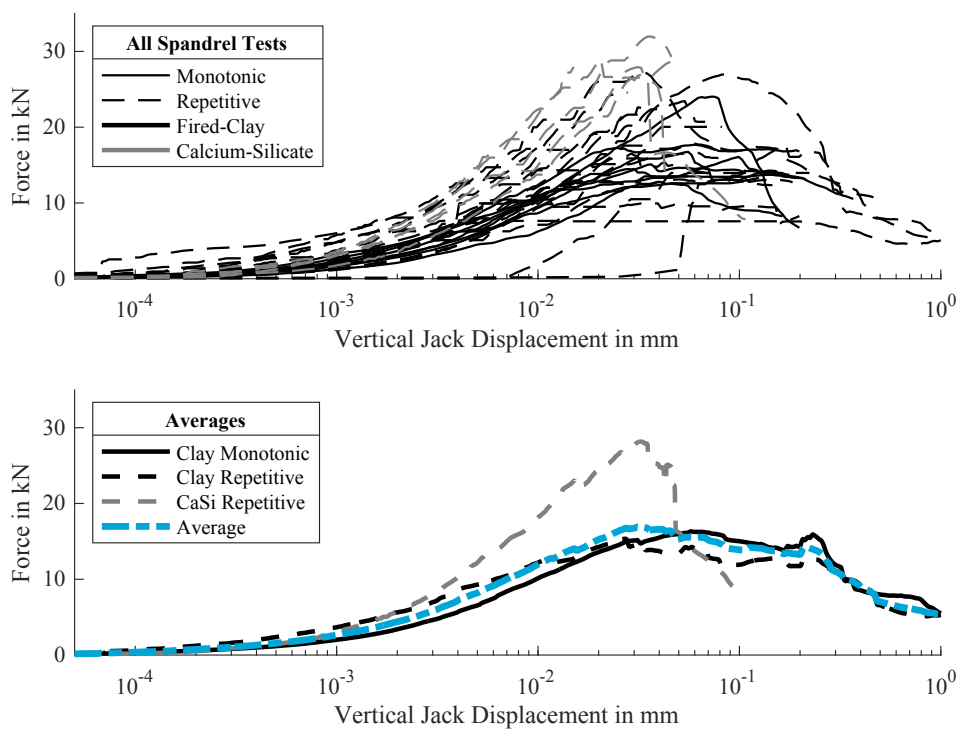


Figure 3.2.6. Force-displacement summary of the spandrel tests using the upper envelopes of the curves. The horizontal scale is logarithmic.

3.2.3. Lessons about Crack Propagation

Many results from the spandrel and wall experiments have been shown in previous sections; glimpses of the influence of cracking have been provided. In this section, a clearer focus is placed on results about crack propagation. Every crack from every experiment cannot be investigated. Instead, a few examples are presented with different types of figures to illustrate and later conclude some lessons about crack initiation and propagation in masonry. The earlier publications and the dataset published along this dissertation (see Appendix F) supply additional details.

First, consider the increase in crack width over repeated cycles. Figure 7 shows the measurement of a CMOD that happened to be located in the correct location to capture the crack forming at the bottom right corner of the first wall tested, Comp40. The value output by this sensor was used to determine the magnitude of the first drift enforced - that which corresponded to an observed crack width of 0.1 mm. During this first step, of three repetitions each, the identical drift didn't lead to any measurable crack increase; however, while the drift was increased by 25% for the second step, the CMOD increased 100% to 0.2mm. Moreover, already during the second step, a slight increase in crack width within the step could be seen. Later steps also saw an increase in crack width measured at the mouth over the repetitions.

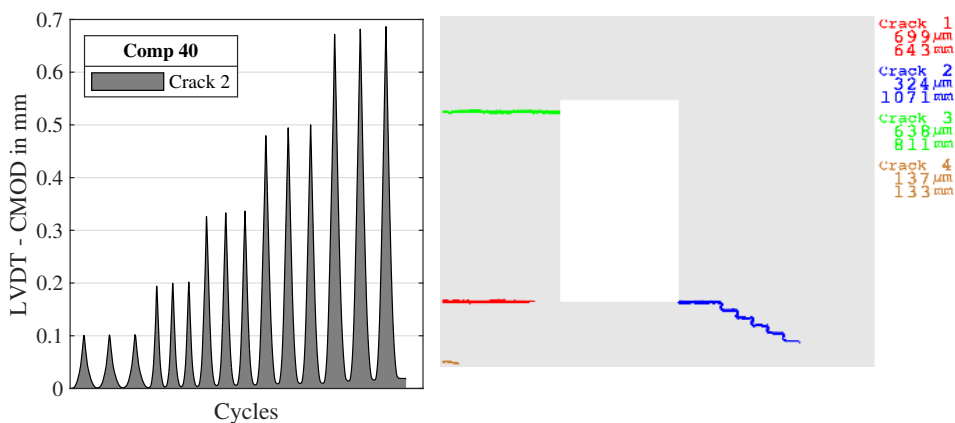


Figure 3.2.7. Crack width of the very first test with three repetitions (TUD-Comp 40). A slight increase can be observed within each incremental step (five of three repetitions each). Measured with an LVDT at the crack mouth of Crack 2 as identified with DIC. The overview, right, is drawn from end of third step.

Figure 8 shows the progression of four cracks, at different locations and in different walls. The progress is shown in terms of crack width, length, and pattern. First, the body shear crack of Comp47 begins at the top. With a small crack width, the length of the crack first increases. Then, both width and length

develop quickly towards the end of the test. This is contrary to the behaviour observed for the example of Comp45. Here, the width and length of the crack, after it has appeared in the very first cycles, gradually progresses over the entire experiment, with an aggravation that follows the applied drift.

The second case of Comp53 also sees a more important crack propagation towards the end of the test. In this case, the length remains mostly constant after the third image since the crack cannot continue extending. Instead, the last steps see a significant increase in width. This is alike the example of Comp49. In this case, the highlighted crack had appeared during the repetitive part of the test, and the figure shows the cyclic portion. Consequently, once the crack opens, the entire length is activated, connecting the corner of the window opening and the edge of the wall on the left side of the pier. Also, the opening of the crack follows the steps in applied drift, though with a small slope of increasing width. Only at the end of the test, when higher values of drift are applied, the crack width displays a steadier increase.

Recalling Figure 3.1.7, where for Comp55 the same crack as Comp45 is highlighted, reveals a comparable behaviour. The nominally identical walls, of the same material and testing protocol only differ in the year of construction and the fact that Comp45 had been pre-damaged with “unbonded” joints. This pre-damage however seems not to have influenced the crack at the top right of the window opening. This is reasonable since the pre-damage was located such that the positive drift direction was affected (see Figure 3.1.8) and the highlighted cracks appear during negative drift. In both cases, the cracks first grow more rapidly in length, while the width develops mostly at the end of the test.

This behaviour can be further studied with a different type of graph for yet additional cracks not yet highlighted. Indeed, the following figures show the “trail plots” of selected cracks. These display the width of the crack along their entire length. The length is followed along the centre line of the crack. In this way, it is possible to see if cracks are tapered, where one end is wider than the other, or, as opposite, if they display a uniform width. The trail plots show crack progression but plotting all instances of the width-length relationship for the given crack. This means that the state of the crack at the beginning of the test (blue) fades over (green, yellow) to the state at the end of the test (red).

Note that the crack width is the principal component of both opening and sliding. Also, the length is the true length following the stair-case path of the crack. For a complex crack (such as later shown for Comp48), the length will be the stair-case length between the most extreme end points of the crack.

The first part of Figure 3.2.9 shows a simple crack forming at the bottom right corner of Comp54. The crack first propagates horizontally and then continues-staircase diagonally. The horizontal portion, both at the beginning as towards the end of the test shows a reasonably constant width with a peak at the very mouth of the crack. The propagating crack through the head joints of the masonry quickly becomes less wide. Throughout this test, the width of the crack increased about 4-fold but its length grew almost 7-fold. The test included five steps of thirty repetitions (5x30). The first and second steps didn't see much crack development. However, between the second and third, and subsequent steps, a clear increase in width and length appeared. Within each step, these increases were minor; yet, especially during the last step, the larger width and length correspond to the last repetitions.

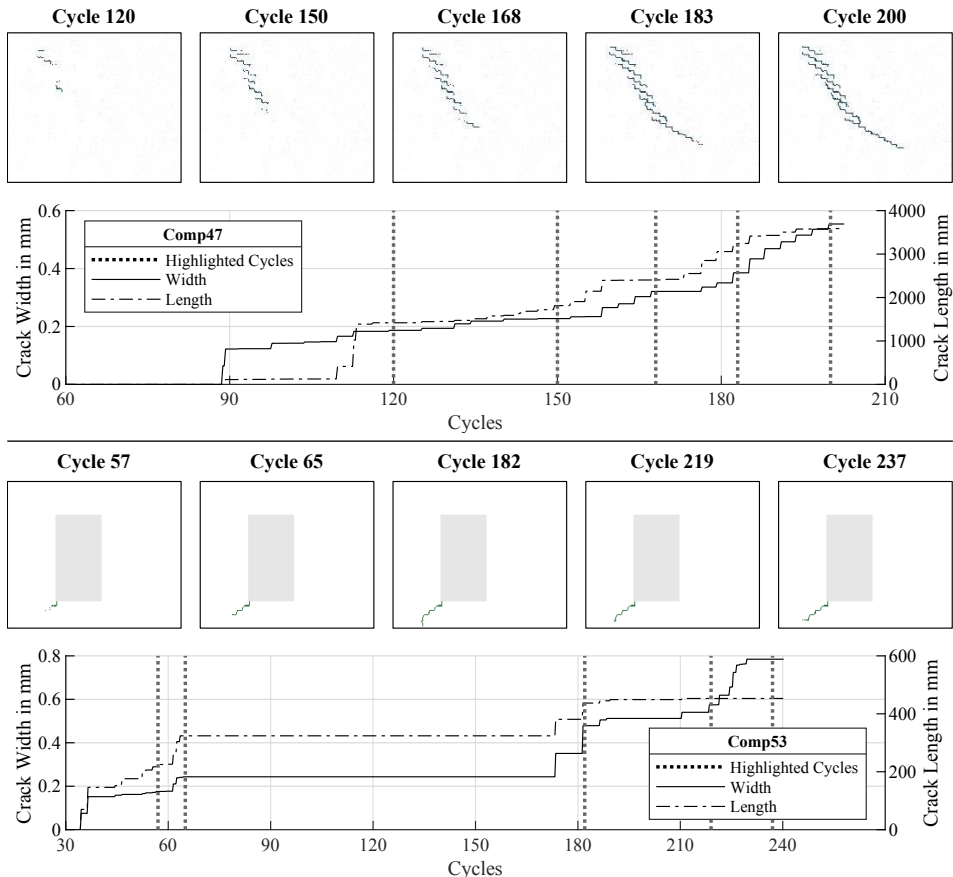


Figure 3.2.8. Progression of selected cracks on selected walls at selected intervals. Crack tracking monitors the progression in terms of crack width as well as crack length is layout; specific instances are highlighted. The cases of Comp47 and Comp53 are shown. See also Figure 3.1.7 for Comp55.

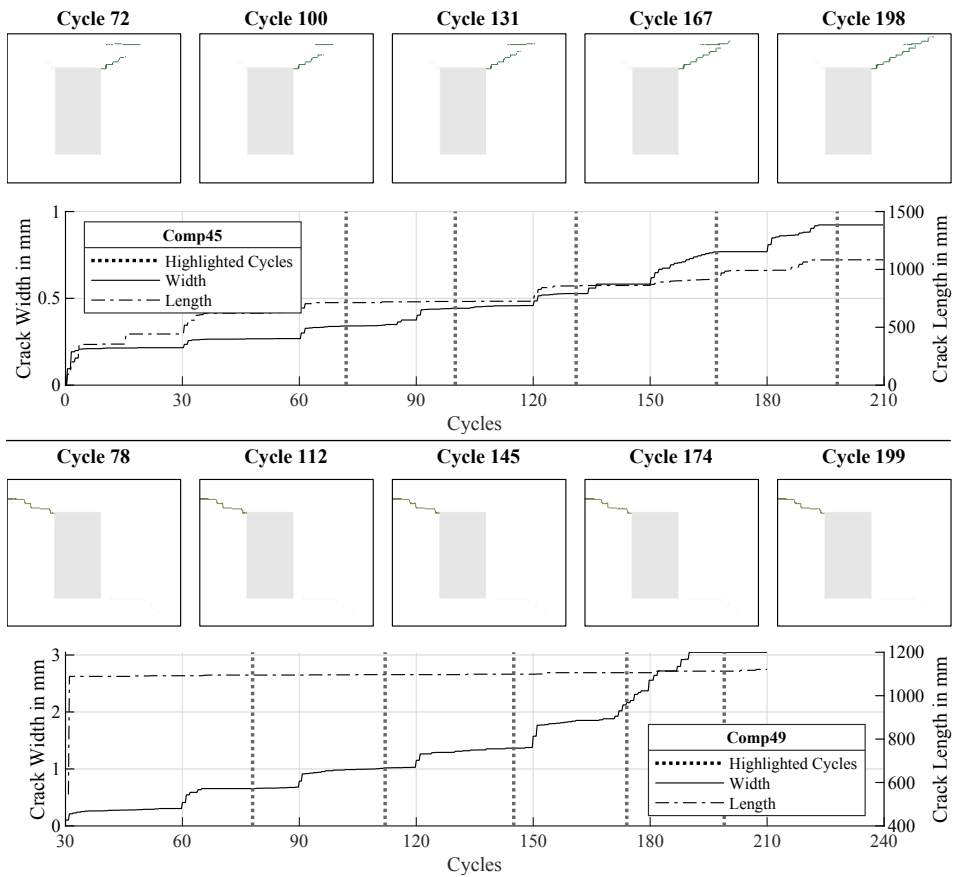


Figure 3.2.8 (continued). Crack tracking for walls Comp45 and Comp49.

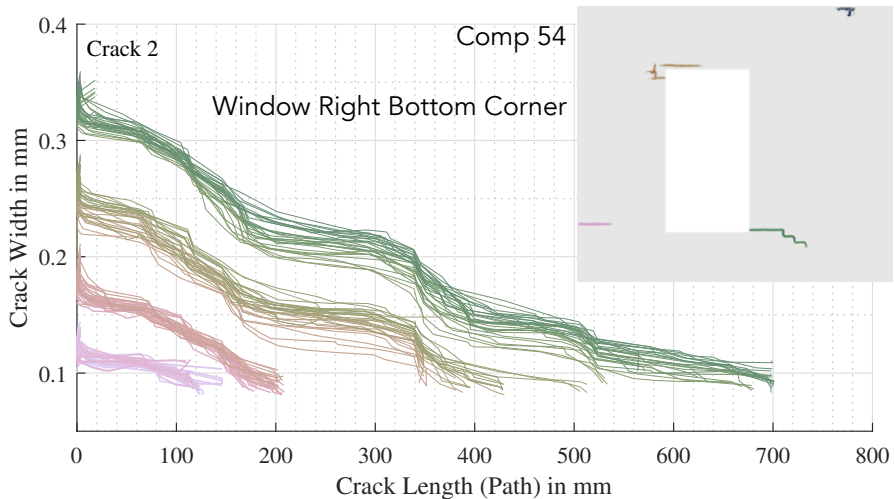


Figure 3.2.9a. Crack width-length plot (Trail plot) for crack 1 at the right bottom corner of the window opening for Comp54, fired-clay wall, repetitive, cantilever test.

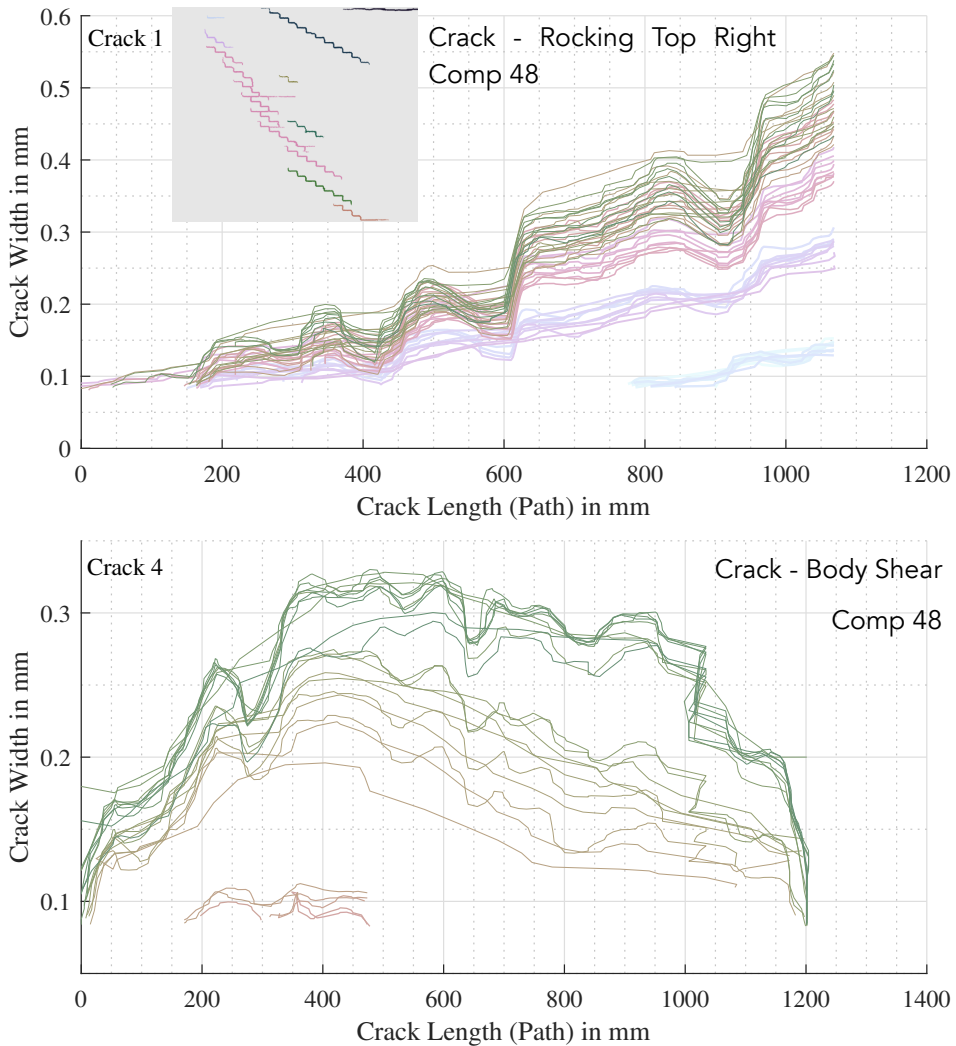


Figure 3.2.9b. Trail plots for cracks 1 and 4, the top rocking crack and the lower body crack for the test of the fired-clay shear wall, Comp48.

Similarly, Figure 9b shows the trail plots for the shear wall, Comp48. In this case, two cracks are selected. The rocking crack at the top forms at the very beginning of the test and displays a clean progression of width and length. The crack is tapered, the larger width is shown always on the left of the plot but corresponds to the right tip of the crack at the crack mouth on the edge of the wall. Around the middle of the test, the crack length stopped increasing substantially and the crack aggravation focused on a progressive increase in width until about 0.55 mm. The body crack behaves differently. The crack width is maximum at the centre of the crack. This is expected for a shear crack; see also the deformed shapes in Figure 3.1.7. The crack also increases in length.

Most of the aggravation, however, occurs in the later cycles. The crack quickly grows once the deformation localises, the head joints open, sections of the crack cut vertically through bricks, and other nearby cracks unload.

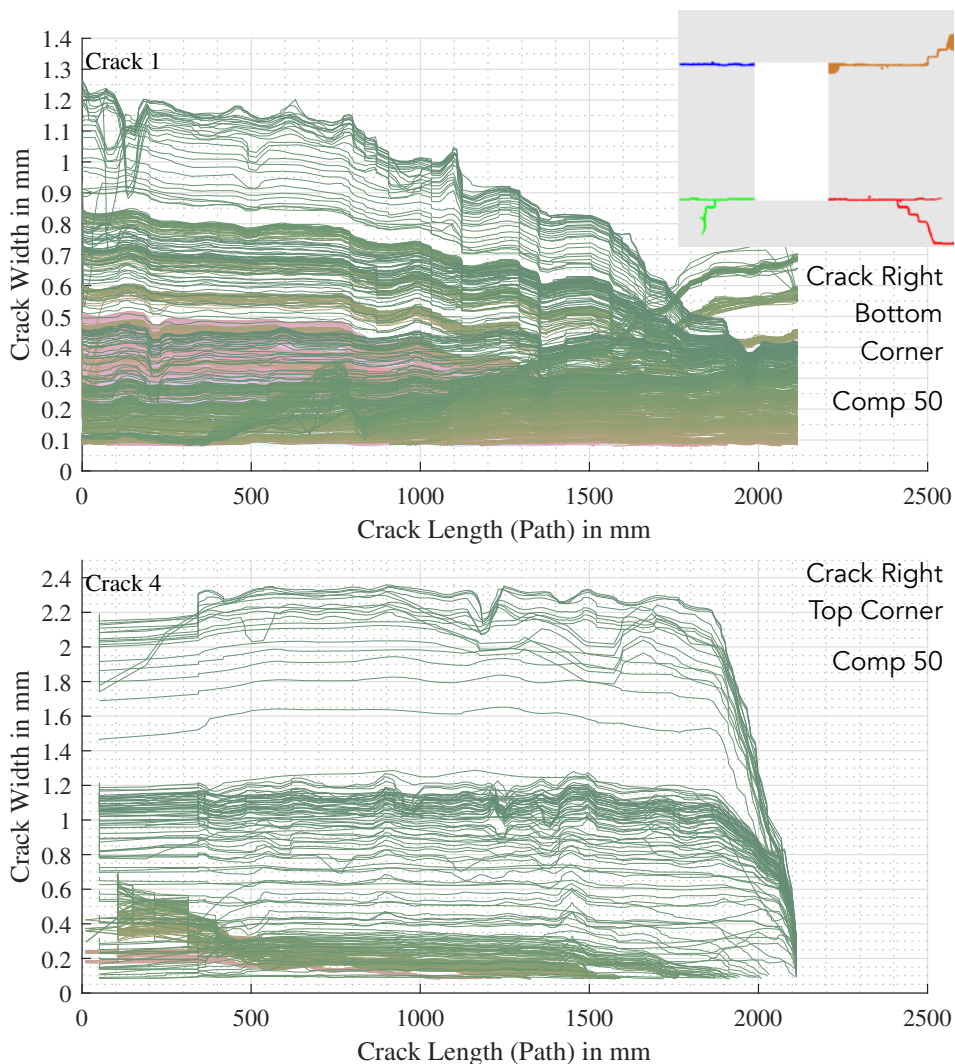


Figure 3.2.9c. Trail plots for cracks 1 and 4, the bottom and top cracks propagating on the right side of the window opening during the repetitive+cyclic tests of the calcium-silicate brick wall, Comp50.

The case of Comp50, one of the calcium-silicate walls where cracks propagating off the four window corners reached the opposite ends of the piers, is presented in Figure 9c. This figure comprises the repetitive and cyclic tests together. Both cracks are quite uniform with a constant width that increases rapidly at the end of the test. Crack 1, opens up for both values of

drift, positive and negative. For the main cracking direction, it is uniform, but for the opposite it is tapered. The other crack, at the bottom corner is also uniform but tapers quickly towards the tip. During rocking, the very tip must remain in compression (toe) and thus the crack width quickly goes to zero.

These graphs show that there are different types of cracks, even in similar tests and in the same specimen. However, the cracks behave consistently during repeated and increasing loading: propagation occurs with increases in width and length.

A similar analysis can be conducted for the spandrels. The centre portion of the window banks was also surveyed with DIC. Figure 3.2.10 shows a few of the crack patterns that arose during the tests. The cracks begin at the top, along one of the three centre head joints, and descend zig-zagging along the joints. Conceptually, this represents a vertical crack in masonry; (smeared) continuum material models would identify them like vertical cracks. The first six specimens selected correspond to the fired-clay material and represent all the variations on crack pattern observed. The last example is one of the few calcium-silicate specimens for which the DIC was able to capture the brick-splitting vertical crack before the sample failed completely. This is probably because the crack bifurcated at the bed joint instead of continuing straight vertically. The figure also reveals that vertical cracks localise less than horizontal cracks. Several neighbouring joints appear open along the main crack path.

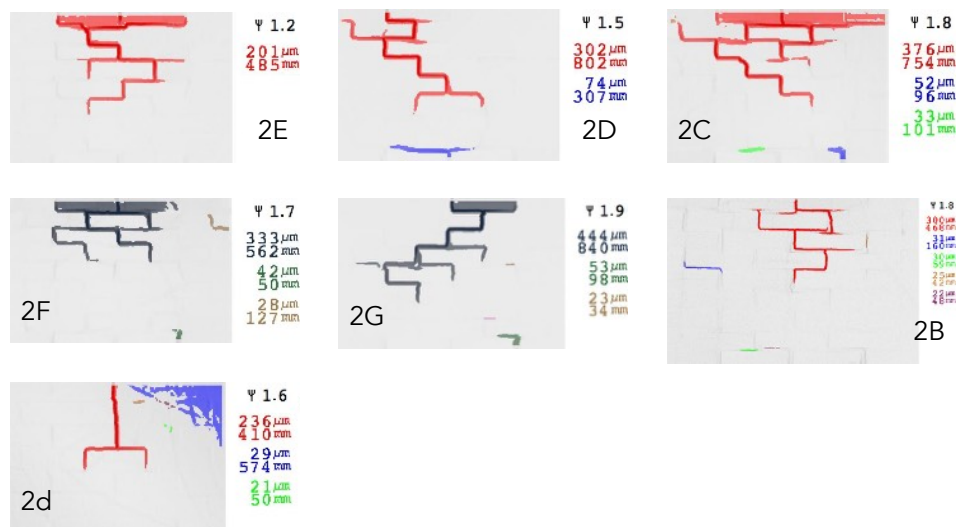


Figure 3.2.10. Examples of crack patterns observed during the window bank tests.

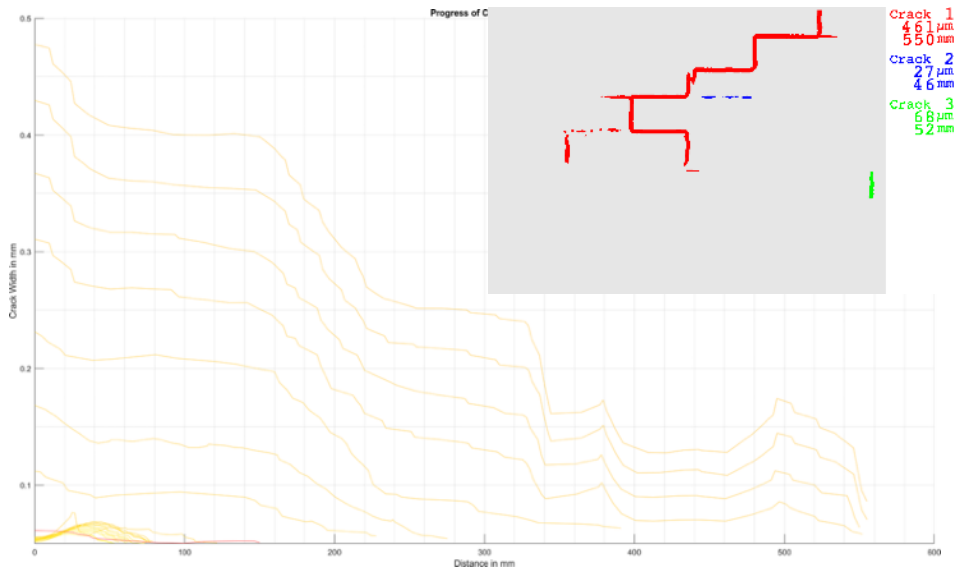


Figure 3.2.11. Crack trail plot for a window bank (2A).

At an increased resolution, it is also possible to present trail plots for the main crack in the window bank tests; the case of specimen 2A is depicted in Figure 11. The crack is invisible during the repetitive portion of the test as the width is much smaller than 0.1 mm, with a length of about 100 mm, corresponding to opening of the head-joint and a part of the bed-joint. During the monotonic part of the test, at much greater CMOD, the crack grows quickly in width and proportionally in length. Around the corners between head- and bed-joints, drastic decreases in width can be observed. The behaviour of this vertical crack in the spandrels doesn't differ much from that of the cracks observed in the walls. This further validates the observation that crack propagation is consistent among different types of cracks.

3.2.4. Conclusions about Crack Propagation

The experiments have demonstrated that cracks mostly initiate from the corners of openings. In some cases also at the lateral edges of walls, and when walls are loaded in shear, also body cracks may appear. For lateral loading, most cracks are horizontal or step-wise diagonal. They begin smeared over multiple joints but coalesce into a single crack. The other nearby cracks unload and close [4].

When cracks propagate, both their width and length grow simultaneously. It is rare for a crack to grow in length but not in width. The opposite is also true: when cracks widen, their length also increases until that is no longer possible.

For example, when a crack spans an entire pier, its length cannot continue increasing. In this case, the width of the crack increases at a higher rate.

The high-resolution monitoring system detected that cracks appear even before they become visible to the naked eye. Many cracks remain 'invisible' while others propagate. Sometimes these invisible cracks never manifest as other cracks become dominant. However, a variation in loading could have aggravated these cracks.

Different types of cracks (horizontal, diagonal, vertical, tapered, or uniform) do not behave too differently in terms of crack propagation. Indeed, similar aggravation in terms of increases in width and length can be expected under similar increases in loading.

Furthermore, repetition has an effect on crack propagation. Under identical loading, cracks still become wider and longer. This effect is minor but measurable and consistent. The effect of repetition is explored in more detail in Sections 3.2 and 6.1.

3.2.5. Four Ways to Utilise the Experimental Results

The experimental tests serve several purposes. Many are specifically exemplified in this report in various sections. First, experiments can be used directly. The results are analysed and observations are drawn from them; this is shown in earlier sections. Additionally, the experiments can be used to test new technologies such as high-resolution DIC. Furthermore, the results can be processed to establish relationships between measured values. For example, in Section 3.3 next, a relation between drift and damage is established, formulating drift limits.

Second, the experimental results can be used to tune or validate numerical models. The input parameters for many material models must be derived experimentally. A calibration of finite element method models is conducted in Chapter 4.

Third, the experiment-calibrated models are used for extrapolations, analysing actions that are difficult to evaluate in experiments. In this way, the experiments are used indirectly. An example is elaborated in Chapter 5.

Finally, the experimental results can be compared to other phenomena. For example, effects observed from monitoring real structures can be contrasted against similar cases investigated experimentally. In Chapter 6, the effect of repetition in various models is compared to the effects of repetition observed in the experiments.

3.3. Crack-Based Drift Limits from Experimental Results

This section presents the first applied results from the experimental campaign in the form of drift limits.

3.3.1. Drift Limits for Light Damage Lacking in Literature

In the realm of structural engineering, the determination of drift limits stands as a pivotal aspect in assessing the performance and resilience of buildings subjected to lateral forces such as wind or those induced by vibrations (FEMA 2013, Crowley et al. 2017). Drift limits serve as invaluable thresholds, facilitating a comprehensive understanding of a structure's behaviour under dynamic loading conditions [3] and some quasi-static actions like differential settlements (Burland et al. 1974). Engineers, during the design or retrofitting phases, routinely employ drift limits as metrics to gauge and ensure the structural integrity of a building, with the aim of meeting specified performance goals when exposed to various hazards (Del Gaudio et al. 2017).

Masonry walls are particularly susceptible to damage resulting from in-plane actions. Thus, it is imperative to verify that in-plane drift remains within acceptable limits to mitigate the risk of (structural) damage (Aldemir et al. 2015). Within performance-based design, frequent vibrations or wind loads should be considered such that masonry components do not enter light damage. Drift limits provide a useful tool for this analysis (Colangelo, 2015).

The current landscape of drift limits for masonry walls often encounters limitations, especially when not derived from crack-based damage assessments. Notably, existing limits, especially those used for DS1, are frequently extrapolated from higher damage grades predicated on the structure's ultimate capacity or ductility (Crowley et al. 2019, Gehl et al. 2013). This extrapolation poses challenges in accurately predicting the threshold at which damage becomes a concern, highlighting the need for more specific and experimentally-derived drift limits. These offer a more granular and realistic understanding of a masonry wall's response to lateral forces. Unlike model-based or extrapolation-based limits, experimentally-derived thresholds for light damage provide a direct and precise measure of the drift at which damage initiates (Magenes et al. 1997, 2010; Giardina et al. 2016). A clear definition of damage must be applied, however; see Chapter 2.

Indeed, most experiments of in-plane walls have focused on establishing thresholds at which the strength capacity of the components is compromised: this is the ultimate limit state or near-collapse. Limits, at which damage begins, where mechanical damage is related to crack-based damage in masonry, have

seldom been directly quantified. They rather have been indirectly extrapolated from the shape of force-displacement curves (Negulescu et al. 2014, Petry & Beyer, 2015). Crack-based light damage, ranging from just-visible cracks to wider cracks not yet compromising the capacity of a wall or component, is nevertheless important to quantify repair and maintenance costs, to prevent additional damage (such as the ingress of water into the structure).

The walls presented in the previous section can be used to define experimental drift limits suitable for light damage. The outcome of these tests is analysed in this section in terms of the relationship between drift and damage with the goal of determining when light damage begins and when it can be considered to end. The section starts with a brief overview of the relevant aspects of the tests and continues with an investigation of drift and crack-based damage as measured with the Ψ parameter. A discussion, including a comparison to other drift limits and a wrap-up conclusion, are included in the last subsection.

This scheme is shown in Figure 1 where the methodology of the section is described in a flow chart. The experimental tests and the definition of light damage from earlier work are brought up to post-process digital-image-correlation measurements from the tests to determine cracking behaviour. This becomes the response variable in a machine learning classification problem that includes other features from the test such as the wall geometries and setup boundaries, though ultimately isolating drift as the main predictor for damage. Moreover, drift thresholds are defined for two types of masonry, namely fired-clay and calcium-silicate brick masonry.

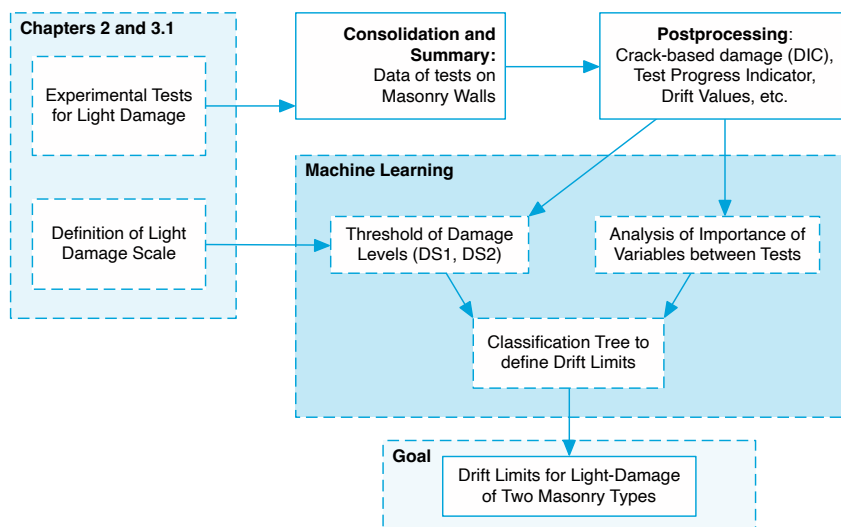


Figure 3.3.1. Flowchart of the process to obtain drift limits from the experiments.

3.3.2. Repetition in the Loading Protocol of Experiments

To characterise the cracking behaviour of masonry at the component scale, that is, to observe how cracks initiate and propagate on full-size elements such as walls, several types of experiments have been conducted. In parallel, tests focused on the fracture mechanics of masonry, at the brick-to-brick scale in tension and shear were analysed, while smaller wallets were included to investigate compressive properties and predominantly vertical cracking in in-plane flexure. The focus, however, was placed on walls about 3.1 meters wide and 2.7 meters tall built of single wythe (about 100 mm) brick masonry in a stretcher bond pattern. Twenty walls have been tested with a light damage protocol and sixteen of them were driven to near-collapse; see Section 3.1. Various experiments focused on different brick materials, initial conditions such as existing cracks represented by “unbonded” joints, varying cycle repetitions, openings, differing boundary conditions, etc. A common thread throughout these, however, was the light damage protocol consisting of a large number of repeated, incremental cycles (Section 3.1.1) surveyed by digital image correlation (Section 3.1.2). In this context, it is possible to link the applied in-plane drift to the cracked conditions of the masonry.

The walls were loaded first, with a one-way, cyclic in-plane drift is enforced with five or six steps of repeated cycles. The amplitude of the first step is that which causes a value of $\Psi=1$; this is repeated 3, 10, 20 or 30 times before increasing this amplitude by 25% for the following step. The magnitude of the increase is kept constant. Second, a two-way cyclic (with both positive and negative) drift is applied. The magnitude of the steps is the same as for the one-way cycles with up to seven steps, meaning that the amplitude of the last step is 2.75 times larger than the first step. Each step consists of 30 or 50 cycles. Third, a near-collapse protocol is applied which comprises fixed displacements: though the tests might be terminated before the last step. Alternatively to the repetitive and cyclic protocols, an asymmetric light-damage protocol may be employed. This one includes cycles in both directions, but the amplitude of the cycles in one direction is halved.

The different stages of the tests have been analysed previously: The repetitive stage only includes drift values in one direction and is associated with a reduction or degradation of the force of each repetition of the drift; the force remains mostly positive. Some residual drift is accumulated towards the end of his stage. The cyclic phase includes drifts in the opposite direction. Most of the force degradation in the positive direction has already occurred while the negative drift still leads to a reduction of the force within every step. This force degradation is linked to a propagation of the cracks in both width and length.

Finally, the near collapse stage offers a more familiar picture with large reductions in lateral capacity at increased drift and a considerable hysteresis envelope during shear failure. See Figure 3.2.1 earlier.

The repetitive, cyclic, and asymmetric protocols enforce in-plane drift values that reach up to the maximum force capacity of the specimens. Up until this point, cracking develops and later worsens during the near-collapse stage until the final failure mechanism. Throughout the experiments, DIC is used to measure a displacement field of the entire surface of the walls. This means that cracks anywhere on the walls can be tracked accurately. For every value of drift and at the intermediate zero drift value, a record of the cracks was captured and the value of Ψ automatically computed based on the width, length and number of cracks.

3.3.3. Relationship between Crack-based Damage and in-plane Drift

The intensity of damage is characterised by the cracks on the walls using Ψ . These are plotted in Figure 3.3.2 against the absolute value of drift. However, the figure includes two horizontal and four vertical thresholds which are dissected in this subsection. The former correspond to the values of Ψ that establish the transition into and out of light damage. The latter are the drift values that are the goal of this section. Note that drift is plotted on a logarithmic scale which suggests an exponential relationship to damage. This relationship is dependent on the formulation of Ψ where the number of cracks and the weighted crack width carry exponents of 0.15 and 0.3, respectively.

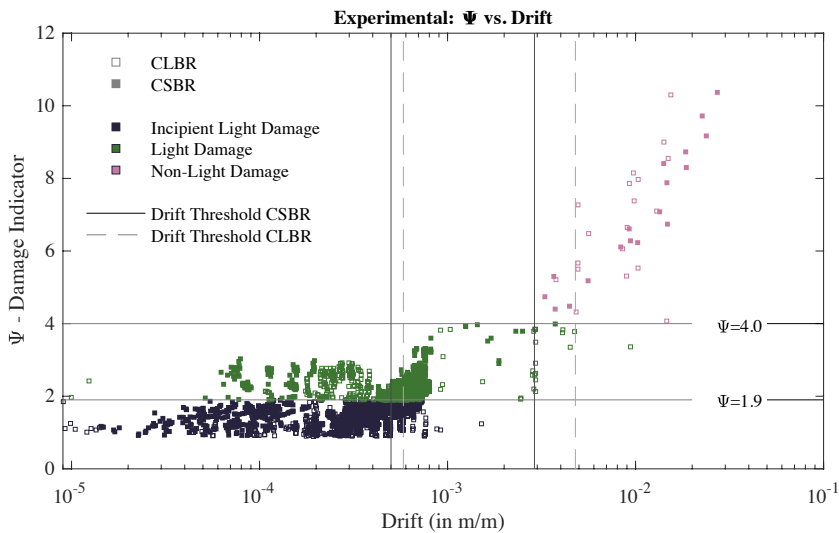


Figure 3.3.2. Wall in-plane drift against crack-based damage measured by Ψ . Proposed thresholds for clay and calcium-silicate brick masonry are included; see next section.

Setting Ψ Thresholds for Light damage based on Experiments

The lowest values of Ψ that can be accurately measured by the DIC system are around 1 with at least one crack with a maximum width of 0.1mm and a minimum length of 100 mm, or two cracks of slightly narrower width (70 μ m). Since the narrower end of a crack must also be reliably detected, in practice, the lowest values of Ψ measured are slightly above 1. This means that the threshold for the beginning of light damage must be set a bit higher. This value and the one for the end of light damage are determined by 'kmeans' clustering to help establish optimum categories (Likas et al. 2003). Additionally, these are verified iteratively by maximising the true positive rate and minimising the false positive rate of a classification model (Narassiguin et al. 2016) while maintaining some realistic values.

The upper threshold of $\Psi=4$, which corresponds to two or three cracks of 5 to 6 mm in width, follows from clustering the data in Figure 3.3.2 also using kmeans clustering. The lower threshold of $\Psi=1.9$, which is linked to about three cracks of 0.5 mm width, is the result of a second clustering step and iterations with the classification model (Osés et al. 2014).

First, this classification model must be introduced. A classification model predicts a category given a set of inputs (Sharafati et al. 2021, Son et al. 2014). The relationship between the inputs and the predictions is set via a training process. For an unrelated example: whether a brick is of fired-clay or calcium-silicate, could be determined based on the color in a photograph. When the photograph is more red, the brick is likely of clay, while a more even distribution between colors (red, green, and blue) would suggest a brick of calcium-silicate. A simple model could employ a linear relationship and determine the ratios of RGB, trained on pre-classified (tagged) photographs, to later make predictions between the two brick categories.

There are many types of classification models with different types of trainable parameters. For a classification problem with a small number of discrete categories and a few predictors, a classification tree will produce good results.

Second, relevant predictors should be defined. From Figure 3.3.2, it should be clear that drift can be used to predict damage, with larger values of damage associated with larger values of drift in a positive correlation. Additionally, Figure 3.3.3 compares the relationship between wall type and damage; see the wall types in Figure 3.1.8.

The ratio of Ψ divided by drift shows that walls of the D type exhibited larger values of Ψ at lower drift when compared to the other wall types. Since D is a CaSi shear wall without openings, it is reasonable that A, the fired-clay shear

walls, display the second highest ratio. The material of the masonry is included in the wall type.

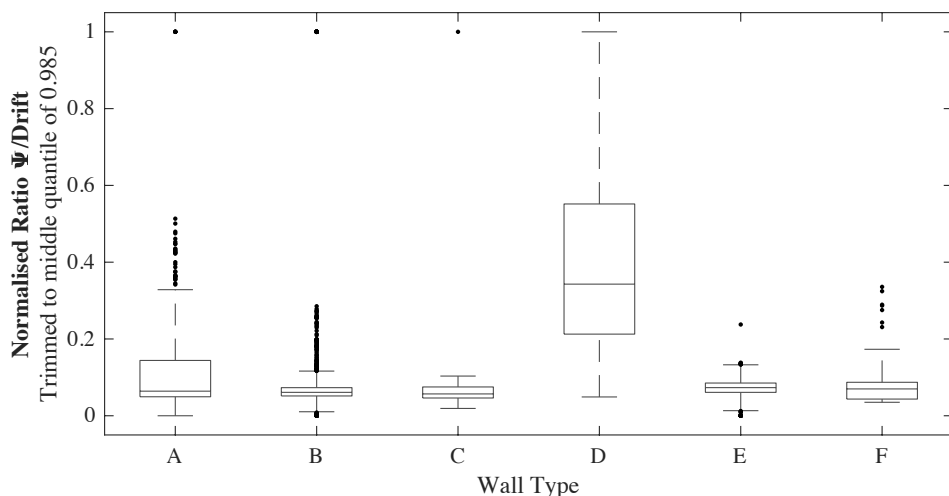


Figure 3.3.3. Influence of wall type, see Table 3.1.9. If Ψ and Drift are linearly correlated, wall type D exhibits, on average, greater damage at equal drift compared to other wall types.

Two additional predictors are available: the boundary during the test that enforces a double-clamped or allows a cantilever condition, and the progress of the test. Since crack damage is accumulated throughout the test, towards the end, even at values of zero drift, residual cracks will be clearly visible. This means that identical values of drift will yield a higher Ψ value if they occur later in the test. To investigate the influence of test progression, an indicator, linearly correlated between the first and last measurement instances, is introduced as additional feature. Furthermore, the data was pre-processed by taking the absolute values of drift and removing measurements with $\Psi=0$, ultimately employing about six thousand data points.

Classification Decision Tree

A decision tree creates nodes between branches to make decisions. For example, if the masonry is fired-clay, the tree would follow the left branch. Ultimately, every leaf at the end of each branch corresponds to a category. The number of times a certain predictor is used at the nodes to make a decision (and the number of leaves affected), corresponds to its importance. The aforementioned predictors are gathered in Table 3.3.1 where their importance is shown. Two variations are presented, one including the wall type as a predictor and another where only the masonry type is considered; these are

mutually exclusive. The wall type, which contains more variability than the masonry type, is also a better predictor for damage, Ψ . The progression of the test is also associated with a relatively high importance of 10%. This means that damage does increase at repeated drift. However, larger values of drift are also imposed towards the end of the tests (as near collapse testing must follow the light damage protocol) so the relationship might be doubly correlated. Finally, the boundary of the test has the lowest importance. Whether the test was in cantilever or double-clamped form seems to be poorly related to the intensity of the cracks.

Table 3.3.1. Description of various potential predictors for Ψ and their importance within a decision tree regression model. Wall type and masonry are mutually exclusive.

Predictor	Importance		Description
Drift	77.2%	79.5%	The in-plane wall drift measured during the tests.
Test Progress	10.6%	11.9%	An indicator, linearly correlated between the first and last measurement instance.
Wall Type	8.7%	NA	The geometry or type of wall, as per Table 1.
Boundary	3.5%	3.4%	The test boundary, Cantilever or Fixed (double-clamped).
Masonry	NA	5.2%	The type of masonry, CLBR or CSBR, included in Wall Type.

The performance of the classification model with the wall types can be evaluated using Receiver Operator Curves (ROC) and confusion charts. These are displayed in Figure 3.3.4. An ROC plots the relationship between the true positive and false positive rate. Ideally, a model should never miss a true result, but this may come at the expense of outputting false positives. This balance can be tuned depending on the application and the desired type of outcome. For example, for this application, it is important that the model never misses a result that exceeds light damage (ELD). This is successfully achieved as evidenced by the 37 cases of ELD that are correctly identified by the model. However, the model also estimates 13 other cases (that were actually LD) as ELD; these are the false positives within the category of ELD. Between incipient LD and actual LD the model is also capable of accurately recalling the true data values with more than 93% accuracy. This is verified by the high AUC (area under curve) values in the ROC plots. The threshold of $\Psi=1.9$ for the beginning of LD, is determined by iteratively adjusting this value and observing the best accuracy and AUC rates.

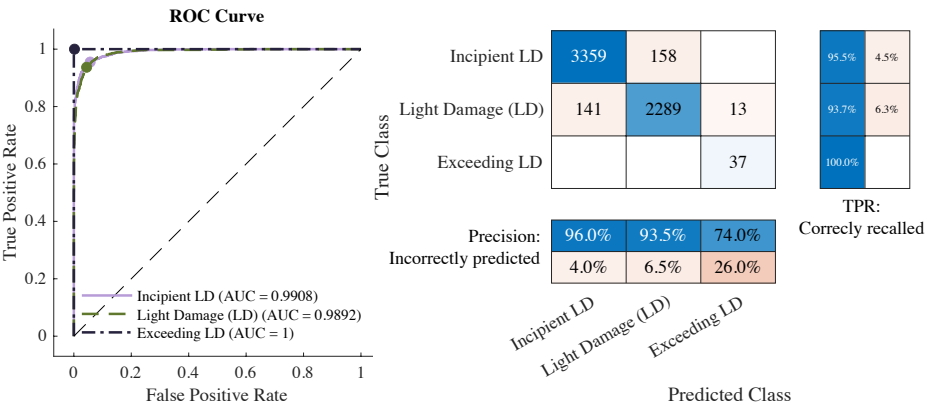


Figure 3.3.4. Confusion chart and ROC curve for an ensemble decision tree model with drift, wall type, boundary, and test progress as predictors of the damage class.

Simplified Models for Drift-Ψ

While the model with four predictors (drift, test progress, wall type, and boundary) is very accurate, it requires several assumptions to be used in practice. For example, the type of wall will depend on the geometry and material of the wall being considered, the boundary will depend on its structural context, and the test progress will have to be linked, perhaps, to the age of the wall. The drift would be the design criterium to limit expected damage. Some of these assumptions can be difficult to define.

For this reason, a simpler model, considering only drift and masonry material as predictors, has been analysed. This can be more easily employed in practice and can be reduced to drift limits which do not require the trained model for making predictions. The performance of the model is segregated by masonry type, fired-clay (CLBR) or calcium-silicate (CSBR) brick masonry in Figure 3.3.5. It is clear that the simpler model is less accurate than the full model; however, the high specificity for ELD is maintained with only 1 false positive for each model. Similarly, both ILD and LD are well discerned though some cross-predictions appear. In general, the models misclassify LD less often, which is desirable.

The results can be employed to derive the drift interval for which the models will classify a wall into light damage. These values are presented in Table 3.3.2. The beginning of LD is fairly consistent between both types of material at about 0.05%, which is an incredibly small value of drift, about 1.35mm for a wall of 2.7m in height. The masonry will remain within LD for a reasonably long interval until a drift of 0.48% for CLBR but only 0.29% for CSBR. Nevertheless, these values fall underneath drift limits employed to assess the ultimate capacity of masonry walls; see next subsection.

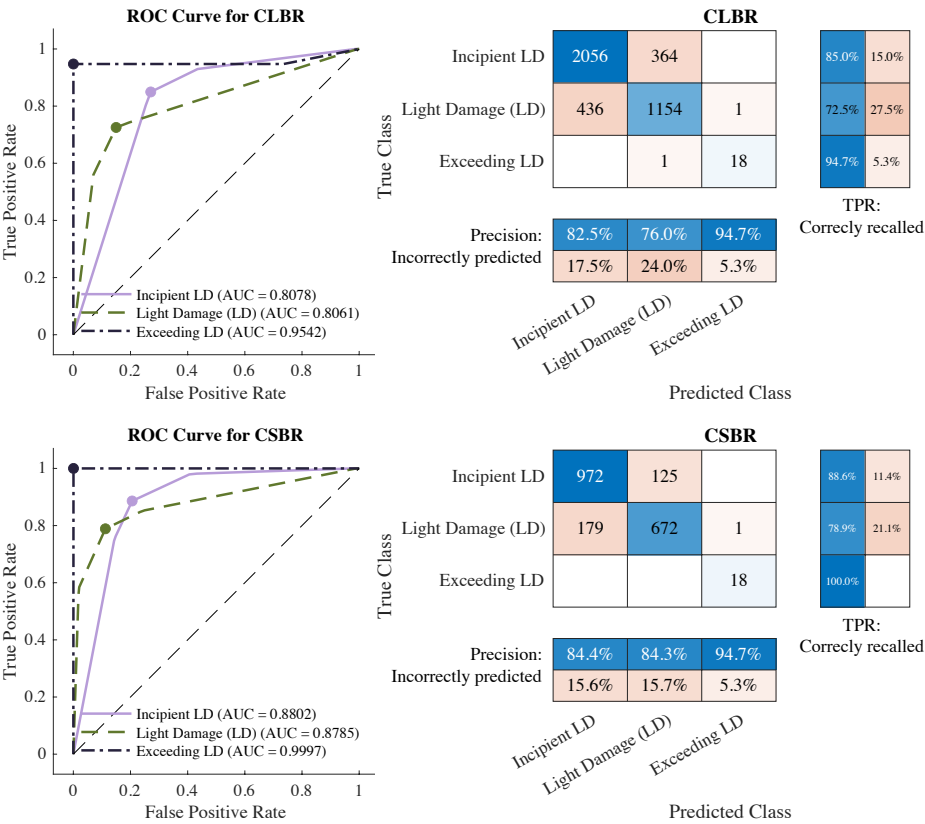


Figure 3.3.5. Confusion chart and ROC curve for clay brick masonry (top) and calcium-silicate brick masonry (bottom) using only Drift and Masonry as predictors of damage class.

Table 3.3.2. Summary drift limits for each masonry type in mm/m or ‰.

Threshold	Fired-Clay Brick Masonry	Calcium-Silicate Brick Masonry
Start of Light Damage	0.58 ‰	0.50 ‰
End of Light Damage	4.78 ‰	2.90 ‰

3.3.4. Discussion and Comparison to Other Drift Limits

Guidelines, codes and the work of many authors have focused on establishing drift limits related to the ultimate capacity of masonry components; see, for example the Swiss, New-Zealand or Italian codes.

Some authors have derived limits associated with the lower damage states as extrapolations from ultimate drift values (Salmanpour et al. 2015). Figure 3.3.6 provides an overview of comparisons against limits defined for ULS, for “significant damage”, and for DS2. Since different approaches consider different parameters, such as the overburden, the compressive strength of the masonry, the height of the walls or only the rotating height of a pier, the expected failure mechanism, etc., for the various walls tested, a range of limits are often obtained depending on the multiple assumptions; these are plotted in a box graph where the middle horizontal lines depict the mean values and the boxes indicate the interquartile range. For this comparison, the individual walls are not observed, but the thresholds defined with the classification tree are used.

The first premise is that ULS limits should be higher than those for lower damage states. Indeed, all formulations result in values larger than the value determined for the upper threshold of light damage. The Italian guideline (MIT, NTC 2008) for example, prescribes values for ultimate drift between 0.6% for shear walls and 1.8% for rocking masonry piers. Both values are significantly higher than that determined herein for the end of light damage at 0.5%. Employing the formulation from the ASCE (ASCE, SEI 41-13, 2014), results in even larger expected ultimate drift values of 2.5%.

The second premise is that limits for significant damage (SD) should be right at the end of the light damage range. Petry & Beyer (2015) propose limits both for ULS and SD, the latter directly preceding the former and slightly above the values defined by the classification model. The New Zealand code (NZSEE 2017) also prescribes values for SD which should correspond to the end of light damage. This seems to agree well with the values derived from the experiments. Similarly, FEMA (Hazardus MH MR5 2013) also specifies drift values to be used for the analysis of pre-code unreinforced masonry structures; this describes the type of masonry components tested and also matches well with the drift values obtained.

With a limited data set part of earlier work [1], it was deduced that DS1 would occur for drift values between 0.3 and 1.1 ‰ for fired-clay brick walls in cantilever tests. Note that the damage state is a range of drift values and not a single threshold. As such, the starting threshold is slightly lower than observed

herein with the extended data and a more rigorous analysis - though the threshold for Ψ was set more strictly, considering just visible damage. The upper threshold, however, is significantly lower. This is because the earlier work investigated only DS1 and forwent DS2 even though the distinctions between the two are seldom strictly defined. In this section, the first two states are clustered into the light damage category, distinguishing between light damage and exceeding it.

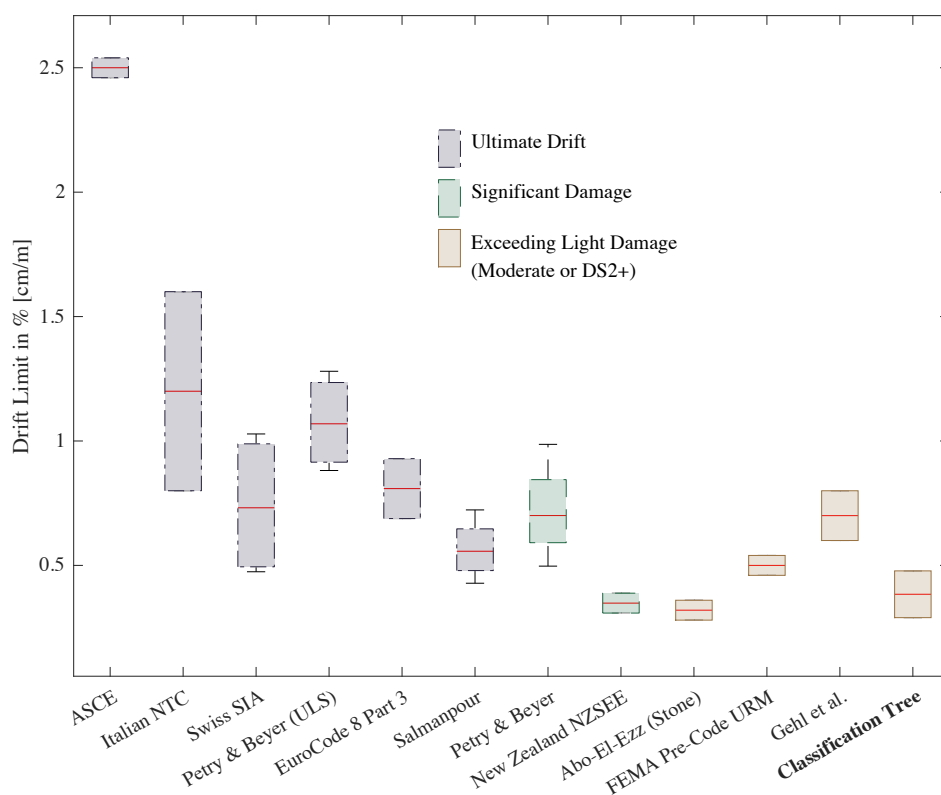


Figure 3.3.6. Comparison with other drift limits for various damage thresholds.

Discussion

Furthermore, the difference between the threshold obtained for masonry with fired-clay or calcium-silicate units should be discussed. In both cases, the mortar joints and size of the units is similar, but the material of the bricks differs. The drift at which light damage can be considered to start is about the same; yet, the drift at which light damage is exceeded is about 40% lower for the calcium-silicate units. This means that calcium-silicate brick masonry is more vulnerable to in-plane inter-storey drift, which might be related to the cracking behaviour that includes brick-splitting cracks and fewer, but wider cracks.

Whether CaSi structures experience or develop equal inter-storey drifts when subjected to damaging actions such as vibrations or settlements and would exhibit thus more damage, still requires additional study. It is likely that such structures, usually in a more modern context with reinforced foundations, rigid floor diaphragms, and updated design and building methods, will better control inter-storey drift.

Finally, the drift limits obtained are linked to the thresholds set for the values of Ψ . A lower Ψ value marking the transition between incipient and light damage will also result in a lower drift value for this threshold. However, this also depends on the available experimental data which is most dense at lower Ψ values. For the upper threshold, clustering of the data was used to determine $\Psi=4$; yet, this threshold is not very sensitive, with values between 3.7 and 4.0 leading to essentially identical upper drift limits (though different in terms of model accuracy). In terms of related cracks, with more than one crack at least 5 mm wide, this upper threshold is also reasonable and comparable to popular damage scales.

The threshold for the beginning of light damage is more sensitive. The strictest formulations consider a crack width of 0.1 mm ($\Psi=1$), just visible cracks, and some begin at 1 mm ($\Psi=2$). Multiple cracks also affect the value of Ψ , so three cracks of 0.5 mm will already reach $\Psi=1.9$. This seems like a reasonable compromise to consider a realistic start of light damage without falling into the most rigorous definition. Moreover, this value is associated with the best model prediction parameters.

3.3.5. Summary of Drift Limits for Light Damage

Results from experimental campaigns on masonry walls have been reinterpreted by post-processing digital image correlation measurements into a crack-based metric and relating it to the in-plane drift of the walls at every measurement instance. Then, the relationship between drift and damage has been explored using a classification model where other predictors are considered. Besides drift, which was found to be highly correlated to damage, the wall type and its material, the boundary of the experimental setup, and the progress of the test were found to be linked to damage. The latter considered that repeated values of drift, occurring later in the tests, were linked to slightly higher damage. Similarly, walls with a cantilever boundary could sustain a slightly larger drift before displaying the same intensity of crack damage than walls subjected to a double-clamped boundary. Moreover, shear walls displayed larger cracks than walls with an opening at similar drift. Analogously, calcium-silicate (CaSi) walls showed more intense damage than fired-clay brick

walls. In fact, when simplifying the classification model to consider only the drift and the masonry material as predictors to establish drift limits for the interval of light damage, CaSi masonry obtained an upper limit 40% lower than fired-clay brick masonry, which exceeds light damage at a value of 0.5%. The upper crack-based light damage threshold corresponds to about three cracks of 6 mm in width. The beginning of light damage, with visible cracks about 1 mm wide, occurs at 0.5 and 0.6 ‰ for CaSi and clay, respectively.

These thresholds may be used directly when designing for performance goals that limit 'significant damage' or even address the serviceability limit state. Older structures, or masonry that is expected to have been subjected to a large number of load repetitions, should be evaluated with slightly reduced drift values (about 10%). Likewise, shear walls, or squat walls connected to rigid floors and foundations, should also consider limits reduced by a similar amount.

Finally, it must be highlighted that these experimentally-derived limits are still related to decisions about the crack-based boundaries for light damage, which inevitably remain somewhat arbitrary. Moreover, future tests should consider additional repetitions to obtain richer drift data around the upper threshold of light damage, which is now slightly scarce. Similarly, additional experiments with varying wall slenderness ratios, could offer a further refinement of the simplified drift limits by incorporating a parameter besides wall material that can be directly used in practice.

3.4. Conclusions: Experiments to Understand Crack Behaviour

Chapter 3 presents a comprehensive study on the initiation and propagation of cracks in masonry, aiming to understand the mechanics behind crack formation and growth. Central to this investigation are laboratory experiments designed to observe crack formation in masonry under various test conditions, extending from small scale tests for assessing the bond between masonry units to large scale tests including full masonry assemblages; the chapter focuses on walls and spandrels.

The chapter details adaptations in traditional testing methods to focus on the early stages of crack formation, emphasising the importance of a loading protocol that slowly increases before reaching the initial damage stage (DS1) and employing an instrumentation system capable of precisely tracking crack development. This methodology allows for an in-depth understanding of crack initiation and progression, highlighting the effects of repeated loading and the significance of in-plane testing on walls to encourage crack formation around openings.

A significant conclusion of the chapter is the establishment of drift limits for light damage based on the experimental observations. Through a detailed classification model, the relationship between drift and the parameter Ψ (representing crack intensity) is explored, defining lower and upper thresholds for light damage. This approach provides a quantifiable measure to assess light damage in masonry structures subjected to lateral loads, potentially guiding the design and evaluation of masonry under load by requiring designers to consider the lateral stiffness of the structures.

Chapter 3 highlights that cracks mostly initiate from the corners of openings or at the lateral edges of walls. In the case of walls subjected to shear forces, body cracks may also manifest. Most observed cracks were either horizontal or step-wise diagonal, coalescing into a single crack from being spread over multiple joints initially. The chapter discusses how the width and length of cracks grow simultaneously, with a notable observation that cracks appear even before they become visible, suggesting the presence of 'invisible' cracks that could potentially propagate if conditions vary. Different types of cracks, whether horizontal, diagonal, vertical, tapered, or uniform, exhibit similar aggravation under increased loading. Moreover, the chapter concludes that repetition affects crack propagation, where identical loading conditions lead to measurable but consistent increases in crack width and length. These insights provide a deeper understanding of crack behaviour in masonry, contributing to better predictive models and mitigation strategies against crack-related damage in masonry structures.

In summary, Chapter 3 advances the knowledge on crack dynamics in masonry through methodical experimentation, contributing to the development of more resilient masonry structures by defining drift limits for light damage and enhancing our understanding of crack formation and propagation mechanisms. The experimental results serve as a basis to calibrate models that, besides the traditional calibration parameters of stiffness, strength, and hysteresis, also strongly consider crack patterns and behaviour.

Chapter 4

Damaging (Multi)Hazards and Modelling their Effects

This chapter begins with a short overview about hazards and the way they act on buildings, Sections 4.1 and 4.2 respectively. Then, Section 4.3 goes back to the experiments of Chapter 3 and reproduces them with finite-element-method models. This is a model calibration conducted in collaboration with other authors [1, 4; see [List of Publications](#)] focused, in contrast to most studies, to reproducing crack patterns and behaviour during light damage.

The calibrated models are then used in Section 4.4 to illustratively model various actions related to (multi-)hazards relevant to Dutch buildings in preparation for their key purpose in Chapter 5.

vibration element displacement
property action micro
test hazard brick
deformation building pattern
calibrate analysis example

Chapter 4: Table of Contents

Calibrating models is not only about defining a modelling strategy that works. The ultimate goal is to have models that can be used to analyse situations that were not, or could not be, tested experimentally; these are extrapolations.

The various loads to be included in models of structures are typically caused by hazards. Therefore, this chapter begins with a definition and overview of hazards followed by a more rigorous description on their actions on masonry buildings.

The models, calibrated against the experiments, are then used to analyse the effects of some of the hazards presented. This is done in preparation for Chapter 5, where the calibrated models are used to analyse the effect of earthquake vibrations.

4.1. Hazards and Multi-hazards	109
4.1.1. Hazards	110
4.1.2. Multi-hazards	111
4.2. Overview of Actions causing Damage to Masonry Buildings	113
4.2.1. Vibrations	114
4.2.2. Restrained Deformations	115
4.2.3. Imposed Deformations	115
4.2.4. Out of Plane Loading	115
4.2.5. Gravity Overloading	116
4.3. Calibrating Crack Behaviour from Experiments into FEM Models	117
4.3.1. Background on Validation Experiments	118
4.3.2. Overview of Calibration Models	119
4.3.3. Model Properties and Boundaries	120
4.3.4. Calibration of Spandrels and Walls with Openings	125
4.3.5. Additional Model for Walls with Pre-Damage	130
4.3.6. FEM Model for Shear Walls	133
4.3.7. Conclusions from the Calibration Process	137
4.4. Modelling Damage: Shrinkage, Settlements, and Vibrations	139
4.4.1. Modelling Restrained Deformations: Shrinkage	139
4.4.2. Modelling Imposed Deformations: Settlements	141
4.4.3. Dynamic, Non-Linear Time History Analysis: Vibrations	143
4.4.4. Modelling Multi-hazards	146
4.5. Conclusions: Modelling and Calibration	147

4.1. Hazards and Multi-hazards

A hazard constitutes a danger to a structure but differs from an action. Traditionally, natural hazards are identified, such as storms or floods, but many anthropogenic hazards, such as terrorist attacks, fires or simply traffic, are also relevant. Any effect that can act on a structure is a hazard. People in a building, because of their weight, represent a hazard. While the building is sufficiently designed for the 'normal' loads of this hazard, an extreme number of people in a building could lead to overloading.

A multi-hazard involves more than one hazard while a single hazard is that which could appear independently. A hazard can act in several ways on a structure. For example, a storm may include wind and rain, and a flood could include hydrostatic or hydrodynamic pressures. Many hazards are linked to a single action, however; for example, a seismic event will lead to vibrations which could also originate from traffic. The actions associated with various hazards are treated in Section 4.2; the hazards are summarised next.

Definition: Hazard

In structural engineering, a hazard refers to any condition, event, or factor that has the potential to cause harm to structures, infrastructure, or the occupants of buildings. Structures are typically designed to withstand the effects of (some) hazards. In many cases, the function of a structure is to withstand a particular hazard. Bridges are designed to handle traffic and wind, buildings are constructed to resist the weight of people and rain, dykes are built to endure waves and erosion. All of these are hazards.

Definition: Action

The action of a hazard is how it affects structures. While the storm is the hazard, the wind pressure on the face of a building is its associated action. Similarly, fire is a hazard, but the action on the structure is described as a temperature increase or gradient on structural elements. Loadings and actions are mostly synonyms, though the term 'loads' is typically employed to describe the forces and strains (vectors, pressures) acting on the structure.

4.1.1. Hazards

The following is a list of hazards. The list focuses on hazards relevant to buildings and infrastructure, and is unlikely to be complete. While the hazards have been distinguished by their natural or anthropogenic character, many of the natural hazards can have anthropogenic triggers or be induced by human activities. For example, seismic events, ground subsidence or even wildfires.

Natural hazards

- seismic activity (earthquakes)
- flooding (heavy rainfall, storm surges, river overflows)
- high winds (hurricanes, tornadoes, severe thunderstorms)
- landslides and mudslides
- tsunamis
- snow and ice accumulation
- volcanic eruptions
- hailstorms
- (extreme) temperatures (cold and heat)
- soil subsidence
- physical or chemical soil changes
- erosion (coastal and riverbank)
- lightning strikes
- wildfires

Anthropogenic (human-made) hazards:

- induced seismicity (mining, geothermal, fracking)
- fire (electrical faults, gas leaks, arson, accidents)
- industrial accidents (chemical spills, blasts, explosions)
- terrorism (bombings, vehicle attacks)
- infrastructure failures (water supply, sewage systems, gas lines)
- aging and neglect (lack of maintenance and repairs, incorrect repairs)
- inadequate renovations (removal of structural elements, etc)
- construction, pile driving, heavy machinery
- excavations, mining, tunnelling

The intensity of hazards can be related to a parameter than can be measured; some examples are provided in Table 4.1.1.

Table 4.1.1. Examples of hazards and some describing parameters with a qualitative intensity categorisation. Adapted from Korswagen et al. (2018), Loat (2010) and Menoni (2016).

Hazard	Intensity Parameter		Intensity		
	Description	Unit	Low	Medium	High
Earthquake	PGA	% of g	<10	10-30	>30
	PGV	mm/s	<5	5-20	>20
Flood	Depth	m	<0.5	0.5-2	>2
	Depth-Velocity	m ² /s	<0.5	0.5-2	>2
Forest Fire	Flame height	m	<1.2	1.2-2.5	>2.5
	Front line power	kW/m	<350	350-1750	>1750
Volcanoes	Mass eruption rate	kg/s	<10 ²	10 ² -10 ⁶	>10 ⁶
	Rate (cm/y or cm/d)	cm	<2/y	>10/y	>10/d
Landslide	Ratio of unstable over stable surface	-	<5	5-15	>15
Debris Flow	Depth & Velocity	m & m/s	n.d.	<1 & <1	>1 & >1
Avalanche	Pressure	kPa	<3	3-10	>10
Rock Fall	Energy	kJ	<30	30-300	>300

4.1.2. Multi-hazards

One hazard can also act together with other hazards. Sometimes these happen to occur simultaneously; or, they act on the structure in sequence but are not related to one another. For example, a wind storm could act on a building after it has been subjected to neighbouring construction activity. These hazards are unrelated and could occur at precisely the same time, compounding their effect on a structure, or most likely, one after another, in which case the earlier hazard could have damaged the structure modifying its response to the following hazard. This represents a multi-hazard analysis.

Simple multi-hazard analyses are embedded into regular structural design in the form of load combinations. For a thorough analysis, hazards behind these loads, especially when considering extreme or accidental loads, should be disentangled.

In some cases the hazards are related. For example, an earthquake may trigger a tsunami. These are coupled or chained multi-hazards. The matrix in Table 4.1.1 draws relationships between various hazards where the primary hazard can trigger the secondary hazard. This multi-hazard analysis is more specific as the hazard combinations are limited.

Table 4.1.2 Interaction of Hazards. Adapted from Korswagen et al. (2018) & Gill (2014).

Primary Hazards		Secondary Hazards (as a result of PH)											
PH		EA	TS	VE	LS	AV	FL	GC	WS	SS	WF	AD	FR
Earthquakes	EA	•	•	•	•	•	•	•					•
Tsunamis	TS			•	•		•	•					
Volcanic Eruptions	VE	•	•		•	•			•	•	•	•	•
Landslides	LS		•		•		•						•
Avalanches	AV			•	•	•	•						•
Floods	FL			•	•			•					
Ground Collapse	GC				•								
(Wind) Storm	WS				•	•	•						•
Hail/Snow Storm	SS			•	•	•	•	•					•
Wildfires	WF				•			•	•			•	•
Ash Deposition	AD				•	•							
Fires	FR										•	•	•

In fact, for Dutch buildings, only certain multi-hazards (coupled or uncoupled) are relevant or worthy of study. For example, volcanic eruptions are not possible and consequently, significant ash deposition is unlikely. These hazards are thus not relevant. Soil subsidence and windstorms, on the other hand, typically affect buildings, and are examples of more relevant hazards for the Dutch context.

More so, those hazards are associated with a limited number of actions. These actions and their typically-associated hazards are treated next.

4.2. Overview of Actions causing Damage to Masonry Buildings

While many hazards can be noted, the number of actions on buildings is limited. Table 4.2.1 collects mechanical actions, or possible loading, on buildings. Note that these actions are related to crack-based damage; other processes resulting from hazards can be linked to other types of damage (see Chapter 2). The location and intensity of the actions will depend on the hazard associated with it. For instance, wind and floods both cause out-of-plane loading on buildings walls; however, floods apply pressure at the bottom of the walls while wind loads are better represented with a higher pressure at the top. The quasi-static ground movements from subsidence phenomena lead to imposed deformations on buildings, but different hazards will lead to (either) horizontal or vertical deformations, resulting in different types of settlements. As such, while actions are similar, hazards can be associated with different failure mechanisms; see de Vent (2011). These differences are considered in the following subsections. Several examples and situations are presented. Nonetheless, this does not constitute an exhaustive nor complete list.

Table 4.2.1. Hazards relevant to the Dutch context and associated mechanical actions.

Actions Hazards	Earthquakes	Regional subsidence	Local soil subsidence	Material Shrinkage	Extreme Temperatures	Renovation / Expansions	Landslides	Avalanches	Floods	(Wind) Storm	Hail/Snow Storm	(Wild)fires	Traffic	Pile Driving
Imposed deformations		•	•			•								
Restrained deformations				•	•							•		
Out of plane pressure							•	•	•	•	•			
Vibrations	•												•	•
Gravity Overloading	•					•			•		•	•		

In computational modelling, actions are translated into loads and a similar terminology is used. Imposed deformations loads, temperature and shrinkage loads, distributed loads (line or surface), and nodal loads are some of the terms. Restrained deformations are the result of a constraining boundary and inner strains derived from temperature or shrinkage loads.

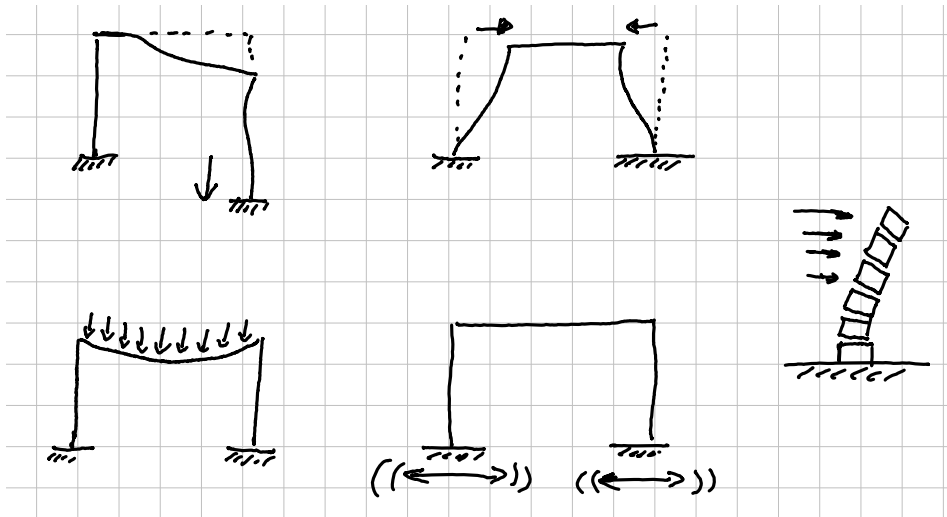


Figure 4.2.1. Overview of various actions on buildings. Imposed deformations, restrained deformations, overloading, vibrations, and out-of-plane loading.

4.2.1. Vibrations

Dutch buildings in general are often subjected to vibrations. These are caused by traffic from nearby roads or railroad tracks, construction activities such as pile driving, wind storms, household activities (such as walking, drilling or slamming doors/windows), and earthquakes. Vibrations are quick, dynamic deformations of building components. Jumping on a wooden floor, for example, causes vibrations that can be easily perceived. Unless inadequately designed, buildings should withstand vibrations from normal use. Therefore, the hazards from outside sources, or hazards unforeseen at design, are the focus of most studies on the effect of vibrations on buildings.

The intensity of the vibrations will depend on the distance of the building to the source. Road traffic vibrations die out quickly with distance, followed by railroad-induced vibrations, and pile driving, with seismic events leading to vibrations that occur over a larger area. This type of vibrations reach the structure via its foundation. However, they can differ in several aspects. Seismic vibrations typically occur uniformly over the entire building foundation, while other sources lead to non-uniform vibrations over the entire foundation. Moreover, vibrations from pile driving usually induce mostly vertical dynamic deformations while distant earthquake events lead to more important horizontal deformations. Similarly, the intensity of the vibrations can be measured in various ways; the peak ground velocity, its duration, the number of effective cycles and the frequency content of the vibrations will differ depending on the responsible hazard.

4.2.2. Restrained Deformations

Building components sometimes need to expand or contract. This is the case for instance, when they are subjected to a temperature increase. Most materials expand proportionally to the temperature increase. Similarly, some materials swell with increases in humidity such as calcium-silicate masonry or timber subjected to moisture. In many situations however, these deformations are constrained. Other building components limit the deformation possible. For example, a recently built masonry wall attempting to shrink over a rigid concrete foundation, will not be able to deform. This limitation leads to stresses in the wall and in the foundation.

In addition, many materials experience creep, like concrete or masonry, where sustained loads lead to plastic deformations over time. Other materials, like steel, are subjected to a similar phenomenon of relaxation, where stresses, product of an imposed deformation, decrease over time.

4.2.3. Imposed Deformations

Opposite to restrained deformations, imposed deformations force structural components to deform. This leads to stresses and potential damage. When other building components shrink or expand, they may be restrained by other elements; in this scenario, one component is forced to deform while the other is constrained. However, imposed deformations can also have outside sources. Settlements, for instance, are the result of a loss of support underneath the foundation of buildings; then, the weight of the building itself forces structural components like walls, to deform, imposing displacements. An external driver in the soil, or a result of detrimental soil-structure interaction or building-component interactions, are also possible situations.

Imposed deformations on certain structural elements are usually restrained by other building components. This interaction can quickly become complex requiring extensive analyses.

4.2.4. Out of Plane Loading

Walls can be subjected to loads perpendicular to their plane. These actions often belong to hazards. Three hazards are noteworthy: wind, floods, and earthquakes. The former apply pressures on the walls, which are most sensitive for out-of-plane pressures. The latter accelerate the building vertically and horizontally. Due to the inertia of the walls themselves, the earthquake leads to an out-of-plane (OOP) distributed load. Wind loads are seldom intense enough to affect walls; roofs instead are usually lifted up.

Buildings components for housing are fragile against out-of-plane loading. Thin, unreinforced walls will fail once their OOP capacity is exceeded.

4.2.5. Gravity Overloading

Overloading is a general term. In essence, any mechanical damage is a consequence of overloading of the material. However, by gravity overloading, one should understand the scenario when gravity loads exceed the design load of the structure. This can occur during a renovation, when heavy finishing floors are laid over structural timber floors. Natural hazards such as snow or heavy rain can accumulate on the roofs of structures and cause overloading. Similarly, an earthquake with a strong vertical component could lead to gravity overloading.

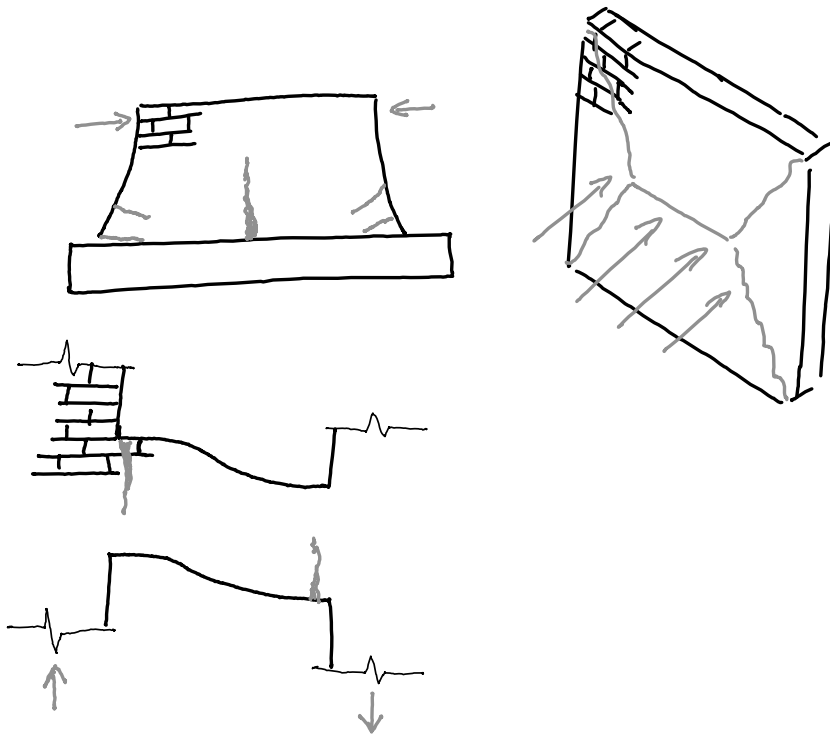


Figure 4.2.2. A scheme of masonry wall subjected to (top left) shrinkage, a deformation with is restrained by the stiff foundation, and (top right) out-of-plane loads resulting in two-way bending. Bottom, a spandrel, between two walls experiencing a relative displacement leading to bending in the spandrel. The schematic location of cracks is highlighted.

4.3. Calibrating Crack Behaviour from Experiments into FEM Models

Hazards and actions have been presented. The goal is to model the effects of these hazards. To do this, however, an intermediate step is needed: to develop accurate models with which to do this. That is the focus of this section.

Indeed, to assess the effects of actions on structures, not only are good models and estimations of actions needed, but a complete understanding of the structure, and its (mechanical) response to the actions, is also necessary. A simple, linear-elastic model of a structure, for instance of a beam, may only require its stiffness (Young's Modulus) and its dimensions. More complex models however, involve many more material parameters, especially non-linear models with other physical non-linearities. These parameters follow from thorough material characterisation campaigns assaying stiffness, strength, and toughness for tension, shear, and compression.

Effective modelling strategies also need to be defined. These are validated against experiments. The models are formulated such that they reproduce the behaviour observed in experiments. Hence, to model the effects of hazards accurately, **calibrated** models are required. These reproduce the behaviour observed in experiments or in monitored field cases and can then be adopted to model the actions of hazards.

Certainly, the experiments of Chapter 3 can be used to calibrate models. The calibration process is presented in this section. These models were elaborated in collaboration with other authors [1, 4, 12]. The experiments provide valuable data for the calibration of finite element models; in this manner, this section builds up on the results from the laboratory tests and describes and discusses the modelling approach used to elaborate models that are capable of reproducing the cracking behaviour of masonry specimens and which later, in Chapter 5, will be used to predict the cumulation of damage from various actions in a probabilistic manner.

The first step is to understand the experiments upon which the modelling calibration process is to be based. The experiments are summarised in one page in section 4.3.1. Next, an overview of the models employed for the calibration is laid out in section 4.3.2. Multiple models of various experiments are required to comprehensively define an effective modelling strategy; the overview is further expanded in section 4.3.3 with the description of the models. The various models are then treated in sections 4.3.4 to 4.3.6.

4.3.1. Background on Validation Experiments

The quasi-static, cyclic experiments were presented in Chapter 3. The most relevant aspects are briefly summarised in this short subsection for clarity: Five nominally identical, single-wythe walls of fired-clay brick masonry approximately 3.1 metres wide and 2.7 m tall with an asymmetrically-placed window opening were tested quasi-statically in-plane by enforcing a controlled displacement at the top of the walls. The walls were pre-loaded vertically to produce an average stress of 0.12 MPa resembling moderate vertical loads; the top of the wall was allowed to rotate freely mimicking a 'cantilever' configuration. The in-plane displacement was applied cyclically with repeated steps of increasing amplitude; the surface of the walls was surveyed with Digital Image Correlation (DIC) to detect and monitor the formation and progression of cracks at a resolution of 20 μm . Two additional walls of identical material without a window opening [3] were tested at a higher vertical overburden of 0.46 MPa and a 'double-clamped' configuration, meaning that the bottom and top edges of the walls were kept parallel during the tests. The first set of walls were seen to correspond to the flexural behaviour, while the latter represented the shear behaviour of masonry walls. Furthermore, two walls with a window opening and pre-damaged crack interfaces [4] were tested in a manner identical to that of the five walls with opening for a window. The pre-damaged interfaces were achieved by incorporating a PVC sheet on some mortar joints strategically located at the corners of the window opening. The built-in pre-damaged pattern was designed to mimic cracking caused by a differential settlement profile and was determined with numerical models and assessment of real case studies [6].

The tests imposed in-plane drifts to the walls of up to 0.1% with some cracks reaching a width of up to 2 mm. The cracks were observed to propagate when identical drifts were enforced repeatedly, though greater crack growth occurred at cycles of amplitude larger than that of the preceding cycle. Pre-existing cracks modified the initial stiffness of the wall and the ultimate crack pattern slightly [4]. Cracks in the flexural walls were mostly horizontal and stair-case-diagonal and propagated off from the corners of the window opening, while cracks in the windowless shear walls were mostly diagonal but steeper than the stair-case motif and started off from the centre of the walls.

Additionally, ten spandrel-type wallets 1.5 m in width and 0.5 m in height were tested in a four-point bending setup such that a flexural vertical crack would cross the specimens in the centre. The cracks were observed to zig-zag around the mortar joints of the fired-clay brick masonry resulting in a toothed crack pattern.

Finally, small companion tests like the bond-wrench test, the shear-triplet test, the compression wallet test, and flexural four-point bending tests in-plane and out-of-plane, were used to determine the material properties of the masonry.

4.3.2. Overview of Calibration Models

To enhance the understanding of experimental tests and apply their findings to various masonry walls, structures, and different load scenarios beyond laboratory capabilities, finite element computational models have been developed and fine-tuned based on experimental data. The modelling of the walls was approached in two ways: first, through a continuum model that combines bricks and mortar into a single composite material for macro-level modelling; and second, by modelling bricks and mortar separately. In the latter approach, while zero-thickness interface elements are commonly used between bricks and mortar, this study employs continuum elements to represent the mortar, thus characterising this approach as a modified micro model. For further details on masonry modelling techniques, readers can refer to the works of Rots et al. (1994), Lourenço (1996), and Lourenço et al. (1997).

Most modelling studies focus on ULS and the ultimate capacity of masonry elements considering large displacements and severe damage; see for instance Rots et al. (1997), Chong (1993), Rots (2000), and Zucchini & Lourenço (2006). These studies are monotonic as are many of the investigations into in-plane loading of masonry. Yet, while the majority of experimental studies do consider the cyclic behaviour (Magenes & Calvi, 1992), few modelling studies do so extensively. Zhai et al. (2016), Mariani et al. (2017), Messali & Rots (2018), and Sarhosis et al. (2019) are useful examples of modelling including cyclic behaviour. The modelling strategies typically include continuum, homogenised material models (Pelà et al. 2014), or even larger elements like various macro-element approaches to represent the behaviour of entire masonry walls or structures (Cannizzaro et al. 2018).

In contrast, this study focuses on SLS with small displacements occurring up until before the maximum capacity of masonry walls. The observation of crack propagation, especially during cyclic loading, plays a major role. Moreover, a novel material model is employed to focus on cracking. Additionally, a micro-modelling strategy is investigated (Almeida, 2012; Ferretti et al. 2018, Rapone et al. 2020).

The micro model, despite being more resource-intensive, allows for a more detailed analysis of cracks. Therefore, it is preferred for smaller, more detailed studies; where computational resources are a constraint, the macro model is more applicable. However, for specific applications like the window-bank test,

where the size of the bricks relative to the sample size is critical, the macro model may not yield as accurate results. As a result, both macro and micro models of the full-scale walls have been developed, with only the micro model being adjusted for the window-bank tests. The micro-model for the spandrels served to help calibrate the micro model for the walls, which in turn, was used to further refine the macro model for the walls. Ultimately, the last model is used in Chapter 5 for the probabilistic explorations. All models were created using the DIANA finite element software.

Table 4.3.1. Overview of models used for calibration.

Model	Approach	Comment	Experiments	Section
Walls with Opening	Homogenised model (macro approach)	Main models	Comp40-Comp43	4.3.3 and 4.3.4
	Detailed model (micro approach)	Cross-validation		
Spandrels	Detailed model (micro approach)	Focus on vertical cracking	Spandrels	
Walls with pre-damage	Homogenised model (macro approach)	Focus on the influence of pre-damage	Comp45, Comp46	4.3.5
Shear walls	Homogenised model (macro approach)	Focus on shear and double-clamped boundary	Comp47, Comp48	4.3.6

4.3.3. Model Properties and Boundaries

This subsection details the calibrated model properties and the replicated experimental boundaries for both wall and spandrel models.

Wall Macro Model

Computational models that had been used to predict the behaviour of the experiments were then improved based on the experimental results to (partly) replicate the observed degradation and better reflect the observed stiffness and crack patterns. As constitutive material model, a smeared, total-strain Engineering Masonry Model (EMM), recently developed by TU Delft and DIANA FEA, see Rots et al. (2016) and Schreppers et al. (2016), was chosen for the elaboration of the macro (or continuum) model with homogenises the properties of the masonry (bricks and joints) into a continuum. The EMM accounts for the orthotropy from bed and head joints, tensile softening with secant unloading, shear friction and cohesion softening with elastic unloading, and compression hardening and softening with bilinear elastic-secant unloading. This makes it particularly suited for the cyclic aspect of repetition.

Moreover, the orthotropy is key in capturing the behaviour of masonry where bricks are laid in bed joints making the horizontal behaviour different from the vertical. Furthermore, the elastic unloading during shear captures sliding at the bedjoints, an important masonry failure mechanism.

The model of the wall includes a linear-elastic, uncracked concrete lintel ($E=31$ GPa), linear beam elements for the bottom and top beams, a fixed boundary at the bottom, and is displacement-driven at the top (see Figure 4.3.1).

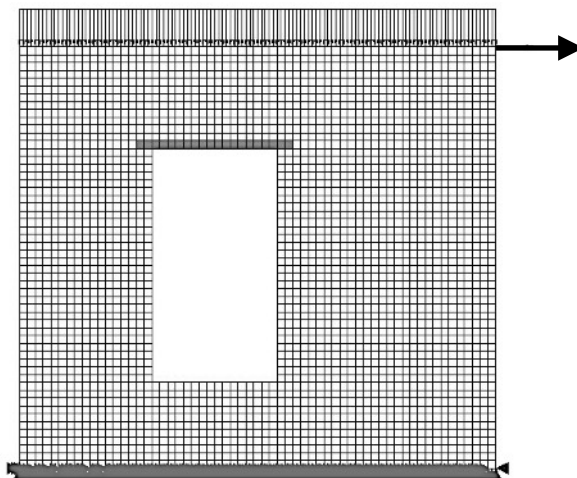


Figure 4.3.1. Finite Element Model showing mesh and boundaries.

Further calibrating the material parameters allowed for results loyal to the experiments. The employed and calibrated parameters for the material model are displayed in Table 4.3.2. Note that the EMM requires the specification of the angle at which stair-case cracks will travel diagonally in masonry, this is related to the geometry of the brick and the masonry pattern (dutch bond, english bond, etc). Moreover, it also requires parameters relating to the compressive strength and softening of masonry, but these did not play a role in any of the models as no compression failure was observed in the tests nor in the models. The light-damage oriented experiments only displayed Mode I tensile fracture and Mode II shear fracture and slip.

These properties are applicable to all the models, including the shear walls and the walls with pre-damage. A summary of the model features is listed next:

- Wall with/without opening from fired-clay brick masonry,
- Dimensions: 3.05x2.70x0.10m,
- 2D Plane Stress Model,
- Bottom (HEB300) and top (HEB600) beam modelled using beam elements,
- 8-Node Quadratic Elements,
- 3x3 Integration scheme,
- 0.12MPa overburden,
- Mesh size 50x50mm,
- Full Newton-Raphson scheme with force or displacement norms with a 1% residual tolerance for convergence.
- Displacement control, small step size
- Constitutive model: EMM

Table 4.3.2. Material properties for FEM models using the EMM.

Material Properties		Clay Masonry	
Elastic	Density	1600 kg/m ³	1
	Elastic Modulus Perpendicular to Bed-Joints	3600 MPa	1
	Elastic Modulus Parallel to Bed-Joints	2500 MPa	1
	Elastic Shear Modulus	1 500 MPa	2
Tension	Bed-Joint Tensile Strength	0.16 MPa	1
	Minimum Head-Joint Tensile Strength	0.16 MPa	2
	Tensile Fracture Energy	11.30 N/m	3
Compression	Vertical/Horizontal Compressive Strength	12.9 MPa	1
	Vertical/Horizontal Compressive Fracture Energy	35 600 N/m	1
Shear	Friction Angle (Friction Coefficient)	0.69 rad	1
	Cohesion	0.17 MPa	1
	Shear Fracture Energy	210 N/m	1
EMM	Head Joint Failure Option	Friction	
	Predefined Angle for Diagonal Cracking	0.50 rad	1

1. From companion tests (material characterisation)
2. From calibration
3. From formulation (Schreppers et al., 2016)

Wall Micro Model

In addition to the macro model, a detailed model was explored as cross-validation. The micro model differs from the macro model in that bricks and mortar are modelled independently, each with their own material properties (see Figure 4.3.2). Since damage was rarely in bricks, these are modelled linear-elastically, significantly improving the computation time of the model and its simplicity. Moreover, since no interface is used between the bricks and the mortar, all non-linear properties are gathered in the mortar; here, the strength of the bond between brick and mortar is used as the strength of the mortar.

Furthermore, it is possible to differentiate between the mortar in the head joints and that in the bed joints. The former being of lower quality (or strength) due to the construction practice where head joints are filled in-between bricks, while bed joints are pressed with the bricks above it. Since the mortar is a homogenous material, a total-strain-based, rotating crack model was used. As its name suggests, this model has a single direction for a stress-strain relationship which rotates in the direction of the principal strain. See Vecchio et al. (1986), Rots et al. (1989), or Feenstra et al., (1998).

The EMM was also explored as a constitutive model for the mortar. Since its loading/unloading design is well suited for the cyclic behaviour of the mortar joint, and because the modelled mortar must include the behaviour of the interfaces 'brick-mortar' which are inherently oriented on the horizontal-vertical axes. However, the EMM requires a larger number of parameters which must also be calibrated. For the monotonic comparison between micro- and macro-modelling strategies, the total-strain model for the joints was deemed sufficient.

Indeed, since the micro model is computationally expensive, it was calibrated only against the monotonic backbone curve of the experiments and a stepwise loading with a single repetition (one-way cyclic). Additional properties in comparison to the macro model are:

- Dimensions: 3.07x2.70x0.10m,
- Brick size: 210x50x100mm,
- Mortar thickness: 10mm,
- 2D Plane Stress Model,
- 4-Node Linear Elements,
- 2x2 Integration scheme,
- Mesh Size: 10x10mm,
- Full Newton-Raphson scheme with force and displacement conditions with a 1% residual tolerance for convergence.

Table 4.3.3. Calibrated properties for the micro model.

Property	Symbol	Bed Joints	Head Joints	Bricks	Units
Density	ρ		1708 ¹	1708 ¹	kg/m ³
Young's Modulus	E		1000 ²	4600 ²	MPa
Poisson's Ration	ν		0.14 ¹	0.14 ¹	-
Tensile Strength	f_t	0.09 ¹	0.05 ²	NA	MPa
Fracture Energy (Tension)	G_f	7.53 ³	4.99 ³	NA	N/m
Compressive Strength	f_c		3.81 ¹	NA	MPa
Fracture Energy (Compression)	G_c		6400 ²	NA	N/m
Shear Retention	-	Damage Based ⁴		NA	-

1. From companion tests (material characterisation)

2. From calibration

3. From formulation (Schreppers et al., 2016)

4. Reduction of Poisson's ratio. See Slobbe et al., (2013).

Window Bank Micro Model (Spandrel)

Due to the reduced size of the spandrels, these were modelled only with the micro-modelling approach. As both the wall and window bank tests served for the same material calibration, these material properties are identical to those used for the full-scale wall micro models. The spandrel was modelled including the contact steel plates for the supports, jacks, and counterweights. The specific model properties are listed next:

- Dimensions: 1.31x0.53x0.10m,
- 2D Plane Stress Model,
- Steel plates, E=200 GPa,
- Counterweight as line force,
- Monotonic Displacement,
- Mesh size 10x10mm.

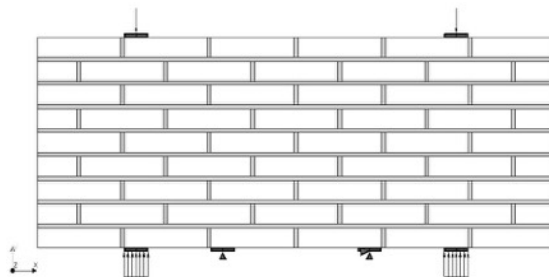


Figure 4.3.2. Spandrel FEM model.

Preface to Sections 4.3.4 - 4.3.6

Three calibration campaigns were performed. First, the walls with openings and the spandrels were used to establish some of the material properties and modelling strategy. This was also complemented by the micro-models of both walls and spandrels {4.3.4}. Second, the two walls with openings and pre-damage were further utilised to verify the selected parameters and strategy {4.3.5}. Third, the two walls without openings (shear walls), served as a final calibration opportunity {4.3.6}. The overview of these phases was presented in Table 4.3.1.

4.3.4. Calibration of Spandrels and Walls with Openings

The focus of the calibration efforts was on the stiffness and strength of the samples, while also capturing the observed crack pattern. In Figure 4.3.3, the calibration against two wall specimens is summarised. It can be observed that the stiffness and strength are both well represented, that there is a loss of strength after the first unloading, and while the hysteresis of the experiments is also well depicted, the degradation observed during the repetitions is not reproduced with the models, mainly because it is also not present in the material model. In the figure the dashed lines appear solid due to the overlay of the repetitions in the cyclic analyses. The inclusion of (cyclic) degradation is hence a point for future improvement (Bindiganavile, 2018).

Furthermore, monotonic analyses were performed. Here, the micro model is more stable than the macro model when applying a monotonic loading protocol (c) and is capable of reaching the degraded step points better (d), yet, there is barely any damaged stiffness (or plastic deformation) at the later steps (d); here the macro models fits the experiments more loyally (b), though for the case of Comp41, the macro model overestimates the plastic deformations (a). Note that the models of the walls with openings focus on Mode I cracks as there is hardly any slip. Mode II cracking becomes more relevant for the shear walls (Section 4.3.6).

In terms of crack patterns, both models represent the three main cracks elegantly (Figure 4.3.4); however, for the case of Comp 41, no model shows the observed crack pattern precisely. Yet, the micro model appears closer to the experiments by displaying the staircase pattern at the bottom of the window, and while it doesn't show a horizontal crack at the top of the window, a staircase crack was observed here in the other walls. This is most likely related to the issue of mesh directional bias for smeared crack band models (e.g. Slobbe et al., 2013) as is the macro model. In contrast to the macro model,

where the narrowest crack computed was actually the largest in the test, for the micro model, the relative crack width is closer to that of the experiments.

In sum, the micro model seems better suited for replicating the experimental test. Especially when crack patterns are of importance, the micro-model excels. Yet, there is an underestimation of the hysteresis, visible in 4.3.3.d likely due to the secant loading/unloading of the total-strain model. This could be remedied by using the EMM for the joints. Regardless, the micro-models is four times more computationally expensive and requires some additional parameters which may not be readily available. For this additional reason, the macro-model is preferred.

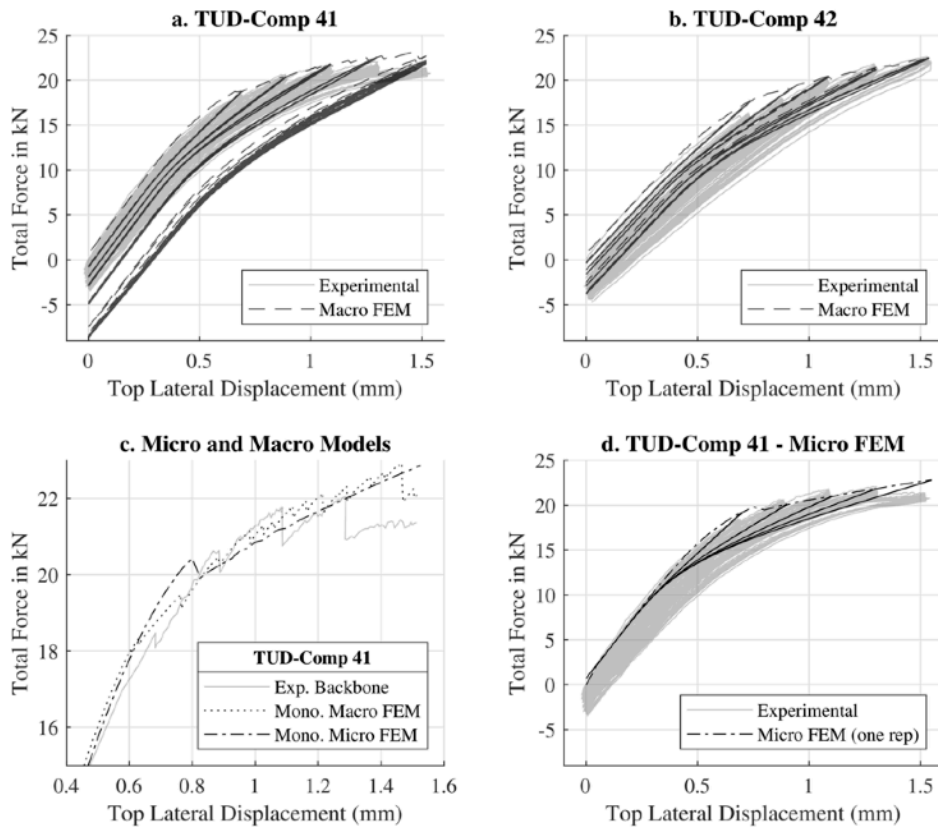


Figure 4.3.3. Calibration force-displacement curves from the models based on two of the test walls, a, b. Monotonic force-displacement curve from both macro and micro models against the experimental backbone curve of wall, c ; and d, force-displacement micro model with 5 steps of one repetition each against the experimental curve.

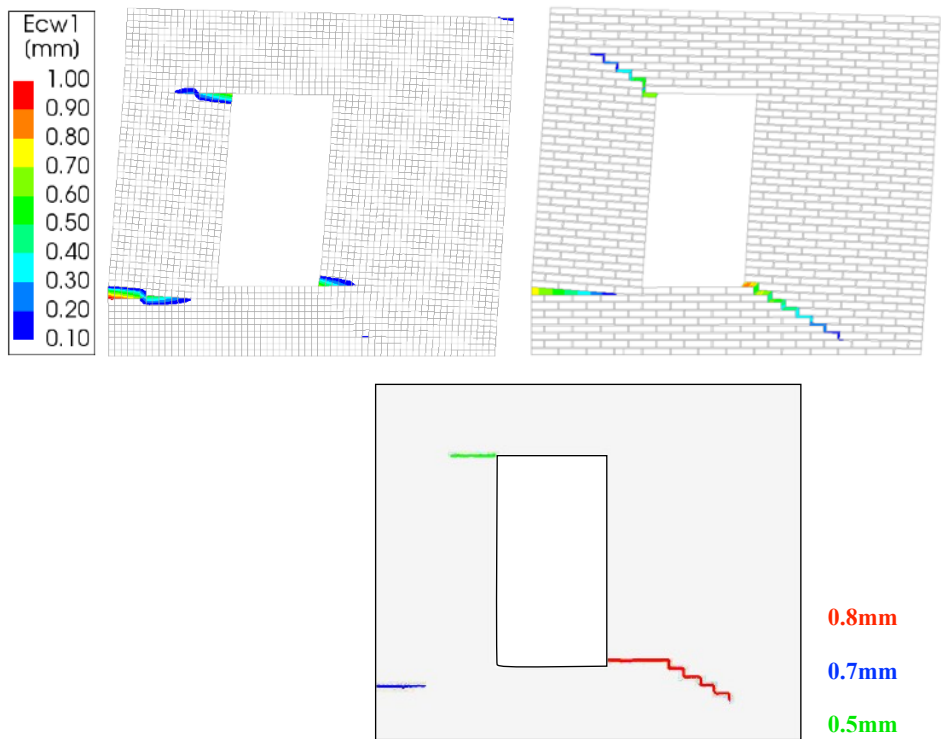


Figure 4.3.4. Comparison between crack pattern from Macro-FEM, Micro-FEM, and TUD-Comp 41 (Exp. DIC) at the end of the repetitive protocol.

Spandrels (Window Bank)

The calibration of the parameters for the material model was further complemented by a replication of the spandrel tests. A set of the spandrels tests were conducted monotonically and a larger set was tested repetitively with up to 300 repetitions; see Chapter 3. Due to the computational expense of the micro modelling approach employed, the models were calibrated only against the monotonic spandrel tests. The inclusion of the repetitive tests is a point for future improvement. Moreover, if the observed degradation can be included in a homogenised material model, then a macro modelling approach may also be possible for these tests.

Nevertheless, a good agreement was achieved between the models and the experimental data (see Figure 4.3.4). Here, the initial stiffness, the maximum strength, and the post-peak plateau were observed. In particular, the inversion point of linear to non-linear behaviour (recognisable on the logarithmic scale around $50\mu\text{m}$ of CMOD) matches the data beautifully. Note that the loss of linearity occurs at approximately half the ultimate capacity of the specimens. This was observed in the model to be related to the exceedance of crack initiation strain for the elements located at the very top of the sample. It also shows how cracks may arise long before the ultimate structural capacity is reached thus leading to the aesthetic DS1.

Further, two variants for the stiffness of the linear-elastic bricks are plotted. The lower Young's modulus corresponds to the stiffness of masonry as a composite material assigned to the brick, while the higher value of 8 GPa belongs to the testing of individual bricks. In the models, a Young's modulus of 1 GPa is given to the mortar elements which represent the mortar and the two mortar-brick interfaces, this value is kept the same for both variations of the brick stiffness. The latter value of 8 GPa for the brick was observed to be slightly too stiff, hence the lower value was also used. It is possible that the poor bond of the replicated masonry leads to an even lower stiffness which is then better captured by reducing the Young's modulus of the bricks.

Additionally, the crack pattern determined by the models was also observed in some of the monotonic tests as is shown in Figure 4.3.5. The spread of the local material property values will affect the precise crack pattern in both experiments and computations. Hence, the vertical crack would begin in one of the three centre head joints.

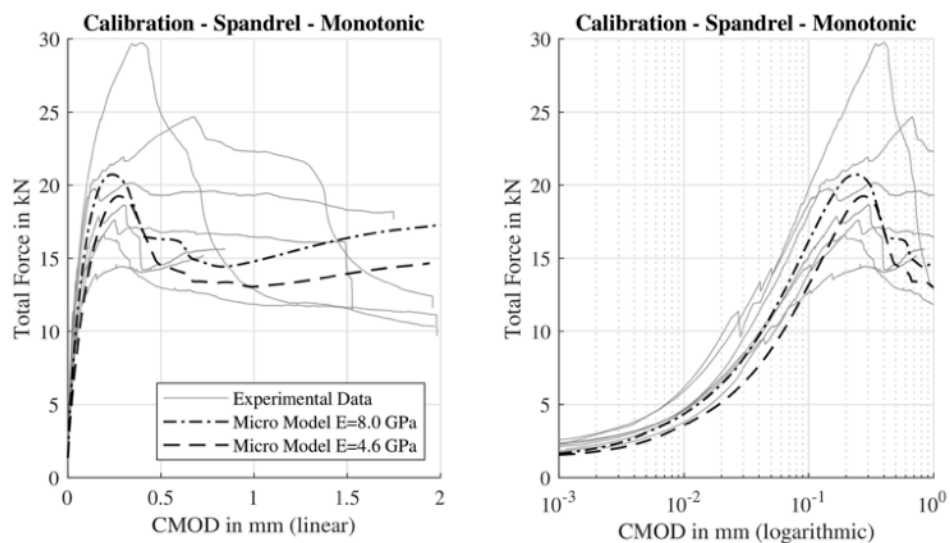


Figure 4.3.5a. Calibration of a spandrel FE model against the monotonic spandrel tests plotted on linear (left) and logarithmic (right) scales.

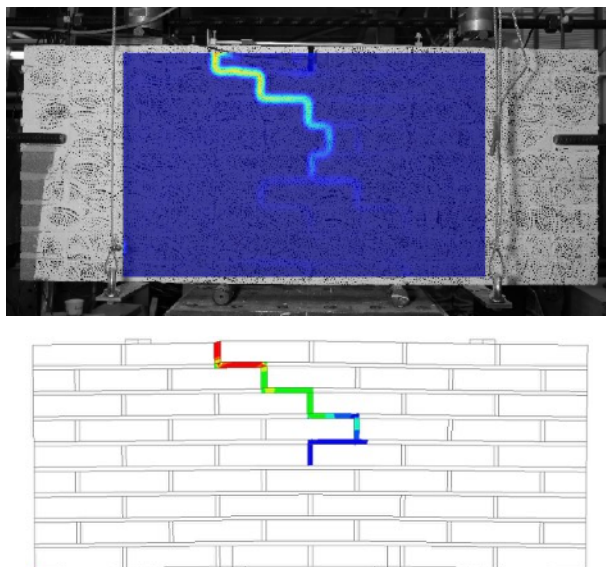


Figure 4.3.5b. Comparison of crack pattern against one of the monotonic spandrel tests. Note that this particular experiment saw a vertical crack through a brick.

4.3.5. Additional Model for Walls with Pre-Damage

This section presents the calibration of the FEM model for the two walls with the local predamage from the unbonded joints. These walls feature joints with reduced bond strength due to plastic strips left during construction, affecting the brick-mortar interface. These zones have no tension and reduced sliding strength. The continuum model mimics this by assigning inferior properties to elements in these weakened areas. In Figure 4.3.6, these elements are marked in a darker colour.

The material properties are identical to the previous walls as are the properties of the steel beams. The focus was on aligning material model parameters with those from smaller tests, too. The Young's modulus perpendicular to the bed joints comes from compression tests on masonry wallets, while the parallel modulus ratio (1.43) follows Jafari et al. (2016). The shear modulus G was calibrated to match wall stiffness, with tensile strength from bond wrench tests and fracture energy from EMM validations (Schreppers et al., 2016). Compressive strength and fracture energy values are extrapolated from masonry wallet tests, with shear parameters from triplet tests. For the weakened elements, elastic moduli are halved, tensile strength is zeroed, and cohesion is reduced to 10% of standard. These values, while somewhat arbitrary, lead to good results. The friction angle also decreases, simulating brick-PVC interaction. Compression properties mirror the rest of the wall. The numerical model's initial stiffness averages the stiffness of Comp 45 and 46 specimens, with Young's moduli already determined from tests.

The analysis has two phases: first, applying gravity load for 0.12 MPa pre-compression; second, introducing lateral displacement. The lateral support is activated only in the second phase. Comparisons between numerical models and the two walls (Comp 45 and 46) are presented in Figures 4.3.7 to 4.3.9. Crack patterns are compared together with load-displacement responses showing slightly overestimated capacities and underestimated energy dissipation on the positive side. The calibration model correctly shows the failure mechanism.

Table 4.3.4. Model components properties of macro-model of TUD-Comp 45/46.

Model Component	Element Type	Number of Nodes	Element Order	Mesh Size	Integration Scheme	Material
Virgin Masonry	CQ16M	8	Quadratic	50x50 mm	Gauss 3x3	EMM
Pre-damaged Masonry	CQ16M	8	Quadratic	50x50 mm	Gauss 3x3	EMM
Lintel	CQ16M	8	Quadratic	50x50 mm	Gauss 3x3	Linear
Beams	CL9BE	3	Class-III	50 mm	Gauss 7	Linear

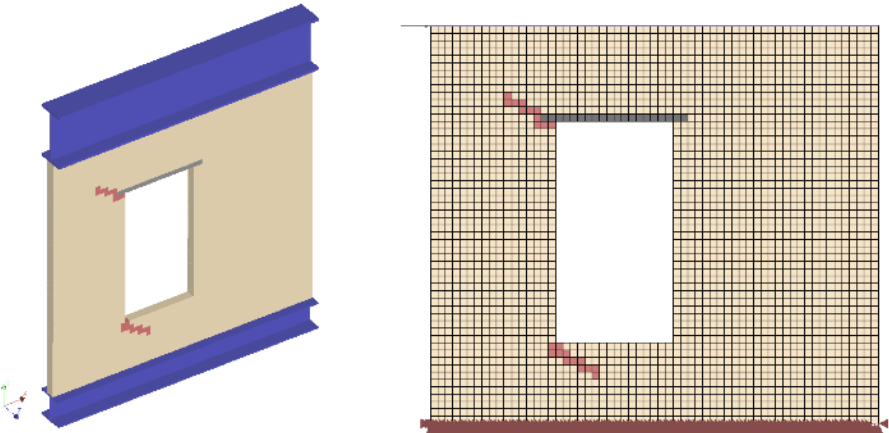


Figure 4.3.6. FE model of Comp 45/46 with pre-damage as weakened elements.

Table 4.3.5. Material properties for the elastic elements.

Material Properties	Concrete Lintel	Steel Beam
Density [Kg/m3]	2 400	45 321
Elastic Modulus [MPa]	31 000	210 000
Poisson's Ratio [-]	0.20	0.30

Figure FEM Notation

Ecw1: Principal crack width from smeared crack strain and crack band width in mm. Cohesion for shear: shear stress in MPa.

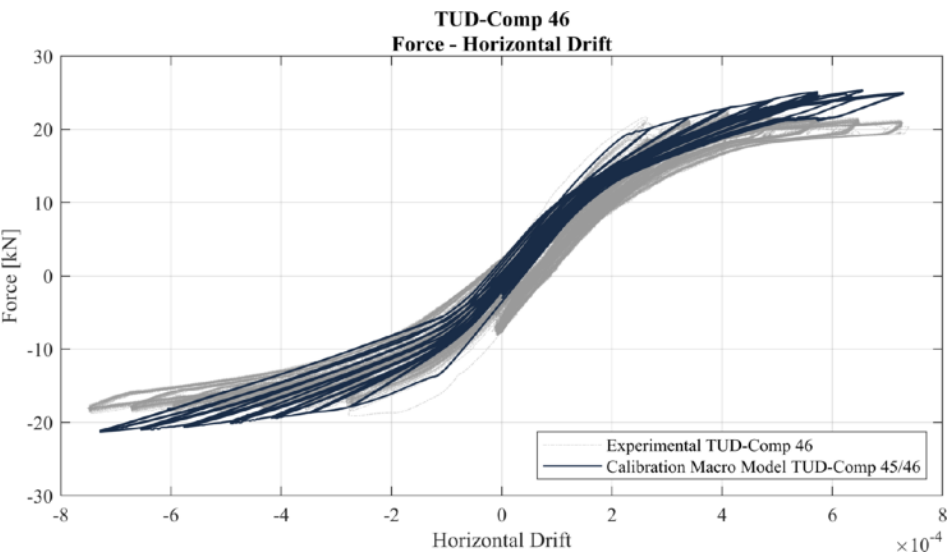


Figure 4.3.7. Force-drift curve of FE model compared with the experimental Comp 46. Drift is the ratio of horizontal deformation over the height of the wall in m/m.

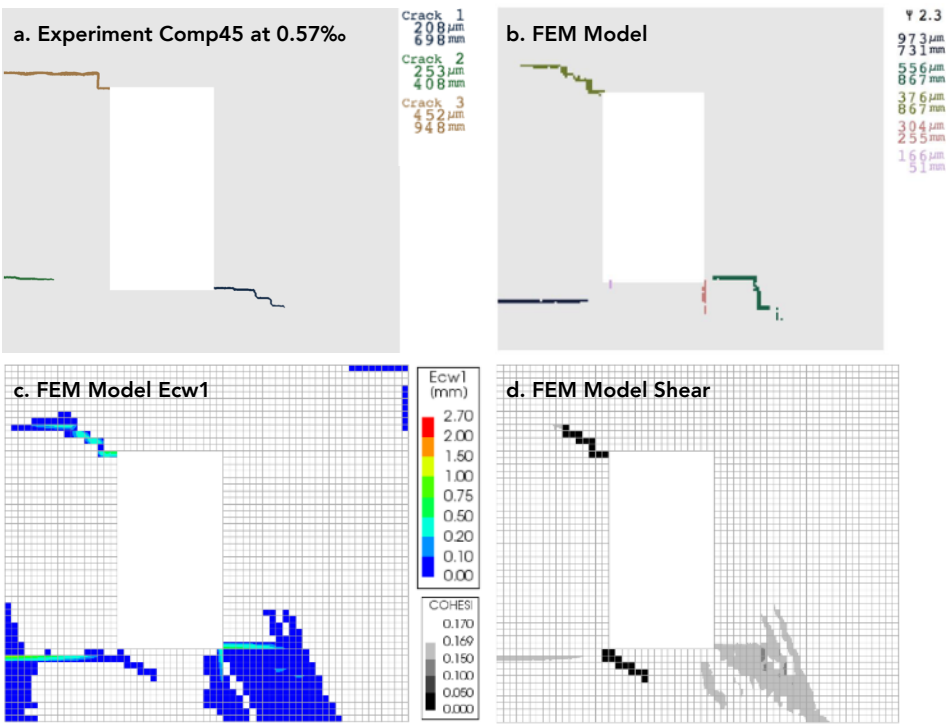


Figure 4.3.8a. a) DIC analysis of Comp46 at a drift of 0.57%, one way cyclic. b to d: he calibrated model at the same drift. (b) shows the interpreted cracks from the FE model.

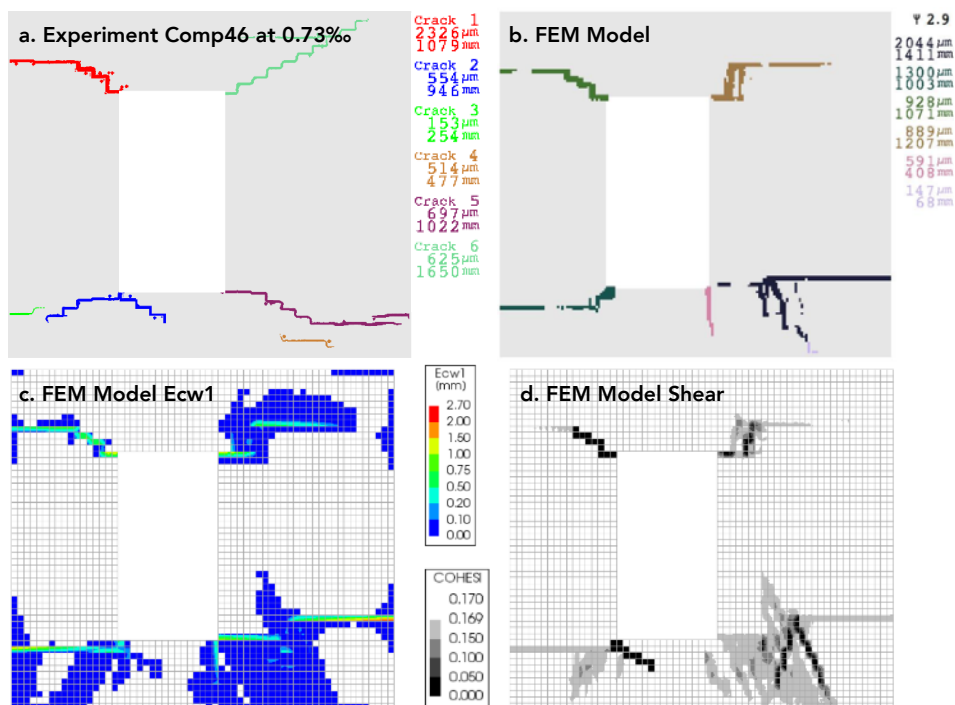


Figure 4.3.8b. a) Idem but for Comp45 at a drift of 0.73%, end of two-way cyclic protocol.

4.3.6. FEM Model for Shear Walls

The shear walls were also part of the calibration. The 2D plane stress model depicts a massive, in-plane clay masonry shear wall without openings, mirroring the dimensions of the other walls but without the opening. Similarly, it's firmly attached to steel beams at the top and bottom; both beams are modelled as line elements with their actual cross-sections. At the top, the overburden consists of a line load to generating a vertical stress of 0.46 MPa. The bottom beam is restricted for two translations and in-plane rotation, while the top beam is only constrained for in-plane rotation. Vertical "tyings" ensure the top beam moves strictly vertically.

The model's initial stiffness, averaging 110.4 kN/mm from specimens Comp 47 and 48, is calculated using the masonry's elastic moduli in both directions and a calibrated shear modulus G .

The analysis involves the two stages, gravity and imposed horizontal deformation. The first phase applies gravity and pre-compression loads up to 0.46 MPa; the model's vertical loading response shows zero horizontal displacement due to model symmetry and the Engineering Masonry Model's zero Poisson's ratio formulation. Phase two resets the displacement field and

activates a lateral horizontal support. Only three of thirty repetitions per step are modelled to reduce the computation expense; the applied load is plotted in Figure 4.3.9.

Force-drift comparisons between experimental test and the numerical model appear in Figure 4.3.10. Crack patterns after the third and last cycles are also compared in Figures 4.3.11 and 4.3.12. The former reveals a slight capacity underestimation on the positive side of the drift but good alignment on the negative. Similarly, the energy dissipation matches experimentally on the negative side but is moderately overestimated on the positive. After cycle 3, the model's shear cracks are more prominent than those in wall Comp 48; indeed, the walls showed $\Psi=1.7$ and $\Psi=1.9$ while the model shows 1.8. And, the final damage patterns are reasonably aligned, although the model's shear cracks are steeper. In terms of Ψ , at the end of the tests, the walls shows 2.6 and 2.3 while the model reaches 2.2, reasonably close.

At first glance, the comparison of crack patterns may appear to yield inadequate results. Two aspects must be noted: First, in the experiments, only cracks with a width higher than 0.1mm are presented, while in the FEM, cracks from a width of 0 mm, indicating a non-zero cracking strain, can be retrieved. In Figure 4.3.11, the 'missing' body cracks in Comp47 might have been there but couldn't be reliably detected. Secondly, the models show both top and bottom rocking cracks. In the experiments, the bottom rocking crack couldn't be fully captured because it was just at the edge of the surveyed area. Measurements with LVDTs, placed at the back of the wall, confirm that such a rocking crack was also present. Hence, the bottom left rocking crack identified by the FE models is correct.

The models fall short in determining the orientation of the cracks. They correctly identify cracks in the body of the walls; but several parallel cracks, at a steeper angle than the experimentally-observed, are depicted. This is partly related to the mesh directional bias and a general deficiency of the EMM in capturing diagonal cracks as opposed to the horizontal (rocking) crack which are well represented. Moreover, the EMM yields more distributed crack patterns instead of localised (Schreppers et.al). Sousamli (2024) has recently tackled some of these issues.

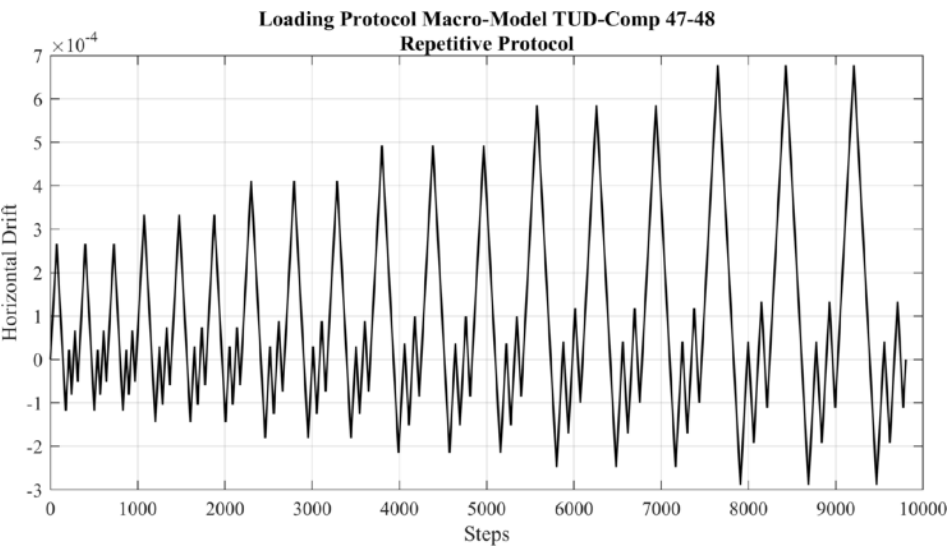


Figure 4.3.9. Simplified loading protocol for the model consisting of only 3 cycles per step.

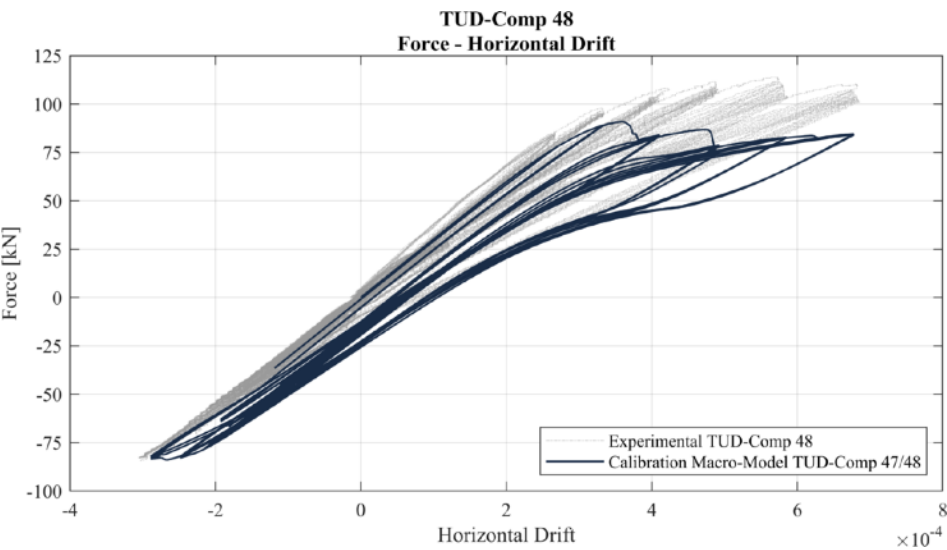


Figure 4.3.10. Comparison of the force-displacement curve between the model and one of the experiments.

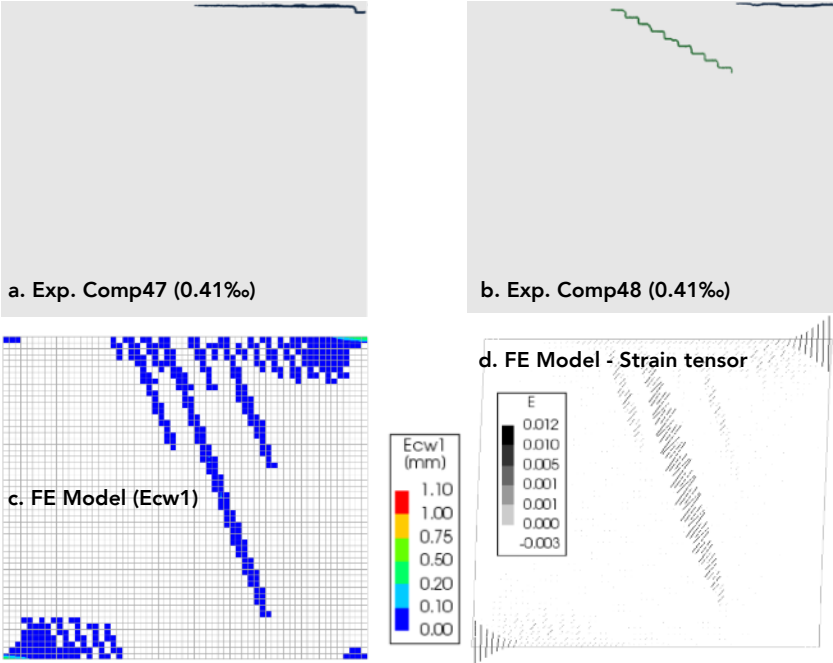


Figure 4.3.11. Comp. of experiments against the calibrated model for a drift of 0.41%.

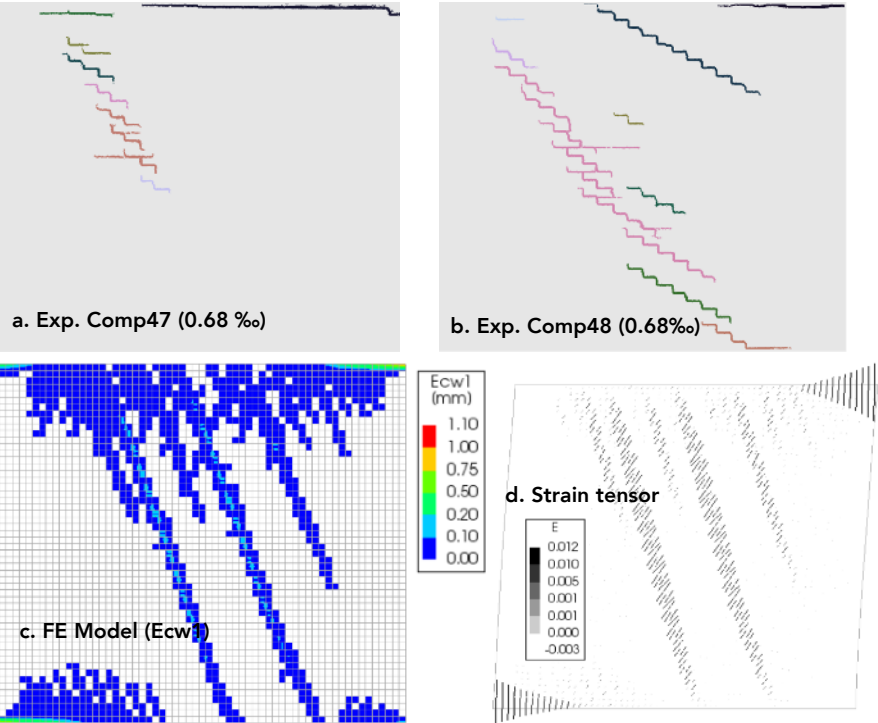


Figure 4.3.12. Experiments against the calibrated model for a drift of 0.68%.

4.3.7. Conclusions from the Calibration Process

The calibration of a wall model that sufficiently represented the experiments was not undergone blindly. A strategy had already been defined based on earlier studies. That a finite-element-method model, with the then recently developed Engineering Masonry Model as constitutive model of the continuum, could be a strong contestant, was already apparent. To the left, other strategies, that can represent crack patterns, are also limited. A micro-model was considered but was foreseen to be expensive. A discrete or distinct-element-method model could have also been successful (Malomo et.al 2018), but work would have had to be invested in an adequate interface model that could capture the behaviour of masonry joints, which was already included in the EMM (Schreppers et.al, 2016).

Therefore, the EMM-based FE model provided a strong starting point. It had to be validated for crack initiation and propagation, which had not been the focus of earlier studies. Additionally, relevant experimental boundaries had to be incorporated in the model, and material parameters had to be extracted from key material characterisation tests. Some other parameters had to be calibrated on the basis of the spandrel and wall tests.

Different tests provided distinct parameters. The choice for the head joint strength option was better defined from the walls without opening which included much more shear behaviour (Mode II). In contrast, the sensitivity of the tensile strength, was more influential in the walls with a window opening, where Mode I behaviour played a stronger role.

The unloading schemes in the EMM were particularly useful to replicate the different Mode I and Mode II cracking that occurs in masonry. Improvements can be made to reproduce diagonal cracks and repetitive degradation.

Three parameters had the largest influence: the tensile strength, the fracture energy in tension and the Young's modulus. Coincidentally, these parameters also have a large variability in experiments. Bond-wrench tests on the replicated masonry samples revealed a deviation of 30% from the mean of the tensile strength. This high variability is likely to be a good representation of the variability in the field between different types of masonry. Fired-clay brick masonry is diverse: the clay and sand composition, firing time and temperature, mould material and shape, all lead to bricks with various properties. Similarly, mortar recipes, lime- or cement-based, curing conditions and masoning practices, will ultimately result in varying mortar, bond, and masonry. While crack patterns were affected by these parameters, the measure of damage in terms of Ψ , which consolidates damage into a single number,

was less sensitive. It follows that damage in general fired-clay brick masonry will be well represented.

A strong point of improvement would lay in the use of probabilistic models. These would output a probable failure mechanism and a band for the force-displacement curve. The probabilistic distributions could be implemented both at the model level, as is done later in Chapter 5 for the extrapolation models, but also at the element level, replicating the fact that materials, especially those like masonry, are never homogenous (Evangeliou, 2016; Roy, 2019). This probabilistic approach would go in hand with additional experimental results; these can also be viewed probabilistically. A larger number of experiments would also yield some insight into the probable failure mechanisms, as the more complex walls do not behave identically. For example, even at the small scale, bond-wrench tests may fail at the mortar-brick interface, in the mortar, or rarely, with delamination at the brick. Probabilistic numerical models could be calibrated such that the ratio of the varying types of failures is reproduced. In this case, various mechanisms and limit states would be predicted by models and specific ones would be more or less likely.

Additional improvements could be further linked to experimental results. DIC has captured displacements over the surface of the wall. The displacement field could be contrasted to that of the numerical models. A comparison could then be made on an element-by-element basis where the deformation of each finite element is linked to the equivalent element on the DIC data. This could also serve to determine the variability in material properties throughout the wall (Sangirardi et.al, Judd et.al, 2023).

Calibrating models is not only about defining a modelling strategy that works. The ultimate goal is to have models that can be used to analyse situations that were not, or could not be, tested experimentally; these are extrapolations. Simultaneously, the first two sections of this chapter have delved into hazards and their actions on structures; the effect of some of these actions can then be explored with the calibrated models. This is performed in the next section.

4.4. Modelling Damage: Shrinkage, Settlements, and Vibrations

Sections 4.1 and 4.2 presented an overview of hazards and multi-hazards. Yet, Dutch buildings are seldom subjected to landslides, for instance, due to the flat nature of the country's geography. Instead, from the effects explored in these earlier sections, three phenomena are most relevant to Dutch buildings: temperature differences and material shrinkage leading to restrained deformations, soil settlements resulting in imposed deformations, and vibrations, as a result from earthquakes, leading to in-plane deformations and damage. These can appear on buildings as a multi-hazard and are the focus of this study.

In this section, an overview of modelling strategies to assess these effects is presented. The models of a masonry wall with an opening, calibrated in Section 4.3, are utilised. These serve as examples.

4.4.1. Modelling Restrained Deformations: Shrinkage

Modelling restrained deformations is straightforward. Analytically, the expected stress is proportional to the Young's Modulus of the material. For uniform axial loads, the stress is $d/L \cdot E$ or simply $E \cdot \epsilon$. This assumes a perfect constraint which is rarely the case. Moreover, walls are seldom uniformly restrained. Typically, the foundation and the floor, if rigid in comparison to the wall, provide a limited amount of restraint. This can also be solved analytically, but only for a linear-elastic situation. If damage needs to be modelled, a FEM model is a good approach.

Figure 4.4.1 displays a masonry wall subjected to internal shrinkage. A strain of $3 \cdot 10^{-3}$ is a common amount of shrinkage for a brick wall with a general cementitious mortar. In this model, the bottom of the wall is fully constrained in the horizontal direction - mimicking the presence of a stiff foundation. The material properties are derived from the calibrated models including smeared cracking in the tensile failure with softening under the EMM. Many factors can influence the intensity of cracking observed in the model. Besides the material properties, boundaries are key. While a fully fixed boundary will lead to higher damage, a partially restrained support will admit some displacement and thus allow for some release in stress.

The figure also includes the stress trajectories on the wall at the load step right before the first element is cracked. For every element a perpendicular set of vectors is drawn; these are rotated according to the principal stress direction in each. At the locations where cracks are about to occur, tensile stress gathers

perpendicular to the potential crack. Three of the window corners develop stress concentrations. However, only the right bottom corner shows later a prominent crack. As this corner cracked, stress re-distributed in the wall.

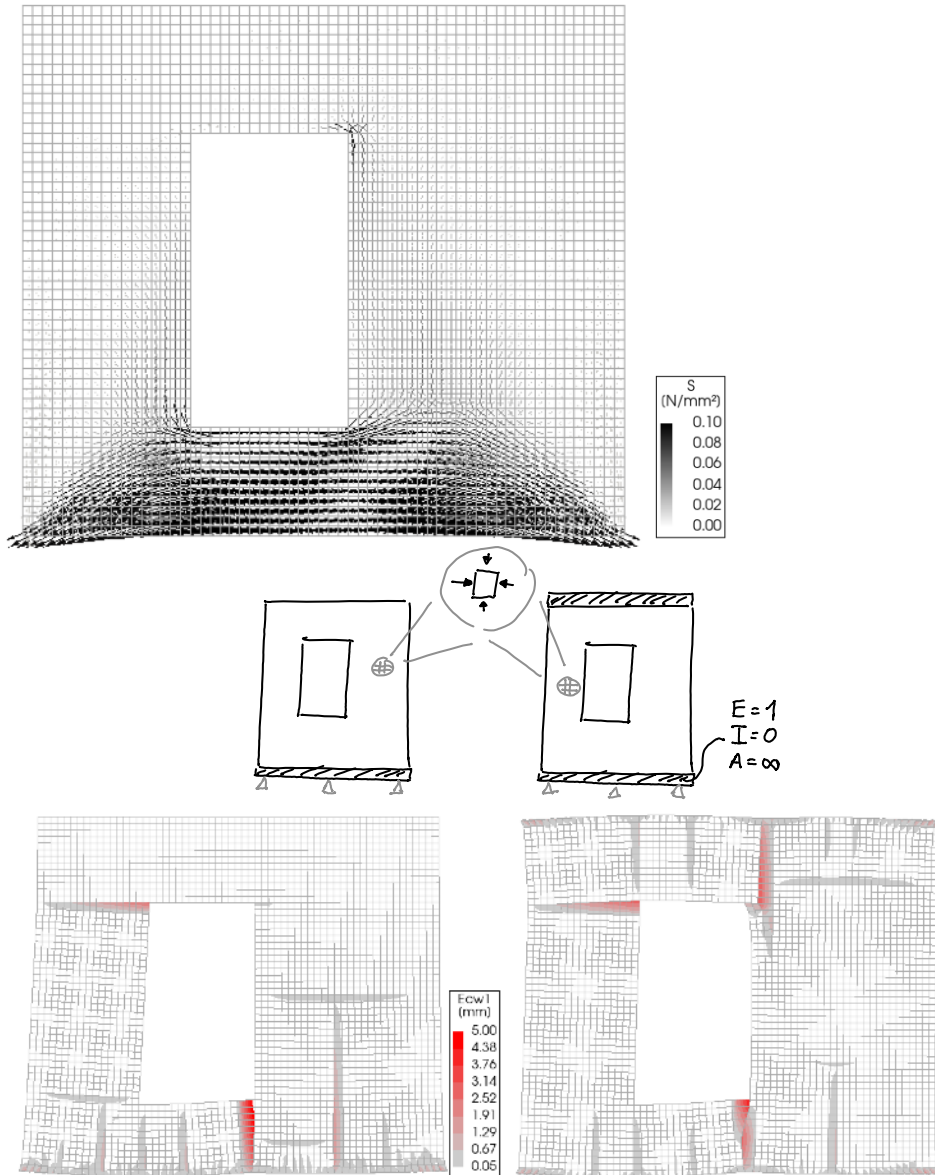


Figure 4.4.1. FEM model of a masonry wall subjected to shrinkage. Left, bottom edge fully constrained. And right, top edge also restrained by a floor. Top, tensile stress trajectories right before cracking for the left case.

In the example on the right of Figure 4.4.1, the upper floor is also viewed as a constraint; therefore, additional cracking is expected. The opening for a window, significantly influences the cracking picture. Moreover, the connection with the boundaries is important: in the examples, a horizontal restraint is enforced, but if crack opening between foundation and wall are possible, the shear transfer may be diminished resulting in delamination but less cracking in the wall. Beyond these examples, modelling of shrinkage is a study in its own; see Rots, Van Der Pluijm, & Vermeltfoort (1997) or de Vent (2011).

4.4.2. Modelling Imposed Deformations: Settlements

The type of imposed deformation will also determine the type of modelling approach. A timber floor expanding due to changes in moisture will push in the out-of-plane of a wall. Such a situation can be modelled by a shell representing the wall supported on three sides and subjected to point loads at the positions of the floor joints. This is illustrated in Figure 4.4.2, left. Here, the plane-stress elements of the calibrated model are replaced by shell elements, which can be loaded perpendicular to their plane. At the top edge of the wall, point loads, distributed every 60 cm, are applied. These represent the contact points with potential floor joists. This results in vertical cracks, especially at the top edge of the window.

Another example is that of settlements. The main load-bearing wall of a simple house may settle uniformly. Because this wall is connected to its transversal walls, they experience a vertical displacement at their extremes. To support this vertical displacement, the bottom edge of the wall is supported by springs (an interface) representing the stiffness of the supporting soil. This is modelled on the right of Figure 4.4.2. Here, the left edge of the wall displaces downwards. This leads to vertical cracks at the corners of the window.

Alternatively, a loss of support of the transversal wall can be modelled. This leads to a similar situation. Here, the boundary nodes of the interface at the bottom edge is subjected to the imposed displacement with an asymmetric hogging shape. This shape could be the result of a similar settlement cause. The result is displayed in Figure 4.4.3. The 'knick' point of the hogging shape, located towards the centre of the wall, leads to a slightly different crack pattern.

For modelling settlements, modelling approaches can become complex. The soil can be included and even the settlement driver within the soil can be modelled. These are not the prime focus of this work but are explored in [6, 9, 22].

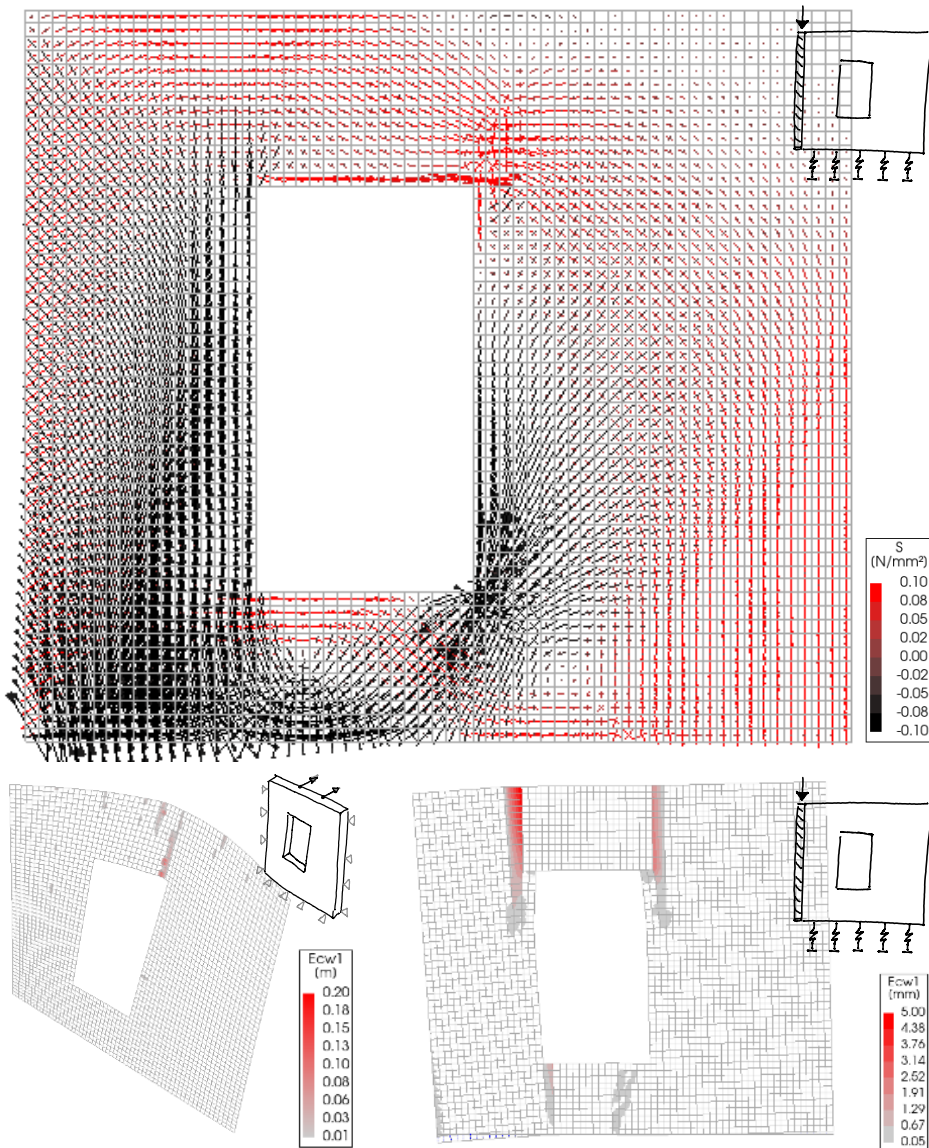


Figure 4.4.2. FEM model of a masonry wall subjected to OOP due to point imposed displacements due to the floor joists. Right, settlement of the façade due to an imposed vertical displacement on the left edge due to settlement of its transversal wall. Top, stress trajectories for the settlement case, one load step before the first element cracks.

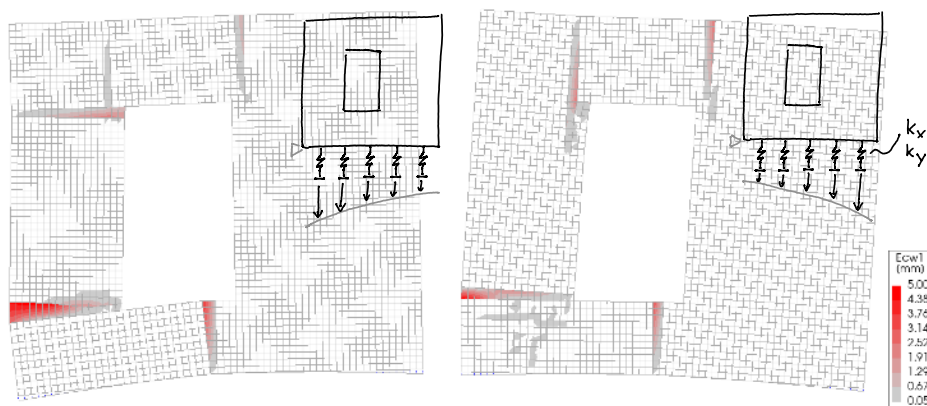


Figure 4.4.3. Model of a façade subjected to an applied settlement shape in the form of asymmetric hogging, with the left or right edges settling.

4.4.3. Dynamic, Non-Linear Time History Analysis: Vibrations

Earthquake actions can be modelled in several ways. Linear elastic approaches, like an equivalent base shear force (static) or the superposition of the structural modal modes and a spectral analysis (dynamic), can offer good results but cannot be used to determine crack-based damage - only the very initiation of cracking when the tensile strength is exceeded.

Pushover against NLTHA

Two non-linear approaches are common, a pushover curve compared against the acceleration and displacement demand of the earthquake record (static) or a non-linear time history analysis (dynamic). Both approaches can be used to estimate damage on a masonry structure. However, the pushover analysis considers a quasi-static force-displacement curve. As the horizontal drift of the structure increases, cracks appear and propagate. Nonetheless, an earthquake is typically a cyclic event, where the drift reverses several times. If the number of effective cycles is considerable, then the pushover analysis will produce a different damage pattern than the NLTHA.

The pushover method has several advantages. First, the comparison against the demand diagram can include several records simultaneously or even idealised spectra from building codes. NLTH analyses require several records to produce the same observations but, in the process, can provide accurate quantifications of the damage variability due to the varying records. Secondly, pushover analyses are significantly cheaper computationally. Thirdly, pushover curves can be compared to the envelope of cyclic experimental tests or monotonic tests; depending on this, a model can be indirectly calibrated for cyclic actions.

Nonetheless, pushover strategies also have some limitations: First, the seismic loading is simplified into a static, incrementally increasing load. This approach cannot capture the dynamic nature of real seismic events, which is a critical limitation compared to NLTHA that models seismic loading as it occurs in time.

Second, they typically focus on the first mode of vibration and assume a predetermined distribution of lateral forces, which may not accurately represent the actual behaviour of the structure under multi-dimensional seismic excitation. NLTHA, on the other hand, can account for higher modes and their effects.

Third, since pushover analyses are a static procedure, they inherently assume that dynamic effects (like inertia and damping) are not significant, which is not always the case in real seismic events. NLTHA include these dynamic effects.

Moreover, pushover methods cannot capture time-dependent phenomena such as the sequence of cracking, yielding, or changes in dynamic properties during an earthquake. NLTHA can account for these effects as it simulates the structural response over time. Similarly, the pushover analysis might not accurately estimate the energy dissipation capacity of a structure during a real earthquake. NLTHA provides a more realistic assessment of how a structure will perform, including its capacity to dissipate energy.

Finally, NLTHA can more effectively incorporate soil-structure interaction effects, which are significant in certain cases.

A sequentially-linear pushover analysis (SLPA) combined in each step with an ADRS could address some of these limitations. The issue of crack snap through, when the brittle formation of a crack unloads the rest of the model, can also be effectively and robustly modelled using SLA; see Pari et al. (2017).

but this is a topic for future study, see also Appendix A.4. For these reasons, NLTHA are employed in the rest of this work to analyse seismic vibrations.

A comparison between the crack pattern observed from a pushover analysis against a NLTHA is performed in Figure 4.4.4 for the earthquake of Zeerijp. This record (see later Figure 5.2.2) has only a few effective cycles. The drift used for the pushover analysis follows from the displacement demand of the record for the first natural period of the structure. For the NLTHA, the maximum crack width is displayed. One can observe some differences between the crack patterns. Many studies focus exclusively in comparing these two approaches (Giusto et.al 2024).

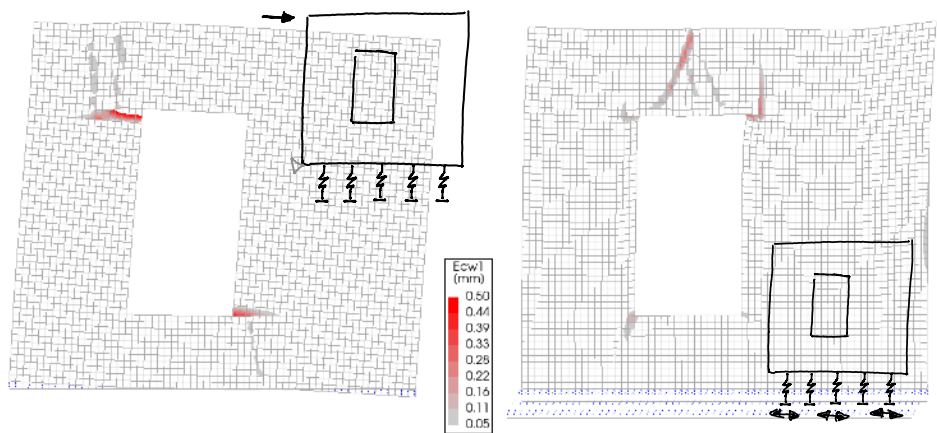


Figure 4.4.4. Left, the crack pattern from a pushover analysis of the Zeerijp near record, and right, the same earthquake evaluated with a NLTHA.

4.4.4. Modelling Multi-hazards

When modelling the effects of a multi-hazard, their respective actions need to be considered. When the actions of the hazards are identical, modelling is straightforward; for example, shrinkage of a wall followed by temperature changes are both hazards that lead to restrained deformations at the same location and can be modelled by enforcing a strain field on the wall or applying a displacement to the supports. Similarly, vibrations from traffic in combination with vibrations from seismic events can be analysed as a single continuous action.

A more thoughtful strategy is needed when the actions from the primary and secondary hazards are different. For example, imposed displacements followed by vibrations, as could be the case for soil subsidence and earthquakes, represent a multi-hazard with different actions. Similarly, overloading followed by restrained deformations, as could be the case of a snowstorm and extreme cold temperatures. In this theoretical example, the snow on a roof can cause overloading and provides additional insulation that creates a difference in temperature between structural components.

For multi-hazards with varying actions, the model must be able to accommodate both types of actions in a way that the damage from both can be calculated. Moreover, the damage of the primary hazard will influence the aggravation of damage from the secondary hazard. A general approach is described extensively in [2], which also includes a case study with an earthquake - flood multi-hazard where a flood (or tsunami) follows an earthquake event. In this case, the structures are weakened by the earthquake accelerations and are more vulnerable to the lateral actions exerted by the flood.

In this work, a multi-hazard consisting of settlement deformations followed by earthquake vibrations is explored. These models are generated in more detail in Chapter 5, but are briefly described next for clarity:

First, a boundary interface is used underneath the wall geometry to apply a settlement shape. The imposed displacement is increased until a pre-defined value of damage ($\Psi=1$ for example) is achieved. Then, in a second phase of the analysis, the interface is locked by increasing its shear stiffness. In this way, an acceleration time history can be applied at the boundary end of the spring and its horizontal displacements are transferred to the wall.

4.5. Conclusions: Modelling and Calibration

This chapter has explored the multifaceted nature of hazards, both natural and anthropogenic, and their specific actions on buildings, with a particular focus on the Dutch context. Through detailed finite-element-method (FEM) model calibrations, informed by experiments and collaborative efforts, the groundwork for understanding and quantifying the impact of various (multi-)hazard scenarios on structures is laid. The calibrated models have not only allowed to replicate the behaviour observed in experimental settings but have also served as a tool for simulating the effects of different hazard actions on buildings.

The calibration process for a wall model was guided by previous studies, using the Engineering Masonry Model (EMM) in a finite-element-method (FEM) for its ability to simulate crack patterns and include masonry loading/unloading behaviour.

The chosen EMM-based FE model needed validation for crack initiation and propagation, incorporating experimental boundaries and extracting material parameters from (companion) tests. The impact of parameters such as tensile strength, fracture energy, and Young's modulus was significant, given their variability and influence on crack behaviour.

Improvements could consider probabilistic models or might integrate more experimental data. For instance, Digital Image Correlation (DIC) has helped align model predictions with observed displacements, providing insights into material variability. The ultimate goal is to extend these models to analyse untested scenarios, leveraging calibrated models to assess hazards and structural responses.

Hazards such as shrinkage and soil movements have been investigated with the calibrated models. The deformation of the wall and the resulting crack patterns were reviewed. Most cracks appeared around window openings, similarly as in the experiments. The cracks developed perpendicular to the tensile stresses on the finite elements. Different hazards also led to distinct crack patterns. However, some cracks were recurrent even between differing hazard actions.

Chapter 5

Fragility

This chapter describes the final step to quantify the probability of light damage or its aggravation. Earlier chapters have looked into how to measure crack-based light damage, both conceptually and in experiments. Its reproduction in models has also been investigated so that extrapolations to new situations could be made. On the basis of these new situations, the influence of variations in building context, which lead to a varying damage response, is observed. How to obtain a probability of damage, or *fragility* from these results is presented next.

This section is loosely based on several works including [7, 15, 23, 24, 27]; see List of Publications.

distribution
event probability present
record value study high
curve parameter initial
number result earthquake
fragility

Chapter 5 : Table of Contents

5.1. Introduction	150
5.2. Extrapolation to Non-Linear Dynamic Analyses	152
5.2.1. Background on Experiments and Calibration	152
5.2.2. Setup of Extrapolation Models (Based on Field Cases).....	153
5.2.3. Results from Extrapolation Models	161
5.3. Regression of Damage Function from FEM Results	167
5.3.1. Reasoned Regression Model Considering Ψ_0	167
5.3.2. Model Uncertainty	173
5.3.3. Surrogate Model with Machine Learning	175
5.4. Fragility Curves for Seismic Vibrations	178
5.4.1. Probabilistic distributions and Parameters.....	178
5.4.2. Results of Monte Carlo Simulation	180
5.4.3. Comparisons to other Studies	184
5.4.4. Fragility Maps	187
5.5. Fragility Curves for Settlements from Soil Curvatures	191
5.5.1. Overview of Semi-Coupled Models of Masonry Façades.....	191
5.5.2. Fragility Curves for Soil Angular Distortion: β vs. Ψ	198
5.6. Conclusions: Probability of Damage and Aggravation	206

5.1. Introduction

The outcome of a numerical model is a deterministic value. This means it is only applicable to a single case. It is unlikely that the case being reproduced will match the model exactly. For this reason, usually a series of models is analysed to obtain a lower and a higher boundary of what is to be expected, varying some of the most sensitive model properties. This is applicable to reproducing experiments where most of the model parameters are reasonably known via measurements and companion tests. For reproducing real cases, a deterministic outcome is naive; in these cases, one should always consider a probabilistic result consisting of an expected value and its uncertainty.

The goal of this work highlights the need to establish the probability of damage, recognising that the behaviour of masonry buildings will be different in many cases. The probability will depend on the expected variations of all the parameters that might affect damage development such as the strength of the material, the shape and geometry of a building, the intensity of the loads, etc. One could analyse a model for each of the possible variations. At some point

however, the number of permutations is so large, that evaluating expensive numerical models becomes unfeasible.

The solution is a hybrid strategy demonstrated in this chapter. First, sufficient numerical models are evaluated to explore the relationship between the hazard, damage and other influential parameters. These relationships are then expressed via a surrogate model: a mathematical formulation that captures the observed relations. Lastly, the surrogate model is used to simulate a larger number of variations thus quantifying the probability of damage.

The calibrated finite-element-method models of chapter 4 are used to investigate two new situations, or extrapolations. In Section 5.2, these extrapolations study the effect of dynamic soil movements (seismic vibrations). Section 5.3 then regresses a relationship between damage and the parameters varied in the models. Next, Section 5.4 conducts a MonteCarlo simulation using probabilistic distributions for the parameters and the intensity of the seismic vibrations. These lead to the probability of damage expressed at increasing seismic intensity, i.e. a set of fragility curves.

The second way in which the models are used to extrapolate is presented in Section 5.5. Here, quasi-static soil movements or deformations leading to settlements are briefly explored. This set of models is used to present a second example of a surrogate function, in this case with a trained neural network, a type of machine learning model well suited for this purpose. The model is then used for a similar MonteCarlo simulation to determine the fragility of masonry buildings against increasing soil curvature or a settlement hazard.

5.2. Extrapolation to Non-Linear Dynamic Analyses

5.2.1. Background on Experiments and Calibration

The experiments have been presented in Chapter 3 and the calibration of FEM models has been treated in Section 4.3. A brief summary of their key aspects is drafted here for clarity. The experiments involved testing five nominally identical, single-wythe walls of fired-clay brick masonry, each 3.1 meters wide and 2.7 meters tall, with an asymmetrically placed window opening. These walls were tested quasi-statically in-plane by enforcing controlled displacement at the top, mimicking a 'cantilever' (flexural) configuration. The walls were pre-loaded vertically to produce an average stress of 0.12 MPa, resembling moderate vertical loads. Two additional walls, identical in material but without a window opening, were tested at a higher vertical overburden of 0.46 MPa in a 'double-clamped' (shear) configuration. Another set of two walls with window openings and pre-damaged crack interfaces was also tested under similar conditions.

The experiments imposed in-plane drifts to the walls of up to 0.1%, with some cracks reaching a width of up to 2 mm. Cracks propagated differently in the flexural walls (mostly horizontal and stair-case-diagonal from the window corners) compared to the shear walls (mostly steeper diagonal cracks starting from the wall centre). Additionally, ten spandrel-type wallets were tested in a four-point bending setup, showing toothed, vertical, crack patterns.

The described experiments, along with standard masonry characterisation tests, informed the development of a modelling strategy using the finite element method (FEM) with DIANA-FEA. This strategy aimed to replicate the specimens' behaviour in terms of stiffness, strength, hysteresis, and crack patterns. The macro approach for masonry was employed, using two-dimensional, plane-stress, quadrilateral, 8-node, quadratic elements (CQ16M) with a mesh size of 50 mm. A non-linear material model (Engineering Masonry Model - EMM) was selected, accounting for different inelastic and elastic properties in directions perpendicular and aligned with the bed-joints.

A single set of parameters was used for all calibration models, reflecting the material characteristics of the masonry that were uniform for the laboratory tests. These models included both physical and geometrical non-linearities and were solved using a quasi-Newton incremental-iterative approach. An overview of the calibration models is presented, juxtaposing experimental and modelled displacement fields, crack patterns, and force-displacement curves, illustrating the various calibration campaigns and their outcomes.

5.2.2. Setup of Extrapolation Models (Based on Field Cases)

The models that were calibrated and validated against the laboratory tests are subsequently extended into the nonlinear time-history domain so as to assess the effect of seismic vibrations and replace the laboratory boundaries with the constraints provided to a masonry wall by a real structure; in this light, these models become **extrapolations** from the validated laboratory scenario to real field cases while maintaining the geometry of the wall. The **adaptations** and **variations** are presented in the following two subsections:

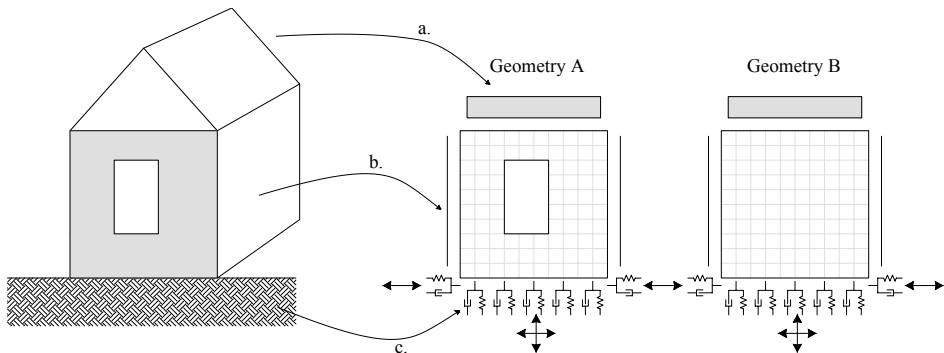


Figure 5.2.1. Schematisation of the model with the representation of some of its features: a) top weight and dynamic mass, b) lateral constraints, and c) soil-structure interaction.

Model Adaptations

The adaptations applied to the models are shown in Figure 1 and are listed below:

- **Overburden:** a vertical pre-compression of 0.12 MPa is applied at the top edge after the self-weight gravity load. This stress corresponds to the weight of one concrete floor or two timber storeys (a storey and a roof).
- **Top boundary:** no steel beam is used at the top of the wall as in the laboratory; instead, a stiffness-free line-mass element is incorporated to mimic the dynamic effect of a floor. The mass is set at 10 ton to simulate the presence of a fictitious rigid floor, an upper masonry wall, an upper floor and a roof. While the wall with an opening doesn't carry the vertical weight of these components, their mass does affect the horizontal in-plane behaviour of the walls; as such, the line mass does not influence the static condition.

The mass is also used to calibrate the natural periods of the walls to match those of low-rise masonry buildings from which the walls are extracted. The flexible wall has a fundamental natural frequency of about 9Hz and the stiff wall of about 13Hz; depending on material, soil and initial masonry condition,

these periods can vary by up to $\pm 2\text{Hz}$. This is deemed an adequate representation in terms of natural periods for masonry buildings.

- Rayleigh damping: a 2% damping based on the first two modes, as judged by order of participating mass, is included in the model.
- Lateral boundaries: two vertical, linear-elastic beam elements, with a fictitious cross-section of one brick, are added to the lateral edges to simulate the constraints of transversal walls. These elements have an elastic modulus equal to 1800 MPa and a Poisson's ratio of 0.16. The density is set to account for the out-of-plane dynamic effect of a wall of 3 m in length along the transversal direction.
- Soil-structure interaction: the bottom steel beam used during the calibration phase is replaced with a combination of springs and dashpots. These are placed underneath the wall in order to simulate the effect of the soil on the structure. Stiffness and damping are provided by two separate interface elements:
 - 1) A non linear 2D line boundary interface (CL6TM-NL), which accounts for the stiffness and for the soil's behaviour, is characterised with a Coulomb friction law. The cohesion is set to 0.1 MPa while the friction and dilatancy angles to 0.61 rad. Additionally, a no-tension criterion is enforced for the springs representing the fact that no tension can develop between soil and foundation.
 - 2) A similar, yet linear-elastic interface (CL6TM-LE), which includes the damping coefficients and offers no stiffness, is also included.

The values of stiffness and damping are varied for two types of soil profiles (and two types of façades) as presented in Table 2. A stiff soil, with higher stiffness and better damping, is contrasted to a poor or soft soil. The methodology employed to determine these coefficients is adapted from NEHRP and described extensively in [5], while the representative soil profiles were obtained from Deltares using insight discussed by Kruiver et al. (2017).
- Input motion: the load introduced as an in-plane, quasi-static displacement at the top of the wall in the experiment is replaced by horizontal and vertical accelerations applied at the base of the wall. This extrapolation is two fold: first, the accelerations become inertia loads, focused at the top (because of the mass) but also distributed throughout the wall; this modifies the validated behaviour slightly. Second, the appearance of cracks could be different when tested dynamically, however, the damage behaviour with dynamic tests has not yet been studied; hence, this becomes a reservation in the present study. Nevertheless, the assumption of transitory or transient damage as the residual damage is conservative (see Section 2.4).

The accelerations applied to the models are derived from four distinct seismic records. Two of these records are from the Zeerijp earthquake captured at the Garsthuizen and Appingedam stations; see Table 1. The other two records are from the Westerwijtwerd earthquake from stations: Stedum and Hoeksmeer. These motions are illustrated in Figure 2 and categorised as 'near' or 'far' based on the station's proximity to the epicentre, with the motion amplitudes normalised to a consistent scale. The expansion in the network of geophones and accelerometers has allowed capturing several records from multiple events; earlier records, like those of the event of Huizinge 2012, are not as complete.

Table 5.2.1. Overview of the four earthquake records employed. For the horizontal Peak Ground Velocity, the maximum rotated component is shown (recorded).

Event	Magnitude	Station	Distance	MaxRot Horz. PGV	Vertical PGV
Zeerijp	3.4	Garsthuizen	2.5 km	31.3 mm/s	6.0 mm/s
8 January 2018		Appingedam	7.5 km	2.4 mm/s	0.8 mm/s
Westerwijtwerd		Stedum	3.2 km	5.4 mm/s	2.5 mm/s
22 May 2019		Hoeksmeer	9.7 km	1.7 mm/s	0.7 mm/s

This classification reflects not only the distance from the epicentre but also similarities in the seismic properties across different records. For instance, the horizontal seismic motions recorded at closer locations ('near') are characterised by arriving earlier and having fewer effective cycles compared to the 'far' records, which show a greater number of cycles with similar amplitudes. This observation is further supported by Fast-Fourier Transform analyses, indicating that the 'far' records are predominantly composed of lower frequency vibrations, ranging from 2 to 4 Hertz, particularly in their horizontal components. Conversely, the frequency content of the vertical components is more consistent across all records. Note that the designations of "near" and "far" for these shallow, induced earthquakes differ from those used for tectonic earthquakes where distances are much larger.

The Arias intensity plots reveal additional distinctions: the energy in the 'near' records is concentrated within a smaller portion of the timeline, whereas in the 'far' records, the energy distribution spans a more extended period. This difference in energy distribution is also evident in the PGV amplitudes; the vertical components of the 'far' records show about a third of the PGV of their horizontal counterparts, while the 'near' records' vertical components exhibit about a fifth.

Spectral amplification analyses show that, although the horizontal components of both 'near' and 'far' records achieve similar levels of amplification, the 'far' records demonstrate activity over a longer range of structural periods. In contrast, the vertical components, particularly in the 'far' records, exhibit higher dynamic amplification but are confined to shorter periods, close to 0.1 seconds. These variations are present when comparing both earthquake types, provided they are scaled to the same peak ground velocity value. The variability in these records arises not only from their different epicentral distances but also from diverse site conditions such as local soil characteristics, soil composition between the epicentre and the station, and the orientation of the fault relative to the station, etc.

Despite the typical practice in structural analysis of utilising a broader spectrum of records (usually seven or more), the computational demands of NLTHAs and their associated complexities in this study necessitated limiting the selection to these four records. This approach allows for a balanced consideration of 'record to record' variability within the constraints of available computational resources.

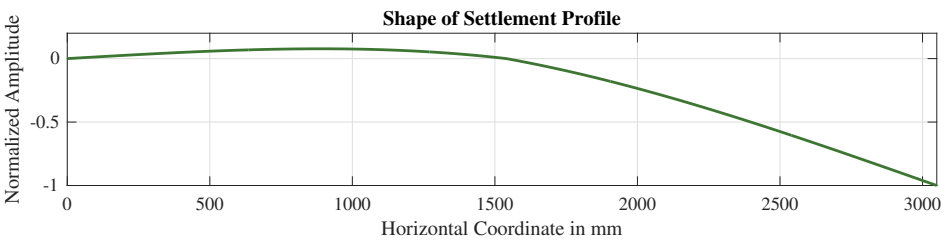


Figure 5.2.3. Normalised profile of the settlement displacement applied to the base of extrapolation models with pre-damage.

Table 5.2.3. Parameters for variations performed in the models.

Binary	Variations	Continuous	Variations
Façade geometry	Flexible (A) or Stiff (B)	Earthquake PGV	2 to 128 mm/s
Soil type	Sand (A) or Peat (B)	Number of earthquakes	1 to 8
Earthquake & event	Near (N) or Far (F)	Material strength	0.5 to 1.5
	Zeerijp (Z) or Westerwijtwerd (W)	Initial damage (Ψ_0)	0 to 1.5

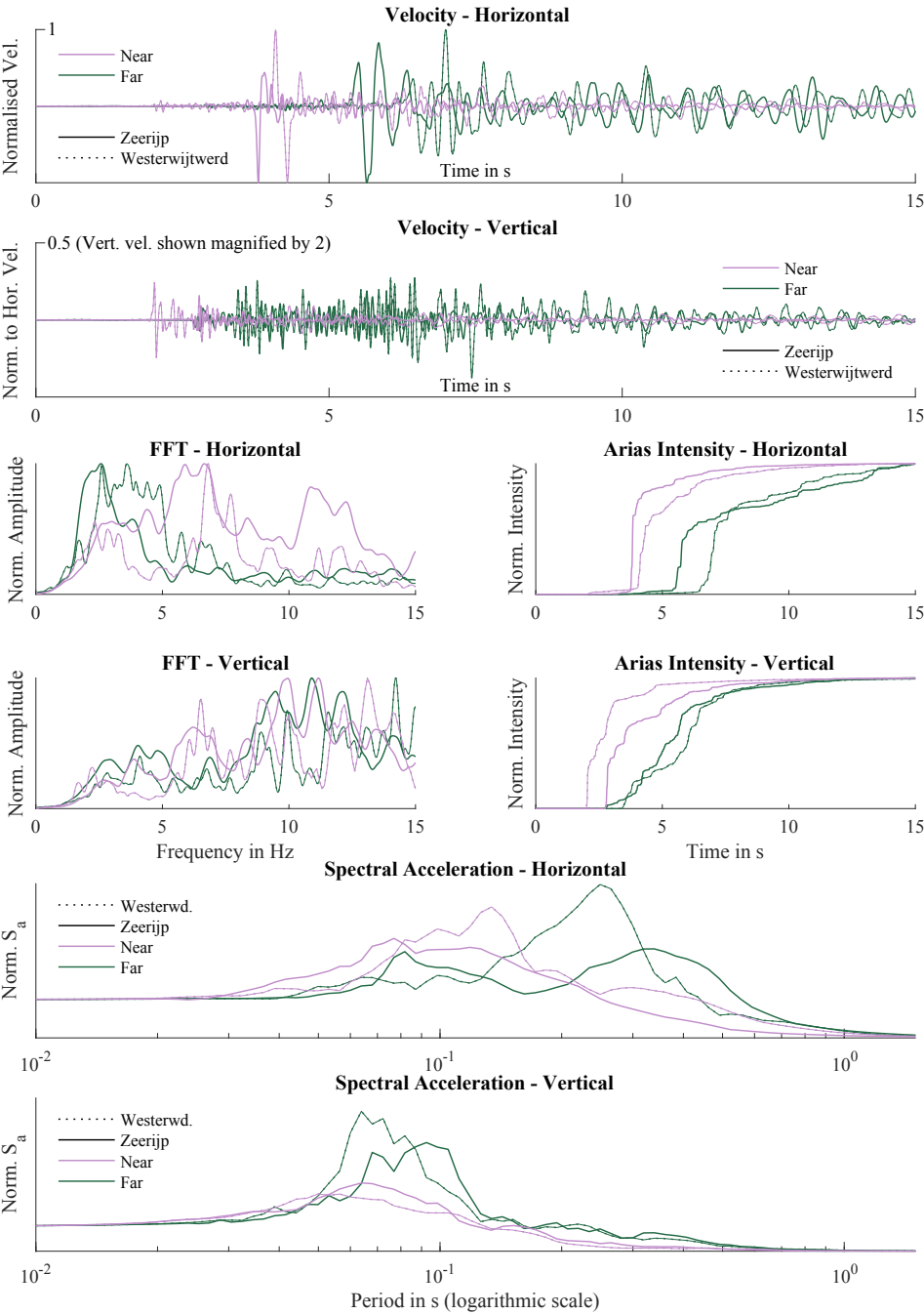


Figure 5.2.2. Comparison between records of the Zeerijp and Westerwijrtwerd earthquakes. For each event two time-series have been selected recorded at relatively near and far stations; see Table 1. Records are normalised to the horizontal peak ground velocity for comparison purposes.

Table 5.2.2. Soil parameters and interface properties. *Average, due to dependency on the properties of the structure. ** For flexible and rigid structures, respectively.

Material Properties		Stiff - Soil A	Soft - Soil B	
		Silty Sand	Peat	
Density	ρ	1700	2000	kg/m ³
Elastic Modulus	E	44.2	26.0	MPa
Elastic Shear Modulus	G	17.0	10.0	MPa
Poisson's Ratio	ν	0.3	0.3	-
Compression Wave Velocity	v_c	187.1	132.3	m/s
Shear Wave Velocity	v_s	100.0	70.7	m/s
Horizontal side stiffness*	kxsi	-	-	N/m
Horizontal side damping*	cxsi	-	-	N/m/s
Horizontal stiffness*	kxi	3.76E+08	1.04E+08	N/m ³
Horizontal damping*	cx	1.10E+05	4.31E+04	N/m/s
Vertical stiffness*	kzi	4.36E+08	1.21E+08	N/m ³
Vertical damping*	cz	2.06E+08	8.07E+04	N/m/s
Vertical stiffness at corners*	kzei	5.66E+08	1.57E+08	N/m ³
Vertical damping at corners**	czei	4.50E+06 8.50E+06	3.50E+03 6.40E+03	N/m/s

Model Variations

In this manner, the light-damage impact of earthquake vibrations can be evaluated on a single masonry wall. The complexity of a three-dimensional structure and the effect of the soil are thus partially included in a model that can be reliably assessed for a multitude of variations while observing the initiation and propagation of damage in the form of cracks. In this context, the variability of light damage is characterised through seven key parameters listed in Table 5.2.3. The parameters are categorised into 'binary or categorical parameters', those that only have two (binary) or four distinct possibilities and for which no trend can thus be observed, and into 'continuous parameters', which may assume any value within a given range. All these parameters are discussed next:

- Firstly, two wall geometries are modelled, with and without a window opening, to consider a more flexible wall with predominantly flexural behaviour, and a more rigid wall with prevalent shear behaviour; these two

typologies correspond to the two types of wall geometry tested experimentally and represent the first binary parameter.

- Secondly, the soil can be varied; the two soil variations used in this study have been discussed in Table 5.2.2.
- Thirdly, the record-to-record variability is provided by four earthquake records; the type of earthquake motion is characterised by the distance to the epicentre with 'near' and 'far' scenarios and belong to two earthquake events; the difference in frequency content, number of effective cycles, and relationship between horizontal and vertical motions for example, are inherent to these records and serve to depict the variability in earthquake motions.
- Fourthly, the variability in the intensity of the motion is considered by scaling the PGV of the horizontal component of the records (and proportionally, the vertical component) to eight different amplitudes: 2, 4, 8, 16, 32, 64, 96, and 128 mm/s. It's important to note that in this context, the distance to the epicentre is decoupled from the amplitude of the record. Moreover, this is the first continuous parameter since the PGV can adopt any value within this range.
- Fifthly, the quantity of earthquake events is also varied; applying the same record for a second time leads to greater accumulated damage in the non-linear model. Thereby, the effect of repeated events on masonry structures can be quantified.
- Sixthly, the masonry material must be varied; three scenarios are considered for the fired-clay brick masonry corresponding to a weak, standard, and strong masonry. Their differences are gathered in Table 5.2.4 and are based on an analysis of masonry characterisation tests (Jafari, 2020).
- Finally, the initial condition of the masonry wall is also varied; this requires some discussion. The intensity of the (pre-)damage is measured using the Ψ damage parameter such that the progression of damage can be quantitatively observed; see Chapter 2. A virgin ($\Psi_0=0$) and three pre-damaged initial conditions ($\Psi_0>0$) are considered; the three scenarios where the wall is already damaged when the earthquake motion is applied, correspond to distinct intensities of differential settlement damage. A settlement profile is enforced as a displacement of the fixed side of the non-linear boundary interface; the normalised profile is shown in Figure 5.2.3 and was fabricated based on the study of real-case deformations via the measurement of masonry bed joint levelling. The amplitude of the profile is adapted such that three intensities of pre-damage are achieved for the wall:

low ($0.25 < \Psi_0 < 0.75$), moderate ($0.75 < \Psi_0 < 1.25$), and high pre-damage ($1.25 < \Psi_0 < 1.75$). It should be noted that sometimes, models of different typology with the same pre-damage value may display a different failure mechanism and, that these initial values are used in the context of DS1 and so the terms 'moderate' or 'high' are relative to these values as pre-damage to assess light damage.

Each analysis is divided into three phases: self-weight and gravity loads, settlement (if present), and earthquake loading. All the models are investigated with the same analysis procedure, keeping load steps, iterative method, norms, and tolerances identical. For the settlement phase the load step changes based on the different properties and the intensity of pre-damage required. After the self-weight and settlement case, the non-linear analysis is continued in a time-history setting with the dynamic load being applied to the deformed model with time-steps of 2 ms. As with the calibration models, physical and geometrical nonlinear effects are considered; yet, in addition, transient effects are activated while considering the dynamic effects using a consistent mass and damping matrix. The Newmark-Beta method ($\beta=0.25$, $\gamma=0.50$) is used as time integration method for these non-linear time-history analyses. Moreover, the Rayleigh damping is kept using the then current stiffness matrix.

Table 5.2.4. Variations in material properties; for unchanged properties, see Table 4.4.1.

Material Properties	Weak/Poor	Standard	Strong/Good	
Elastic Modulus Perpendicular to Bed-Joints	2747	3571	5101	MPa
Elastic Modulus Parallel to Bed-Joints	1921	2497	3567	MPa
Elastic Shear Modulus	1154	1500	2143	MPa
Bed-Joint Tensile Strength	0.112	0.16	0.208	MPa
Minimum Head-Joint Tensile Strength	0.112	0.16	0.208	MPa
Tensile Fracture Energy	5.6	11.30	19.0	N/m
Cohesion	0.119	0.17	0.221	MPa
Shear Fracture Energy	102.5	209	353.0	N/m

5.2.3. Results from Extrapolation Models

The permutation of the seven parameters to vary in the models results in more than six thousand different scenarios; however, only 3840 cases were run by neglecting cases where key, previously-run models indicated that no damage was expected. For example, for the cases where the earthquake intensity of 4 and 8 mm/s did not lead to any damage (increase), the case of 2 mm/s was not run. Similarly, when two repetitions and a PGV of 2 mm/s didn't lead to a damage (increase), the case for one repetition was spared.

Figure 5.2.4 presents a coloured overview of the results, where each model was evaluated by automatically computing its damage value Ψ and its initial damage Ψ_0 . Note the four quadrants delimited by dark lines which correspond to the 2x2 permutations of the two binary variables (wall type, and soil) and that each square is divided into four triangles for the two events of Zeerijp and Westerwijtwerd (ZN, ZF, WN, WF). The effect of each variable is discussed next and some examples from the pool of analyses are picked.

First, the **wall type or façade type** revealed that the flexible wall (A) showed a higher increment of damage ($\Delta\Psi$) in respect to façade B, consistently, at least for the near-type earthquake records. An example is provided in Figure 5.a in which two damage patterns of different façades are presented. The window opening of façade A contributes to an easier initiation of cracks due to stress concentration at the window corners. The lateral constraints and top mass enhance the damage to the lateral side and above the window opening respectively. Façade B presents minor shear cracking at the mid-left of the model and some smeared cracking to the lateral side. Horizontal cracks at the bottom are also visible. For the case represented in 5.a, when the two façades are placed on soil A, having weak material, no pre-damage, and subjected to a single, near Zeerijp event of 32 mm/s, façade A experiences 25% more damage than façade B. In other words, for most of the cases, the wall with the window appears more vulnerable to damage than the rigid wall. It should be noted that these results display the maximum of crack strain in all Gauss points that occurred over the entire NLTH analysis. This explains the rather wide zones or 'clouds' of smeared cracks. At certain discrete times, the crack strain plots show a more localised pattern as some Gauss points soften while others unload. As an alternative, discrete crack/slip micro-models in predefined interface elements were used to study these localisations [3]; yet, these more detailed models are severely more computationally expensive and did not lead to significantly better calibration results; hence, they were not considered for this large number of analyses.

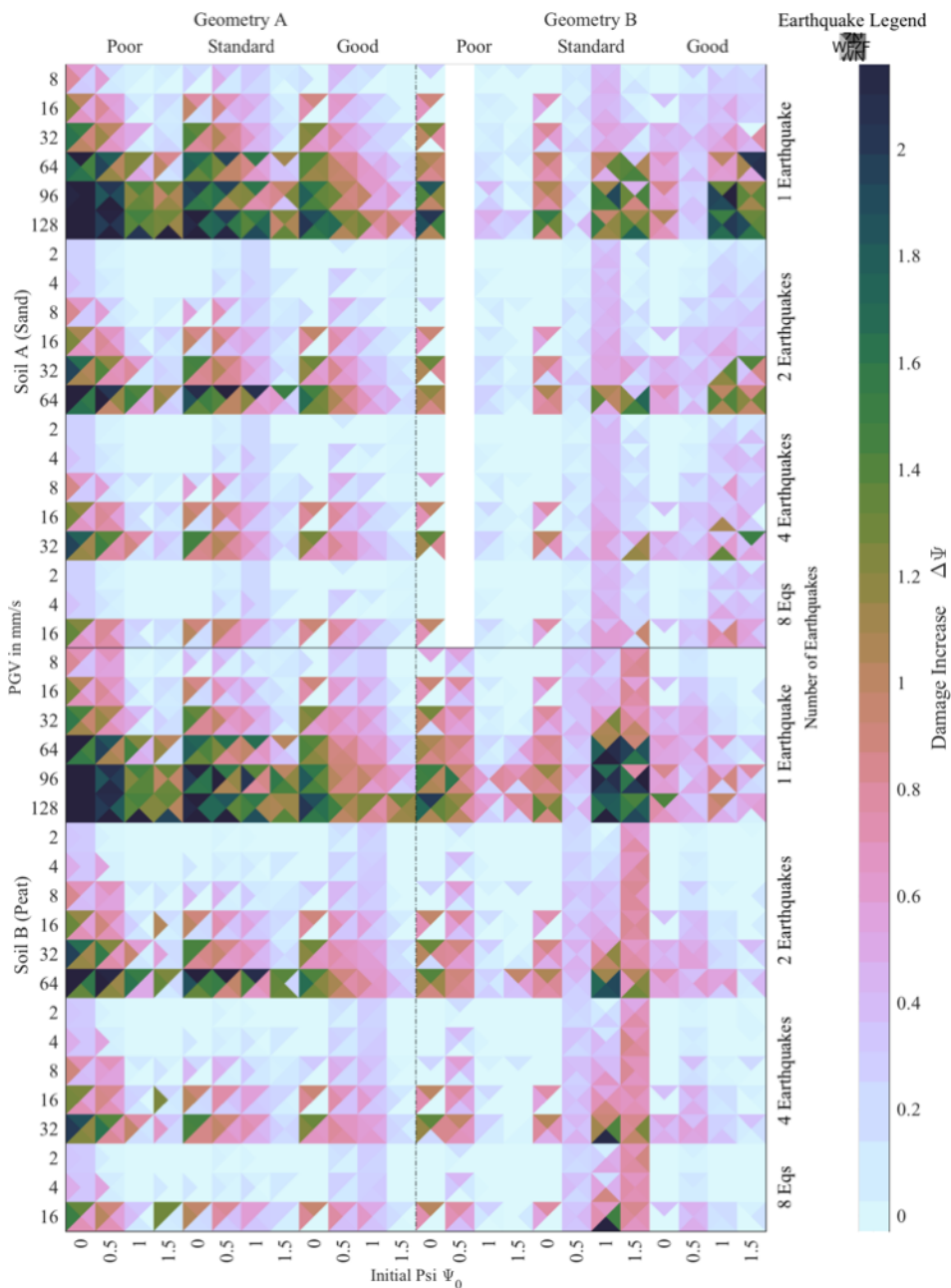


Figure 5.2.4. Results in terms of $\Delta\Psi$ from the permutations with the extrapolation models for fired-clay brick. There are 40x24 squares, each divided into 4 triangles. In total, 3840 results are displayed. This type of graph is referred to as the 'colour diamonds' table.

Secondly, the **soil type**: the softer soil (B) requires a higher settlement amplitude to produce the same damage level obtained in a façade modelled

with soil A. This is because, for the same enforced soil deformation, the more flexible soil better accommodates the desired deformation of the structure, while the stiffer soil leads to sharper curvatures and hence higher stresses and damage in the walls. Figure 5.b shows the virgin, rigid wall with weak material and subjected to a single, near earthquake (ZN) of 96 mm/s as PGV, analysed with two different soils. A similar crack pattern is detected for the two models, which depict diagonal shear cracking at the middle of the wall; see Figure 5.2.5. Cracks in models with soil A appear more concentrated and wider than the smeared shear cracking of the one on the weaker soil B. In this case the difference in damage at the end of the protocol reaches about 20%.

For the **earthquake type**, near or far from the epicentre using the two records of the Zeerijp event, Figure 5.c presents the effect on façade B on soil B with standard material and moderate pre-damage. Both earthquake types are scaled to a PGV of 32 mm/s and a single motion is run. The results show a different crack propagation; while for the near-field motion the existing crack pattern grows mainly in length with some additional parallel lateral cracks, the far motion depicts mainly an increase in width without affecting much its length. This behaviour is frequently seen in façade B when the far record often produces higher damage. On the other hand, the flexible façade (A) appears more sensitive to the near motion. This observation is likely related to the different frequencies present in the two signals which interact in distinct manners with the two types of walls.

Next, Figure 6.a. depicts the effect of different **pre-damage** situations on the final damage condition at the end of one motion; only the cases subjected to settlement are shown in the graph. The analyses concern façade A with standard material on soil A and subjected to one near earthquake (ZN) of 16 mm/s. The pre-damage values (Ψ_0) are about 0.5, 1.0 and 1.5 respectively for low, moderate and high pre-damage cases. As can be seen, increasing the damage at the initial condition, produces higher final damage. The detected values are 1.2, 1.4 and 1.6 Ψ with increasing level of pre-damage. The model of the same category without initial settlement loading, generates a final damage of 0.8 Ψ . It must be noted that, the increment of damage $\Delta\Psi$ diminishes when a higher pre-damage is adopted. In fact, considering the initial state, the difference between final and initial damage ($\Delta\Psi$) is equal to 0.8, 0.7, 0.4, and 0.1, respectively for no, low, moderate and high pre-damage. This observation can be generalised for many other cases.

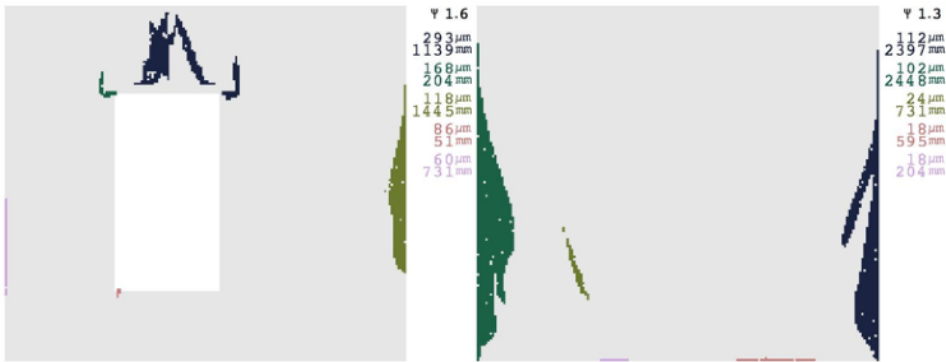
Regarding the quantity or **number of earthquake** records, the cumulation of damage gained from multiple earthquakes in a row is summarised in Figure 6.b. The presented façade B on soil A with weak material and no pre-damage

is subjected to three different number (repetitions) of near-type earthquakes (ZN), all with PGV of 16 mm/s; one, four and eight motions are applied. As expected, a higher number of earthquakes leads to a higher value of final damage. After each earthquake motion, the cracks increase in width and in length. The increase is minor, about 2 to 5%, but consistent throughout the entire table of results; lower PGVs are also associated with a smaller increment rate.

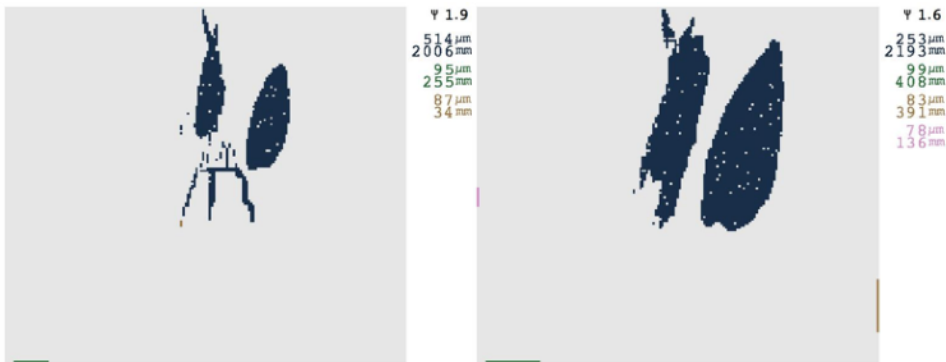
Similarly, the **variation in material** presents a congruous observation: the weaker masonry material leads to a more flexible model, but also to lower values of resistance to tensile and shear failure, consequently, a larger increment of damage can be observed when the material properties are weak. An example of this trend is shown in Figure 6.c where the flexible façade A is subjected to a 96 mm/s far-field earthquake (ZF). The model is placed on soil A and has no pre-damage, and the results at the end of the motion of the three different material configurations are shown in the figure. The façade with weak material develops two cracks at the top window corners, together with damage in the top spandrel. The two stronger material variations depict additional tiny cracks located at the other window corners and a more distributed damage to spandrel and lateral sides; nevertheless, the width of these cracks and their length result in a final damage value lower than that of the case with the weak material.

Finally, varying the **intensity of the earthquake motion**, where the intensity is given by the scaled value of peak ground velocity, offers the expected relationship that, at higher intensity, the increase in damage is also higher. The effect of different PGVs on façade A is shown as an example in Figure 6.d; the model is placed on soil B, with standard material and virgin initial condition. The wall is subjected to one earthquake of the near type (ZN) and three PGVs are selected: 8, 16 and 64 mm/s. The final damage is remarkably different between the three models with an almost 100% increase between them. This underlines the large effect of this parameter on the results.

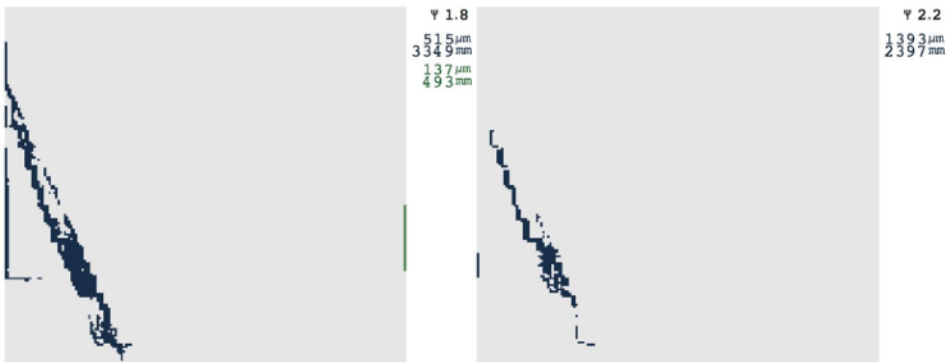
The hand-picked examples have been selected to show the variability in crack patterns that can be represented by the models. For example, while the walls without openings in Figure 5.2.5 (b and c) are similar, the crack patterns differ. This is because the cases displayed in (c) began with some pre-damage. Consequently, the vibrations further aggravated these existing cracks. Conversely, the cases from (b) did not have existing cracks so new cracks in the body of the wall were generated by the vibrations; the smeared model represents these diagonal shear cracks in clouds.



a. Final damage of two different façades on soil A, near earthquake, weak material, no pre-damage, one earthquake with PGV of 32 mm/s: façade A (left) and façade B



b. Final damage of façade B on two different soils. Results of near earthquake, weak material, no pre-damage, one earthquake with PGV of 96 mm/s: soil A (left) and soil B.



c. Final damage of façade B subjected to two different earthquakes. Results of soil B, standard material, moderate pre-damage, one earthquake with PGV of 32 mm/s: near field (left) and far field earthquake (right).

Figure 5.2.5. Hand-picked examples for comparison of the effect of the three binary variables: flexible or rigid wall type (top row), good or poor soil type (middle row), and near or far earthquake type, both for the Zeerijp event (bottom row).

5.3. Regression of Damage Function from FEM Results

While the generated pool of models provides a large amount of data, it is not sufficient to determine the probability of certain damage levels. Moreover, the distributions of the data do not resemble the expected distributions of the parameters. For example, an equal number of models with the *weak*, *standard*, and *strong* material were analysed, but the material strength is normally distributed, so the results of the *standard* material would be more likely.

There are two approaches to solve this problem. First, the results can be weighted according to the distributions of the parameters so that the more likely results influence the probability more prominently. This is explored later on. Second, a surrogate function can be regressed which reproduces the data and its results. Then, this function can be used within a Monte Carlo simulation to predict the results of samples generated from the probabilistic distributions of each parameter. This is treated next.

5.3.1. Reasoned Regression Model Considering Ψ_0

The trends observed in the multitude of analyses run to produce Figure 5.2.4 can be captured in a regression model that incorporates the effect of every parameter varied and the relationship between the most relevant of these parameters. To avoid a 'black box' effect where an arbitrary model is fit precisely to the existing data points but may produce unexpected results outside of the domain of the data (see section 5.3.3), a 'reasoned model' is employed where the relationship between the input parameters and damage can be understood. First, clear trends are gathered in the following order:

- The higher the PGV, the more damage is expected;
- The higher the pre-damage value, the higher the final damage. However, the difference between initial damage and final damage diminishes when the initial damage is higher;
- The weaker the material, the higher the final damage;
- The more flexible soil (B) led to lower damage, albeit not significantly so. Note that the amplification that soft soils produce is not considered here since the PGV is being used directly;
- The more flexible façade (A) showed higher damage for the near records, while the rigid façade showed more damage for the far records;
- The larger the number of earthquakes, the higher the final damage. This increase was marginal but consistent.

To gain additional insight into these relationships, the three discrete variables (soil, façade, and earthquake record) were considered independently while the four continuous variables (PGV, material, number of events and pre-damage) were included in a multi-variate function, and a linear Pearson correlation between the increase in damage ($\Delta\Psi$) and the various parameters was observed; see Figure 5.3.1.

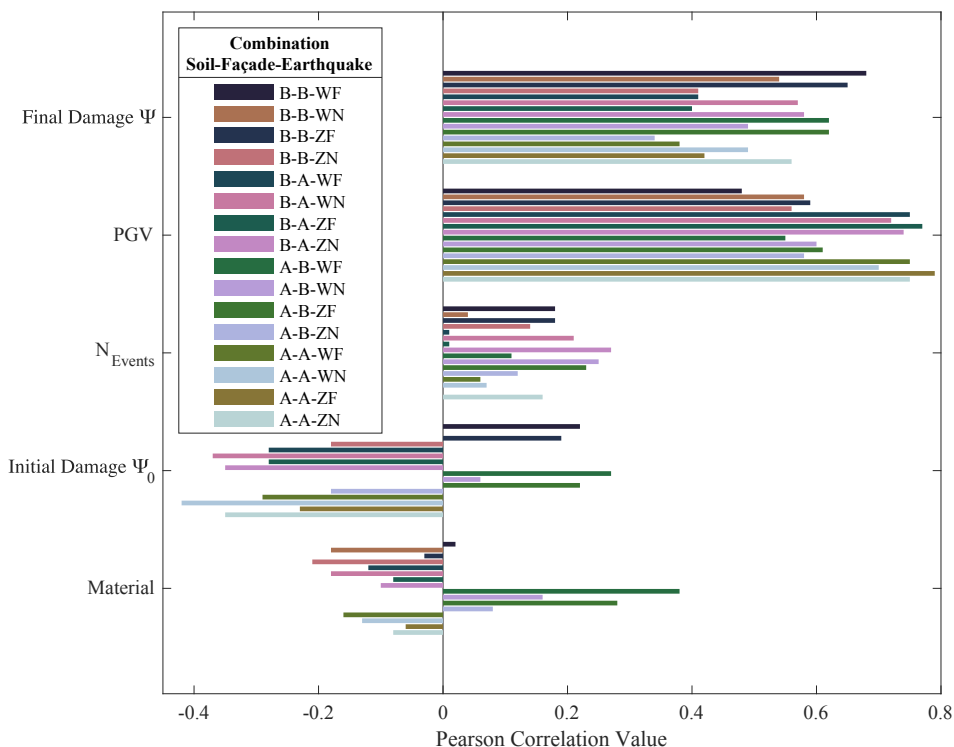


Figure 5.3.1. Pearson correlation values between $\Delta\Psi$ and the different variables in the regression model.

The Pearson correlation values range from -1 to +1, indicating perfect inverse correlation or perfect positive correlation, respectively. A perfect correlation is achieved when changes in one parameter are precisely reflected in the other. First, it can be observed that the correlation of the material is slightly negative; this means that as the material strength increases, the damage decreases. Similarly, the initial damage has also a negative correlation, meaning that, when the initial damage is high, the increase in damage reduces; this influence is more important than that of the material since the values are closer to -1. Next, the number of earthquakes has a small positive correlation indicating that a larger number of earthquakes will also cause more damage. Comparably, the PGV has a strong positive correlation; this is expected as the PGV is the hazard

variable causing damage. Lastly, the final value of Ψ has been included in the table to illustrate that the increase in damage $\Delta\Psi$ is not perfectly correlated with the final damage; this hints at the importance of the initial damage condition.

Moreover, differences between the soil, façade and earthquake type can also be recognised: First, the initial damage and material strength seem to be more relevant for earthquakes occurring nearby, while earthquakes farther away are more damaging regardless. This is also reflected in the higher correlation with the PGV. Conversely, the soft soil (B) increases the importance of the material and the initial damage, suggesting that the damage of structures on soft soil is more dependent on their condition, where also the repetition of earthquakes has a larger effect as seen from the higher values associated with the correlation of the number of earthquakes. Interestingly, the far records show a slight inverse of the correlation between the initial damage and the increase in damage for the stiff facade, suggesting that in these cases, the more damaged and thus more flexible state of the wall in combination with the specific spectral content of the far records, leads to an increase in damage. Yet, a distinct behaviour difference cannot be established between the stiffer façade without a window opening (B), and the more flexible façade (A).

Model Formulation

Accordingly, the model function was shaped so as to fulfil the observations presented and the trends observed in Figure 5.3.1 while simultaneously employing the fewest possible number of regression coefficients. Various regression models were tested and evaluated based on the mean value of the residuals, the number of coefficients, and their fit to the observations. The best model is herein presented; it constitutes a scaled sum of a logistic component and a linear component with the PGV as the argument and the increase in damage ($\Delta\Psi$) as the ordinate value. Both components of the function depend on the inverse of the material and the initial damage, while the number of earthquakes and initial damage also participate in the scaling factor.

$$\Psi_f = \Psi_0 + \Delta\Psi \quad \text{Eq. 5.1}$$

$$\Delta\Psi = \beta_1 \cdot \left(\frac{1}{1 + e^{\beta_2}} + \beta_3 \right) \quad \text{Eq. 5.2}$$

Where β_1 is the scaling factor in the function, β_2 is the exponent of the logistic component and β_3 is the linear component; these are in turn defined as:

$$\beta_1 = \frac{\alpha_1 \cdot N^{\alpha_2}}{1 + \Psi_0^{\alpha_3}} \quad \text{Eq. 5.3}$$

$$\beta_2 = 5 - \frac{\frac{1}{2} \cdot \text{PGV}}{1 + \alpha_4 \cdot \Psi_0^{\alpha_5} + \alpha_8 \cdot m^{\alpha_9}} \quad \text{Eq. 5.4}$$

$$\beta_3 = \frac{\text{PGV}}{1 + \alpha_6 \cdot \Psi_0^{\alpha_7} + \alpha_{10} \cdot m^{\alpha_{11}}} \quad \text{Eq. 5.5}$$

Where N is the number of consecutive, identical events, m is the normalised material strength given by the ratio of tensile strength over the tensile strength of the standard material, and α are the eleven regression coefficients. Their values are gathered in Figure 5.3.2 for each of the sixteen combinations of binary variables. The fit of the model is evaluated using the mean of the absolute values of the residuals, which is in average 0.15 Ψ points with a deviation of 0.16 points over the sixteen sets of coefficients. This is deemed a reasonable fit due to the scatter in the analyses' results; the logistic component of the model allows for a good fit to low values of damage for low values of PGV and introduces a steepening of the relationship at a certain PGV value (around 10 mm/s) which follows the data points adequately; this can be observed in Figure 5.3.3. This figure also illustrates how damage remains close to zero for very low values of PGV but then starts to increase rapidly between values of 5 to 20 mm/s; however, for stronger materials ($m=1.5$), this transition occurs more gradually into well around 50 mm/s. Therefore, the value of $\Psi \geq 1$ corresponding to the start of visible damage, appears significantly earlier for the weaker masonry.

The regression coefficients are restricted to an interval that leads to a smooth surface over the material parameter where only three data points are available (weak, standard, and strong). This follows the assumption that the behaviour of real world structures is expected to be a smooth curve. The values of the regression coefficients, like the Pearson correlation values, hint at the relationship between the parameters and the light damage of a masonry wall. The regression coefficient α_2 for example, indicates the influence of the number of earthquakes; a positive number slightly larger than zero suggests a proportional relationship between the number of earthquakes and the increase in damage. Similarly, α_3 establishes a link between the initial condition and the increase in damage; its values in Figure 5.3.2 suggest that this link is stronger for the flexible façade but weaker for the stiffer façade. Next, α_4 and α_5 determine the effect of the initial damage on the logistic part of the function (principally for lower PGV values), while α_6 and α_7 , indicate its effect on the linear component of the function. Likewise, α_8 and α_9 link the material to the logistic part of the model and α_{10} and α_{11} to the linear part. Strong, clear relationships can be established in this manner, for instance, for the case of the rigid wall (B) on soft soil (B) subjected to near Zeerijp (ZN) earthquake (B-B-ZN)

and its material strength where the regression coefficients (α_8 to α_{11}) show comparatively high values.

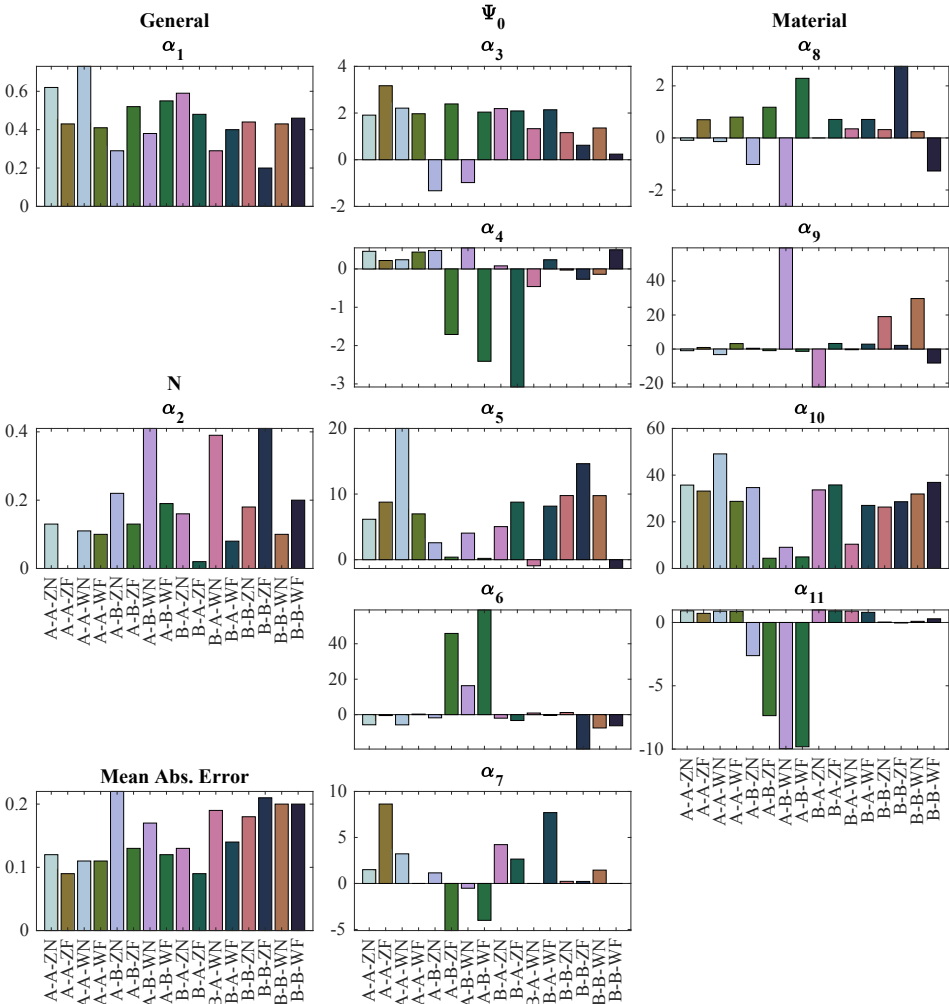


Figure 5.3.2. Values of the regression coefficients (α : 1 to 11) and mean absolute error (in Ψ) for the sixteen sets of binary parameters.

To improve the behaviour of the regression for the sensitive and more commonly-occurring low values of PGV, the data points below or equal to 16 mm/s are considered twice as important as the higher values by using a weight of 2 in the least-squares model fit. The threshold of 16 mm/s was chosen, first, because extrapolation models were available for all four earthquake repetitions while the following model set, run at 32 mm/s, had twice the PGV value and was present in only three of the sets. This means that the confidence to the model fit up to 16 mm/s is higher than for points later on, and setting the

threshold at any value between 16 and 31 would yield the same result. Secondly, in comparison to the PGV values that have been recorded in the field and to the four earthquake motions, which reached PGV values below 32 mm/s, a threshold above this interval would be too high. Since the present study focuses on damage at low PGV values, these should be preferred in the fit. Moreover, as seen in Table 5.2.1, the original records achieved PGV values between 1 and 32 mm/s; scaling these records too far beyond their original PGVs may introduce a bias further decreasing the confidence in the data points at and above 32 mm/s. On the other hand, the value of 2 for the weight of the fit is rather arbitrary; for a higher weight, the points above 16 mm/s become irrelevant and are ignored, so the largest reasonable value was selected.

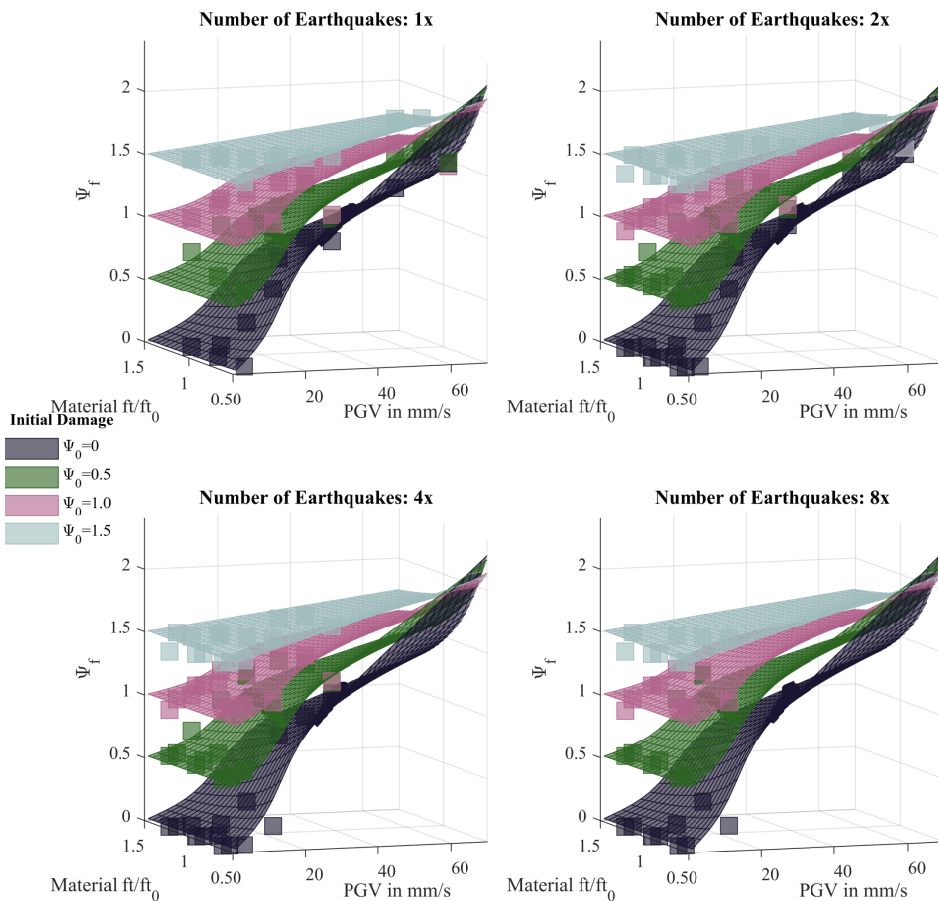


Figure 5.3.3. Example of the model shape and fit to the data points (squares) for the combination of soil A, façade A and far record of the Zeerijp event.

5.3.2. Model Uncertainty

The imperfect fit of the regression model, due partly to the non-smooth trends of the data points provided by the extrapolation FE models, can be captured by a model uncertainty parameter, ε . The parameter is considered by modifying equation 1 such that the increase in damage, $\Delta\Psi$, is affected by ε , which, using a Generalised Extreme Value, is randomly distributed, satisfying the condition that the final damage can never be lower than the initial damage; this is expressed in the following equations:

$$\Psi_f = \Psi_0 + \Delta\Psi' \quad \text{Eq. 5.6}$$

$$\Delta\Psi' = \Delta\Psi + \varepsilon \geq 0 \quad \text{Eq. 5.7}$$

$$\varepsilon = GEV(k_{gev}, \sigma_{gev}, \mu_{gev}) \quad \text{Eq. 5.8}$$

$$\sigma | k_{gev} = \gamma_1 \cdot e^{(PGV \cdot \gamma_2)} + \gamma_3 \cdot e^{(PGV \cdot \gamma_4)} \quad \text{Eq. 5.9.a}$$

$$\mu_{gev} = \gamma_5 \cdot (1 - PGV^{\gamma_6}) \quad \text{Eq. 5.9.b}$$

The value and distribution of ε can be approximated to the average mean of the absolute value of the residuals of the model regression and distributed normally. However, the variability in the fit appears to be dependent on the PGV as is visualised in Figure 5.3.4 and, moreover, the residuals are better represented with an extreme value distribution where the actual value of Ψ may be much larger than what is predicted by the regression model.

A three-parameter Weibull distribution, or Generalised Extreme Value distribution, accurately follows the shape of the residuals and can be adjusted such that its parameters (shape, scale and location, k_{gev} , σ_{gev} and μ_{gev} , see Table 5.3.1) become functions of PGV as is specified in Eq. 9 and are thus defined for any value of PGV ($PGV \geq 1$ mm/s). The use of a Weibull distribution is slightly conservative because it allows for relatively large values of ε due to its long tail to the right, yet limits the underestimation of Ψ because of the truncated tail at its left. In this sense, the uncertainty parameter can be assumed to include not only a degree of aleatoric uncertainty but also the epistemic uncertainty in the FE modelling approach and crack characterisation processes, where unforeseen conditions may trigger much-larger-than-anticipated damage.

Table 5.3.1. Coefficients to determine k , σ , and μ of the generalised extreme value distribution for the PGV-dependent uncertainty of the regression model. See equation 5.9.

Coefficient	Y_1	Y_2	Y_3	Y_4	Y_5	Y_6
k	2814	-0.239	-2813	-0.239	-	-
σ	0.168	0.008	-0.202	-0.255	-	-
μ	-	-	-	-	0.010	0.678

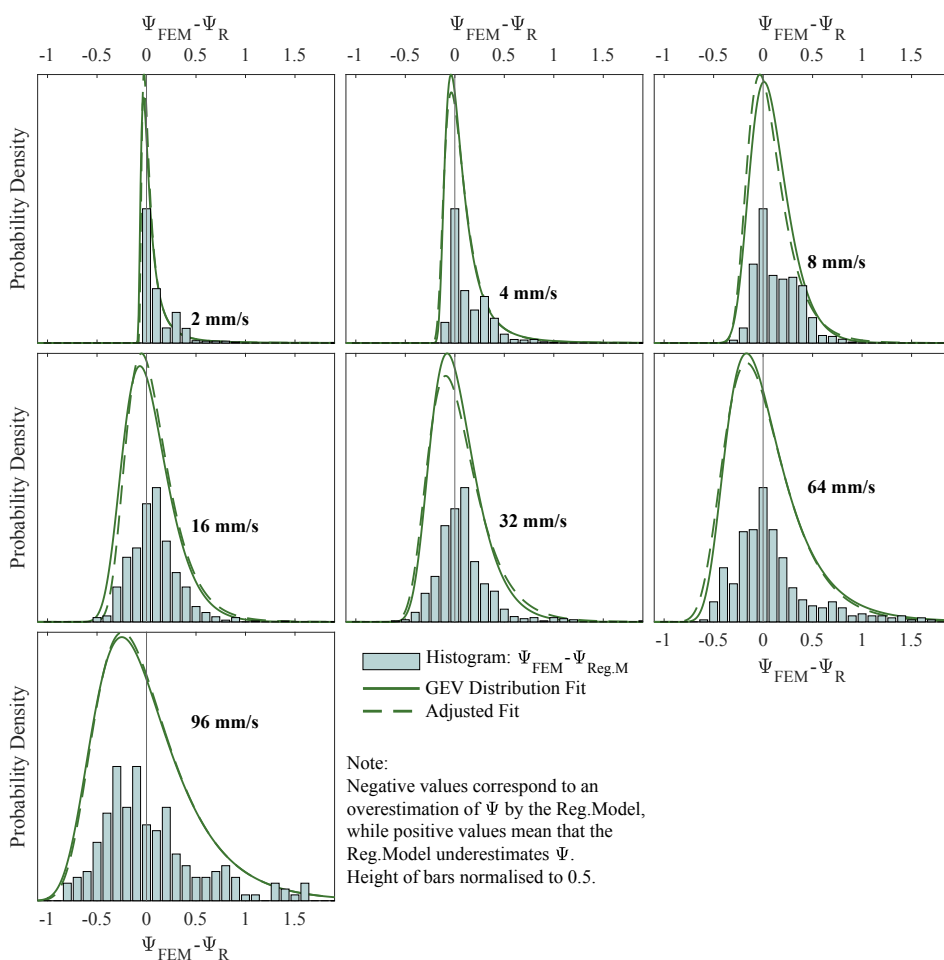


Figure 5.3.4. Residuals to the fit of the regression model segregated by PGV and Generalised Extreme Value (GEV) distribution fit for the uncertainty parameter.

5.3.3. Surrogate Model with Machine Learning

The regression model presented in the previous section uses domain knowledge to define a function with parameters that are then fitted using a non-linear algorithm. While this is already an example of heavily supervised machine learning, a surrogate model can also be formulated by training different types of regression models, as is done in this section. With the adequate software, it is trivially easy to generate any type of model including neural networks, multi-dimensional linear models, (binary) decision tree models, kernel or support-vector machine models, etc. These types of models, however, must be properly evaluated to verify that they generalise well outside the interval (and sometimes also within) represented by the data. Expected trends, like a positive proportional relationship between PGV and Ψ , cannot be enforced and may be poorly represented by these models if the data is noisy or inconsistent since they try to minimise the error between results and predictions. While some of these issues can be addressed by pre-processing the data and removing conflicting data points, these efforts negate the advantages of using these automatised types of models.

The table next compares a few of the most suited models. The Root Mean Squared Error (RMSE), which is expressed in units of Ψ and is about 0.15 for the reasoned regression model, is displayed for each model. Note that this value differs from Figure 5.3.2 because the data set has been cleaned removing outliers based on the quadrants of Figure 5.2.4. The RMSE shows that some models provide theoretically better fits to the data; the same is reflected by the Mean Absolute Error (MAE). However, Figure 5.3.5 reveals that this is not the case.

This figure collects one case where the data was incomplete and/or several outliers were removed. Based on the rest of the data, the models can still make predictions. Some models suffer from overfitting, where the data points are followed accurately but their behaviour is chaotic outside the data. Other models manage to capture the general trends but include behaviour that is not expected. The decision trees, for example, reveal the expected trends for the PGV, the Material and the Number of Earthquakes, but their discontinuous nature makes them less suited to regression problems (they are strong for classification problems). The Gaussian Process is very accurate in capturing the data but also captures some of the noise present in it. The neural network presents a similar behaviour. For this reason, another network is trained with a limited small layer so that it would replicate only the most general and strongest trends. This is somewhat successful but is shadowed by the behaviour of the reasoned model.

Table 5.3.2. Comparison between various types of machine learning models.

Model	RMSE	MAE	R ²	Captured observed trends	Description
Reasoned (Section 5.3.1)	0.136	0.077	0.927	Very Good	176 α parameters
Ensemble Tree	0.081	0.042	0.974	Poorly	Discontinuous
Binary Tree	0.072	0.024	0.980	Good	Discontinuous
Neural Net	0.060	0.030	0.986	Good	2 layers of 100 and 50
Gaussian Proc.	0.024	0.009	0.998	Very Good	Probabilistic
Kernel	0.148	0.082	0.914	Very Poor	Quick
Neural Net (Limited)	0.151	0.086	0.910	Good	One Layer of 5

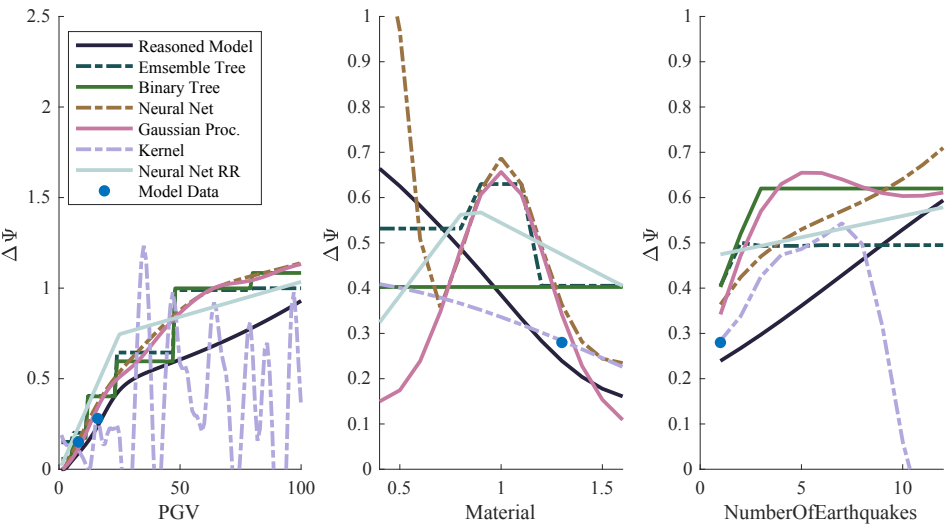


Figure 5.3.5. Trends and comparisons between various model predictions for combinations of poor data availability.

The reasoned model is employed in subsequent sections. This is because the generalised surrogate models lack physical accuracy in between data points and outside the interval of the data, and because the reasoned model performs sufficiently well with a clear error that can be assigned into a model uncertainty parameter. In future studies, additional data could be generated by

running models at intermediate points where the surrogate models produce unreliable results. Alternatively, several surrogate models could be used simultaneously to make predictions with varying degrees of confidence depending on the agreement of the various models. The error of the models can also be used to fabricate an uncertainty parameter. These approaches have not been further explored herein.

5.4. Fragility Curves for Seismic Vibrations

5.4.1. Probabilistic distributions and Parameters

The implementation of a regression model within a Monte-Carlo simulation framework is key to determining the probability of damage in the analysed masonry structures. This simulation method involves taking individual samples for each variable and determining outcomes based on these specific combinations. The process is repeated until a sufficient number of outcomes are evaluated, ensuring the reliability of the results. The assignment of appropriate distributions for each relevant parameter is a crucial first step in this process.

Material Strength: In the regression model, material strength is represented as the ratio of the direct tensile strength to the tensile strength of a standard or mean material. This ratio reflects the most influential material properties identified in the Finite Element (FE) models. The tensile strength's coefficient of variation, measured at about 30% in material tests and normally distributed, leads to characterising the variable 'm' with a normal distribution. This distribution has a mean of 1 and a standard deviation of 0.3. To maintain consistency with the calibrated values (0.7, 1.0, and 1.3), the distribution is truncated at two standard deviations.

Initial Condition of Masonry: The condition of structures in the region is still under study, and the high variability in factors like settlements and stresses from restrained shrinkage or thermal movements makes it challenging to assign a specific distribution for this variable. Therefore, the simulation evaluates discrete values for initial conditions: no-damage ($\Psi_0=0$), invisible damage ($\Psi_0=0.5$), and light visible damage ($\Psi_0=1$).

Peak Ground Velocity is employed as the hazard variable to assess the probability of light damage. The simulations explore various PGV values within the 1 to 100 mm/s range, aiming to establish a relationship between PGV and damage. However, the simulation excludes the variable of multiple identical seismic events, considering that identical amplitude events are unlikely and require further investigation. This is explored in Chapter 6.

Masonry Wall Types: The study modelled two types of masonry walls: a rigid, windowless shear wall and a flexible wall with a window opening. These models introduce variability in geometry and dynamic behaviour. Since it's impractical to assign a specific state to existing structures, a uniform distribution is used, with each wall type assigned an arbitrary 50% probability.

Type of Earthquake Motion and Soil Type: The correlation between PGV and the proximity of an earthquake (near or far) is intuitive, with higher PGVs likely caused by nearby events. A statistical study on historical data from January 1993 to December 2019 (for earthquakes with at least $M_w \geq 1.5$) was conducted, using GMPEs by Bommer et al. to compute regional PGVs. This study, coupled with a simplified database of buildings (see Appendix A), helped determine the distance and intensity of seismic events relative to buildings. Figure 5.4.1 illustrates the ratio of near to far events for various PGV intervals, showing a trend where higher local PGVs often correspond to events within a 2 km radius. A correlation function is used in the simulation, assigning a 10% probability of a nearby event at 1 mm/s PGV and a 90% probability at 35 mm/s PGV. This is formulated into Equation 5.10.

$$f_{\frac{Near}{Near + Far}}(PGV) = \frac{1.9}{1 + e^{-0.08 \cdot (1 + PGV)}} - 0.9 \quad \text{Equation 5.10}$$

Where f is the probability of an event being near given the PGV.

Soil Type Probability: The likelihood of encountering stiff or soft soil was statistically determined for buildings experiencing at least 1 mm/s PGV. The vertical shear wave velocity (V_{s10}) of the soil was calculated based on microzonation studies (Kruiver et al. 2017). Locations with V_{s10} greater than 100 m/s were classified as stiff soil, and those with lower V_{s10} as soft soil. This classification aligns with soil parameters in Table 2, resulting in a binary distribution that assigns a 95% probability to stiff soil (A) and 5% to soft soil (B).

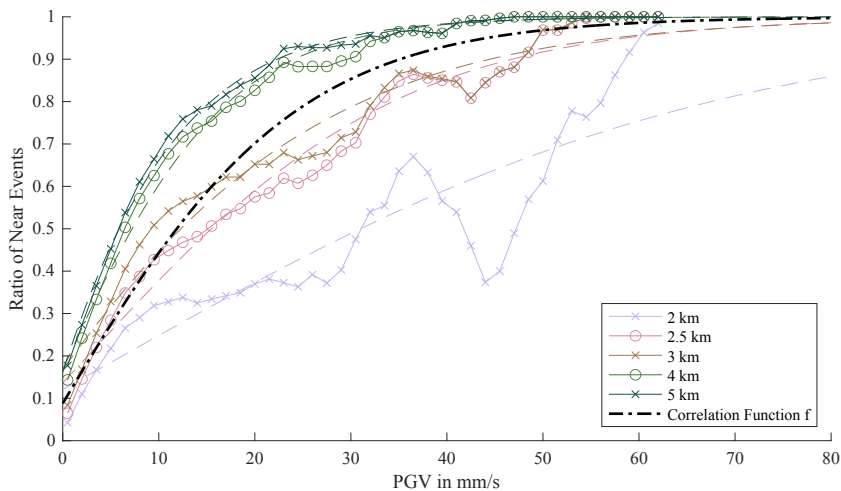


Figure 5.4.1. Correlation between PGV and near-type records from statistical, historical data. Low PGV values often correspond to events with an epicentre located farther away, while PGV values above 10 mm/s are more likely to correspond to events originating less than 3 km away.

5.4.2. Results of Monte Carlo Simulation

In the Monte Carlo simulation, values for material strength, soil type, earthquake type, model uncertainty, and wall type are sampled from their respective distributions. Equation 5.6 is then used to determine the final damage for discrete values of initial condition ($\Psi_0 = 0, 0.5, 1, \text{ and } 1.5$) and PGV. The final damage values are categorised into intervals between zero and three in half-point increments. The simulation was executed with over ten million points for each discrete combination of initial condition and PGV to ensure sufficiency. The results are illustrated in Figure 5.4.2 as fragility curves, depicting the probability of exceeding various light damage levels based on the initial masonry condition and PGV. The discrete values obtained from the simulation are indicated, and a simple spline is fitted to these points.

At a PGV of 10 mm/s, the probability of reaching or exceeding visible damage ($\Psi \geq 1$) is only 5% when no initial damage is present (Figure 2.a). This probability significantly increases to about 20% when minor, initially invisible damage ($\Psi_0 = 0.5$) is present (Figure 2.b). The curves are relatively flat, indicating a wide variability in input parameters. However, for low pre-damage ($\Psi_0 \leq 0.5$), the curves for visible damage initially steepen, suggesting vulnerability to light cracking at low PGV values. The graphs in Figures 2.c and 2.d, corresponding to already visible initial damage ($\Psi_0 \geq 1$), show that light damage is unlikely to worsen significantly unless earthquake vibration intensity is relatively high, with PGV values above 40 mm/s (approximately 0.12g PGA).

The simulations also indicate that near-type records are more damaging to masonry walls, suggesting a more conservative assessment for low-rise masonry buildings using near-type earthquake records. Despite using only two types of masonry walls to represent in-plane behaviour, the variability introduced should capture the probabilistic spread for a broader range of buildings. However, it is essential to note that the study focuses on damage in bare masonry or at continuous corners, not on connections between walls and floors or adjacent walls. The light damage in these joint areas, which this study does not contemplate, is also challenging to quantify and is a future topic.

A notable aspect in the graphs is the initial plateau between 1 and 10 mm/s before the curves slope upward. This plateau indicates a consistent probability of damage at low PGV values, likely due to the model uncertainty parameter ϵ , based on variability observed in the limited number of FE models. This suggests that low PGV values can trigger visible damage in certain scenarios, especially when initial damage and residual stresses are present. Further studies are needed to analyse very low vibrations combined with multiple initial damage factors, particularly relevant for regions like Groningen.

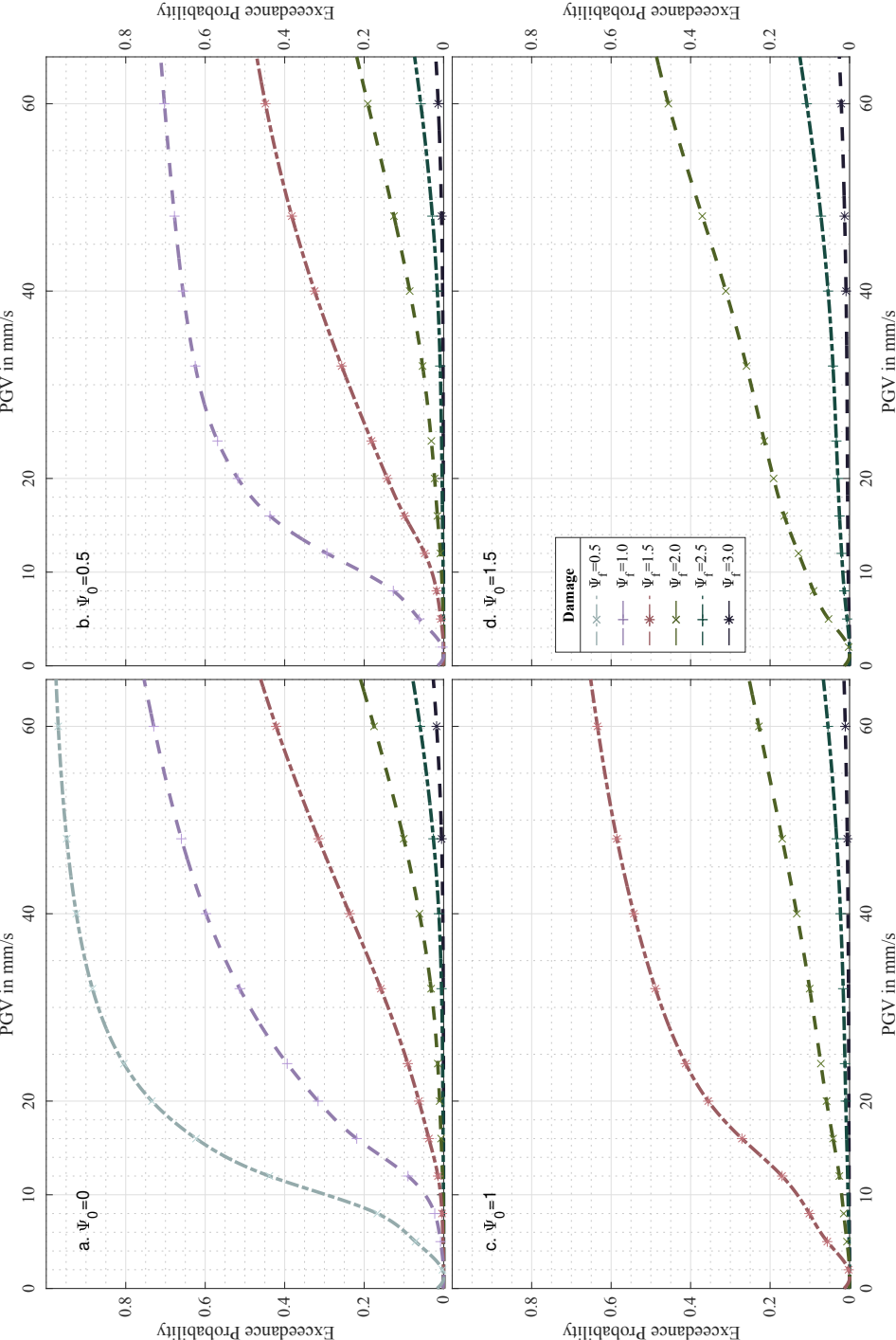


Figure 5.4.2. Fragility or vulnerability curves for various initial damage conditions (ψ_0) and final damage thresholds (ψ_f).

The curves show that the probability of exceeding $\Psi=3$ are comparatively small even at higher values of PGV. However, given that these Ψ values approach the end of light damage (and continue towards near-collapse) and that the consequences of failure can be severe, probabilities of around 1% are not small. The Eurocode prescribes, for instance, a failure probability of 10^{-5} against structural failure. Nevertheless, the fragility curves focus on the lower damage and should be viewed in that context. A log-normal fit to the curves is provided in Figure 5.4.3 for future reference, with parameters detailed in Table 5.4.2.

Table 5.4.2. Lognormal parameters for the start of the fragility curves determined.

Ψ_{final}	$\Psi_0 = 0$		$\Psi_0 = 0.5$		$\Psi_0 = 1.0$		$\Psi_0 = 1.5$	
	μ	σ	μ	σ	μ	σ	μ	σ
0.5	2.604	0.624	NA		NA		NA	
1.0	3.370	0.725	3.002	0.931	NA		NA	
1.5	4.323	0.860	4.070	0.983	3.411	1.034	NA	
2.0	5.518	1.082	5.523	1.259	5.293	1.444	4.631	1.860
2.5	7.416	1.516	7.758	1.780	7.955	2.091	7.929	2.585
3.0	8.869	1.729	11.287	2.606	11.913	3.034	12.363	3.610

Table 5.4.1. Results of vulnerability curves for key PGV values. The table shows the probability of fired-clay brick masonry walls entering the Damage State 1 range at $\Psi=1$ and the probability of exceeding DS1 with $\Psi=2$, for two different initial conditions of the masonry (Ψ_0), where sensitive, pre-cracked masonry is characterised with $\Psi_0 \approx 0.5$.

PGV Peak Ground Velocity	Probability of DS1 ($1 \leq \Psi \leq 2$)			
	No initial damage $\Psi_0=0$		Light, yet imperceptible initial damage $\Psi_0 \approx 0.5$	
	$\Psi \geq 1$	$\Psi \geq 2$	$\Psi \geq 1$	$\Psi \geq 2$
5 mm/s	1%	< 0.1%	6%	0.1%
10 mm/s	6%	0.2%	21%	0.6%
15 mm/s	19%	0.5%	40%	1%
20 mm/s	32%	1%	52%	2%
30 mm/s	48%	3%	61%	5%
40 mm/s	60%	6%	66%	9%

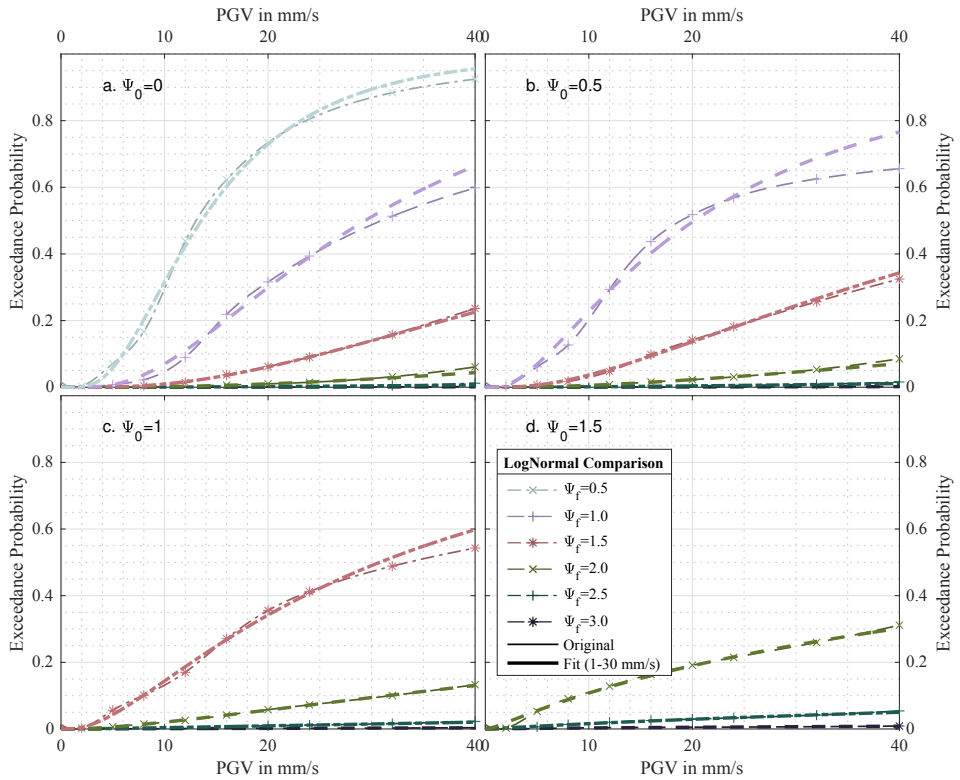


Figure 5.4.3. LogNormal fit to fragility curves.

The key values extracted from the curves are compiled in Table 5.4.1. These results underline the importance of considering a range of factors, including initial damage and model uncertainty, in assessing the probability of light damage in masonry structures due to seismic vibrations. The study's approach to defining damage probabilistically based on visible cracks provides a more precise understanding of seismic vulnerability, especially for low earthquake vibrations.

5.4.3. Comparisons to other Studies

Comparing the fragility curves developed in this study, which outline a range for Damage State 1 (DS1) with Ψ values between one and two ($1 \leq \Psi \leq 2$), to those from other authors is crucial. Typically, other studies define DS1 or DS2 with a single line indicating exceedance probability, often without clear differentiation between incursion into or exceedance of a damage state. However, before making any comparisons, several key aspects need to be underscored. Chief among these are the metrics used for quantifying damage and the representation of the seismic hazard.

In this study, PPGV serves as the primary measure of the seismic hazard. This choice is influenced by guidelines and studies on low structural vibrations, including non-earthquake-related vibrations, where PGV is preferred due to its better correlation with vibration energy. Given the focus on low earthquake vibrations, PGV was chosen to facilitate comparisons with other vibration sources, such as trains, construction activities, and normal structural use. Traditionally, earthquake intensity is gauged using Peak Ground Acceleration (PGA), which relates more directly to the forces acting on structures—a crucial factor when assessing structural strength capacity, but less relevant for evaluating light damage. Pseudo acceleration (S_a) is also employed to describe amplified dynamic forces on structures, but its dependency on a structure's natural vibration period makes it less suitable for a singular hazard measure.

For the upcoming comparisons, the average transfer factors from this study's four signals are used to approximate the relationship between PGA and PGV (26.4 s/s^2). For S_a , the upper envelope of the spectra in Figure 5.2.2 aids in establishing the ratio between S_a and PGA at different structural periods. Next, the study's unique approach to measuring damage, focusing explicitly on light damage quantified by visible cracks on masonry walls, must be noted. This contrasts with most other studies that either use qualitative descriptions of light damage or infer it indirectly based on parameters related to ultimate structural strength. Hence, comparing DS1 outcomes from this study to others presents challenges.

Furthermore, factors like geometry and material, structural configuration and connections, earthquake types, and soil and foundation considerations vary significantly across studies, making direct comparisons feasible only within an order of magnitude. Figure 5.4.4 attempts to make these comparisons, despite the detailed and complex nature of the data.

In Figure 3.a, FEMA guidelines specify drift limits for DS1. Assuming these limits correspond to a 5% exceedance probability of DS1 (with a 50%

probability at twice the drift limit), the light damage probabilities for infill and non-infill masonry walls align with the highlighted PGV range up to 60 mm/s. Okada et al.'s study on timber-frame buildings, Gehl et al.'s study using 3Muri software, and Abo-El-Ezz et al.'s research on Canadian rubble stone masonry provide contrasting curves, reflecting differences in structural vulnerability and modelling approaches.

Empirical DS1 curves from Crowley et al., based on regional damage data up to 2015, present a closer fit to the DS1 range defined in this study. These curves, particularly for post-1940 unreinforced masonry and vulnerable masonry farmhouses, align well with the upper threshold of $\Psi=1$ and the mid-range of the DS1 interval. However, these empirical curves, extrapolated from data points available only for PGV values below 20mm/s, seem to slightly underestimate light damage compared to the fragility curves developed in this study.

Other studies examining DS2, compared in Figure 3.b, include Kallioras et al.'s dynamic tests on calcium-silicate masonry terraced houses and Crowley et al.'s DS2 fragility curve. These studies, while offering insights, highlight differences in structural typology and material vulnerability, affecting the positioning of their curves relative to the DS1 range.

HAZUS guidelines and Van Elk et al.'s building fragility curves, alongside Milosević et al.'s research on unreinforced masonry with rubble stone and hollow brick, also offer comparative insights. Waarts' linear-elastic analyses on masonry façades further illustrate the variance in perceived damage at low PGVs.

In summary, the DS1 range defined by Ψ values of 1 to 2, despite differences in structural typology and masonry material, is comparable to other studies focusing on low damage states in masonry. While the strength of this work lies in its precise definition of damage and the use of complex FEM models for realistic crack monitoring, the limitation in the number of earthquake motions analysed is a notable weakness. This constraint results from the high computational demands of these models, which in turn limits the representation of record-to-record variability. Future advancements in computational capabilities and modelling strategies are anticipated to allow for more comprehensive analyses and a better depiction of the inherent uncertainty in seismic fragility curves.

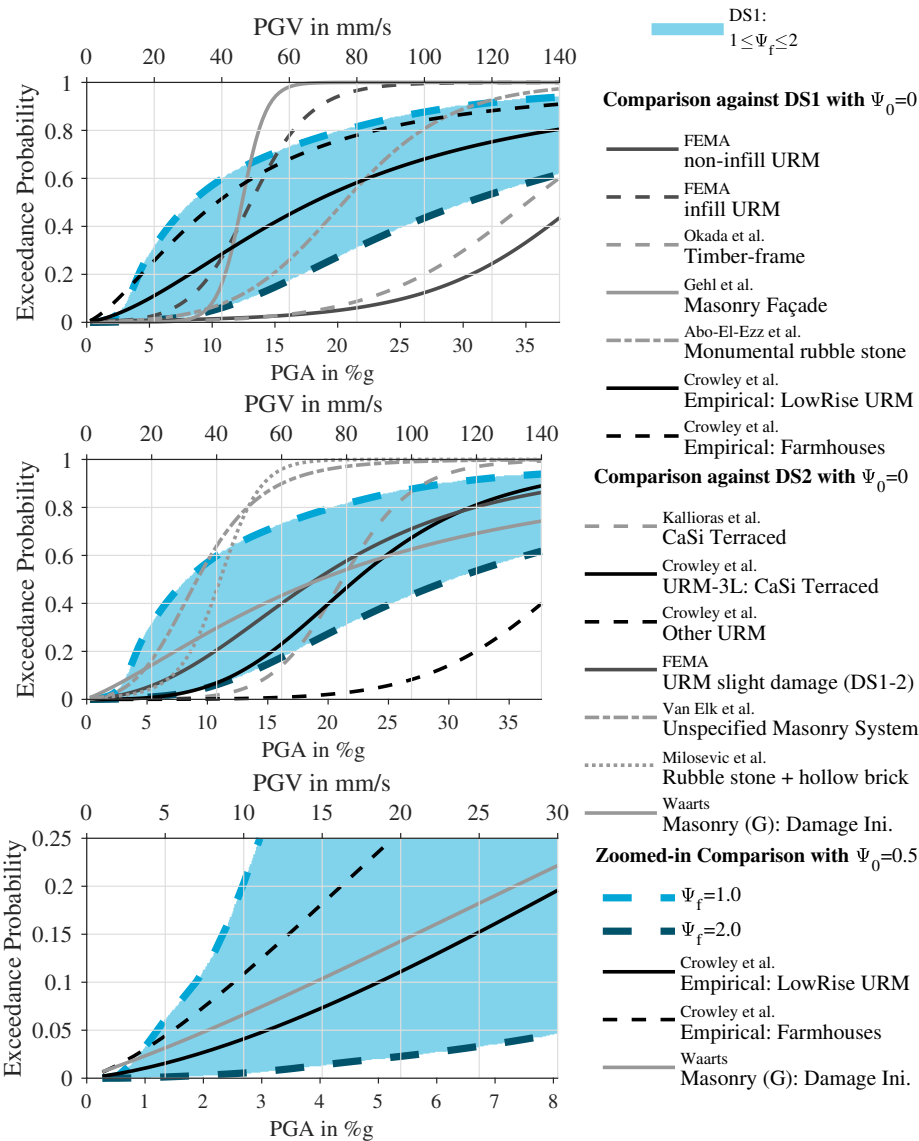


Figure 5.4.4. Comparisons with other authors.

5.4.4. Fragility Maps

The fragility curves can be superimposed with the earthquake hazard at the spacial scale. Bommer et al. (2019) formulated GMPEs that describe the hazard's intensity in a probabilistic manner at any location in the Groningen region. The probabilistic distribution in PGV can then be convoluted and integrated with the fragility curves, which describe the probability between PGV and damage in terms of Ψ , so that the probability of damage given a certain event can be computed. The epicentres of earthquakes events are known from the database of the Dutch meteorological institute, KNMI. Hence, this exercise is conducted for a few illustrative events and the result is drawn in Figure 5.4.5. Each event is described with a distribution of PGV at any location.

This is an example of the potential application of the proposed fragility curves. The figure includes six cases distributed for three relevant seismic events and two cases of $\Delta\Psi$ for the threshold of visible damage ($\Psi=1$). This is the strictest threshold for the initiation of light damage. The maps show the probability depending on the distance and magnitude to the epicentres of the events using the empirical formulation of ground motion prediction equations of Bommer et al. (2019); these equations include probabilistic terms. The earthquake of Huizinge of 2012 leads to the highest probabilities with most of the region being enclosed by the contour indicating that invisible damage ($\Psi_0=0.5$) has a 1% probability of being aggravated to visible damage due to this event.

Finally, a summarising figure is elaborated: Figure 5.4.6. Here, the history of all earthquake events, with a magnitude of $M_w=2$ or more, is analysed to determine the distribution of maximum PGV at any location. Based on this distribution, the probability is computed for a $\Delta\Psi$ of 0.5 with a $\Psi_0=1$. This corresponds to masonry structures that were exhibiting just visible damage before the seismicity begun; this damage was then worsened such that its cost for repair is mostly linked to the earthquake vibrations; see Table 2.2.4. Note that this figure considers only the maximum PGV and not the accumulation of damage from repeated events; this is treated in Chapter 6. Whether progressively accumulating damage over time due to smaller and larger events will lead to a worse situation will be examined.

Indeed, Figure 6 reveals an interesting observation: for older masonry structures, which are likely to display some visible damage and for which the material properties of this study have been tailored to, there is a small probability ($>1/1000$) of considerable damage aggravation ($\Delta\Psi=0.5$) within the entire Groningen region. There are about 100 thousand buildings from before 1945 within the entire region; see Appendix A.2. Given this small probability

and the number of buildings, one can determine the probability of at least n buildings showing this level of aggravated damage using the following equation derived from a binomial distribution:

$$P(X \geq n) = 1 - \sum_{k=0}^{n-1} \binom{N}{k} p^k (1-p)^{N-k} \quad \text{Equation 5.11}$$

where N is the total number of buildings in the region (assumed 100 thousand), p is the failure probability of each building (assumed 1/1000), and n is the minimum number of buildings with failure. Note that N over k represents the number of possibilities to choose k from N . This equation might be numerically challenging for small values of p and k , but can be solved with specific computational methods.

It is almost certain that at least ten buildings ($n=10$) have developed a $\Delta\Psi=0.5$, assuming that all $N=100'000$ buildings started with $\Psi_0=1$ and neglecting the higher probabilities towards the centre of the region. However, the probability of at least 100 buildings ($n=100$) showing this damage quickly diminishes to 50%, and the probability of 150 buildings is below 1%; again, under the aforementioned assumptions. In addition, this calculation assumes independence between buildings; this means that parameters are not correlated between buildings. While the strength of the buildings, for instance, is unlikely to be correlated between buildings, the near-far distribution of the earthquake type, could be.

To determine a more accurate probability, the initial condition of all the structures would need to be estimated. Moreover, when each building has a different probability (dependent on its location on the map), the problem cannot be solved analytically. Instead, a simulation is needed. This requires additional study.

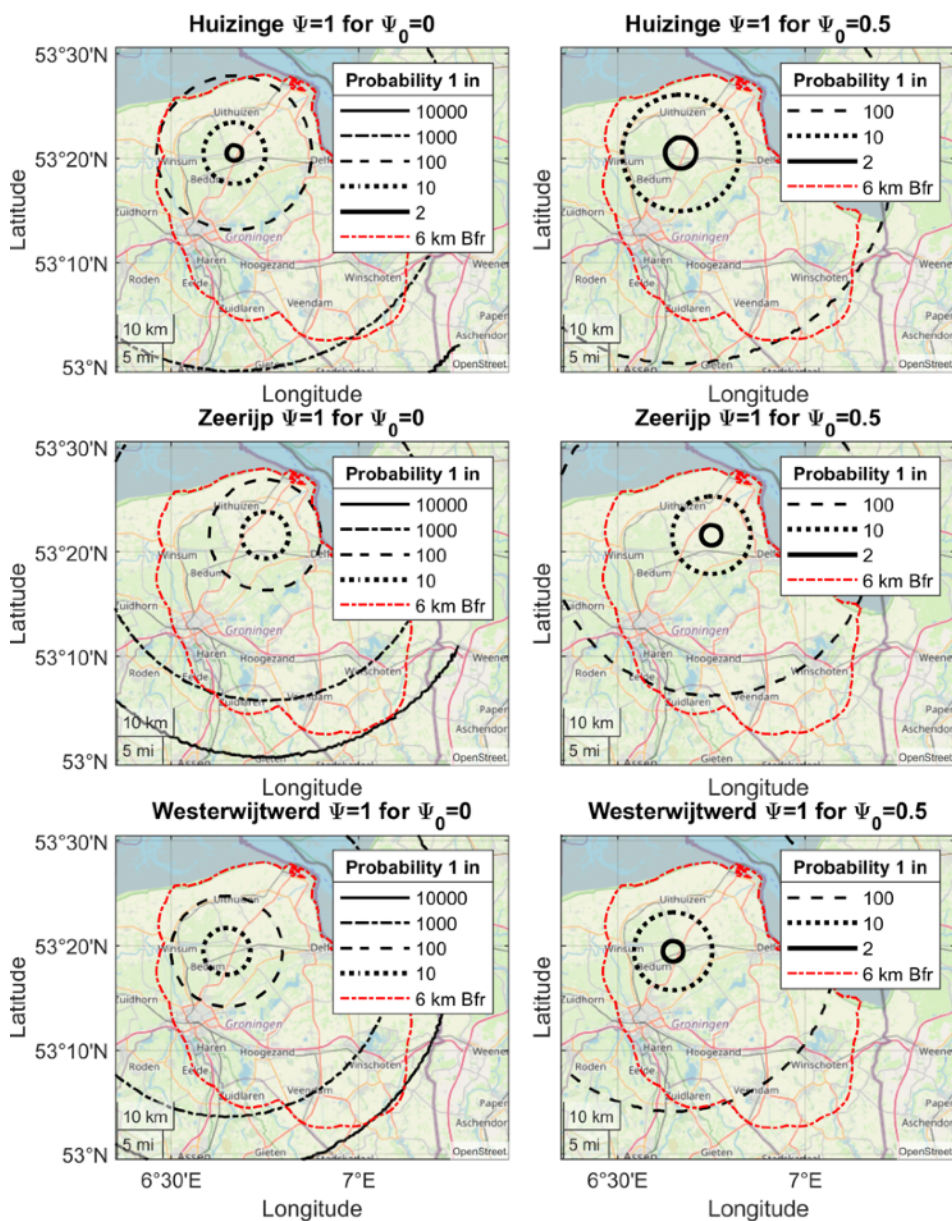


Figure 5.4.5. Probability maps from the convolution of PGV distributions and the fragility curves proposed. The buffer zone of 6 kilometres around the Groningen gas field is demarked.

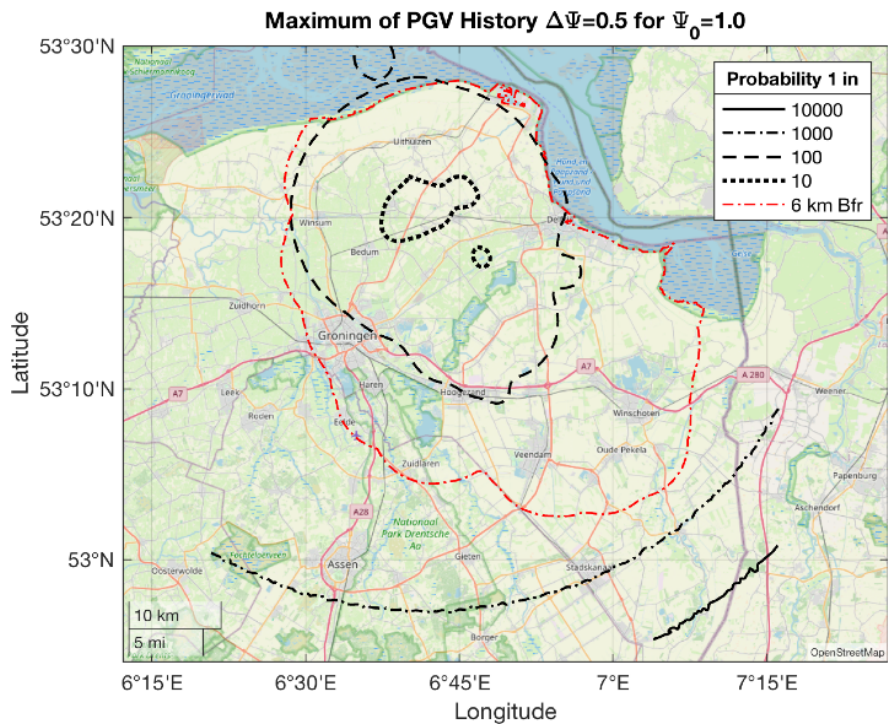


Figure 5.4.6. Probability map for the historical maximum PGV convoluted with the masonry fragility determined in this chapter. The case of $\Delta\Psi=0.5$ for an initial condition of just visible damage is exemplified. Note that the lines are truncated do the model domain.

5.5. Fragility Curves for Settlements from Soil Curvatures

In a related study [27], the extrapolated models of Section 5.2 were further modified to consider façade geometries. Moreover, the goal was adapted to determine the fragility of buildings for slow, vertical soil movements.

Indeed, instead of applying a dynamic soil motion underneath the foundation, a quasi-static displacement was applied similar to the pre-damage phase of the models in the previous sections. The shape and intensity of this displacement was varied in order to relate the intensity of the static soil motion to the probability of damage. In this manner, following a similar approach as sections 5.2 to 5.4, fragility curves can be produced. See also Appendix A.13.

5.5.1. Overview of Semi-Coupled Models of Masonry Façades

Displacement at the Foundation

The displacement applied underneath the foundation depends on the type of hazard that is being modelled. In general, horizontal and vertical displacements can be applied and will correspond to different hazards. For instance, land subsidence over large regions may lead to more prominent horizontal deformations as the vertical deformations are smeared out over a large area. Conversely, local effects, such as swelling of sensitive clays, will impart mostly vertical displacements and negligible horizontal displacements. Analysing a combination of both effects is an intricate problem reserved for another study. In this work, the effect of vertical displacements will be used to illustrate the approach for relating soil movements to light damage fragility.

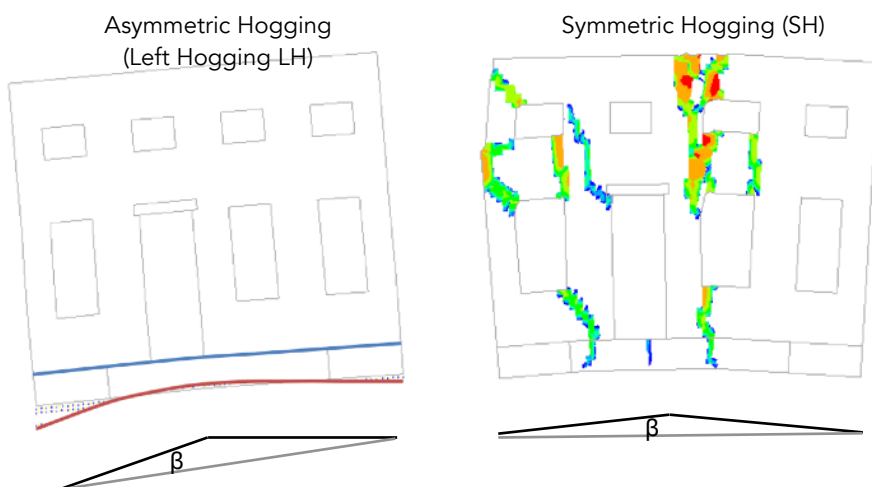


Figure 5.5.1. Scheme of a model of a façade subjected to a deformation of which the idealised shape is characterised with the angular distortion, β .

If the vertical displacements applied underneath a foundation are completely uniform, then no damage will arise. It is a varying displacement field, leading to differential settlements, that will lead to deformations, stresses, and cracks in a masonry façade. There are several parameters that can be used to characterise the intensity of the applied displacement, analogous to the PGV or PGA of an earthquake vibration. Prosperi et al. (2020) showed that the angular distortion is better correlated to visible masonry damage. If the displacement shape is idealised as a bilinear curve, then the angle these curves and the overall tilt would be the angular distortion; see Figure 5.5.1. Hence, in this work, the angular distortion, β , as proposed by Boscardin & Cording (1989), is used as the intensity parameter of the subsidence hazard.

Masonry Façades

Subjecting walls to vertical soil deformations is insufficient to adequately characterise the sensitivity of masonry façade to static soil movements. This is because longer façades are more vulnerable to differential settlements. For this purpose, several geometries for masonry façades were collected, inspired by real damage cases (Van Staalduinen et al. 2018, for instance) and cadaster information (Appendix A.2). The goal was to elaborate representative geometries with which the effect of the length of the façade could be evaluated. The foundation of the façades is also included since it plays a crucial role. For this study, only unreinforced foundations, such as traditional masonry foundations employed in older structures, typically erected before 1945, are considered.

Model Variations

As with the walls, several parameters are varied to evaluate the sensitivity and vulnerability of the façades. Firstly, the material is modified with five variations, a weaker and a stronger version than already evaluated, thus with relative tensile strength of 0.5 and 1.5 in addition to 0.7, 1.0, and 1.3. Secondly, the soil profile, idealised underneath the façade with the interface, is also varied as in Section 5.2 with Soils A and B corresponding to a sandy and a peaty clay.

Thirdly, in addition to the soil profile which determines the properties of the interface as per Table 5.2.2, one of the properties is varied independently. The normal interface stiffness has a large influence in how the deformations are transferred from the soil (bottom of the interface) to the masonry (top of the interface). For this reason, a low and a high stiffness are also considered in the variations. For these, the original value is divided or multiplied by ten.

Fourthly, some variations are assigned to the representation of the hazard. Two settlement shapes are considered: a symmetric hogging and an asymmetric

hogging. Additionally, the shapes are modified by varying the location of the 'knick' point. This results in four displacement shapes as illustrated in Figure 5.5.3. The intensity of the displacements, measured by the angular distortion, is increased continuously in the analyses over the load steps. This is unlike the PGV intensity which had to be scaled for each analysis. The continuous variation allows extracting the β values for which key values of Ψ are displayed.

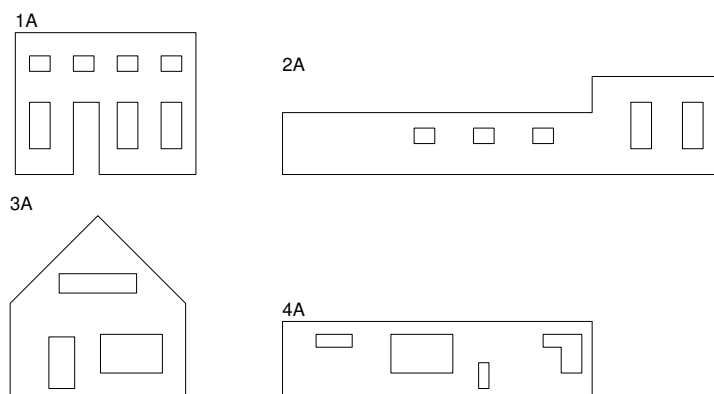


Figure 5.5.2. Four façade geometries for fired-clay brick. These are identical to existing buildings.

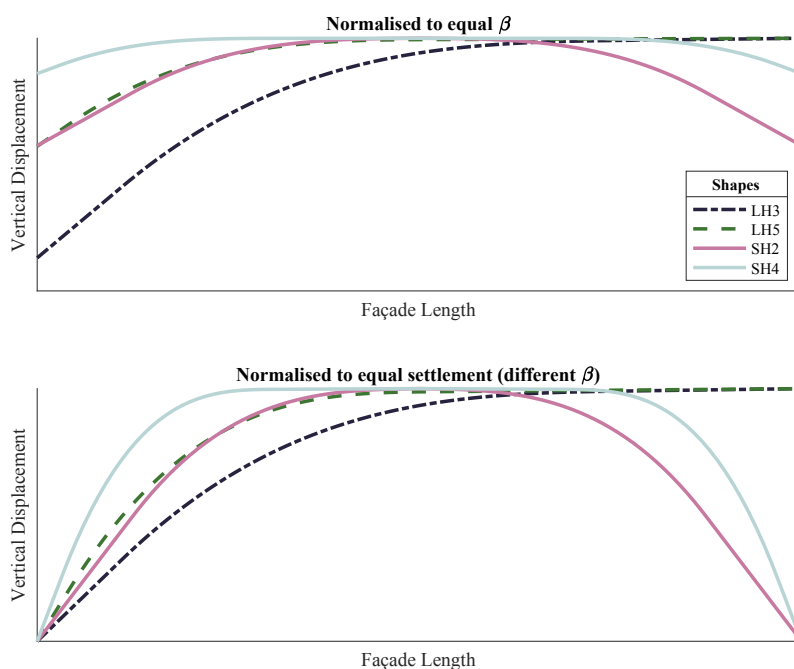


Figure 5.5.3. Four settlement shapes. The numbers after the shapes (left or symmetric hogging) indicate the location of the 'knick': at a third, a fifth, a quarter or in the middle. Sagging shapes were not considered.

Finally, geometric variations are included. These are not limited to the four main façade geometries presented but permute variations in length and opening ratio. A list of the geometries considered is collected in Table 5.5.1. Also, Figure 5.5.2b shows an overview of the geometry variations.

Table 5.5.1. List of façade geometries and their geometrical features.

Façade Variation	Length (m)	Height (m)	Opening Ratio	Large Openings	L/H
1A	7.00	5.50	0.235	FALSE	1.27
1B	5.50	5.50	0.235	FALSE	1.00
1C	8.48	5.50	0.235	FALSE	1.54
1D	7.00	7.00	0.235	FALSE	1.00
1E	7.00	3.80	0.235	FALSE	1.84
1F	7.00	5.50	0.317	FALSE	1.27
1G	7.00	5.50	0.416	FALSE	1.27
1H	7.00	5.50	0.145	FALSE	1.27
1I	7.00	5.50	0.317	TRUE	1.27
1J	7.00	5.50	0.416	TRUE	1.27
2A	17.00	3.80	0.09	FALSE	4.47
3A	6.80	7.10	0.214	TRUE	0.96
3B	4.80	7.10	0.214	TRUE	0.68
3C	8.80	7.10	0.214	TRUE	1.24
3D	6.80	10.00	0.214	TRUE	0.68
3E	6.80	4.20	0.214	TRUE	1.62
3F	6.80	7.10	0.13	FALSE	0.96
3G	6.80	7.10	0.304	TRUE	0.96
4A	12.00	3.00	0.174	TRUE	4.00
4B	6.00	3.00	0.174	TRUE	2.00
4C	9.00	3.00	0.174	TRUE	3.00
4D	12.00	4.80	0.174	TRUE	2.50
4E	12.00	6.60	0.174	TRUE	1.82
4F	12.00	3.00	0.1	TRUE	4.00
4G	12.00	3.00	0.328	TRUE	4.00

These permutations sum up three thousand variations without considering the values for the angular distortion. If the β values corresponding to Ψ of 0.5, 1.0, 1.5, 2.0, 2.5 and 3.0 are extracted, then over 15 thousand data points are collected. However, some models never reach the upper values of Ψ for the angular intensities applied. Unrealistic values of β , above 1/100, would have to be applied for these models to display large values of Ψ . This is because those particular cases, a slender façade with few openings and strong material for example, are particularly robust.

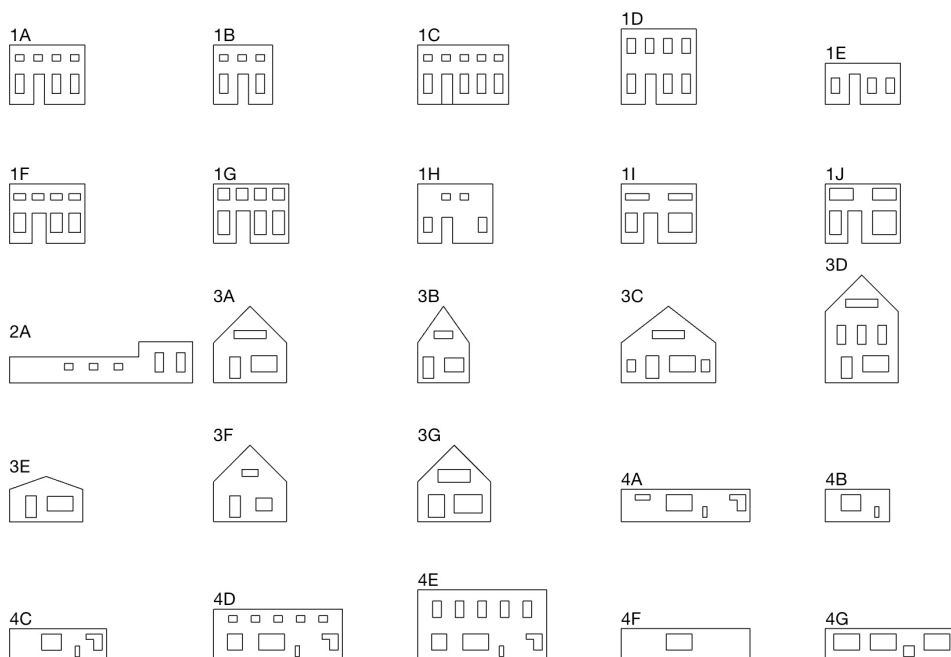


Figure 5.5.2b. Geometry variations of the 25 façades.

Model Results

The entire pool of results is presented in Figure 5.5.4 which indicates, as a table but with colour, the value of applied angular distortion (β) required to generate damage measured with a $\Psi=1$. The lighter the colour, the smaller the β required to cause damage, meaning that the particular façade is susceptible to damage. This is the case of façade 4G which sports the lowest values overall besides façade 2A for which only a few models were run. In contrast, façade 3B is linked to dark colours and missing values. This observation is linked to the large difference in L/H ratio of the façades; the long façade with large openings is most vulnerable to soil deformations, while the slender, tall façade remains rigid against settlement shapes and thus also undamaged.

Other effects are also recognisable. For instance, the settlement shapes that affect most of the façade (LH3 and SH2) are more damaging than the once affecting only the corners; also, asymmetric shapes are more serious than symmetric shapes. Furthermore, the softer Soil B allows for larger β before reaching $\Psi=1$. This is because its lower stiffness helps accommodate the soil deformation and 'cushions' the façade. Similarly, the material strength affects the required β ; the better material (1.5), both stiffer and stronger, resists cracking. The stiffness of the interface has a less discernible influence. The lower stiffness makes the buildings slightly more vulnerable than the original

value, but the higher stiffness makes them a bit more vulnerable, too. For the stiffer case, this is reasonable since the interface doesn't help accommodate the applied settlement. For the interface with the low stiffness, the lack of support makes the deformation on the building more pronounced. The normal interface is thus the least detrimental to the façades. Finally, the various façades differ in their geometry, the size and relative ratio of the openings, and principally, in the length/height ratio. From these, one can observe that the longer façades, with a higher L/H ratio are most vulnerable. Larger opening ratios and larger openings are also unfavourable.

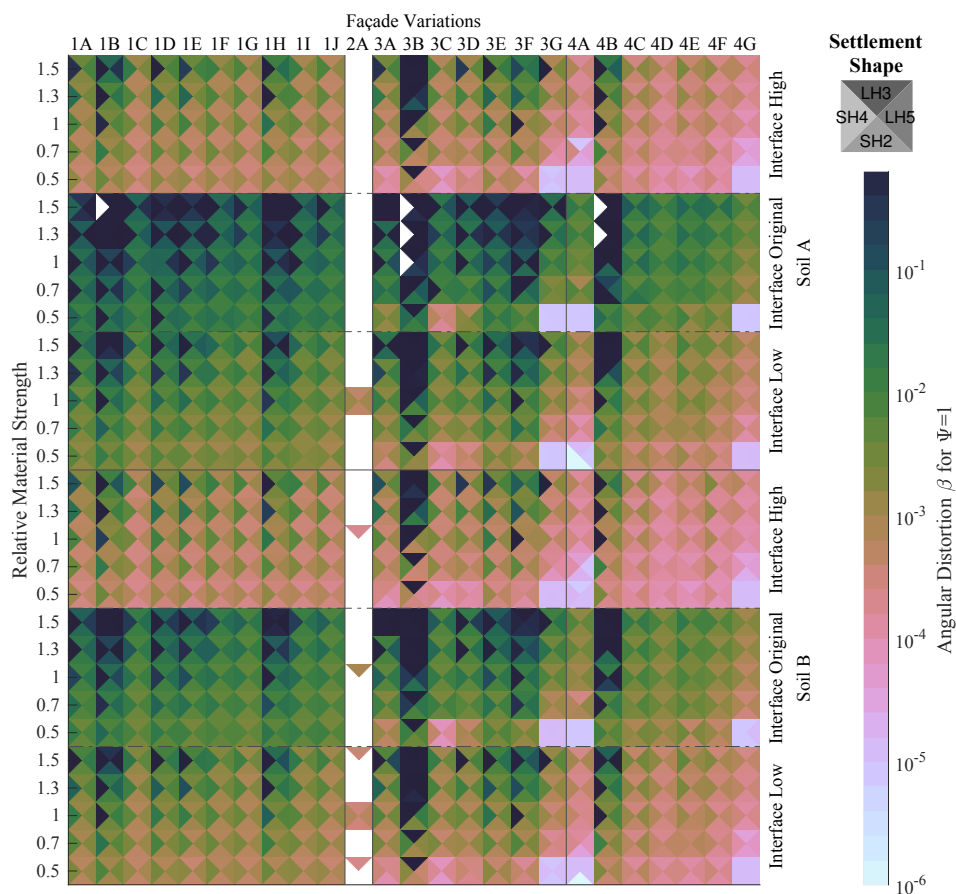


Figure 5.5.4. Color Diamonds for the almost three thousand FEM model results with several façade geometry variations.

As a few examples, Figure 5.5.5 collects the crack analyses of four different façades at similarly large values of Ψ . The applied distortion to generate this damage is very different, however. For façades 1B, 1C, 3C, and 3D, β are 1/100, 1/1300, 1/150, 1/400 for shapes SH2, SH4, SH2, and SH4 respectively.

All but façade 1C are on Soil B. Both façades 1 are of the weakest material, while façades 3C and 3D are of the standard (1.0) and slightly strong material (1.3). Façade 1B has the low stiffness interface, façade 1C the high stiffness, and the rest the original stiffness.

These permutations allow some specific comparisons besides some general observations. First, cracks form around windows, typically at corners, at the centre or around lintels. Most cracks are horizontal or vertical, which is consistent with settlement-related cracking (de Vent, 2011). In most cases, the widest cracks are vertical and are the result of bending of the façade. The longer façade 1C reaches higher damage at a tenth of the soil distortion applied to 1B even though the SH4 shape acting on 1C is less damaging.

The cases selected for façades 3C and 3D are exceptions to the general trends: the taller façade is more vulnerable. This seems to be related to the geometry and the settlement shape. The symmetric shape at a quarter of the façade length (SH4) is typically less damaging than the shape that goes to the centre of the façade (SH2). For the geometry of façade 3D, because of the window layout, two piers at the edges carry most of the weight. This forces additional bending of the spandrel underneath the large window which results in a wider crack than the similar crack of its sibling, 3C. In this case, the stronger and stiffer material of façade 3D is detrimental.

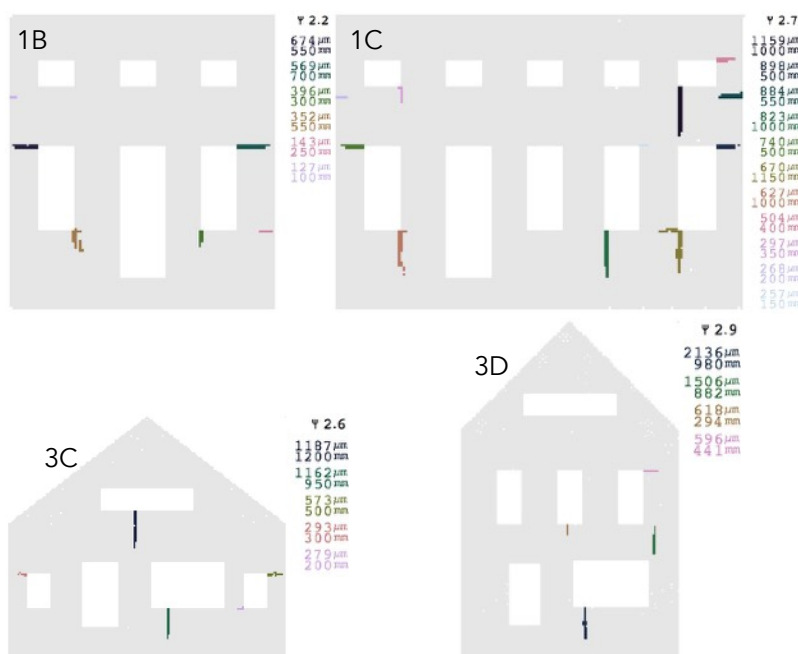


Figure 5.5.5. Crack plots of 4 façades with values around $DS1/DS2$ ($\Psi \approx 2.5$).

5.5.2. Fragility Curves for Soil Angular Distortion: β vs. Ψ

The ultimate goal, as with the relationship between PGV and Ψ , is to produce fragility curves in terms of Ψ for increasing β intensity.

Damage Regression

Since the number of data points is reasonably large, there are three good possibilities to shape a relationship between the varied parameters and damage. First, a **reasoned model** could be shaped to capture this relationship, as was done in Section 5.3. However, the number of parameters being varied is large and there are inter-relationships that could play an important role, especially within the variations of the hazard and the geometry. This exercise, to formulate a set of equations that capture these relationships, quickly becomes unfeasible.

Second, the large number of results can already be used to determine a probability of failure using **weights**. For example, for an applied distortion value of 1/500, about 20% of the two thousand models have exceeded a damage level corresponding to $\Psi = 2.5$. Given the limited number of models, this approach loses confidence at very low values of probability where only one or two models have crossed the threshold. This can be reasonably compensated by applying a log-normal distribution fit to the results. Furthermore, not all models should be considered equally. Houses built with masonry that closely matches the average material properties are more likely to appear in the region than houses that correspond to the 'very strong' set of material parameters. This spread in material parameters can be captured with a probabilistic distribution; characterisation experiments in the lab have shown that the tensile strength follows a normal distribution with a 30% variance, for example.

Similarly, the distributions of the other parameters that have been varied, such as the soil type, the settlement profile shape, etc. can be determined. Then, the models can be weighted so as to reproduce the likelihood of their combination of parameters appearing in buildings in the region; in this manner, the probability of failure for a more realistic combination of situations can be estimated. Correlations between the various parameters, such as weaker soil-structure interfaces being more likely on the softer soil for instance, can also be included. A structure with a material far from average, on bad soil but with a stiff soil-structure interface, subjected to a symmetric soil settlement profile that only deforms the ends of a short foundation, would receive the lowest weight possible of 0.06; while, a structure of average material, on the stiff soil and also a stiff soil-structure interface that transfers an asymmetric settlement distortion

to a long foundation, would receive the highest weight of 4.5. These examples exclude weights assigned due to the geometry of the walls. It must be said, that this weighing approach can only be used if the various model variations cover the range of typical parameters found in real cases. This comprises some limitations.

Third, a (semi-)unsupervised **machine learning model** could be trained. Since β is varied continuously, Ψ is extracted at discrete intervals. This means that the response variable, Ψ , has distinct values or categories. The model to train is thus a classification model. These types of models are usually more successful than general regression models. Once the model is trained and validated against a (reserved) portion of the data, it can be used to predict values of Ψ for any combination of parameters. Hence, the parameters can be assigned realistic, probabilistic distributions and sampled within a MonteCarlo simulation. Weighting is not required since the samples follow the assigned distributions. In this manner, the probability of damage can be computed, and unlike the weighting approach, small probabilities can also be more reliably simulated.

In [27] the weighting approach has been employed on the basis of the same model results. In this section, however, a machine learning model is trained. Specifically, a classification neural network is chosen since it may provide accurate predictions for a high invariance in the importance or relevance of the input parameters as is the case for the leading variable, the angular distortion, which determines the degree of damage of the masonry façades.

Other types of models were also tested, such as (ensemble) trees, kernels, naive Bayes models, and (optimised) linear models, but their accuracy was limited to 30% of correct predictions or less. A support vector machine model reached an accuracy of 55% but was very slow. In contrast, the neural network with three interconnected layers achieved an accuracy of 70% for Ψ classes at intervals of 0.5 and a prediction speed of millions of points per second; see Figure 5.5.6. Given the façade's length, its opening ratio, its length/height ratio, the shape and location of the knick of the applied displacement profile, the relative material strength, the soil type, the interface stiffness type, and the applied angular distortion, the model predicts the category of Ψ . See later Table 5.5.2 for a summary of these predictors.

FEM Model Result	$\Psi < 1$	$\Psi = 1.0$	$\Psi = 1.5$	$\Psi = 2.0$	$\Psi = 2.5$	$\Psi \geq 3.0$	
	2567 16.3%	148 0.9%	37 0.2%	22 0.1%	18 0.1%	15 0.1%	91.4% 8.6%
	159 1.0%	2345 14.9%	150 1.0%	55 0.3%	40 0.3%	34 0.2%	84.3% 15.7%
	50 0.3%	166 1.1%	2147 13.6%	183 1.2%	74 0.5%	68 0.4%	79.9% 20.1%
	22 0.1%	37 0.2%	190 1.2%	1922 12.2%	332 2.1%	187 1.2%	71.4% 28.6%
	14 0.1%	18 0.1%	36 0.2%	229 1.5%	1446 9.2%	531 3.4%	63.6% 36.4%
	19 0.1%	36 0.2%	73 0.5%	164 1.0%	616 3.9%	1621 10.3%	64.1% 35.9%
	90.7% 9.3%	85.3% 14.7%	81.5% 18.5%	74.6% 25.4%	57.2% 42.8%	66.0% 34.0%	76.4% 23.6%
NN Prediction							

Figure 5.5.6. Confusion chart of the classification neural network.

Uncertainty

The classification model can then be used for a MonteCarlo simulation. Yet, the model is not perfectly accurate; it fails to correctly predict about 30% of the training data. In most cases, the prediction is one category away from the true value, so if the numerical model determined $\Psi=2.0$, the classification model predicts $\Psi=2.5$ or $\Psi=1.5$. A slightly higher accuracy could be achieved by overfitting the model to the training data. This is not desired, since the model could produce unexpected values if the input parameters differ from the precise training inputs employed. To prevent overfitting, a 5-fold validation scheme was used.

Another strategy to improve the model's accuracy is by finding predictors that are better related to damage. For example, other geometric features of the

façades, like the distance between the windows or the heights of the spandrels could better reflect the vulnerability of the buildings. Perhaps the location of the knick point in relationship to the location of the façades' openings could also function as an alternative predictor yielding higher accuracy. Furthermore, 'deep learning' could be employed to extract additional predictors. This is outside of the scope of this work, however.

Consequently, the original predictors have been maintained. In fact, the small inaccuracy of the model has its advantages. The errors in the confusion matrix (Figure 5.5.6) can be used in a model uncertainty parameter. This parameter not only helps represent the uncertainty in the classification model but also that in the FEM modelling strategy. Though great care has been exercised in modelling the behaviour of the façades, uncertainties about the soil-structure interface strategy, the application of the displacement, the choice in material model and soil profiles, and some of the values assumed for the models for instance, will impact the final probability in a way which would difficult to quantify. The uncertainty parameter derived from the confusion matrix can help represent these effects.

The uncertainty is modelled directly from the confusion matrix. Since the classification problem leads to discrete values, if the model predicts a certain value of Ψ , the other values in the column give the probability that the true value was a different one. For example, for a prediction of $\Psi=1$, there is a probability of 10% that the true value was $\Psi=0.5$ or $\Psi=1.5$ (about 5% each) and approximately 2% that it was $\Psi=2.0$.

Damage Simulation

The various input parameters for the regression model are assigned probabilistic distributions as per Table 5.5.2. These distributions are assumed from various sources. First, the geometry of the façade is represented by four parameters: its length, its length/height ratio, its opening ratio and whether there are large openings. The first two are sourced from the 3D-BAG database; see Appendix A.2. Post-processing the database for the length and height of walls reveals a log-normal distribution where walls about three meters in width are most common and a long tail shows walls of fifteen metres are also present. Similarly the height is characterised to then extract the length/height ratio. To date, the 3D-BAG database does not yet include openings such as doors or windows. Therefore, a distribution is derived from the opening ratios present in the modelled façades. These have been inspired by historic structures and compared to reports of damage cases. Finally, the indicator for large openings (true/false) is correlated to the opening ratio. An opening ratio of 30% for

example, is linked to a 30% probability of large openings. A smaller opening ratio will be less likely to contain large openings. While it was considered to remove the predictor of large openings, re-evaluating the model without it led to a 3% decrease in accuracy, hence all seven predictors were kept.

For the settlement shapes, damage cases are investigated from literature (Van Staaldin et al. 2018, Prosperi et al. [20]). Four different shapes were included in the FEM models; all are hogging-based shapes which are more damaging to buildings and thus appear more frequently in damage reports. However, the symmetric hogging is less likely (42 vs 58%) and the knick points involve most of the deformation (located at half and third being thus more likely). Yet, these are correlated to the length of the façades. Longer façades are more likely to have shapes only affected at their corners (at a fourth or a fifth of the length). Hence, for façades with length larger than the mean length, shorter knick points are twice as likely while for shorter façades they are half as likely. This precise distribution is an assumption from the empirical observations. The relative material strength follows a normal distribution with a 30% variation; see section 5.2.

Two soil profiles were investigated: the sandy soil A and the peaty profile B. The micro-zonation study of Kruiver et al. (2017), was used to determine which was more likely on the province scale. It follows that the sandy soil appears in 60% of the cases and the peaty soil in the remaining 40%. This also follows into a binary distribution. The normal stiffness of the interface representing the soil is also affected. Three possibilities were studied: low, original and high normal stiffness. For soil A, the stiffer option is more likely with a distribution of 0.7:1.0:1.5 (L:O:H); while for soil B, the lower options becomes more likely with the inverse assignments (1.5:1.0:0.7). The exact values are somewhat arbitrary but corresponds to the weights assigned in [27].

Finally, the parameter with the most influence in the classification model is the angular distortion. For this, no distribution is assumed since this is the hazard intensity parameter. Instead, the values are varied between $1 \cdot 10^{-5}$ and 0.01 (or 1/100) and the probability of damage is determined based on a simulation with a million samples per value of β . The probability of reaching or exceeding various values of Ψ is then determined based on the number of models that exceed those values at the ordinal β s. The result is plotted as fragility curves in Figure 5.5.7. One can observe their characteristic S-shape. However, especially the curve for $\Psi=1$, does not start from the origin but at a higher probability. This is explained by some models that already start with some degree of damage due to gravity effects. This could be addressed by considering the $\Delta\Psi$, but that conveys other issues when the geometries of the façades differ. At

the right side of the curves, one can also see that the probabilities do not reach 1 at the high values of β investigated. This is particularly clear in the bottom figure for geometries with L/H smaller than 1.5.

Table 5.5.2. Predictors and distributions assumed. \bar{L} is the mean of L .

Predictor	Symbol	Distribution	Parameters / Formulation	Units / Values
Length	L	LogNormal	$\mu=1.482, \sigma=0.677$	m
Height	H	LogNormal	$\mu=1.282, \sigma=0.428$	m
Opening Ratio	O_R	LogNormal	$\mu=-1.51, \sigma=0.342$	-
Large Openings	O_T	Uniform Correlated	$p(\text{true})=O_R$	true; false
Settlement Shape	A_β	Uniform	$p(AS)=0.58$	AS; S (symmetric)
Knick Location	p_k	Uniform Correlated	$p(E L > \bar{L})=2/3$ $p(C L > \bar{L})=1/3$	E (edge); C (centre)
Soil Profile	S	Uniform	$p(A)=0.6$	Soil A; Soil B
Interface Normal Stiffness	k_n	Uniform Correlated	$p(L S=A)=0.22$ $p(L S=B)=0.47$ $p(H S=A)=0.47$ $p(H S=B)=0.22$	L; O; H (high)
Relative Material Strength	m	Normal	$\mu=1, \sigma=0.3$	-
Angular Distortion	β_A	Fragility Parameter	$10^{-5} \dots 10^{-1}$	rad

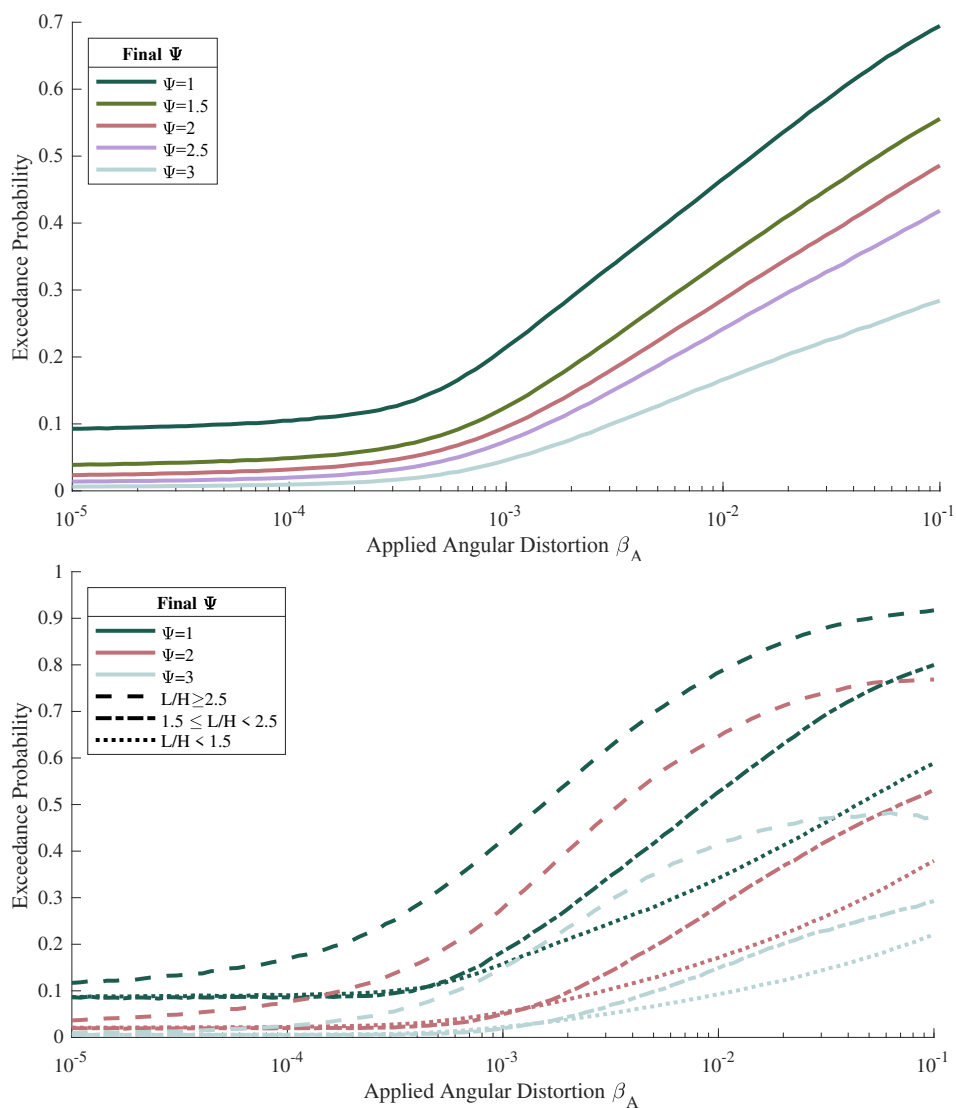


Figure 5.5.7. Fragility curves for soil angular distortion β . Bottom, segregated by L/H ratio.

Indeed, the curves are also plotted distinguishing between long façades, for which the L/H is larger than 2.5, and short or slender façades. Besides the angular distortion, this is the most influential parameter, clearly demonstrated by the significantly higher probability of damage of the longer façades. This makes sense since an equal value of angular distortion will lead to higher differential settlements on a longer façade. If the façade is not very tall, it acts as a slender beam subjected to high deformations. This leads to large tensile stresses at the top of the façades (for hogging), which results in cracks. The

geometries with a low L/H ratio instead, even if subjected to larger angular distortions, are sufficiently stiff and do not deform under their own weight and associated vertical loads.

The fragility curves are fitted with a log-normal distribution as in Section 5.4. This eliminates the abnormal effects at the tails of the curves and makes them more comparable to others in literature. In particular, earlier work employed the same model results to draw weighted exceedance curves where the number of model results were counted and their count weighted with their likelihood or appearing in real distributions. This comparison is conducted in Figure 5.5.8 for the range of β between $1/10000$ (10^{-4}) and $1/100$ (10^{-2}) between the sets of log-normal curves. The reference value of $1/500$, used to evaluate if buildings are sensitive to angular distortions is also highlighted for the comparison. At this value, the curves are well comparable. For larger distortions, the weighted exceedance lines display larger probabilities. This is due to the geometries employed. The weighted approach attempts to weigh the number of models so that the distribution of geometries match the distributions of Length and Height observed from the 3D-BAG database which are represented by lognormal distributions. Neither weight matching nor log-normalisation are perfect (especially for the Height) which makes the weighted approach, with its purposely vulnerable geometries, more conservative.

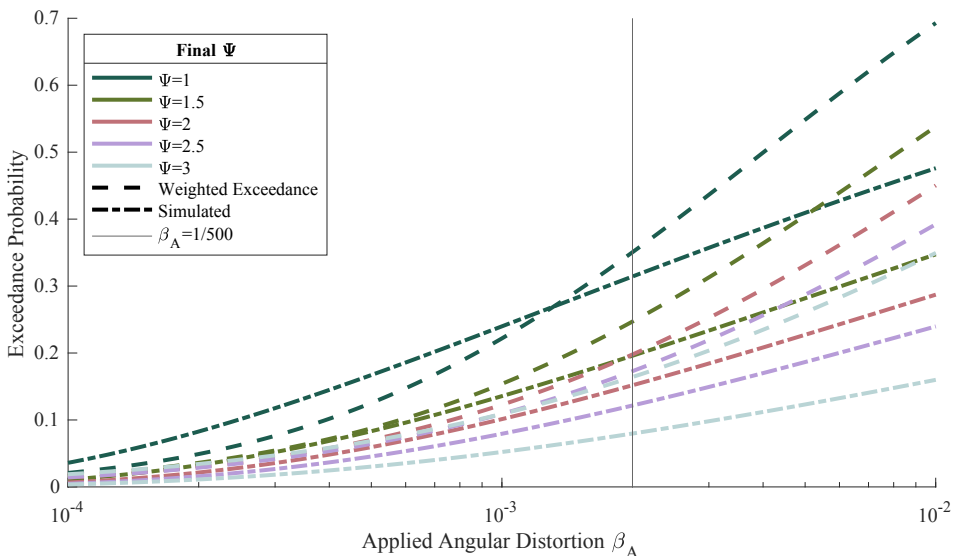


Figure 5.5.8. Comparison of fragility curves against weighted exceedance curves from [27].

Conclusion

The fragility curves for quasi-static soil movements are another example of crack-based damage probabilities for masonry buildings. The set of curves, determined for soil deformations in terms of curvatures with negligible horizontal strains expressed as angular distortion, β , give the probability of light damage in the damage scale of the parameter Ψ . The relationship β - Ψ can help establish the initial condition of buildings when subsequently subjected to vibrations.

5.6. Conclusions: Probability of Damage and Aggravation

In this study, a five-step process was employed to quantify the likelihood of light damage, characterised as visible cracks of at least 0.1 mm, in bare, fired-clay-brick masonry walls. Initially, wall experiments calibrated nonlinear FE models, focusing on crack behaviour, and these models were then extrapolated to assess the dynamic impact of seismic vibrations on crack initiation and propagation, including cases with pre-existing micro-cracks or invisible damage from differential settlements.

The study revealed quantifiable relationships between damage intensity and various factors like material strength, pre-damage condition, soil type, and Peak Ground Velocity (PGV). For instance, it was found that weaker masonry materials saw larger damage increases, with models on peat (soft soil) accruing 33% more damage than those on stiffer sandy soil, and walls with windows experiencing 25% more damage than those without. Additionally, walls undergoing two consecutive seismic events showed an average of 10% more damage than those subjected to a single event. The final step involved creating a set of 'fragility or vulnerability curves', that present the probability of exceeding a value of Ψ given an initial condition Ψ_0 . These curves demonstrated for example, that walls with no pre-damage ($\Psi_0=0$) had a 5% chance of light damage at a PGV of 10 mm/s, a probability that rose to 20% if the walls had some undetectable pre-existing damage ($\Psi_0=0.5$). A lower PGV would be associated with a lower probability of damage; for instance, at 5 mm/s, the probability of exceeding $\Psi \geq 1$ when $\Psi_0=0.5$ is 6% and for exceeding $\Psi \geq 2$, it is below 0.1%.

While the fragility curves determined herein are specific to the situation in the north of the Netherlands and are constrained by certain limitations such as the type of masonry and structural geometry, the reduced number of earthquake motions, and the type of pre-damage selected; the methodological approach employed comprising FE calibration, extrapolation, and probabilistic extension, can be used in other situations to determine the probability of light damage.

Indeed, in addition to the light damage fragility for seismic vibrations, this chapter presents a comprehensive analysis of the relationship between soil angular distortion and the fragility of masonry façades, contributing to the understanding of static soil movement impacts on structural integrity. By employing a combination of finite element modelling and data analysis techniques, including machine learning, the research provides a nuanced perspective on the susceptibility of various façade geometries and material compositions to soil-induced damages.

The semi-coupled models developed in this work reveal the intricate interplay between soil movements and masonry façade damage. By systematically varying parameters such as material strength, soil profile, interface stiffness, and displacement shapes, the study offers a detailed exploration of the factors influencing façade vulnerability. This comprehensive approach, encompassing over 15 thousand data points, enables the derivation of fragility curves that effectively correlate soil angular distortion with damage probability.

Furthermore, the use of a classification neural network to predict damage levels marks a significant methodological advancement. Despite some inherent limitations and uncertainties, this model serves as a powerful tool for estimating the likelihood of masonry wall damage under various conditions. The study's findings are further strengthened by the incorporation of realistic probabilistic distributions for key parameters, ensuring that the model outcomes mirror real-world scenarios. The fragility curves exhibit the characteristic S-shape, providing clear insights into the damage probability at different levels of soil angular distortion. Notably, the study highlights the critical influence of the length-over-height ratio on façade vulnerability, with longer façades demonstrating a higher propensity for damage. This finding underscores the importance of considering façade geometry in assessing structural risk.

The conclusions can be further summed up:

Impact of Pre-existing Conditions: The analysis underscores the significant role of pre-existing, undetectable damage in increasing seismic vulnerability. Structures with prior damage exhibited a 20% increase in the probability of light damage at a Peak Ground Velocity (PGV) of 10 mm/s, compared to a 5% probability for structures with no prior damage. This highlights the necessity for thorough pre-seismic assessments to accurately gauge vulnerability; a zero measurement or in Dutch a “nulmeting”.

Material Properties and Damage Susceptibility: Weaker masonry materials experienced a 33% greater increase in damage compared to stronger variants.

This insight is crucial for material selection and emphasises the need for material-specific considerations in seismic risk assessments.

Influence of Geometric Variations: The study revealed that wall geometries and façade types significantly affect damage susceptibility. For example, walls with window openings were found to be 25% more vulnerable to seismic-induced damage than walls without openings, highlighting the importance of considering architectural design in seismic resilience planning. Longer walls are more susceptible to settlement-induced damage.

Seismic Risk Management Applications: The study contributes fragility curves that correlate PGV with the probability of light damage. These curves can be instrumental for seismic damage assessment, providing a more nuanced understanding of damage probabilities under varying seismic intensities. These can be further employed in risk management decision support.

Chapter 6

Hastening: Damage Accumulation Function

The effect of repetition when considering damage to masonry structures is exhaustively investigated in this final chapter. A lengthened introduction details the motivations and the layout of the chapter. The section considers new insights developed upon earlier work [17, 23, 24]; see [List of Publications](#).

hasten | 'heɪsn |

verb [*no object, with infinitive*]

be quick to do something: *he hastened to refute the assertion.*

- [*with adverbial of direction*] move or travel hurriedly: *we hastened back to Paris.*
- [*with object*] cause (something, especially something undesirable) to happen sooner than it otherwise would: *this tragedy probably hastened his own death from heart disease.*

[Oxford Dictionary of English]

- the earthquakes hastened the inevitable damage on that poorly-built house.

[Own Example]

example force earthquake
number value vibration
effect event repeat
repetition large result
hazard similar
sequence

Chapter 6: Table of Contents

6.1. Analysis of Repetition Effect in Experiments	212
6.2. Damage Accumulation due to Repetition in FEM Models	218
6.2.1. Methodology: Brief Description of the FE Models.....	218
6.2.2. Variations investigated with the FE Models.....	221
6.2.3. Model Results: Effect of Repetition	223
6.2.3. Summary of Observations from Repetitions Models	228
6.3. Damage Accumulation Function (DAF)	229
6.3.1. Function for Ψ from Variable PGV Sequences.....	229
6.3.2. Comparison of DAF against Model Results.....	235
6.3.3. Comparison of DAF against Experimental Results	241
6.3.4. Application: Probability Maps for Accumulated Damage	244
6.4. Concept of Damage Hastening	248
6.4.1. Definition of 'Hastening' in the Context of Damage	249
6.4.2. Time as the Hazard	252

Prologue

Repeated vibrations may cause an accumulation of damage. The experiments of Chapter 3 have shown that cyclic loading, or repeated loading without a reversal in direction, leads to a degradation of the masonry and an increase in visible crack-based damage. As in the experiments, masonry structures are exposed to repeated loading from several sources such as wind, gravity loading/unloading, temperature variations, seasonal soil changes, and vibrations, among many others. See earlier Chapter 4 for a more extensive overview of loads on masonry buildings.

The goal of this work is to assess the effect from vibrations, in particular, from repeated vibrations. These may come from several sources, such as construction or industrial activities, traffic, or seismicity, though the focus is placed on the latter source.

Often, repeated iterations of the same load are similar. Construction activities, for instance, could be caused by machinery operating at a certain load and at a specific distance from neighbouring structures, which would to similar repetitions. In other cases, like for traffic vibrations, only the larger events have an influence on structures. For example, larger trucks driving by a house would trigger vibrations in the structure while passenger vehicles would have no effect. In this case, most of the larger vibrations are again similar.

In the case of seismic vibrations, however, repeated events could be markedly different and all types of events could have a damaging influence on masonry structures. Figure 6.0 presents the peak ground velocity in the town of Loppersum considering events with an intensity of at least 2 mm/s. Two observations can be made from this figure. First, that in the past two decades, structures in the exemplified city have been subjected to more than 30 relevant events. Second, that the events have varied significantly in their intensity, with many events more than five times more intense than the smaller ones.

This means that when evaluating the effects of repetition, one must also consider that the repetitions might have varying intensities. And, unlike during the experiments on masonry walls, the intensity of the repetitions will not be gradually increasing but mark a random sequence of alternating events.

This chapter begins with an analysis of the effects of repetition on the experiments on walls and spandrels in Section 6.1; this is a more in-depth examination that continues the analysis of Chapter 3. This is followed by an exploration of repetition effects on the extrapolated finite-element-method models of Chapter 5. These models, calibrated on the experiments, were subjected to repeated earthquake records via non-linear time-history analyses. The increase in damage because of the repeated records is then examined in Section 6.2.

Next, the chapter delves into a proposal for a formulation that enables computing the (probability of) damage and its increase for a sequence of earthquake events, just like the one illustrated in Figure 6.0. This formulation is validated by contrasting its results against the repetition effect in the experiments and in the FEM models. This is elaborated in Section 6.3.

Finally, the chapter coins the concept of 'damage hastening' in Section 6.4. This concept acknowledges that building damage is a continuous process which might be exacerbated by singular (repeated) events. Over time, this aggravation leads to the need for earlier (maintenance) interventions. It also means that damage will be earlier visible. Moreover, the influence of a hazard can be quantified by its hastening of damage. Similarly, this section places time on the hazard axis: the longer a structure is exposed to seismicity, the higher the probability of damage. For this case, various idealised seismicity scenarios are evaluated. This approach could be employed for other hazards, too, like distinct policies on water level management. These notions are explored in this last section of this work.

The town "Loppersum" is used as an example for a location in this Chapter. It is located close to the centre of the region and was exposed to many of the

It was observed that thirty repetitions were sufficient to reach a stabilised force degradation. Walls were tested with thirty and fifty repetition variants, and thirty was again confirmed to be sufficient to observe the effect. Consequently, most tests were consistently conducted with thirty repetitions to ensure comparability and reduce the quasi-static tests' durations.

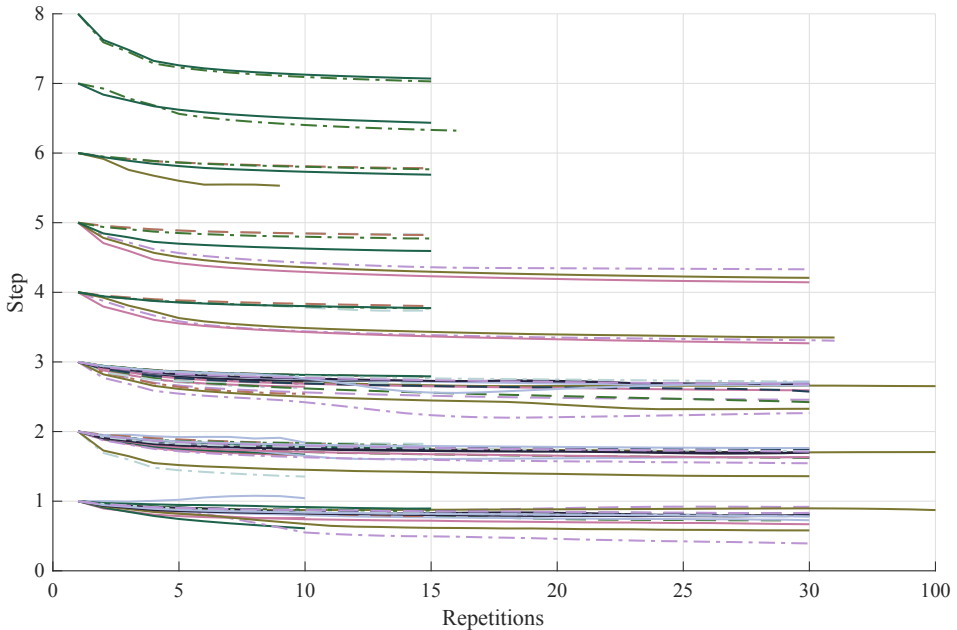


Figure 6.1.1. Force degradation for the spandrels segregated by step. Different lines are used only to distinguish overlapping instances; style and colour have no legend. Chapter 3.

In the figure, every increase in displacement is noted as an additional step. In some cases, eight increases (8x15) were performed. For later steps, the degradation is about twice (proportionally) than for earlier steps. However, steps with a large number of repetitions, also saw a larger degradation at later steps. Except for a single case, all examples show a reduction in force as displacements are repeated.

The effect of force degradation is further illustrated in Figure 6.1.2 for the case of the full-scale walls. Here, in-plane lateral drift is enforced repeatedly, first in one direction, and then in two-way cyclic tests. Only the wall tested with the repetitive and cyclic protocols and surveyed with the high-resolution DIC system are collected. Nonetheless, thirteen walls show decreases in force when drifts were repeated.

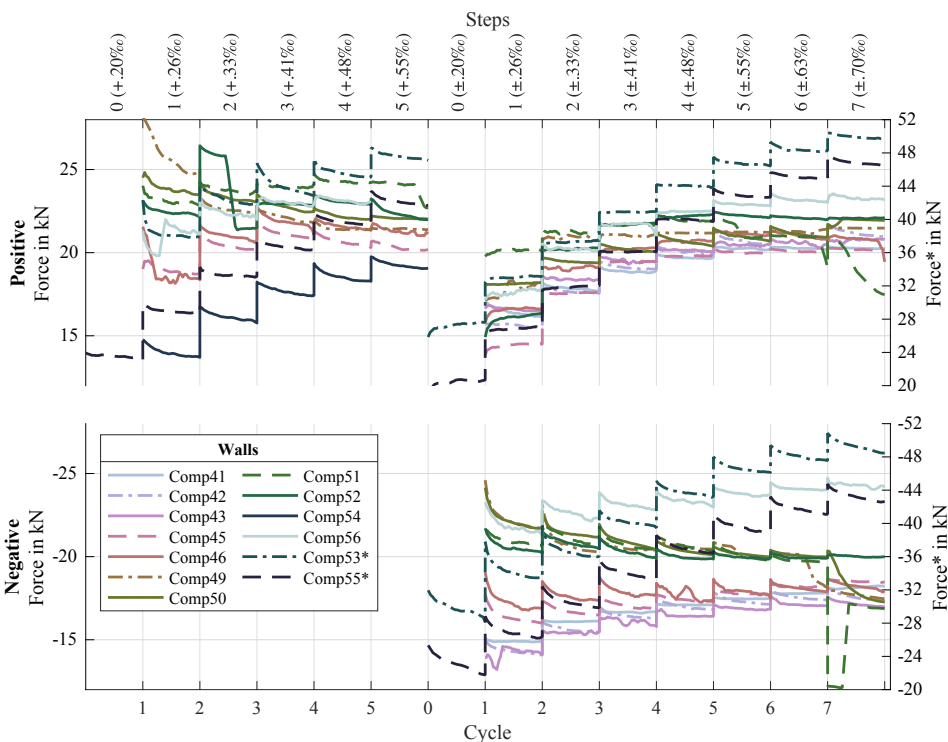


Figure 6.1.2. Force degradation for walls positive, cyclic.

These values are quantified in Table 6.1.1. The degradation is measured by fitting a straight line to every step. Then, the slope of the line is linked to the average decrease in force during every step expressed as Newtons per repetition. In some cases, the slopes are positive indicating an increase. The median values for every wall during the repetitive, positive cyclic and negative cyclic are calculated. This reveals that little degradation occurs for positive loading during the cyclic portion of the tests. However, the degradation during the repetitive part and the negative drift are similar. This is reasonable, since the positive direction during cyclic loading was already damaged during the repetitive part. Indeed, while a large variation is present in the values, the resulting averages for the three categories are similar.

Table 1 also includes the median values between all the walls for a given step. Here, one can observe that the sixth and seventh steps during cyclic positive loading do lead a force reduction in comparison to the earlier five steps; this is likely because these steps enforce a larger drift than what was tested during the repetitive protocol.

Table 6.1.1. Left, median slope from the various steps in the repetitive and cyclic protocols for each wall. Right, median slope from the various walls for each step. The slope is expressed in Newtons per repetition; a negative slope indicates a decrease in force. See Figure 6.1.1.

Walls	Median N/rep			Protocol / Direction	Step	Median N/rep
	Repetitiv	Cyclic +	Cyclic -			
Comp41	NA	-6.8	0.5	Repetitive	1	-20.1
Comp42	NA	-12.1	-17.1		2	-24.6
Comp43	NA	-3.9	-4.0		3	-25.6
Comp45	-21.7	0.7	-10.9		4	-21.6
Comp46	-17.9	-0.5	-21.2		5	-19.5
Comp49	-16.8	0.1	-34.2	Cyclic Positive	1	11.7
Comp50	-24.6	-13.2	-22.3		2	-1.0
Comp51	-15.7	-7.2	-24.8		3	-2.2
Comp52	-16.5	3.7	-16.2		4	0.1
Comp53	-50.8	3.4	-46.3		5	-9.5
Comp54	-24.6	NA	NA		6	-11.6
Comp55	-25.6	2.5	-56.8		7	-12.2
Comp56	-17.4	-7.7	-18.6	Cyclic Negative	1	-34.7
Median	-23.8	-3.9	-21.9		2	-25.6
					3	-24.5
					4	-18.6
					5	-16.1
					6	-12.0
					7	-9.8
				Repetitive		-23.8
				Median Cyclic +		-3.9
				Cyclic -		-21.9

Since identical displacements were applied in each step, cracks were expected to remain unchanged within a step, with the effect of the damage concentrating in the reduction in force. The degradation of force at equal drift could be compared to the increase of displacement at equal force, a situation more analogous to a repeated dynamic excitation. However, repeating an identical force is experimentally challenging. Nonetheless, at later steps, even during identical values of drift, cracks grew both in width and in length. This was especially true during two-way cyclic steps where the reversal of the load seems to have caused local damage within the crack interface. Figure 6.1.3 demonstrates this for a horizontal crack in a wall. See also similar figures for other walls in Chapter 3. Here, some of the cracks increase considerably in width even within steps; this is then linked to an increase in Ψ . This means that

repeated effects are not only expressed as a force degradation in the experiments but also lead to a direct increase in measurable damage.

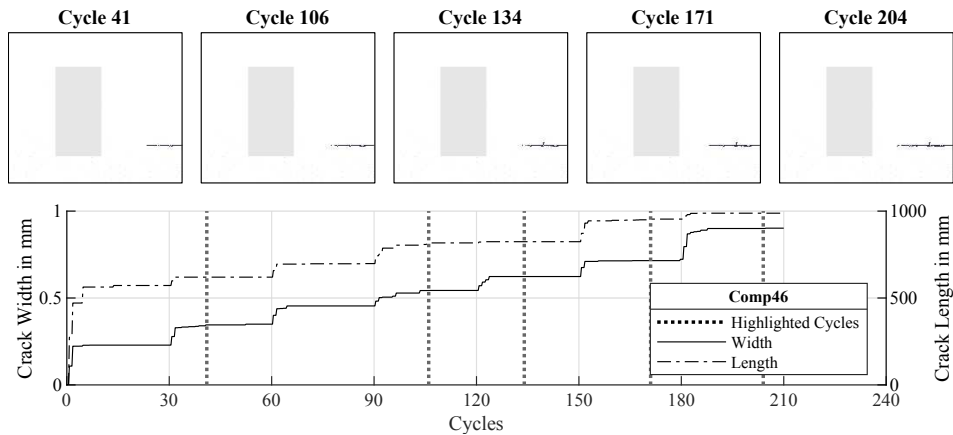


Figure 6.1.3. Progression of crack width and length for a selected crack of Comp46. See also Figures 3.1.7 and 3.2.8.

The evolution of Ψ , as measured by the cracks identified with the DIC system, is presented in Figure 6.1.4 in a way similar to that of Figure 6.1.2. In this case, the increase in Ψ over the steps can be observed. This increase is not as consistent as the decrease in force. In some cases, Ψ appears to decrease or is noisy. This is because of the several steps involved between the actual cracks appearing on the masonry and the expression of Ψ . Unlike the force, which is measured directly; cracks are inferred from the displacement field of the wall. This field in turn, is extracted from the correlation of pixels in a pair of digital images which are captured by a camera. The crack width and length are computed from the displacement field, which also carries uncertainties. Under these limitations, it is remarkable that the small, general trend of increasing Ψ within the steps can be observed.

The spandrels were controlled with the crack mouth opening displacement and thus showed a proportionally large degradation in force. The walls, controlled by in-plane drift, saw both a reduction in force and an increase in damage. It follows that if identical forces were repeatedly applied, a larger increase in crack-based damage would be expected. A hybrid force-displacement control system for new experiments could be designed to test this hypothesis.

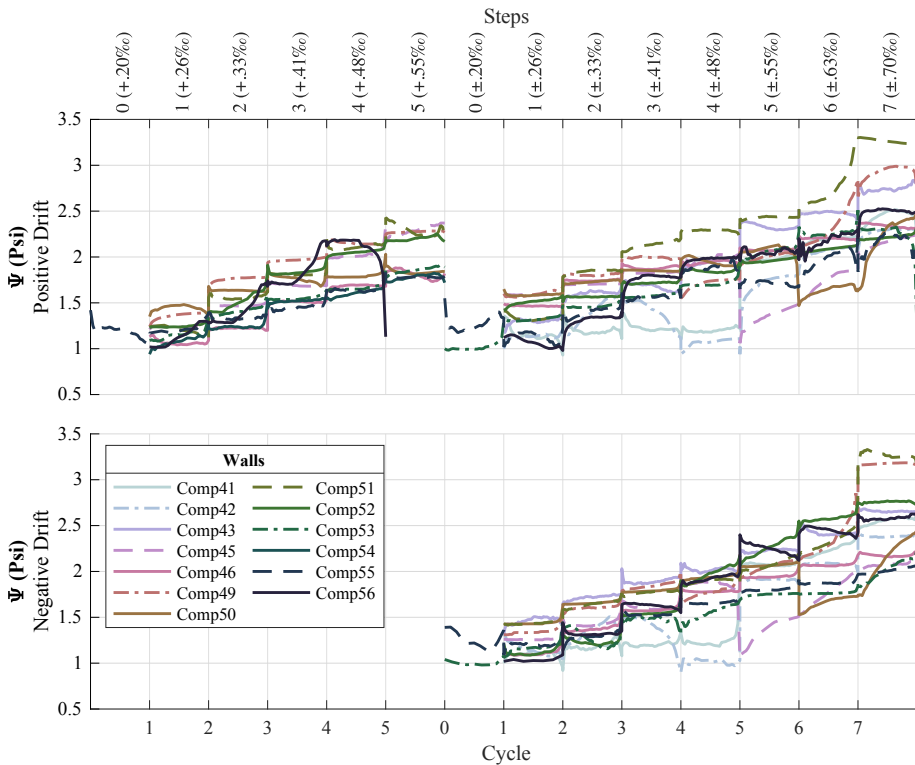


Figure 6.1.4. Evolution of Ψ over the repetitive and cyclic wall experiments.

The experiments demonstrate an increase in damage during repeated loading. For actions such as temperature variations, for which identical displacements are enforced over regular daily or seasonal cycles, this observation can be directly applied. Other actions, like differential settlements, can also lead to cyclic displacements when the causes are linked to changes in the ground water table or seasonal patterns of underground (gas) storage.

For dynamic actions, the observations based on repeated displacements can only be adopted qualitatively since dynamic actions are associated with a repetition in (inertial force) which, if leading to damage, can then be associated with a varying displacement amplitude. The effect of repetition is thus better evaluated with numerical models calibrated on the experiments; see next section.

6.2. Damage Accumulation due to Repetition in FEM Models

The aim of this section is to explore the effect of repeated earthquake vibrations via the use of non-linear finite element models previously calibrated against experiments on masonry walls. The objective is to quantify the effect of multiple repeated events and observe which combinations are most influential for the progression of damage. The study looks at damage on bare, fired-clay brick masonry walls without finishing; window frames are not included and connections at the ends of the walls are approximated while connections with the floors are not represented. The effect of repeated acceleration signals is presented.

6.2.1. Methodology: Brief Description of the FE Models

Models of masonry walls, as a proxy of masonry structures, are used to analyse a multitude of parameters and their influence on the final damage. The models have been calibrated against experiments (Chapter 3) and validated against further tests (Chapter 4). A main strategy, consisting of experiments, calibrated models, and extrapolation models, is used to explore the effect of earthquake vibrations in several previous publications [1,2,3,4]. The damage contemplated is crack based and measured predominantly by the width of the cracks using the damage parameter, Ψ ; see Chapter 2.

Figure 6.2.1 depicts the two geometries of the finite-element models. They consist of 100 mm thick, fired-clay-brick masonry walls 3.10 m tall and 2.70 m high, one with an opening for a window placed asymmetrically and another without openings, both sporting a mesh of 50x50 mm plane-stress, and 8-node quadratic elements with a 3x3 Gaussian integration scheme. The elements were assigned the Engineering Masonry Model for DIANA FEA, an orthotropic non-linear material model which includes different properties for the two directions for both elastic and inelastic behaviour: tensile cracking with softening and secant nonlinear unloading/reloading behaviour, Coulomb friction with cohesion softening and elastic unloading/reloading, and compression crushing (in both horizontal and vertical directions) with mixed secant/elastic unloading and reloading (Schreppers et al. 2017, Rots et al. 2016). This material model, purposely developed to depict the inelastic behaviour of masonry, is key when assessing the accumulation of damage. However, the material degradation observed in the experiments as a force reduction (see Section 6.1) is not implemented. This is discussed by Bindiganavile-Ramadas (2018), where the EMM is expanded to account for the repeated degradation. Yet, this model has not been validated for NLTHA.

The models include an interface at their base to simulate the local soil-structure interaction. The interface is provided with springs and dampers which simulate the presence of the soil around the foundation of the structure following the methodology proposed by Gazetas (1991), adapted from NEHRP (2012) and further explored in Longo et al. (2021). The boundary interface does not allow tension so that applying a settlement shape does not pull on the masonry and allows it to deform freely instead. The masonry elements are assigned 2% of Rayleigh damping based on the first two modes. Additionally, a line mass of 10,000 kg at the top, represents the dynamic effect of floors and transversal walls experienced by the walls if they were part of a structure; similarly, an overburden of 0.12 MPa is applied as a gravity load.

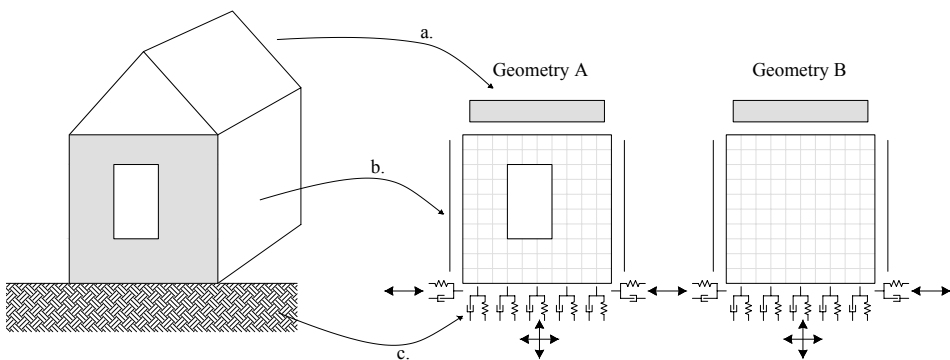


Figure 6.2.1. Two geometries of the FEM model. a) Mass from the roof, b) effect of lateral walls, c) local soil-structure interaction.

The effect of transversal walls was also included in the same manner as in the parallel study focused on settlement deformations [27], namely with linear-elastic beam elements placed vertically on the sides of the walls and simulating the stiffness of a flange connected via the corners to the modelled walls, typical for Dutch masonry buildings before 1970.

The models included three phases: first, the gravity load was evaluated for which no cracking strains were observed. Secondly, a settlement deformation was applied underneath the boundary interface which led to small cracks in the walls depending on the intensity of the applied profile, for some walls no pre-damage was generated; see next section. Thirdly, sliding at the interface was locked, the displacement field of the wall was cleared but cracking strains were retained, and a time-history analysis was performed in which the acceleration time series of four distinct earthquake records was evaluated (in different models). The settlement shape and earthquake records, also employed in other chapters of this work, are detailed in Figure 2. To adequately represent the record-to-record variability of the earthquake vibrations, four records from two

events were selected. By employing recordings registered near and far from the epicentres, with both horizontal and vertical components, additional variability is introduced as the records are clearly distinguished by their number of effective cycles and frequency content.

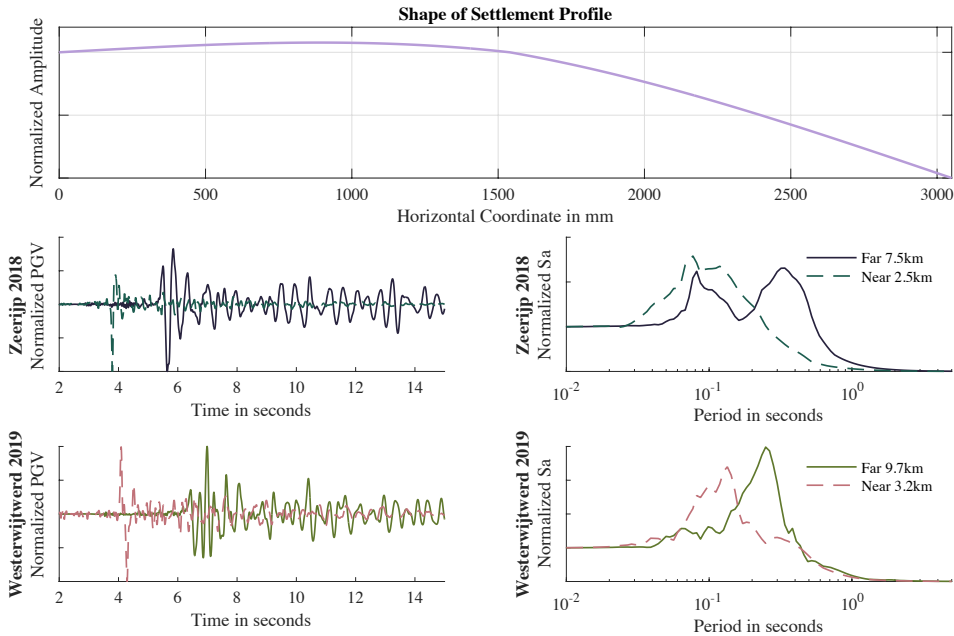


Figure 6.2.2. Top, settlement shape for the pre-damage scenarios. Bottom four, horizontal components of the normalised velocity time series corresponding to two events, each recorded at two different stations, near and far to their respective epicentres and, the normalised spectral acceleration of the signals. Normalised graphs are valueless and show shape and comparison between records.

6.2.2. Variations investigated with the FE Models

A large number of variations were automatically set to run to investigate the influence of: the two geometries presented, the material strength, the intensity of the initial pre-damage, the stiffness of the soil-structure interface, the type of earthquake record, the intensity of the vibration, and the number of repeated vibrations.

In particular, two distinct batches of models can be identified. One where the intensity of the vibrations was always identical, so a sequence of two, four or eight times the same acceleration signal amplified to the same PGV was evaluated in the model. This allowed for a more direct comparison to the experimental results, where identical values of drift were applied to masonry walls, and for a more precise evaluation of the repetition, where only one factor was being varied in the analyses. For the second batch of heterogeneous models, the PGV was varied to analyse the effect of a small vibration following a large vibration or vice versa. These two batches are herein referred to as the homogenous and heterogenous sequences, respectively. Table 6.2 summarises the potential variations; the number of permutations is about three thousand.

6.2.3. Model Results: Effect of Repetition

The results of the individual models have been discussed earlier; here, only a few cases are highlighted instead. Figure 6.2.3 details the initial damage condition of a wall; the cracks were created by allowing the wall to settle under the gravity load and the deformed lower boundary of the supporting interface. The settlement shape was modified such that the initial damage fell into one of the three categories listed in Table 6.2. The cracks are relatively small, pertaining to light damage, and are then aggravated in both width and length by the subsequent vibrations applied during the following time-history phase. In this example, the opening for a window causes stresses to localise and cracks to appear around the opening. Bending in the bottom spandrel results in a vertical crack, common for settlement-based damage observed in damage reports (Van Staaldunin et al., 2018). At the top corner of the window, a vertical-diagonal cracks also appears. Also in Figure 3, the case of cracks during the earthquake motion is depicted. The lateral loading produces a diagonal crack in the body of the wall (example without an opening) and small rocking or flexure cracks at the edges.

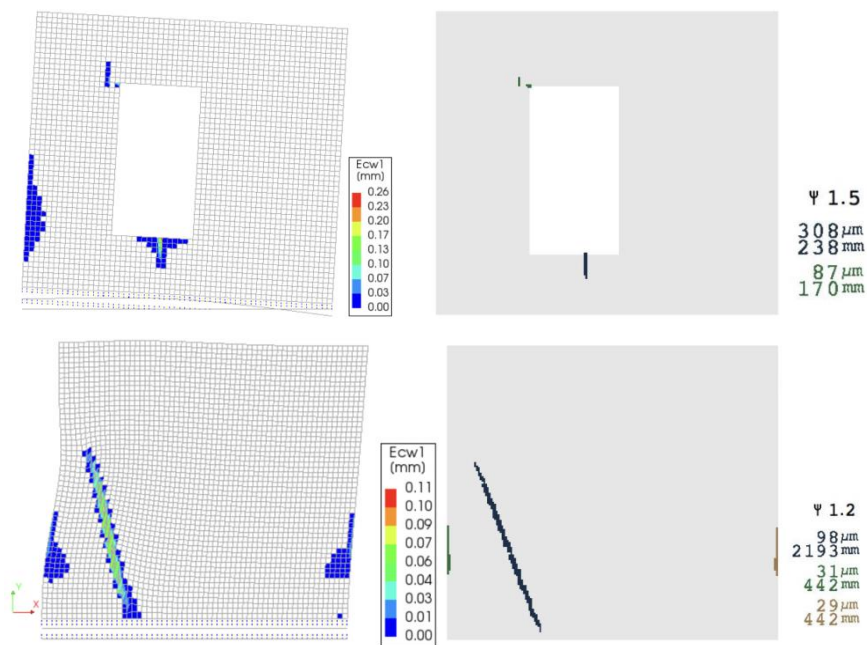


Figure 6.2.3. Example of two model variations (wall with a window, top, and without, bottom) for the initial condition before the earthquake phase, top, and after earthquake motion, bottom. Showing the cracking from the FEM model, left, crack width per element, and right, the automatically-processed damage evaluation. Widths below 0.01 mm are excluded; shear crack width (E_{cw3}) is included but not shown.

The results were automatically processed to recognise the individual cracks and the intensity of the damage. Then, the difference between the initial damage and the final damage ($\Delta\Psi$) was quantified for each model.

Several interesting observations were drawn from the pooled results. For example, the weaker masonry material led to a larger damage increase in comparison to the stronger materials. Also intuitively, the larger PGV caused greater damage. In contrast, the softer soil resulted in slightly less damage since it offered more damping; note that the PGV value is fixed in these comparisons, so the amplification typically associated with soft soils is not included. Similarly, the higher the value of pre-damage, the larger the final damage, yet the increase in damage diminished as the initial damage increased. Regardless of wall material or soil type, the settlement was adjusted to achieve specific values of initial damage; consequently, the effect of individual parameters could be assessed. Additionally, the more flexible wall displayed more damage for earthquakes recorded nearby the epicentre, while the rigid wall was more vulnerable to the records registered far from the epicentre. These observations have been discussed in depth in Chapter 5.

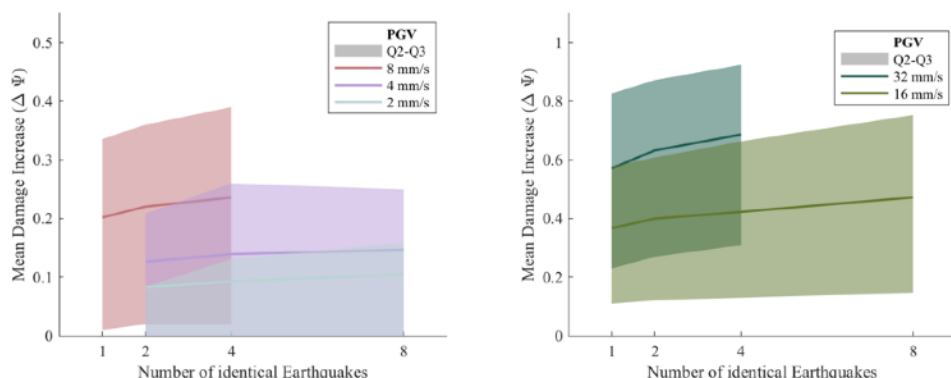


Figure 6.2.4. Mean increase in damage ($\Delta\Psi$) and quantile range of 25-75% (shaded) for the models with homogeneous sequences of PGV. Left, for relatively small values of PGV, 2, 4 and 8 mm/s; and right, for values of 16 and 32 mm/s. Note that the vertical scales differ by a factor 2 and that the centreline corresponds to the average (mean) and the shaded areas to percentiles. See Figure 5.2.4.

Instead, the focus of this section is on the effect of the repeated vibrations. Figure 6.2.4 presents a first look into the results where all models have been pooled together and only segregated by PGV and number of repeated events. Since pre-damage has an effect on the progression of damage caused by earthquakes, the absolute damage increase between the initial damage and the final damage after all events were evaluated is shown on the vertical axes. The graphs illustrate that a more intense PGV results in a larger increase of

damage, with an event of 8 mm/s increasing the damage by 0.21 points on average, while an event of 32 mm/s produces almost three times more damage. Similarly, repeated events also lead to an increase in damage, but this is dependent on the intensity of the vibration. For very small values of PGV, the increase seems minimal, while the larger PGVs can lead to an average increase of 10% for a second identical event. However, further repetitions seem to result in ever smaller increases in damage. The figure also shows the quartiles corresponding to the 25th and 75th percentiles. For low PGVs, many models did not show any damage increase at all, for example; while for large values of PGV, most models showed damage and the variability between models was about twice as large than for the smaller PGV values.

The results can be further dissected to compare the difference between the homogeneous and heterogeneous sequences; this is realised in Figure 5. Here, the two or three event sequences are decomposed into the earlier events; so, the sequence of 2 times 16 mm/s followed by 1 time 8 mm/s ($2 \times 16 + 1 \times 8$) for example, is the composition of 1×16 , 2×16 and the entire sequence $2 \times 16 + 1 \times 8$. This compares the various events and shows which contributed most to the final increase in damage.

The graph shows how larger events impart most to the increase in damage, while a small event following a large event adds little damage. Moreover, the greater number of events usually reduces the standard deviation in the results, meaning the increase in damage becomes more uniform. In particular, comparing the combinations of $2 \times 8 + 1 \times 16$ and $2 \times 16 + 1 \times 8$ shows that the final damage is very similar, but in the first sequence most of the damage appears during the last event, while in the second sequence the damage appears with the first event and progresses slightly afterwards. This is better observed when comparing the last two series of three records each; the sequence with 2×32 yields slightly larger damage.

Furthermore, the comparison of 1×16 against $1 \times 16 + 1 \times 4$ for instance, proves that the small event does have a small, yet measurable contribution to the final damage. However, the median is skewed in the second case and appears to show a much larger damage increase. Indeed, some results seem slightly inconsistent. For example, in the combinations of $1 \times 16 + 1 \times 4$ and $1 \times 16 + 1 \times 8$, the damage increase caused by both second events seems much alike even though the latter combination has a larger PGV. Similarly, it can also be observed that the quartile range of the sequences with heterogeneous PGV values is usually wider than that of the homogeneous sequences. This means that there is more variability between the distinct models pooled in these

groups which in turn suggests that different models also respond differently to the mixed PGV values.

To further improve these observations, additional model variations with different geometries and sequences of PGV from more varied acceleration records will need to be analysed. Moreover, observations from the field, where cracks reported in earlier damage claims can be compared to subsequent visits, will help validate the observations gathered in this modelling study.

The experiments on masonry walls show that repetition leads to degradation. Unlike the models, where the excitation of the earthquakes leads to larger wall drifts in each repetition, in the quasi-static experiments the in-plane wall drift is repeated identically and the reduction in the strength and stiffness response of the wall is measured. This reduction was observed to be highest at the second repetition but stabilised after approximately 30 repetitions when the walls did not lose additional stiffness nor strength. The experiments evidenced that damage would increase slightly even when the enforced drift was identical. This slight increase in damage and associated reduction in wall stiffness is reflected in the results of the wall models; however, a direct, quantitative comparison is difficult.

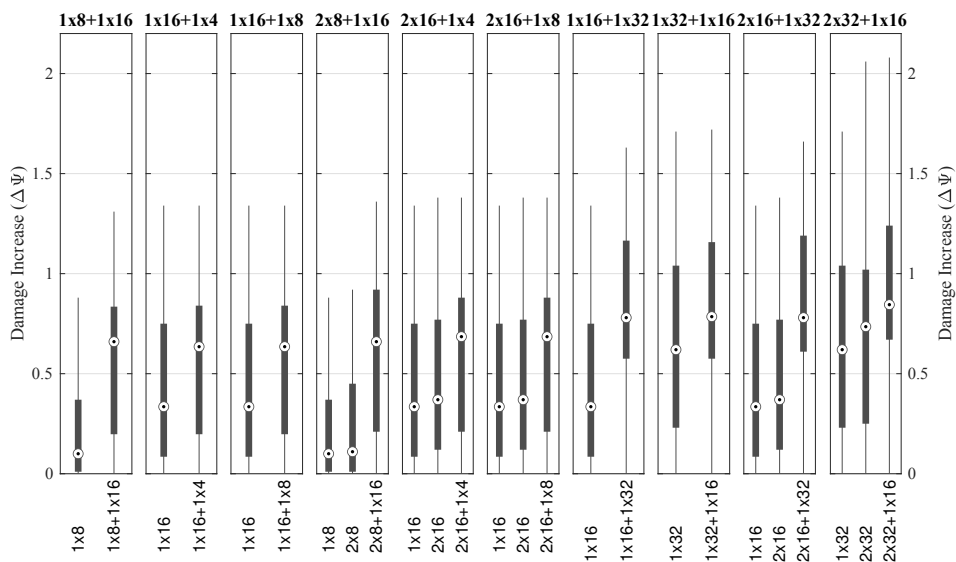


Figure 6.2.5. Box-plot with decomposed PGV sequences. The white ball indicates the median, the box corresponds to the second and third quartiles and the lines (or whiskers) correspond approximately to the interval defined by 2.5 times the standard deviation.

The effect of the repetitions can be approximated by a power law dependent on the number of repetitions and the intensity of the PGV. This is illustrated in

Figure 6 where the increase in damage for subsequent repetitions has been related to the increase caused by the first instance of the earthquake vibration. The data points of the mean increase in damage are included and, while the data is limited, the power law follows the general trend. This simple formulation can then be used to estimate the contribution of subsequent repeated events of similar intensity for any number and combination of peak ground velocity values.

The fit of the power law seems inaccurate or insufficient. There are several reasons for this. First, the function has been conceived using only two parameters that are expected to have the most influence: the PGV and the number of repetitions. But, there are other parameters that will have an influence on the increase in damage such as the material strength or the earthquake record. Secondly, the data points represent the mean of a pool of model results segregated only by PGV and repetition. Yet, the number of models evaluated for the various PGVs and repetitions is not the same. Lower PGV values have been modelled more often thus introducing a bias to the results of Figure 6. Finally, the number of models is limited and only permits observing general trends. These shortfalls will be partly remedied in the following section.

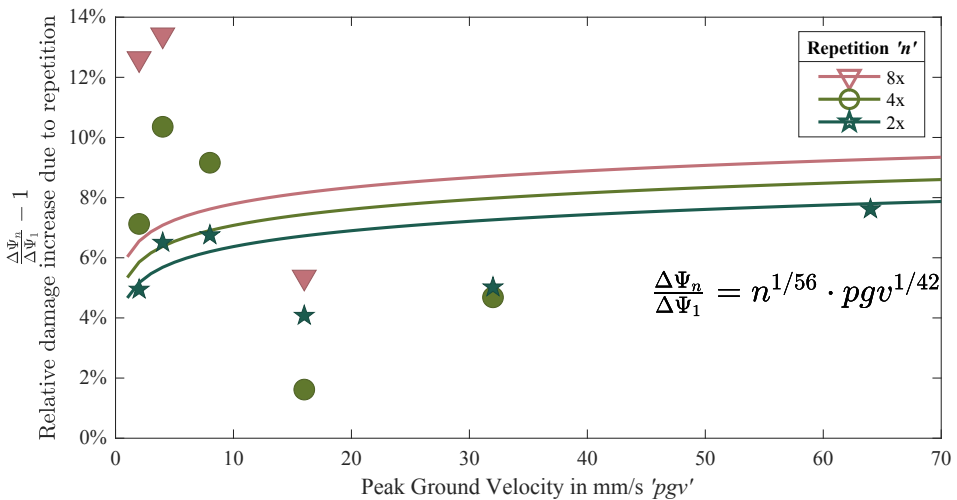


Figure 6.2.6. Additional damage expected for repetition of earthquake vibrations. Approximate power law and mean sample points are shown.

6.2.3. Summary of Observations from Repetitions Models

This study has employed non-linear finite-element models to quantify in-plane, light, crack-based damage in bare masonry walls and investigate its sensitivity towards repeated vibrations. Time history analyses with one or multiple earthquake time series, amplified to identical or varying intensities, were used to evaluate the influence of these repeated events. It was observed that,

- repeated events do lead to an accumulation in damage, albeit in small quantities,
- vibrations of lower intensity than previous vibrations increase damage negligibly, while
- vibrations of similar or larger intensity than previous vibrations may increase damage by 10%, though this is dependent on the intensity of the vibrations and the number of repetitions.
- For a second vibration of 10 mm/s for example, damage is expected to increase by 6%.
- The limited number of models and variations, and lack of comparison field data, should be further expanded to validate these model-based observations.

6.3. Damage Accumulation Function (DAF)

The goal of this section is to elaborate a procedure using the surrogate function of Chapter 5 to predict the increase in damage even for sequences of varying PGV values. The models of Section 6.2 provide a background for validation of this function against homogenous and heterogeneous sequences of PGV. Additional validation is provided by the experimental results of Section 6.1. These help tackle some of the limitations of the models. For example, the capacity of the models to describe the degradation observed in the experiments is limited because of the lack of explicit degradation in the material model. Contrasting the Damage Accumulation Function (DAF) against the experiments helps to verify that the effect of repetition is correctly captured.

The DAF is then used to analyse real, historic sequences of seismic events expressed as PGV histories.

6.3.1. Function for Ψ from Variable PGV Sequences

In Section 5.3, a function for estimating damage was formulated in the form:

$$\Psi_F = \Psi_0 + \Delta\Psi(\sim) + \epsilon(V) \quad \text{Equation 6.1.}$$

where the final value of Ψ (or Ψ_F) is composed by the initial value Ψ_0 , the damage increase $\Delta\Psi$ and an uncertainty term ϵ dependent on the intensity of the peak ground Velocity (V or PGV). The sum of $\Delta\Psi$ and ϵ should always be equal or greater than zero. $\Delta\Psi$ itself is a function of several parameters such as the material strength, the façade type, the soil type, etc. In Equation 6.1 these are denoted with a tilde (\sim). This can be rewritten simply as Ψ being a function of several variables, where the variables are separated by a vertical bar ($|$):

$$\Psi = f(\Psi_0 | V | \sim) \quad \text{Equation 6.2.}$$

One of the variables that is not evaluated in the model of Chapter 5 is the number of repetitions of the earthquake “ N ” (see Equation 5.3). While N appears in the formulation, for the subsequent analyses it was assumed to be $N=1$. For the DAF however, N must be any natural number:

$$\Psi = f(\Psi_0 | V | N | \sim) \quad \text{Equation 6.3.}$$

Yet, with this formulation, the PGV would adopt a single value, thus forming a homogenous sequence of PGV. Real PGV histories are rarely homogeneous, so a new formulation is required: this is the Damage Accumulation Function.

Damage Accumulation Function

For the DAF, the value of Ψ following an earlier value of Ψ will be the sum of the earlier value (Ψ_{i-1}), the instant damage increase $\Delta\Psi$, and the uncertainty term ε .

$$\Psi_i = \Psi_{i-1} + \Delta\Psi(\sim) + \frac{\varepsilon(V_i)}{i} \quad \text{Equation 6.4}$$

In this sequence, the following sets can be defined for Ψ and the PGVs (V):

$$\Psi = \{\Psi_1, \Psi_2, \Psi_3, \dots, \Psi_i, \dots, \Psi_N\} \quad \text{Equation 6.5}$$

$$V = \{V_1, V_2, V_3, \dots, V_i, \dots, V_N\} \quad \text{Equation 6.6}$$

From models and experiments, three distinct observations stand out regarding the influence of repeated loading. The loading consists of imposed drift in the experiments and of PGV in the models: 1) A larger load leads to greater damage; 2) repeated loading of similar amplitude leads to a slight increase in damage; and 3) a repeated load, larger than any previous loads, causes a clear increase in damage. This is captured into a formulation with two parts for $\Delta\Psi$:

Equation. 6.7 Parts a & b

$$\Delta\Psi_{\rightarrow i} = \begin{cases} \Psi(\Psi_{i-1} | V_i | N_{eq} + 1 | \sim) - \Psi(\Psi_{i-1} | V_i | N_{eq} | \sim) & \text{if } V_i \leq (1 - \rho) \cdot V_{\rightarrow i} \text{ (a)} \\ \Psi(\Psi_{i-1} | V_i | 2 | \sim) - \Psi(\Psi_{i-1} | V_{\rightarrow i} | 1 | \sim) & \text{if } V_i > (1 + \rho) \cdot V_{\rightarrow i} \text{ (b)} \end{cases}$$

where: V_i is the PGV at instance i and $V_{\rightarrow i}$ is the largest PGV up until i , without including V_i , or:

$$V_{\rightarrow i} = \max[V(1 \dots i - 1)] \quad \text{Equation 6.8}$$

ρ is a factor determining the similitude of the earthquakes' intensities. If $\rho=0.25$ then a PGV that is larger than 25% the maximum PGV occurred until then ($V_{\rightarrow i}$) will be considered a comparably large event and the second line of Equation 6.7 becomes applicable. Similarly, N_{eq} is the number of equivalent PGV occurred until instance i . In other words, the count of all the events with a PGV within the interval 25% smaller or larger than V_i . This is expressed as:

$$N_{eq} = \sum_{j=1}^{i-1} I_N(V_j)$$

$$I_N(V_j) = \begin{cases} 1 & \text{if } -\rho < \frac{V_j}{V_i} - 1 \leq \rho \\ 0 & \text{otherwise} \end{cases} \quad \text{Equation 6.9}$$

Phrased differently: the increase in damage at any instance will depend on whether the PGV is similar (Eq. 6.7a) or comparably larger (Eq. 6.7b) than the PGVs of events in the sequence up until that moment. If it is similar, then

damage can be computed by evaluating the surrogate function for $\Psi(\sim)$ considering the difference between a homogenous sequence of PGVs with the number of similar events and the same sequence with a number of similar events plus one. This means that $\Delta\Psi$ is indeed the difference in the homogenous sequence for an increase in the number of events by exactly one. If the PGV is much larger than earlier events, then the increase in damage will be the difference between that of 2 large events and 1 event with the previous largest PGV. The entire process is schematised in Figure 6.3.1.

The value of p is somewhat arbitrary. What constitutes similar events and when can an event be considered large in comparison to earlier events? From an iterative calibration process considering the results of the next two sections, good agreement was found by setting $p=0.25$.

Uncertainty

Equation 6.4 also contains an uncertainty term. As was determined in Chapter 5, the uncertainty is best characterised as a function of the value of PGV. Small values of PGV carry a smaller uncertainty than larger values. This relationship, a generalised extreme value distribution (see Section 5.3.2), is maintained. However, adding this uncertainty at every iteration of $\Delta\Psi$ would lead to an unreasonably large total uncertainty. For this reason, the uncertainty term is weighted by its position in the sequence. The first value would receive the complete uncertainty. For the second value, only half of the new uncertainty is added; for the third, only a third; and so on:

$$\epsilon_{Total} = \frac{\epsilon(V_1)}{1} + \frac{\epsilon(V_2)}{2} + \frac{\epsilon(V_3)}{3} + \dots + \frac{\epsilon(V_N)}{N} \quad \text{Equation 6.10}$$

The last value in the series will receive a relative small contribution of additional uncertainty. This is reasonable since a large amount of uncertainty has been considered already.

This means also that the influence of a large earthquake will be different if it occurs early or later in the series. Towards the beginning, the uncertainty might receive a larger value while at the end, the value will be smaller. This is also reasonable since the evaluation of the surrogate function also depends on the initial value of Ψ (in this case Ψ_{i-1}). Towards the end of the series, this value will have been affected more by the accumulated uncertainty which will lead to a larger increase without the need of considering the specific uncertainty term corresponding to the large event at the end.

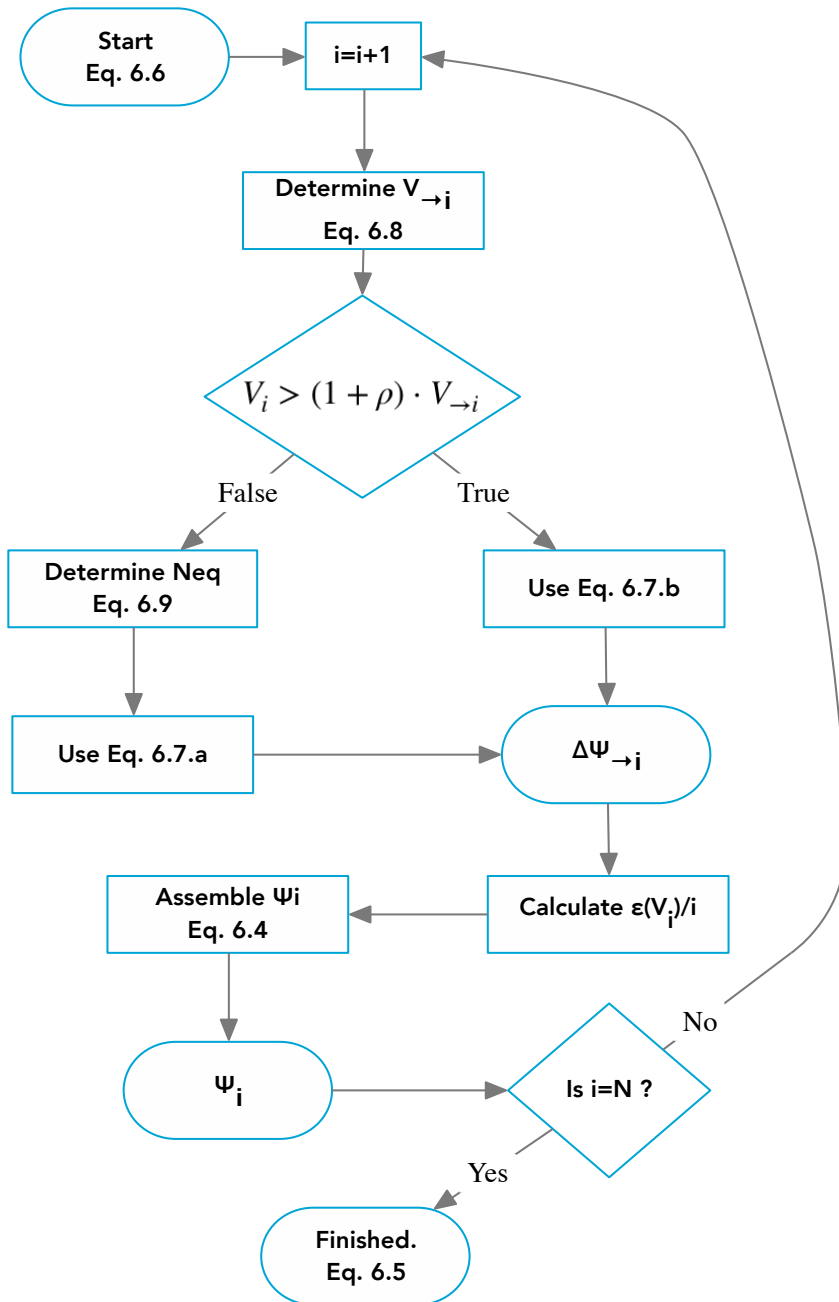


Figure 6.3.1. Flowchart of the DAF procedure.

Equations (Reprised & Reordered)

$$V = \{V_1, V_2, V_3, \dots, V_i, \dots, V_N\} \quad \text{Equation 6.6}$$

$$V_{\rightarrow i} = \max[V(1 \dots i - 1)] \quad \text{Equation 6.8}$$

Equation. 6.7 Parts a & b

$$\Delta\Psi_{\rightarrow i} = \begin{cases} \Psi(\Psi_{i-1} | V_i | N_{eq} + 1 | \sim) - \Psi(\Psi_{i-1} | V_i | N_{eq} | \sim) & \text{if } V_i \leq (1 - \rho) \cdot V_{\rightarrow i} \text{ (a)} \\ \Psi(\Psi_{i-1} | V_i | 2 | \sim) - \Psi(\Psi_{i-1} | V_{\rightarrow i} | 1 | \sim) & \text{if } V_i > (1 + \rho) \cdot V_{\rightarrow i} \text{ (b)} \end{cases}$$

$$N_{eq} = \sum_{j=1}^{i-1} I_N(V_j)$$

$$I_N(V_j) = \begin{cases} 1 & \text{if } -\rho < \frac{V_j}{V_i} - 1 \leq \rho \\ 0 & \text{otherwise} \end{cases} \quad \text{Equation 6.9}$$

$$\epsilon_{Total} = \frac{\epsilon(V_1)}{1} + \frac{\epsilon(V_2)}{2} + \frac{\epsilon(V_3)}{3} + \dots + \frac{\epsilon(V_N)}{N} \quad \text{Equation 6.10}$$

$$\Psi_i = \Psi_{i-1} + \Delta\Psi_{\rightarrow i}(\sim) + \frac{\epsilon(V_i)}{i} \quad \text{Equation 6.4}$$

$$\Psi = \{\Psi_1, \Psi_2, \Psi_3, \dots, \Psi_i, \dots, \Psi_N\} \quad \text{Equation 6.5}$$

Example Histories with DAF

The application of the DAF is discussed later on in section 6.3.4 after comparisons and validation in sections 6.3.2 and 6.3.3. However, a few examples of Ψ sequences determined with the DAF are presented here. Figure 6.3.2 shows a sequence of PGV as determined for one location in Appingedam using GMPEs (Bommer et al. 2019). This sequence is deterministic using the PGV associated with the 75% probability. To consider a distribution of PGV, a MonteCarlo simulation of probable timelines can be performed; see Section 6.3.4.

The sequence leads to an accumulation of damage. Larger events are linked to a noticeable increase in damage. For example, the event with epicentre in Appingedam in 2009 resulted in a $\Delta\Psi$ of about 0.2. A similar event in 2015 led to a smaller increase. In Loppersum, significantly more events with a PGV larger than 2 mm/s have been experienced; the values of PGV have also been higher. This also results in a higher value of Ψ as depicted in Figure 6.3.3 with a likely $\Delta\Psi$ higher than 1.

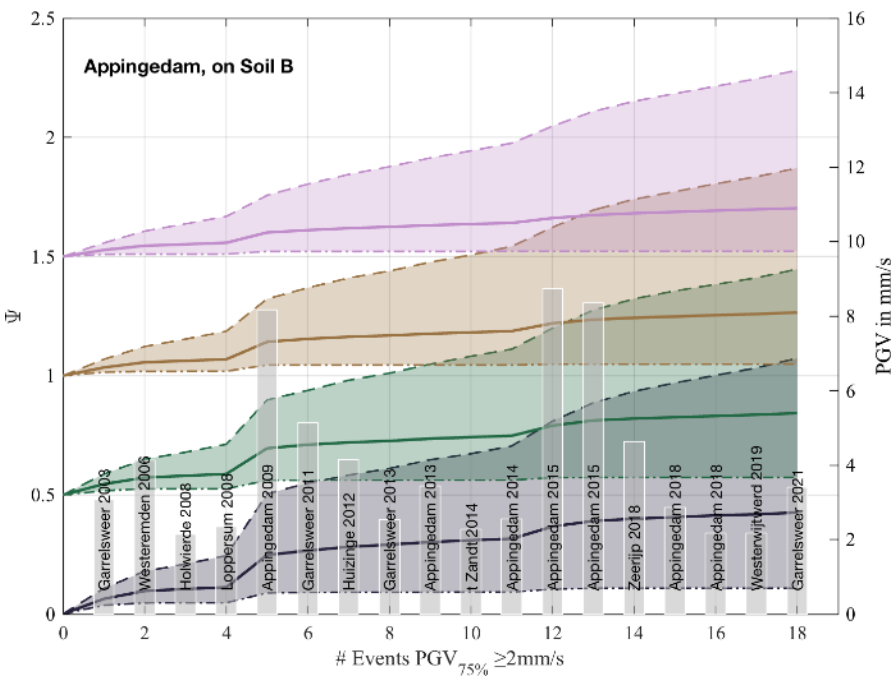


Figure 6.3.2. An example history for the sequences of PGV measured in Appingedam. Four initial values of Ψ are considered ranging from 0 to 1.5. The expected accumulated Ψ is marked with a solid line and the confidence interval 5-95% is highlighted for every case. Analysis based on wall of fired-clay brick masonry.

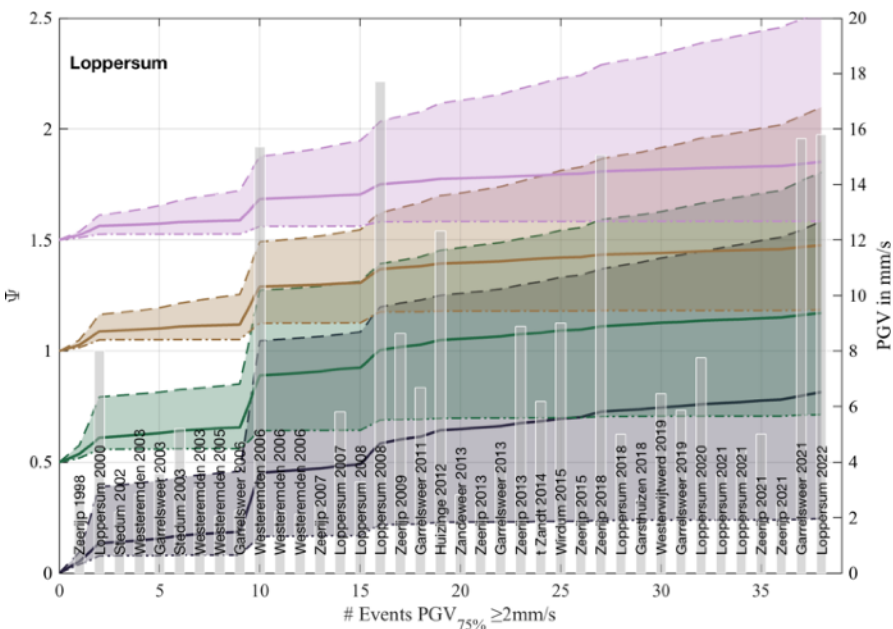


Figure 6.3.3. Similar to Figure 2 but for the town of Loppersum. See Figure 6.0.

6.3.2. Comparison of DAF against Model Results

Chapter 5 describes the learnings from about 3500 FEM models that were run to analyse the influence of various parameters. The effect of parameters such as initial Ψ value, façade stiffness, soil type, earthquake record, distance and PGV, and number of subsequent earthquake vibrations, on the final value of damage, as measured by Ψ , was examined. These models were then employed to derive fragility curves to estimate the probability of light damage at increasing PGV intensity. The focus of Chapter 5 was not placed, however, on assessing the effect of repetition. This was further studied, instead, in section 6.2. Here, additional models were considered including heterogeneous sequences of PGV. Based on this pool of data, the DAF has been formulated. A stricter comparison, with the goal of validation, is presented in this subsection. In this manner, the behaviour of the DAF is evaluated against homogeneous and heterogeneous sequences of vibrations.

Figure 6.3.4 shows the mean increase in damage ($\Delta\Psi$, from the initial Ψ for the models with pre-damage to the final Ψ) for all the models segregated by the number of repeated identical PGVs; the graphs include the 25% to 75% quantile (or from the end of the first to the third quartile). It can be observed that damage increases as the repetitions of the PGV increase; moreover, larger PGVs lead also to a larger increase in damage and a larger relative influence of the repetition effect. It can also be seen that the higher PGVs also produce a greater spread in the mean with the larger interquartile areas. These differences arise because different initial conditions, varying soil, facade type, and material strength also lead to a distinct $\Delta\Psi$ for every model. The middle column of graphs shows the same model parameters evaluated with the DAF function. In general, the observed trends are well reproduced by the DAF but the spread in the results is lacking, especially for the low PGV values. This is because the uncertainty parameter ε is a key component of the DAF, especially because it is PGV-dependent and its mean is not zero. See equations 5.8 and 6.4. When a sufficient number of samples is simulated to reproduce the FEM parameter combinations, as is depicted in the third column, the interquartile spread has a better agreement with the FEM graphs on the first column of curves. However, the DAF appears more conservative with an interquartile range that achieves higher values compared to the FEM results.

This is further explored in Figure 6.3.5, which includes the results of the heterogeneous models. The first three rows of graphs show essentially the same data presented in Figure 4. Here, the larger spread of the FEM models is observable. This is also related to the size of the data: the lower number of

observations from the FEM models may present a larger spread than what a larger population would show. The DAF data comprises thousands of points.

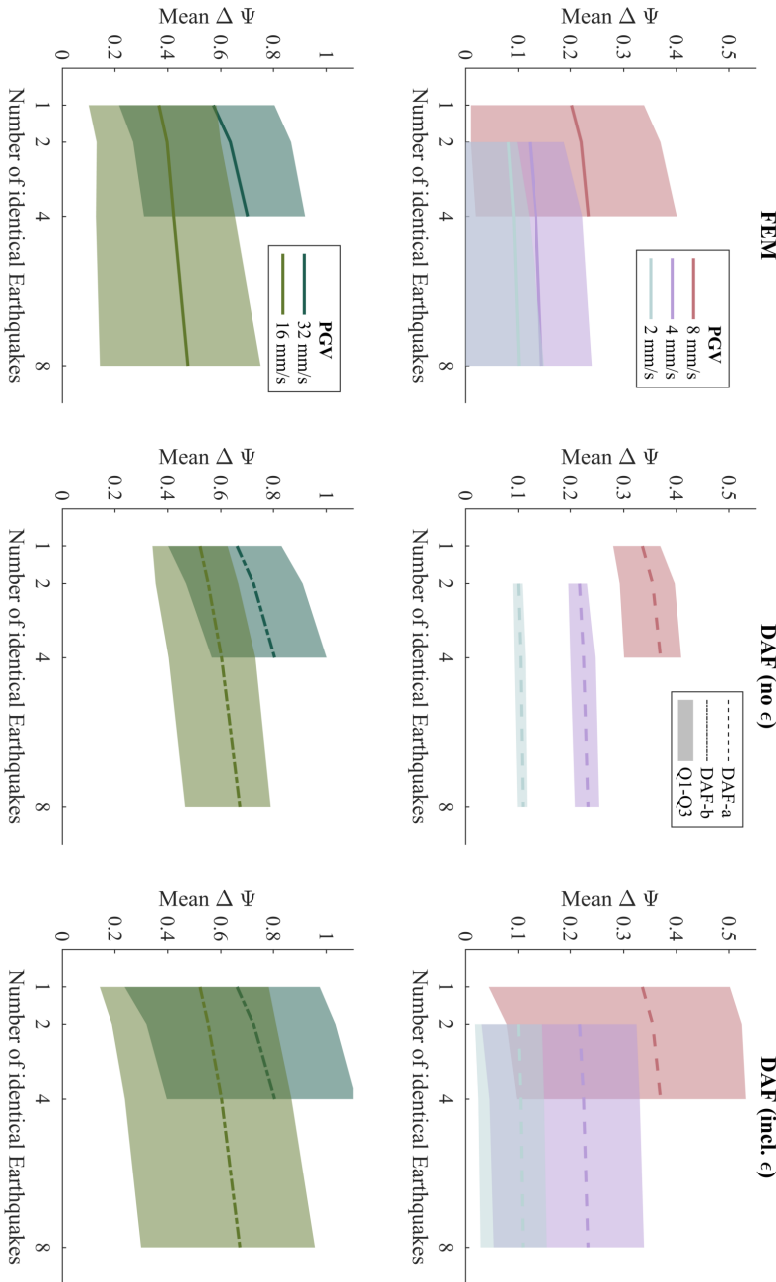


Figure 6.3.4. Mean increase in damage ($\Delta \Psi$) from the 3572 homogenous models and their reproduction using the DAF, without and with its uncertainty parameter ϵ . Results based on FEM results from Figure 5.2.4.

The last row of Figure 6.3.5, with many more bars, includes the heterogeneous models. Here, the difference between 1x8+1x16 and 2x16 can be observed. However, this comparison is unfair, since the 2x16 group includes many more models with variations. A better comparison is done later in Figures 6 and 7. Nonetheless, the graph serves to compare the FEM results against the DAF estimation. The mean $\Delta\Psi$ of the FEM models is higher than the mean produced by the DAF, but the interquartile boxes are very much in agreement. This is because the FEM results seem skewed, with a mean close to the upper 75% quantile. This is probably the result of the limited number of models and the specific parameters chosen for these.

Figure 6.3.6 compares the FEM and DAF results employing only the parameters present in the heterogeneous models, so only Westerstjwerd records and only initial Ψ of 0.5 and 1, for example. The number of FEM models reduces but the comparisons are straightforward. The graph shows for example, that indeed, 1x16 outputs a smaller damage increase than 1x4+1x16. The plots also show a good agreement between the sequences observed from the models and from the DAF when looking at the interquartile boxes, though the means of the FEM models seems higher. This is again visible in Figure 7, which has the data neatly arranged to show the final sequences present in the models. This figure emphasises the key observations from the FE models and which are reproduced in the DAF:

- repeated earthquakes lead to additional damage,
- the higher the PGV, the larger the damage increase,
- in a history with low PGV values, a relatively large value leads to a stark increase,
- in a history with similar PGV values, an additional event leads only to a small increase,
- the final values of damage between a large and a small, and a small and a large PGV values are similar (see 32+16 and 16+32).

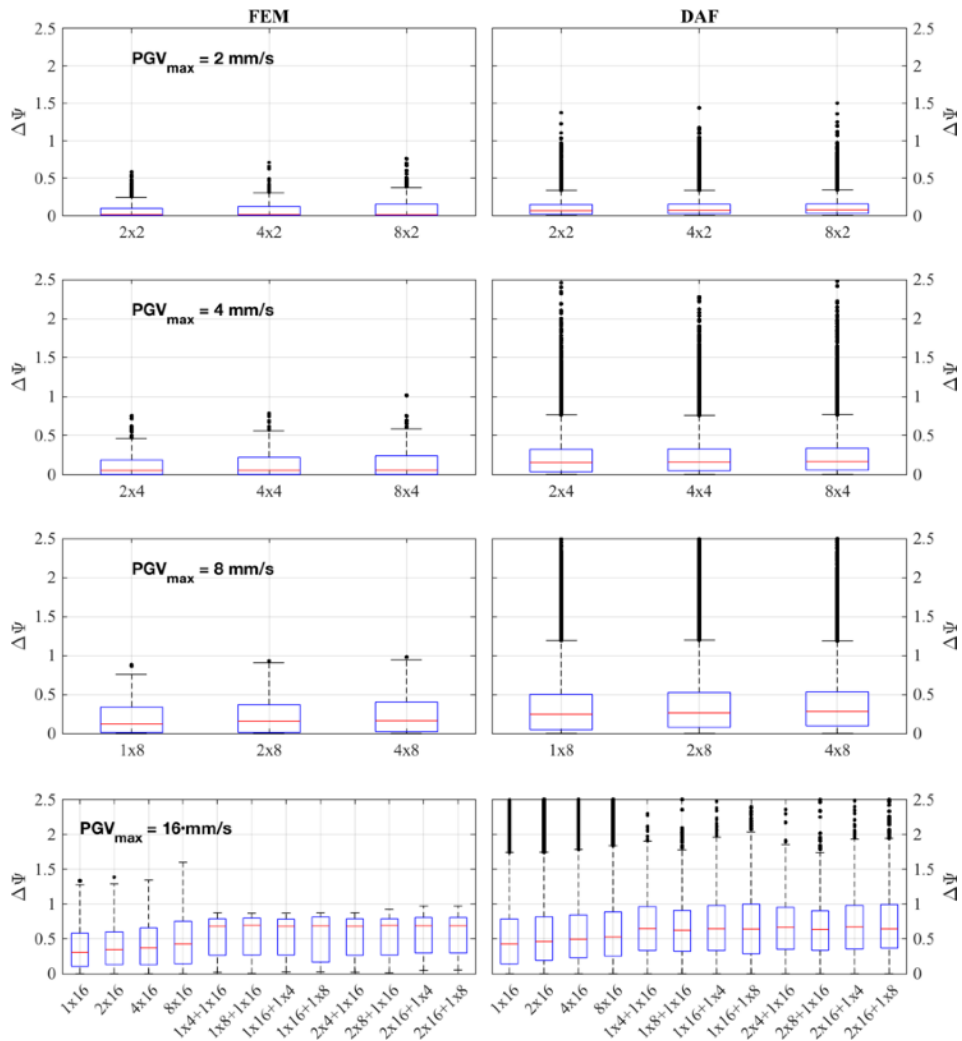


Figure 6.3.5. Box plot of the various combinations segregated by maximum PGV. The mean is shown with a horizontal red line, the blue box encompasses the second and third quartiles (25-75%) and the lines show approximately the 1% to 99% confidence range of results (using the standard deviation of a normal distribution). Values outside this range are considered outliers and appear as dots.

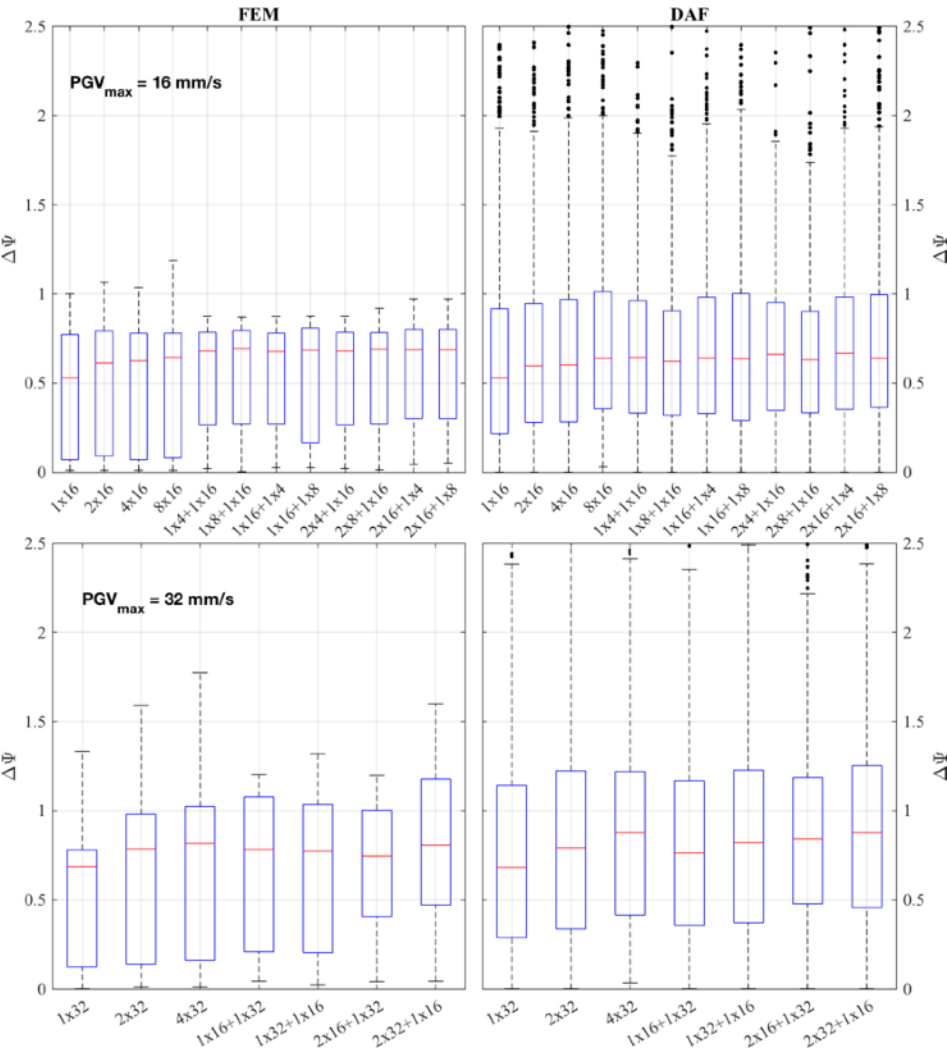


Figure 6.3.6. Similar as Figure 2 but only matching model parameters present in the new models.

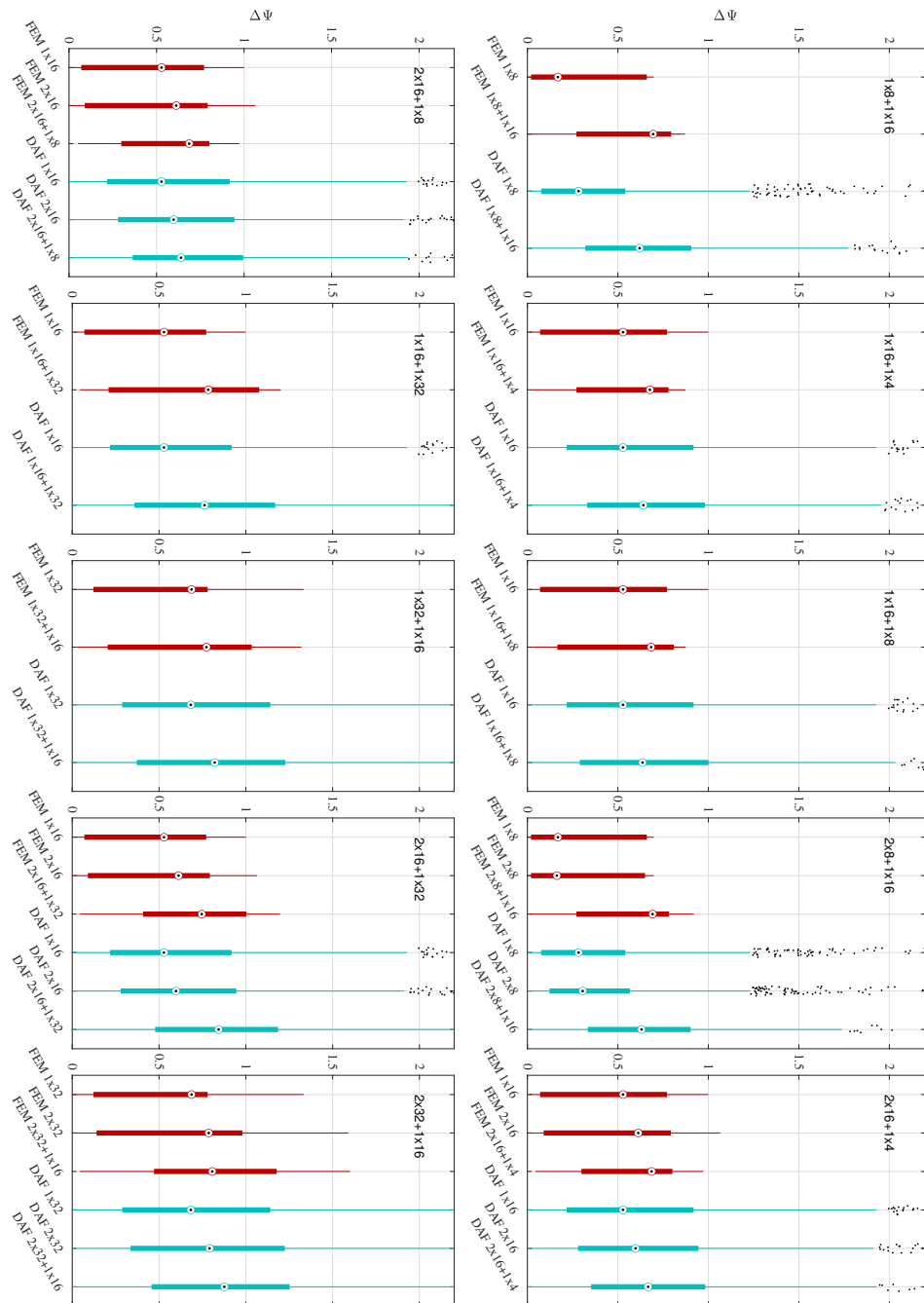


Figure 6.3.7. Similar as Figures 2 and 3 but for specific combinations with the related preceding earthquakes extracted from the data and displayed in sequence.

6.3.3. Comparison of DAF against Experimental Results

It is difficult to validate the DAF on the basis of experimental results because of several reasons. First, the experiments repeated displacements while the DAF evaluates the results of repeated forces. The earthquake vibrations applied at the base of the structures represent an acceleration which translates to inertial forces. Similar events, with a similar frequency content, will result in similar induced forces. This assumes that the progression of damage does not modify the dynamic response of the structure too much - though this effect is considered in the FEM models. Regardless, the experiments were displacement-controlled, and could not have been force-controlled since cracking leads to non-linear behaviour that would have resulted in a loss of control. This means that, to compare the DAF behaviour to that observed in experiments with repetitions, an assumption must be made: that the increase in damage while repeating force-based events should be similar to the decrease in force while repeating displacement-based actions.

The experiments observed a clear relationship between drift (or displacement) and damage. This comparison is presented in Figure 6.3.8 for the walls; the reduction in force is relative to the initial force at each step in the same manner that the increase in damage is presented relative to the damage at the first repetition. One can observe that the behaviour between the experiments and the DAF is similar, with a decreasing slope as repetitions increase.

Nonetheless, a true quantification remains difficult. This is partly because the experiments also showed an increase in damage simultaneously with the reduction in force. However, the reduction in force is also visible for the spandrels. In this case, damage was kept constant since the spandrels were controlled by the width at the crack-mouth; see section 3.1. Consequently, the comparison should be more direct, but the spandrels represent a smaller portion of masonry and focused on a single crack. This contrasts with the objective of the DAF which is meant to represent larger masonry components with various cracks comprised by Ψ .

The spandrels, shown on the last row of Figure 6.3.8, are segregated by step, which in their case, is related to the initial force before the reduction. This is more comparable to the increasing PGV employed for the DAF graphs. Hence, one can also observe that the force reduction, and increase in damage with the DAF, are greater for the larger steps or PGVs.

Second, the experiments included a large number of repetitions. In most cases thirty repetitions were applied to see a stabilisation in the force reduction. In total, about three hundred repetitions happened during the tests. Yet, thirty

repetitions of similar earthquake events is already a large amount of repetitions. The larger number of repetitions was envisioned to consider that vibrations contain several effective cycles. Nevertheless, this disparity obfuscates the comparison.

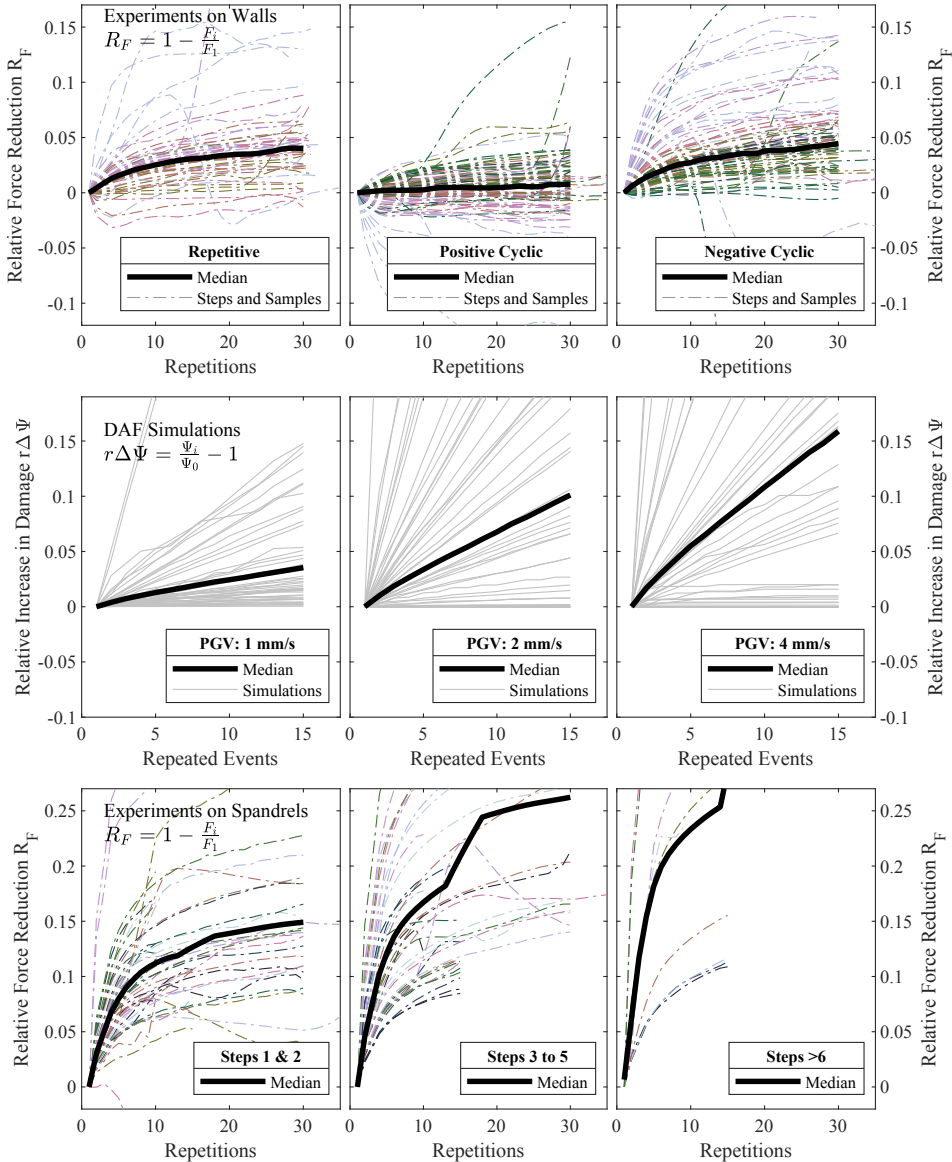


Figure 6.3.8. Comparison of force reduction during wall experiments with the repetitive protocol against expected damage increase evaluated with the DAF for various PGV values. Bottom row, force reduction for the various steps of the spandrel tests.

A third difficulty rests on the fact that the DAF has been mainly formulated to evaluate heterogeneous sequences of PGVs. In the experiments this effect is limited but not entirely absent. Indeed, the way the loading protocols were formulated and arranged one after another reveals the same behaviour from the FE models, also reproduced by the DAF. First, the repetitive protocol considered five steps in a one-way cyclic tests. Then, the cyclic protocol applied seven steps in a two-way cyclic fashion. The first five steps of the cyclic protocol see little force reduction. This is analogous to the observation that events, with a PGV smaller than what has occurred before, do not lead to a damage increase. The last two steps, however, do lead to a noticeable force reduction; which compares to larger PGV events increasing damage even if other events have happened before.

This effect is further reflected during the tests with the asymmetric loading protocol. Unlike the repetitive and cyclic protocols, which applied symmetric and regular cycles during each step, each step of the asymmetric protocol comprised sub-steps more alike the various cycles within an earthquake record; see section 3.1.1. The larger cycles within the sub-step led to a reduction in force, but the smaller cycles did not. The overall reduction is more inline with what is predicted by the DAF. The fewer asymmetric steps (but including sub-steps) represent the loading by the vibrations more loyally.

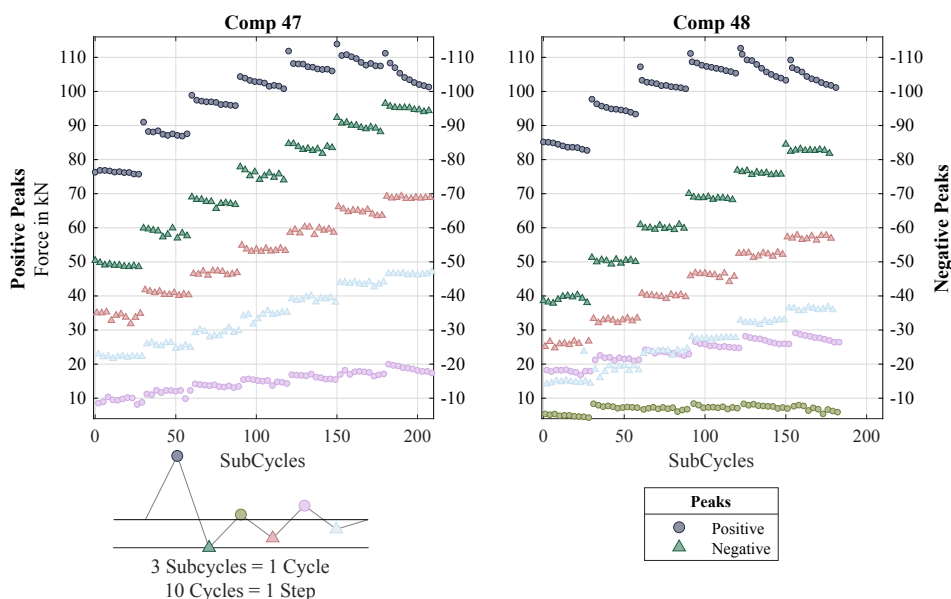


Figure 6.3.9. Force reduction during two wall tests with the asymmetric loading protocol.

In conclusion, a direct comparison to investigate the behaviour during repetitions between the experiments on walls and spandrels, and the damage evolution predicted by the Damage Accumulation Function is problematic. Nevertheless, the effect of repetition observed in the experiments is reflected in the results output by the DAF.

6.3.4. Application: Probability Maps for Accumulated Damage

In Chapter 5, fragility maps were produced. These combined the hazard, represented by its distribution of the PGV, with the response of the buildings, depicted by their fragility curves. The DAF allows a similar procedure. In this case, the result is a set of maps that include the history of PGV and their compounding effect on damage of the masonry buildings. Both the PGV values and the vulnerability of the buildings can be represented probabilistically. The spatial and temporal distributions of the events are depicted in the following map, Figure 10.

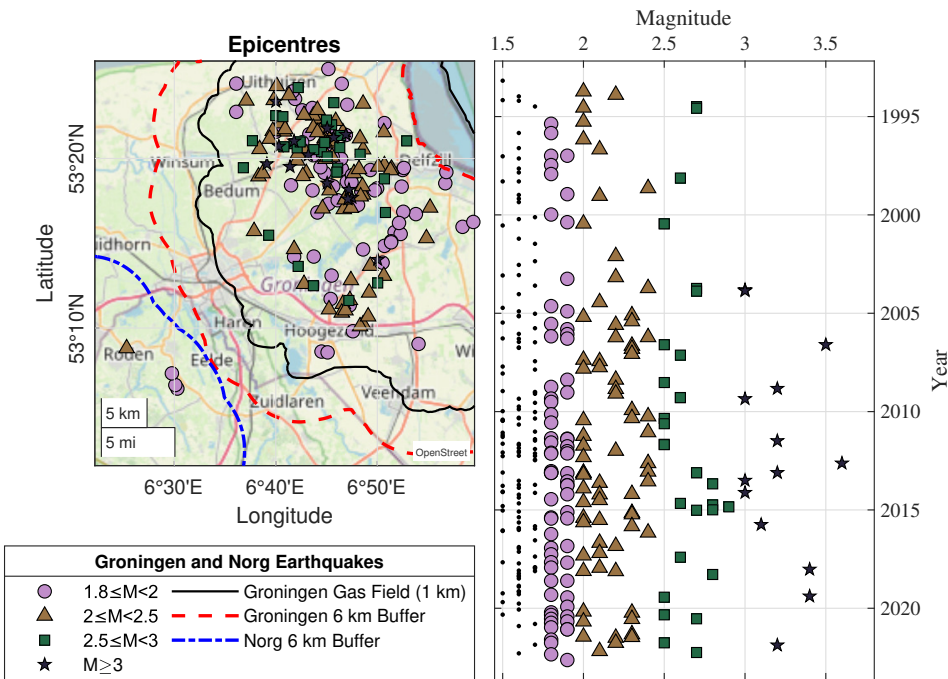


Figure 6.3.10 Overview of earthquake epicentres in the northeastern region. Right, magnitude of the events over time.

The map can be divided into cells. For each cell, the history of PGV can be determined based on the epicentre and magnitude of each event using ground motion prediction equations; for this example, the empirical formulation of GMPEs by Bommer et al. (2019) are employed. The result is displayed in Figure 6.3.11 for a few combinations of initial damage, Ψ_0 , and final damage in terms of probability contours. The distributions for the other parameters, such as the material strength, or the soil type, are sampled as in Section 5.4.1.

The contours encircle the areas for which the probability of the specified $\Delta\Psi$ is at least $1 \cdot 10^{-4}$ (or 1 in 10'000). Towards the centre north of the gas field, the induced seismicity has caused the most events and with the highest magnitudes, as was presented in Figure 10. This is also associated with a very high probability of displaying visible damage ($\Psi=1$) for initially undamaged masonry structures. Most of the buffer zone of the gas field is computed to have a probability of at least 0.1% of displaying visible damage accumulated over the past three decades of seismicity. In contrast, only the very centre of the region is determined to exhibit a similar probability of having exceeded DS1 ($\Psi \geq 2.5$). If the masonry walls considered, already presented visible initial damage ($\Psi_0=1$), then the region enlarges. In this case, most of the buffer zone, excluding the southeastern cities of Veendam and Winschoten, displays a probability of 1:10'000 of reaching or exceeding $\Psi \geq 2.5$.

To evaluate the contribution of considering the accumulation of damage with the DAF, a comparison is drawn against the maps produced in Chapter 5. Figure 5.4.4 presents the probability contours for three important events; the event of Huizinge of 2012 is reprised in Figure 6.3.12 for the same $\Psi \mid \Psi_0$ as in Figure 6.3.11 thus expanding on Figure 5.4.4. This allows a direct comparison for the effect of the most influential event against that of the entire history of events.

First, the shape of the contours from the single event is mostly circular as the propagation in the GMPE depends on the distance to the epicentre. For the DAF map, multiple events are considered with their own epicentres. Second, the outer probability contours from the single event encircle slightly smaller regions. This means that considering the accumulated effect of multiple events leads to higher probabilities; this is an expected result. Third, the contours towards the centre of the region are much larger for the DAF case. This is because of the larger number of events and the fact that their epicentres are spread out thus modifying the shape of the contours.

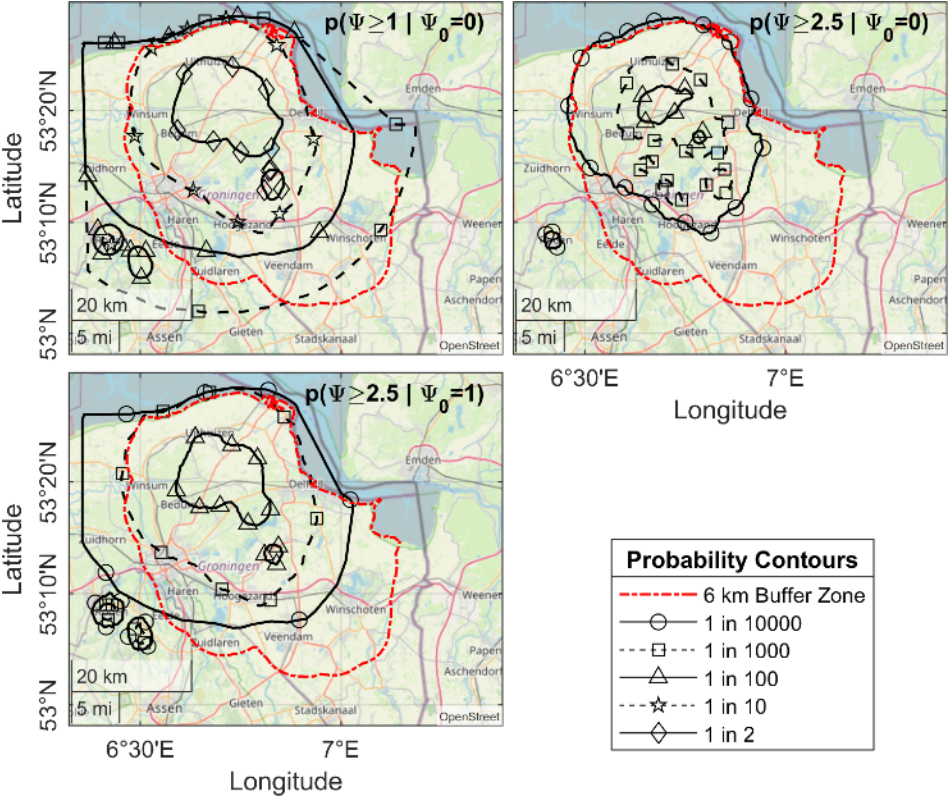


Figure 6.3.11. Probability contours for the accumulation of damage due to a history of events.

For a specific location, the DAF can lead to a significant influence. This is the case for places close to the centre of the region but relatively far from the specific event of Huizinge. In Delfzijl, for instance, the probability of displaying visible damage is less than 1% in the case of Huizinge, but considering the entire history of events, this probability rises to 10%. However, the probability of exceeding $\Psi \geq 2.5$ is virtually unaffected regardless of the initial damage condition. For this case, the single, large event plays a more important role than the accumulated effect of multiple smaller events.

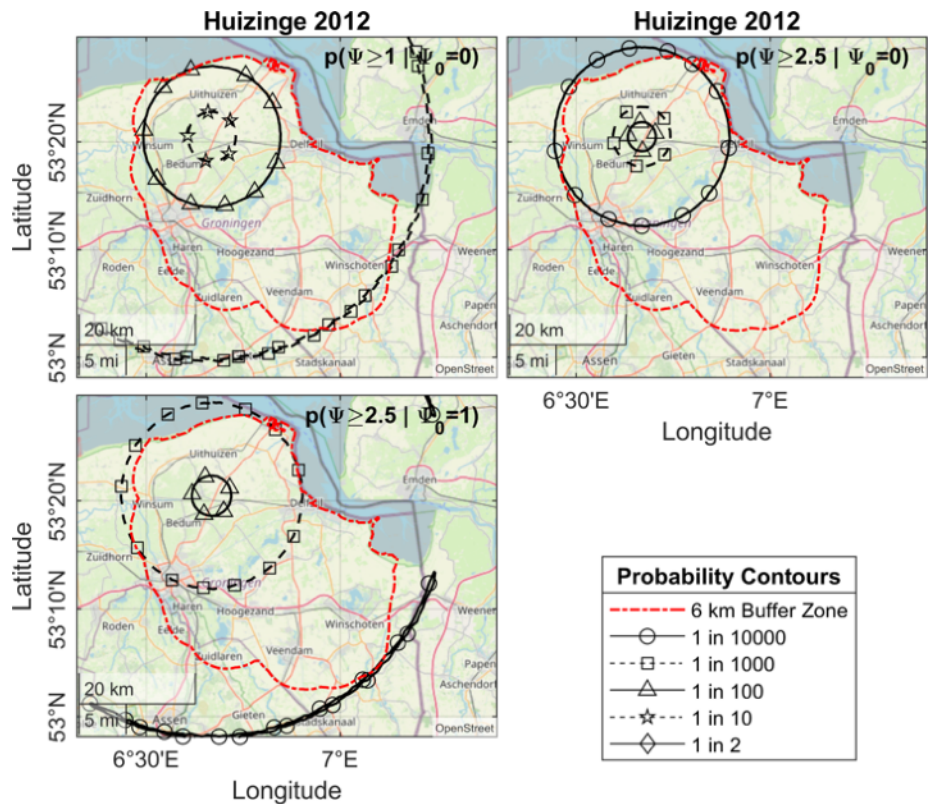


Figure 6.3.12. For comparison against the DAF map, which considers the accumulation of damage due to repeated events over thirty years, and a fragility-based map (Chapter 5) for the single event of Huizinge of August of 2012.

6.4. Concept of Damage Hastening

When observing the accumulation of damage due to a specific hazard, one should not neglect the ongoing effects of other hazards. In this work, an initial condition, Ψ_0 , has been employed to evaluate the aggravation of damage due to earthquake vibrations. However, the hazard that caused Ψ_0 may still be acting on the structure. Settlements, for example, often take place over many years. During this time, damage increases. Seasonal temperature effects, for instance, can accumulate damage over several seasons, capitalising on the effect of repetition. Other hazards, like material-induced shrinkage, only affect structures at the beginning of their service life. Over decades, masonry buildings subjected to the weathering of wind, sun, and rain, will require repair to replace affected units and repoint weakened mortar to prevent further damage such as that caused by frost-thaw cycles on wet masonry, which can lead to visible cracks.

Preventive maintenance indeed, is not unique to masonry structures. Steel elements must be recoated and painted to avoid corrosion, while timber needs to be treated regularly to prevent rot. Concrete structures suffer from other problems.

One can argue that buildings naturally display damage over time. This is the essence for the need of maintenance. Masonry buildings on soft soils will inevitably display visible cracks as they move, together with the soil, throughout the seasons. In this context, extraneous hazards, like earthquake vibrations, do not cause damage but **aggravate**, instead, existing damage. They accelerate the development of damage that would eventually have appeared on the structure without the hazard regardless. It is this acceleration of damage, herein denoted as 'damage hastening' that should be quantified.

This section does not attempt to measure the effect of earthquakes using their damage hastening. This would first require to have a thorough understanding of the autogenous progression of damage in masonry structures, which would comprise a study on its own. The section provides instead a reflection on the true damage aggravation effect of earthquake vibrations and a methodology to determine damage hastening.

6.4.1. Definition of 'Hastening' in the Context of Damage

Damage hastening can be defined as the reduction in the time that a structure would show a specific level of damage because of the influence of a particular hazard. When speaking of hastening, there are usually two or more hazards involved, though one can also consider a change in a single hazard. In the case of a multi-hazard, the first hazard causes a progression of damage and the second hastens this progression. For example, a masonry structure on a soft soil will likely experience settlement damage over time; let us assume that after five years, the building would display a $\Psi=1$. If this building is located in a region of seismicity, it will be affected by this second hazard with earthquake vibrations. Because of this additional hazard, the building displays $\Psi=1$ after only three years. A $\Psi=1$ has been hastened by two years; this represents a speed up of about 1.7x.

A similar example can be reversed. A certain building next to a road will develop a Ψ of 2 in ten years due to traffic-induced vibrations. The construction of a new neighbouring building can lead to settlements which take place in the first five years of the new construction. After the five years, the building has developed $\Psi=2$; this results in a hastening value of 2x as the time required to progress to the same damage has halved. If the new building is erected after the original building has already been subjected to five years of vibrations, the effect might be different. The progression of damage due to the traffic vibration is not likely to be linear. Also, the effect of the settlements on a certain value of Ψ_0 will change.

Indeed, because evaluating hastening considers two alternative timelines, one with and without the affecting multi-hazard, it is always based on predictions for both scenarios. In these predictions, it is difficult to determine the progression of damage from the first hazard and the effect of the second hazard. Moreover, both hazards could continue acting together and thus the effect of the second hazard will affect the progression of damage from the first hazard.

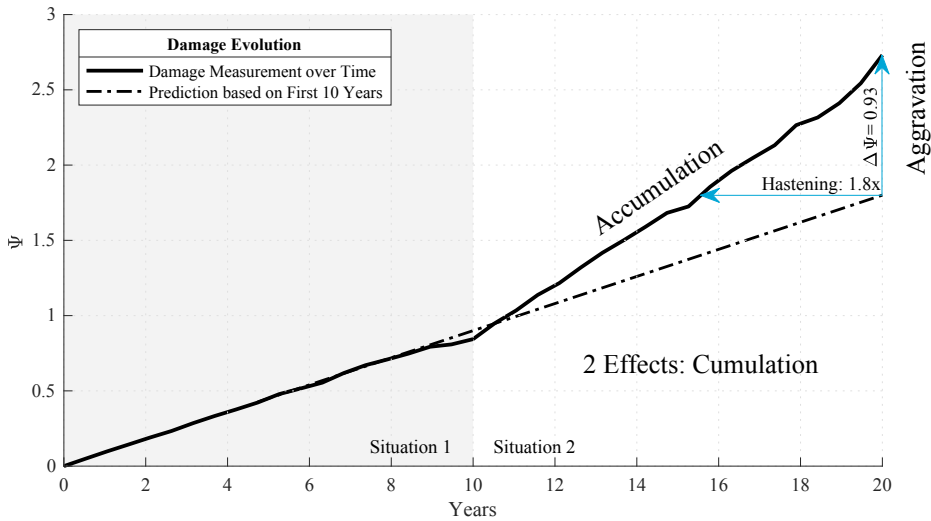


Figure 6.4.1. The damage evolution of an example building over 20 years.

A first example is provided in Figure 6.4.1. Here, two situations are considered. This could represent the case of a masonry building settling under its own weight. After ten years, an expansion is made which accentuates the settlement and increases the rate in which damage appears. The renovation could be considered as the second hazard. Similarly, the figure could represent a single hazard but its intensity is changed after 10 years. For example, traffic vibrations are intensified as a result of changes in the pattern of traffic.

In this fabricated example, the evolution of damage during the first period is linear. This makes it easy to conceive an empirical prediction for the absence of the second hazard or the change in the second period by extrapolating the linear trend. The difference between the predicted final damage without the contribution of the second hazard can be computed; this is the value of $\Delta\Psi$. One could assess the influence of the second situation by observing $\Delta\Psi$; this is also performed in Chapter 5. However, the concept of hastening emphasises that damage may be accumulated over time and the effect of repetition could play a role. For this example, the second hazard hastens damage, observed at the end of the 20-year period, by 1.8x.

A second example considers repeated earthquake vibrations. This is computed using the DAF with a real history of earthquake events; see Figure 6.0. The progression of damage without the earthquake hazard is idealised as a linear trend between $\Psi_0=0.5$ and $\Psi=1.5$ after thirty years - the cause could be related to settlements. Over this time, the earthquake hazard aggravates the initial damage, accumulating additional damage until a $\Psi=1.5$ is reached after only 20 years. This corresponds to a hastening of 1.7x. Damage continues

increasing until $\Psi \approx 2.3$ is reached, resulting in a damage increase of 55%. In this simulation, before the effect of each repetition is computed with the DAF (flowchart of Figure 6.3.1), Ψ is adjusted to consider the linear increase given by the first hazard. No effect on the damage caused by the first hazard is assumed because of the damage increase exerted by the hastening hazard.

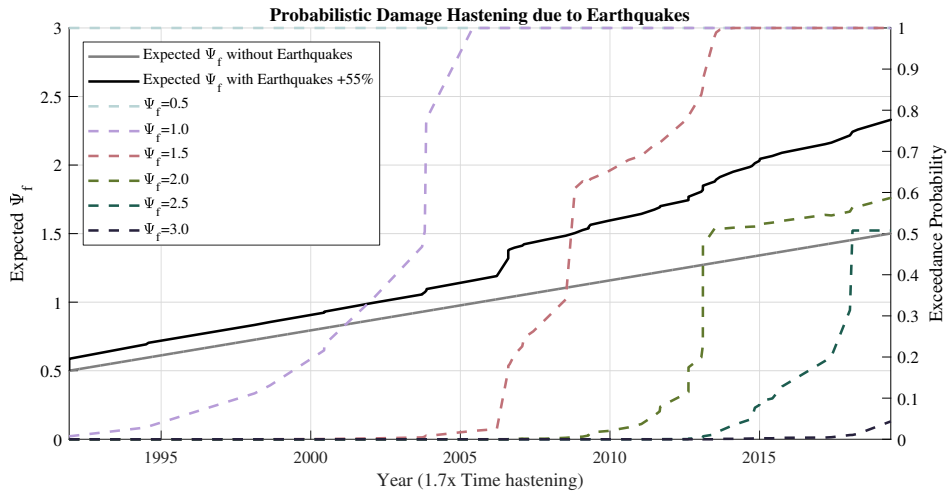


Figure 6.4.2. Example of damage progression for a building in Loppersum with a $\Psi_0=0.5$ that would have reached $\Psi=1.5$ after 30 years. Because of seismicity, the final expected damage is increased by 55%. The exceedance probability curves are on the right axis.

Since the DAF considers a term of uncertainty, its predictions are probabilistic; see Figure 6.3.3. The dark line in Figure 6.4.2 corresponds to the expected value of Ψ , but it is possible that Ψ is higher or lower, though never lower than the damage progression bound by the first hazard. The exceedance probability of specific values of Ψ is included in the figure. While the expected Ψ at the end of the period is about 2.3, there is a 5% probability that a value of $\Psi=3$ has been reached or exceeded.

Damage hastening can be used as an additional or alternative metric to quantify the effect of a hazard. This is especially useful and relevant if the hazards considered lead to an accumulation of damage over time. The hastening values can be employed directly when determining when to schedule maintenance or interventions.

6.4.2. Time as the Hazard

In the definition of damage hastening, time plays a crucial role. Time itself cannot be a hazard, but given specific scenarios of multi-hazards, the passage of time will lead to damage. As such, time can be placed on the hazard axis instead of, for example, PGV.

Because of its effects on buildings, the Dutch government considered different scenarios of gas production to reduce seismicity. The change in seismicity would occur over time and lead to a different number and magnitude of events in the future. Every scenario would convey a distinct seismicity. Hence, each scenario would be associated with a different progression of damage on masonry buildings. This is a problem for which the DAF is ideally suited.

Let us consider three different scenarios of gas production which in turn lead to different yearly rates of events. The magnitude of the events is also affected. The physical relationship between the dynamics of gas production throughout the gas field and the resulting seismicity is a topic on its own which cannot be contemplated here. Instead, reasonable assumptions are made regarding the yearly rate of events as per Table 6.4.1 for three imagined scenarios. The statistical distribution of past events with a magnitude greater than 1.5 is employed to determine a mean yearly rate of events. This mean yearly rate is reduced for two of the scenarios.

Table 6.4.1. Three scenarios for potential future seismicity distinguished by their mean yearly rate of events.

Scenario	Initial Yearly Rate (year 0)	Final Yearly Rate (year 50)	Decrease
Continued	11.5	11.5	-
Reduced	11.5	$\frac{1}{2} \cdot 11.5$	linear
Stopped	11.5	0	linear

The distribution in the magnitude of the events is unaffected for this example. Similarly, the spatial distribution of the epicentres is kept identical to the statistical distribution of past years and a correlation with the magnitude is drawn. Whether these assumptions are realistic is not investigated.

Figure 6.4.3 presents the past events and a histogram of their magnitude. To aid in visualising a Weibull probabilistic distribution, magnitude values from 0 upwards are included. However, since the focus is on the larger events, an adjusted curve, fit to the tail end of the distribution, is considered. The number of events with a magnitude of at least 1.5 is counted per year in the bottom of the figure. The mean trend in the period 1990-2023 is about 11.5 events/year.

Based on the three scenarios of Table 1, the projection of the yearly rate is drawn.

The second part of the figure considers the spatial distribution of events. Based on the historical epicentres, two beta distributions are fit to the latitude and longitude coordinates of the events. The distributions can be adjusted based on the magnitude of the events since the largest events have been more clustered.

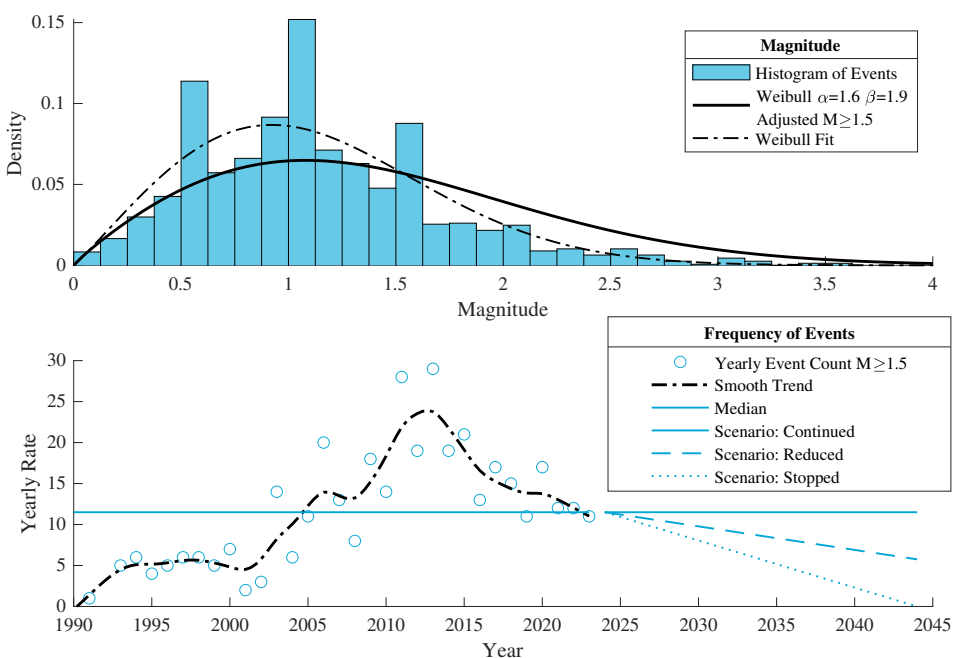


Figure 6.4.3a. Overview of the Weibull distribution for the Magnitude of events, the correlated latitude and longitude for the epicentre of events, and the frequency or yearly rate of potential events. These are based on statistical analysis of past events; updated March of 2024.

A simulation to generate a timeline of events is performed. Using the yearly rate, it is possible to sample, on a daily basis, whether an event will occur. If it does, its location and magnitude are sampled from the aforementioned distributions. For each of the scenarios, hundreds of timelines are generated in order to produce a good probabilistic depiction of the scenario. For every timeline, an evolution of damage is calculated at given locations using the DAF as in Section 6.3.1. The timelines of each scenario are then combined to generate fragility curves where the number of years appears on the horizontal axis. This comparison appears in Figure 6.4.5 for the location of Loppersum, exemplified in this section.

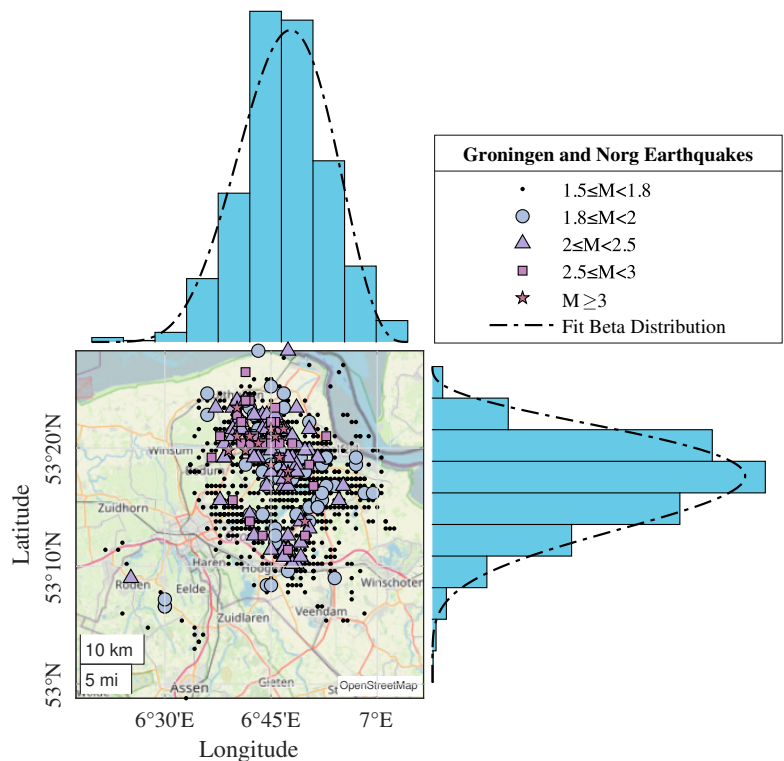


Figure 6.4.3b. Distribution of epicentres of historical events.

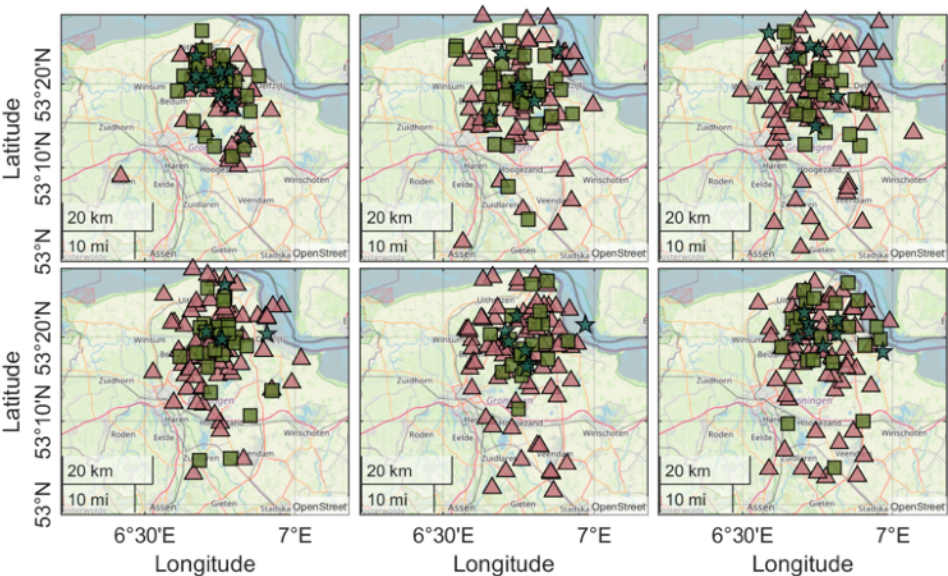


Figure 6.4.4. Comparison of the historical timeline (top left) and five simulated timelines of events.

The curves reveal the differences in exceedance probability and expected Ψ for each scenario. Two cases of Ψ_0 and threshold for Ψ are analysed. The trends are as expected, with the scenario of the smallest seismicity also producing the lowest values of damage. The probability of exceeding DS1, even considering visible damage at the beginning of the period, is very small. Between scenarios, the differences appear relatively small. This is due to the simulation of the hazard and its seismicity. Whether these assumptions are realistic is not investigated; still, the DAF is successfully employed to contrast the scenarios.

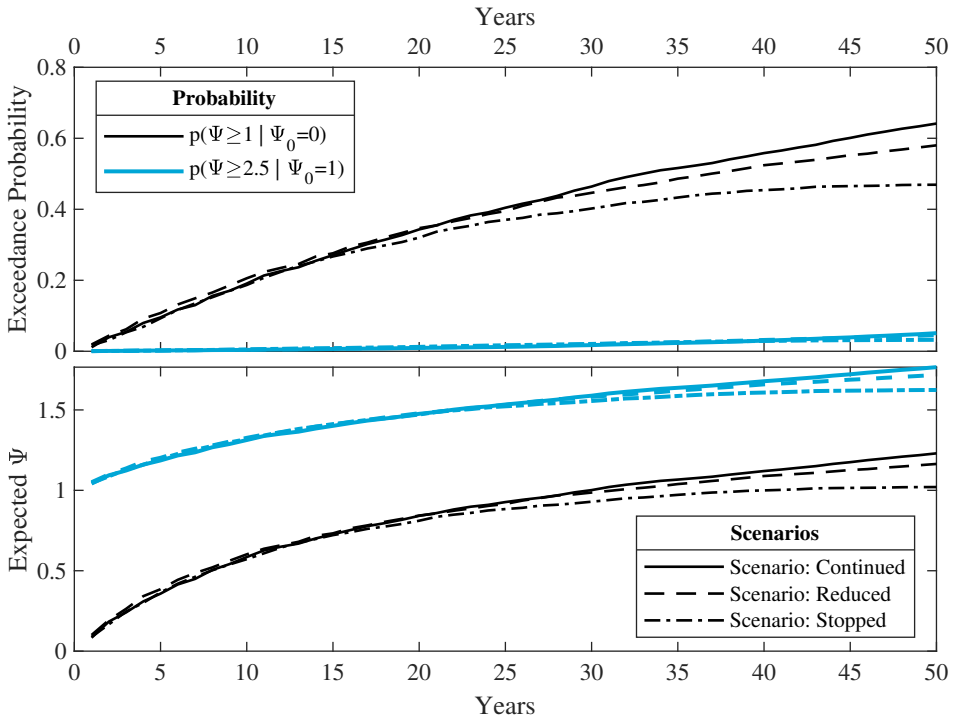


Figure 6.4.5. Fragility curves for the three scenarios as determined with the DAF analysis of multiple timelines per scenario. These are the fragility curves at the location of Loppersum based on idealised future scenarios with simplified assumptions. Year zero of the simulation corresponds to last year of the real history.

Furthermore, for the probability of damage at the end of the 50 years, a map of probability contours is calculated as in Section 6.3.4. The three scenarios can thus be compared in terms of the final probability contours; see Figure 6.4.6. As expected, the inner regions encircled by the contours determined for the Reduced and Stopped scenarios are smaller than for the Continued scenario, but the outer regions, representing the very low probabilities, are similar between the scenarios. This is because the very low probabilities, appearing far from the centre of the region, are mostly determined by the influence of the

events with a relative large magnitude which occur at the centre of the region; see also Figure 6.3.12. The inner circles are affected instead by the repetition of events, for which the Continued scenario, with a higher rate of events, is dominant.

These simulations serve to highlight the importance of time for repeated events and the versatility of the DAF formulation. While the concept of hastening is not directly applied, a multi-hazard could be included. The result would be a combination of figures 2 and 4. For clarity in the example, a starting hazard has been omitted. Nonetheless, the scenarios considering a reduction in seismicity, lead to the opposite of hastening: retardation. For the expected Ψ , damage appears slower than in the scenario where the current rate of events is maintained, in this case a retardation of certain values of Ψ can be observed.

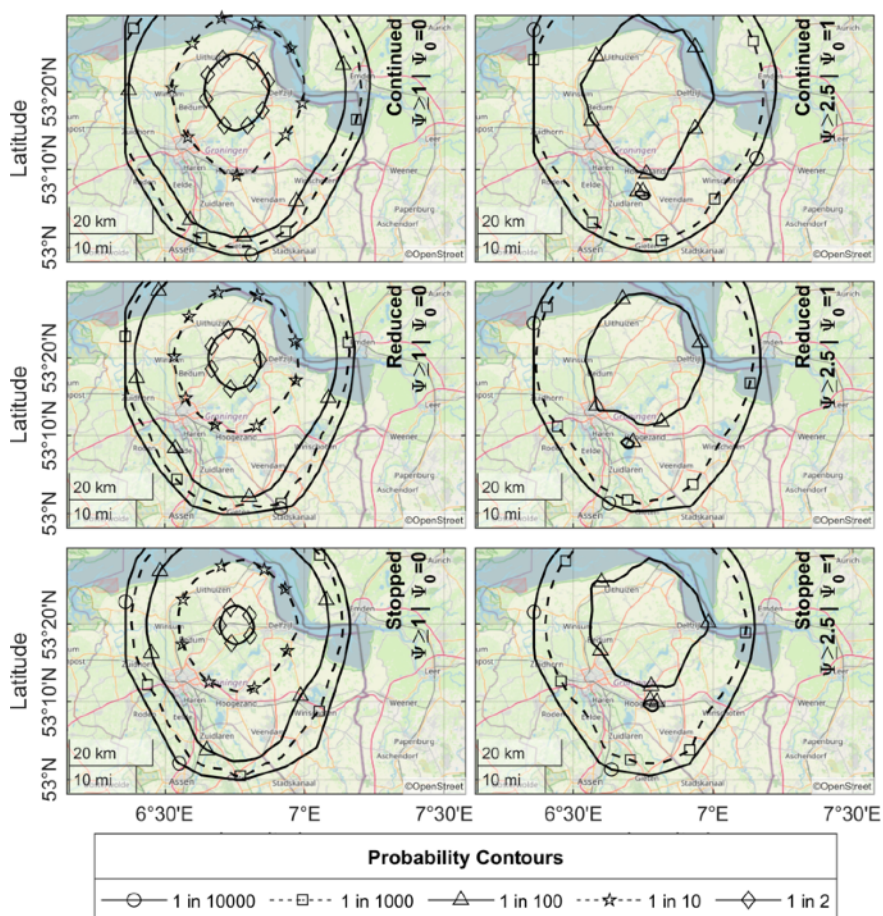


Figure 6.4.6. Probability contours for the three scenarios, at the end of the period considered, for the case exceeding DS1 or $\Psi=2.5$. The initial condition is $\Psi_0=1$.

Chapter 7

Conclusions and Outlook

This final chapter consolidates the findings from this investigation into light damage in masonry structures due to seismic vibrations. This study embarked on a detailed journey to understand and quantify light, crack-based damage in masonry, a subject of significant importance in regions prone to seismic activities in the Netherlands.

The approach was multi-faceted, involving the development of a new scale for measuring light damage, conducting innovative experiments for monitoring crack initiation and progression, and collaborating on calibrating numerical models to reflect observed damage behaviours. This comprehensive method allowed me to explore the probability of damage under varying seismic conditions, adding a crucial layer of understanding to the field.

The conclusions presented in the following sections, and focused on the research questions (Section 7.1), are drawn from an extensive analysis of each aspect of the research, enriched by collaborations and comparisons with other experts. These insights provide a nuanced view of how masonry structures react to seismic actions and the potential risks involved in terms of light damage. As the discussion is wrapped up, I will also reflect on the relevance (Section 7.2) and limitations of the study (Section 7.3) and suggest directions for future research (Section 7.4). This chapter not only aims to summarise the key findings but also to offer a perspective on the broader implications of the research in the context of changing environmental conditions and societal attitudes towards (infrastructure) resilience and damage (Section 7.5).

7.1. Answers and Conclusions

This work set out to investigate 'light damage' in masonry and its relationship to seismic vibrations. This not only concerned the initiation of new damage but, in particular, an aggravation of existing damage, being present in structures due to e.g. uneven settlements, was to be examined. Additionally, an accumulation of damage due to repeated seismic events was a concern. To accurately portray these relationships, damage and its exacerbation had to be precisely quantified. Since light damage represents mainly crack-based damage in masonry, this translates to understanding the initiation and propagation of cracks in masonry and linking it to the repeated potential seismic vibrations. Moreover, since masonry and damage have a large variability, the potential damage should be quantified in terms of its probability. This led to the formulation of the following research goal:

To objectively and probabilistically quantify the initiation and aggravation of crack-based damage in (pre-damaged) masonry for (repeated) seismic events.

To achieve this goal, a five step, physics-based process was devised. To list: First, the definition of a scale with which to measure light damage (increments). Second, the design and realisation of experiments to observe crack initiation and propagation, also due to the repetition. Third, the calibration of numerical models accurately reproducing the light damage behaviour. Fourth, the extrapolation of the calibrated models to analyse the effect of seismic vibrations also on an initial damage condition. And fifth, the analysis of variations in the models and their relationship to damage to establish the probability of damage in fragility curves and maps.

This five step process has been successfully implemented in this work. Some of the steps have been worked on with the collaboration of other authors. The conclusions of individual subquestions formulated as part of the main research question is presented next.

7.1.1. Objective, Continuous Scale for Damage and its Aggravation

What is a damage scale or measure capable of objectively characterising masonry light damage (for various relevant causes)?

Seismic vibrations and quasi-static soil movements due to subsidence generally lead to cracks in masonry structures. Other types of masonry damage, such as crushing or spalling, are linked to other causes or actions. Moreover, damage in masonry for the serviceability limit state, also known as damage states one and

two (DS1+DS2) or simply 'light damage', consists of narrow cracks, up to five millimetres in width.

To objectively measure masonry damage, a continuous scale has been proposed. The scale or parameter does not depend on subjective descriptions of the damage but can be calculated based on the measured crack width, length and number of cracks. These are computed together to produce a scalar measure that is related to crack-based damage. In this way, the parameter maintains a degree of comparability to existing damage scales based on cracks. The parameter, Ψ , is tuned in such a way that a value of $\Psi=1$ marks the threshold for visible damage with cracks of about 0.1mm in width; a value of $\Psi=2$ denotes easily observable damage (crack width ≈ 1 mm), and the upper threshold for light damage, encompassing DS1 and DS2, is set at $\Psi=4$. Moreover, the value of Ψ gives an indications as to the ease and cost of repair of masonry damage.

Furthermore, the continuous parameter allows for investigations into $\Delta\Psi$ or the increase, aggravation, or accumulation of damage. Values of $\Delta\Psi$ are associated with different degrees of detectability, whether the increase in damage can be observed, and contribution to the cost of repair. The cost of repairing damage increased by $\Delta\Psi=1$ is entirely attributable to the cause aggravating the initial damage, while a $\Delta\Psi\leq 0.1$ cannot be discerned by the naked eye, and in practice, cannot be measured by observation only. A threshold of $\Delta\Psi=0.2$ is set as a marker for a visible or noticeable damage increase. Lower increases of damage can of course be measured with dedicated monitoring equipment.

The continuous and objective parameter is extremely well suited to monitor damage and evaluate small increases in damage from laboratory experiments and numerical models automatically. These small increases can be related to purposed changes in the experiments and models to detect the influence of variations in the boundary conditions or the strength of the materials, for example. For investigations in real structures, Ψ can be used to compare increases in damage against earlier inspections. However, comparisons between different buildings are less practical unless the differences in size and materials can be accounted for in the cost of repair.

The damage parameter devised has been successfully used in this work to investigate the influence of repeated seismic vibrations and certain soil deformations on typical Dutch masonry. In this manner, the first step is completed.

7.1.2. Monitoring Crack-Based Damage Aggravation from Experiments

How can cracking, relevant for light damage, be accurately surveyed in masonry experiments?

Answering of this research question required two elements. One, that experiments had to be designed and executed such that they actually display (repeated) light damage; and two, that this light damage can be measured in an accurate manner.

For the former, a loading protocol was drafted based on an imposed in-plane drift on full-scale masonry walls such that one crack with a width of 0.1 mm appeared. Then, based on this initial drift, subsequent cycles of imposed drift were applied. These cycles followed increasing steps of repeated displacements so that the effects of repetition could also be evaluated. This guaranteed that the specimens displayed cracks in the light damage range.

To measure these cracks, which could appear anywhere on the surface of the specimen, photogrammetry was used. In order to employ Digital Image Correlation (DIC) to observe the entire full-scale walls while detecting and tracking cracks narrower than 0.1 mm, several improvements were applied:

First, a high-resolution camera, linked to a high-speed flash and timed by the computer controlling the test, was implemented. This setup allowed to accurately capture the displacement field of the surface of the wall at the instances of maximum and zero drift. The camera settings were configured and a lens was selected such that the sharpest possible image was achieved without distortion. A camera with 51 M pixels with a 35 mm lens capable of f/2.0 was stepped down to f/9.0 with an exposure of 1/100 of a second. The exposure was controlled with the flash illuminating the sample for 1/63'000 s to prevent motion blur from vibrations (in the camera) and mitigate the influence of any other lightning sources in the laboratory.

Second, the surface of the masonry was painted with a high-contrast black-and-white speckle pattern. Unlike typical applications, the minimum and maximum size of the speckles was controlled using a stencil in order to achieve the maximum resolution and measurement density. The stencil was laser-cut out of a flexible polycarbonate sheet and designed with a program that randomly located speckles with a size and spacing drawn from a uniform probabilistic distribution that would translate to 2-5 pixels for the camera. This was determined to be the optimum configuration to produce efficient subsets of pixels that could be tracked later by software maximising the density of measurement points.

Finally, a DIC post-processing program was written to analyse the images and focus on the displacement fields and its local discontinuities. Common applications emphasise post-processing to obtain a strain field, but for tracking cracks, displacement discontinuities are desired. The program was integrated with a crack-detecting algorithm that characterised individual cracks and monitored them throughout the loading history.

In summary, this approach presents an effective method for accurately surveying light damage in masonry via cracking. Through a carefully designed loading protocol, light damage was consistently induced in masonry walls, producing identifiable cracks. The utilisation of Digital Image Correlation (DIC) with a high-resolution camera and a specialised speckle pattern enabled precise crack detection and monitoring. The development of a DIC post-processing program, focused on displacement discontinuities, further enhanced the accuracy of crack tracking. This integrated approach marks a significant advancement in masonry research, offering a reliable technique for assessing light damage in masonry experiments.

7.1.3. Damage Aggravation by Subsequent Actions

How is light damage, caused by settlements or other autogenous actions in masonry buildings, aggravated by seismic vibrations, especially after multiple seismic events?

Existing light damage is worsened by the propagation of cracks. These grow in width and length, while new cracks become visible. This intuitive observation was further studied and quantified in two ways:

First, experiments were tested under repeated and increasing loading. These showed that cracks from previous loading cycles would propagate even at repeated, identical loading and certainly at larger loads. When imposed in-plane drifts were increased by 25%, crack widths would double. The length of the cracks increased about 50%. Additionally, two specimens were constructed with unbonded joints in locations that resemble settlement-induced cracks. When these 'existing cracks' were in a region where cracks due to lateral loading would naturally appear, they aggravated. When they were in other parts of the specimen, the cracks would activate but seldom propagate.

Second, the numerical models, calibrated on the experiments, were used to investigate how damage from specific actions would worsen. Various models of masonry walls were first subjected to settlement actions by applying a settlement shape in the form of a vertical displacement underneath an interface at the base of the models. The no-tension interface allowed the walls to deform and develop cracks consistent with those observed in real structures

under similar actions. The settlement action was applied in such a way that cracks constituted light damage at various intensities of Ψ (Ψ_0 : 0 to 1.5 in 0.5 increments). Subsequently, earthquake vibrations were applied at the base also at varying intensities. The model variations established for instance, that weaker masonry experienced a larger increase in damage and that higher values of Peak Ground Velocity (PGV) led to even larger increases. While these relationships are not unexpected, they have been well quantified. For example, models of walls on peat (soft soil) accumulated 33% more damage than walls on the comparatively stiff sandy soil; while, models of walls with a window opening attained a 25% higher increase in damage than walls without a window. Similarly, models of walls subjected to two consecutive identical seismic events displayed on average 10% higher damage increase than those subjected to only one event.

What is the probability of visible light damage for masonry structures in the region of Groningen, primarily due to seismic actions, but considering the probable current state of the buildings?

From the relationships observed, a surrogate function was regressed. The regression was performed with a custom model and a non-linear fit. Comparatively, a neural network (NN) model was also fitted to the models' results. However, the NN did not reproduce the expected behaviour in some cases in between data points and outside the calibrated interval. The custom, or 'reasoned' model, was designed such that the physical relationships would be maintained. For example, at increasing PGV, also increasing damage is expected. The surrogate models allowed to conduct a MonteCarlo simulation where the various parameters were assigned probabilistic distributions and (co)relationships. This analysis enabled the estimation of damage probabilities for different PGV values and initial conditions (Ψ_0). The resulting 'fragility or vulnerability curve' indicates, for example, that a masonry wall at 10 mm/s PGV has a 5% chance of sustaining light damage, defined as visible cracks of at least 0.1 mm. This probability increases to 20% if the wall has pre-existing, undetectable damage, like that caused by differential settlements. At lower PGVs, the probability of damage is accordingly lower.

This highlights the importance of considering a structure's existing condition when assessing seismic impacts, particularly for low PGV vibrations. It suggests that damage claims should account for both new and exacerbated pre-existing damage. Compared to other studies on masonry fragility curves for 'damage state 1', the range defined in this study aligns well with empirical curves derived from claims data, especially the curves considering initial undetectable damage ($\Psi_0=0.5$).

7.1.4. The Effect of Repetition on Damage Accumulation

How is intrinsic light damage hastened by seismic vibrations?

The final subquestion deals specifically with the effects of repeated vibrations on existing damage. Repetition has been a consistent topic throughout several chapters in this work. Experiments demonstrated that cracks grow under identical repeated cycles. Calibrated numerical models showed damage increase under repeated actions. And, extrapolated models displayed aggravation of existing damage by different subsequent actions. Nonetheless, these increases are minor; for repetitions of high intensity (PGVs larger than 30 mm/s), damage can increase by up to 10% on average.

The final chapter treated intrinsic light damage in masonry structures and its natural development over time. Natural soil movements, material shrinkage, and thermo-hygral variations lead to intrinsic damage that require periodic maintenance; though many masonry buildings are seldom given proper maintenance. Under the assumption that intrinsic or autogenous damage advances over time, the effect of foreign actions can be compared. In this manner, another measure with which to evaluate the effect of repetition is crafted: damage hastening. Hastening is defined in the dictionary as *to cause something undesirable to happen sooner than it otherwise would*.

Since repeated actions accumulate damage over time, they are comparable to progressive autogenous damage. The foreign actions will cause visible damage ($\Psi=1$ or $\Psi=2$) to occur earlier than only due to autogenous causes. It is thus dependent on the intrinsic damage development of a structure and the history or sequence of repeated actions. In Loppersum, a village in the centre of the Groningen province, where frequent PGVs have been measured in the last two decades, a masonry structure that would have developed a $\Delta\Psi$ of 1 due to autogenous causes in the same period, would see this increase occur 40% earlier, or with a 1.7x hastening, due to the vibrations. In Delfzijl, where fewer significant events have been experienced, the hastening is about 1.3x. These results can also be assessed in a probabilistic manner; however, these findings are highly dependent on the intrinsic progression of damage in masonry structures and will require more exhaustive research before additional results can be confidently analysed.

7.1.5. Answer to the Main Objective

The five-step approach employed herein, i.e. the 'how' to answer the sub-questions, is part of this work's goal. As Step 1, the research developed an ingenious approach to objectively quantify light damage in masonry structures, particularly in the context of seismic events. A novel damage parameter, Ψ , was introduced to measure light damage based on crack dimensions, offering a scalar value that reflects different damage levels. This parameter also facilitates the assessment of damage increase ($\Delta\Psi$), integrating factors like visibility and repair costs. To precisely track crack-based damage, the study employed a sophisticated technique using Digital Image Correlation (DIC) coupled with high-resolution imaging and a specialised speckle pattern. This approach enabled accurate monitoring of light damage in full-scale masonry wall experiments, effectively capturing the initiation and progression of cracks; observing damage in these experiments constitutes Step 2.

The research further examined the aggravation of light damage due to seismic vibrations, employing both experimental and numerical modelling techniques. Experiments demonstrated the propagation of cracks under repeated seismic loading, while non-linear finite-element numerical models, calibrated on these experiments (Step 3), simulated the impact of seismic vibrations on masonry with pre-existing light damage. These models highlighted how various factors, including soil type and structural features like window openings, affect the extent of damage aggravation (Step 4). Additionally, a probabilistic analysis was conducted, creating a model to estimate the likelihood of visible light damage under different seismic intensities and pre-existing conditions (Step 5). The study also explored the effect of repeated seismic events on accelerating intrinsic light damage, revealing that such events can hasten the appearance of visible damage in masonry structures, a crucial insight for understanding the cumulative impact of seismic activity in regions prone to such events.

7.2. Relevance and Contributions

7.2.1. Scientific Relevance

In comparison to literature, this bottom-up approach presents several scientific contributions. Three types of reference studies can be identified from literature: First, empirical analyses, which are drawn from damage claims or reports. These have difficulty isolating the origin of the reported damage and thus cannot draw reliable quantitative conclusions about the effects of earthquakes, accumulation, or repetition. A physical, bottom-up approach, seeks to understand the process leading to damage. This is accomplished with the experiments and models in this study.

Second, extrapolative curves, on the basis of ULS values or a pushover curve, infer the behaviour or limits for light damage. These cannot express clear limits for visible damage or its propagation since this is not explicitly modelled. Nonetheless, many of these fragility curves fall within the thresholds established in this work, where clear limits are established.

Third, studies which do look at crack formation but where damage is insufficiently quantified; these rarely take the step to calibrate models and employ them to investigate the effect of earthquakes. This step is explored in this work and so a good damage quantification method is transferred to the assessment of earthquake damage probability.

Many studies are affected by more than one of these shortages. Empirical studies monitoring damage sometimes lack accurate definitions for damage; the assignment of a damage grade is left to the inspector. Similarly, experiments where light damage is monitored, often do not establish a clear relation between the load acting on the specimens and its counterpart in actual buildings.

In this context, the present work adds upon these shortages.

7.2.2. Societal Relevance

Moreover, the study is socially relevant on several aspects; these are gathered in this separate subsection. It is clear that the Groningen region has experienced significant societal and economic unrest due to the seismic activities linked to gas extraction. The Dutch government established plans to reimburse damage due to the consequences of this activity. With the inverse of proof, where all cracks are deemed related to this mining activity, unless proven otherwise, a significant advantage was given to the inhabitants. Still, one asks, in which region should this ruling be effective? One can imagine that buildings located in the other side of the country, far away from the seismic area, which

may also have cracks due to settlements, temperature effects, etc., should not be considered. The fragility maps developed in this thesis may help to answer such questions.

Yet, this study does not help to answer what is an acceptable probability of damage; this is left to policy makers and sociologists. Instead, this work helps to determine which probabilities of damage are associated to which intensities of damage (or the probability of small cracks). Furthermore, it quantifies that repetition affects the expected damage, and that initial damage will also alter the progression of further damage. For damage on bare, fired-clay brick masonry walls, the thresholds at which increases in damage are actually noticeable, have also been defined. This contributes to the statement that while an aggravation of the existing damage cannot be excluded, this increase has seldom an effect in the visibility or the cost of repair of the damage. The regions and cases when it does, can be determined.

Indeed, this quantitative knowledge will be useful when formulating strategies for damage compensation. Additionally, it should have an effect on the perception of safety, demonstrating that the aggravation of damage is unlikely to lead to an exceedance of light damage - transitioning into structural damage with associated safety issues - at least for the in-plane actions evaluated in this study. Moreover, it should help define repair and mitigation strategies (see 7.4.4) that would be effective in the region and in future cases of mining and building damage.

Understanding and addressing minor damage is thus crucial for maintaining public trust and ensuring that the social fabric of the region remains intact. Similarly, understanding the nature of light damage and developing methods to quantify and manage it can help in better planning and decision-making, potentially reducing economic costs and social tensions related to property damage and safety concerns. Communities in affected regions can be better educated about the risks and appropriate responses, enhancing community resilience and institutional trust.

In summary, the work herein is highly relevant from a societal perspective as it intersects with public safety, economic stability, legal and policy frameworks, and scientific innovation. It contributes valuable knowledge that can be used to mitigate the negative impacts of seismic activities associated with gas extraction, enhancing community resilience and informing socially-fair practices.

7.2.3. Utilisation

The way these results can be used is hinted at in the preceding subsections. Here, a more specific list is gathered. First, experiments on cracks and crack propagation, together with the improvements to DIC on masonry, will help to understand damage in the field. It contributes to the pool of crack patterns related to (earthquake) loading, and to crack propagation, among others. Monitoring strategies could take advantage of DIC. The calibration models also reflect on successful strategies to replicate crack propagation and identify subjects for further study. Similarly, the extrapolation models and the exploration models in Chapter 4, suggest strategies to evaluate relevant effects in the study of damage for various hazards. These can be further expanded.

Moreover, a compilation of results from experimental tests has been consolidated. These are published (see Appendix F) and can thus be used by other researchers as a benchmark to calibrate (other types of) numerical models or compare against other types of tests.

Furthermore, the probabilistic strategy to assess the probability of damage and its aggravation, on the basis of a surrogate model and a Montecarlo simulation, can be adapted and applied to other hazards. In this work, it is employed with two examples: settlements from soil distortions, and vibrations from earthquakes; other actions and hazards, such as flooding, could also be quantified.

The utilisation of the results of these analyses have already been mentioned: insight into damage and its probability will help policy and compensation strategies. Moreover, the study into the accumulation of damage, with the Damage Accumulation Function (DAF), revealed several uses: first, a quantification of accumulated damage from decades of past earthquake events; second, a method to forecast future damage, including the evaluation of different scenarios. This can be used to take informed decisions about the impact of gas mining in the future.

7.3. Limitations - Restrictions of the Scope

Several aspects of this study must be contemplated within their limitations. This section presents some of the key constraints within which to frame the afore-listed conclusions.

7.3.1. One Parameter to Describe it All

In several areas, one measure or one parameter is employed to represent a more complex situation or variability. These simplifications have enabled several stages of the method, but also represent a limitation. These one-for-all limitations are discussed next:

Ψ Damage Parameter

One of the main advantages of the Ψ damage measure, that damage can be captured in a single scalar, can also be a major limitation. A single number cannot express the location of the damage, the direction or shape of cracks, the number of cracks, or give insight into the cause of the damage. This crack pattern information is lost in the scalar. This is one of the reasons that using Ψ to compare damage from different structures subjected to different causes can be difficult. To more reliably realise these comparisons, a second parameter would have to be considered, perhaps including the 'taperedness' of the cracks [2.4.3]. This study has focused on the increase in damage ($\Delta\Psi$) and comparisons have been drawn between similar cases. Yet, to study the difference between damage causes would require a more comprehensive description of the damage included into the parameter.

Walls

Similarly, to study the effect of vibrations, walls have been used as a proxy of more complex geometries like façades and buildings. Two distinct walls served to study the effects of geometry on the probability of damage. In other collaborations, more varying geometries have also been considered, though not as extensively in terms of the variations of other parameters like soil type or earthquake record. In these comparisons, the proxy walls seem to act well. However, additional geometries provide a greater variability and can reveal more intricate relationships. They are also subjected to specific failure mechanisms that may not be common outside their particular geometry. To consider the potential variations accurately, a large number of expensive models would have been needed. This was unfeasible and thus remains a limitation of this work. Moreover, the differences with models of buildings, with 3D effects and other complexities, have only been checked in parallel and must be further quantified.

Fired-Clay Brick

Furthermore, light damage has been studied predominantly for one material: fired-clay brick masonry. Limited experiments have been conducted also for calcium-silicate brick masonry but calibrations and simulations have not considered it. While the type of fired-clay brick masonry is representative of older, more vulnerable structures in the Netherlands, the behaviour of newer types of masonry will differ. The conclusions drawn here, especially those that quantify damage, are thus strictly applicable to the older masonry type. Other masonry, with different bricks and mortars, should also be explored.

Damage on Bare Walls

The study has looked at damage in masonry. This means that connections have not been explored. Also, damage on finishings, like plaster, paint or coatings, which could increase the visibility of cracks, have been neglected (see Appendix B). The connections comprise continuous or discontinuous wall-to-wall connections, wall-to-floors, etc.

In sum, it becomes evident that while the Ψ damage measure offers a streamlined approach to quantifying structural damage, it inherently lacks the depth to convey detailed damage characteristics such as location, orientation, and specific cause. This limitation is particularly pronounced when attempting to compare damages across different structures or damage causes, suggesting the need for a more multifaceted approach or additional parameters. The use of walls as a simplified proxy for more complex structures, although effective to a degree, falls short in capturing the full spectrum of potential damage scenarios, especially those unique to specific geometries. Furthermore, the study's focus on a single material type limits the generalisability of its findings, as different materials exhibit varied damage behaviours.

7.3.2. Single-Wythe Brick Walls and In-Plane Damage

Furthermore, this study has focused on in-plane damage for single wythe walls. Damage in single wythe walls is easier to track in experimental setups and to reproduce in numerical models. Yet, many older structures possess double wythe walls. For damage that occurs in the plane of walls, cracks are expected to be similar between single or double wythe walls. However, these differences should be more accurately investigated. 3D DIC or embedded fibre optics could be used to explore crack propagation throughout the masonry thickness.

Moreover, while light damage typically occurs in the plane of the walls (De Vent, 2011; Van Staalduinen et.al 2018), combinations with out-of-plane actions could lead to asymmetry in crack-based damage between one face of a

wall and the other. This effect would be especially marked in thicker double wythe masonry. This 'mixed mode' of in-plane and out-of-plane effects has not been considered in this work and remains to be further researched.

7.3.3. Quasi-static Extrapolation to Dynamic Actions

In the fourth step of the five step approach to quantify light damage, extrapolations are made using calibrated models. The extrapolation consists of employing the models, calibrated against the experiments, to investigate the effects of soil movements. However, the experiments were quasi-static, applying a slowly enforced in-plane drift, while soil movements can be dynamic, as is the case of earthquake vibrations. A more direct approach would have considered models calibrated against dynamic experiments.

However, dynamic tests should always be considered as supplemental since their interpretation is more difficult than that of quasi-static tests. The dynamic effects imparted by the setup and its interaction with the loading signal, as well as the boundaries applied to the specimen, can significantly alter the damage evolution in a test. For the dynamic loading to be sufficiently representative, the test of a wall should include an inertial mass on top. Still, the dynamic interaction of the other walls in a real structure, which will modify the way in which a single wall is loaded, is nearly impossible to reproduce. For this reason, accurate dynamic tests usually employ an assemblage of walls into a true building. Then, testing a relatively large number of buildings becomes unfeasible, unless these are scaled, which interferes with the development of light damage and the size effect associated with softening. Moreover, capturing damage and its propagation becomes exceedingly more problematic during dynamic tests since damage can develop within milliseconds. In this light, quasi-static tests offer better calibration possibilities for models attempting to reproduce masonry cracking at the initiation stages. Nonetheless, additional verifications are needed against dynamic tests to confirm the accurate behaviour of the calibrated models when extrapolated to dynamic situations.

Consequently, the observations presented here should be viewed within this limitation. For high values of PGV (>30 mm/s), where dynamic effects can play a more important role, the damage behaviour could differ slightly. As such, the conclusions are better applicable for the low values of PGV, where light damage is also expected to occur.

7.3.4. Repetition at the Material Model

The effect of the degradation observed because of repetition in experiments is only partly reflected in the numerical models. In the models reproducing the test, the reduction in force levels out after three or four repetitions, while the degradation of force in experiments reaches an asymptote after about thirty repetitions. Since the overall decrease has been captured well, and the propagation of damage within identical steps is correctly reflected in the models, the calibration in terms of degradation has been deemed sufficient. Moreover, the Damage Accumulation Function has been validated directly to experimental results. However, repetition has proven to be influential in damage accumulation. It is not clear to which degree the additional degradation would modify the damage behaviour observed in this work, but it must be highlighted as a limitation, that the material degradation observed in experiments is not fully implemented yet in numerical models. Therefore, additional emphasis on capturing all aspects of repetition should be a focus of future studies.

7.4. Recommendations for Further Study

If the previous section identified specific limitations that constrain the conclusions of this work and suggestions to address them have been made, this section highlights additional topics that could further expand this study.

7.4.1. Crack-Based Damage in Modern Masonry

This work has focused on experiments replicating the properties of aged or older masonry and models calibrated to their behaviour. However, modern masonry, with joints of adhesive mortar between calcium-silicate units, or veneers of factory-quality fired-clay bricks with cement mortars designed for a low CO₂ footprint, will have differing properties and present a distinct cracking behaviour. Modern structures, with reinforced concrete foundations supported by piles, are less vulnerable to static soil movements, but problems may still arise. In particular, these structures, built with shrinkage-sensitive materials or heavy, pre-fabricated concrete floors, are vulnerable to shrinkage cracking or vibrations, for example. Hence, it is also important to understand the light-damage behaviour of buildings with a more modern type of masonry; this should be more thoroughly investigated.

Furthermore, this work has observed cracks within masonry components, but part of the damage observed in real situations in buildings in the Netherlands, older or newer structures, does not occur in the masonry but at discontinuous connections between elements. These comprise for instance, the connections

between walls and floors (concrete or timber) at the ceiling or on the floor side, or between non-structural walls and floors or walls. In some cases, structural walls are also purposely disconnected at corners. Whether such corner cracks can be considered damage or are part of the normal behaviour of a structure, is still being discussed. In many cases, a flexible finishing is capable of accommodating the normal expansion and contractions of a structure during its daily life. Dilation joints are included in modern constructions, accommodating thermal and hygral 'breathing' of the masonry.

For static or dynamic movements of somewhat greater intensity, these connections may open up as out-of-plane or rocking cracks, or present sliding from in-plane effects. This topic requires further study. Its main challenge would be the great variability in types of connections and their structural behaviour. A few MSc projects (see Appendix C) have begun a theoretical study into the dynamic cracking of the connections between non-structural walls and ceilings and other walls.

7.4.2. Mixed-Mode Fracture and Degradation

Degradation, when repeated actions lead to reduced material strength, was clearly observed in experiments; see Chapter 3. The material model employed in models (EMM) considers damage as part of the secant unloading/reloading for cracks in tension (Mode I) and with elastic unloading/reloading and residual shear strains in shear (Mode II). However, these effects do not seem to fully account for the material degradation observed in the experiments. Moreover, cracking behaviour when both modes are combined (mixed mode), a situation that can arise due to vertical soil movements for instance, should also be studied further both within the material modelling strategy, as with tailored experiments specifically designed to investigate this behaviour. On the τ - σ space, strategies for a smooth or discontinuous failure curve (or surface) exist but a mixed-fracture energy is not clearly defined with a basis on experiments.

An improvement to the material model, based on tailored experiments and that explicitly considers degradation and has clearer parameters for a mixed mode situation could be further studied. The former has been partly investigated (Bindiganavile, 2018) but an implementation that can also handle dynamic loading is still needed. Alternatively, brick-to-brick micro models offer promising possibilities as computational costs reduce and make them more feasible.

7.4.3. Monitoring Damage in the Field

This work has looked into laboratory experiments and models to investigate damage. These have been used to estimate damage as a result from seismicity. However, a third aspect, key in evaluating whether experiments and models reflect the behaviour of real buildings, is monitoring in the field.

Monitoring plays a crucial role in bridging the gap between theoretical models and the actual response of buildings to seismic events. By incorporating real-time data collection and analysis, monitoring allows for the validation and refinement of existing models. Advanced techniques like structural health monitoring (SHM) systems, which employ sensors to detect changes in a building's integrity, are instrumental in this process. The behaviour observed in experiments should also be observable in real situations. Monitoring allows for these types of verifications. Additionally, in-situ or field tests provide real-life tests to further enrich models and verify the results of laboratory experiments.

In this sense, monitoring is the missing third pillar in the framework of experiments and models attempting to understand and quantify cracking in masonry. In future research, monitoring and potential in-situ tests should be considered to provide additional validations to insights gained in this study.

7.4.4. Strategies for Repair, Mitigation, and Adaptation

Understanding the causes of crack-based damage and accurately determining how much damage can be expected in masonry structures can be useful for many purposes. One of these purposes may be the development of strategies to repair the damage. Another purpose would be the design of mitigation solutions such that the damage is prevented in the future. Yet another is adaptation, where new structures are built in such a way that damage is less likely. Dilation joints are an excellent example of an adaptation measure against thermal and shrinkage damage in masonry.

In the realm of repair strategies, various approaches can be employed depending on the severity and type of crack-based damage in masonry. For minor cracks, techniques such as crack injection, where an epoxy or polyurethane resin is injected into the crack, can be effective. This not only seals the crack but also restores the structural integrity of the masonry. For more extensive damage however, more comprehensive methods like stitching or rebuilding portions of the structure may be necessary. Yet, additional studies have been recently started in the field of innovative repair strategies, such as self-healing mortars [10]. Note that, the behaviour of repaired cracks, also subjected to repeated loading, will have to be investigated, too.

In terms of mitigation, regular maintenance and monitoring play crucial roles. By implementing a schedule for regular inspection and maintenance, early signs of cracking can be detected and addressed before they develop into significant problems. Additionally, using materials that are more resistant to environmental factors such as temperature changes, moisture, and chemical reactions can greatly reduce the likelihood of crack formation.

Adaptation strategies, on the other hand, focus on designing buildings with the foresight of potential damage. This includes not only the use of dilation joints as mentioned, but also the integration of flexible materials and advanced design techniques such as seismic retrofitting for earthquake-prone areas. These adaptation measures aim to make structures more resilient to the stresses they are likely to encounter over their lifespans. Future research may also focus in new adaptation techniques such as the use of structural glass for in-plane strengthening of masonry structures [19].

Furthermore, advancing technology, such as the use of sensors and connected devices, can provide real-time monitoring of structures, allowing for prompt identification and response to any signs of distress. This integration of technology in masonry work can revolutionise the way buildings are maintained and safeguarded against damage. Studies into the implementation of sensors like accelerometers, tilt-meters, embedded fibre-optic strain sensors, etc. could be fruitful.

In conclusion, addressing crack-based damage in masonry structures requires a multifaceted approach that encompasses repair, mitigation, and adaptation strategies. By understanding the underlying causes and employing the right combination of techniques, the longevity and safety of masonry structures can be significantly enhanced.

7.5. Outlook

The previous section looked at specific aspects or topics that should be studied following this work. This section instead, provides a more general outlook on the challenges surrounding building damage.

7.5.1. Climate Change and Building Fragility

Apart from gas extraction and mining, also climate change is an upcoming threat to buildings. Climate change and building fragility may seem unrelated at first glance. However, many effects of climate change have been demonstrated and these indirectly affect buildings. Consider first, more extreme weather events such as stronger wind storms, drought, heavy rainfall, and heat waves. These alone affect buildings in several ways. Strong and more frequent storms may damage roofs or walls. Droughts will lead to soil changes (like drying and wetting of peat and clay) that ultimately can lead to settlements in buildings. Heavy rainfall can saturate unprepared roofs causing overloading, or it can lead to erosion on foundations. Similarly, quickly changing water table levels may again lead to settlements. Heatwaves can also cause problems with thermal expansion for buildings or infrastructure never designed for those (rapid changes in) temperatures.

Secondly, observe the higher risk of (flash) floods due to heavy rainfall, riverine floods, and sea level rise. The flood fragility of buildings will become ever more relevant. Thirdly, to mitigate climate change, underground storage of carbon-dioxide may prove to be a viable solution; its effects at the ground surface will need to be studied. The multi-hazard framework presented in this work may help in this matter.

7.5.2. Cracking and the Energy Transition

Similarly, the energy sector is transitioning from fossil-based energy to renewable sources as part of climate-change mitigation. One of such options is geothermal energy which requires drilling and interacting with the underground. Other renewable sources, like wind or solar, also require energy storage which can be achieved underground. These ground-based solutions may have similar effects on buildings and infrastructure as mining-induced subsidence and vibrations.

Moreover, the relationship between the energy transition and cracking can be more straightforward. As homeowners implement insulation measures, install photovoltaic or adiabatic solar collectors, replace old furnaces with more efficient, hybrid or electric devices, their renovation efforts will lead to changes

in buildings that should be properly conducted to avoid problems and damage.

7.5.3. Risk Reluctance, Acceptance and Damage Policy

In the case of gas extraction in the North of the Netherlands, knowledge, policy and communication about the effects of induced seismicity and subsidence came too late (Palomo-Vélez et al. 2023). Public perception regarding these issues has been overwhelmingly negative (Van der Voort & Vanclay, 2015; Mulder & Perey, 2018). Besides the cost of repair, which affects a limited area, the loss of property value and immaterial damage has been greater and more widespread. Moreover, the uncertainty, especially due to lack of clear communication, regarding the aforementioned points and in particular, the matter of safety, has upset many. This has led to a risk-reluctant stance where no potential effects are tolerated. The probability of damage considered, that of just-visible cracks appearing, is comparable to that of failure of critical flood defences of the Netherlands (1 in 10'000 yearly). In the case of building damage due to mining activities, these probabilities are so small that their uncertainty affects them by their order of magnitude. These policies seem unreasonable but are the result of a society that does not accept, or has become unaccepting, of the risks associated with mining. Perhaps this situation is analogous to that of nuclear energy, for which there is a large risk aversion, too.

Thus, one additional strategy for mitigation and adaptation can be noted: acceptance. Small cracks could be accepted as normal behaviour. With the acceptability of imperfections to a certain degree, as in many other industries, many of the suggested measures would not be necessary.

With an outlook towards the future, work needs to be exerted into forming a more risk-accepting society. Climate change will carry greater risk to buildings, as problems of water management, energy, and housing, will require new solutions. These new solutions, such as underground carbon capture or storage, geothermal energy, more variable water table levels, etc. are not without risk. To reduce societies' effect on the climate and adapt to its inevitable changes, the risk associated with these solutions will need to be managed. Clear damage policies will give confidence that problems will be handled fairly if they arise.

List of Publications

References in this work are cited with authors names; see *Bibliography*. References in numbered squared brackets [1 - 33] are own publications or collaborations; see this section. References in curly brackets {2.2} indicate sections within this text.

Journal Papers

1. P.A. **Korswagen**, M. Longo, E. Meulman, J.G. Rots (2019). Crack initiation and propagation in unreinforced masonry specimens subjected to repeated in-plane loading during light damage. *Bulletin of Earthquake Engineering* (2019) 17:4651–4687 doi.org/10.1007/s10518-018-00553-5
2. P.A. **Korswagen**, S.N. Jonkman, K. Terwel (2019). Probabilistic assessment of structural damage from coupled multi-hazards. *Structural Safety* Volume 76, 2019, 135-148, ISSN 0167-4730 doi.org/10.1016/j.strusafe.2018.08.001
3. P.A. **Korswagen**, M. Longo, J.G. Rots (2020). Calcium silicate against clay brick masonry: an experimental comparison of the in-plane behaviour during light damage. *Bulletin of Earthquake Engineering* (2020) 18:2759–2781 doi.org/10.1007/s10518-020-00803-5
4. P.A. **Korswagen**, M. Longo, J.G. Rots (2020). High-resolution monitoring of the initial development of cracks in experimental masonry shear walls and their reproduction in finite element models. *Engineering Structures* 211 (2020) 110365 doi.org/10.1016/j.engstruct.2020.110365
5. L. Jansen, P.A. **Korswagen**, J.D. Bricker, S. Pasterkamp, K.M. de Bruijn, S.N. Jonkman (2020). Experimental determination of pressure coefficients for flood loading of walls of Dutch terraced houses. *Engineering Structures* 216 (2020) 110647, doi.org/10.1016/j.engstruct.2020.110647
6. M. Longo, M. Sousamli, P.A. **Korswagen**, P.C. Van Staalduinen, J.G. Rots (2020). Three-tiered finite element approach to soil-masonry-wall interaction for light seismic motion. *Engineering Structures* 245:2021. doi.org/10.1016/j.engstruct.2021.112847
7. P.A. **Korswagen**, M. Longo, J.G. Rots (2022). Fragility curves for light damage of clay masonry walls subjected to seismic vibrations. *Bull Earthquake Eng* 20, 6193–6227 (2022). doi.org/10.1007/s10518-022-01404-0
8. A. Prosperi, P. A. **Korswagen**, M. Korff, R. Schipper, J. G. Rots, Empirical fragility and ROC curves for masonry buildings subjected to settlements. *Journal of Building Engineering*, 68, 106094 (2023).

9. A. Prosperi, M. Longo, P. A. **Korswagen**, M. Korff, J. G. Rots, Sensitivity modelling with objective damage assessment of unreinforced masonry facades undergoing different subsidence settlement patterns. *Engineering Structures*, 286, 116113 (2023).
10. A. Prosperi, M. Longo, P. A. **Korswagen**, M. Korff, J. G. Rots, 2D and 3D modelling strategies to reproduce the response of historical masonry buildings subjected to settlements. *International Journal of Architectural Heritage* (2024).
33. Gaggero, M. B., **Korswagen**, P. A., Esposito, R., & Rots, J. G. (2023). In-Plane Behaviour of Unreinforced Masonry Strengthened with a Structural Glass Window: A Proof of Concept. *Buildings*, 13(2), 361.
34. P. A. **Korswagen**, J. G. Rots, K. C. Terwel (2024). Experimentally-based in-plane Drift Limits for the Upper Threshold of Masonry Light Damage. *Earthquake Engineering and Structural Dynamics*.

Conference Papers

11. P.A. **Korswagen**, E. Meulman, M. Longo, J.G. Rots (2018). Crack Initiation And Propagation In Unreinforced Masonry Structures Subjected To Repeated Load And Earthquake Vibrations. 10th International Masonry Conference, Milan, Italy 2018
12. P. **Korswagen**, M. Longo, E. Meulman, J.G. Rots (2019). Experimental and Computational Study of the Influence of Pre-Damage Patterns in Unreinforced Masonry Crack Propagation Due to Induced, Repeated Earthquakes. 13th North American Masonry Conference, Utah, USA 2019
13. P.A. **Korswagen** & J.G. Rots (2020). Older clay masonry can be more earthquake-resistant than calcium-silicate masonry for light damage. 17th International Brick and Block Masonry Conference (IB2MaC), Krakow, Poland 2020
14. P.A. **Korswagen** & J.G. Rots (2020). Monitoring and quantifying crack-based light damage in masonry walls with Digital Image Correlation. 1st International Conference on Structural Damage Modelling and Assessment (SDMA), Gent, Belgium 2020
15. P.A. **Korswagen**, M. Longo, J.G. Rots (2020). Experimental and computational research into the lower damage state DS1 for masonry structures. 17th World Conference on Earthquake Engineering, 17WCEE, Sendai, Japan 2021

16. P.A. **Korswagen**, M. Longo, J.G. Rots (2021). Experimental and computational study into the onset of light damage of Dutch masonry structures. *HERON* Volume 66 (2021), issue 1.
17. Paul A. **Korswagen**, Michele Longo, Jan G. Rots, Karel C. Terwel (2023). Sensitivity of Damage Accumulation of Masonry Walls due to Earthquake Vibrations via Finite-Element Models. 14th North American Masonry Conference (NAMC), Nebraska, USA 2023.
18. Francesco Messali, Rita Esposito, Samira Jafari, Geert Ravenshorst, Paul **Korswagen**, Jan G. Rots (2018). A Multi-scale Experimental Characterisation Of Dutch Unreinforced Masonry Buildings. 16th European Conference on Earthquake Engineering. Thessaloniki, Greece, 2018.
19. Gaggero, M. B., **Korswagen**, P. A., Esposito, R., & Rots, J. G. (2023, September). Innovative Application of Self-healing Technology to Masonry: A Proof of Concept. In *International Conference on Structural Analysis of Historical Constructions* (pp. 332-345). Cham: Springer Nature Switzerland.
20. P. A. **Korswagen**, M. Longo, A. Prosperi, J. G. Rots, K. C. Terwel (2023). Modelling of Damage in Historical Masonry Façades Subjected to a Combination of Ground Settlement and Vibrations. In *International Conference on Structural Analysis of Historical Constructions* (pp. 904-917) (2023).
21. Maria B. Gaggero, Paul A. **Korswagen**, Rita Esposito, Jan G. Rots. Exploring Bacteria-Based Self-Healing Potential in Cement-Lime Mortar Masonry. IB2MaC, Birmingham, UK 2024.
22. A. Prosperi, M. Longo, **P. A. Korswagen**, M. Korff, J. G. Rots (2023), Accurate and Efficient 2D Modelling of Historical Masonry Buildings Subjected to Settlements in Comparison to 3D Approaches. In *International Conference on Structural Analysis of Historical Constructions* (pp. 232-244) (2023).
31. Paul **Korswagen**, M. Belen Gaggero, Jan G. Rots (2024). Experimental comparison of cracking in four masonry walls with different boundaries and material. IB2MaC, Birmingham, UK 2024.
32. A. Prosperi, M. Longo, P. A. **Korswagen**, M. Korff, J. G. Rots (2023). Shape matters: Influence of varying settlement profiles due to multicausal subsidence when modelling damage in a masonry façade. In *Tenth International Symposium on Land Subsidence* (2023).

Scientific Reports

23. **Korswagen**, Longo, Meulman, Van Hoogdalem. (2017). Damage sensitivity of Groningen masonry structures – Experimental and computational studies. TU Delft Report number C31B69WP0-11, v.1.2. (Stream 1)
24. Damage sensitivity of Groningen masonry structures - Experimental and computational studies - Stream 2
 - a. **Korswagen**, P., Longo, M., Meulman, E., (2019). Damage sensitivity of Groningen masonry structures - Experimental and computational studies - Stream 2 - Part 1. Report number C31B69WP0-14, Report, version 2.0, 1 of December of 2019
 - b. **Korswagen**, P., Longo, M (2019). Damage sensitivity of Groningen masonry structures – Experimental and computational studies - Stream 2 - Part 2. Report number C31B69WP0-14-2, Report, version 1.0, 1 of December of 2019.
25. **Korswagen**, P., Meulman, E., Mariani, V. (2017). Testing, Characterisation, and Modelling of NeHoBo Floors for Groningen Seismic Assessment. Report number C31B71WP0-1, Intermediate Report, version 3.3, January of 2018.
26. **Korswagen**, P., Harish, S., Oetjen, J. & Wüthrich, D. (2022). Post-flood field survey of the Ahr Valley (Germany) - Building damages and hydraulic aspects – TU Delft Report, 69 pages (DOI: 10.4233/uuid:3cafd772-facd-4e3a-8b1a-cee978562ff1) and MetaData (DOI: 10.4121/19222656).
27. P.A. **Korswagen**, M. Longo, J.G. Rots, A. Prosperi (2022). Supporting analyses to determine probability of damage and fragility curves due to indirect subsidence effects. Delft University of Technology. Report number 00, Final Version 2, October 3, 2022.
28. Rots, J.G., **Korswagen**, P.A., Longo, M. (2021). Computational modelling checks of masonry building damage due to deep subsidence. Delft University of Technology. Report number 01, Version 05, February 18, 2021.
29. **Korswagen**, P., Pari, M., Rots, J.G. (2023). Fragility curves and maps for calcium-silicate brick masonry light damage vulnerability (fragility v2). Report number IMGWP3.3_5, Draft report, version 1.0, 31 May 2023
30. Pari, M., **Korswagen**, P., Rots, J.G. (2022). Calibration of Computational models for the reproduction of damage in calcium-silicate masonry walls. Report number IMGWP3.3_4, Intermediate draft report, version 1.1, 24th of February 2022

Bibliography

- Abo-El-Ezz et al. (2013)
A. Abo-El-Ezz, M. Nolle, M. Naste. Seismic fragility assessment of low-rise stone masonry buildings. *Earthq Eng & Eng Vib* (2013) 12-87-97.
- Ademović et al. (2020)
N. Ademović, T.K. Šipoš, M. Hadzima-Nyarko. Rapid assessment of earthquake risk for Bosnia and Herzegovina. *Bull of Earthq Eng* (2020) 18:1835–1863. doi.org/10.1007/s10518-019-00775-1
- AeDES (2007)
AeDES. Field Manual for post-earthquake damage and safety assessment and short term countermeasures. European Commission - Joint Research Centre - Institute for the Protection and Security of the Citizen.
- Aguilar et al. (2016)
V. Aguilar, C. Sandoval, J.M. Adam, J. Garzón-Roca, G. Valdebenito. Prediction of the shear strength of reinforced masonry walls using a large experimental database and artificial neural networks. *Structure and Infrastructure Eng*. doi.org/10.1080/15732479.2016.1157824
- Akhavissy (2012)
A.H. Akhavissy. The DSC Model for the Nonlinear Analysis of In-plane Loaded Masonry Structures. *The Open Civil Eng J*, 2012, 6, (Suppl 1-M8) 200-214.
- Akhavissy & Milani (2013)
A.H. Akhavissy, G. Milani. A numerical model for the analysis of masonry walls in-plane loaded and strengthened with steel bars. *Intl J of Mech Sciences* 72 (2013) 13–27.
- Alberto et al. (2011)
A. Alberto, P. Antonaci, S. Valente. Damage analysis of brick-to-mortar interfaces. *Procedia Eng* 10 (2011) 1151–1156.
- Aldemir et al. (2015)
A. Aldemir, B. Binici, E. Canbay, A. Yakut. Lateral load testing of an existing two story masonry building up to near collapse. *Bull Earthq Eng DOI*. doi.org/10.1007/s10518-015-9821-3
- Allen et al. (2015)
C. Allen, M.J. Masia, A.W. Page, M.C. Griffith, H. Derakhshan. Cyclic in-plane shear testing of unreinforced masonry walls with openings. *Procdngs of the Tenth Pacific Conf on Earthq Eng Bldg an Earthq-Resilient Pacific* 6-8 November 2015, Sydney, Australia.
- Almeida et al. (2012)
J.C. Almeida, P.B. Lourenço, J.A. Barros. Characterisation of brick and brick–mortar interface under uniaxial tension. *Intl Seminar of Struct Masonry for Developing Countries*.
- Almeida & Monteiro (1999)
J.C. Almeida, S.N. Monteiro. The Iosipescu test method as a method to evaluate the tensile strength of brittle materials. *Polymer Testing* 18 (1999) 407–414.
- Anania et al. (2012)
L. Anania, C. Giaquinta, G. D'Agata. The Reinforcement of Multiple-Leaves Masonry Walls using Carbon Fibre Reinforced Polymer: A Theoretical Approach. *Procdngs of the Eleventh Intl Conf on Comput Structs Tech, BHV Topping, (Editor), Civil-Comp Press, Stirlingshire, Scotland*.
- Anania et al. (2014)
L. Anania, G. D'Agata, C. Giaquinta, A. Badalà. Out of Plane Behavior of Calcareous Masonry Panels Strengthened by CFRP. *APCBEE Procedia* 9 (2014) 401 – 406.
- Anania & D'Agata (2014)
L. Anania, G. D'Agata. Performance Of a Multiple-leaf Masonry Wall Under Eccentric Loads. *Department of Civil Eng and Architecture, U of Catania*.
- Anthoine et al. (1995)
A. Anthoine, G. Magonette, G. Magenes. Shear-compression testing and analysis of brick masonry walls. *10th European Conf on Earthq Eng, Duma (ed)© 1995 Balkema, Rotterdam* ISBN 90 5410528 3.
- Anthoine & Molina (2008)
A. Anthoine, F.J. Molina. Pseudo-dynamic Testing Of Full Scale Masonry Structures: Preparatory Work. *European Laboratory for Struct Assessment (ELSA) Joint Research Centre of the European Commission Ispra, Italy*.
- Arias (1970)
A. Arias. A measure of earthquake intensity. *Hansen RJ (ed) Seismic design for nuclear power plants MIT Press, Cambridge MA, pp 438–483*.

- Arup (2013)
Arup. Groningen 2013 - Implementation Study. Arup.
- Arup (2015)
Arup. Groningen Earthquakes Structural Upgrading - Site Response Analysis. ARUP.
- Arup et al. (2015)
Arup, Eucentre, TUDelft, Mosayk. LNEC-BUILD-1 - Modelling Predictions and Analysis Cross Validation. ARUP, 229746_0310_REP2004 Issue I 8 September 2017.
- Arup (2016a)
Arup. Groningen Earthquakes Structural Upgrading - Martini Type K As-Built Assessment Report. ARUP.
- Arup (2016b)
Arup. Groningen Earthquakes - Structural Upgrading - Expert System Modelling Methods and Assumptions. Arup.
- Arup (2018a)
Arup. Equivalent viscous damping for secant stiffness method with Draft NPR 9998:2017 ground motions for unreinforced masonry building super structures. Nen, Arup.
- Arup (2018b)
Arup. Exposure Database (EDB) V5. ARUP 229746_0520_REP2014 Rev009 ISSUE_DEF, 18 January 2018.
- Arya et al. (2013)
A.S. Arya, T. Boen, Y. Ishiyama. Guidelines For Earthquake Resistant Non-engineered Construction. United Nations Educational, Scientific and Cultural Organization, 7, place de Fontenoy, 75352 Paris 07 SP, France.
- Astroza et al. (2012)
M. Astroza, O. Moroni, S. Brzev, J. Tanner. Seismic Performance of Engineered Masonry Buildings in the 2010 Maule Earthquake. *Earthq Spectra*, Volume 28, No S1, pages S385–S406, June 2012.
- Atkinson (2015)
G.M. Atkinson. Ground-Motion Prediction Equation for Small-to-Moderate Events at Short Hypocentral Distances, with Application to Induced-Seismicity Hazards. *Bull of the Seismological Soc of America*, Vol 105, No 2a, pp –, April 2015. doi.org/10.1785/0120140142
- Bakema et al. (2018)
M.M. Bakema, C. Parra, P. McCann. Analyzing the Social Lead-Up to a Human-Induced Disaster: The Gas Extraction-Earthquake Nexus in Groningen, The Netherlands. *Sustainability* 2018, 10, 3621;. doi.org/10.3390/su10103621
- Bal et al. (2018)
I.E. Bal, D. Dais, E. Smyrou. "Differences" Between Induced And Natural Seismic Events. 16th European Conf on Earthq Eng, Thessaloniki 18-21 June, 2018.
- Bal et al. (2021)
I.E. Bal, D. Dais, E. Smyrou, V. Sarhosis. Novel invisible markers for monitoring cracks on masonry structures. *Construction and Bldg Mats* 300 (2021) 124013.
- Basilio et al. (2014)
I. Basilio, R. Fedele, P. Lourenço, G. Milani. Numerical and experimental analysis of full scale arches reinforced with GFRP materials. *Key Eng Mats Online*: 2014-09-12 ISSN: 1662-9795, Vol 624, pp 502-509. doi.org/10.4028/www.scientific.net/KEM.624.502
- Belletti et al. (2014)
B. Belletti, C. Damoni, M.A.N. Hendriks, A. de Boer. Analytical and numerical evaluation of the design shear resistance of reinforced concrete slabs. *Struct Conc* 15 (2014), No 3.
- Benedetti et al. (1998)
D. Benedetti, P. Carydis, P. Pezzoli. Shaking Table Tests On 24 Simple Masonry Buildings. *EARTHQUAKE ENGINEERING AND STRUCTURAL DYNAMICS*, VOL 27, 67—90 (1998).
- Bernat et al. (2014)
E. Bernat, P. Roca, L. Gil. Experimental study of brick masonry walls strengthened with textile reinforced mortar. *Key Eng Mats Online*: 2014-09-12 ISSN: 1662-9795, Vol 624, pp 397-404. doi.org/10.4028/www.scientific.net/KEM.624.397
- Beyer & Mergos (2015)
K. Beyer, P. Mergos. Sensitivity Of Drift Capacities Of Urm Walls To Cumulative Damage Demands And Implications On Loading Protocols For Quasi-Static Cyclic Tests. 12th North American Masonry Conf, Denver, Colorado May 17-20, 2015.
- den Bezemer & van Elk (2018)
T. den Bezemer, J. van Elk. Special Report on the Zeerijp Earthquake – 8th January 2018. NAM.
- Bindiganavile-Ramadas (2018)
S. Bindiganavile-Ramadas. A Hyperbolic model for Degradation in Tension mode-I Fracture of

- Masonry - Implementation and Validation in Engineering masonry model. Delft U of Tech. Bird et al. (2006)
- J.F. Bird, J.J. Bommer, H. Crowley, R. Pinho. Modelling liquefaction-induced building damage in earthquake loss estimation. *Soil Dyns and Earthq Eng* 26 (2006) 15–30.
- Blaber et al. (2015)
- J. Blaber, B. Adair, A. Antoniou. Ncorr- Open-Source 2D Digital Image Correlation Matlab Software. *Experimental Mech*s DOI. doi.org/10.1007/s11340-015-0009-1
- Blong (2003)
- R. Blong. A new Damage Index. *Natural Hrzrds* 30: 1–23, 2003.
- de Boer et al. (2016)
- S.J. de Boer, A. van den Bos, J. van Es, N. Kostense, H. Krijgsman, J. Manie, P. Meijers, R. Ringers, R. Roijakkers, A. Verweij, C. van der Vliet, R. Vonk, P.A. Vázquez Gutiérrez. Guideline for NLTH Earthquake Analyses of Existing Buildings in Groningen Performed with DIANA FEM Software. ABT-Wassenaar, ARCADIS, ROYAL HASKONINGDHV, TNO.
- Boffi & Castellani (1988)
- G. Boffi, A. Castellani. Effects of Surface Waves on the Rotational components of earthquake motion. *Procdngs of Ninth World Conf on Earthq Eng*, 1988 Tokyo-Kyoto, Japan.
- Bommer et al. (2013)
- J. Bommer, H. Crowley, R. Pinho. Review of Arup Report “Seismic Risk Study: Earthquake Scenario-Based Risk Assessment. NAM.
- Bommer et al. (2015a)
- J.J. Bommer, B. Dost, B. Edwards, A. Rodriguez-Marek, P.P. Kruiver, P. Meijers, M. Ntinalexis, P.J. Stafford, J. van Elk, D. Doornhof. Development of Version 2 GMPEs for Response Spectral Accelerations and Significant Durations from Induced Earthquakes in the Groningen Field. NAM.
- Bommer et al. (2015b)
- J.J. Bommer, P.J. Stafford, B. Edwards, B. Dost, M. Ntinalexis. Development of GMPEs for Response Spectral Accelerations and for Strong-Motion Durations. NAM.
- Bommer et al. (2017a)
- J.J. Bommer, P.J. Stafford, M. Ntinalexis. Empirical Ground-Motion Prediction Equations for Peak Ground Velocity from Small-Magnitude Earthquakes in the Groningen Field Using Multiple Definitions of the Horizontal Component of Motion. NAM.
- Bommer et al. (2017b)
- J.J. Bommer, P.J. Stafford, B. Edwards, B. Dost, E. van Dedem, A. Rodriguez-Marek, P. Kruiver, J.F. van Elk, D. Doornhof, M. Ntinalexis. Framework for a Ground-Motion Model for Induced Seismic Hazard and Risk Analysis in the Groningen Gas Field, The Netherlands. *Earthq Spectra*: May 2017, Vol 33, No 2, pp 481–498.
- Bommer et al. (2017c)
- J.J. Bommer, B. Dost, B. Edwards, P.P. Kruiver, M. Ntinalexis, A. Rodriguez-Marek, P.J. Stafford, J. van Elk. Developing a model for the prediction of ground motions due to earthquakes in the Groningen gas field. *Netherlands J of Geosciences — Geologie en Mijnbouw* 196 – 5 | s203–s213 | 2017.
- Bommer et al. (2019)
- J.J. Bommer, P.J. Stafford, M. Ntinalexis. Updated Empirical GMPEs for PGV from Groningen Earthquakes – March 2019. Imperial College & NAM.
- Bommer & van Elk (2017)
- J.J. Bommer, J. van Elk. Comment on “The Maximum Possible and the Maximum Expected Earthquake Magnitude for Production-Induced Earthquakes at the Gas Field in Groningen, The Netherlands” by Gert Zöller and Matthias Holschneider. *Bull of the Seismological Soc of America*, Vol 107, No 3, pp 1564–1567, June 2017. doi.org/10.1785/0120170040
- Bommer & MartinezPereira (1998)
- J.J. Bommer, A. MartinezPereira. The Prediction of Strong-Motion duration for engineering design. *Eleventh World Conf on Earthq Design Paper* no 84.
- Boonpichetvong et al. (2004)
- M. Boonpichetvong, H. Netzel, J.G. Rots. Numerical Analyses of Soil-Foundation-Building Interaction due to Tunnelling. *5th Intl PhD Symp in Civil Eng - London*.
- Borzi et al. (2001)
- B. Borzi, G.M. Calvi, A.S. Elnashai, E. Faccioli, J.J. Bommer. Inelastic spectra for displacement-based seismic design. *Soil Dyns and Earthq Eng* 21 (2001) 47–61.
- Borzi et al. (2008)
- B. Borzi, R. Pinho, H. Crowley. Simplified pushover-based vulnerability analysis for large-

- scale assessment of RC buildings. *Eng Structs* 30 (2008) 804–820.
- Boscardin & Cording (1989)
M.D. Boscardin, E.J. Cording. Building response to excavation-induced settlement. *J of Geotechnical Eng*, 115(1):1–21, 1989.
- Bosiljkov et al. (2008)
V. Bosiljkov, A.W. Page, V. Bokan-Bosiljkov, R. Zarnić. Evaluation of the seismic performance of brick masonry walls. *STRUCTURAL CONTROL AND HEALTH MONITORING Struct Control Health Monit* 2010; 17:100–118
Published online 22 December 2008 in Wiley InterScience (www.interscience.wiley.com). doi.org/10.1002/stc.299
- Boulanger & Idriss (2014)
R.W. Boulanger, I.M. Idriss. CPT and SPT based Liquefaction Triggering Procedures. Center for Geotechnical Modeling - Department of Civil and Environmental Eng - U of California.
- Bourne et al. (2015)
S.J. Bourne, S.J. Oates, J.J. Bommer, B. Dost, J. van Elk, D. Doornhof. A Monte Carlo Method for Probabilistic Hazard Assessment of Induced Seismicity due to Conventional Natural Gas Production. *Bull of the Seismological Soc of America*, Vol 105, No 3, pp 1721–1738, June 2015. doi.org/10.1785/0120140302
- Bourne et al. (2018)
S.J. Bourne, S.J. Oates, J. van Elk. The exponential rise of induced seismicity with increasing stress levels in the Groningen gas field and its implications for controlling seismic risk. *Geophys J Int* (2018) 213, 1693–1700. doi.org/10.1093/gji/ggy084
- Bourne & Oates (2017)
S.J. Bourne, S.J. Oates. Development of statistical geomechanical models for forecasting seismicity induced by gas production from the Groningen field. *Netherlands J of Geosciences — Geologie en Mijnbouw* 196 – 5 | s175–s182 | 2017.
- BouwenmetStaal (2015)
BouwenmetStaal. Aardbevingsbestendig Ontwerpen. Bouwen met Staal.
- Brzev (2019)
S. Brzev. Earthquake-Resistant Confined Masonry - Construction. National Information Center of Earthq Eng Indian Institute of Tech Kanpur India.
- Bultot et al. (2012)
E. Bultot, L.V. Parys, S. Datoussaid. Out-of-plane Behaviour of URM Walls: Experimental studies. 9th National Congress on Theoretical and Applied Mechs, Brussels, 9-10-11 May 2012.
- Burland et al. (1977)
J.B. Burland, B.B. Broms, V.F.B.D. Mello. Behaviour of Foundations and Structures. Bldg Research Establishment. doi
- Burland et al. (2001)
J.B. Burland, J.R. Standing, F.M. Jardine. Building response to tunnelling Case studies from construction of the Jubilee Line Extension, London. CIRIA Special Publication 200.
- Burland & Wroth (1974)
J.B. Burland, C.P. Wroth. Settlement of buildings and associated damage. *Procings of Conf on Settlement of Struts*, pages 611–654, Cambridge, 1974 Pentech Press.
- Burnett et al. (2007)
S. Burnett, M. Gilbert, T. Molyneaux, G. Beattie, B. Hobbs. The performance of unreinforced masonry walls subjected to low-velocity impacts: Finite element analysis. *Intl J of Impact Eng* 34 (2007) 1433–1450.
- CUR et al. (1990)
CUR, Jansen, J.G. Rots, Walraven. Pre-advice Computational Masonry Mechanics, final report CUR committee PA33 'Masonry Mechanics'. CUR, Gouda, 1990, CUR-report-90-6.
- Calderini et al. (2008)
C. Calderini, S. Cattari, S. Lagomarsino. In-plane strength of unreinforced masonry piers. *Earthq Engng Struct Dyn* 2009; 38:243–267.
- Calderini et al. (2015)
C. Calderini, S.D. Abbati, P. Cotič, M. Kržan, V. Bosiljkov. In-plane shear tests on masonry panels with plaster: correlation of structural damage and damage on artistic assets. *Bull Earthq Eng* (2015) 13:237–256 DOI. doi.org/10.1007/s10518-014-9632-y
- Calduran (2004)
Calduran. Kalkzandsteen Dilatatierichtlijnen. Calduran Kalkzandsteen Bouwtechniek en Voorlichting.
- Calvi et al. (2006)
G.M. Calvi, R. Pinho, G. Magenes, J.J. Bommer, L.F. Restrepo-Vélez, H. Crowley. Development Of Seismic Vulnerability Assessment Methodologies Over The Past 30 Years. *ISIT J*

- of Earthq Tech, Paper No 472, Vol 43, No 3, September 2006, pp 75-104.
- Calvi & Kingsley (1996)
G.M. Calvi, G.R. Kingsley. Problems and certainties in the experimental simulation of the seismic response of MDOF structures. EngStructs, Vol 18, No 3, pp 213-226, 1996.
- Cannizzaro et al. (2018)
F. Cannizzaro, B. Pantò, S. Caddemi, I. Calì. A Discrete Macro-Element Method (DMEM) for the nonlinear structural assessment of masonry arches. Eng Structs 168 (2018) 243–256. doi.org/10.1016/j.engstruct.2018.04.006
- Casapulla et al. (2016)
C. Casapulla, L.U. Argiento, F.d. Porto, D. Bonaldo. The relevance of frictional resistances in out-of-plane mechanisms of block masonry structures. Procdngs of the 16th Intl Brick and Block Masonry Conf, Padova, Italy, 26-30 June 2016.
- Casapulla & Argiento (2016)
C. Casapulla, L.U. Argiento. The comparative role of friction in local out-of-plane mechanisms of masonry buildings. Pushover analysis and experimental investigation. Eng Structs 126 (2016) 158–173.
- Casapulla & Portioli (2015)
C. Casapulla, F. Portioli. Experimental investigation on the torsion- shear interaction between stone blocks in frictional contact. WIT Transactions on the Built Environment · July 2015.
- Castellani & Boffi (1986)
A. Castellani, G. Boffi. Rotational components of the surface ground motion during an earthquake. Earthq engineering and structural dynamics vol 14, 751-767.
- Castellazzi et al. (2017)
G. Castellazzi, A.M. D'Altri, S. de Miranda, A. Chiozzi, A. Tralli. Numerical insights on the seismic behaviour of a non- isolated historical masonry tower. Bull Earthq Eng DOI. doi.org/10.1007/s10518-017-0231-6
- Caudron et al. (2008)
M. Caudron, M. Al Heib, F. Emeriault. Collapses of underground cavities and soil-structure interactions - influences of the position of the structure relative to the cavity. Intl Association for Computer Methods and Advcs in Geomechanics (IACMAG). doi
- Causevic & Mitrovic (2010)
M. Causevic, S. Mitrovic. Comparison between non-linear dynamic and static seismic analysis of structures according to European and US provisions. Bull Earthq Eng DOI. doi.org/10.1007/s10518-010-9199-1
- Ceran & Erberik (2013)
H.B. Ceran, M.A. Erberik. Effect of out-of-plane behavior on seismic fragility of masonry buildings in Turkey. Bull Earthq Eng (2013) 11:1775–1795 DOI. doi.org/10.1007/s10518-013-9449-0
- Chacko et al. (2018)
J. Chacko, A. Giannakou, V. Drosos, P. Tasiopoulou. Evaluation of Liquefaction- Induced Settlements of typical Residential Buildings on Shallow Foundations Groningen, The Netherlands. Nam.
- Chaimoon & Attard (2009)
K. Chaimoon, M.M. Attard. Experimental and numerical investigation of masonry under three-point bending (in-plane). Eng Structs 31 (2009) 103–112.
- Chong (1993)
V.L. Chong. The Behaviour Of Laterally Loaded Masonry Panels With Openings. School Of Civil and Struct Eng U Of Plymouth.
- Chopra & Goel (1999)
A.K. Chopra, R.K. Goel. Capacity-Demand-Diagram Methods for Estimating Seismic Deformation of Inelastic Structures: SDF Systems. Pacific Earthq Eng Research Center - College of Eng U of California, Berkeley.
- Chuang et al. (2004)
S. Chuang, Y. Zhuge, P.C. McBean. Seismic Retrofitting Of Unreinforced Masonry Walls By Cable System. 13th World Conf on Earthq Eng Vancouver, BC, Canada.
- Chummar (1984)
A.V. Chummar. Excessive Settlement in Buildings. Intl Conf on Case Histories in Geotechnical - Eng Paper 17.
- Chung & Park (2016)
L. Chung, T. Park. Evaluation of Natural Frequency Through Measurement of Ambient Vibration for Wall-type RC Structures. J of Asian Architecture and Bldg Eng/May 2016/301.
- Colangelo (2015)
F. Colangelo. On the code-compliant verification of seismic damage to non-structural

- masonry infills. *Bull Earthq Eng* (2015) 13:2051–2072 DOI. doi.org/10.1007/s10518-014-9704-z
- Mine Subsidence Engineering Consultants (2007)
- M.S.E. Mine Subsidence Engineering Consultants. Mine Subsidence Damage to Building Structures. Revision A. doi
- Cornelissen et al. (1986)
- H.A.W. Cornelissen, D.A. Hordijk, H.W. Reinhardt. Experimental determination of crack softening characteristic of normal weight and lightweight concrete. *Heron* 31 (2), 45-56.
- Correia et al. (2018)
- A.A. Correia, U. Tomassetti, A. Campos-Costa, A. Penna, G. Magenes, F. Graziotti. Collapse Shake-table Test On a Urm-timber Roof Substructure. 16th european conference on Earthq engineering, Thessaloniki.
- Costa et al. (2007)
- A.A. Costa, A. Arêde, A. Costa. Experimental Tests On Masonry Structures: From the Simplest In-situ Test To Complex Lab Test Setups. 2nd Intl Conf on Advcs in Experimental Struct Eng Tongji Univ, Shanghai 200092, China.
- Costa et al. (2012a)
- A.A. Costa, A. Arêde, A. Costa, C. Sousa-Oliveira. Out-of-plane behaviour of existing stone masonry buildings: experimental evaluation. *Bull Earthq Eng* (2012) 10:93–111 DOI. doi.org/10.1007/s10518-011-9332-9
- Costa et al. (2012b)
- A. Costa, A. Arêde, F. Garcia, A.A. Costa, C. Quintela, C.S. Oliveira. Out-of-Plane Cyclic Experimental Testing of Traditional Stone Masonry Walls with Distributed Loads. 15 Wcee.
- Costley & Abrams (1996)
- A.C. Costley, D.P. Abrams. Dynamic Response of Unreinforced Masonry Buildings with Flexible Diaphragms. Technical Report NCEER-96-0001, U of Illinois at Urbana-Champaign.
- Crammond et al. (2013)
- G. Crammond, S.W. Boyd, J.M. Dulieu-Barton. Speckle pattern quality assessment for digital image correlation. *Optics and Lasers in Eng* 51 (2013) 1368–1378.
- Crowley et al. (2004)
- H. Crowley, R. Pinho, J.J. Bommer. A Probabilistic Displacement-based Vulnerability Assessment Procedure for Earthquake Loss Estimation. *Bull of Earthq Eng* 2- 173–219, 2004.
- Crowley et al. (2015)
- H. Crowley, R. Pinho, B. Polidoro, P. Stafford. Development of v2 Partial Collapse Fragility and Consequence Functions for the Groningen Field. NAM.
- Crowley et al. (2017a)
- H. Crowley, R. Pinho, B. Polidoro, J. van Elk. Developing fragility and consequence models for buildings in the Groningen field. *Netherlands J of Geosciences — Geologie en Mijnbouw* 196 – 5 | s247–s257 | 2017.
- Crowley et al. (2017b)
- H. Crowley, B. Polidoro, R. Pinho, J. van Elk. Framework for Developing Fragility and Consequence Models for Local Personal Risk. *Earthq Spectra* · August 2017. doi.org/10.1193/083116EQS140M
- Crowley et al. (2018)
- H. Crowley, R. Pinho, J. Van Elk, J. Uilenreef. Probabilistic damage assessment of buildings due to induced seismicity. *Bull of Earthq Eng*. doi.org/10.1007/s10518-018-0462-1
- Crowley et al. (2019)
- H. Crowley, R. Pinho, F. Cavalieri. Report on the v6 Fragility and Consequence Models for the Groningen Field. Nam.
- Curtin et al. (2008)
- Curtin, Shaw, Beck, Bray, Easterbrook. *Structural masonry designers' manual..* John Wiley & Sons.
- Custer (2015)
- R. Custer. Hierarchical Modelling of Flood Risk for Engineering Decision Analysis. Technical U of Denmark Department of Civil Eng.
- Dalgic et al. (2023)
- K.D. Dalgic, B. Gulen, Y. Liu, S. Acikgoz, H. Burd, M. Marasli, A. Ilki. Masonry buildings subjected to settlements: Half-scale testing, detailed measurements, and insights into behaviour. *Eng Structs* 278 (2023) 115233. doi.org/10.1016/j.engstruct.2022.115233
- Damiola et al. (2018)
- M. Damiola, R. Esposito, F. Messali, J.G. Rots. Quasi-Static Cyclic Two-Way Out-Of-Plane Bending Tests And Analytical Models Comparison For Urm Walls. 10th Intl Masonry Conf, Milan.

- DeJong et al. (2009)
M.J. DeJong, B. Belletti, M.A.N. Hendriks, J.G. Rots. Shell elements for sequentially linear analysis: Lateral failure of masonry structures. *Eng Struct* 31 (2009) 1382–1392.
- DeSantis et al. (2016)
S. DeSantis, P. Casadei, G. DeCanio, G. deFelice, M. Malena, M. Mongelli, I. Roselli. Seismic performance of masonry walls retrofitted with steel reinforced grout. *Earthq Engng Struct Dyn* 2016; 45:229–251.
- Debailleux (2019)
L. Debailleux. Suggested Method for the Determination of the Weathering Index of Ancient Fired Clay Bricks. 13th North American Masonry Conf, SLC, Utah.
- Deckner (2013)
F. Deckner. Ground vibrations due to pile and sheet pile driving – influencing factors, predictions and measurements. KTH Royal Institute of Tech.
- Degée et al. (2008)
H. Degée, V. Denoel, P. Candeias, A. Campos-Costa, E. Coelho. Experimental investigations on non-engineered masonry houses in low to moderate seismicity areas. The 14 World Conf on Earthq Eng, China.
- Dempsey & Suckale (2017)
D. Dempsey, J. Suckale. Physics-based forecasting of induced seismicity at Groningen gas field, the Netherlands. *Geophys Res Lett*, 44, 7773–7782. doi.org/10.1002/2017GL073878.
- Derakhshan (2011)
H. Derakhshan. Seismic Assessment of Out-of-Plane Loaded Unreinforced Masonry Walls. The U of Auckland Department of Civil and Environmental Eng New Zealand.
- Derakhshan et al. (2013a)
H. Derakhshan, M.C. Griffith, J.M. Ingham. Airbag testing of multi-leaf unreinforced masonry walls subjected to one-way bending. *Eng Struct* 57 (2013) 512–522.
- Derakhshan et al. (2013b)
H. Derakhshan, M.C. Griffith, J.M. Ingham. Out-of-Plane Behavior of One-Way Spanning Unreinforced Masonry Walls. *J Eng Mech* 2013139:409–417.
- Derakhshan et al. (2018a)
H. Derakhshan, W. Lucas, P. Visintin, M.C. Griffith. Out-of-plane Strength of Existing Two-way Spanning Solid and Cavity Unreinforced Masonry Walls. *Structs* 13 (2018) 88–101.
- Derakhshan et al. (2018b)
H. Derakhshan, Y. Nakamura, H. Goldsworthy, K.Q. Walsh, J.M. Ingham, M.C. Griffith. Peak Floor Accelerations in Unreinforced Masonry Buildings With Flexible Diaphragms. *10amc*.
- Dhanasekar et al. (2019)
M. Dhanasekar, P. Prasad, J. Dorji, T. Zahra. Serviceability Assessment of Masonry Arch Bridges Using Digital Image Correlation. *J Bridge Eng*, 2019, 24(2): 04018120.
- Didier et al. (2017)
M. Didier, G. Abbiati, M. Broccardo, K. Beyer, L. Danciu, M. Petrović, N. Mojsilović, B. Stojadinović. Quantification of Non-Structural Damage in Unreinforced Masonry Walls Induced by Geothermal Reservoir Exploration using Quasi-Static Cyclic Tests. *Procngs of the 13th Canadian Masonry Symp*, Halifax, Canada, June 2017.
- Didier et al. (2018)
M. Didier, G. Abbiati, F. Hefti, M. Broccardo, B. Stojadinovic. Damage Quantification In Plastered Unreinforced Masonry Walls Using Digital Image Correlation. 10th Australasian Masonry Conf, 14–18 February, 2018.
- Dizhur et al. (2010)
D. Dizhur, N. Ismail, C. Knox, R. Lumantarna, J.M. Ingham. Performance Of Unreinforced and Retrofitted Masonry Buildings During the 2010 Darfield Earthquake. *BULLETIN OF THE NEW ZEALAND SOCIETY FOR EARTHQUAKE ENGINEERING*, Vol 43, No 4, December 2010.
- Dizhur et al. (2011)
D. Dizhur, J. Ingham, L. Moon, M. Griffith, A. Schultz, I. Senaldi, G. Magenes, J. Dickie, S. Lissel, J. Centeno, C. Ventura, J. Leite, P. Lourenco. Performance of masonry buildings and churches in the 22 February 2011 Christchurch earthquake. *BULLETIN OF THE NEW ZEALAND SOCIETY FOR EARTHQUAKE ENGINEERING*, Vol 44, No 4, December 2011.
- Dizhur et al. (2014)
D. Dizhur, M. Griffith, J. Ingham. Out-of-plane strengthening of unreinforced masonry walls using near surface mounted fibre reinforced polymer strips. *Eng Struct* 59 (2014) 330–343.
- Dizhur et al. (2017)
D.Y. Dizhur, M. Giaretton, I. Giongo, J.M. Ingham. Seismic Retrofit Of Masonry Walls

- Using Timber Strong-walls. *J of the Struct Eng Soc of New Zealand Inc*, Vol 30 No 2.
- Doherty (2000)
K.T. Doherty. An investigation of the weak links in the seismic load path of unreinforced masonry buildings. Department of Civil and Environmental Eng, The U of Adelaide, Australia.
- Doherty et al. (2002)
K. Doherty, M.C. Griffith, N. Lam, J. Wilson. Displacement-based seismic analysis for out-of-plane bending of unreinforced masonry walls. *EARTHQUAKE ENGINEERING AND STRUCTURAL DYNAMICS Earthq Engng Struct Dyn* 2002; 31:833–850 (. doi.org/10.1002/eqe.126)
- Dolatshahi et al. (2015)
K.M. Dolatshahi, A.J. Aref, A.S. Whittaker. Interaction Curves for In-Plane and Out-of-Plane Behaviors of Unreinforced Masonry Walls. *J of Earthq Eng*, 19:60–84, 2015.
- Dolatshahi & Aref (2011)
K.M. Dolatshahi, A.J. Aref. Three Dimensional Modeling of Masonry Structures and Interaction of In-Plane and Out-of-Plane Deformation of Masonry Walls. *Eng Mechs Institute Conf (EMI2011)*.
- Dolšek & Fajfar (2008)
M. Dolšek, P. Fajfar. The effect of masonry infills on the seismic response of a four-storey reinforced concrete frame — a deterministic assessment. *Eng Struct* 30 (2008) 1991–2001.
- Dost et al. (2013)
B. Dost, M. Caccavale, T. van Eck, D. Kraaijpoel. Report on the expected PGV and PGA values for induced earthquakes in the Groningen area. KNMI.
- Dost & Kraaijpoel (2012)
B. Dost, D. Kraaijpoel. The August 2012 earthquake near Huizinge. KNMI.
- Dungca et al. (2016)
J.R. Dungca, D.Y. Acosta, M.B. Juego, Sanches H., Sanches I.. The Propagation Behavior Of Pile-Driving-Induced Vibration Done On Soil At Varying Distances And Its Effects On Existing Structures. *Intl J of GEOMATE*, May, 2016, Vol 10, Issue 21, pp 1877-1883.
- D'Altri (2017)
A.M. D'Altri. A Computational 3D Model For In-Plane And Out-Of-Plane Analysis Of Masonry Structures. U of Bologna.
- D'Altri et al. (2017)
A.M. D'Altri, G. Castellazzi, S. de Miranda, A. Tralli. Seismic-induced damage in historical masonry vaults: A case-study in the 2012 Emilia earthquake-stricken area. *J of Bldg Eng* 13 (2017) 224–243.
- Edwards et al. (2019)
B. Edwards, B. Zurek, E. van Dedem, P.J. Stafford, S. Oates, J. van Elk, B. deMartin, J.J. Bommer. Simulations for the development of a ground motion model for induced seismicity in the Groningen gas field, The Netherlands. *Bull of Earthq Eng* (2019) 17:4441–4456. doi.org/10.1007/s10518-018-0479-5
- El-Dakhkhni et al. (2013)
W.W. El-Dakhkhni, B.R. Banting, S.C. Miller. Seismic Performance Parameter Quantification of Shear-Critical Reinforced Concrete Masonry Squat Walls. *J Struct Eng*, 2013, 139(6): 957-973.
- ElGawady et al. (2005)
M.A. ElGawady, P. Lestuzzi, M. Badoux. Seismic performance of URM walls retrofitted using FRP. *NZSEE Conf*.
- ElGawady et al. (2006)
M.A. ElGawady, P. Lestuzzi, M. Badoux. Aseismic retrofitting of unreinforced masonry walls using FRP. *Composites: Part B* 37 (2006) 148–162.
- ElGawady et al. (2016)
M.A. ElGawady, P. Lestuzzi, M. Badoux. Retrofitting of Masonry Walls Using Shotcrete. 2006 NZSEE Conf.
- Elenas (2000)
A. Elenas. Correlation between seismic acceleration parameters and overall structural damage indices of buildings. *Soil Dyns and Earthq Eng* 20 (2000) 93±100.
- Van Elk et al. (2017)
J. Van Elk, J. Uilenreef, D. Doornhof. Methodology Prognosis of Building Damage and Study and Data Acquisition Plan for Building Damage. *Nam © Ep201701249834*.
- van Elk et al. (2019)
J.F. van Elk, S.J. Bourne, S.J. Oates, J.J. Bommer, R. Pinho, H. Crowley. A Probabilistic Model to Evaluate Options for Mitigating Induced Seismic Risk. *Earthq Spectra* · January 2019. doi.org/10.1193/050918EQS118M
- van Elk & Doornhof (2019a)
J. van Elk, D. Doornhof. Study and Data

- Acquisition Plan Induced Seismicity in Groningen. Nam.
- van Elk & Doornhof (2019b)
J. van Elk, D. Doornhof. Special Report on the Westerwijtwerd Earthquake 22nd May 2019. Nam.
- Ellsworth & McGarr (2016)
W.L. Ellsworth, A.F. McGarr. Review of "Hazard and Risk Assessment for Induced Seismicity in Groningen – Update 7th November 2015". USGS.
- Elmenschawi et al. (2010)
A.E. Elmenschawi, M. Sorour, A. Mufti, L.G. Jaeger, N. Shrive. In-plane Seismic Behaviour of Historic Stone Masonry. *Canadian J of Civil Eng*, 37(3): 465–476.
- Erdal (2010)
M. Erdal. Improving out-of-plane strength and ductility of unreinforced masonry walls in low-rise buildings by centrally applied FRP strip. *International J of the Physical Sciences Vol 5 (2)*, pp 116-131, February, 2010.
- Esposito et al. (2016)
R. Esposito, F. Messali, J.G. Rots. Tests For the Characterization Of Replicated Masonry and Wall Ties. C31B60 TU Delft.
- Esposito et al. (2017)
R. Esposito, K. Terwel, G.J.P. Ravenshorst, H.R. Schipper, F. Messali, J.G. Rots. Cyclic pushover test on an unreinforced masonry structure resembling a typical Dutch terraced house. 16th World Conf on Earthq Eng: Santiago, Chile.
- Esposito et al. (2018)
R. Esposito, S. Jafari, G.J.P. Ravenshorst, H.R. Schipper, J.G. Rots. Influence Of The Behaviour Of Calcium Silicate Brick And Element Masonry On The Lateral Capacity Of Structures. 10th australasian masonry conference, sydney australia.
- Esposito et al. (2019)
R. Esposito, F. Messali, G.J.P. Ravenshorst, H.R. Schipper, J.G. Rots. Seismic assessment of a lab-tested two-storey unreinforced masonry Dutch terraced house. *Bull Earthq Eng* 17, 4601–4623 (2019). doi.org/10.1007/s10518-019-00572-w
- Esposito & Ravenshorst (2017)
R. Esposito, G. Ravenshorst. Quasi-static Cyclic In-plane Tests On Masonry Components 2016/2017. Delft U of Tech Report number C31B67WP3-4, version 1, 10 August 2017.
- Evangelidou (2016)
P. Evangelidou. Probabilistic nonlinear finite element analysis of reinforced concrete beams without shear reinforcement. TU Delft.
- Ewing & Kowalsky (2004)
B.D. Ewing, M.J. Kowalsky. Compressive Behavior of Unconfined and Confined Clay Brick Masonry. *J Struct Eng*, 2004, 130(4): 650-661.
- FEMA (2000)
FEMA. Pre-Standard and Commentary for the Seismic Rehabilitation of Buildings. FEMA.
- FEMA (2012)
FEMA. Hazus MH 2.1. FEMA.
- FEMA (2013)
FEMA. Hazus MH MR5. FEMA.
- Farhidzadeh et al. (2013)
A. Farhidzadeh, E. Dehghan-Niri, A. Moustafa, S. Salamone, A. Whittaker. Damage Assessment of Reinforced Concrete Structures Using Fractal Analysis of Residual Crack Patterns. *Experimental Mech* (2013) 53:1607–1619. 10.1007/s11340-013-9769-7
- Farrell et al. (2014)
R. Farrell, R. Mair, A. Sciotti, A. Pigorini. Building response to tunnelling. *Soils and Foundations* 2014; 54(3):269–279.
- Fathy et al. (2008)
A.M. Fathy, J. Planas, J.M. Sancho. A numerical study of masonry Cracks II. *Anales de Mecánica de la Fractura* 25, Vol 1 (2008).
- Feenstra et al. (1998)
P.H. Feenstra, J.G. Rots, A. Arnesen, J.G. Teigen, K.V. Hoiseth. A 3D constitutive model for concrete based on a co-rotational concept. *Proc Euro-C Conf Comput Modelling of Conc Strucs*, Balkema.
- Fema (2020)
Fema. A Practical Guide to Soil-Structure Interaction. Fema P-2091. doi
- Ferreira et al. (2015)
T.M. Ferreira, A.A. Costa, A. Costa. Analysis of the Out-of-Plane seismic behaviour of unreinforced masonry: a literature review. *Intl J of Architectural Heritage* 9, 949-942.
- Ferretti et al. (2018a)
F. Ferretti, C. Mazzotti, R. Esposito, J.G. Rots. Shear-sliding behavior of masonry: numerical micro-modeling of triplet tests. Delft U of Tech.

- Ferretti et al. (2018b)
F. Ferretti, S. Jafari, R. Esposito, J.G. Rots, C. Mazzotti. Investigation of the shear-sliding behavior of masonry through shove test: experimental and numerical studies. SAHC.
- Ferris & Tin-Loi (2001)
M.C. Ferris, F. Tin-Loi. Limit analysis of frictional block assemblies as a mathematical program with complementarity constraints. *Intl J of Mech Sciences* 43 (2001) 209}224.
- Fiore et al. (2012)
A. Fiore, A. Netti, P. Monaco. The influence of masonry infill on the seismic behaviour of RC frame buildings. *Eng Struct* 44 (2012) 133–145.
- Fiore et al. (2014)
A. Fiore, G.C. Marano, D. Laucelli, P. Monaco. Evolutionary Modeling to Evaluate the Shear Behavior of Circular Reinforced Concrete Columns. *Advcs in Civil Eng Volume 2014*, Article ID 684256. doi.org/10.1155/2014/684256
- Foraboschi (2009)
P. Foraboschi. Coupling effect between masonry spandrels and piers. *Material and Structs*, 42, 279-300.
- Forbes & Camp (2013)
R.H. Forbes, W.M. Camp. Settlement & Vibration Monitoring for Transmission Line Foundation Installation. S&ME, NCDOT Conf.
- Forrest (1999)
J.A. Forrest. Modelling of Ground Vibration from Underground Railways. U of Cambridge.
- Franchin et al. (2009)
P. Franchin, P.E. Pinto, P. Rajeev. Confidence in the Confidence Factor. Eurocode 8 Perspectives from the Italian Standpoint - Workshop, 25-38, Doppiovoce, Napoli, Italy.
- Friedland (2009)
C.J. Friedland. Residential Building Damage From Hurricane Storm Surge: Proposed Methodologies To Describe, Assess And Model Building Damage. The Department of Civil and Environmental Eng, Louisiana State U.
- Fuente et al. (2010)
J.V. Fuente, R. Fernandez, V. Albert. Brick masonry elastic modulus determination using the numerical simulation and experiments of sonic wave propagation. Simulation in NDT Online Workshop in www.ndtnet in September 2010.
- Gams et al. (2014)
M. Gams, M. Tomazevic, A. Kwecien. Strengthening brick masonry by repointing – an experimental study. *Key Eng Mats Online*: 2014-09-12 ISSN: 1662-9795, Vol 624, pp 444-452.
- Ganz & Thürlimann (1984)
H. Ganz, B. Thürlimann. Versuche an Mauerwerksscheiben unter Normalkraft und Querkraft. Institut für Baustatik und Konstruktion, ETH Zürich; Nr 7502-4, Birkhäuser Verlag Basel ISBN 3-7643-1665-9.
- García-Macías & Ubertini (2019)
E. García-Macías, F. Ubertini. Seismic interferometry for earthquake-induced damage identification in historic masonry towers. *Mech Systems and Signal Processing* 132 (2019) 380–404.
- Gattesco et al. (2016)
N. Gattesco, L. Macorini, A. Dudine. Experimental Response of Brick-Masonry Spandrels under In-Plane Cyclic Loading. *ASCE J of Struct Eng Vol 142*, Issue 2 (February 2016).
- Del Gaudio et al. (2017)
C. Del Gaudio, M.T. De Risi, P. Ricci, G.M. Verderame. Drift-based fragility functions for hollow clay masonry infills in RC buildings under in-plane seismic actions. Anidis, 2017, Pistoia.
- Gazetas (1991)
G. Gazetas. Formulas and Charts For Impedances Of Surface and Embedded Foundations. *J of Geotechnical Eng*, Vol 117, No 9, September, 1991 ©ASCE, ISSN 0733-9410/91/0009-1363.
- Gehl et al. (2013)
P. Gehl, D.M. Seyed, J. Douglas. Vector-valued fragility functions for seismic risk evaluation. *Bull Earthq Eng* (2013) 11:365–384 -DOI. doi.org/10.1007/s10518-012-9402-7
- Gehri et al. (2020)
N. Gehri, J. Mata-Falcón, W. Kaufmann. Automated crack detection and measurement based on digital image correlation. *Construction and Bldg Mats* 256 (2020) 119383.
- Ghandil & Behnamfar (2015)
M. Ghandil, F. Behnamfar. The near-field method for dynamic analysis of structures on soft soils including inelastic soil–structure

- interaction. *Soil Dyns and Earthq Eng* 75 (2015) 1–17.
- Ghobarah & Mandooh-Galal (2004)
A. Ghobarah, K.E. Mandooh-Galal. Out-of-Plane Strengthening of Unreinforced Masonry Walls with Openings. *J Compos Constr*, 2004, 8(4): 298–305.
- Ghorbani et al. (2015)
R. Ghorbani, F. Matta, M.A. Sutton. Full-Field Deformation Measurement and Crack Mapping on Confined Masonry Walls Using Digital Image Correlation. *Experimental Mech* (2015) 55:227–243.
- Giardina et al. (2008)
G. Giardina, M.A.N. Hendriks, J.G. Rots. Numerical analyses of tunnel-induced settlement damage to a masonry wall. 7th fib PhD Symp in Stuttgart, Germany.
- Giardina et al. (2012)
G. Giardina, A. Marini, M.A.N. Hendriks, J.G. Rots, F. Rizzardini, G. Giuriani. Experimental analysis of a masonry façade subject to tunnelling-induced settlement. *Eng Struct* 45 (2012) 421–434.
- Giardina et al. (2013a)
G. Giardina, A.V. van de Graaf, M.A.N. Hendriks, J.G. Rots, A. Marini. Numerical analysis of a masonry façade subject to tunnelling-induced settlements. *Eng Struct* 54 (2013) 234–247.
- Giardina et al. (2013b)
G. Giardina, J.G. Rots, M.A.N. Hendriks. Modelling of Settlement Induced Building Damage. TU Delft.
- Giardina et al. (2015a)
G. Giardina, M.A.N. Hendriks, J.G. Rots. Sensitivity study on tunnelling induced damage to a masonry façade. *Eng Struct* 89 (2015) 111–129.
- Giardina et al. (2015b)
G. Giardina, M.J. DeJong, R.J. Mair. Interaction between surface structures and tunnelling in sand: Centrifuge and computational modelling. *Tunnelling and Underground Space Tech* 50 (2015) 465–478.
- Giaretton et al. (2015)
M. Giaretton, D. Dizhur, C. Qian, F.d. Porto, J. Ingham. Dynamic behaviour of seismically retrofitted clay brick masonry cavity walls. *Procdngs of the Tenth Pacific Conf on Earthq Eng Bldg an Earthq-Resilient Pacific* 6-8 November 2015, Sydney, Australia.
- Giaretton et al. (2016a)
M. Giaretton, K. Walsh, D. Dizhur, F. daPorto, J. Ingham. Retrofitting URM cavity walls for out-of-plane composite behaviour. *Brick and Block Masonry – Trends, Innovations and Challenges – Modena, da Porto & Valluzzi (Eds)*.
- Giaretton et al. (2016b)
M. Giaretton, D. Dizhur, J.M. Ingham. Shaking table testing of as-built and retrofitted clay brick URM cavity-walls. *Eng Struct* 125 (2016) 70–79.
- Giaretton et al. (2016c)
M. Giaretton, D. Dizhur, F. daPorto, J.M. Ingham. Construction Details and Observed Earthquake Performance of Unreinforced Clay Brick Masonry Cavity-walls. *Structs* 6 (2016) 159–169.
- Gilbert et al. (2002)
M. Gilbert, B. Hobbs, T.C.K. Molyneaux. The performance of unreinforced masonry walls subjected to low-velocity impacts: experiments. *Intl J of Impact Eng* 27 (2002) 231–251.
- Gill & Malamud (2014)
J.C. Gill, B.D. Malamud. Reviewing and visualizing the interactions of natural hazards. *Rev Geophys*, 52, 680–722. doi.org/10.1002/2013RG000445
- Gilstrap & Dolan (1998)
J.M. Gilstrap, C.W. Dolan. Out-of-plane Bending Of Frp-reinforced Masonry Walls. *Composites Science and Tech* 58 (1998) 1277–1284.
- Giongo et al. (2014)
I. Giongo, A. Wilson, D.Y. Dizhur, H. Derakhshan, R. Tomasi, M.C. Griffith, P. Quenneville, J.M. Ingham. Detailed Seismic Assessment And Improvement Procedure For Vintage Flexible Timber Diaphragms. *Bull Of The New Zealand Soc For Earthq Eng*, Vol 47, No 2, June 2014.
- Giongo et al. (2019)
I. Giongo, D. Dizhur, R. Tomasi, J.M. Ingham. In-plane assessment of existing timber diaphragms in URM buildings via quasi-static and dynamic in-situ tests. doi.org/10.4028/www.scientific.net/AMR.778.495
- Giusto et al. (2024)
S. Giusto, S. Cattari, S. Lagomarsino. Investigating the Reliability of Nonlinear Static

- Procedures for the Seismic Assessment of Existing Masonry Buildings. *Appl Sci* 2024, 14, 1130. doi.org/10.3390/app14031130
- Godio et al. (2019)
M. Godio, F. Vanin, S. Zhang, K. Beyer. Quasi-static shear-compression tests on stone masonry walls with plaster: Influence of load history and axial load ratio. *Eng Struct* 192 (2019) 264–278.
- Grant et al. (2015)
D. Grant, G. Magenes, J. Rots, J. Van Elk, D. Doornhof. Groningen Earthquakes – Structural Upgrading – URM Modelling and Analysis Cross- Validation. Nam.
- Graziotti et al. (2015)
F. Graziotti, U. Tomassetti, A. Rossi, S. Kallioras, M. Mandirola, E. Cenja, A. Penna, G. Magenes. Experimental campaign on cavity walls systems representative of the Groningen building stock. Report, EUC318/2015U, EUCENTRE, Pavia, Italy.
- Graziotti et al. (2016a)
F. Graziotti, U. Tomassetti, A. Rossi, B. Marchesi, S. Kallioras, M. Mandirola, A. Fragomeli, E. Mellia, S. Peloso, F. Cuppari, G. Guerrini, A. Penna, G. Magenes. Experimental campaign on a clay URM full-scale specimen representative of the Groningen building stock. Report EUC128/2016U, Eucentre, Pavia, IT.
- Graziotti et al. (2016b)
F. Graziotti, U. Tomassetti, A. Penna, G. Magenes. Out-of-plane shaking table tests on URM single leaf and cavity walls. *Eng Struct* 125 (2016) 455–470.
- Graziotti et al. (2016c)
F. Graziotti, A. Rossi, M. Mandirola, A. Penna, G. Magenes. Experimental characterisation of calcium-silicate brick masonry for seismic assessment. 16th Intl Brick and Block Masonry conference ISBN 978-1-138-02999-6.
- Graziotti et al. (2017a)
F. Graziotti, U. Tomassetti, S. Kallioras, A. Penna, G. Magenes. Shaking table test on a full scale URM cavity wall building. *Bull of Earthq Eng*, 15 (12), pp 5329-5364.
- Graziotti et al. (2017b)
F. Graziotti, U. Tomassetti, L. Grottoli, S. Dainotti, A. Penna, G. Magenes. Shaking table tests of URM walls subjected to two-way bending out-of-plane seismic excitation. *Anidis* 2017, Pistoia.
- Graziotti et al. (2018)
F. Graziotti, U. Tomassetti, L. Grottoli, A. Penna, G. Magenes. Full-scale Out-of-plane Shaking Table Tests Of Urm Walls in Two-way Bending. 10amc.
- Green et al. (2019)
R.A. Green, J.J. Bommer, A. Rodriguez-Marek, B.W. Maurer, P.J. Stafford, B. Edwards, P.P. Kruiver, G. de Lange, J. van Elk. Addressing limitations in existing ‘simplified’ liquefaction triggering evaluation procedures: application to induced seismicity in the Groningen gas field. *Bull of Earthq Eng* (2019) 17:4539–4557. doi.org/10.1007/s10518-018-0489-3
- Green et al. (2020)
R.A. Green, J.J. Bommer, P.J. Stafford, B.W. Maurer, P.P. Kruiver, B. Edward, A. Rodriguez-Marek, G. de Lange, S.J. Oates, T. Storck, P. Omid, S.J. Bourne, J. van Elk. Liquefaction Hazard in the Groningen Region of the Netherlands due to Induced Seismicity. *J Geotech Geoenviron Eng*, 2020, 146(8): 04020068.
- Griffith (2000)
M.C. Griffith. Experimental Study of the Flexural Strength of URM Brick Walls. Research Report R169, Department of Civil and Environmental Eng, Adelaide U.
- Griffith et al. (2003)
M.C. Griffith, G. Magenes, G. Melis, L. Picchi. Evaluation Of Out-of-plane Stability Of Unreinforced Masonry Walls Subjected To Seismic Excitation. *J of Earthq Eng*, 7:S1, 141-169. doi.org/10.1080/13632460309350476
- Griffith et al. (2004)
M.C. Griffith, N.T.K. Lam, J.L. Wilson, K. Doherty. Experimental Investigation of Unreinforced Brick Masonry Walls in Flexure. *J Struct Eng* 2004130:423-432.
- Griffith et al. (2005)
M.C. Griffith, S.J. Lawrence, C.R. Willis. Diagonal Bending of Unreinforced Clay brick masonry. *J of the british masonry society*, masonry international Vol 18, No 3.
- Griffith et al. (2007)
M.C. Griffith, J. Vaculik, N.T.K. Lam, J. Wilson, E. Lumantarna. Cyclic testing of unreinforced masonry walls in two-way bending. *Earthq Engng Struct Dyn* 2007; 36:801–821.
- Griffith & Vaculik (2007)
M.C. Griffith, J. Vaculik. Out-of-Plane Flexural

- Strength of Unreinforced Clay Brick Masonry Walls. TMS J September 2007.
- de Groot (2019)
A. de Groot. Structural window design for in-plane seismic strengthening. MSc Thesis, TU Delft.
- Grottoli et al. (2019)
L. Grottoli, S. Kallioras, P. Korswagen, F. Graziotti. In-plane and out-of-plane quasi-static cyclic tests on unreinforced calcium-silicate masonry walls under high compressive load. Technical Report EUC067/2019U, EUCENTRE Foundation, Pavia, Italy Available online at www.eucentre.it/nam-project.
- Grünberg et al. (2005)
J. Grünberg, S. Meincke, F. Radtke. Experimentelle und numerische Untersuchungen des Materialverhaltens von Mauerwerk unter Erdbelastungen. Ernst & Sohn Verlag für Architektur und technische Wissenschaften GmbH & Co KG, Berlin · Mauerwerk 9, Heft 6.
- Grünthal et al. (1998)
G. Grünthal, R.M.W. Musson, J. Schwarz, M. Stucchi. European Macroseismic Scale 1998 (EMS-98). European Seismological Commission, sub commission on Eng Seismology, Working Group Macroseismic Scales Conseil de l'Europe, Cahiers du Centre Européen de Géodynamique et de Séismologie, Vol 15, Luxembourg.
- Guerrini et al. (2017a)
G. Guerrini, F. Graziotti, A. Penna, G. Magenes. Dynamic shake-table tests on two full-scale, unreinforced masonry buildings subjected to induced seismicity. Experimental vibration analysis of civil engineering structures, San Diego, USA.
- Guerrini et al. (2017b)
G. Guerrini, F. Graziotti, A. Penna, G. Magenes. Improved evaluation of inelastic displacement demands for short- period masonry structures. Earthq Engng Struct Dyn 2017; 46:1411–1430.
- Gupta & Baker (2019)
A. Gupta, J.W. Baker. A framework for time-varying induced seismicity risk assessment, with application in Oklahoma. Bull of Earthq Eng (2019) 17:4475–4493. doi.org/10.1007/s10518-019-00620-5
- Gálvez et al. (2017)
F. Gálvez, K. Ip, J. Vaculik, M.C. Griffith, L. Sorrentino, D. Dizhur, J.M. Ingham. Discrete Element Modelling To Predict Failure Strength Of Unreinforced Masonry Walls. Australian Earthq Eng Soc 2017 Conf, Nov 24-26, Canberra, ACT.
- De Haan (2016)
F.S. De Haan. Dynamic loading of existing quay structures by induced earthquakes - A case-study regarding the quay structures of Groningen Seaports. Delft U of Tech.
- Hak et al. (2017)
S. Hak, P. Morandi, G. Magenes. Verification Of Drift Demands in the Design Of Rc Buildings With Masonry Infills. 16th World Conf on Earthq Eng, 16WCEE 2017 Santiago Chile, January 9th to 13th 2017.
- Hamed & Rabinovitch (2010)
E. Hamed, O. Rabinovitch. Lateral Out-of-Plane Strengthening of Masonry Walls with Composite Materials. J Compos Constr 2010;14:376-387.
- Hancock (2006)
J. Hancock. The Influence of Duration and the Selection and Scaling of Accelerograms in Engineering Design and Assessment. Department of Civil and Environmental Eng Imperial College U of London March 2006.
- Hancock & Bommer (2004)
J. Hancock, J.J. Bommer. Predicting the number of cycles of ground motion. 13th World Conf on Earthq Eng Vancouver, BC, Canada August 1-6, 2004 Paper No 1989.
- Hatzigeorgiou (2010)
G.D. Hatzigeorgiou. Damping modification factors for SDOF systems subjected to near-fault, far-fault and artificial earthquakes. Earthq Engng Struct Dyn 2010; 39:1239–1258.
- Heath et al. (2008)
D.J. Heath, E.F. Gad, J.L. Wilson. Damage Thresholds in Unreinforced Masonry. Australian J of Struct Eng, 8:2, 145-158. 10.1080/13287982.2008.11464994
- van Hees et al. (2004)
R.P.J. van Hees, L. Binda, I. Papayianni, E. Tombakari. Characterisation and damage analysis of old mortars. Mats and Structs, Vol 37, pp648-664.
- Al Heib et al. (2013)
M. Al Heib, H.L. Nghiem, Fabrice, Emeriault. Understanding Sinkhole Consequences on Masonry Structures Using Large Small-Scale

- Physical Modeling. Intl Conf on Case Histories in Geotechnical Eng 12.
- Hendriks et al. (1995)
M.A.N. Hendriks, J.G. Rots, P.C. Van Staalduijn. Onderzoek naar te verwachten zettingschade bij aanleg van de noord/zuidlijn in Amsterdam. 95 Con-r0343, Tno. doi
- Hendriks & Rots (2013)
M.A.N. Hendriks, J.G. Rots. Sequentially linear versus nonlinear analysis of RC structures. Eng Computations: Intl J for Computer-Aided Eng and Software, Vol 30 No 6, 2013.
- Hendry (2001)
E.A.W. Hendry. Masonry walls: materials and construction. Construction and Bldg Mats 15 (2001) 323-330.
- Hildebrand et al. (2008)
R. Hildebrand, E. Keskinen, J.A. Romero Navarrete. Vehicle vibrating on a soft compacting soil half-space: Ground vibrations, terrain damage, and vehicle vibrations. J of Terramechanics 45 (2008) 121–136.
- Hillerborg (1985)
A. Hillerborg. The theoretical basis of a method to determine the fracture energy of concrete.. Rilem Technical Committees, Vol 18- N ~ 106 - Matériaux et Constrcs.
- Hojdys & Krajewski (2014)
Ł. Hojdys, P. Krajewski. Laboratory Tests on Masonry Vaults with Backfill Strengthened at the Extrados. Key Eng Mats ISSN: 1662-9795, Vol 624, pp 510-517. doi.org/10.4028/www.scientific.net/KEM.624.510
- Ingham & Dizhur (2015)
J. Ingham, D. Dizhur. Seismic Improvement of Load-bearing Unreinforced Masonry Cavity Walls. U of Auckland funded by the Bldg Research Levy.
- Ingham & Griffith (2011)
J.M. Ingham, M.C. Griffith. The Performance of Earthquake Strengthened URM Buildings in the Christchurch CBD in the 22 February 2011 Earthquake. Technical Report. doi.org/10.13140/RG.2.1.1548.6166
- Invernizzi et al. (2011)
S. Invernizzi, D. Trovato, M.A.N. Hendriks, A.V. Van De Graaf. Sequentially linear modelling of local snap-back in extremely brittle structures. Eng Struct 33 (2011) 1617–1625.
- Jafari et al. (2017a)
S. Jafari, R. Esposito, J.G. Rots, F. Messali. Characterizing the Material Properties of Dutch Unreinforced Masonry. Procedia engineering, 193, 250-257.
- Jafari et al. (2017b)
S. Jafari, R. Esposito, J.G. Rots. Literature Review On The Assessment Of Masonry Properties By Tests On Core Samples. 4th WTA Intl PhD Symp – Delft 2017.
- Jafari et al. (2018a)
S. Jafari, R. Esposito, J.G. Rots. A Comparative Study On The Different Testing Methods: Evaluating The Compression Properties Of Masonry. 10th Intl Masonry Conf, Milan.
- Jafari et al. (2018b)
S. Jafari, R. Esposito, J.G. Rots. From Brick to Element: Investigating the Mechanical Properties of Calcium Silicate Masonry. SAHC.
- Jafari & Esposito (2016)
S. Jafari, R. Esposito. Material Tests for the Characterisation of Replicated Solid Clay Brick Masonry. Delft U of Tech Report number C31B67WP1-12, version 01, 16 August 2017.
- Jafari & Esposito (2019)
S. Jafari, R. Esposito. Summary of material properties of existing Dutch masonry - updated URM abacus (version 2). Delft U of Tech Report number C31B67WP1-16, version 02.
- Jafari & Rots (2015)
S. Jafari, J.G. Rots. Conclusive summary report – Masonry material testing 2014. TU Delft.
- Jalayer et al. (2009)
F. Jalayer, L. Elefante, I. Iervolino, G. Manfredi. Confidence Factors and Structural Reliability. Department of Struct Eng, U of Naples.
- Jeary et al. (2015)
A.P. Jeary, T. Winant, J. Bunyan. Some Aspects Of The Measurement Of Vibration Intensity For The Assessment Of Building Structures. Forensic Eng 7th Congress Performance of the Built Environment November 15 – 18, 2015.
- Jonaitis et al. (2009)
B. Jonaitis, G. Marciukaitis, J. Valivonis. Analysis of the shear and flexural behaviour of masonry with hollow calcium silicate blocks. Eng Struct 31 (2009) 827–833.
- Jongejan et al. (2019)
R. Jongejan, V. Drosos, A. Giannakou, J. Chacko, P. Tasiopoulou, N. Zuideveld-Venema, S. de Wit, H. Huissoon. Probabilistic assessments of flood defence performance subject to induced seismicity. Bull of Earthq

- Eng (2019) 17:4517–4537. doi.org/10.1007/s10518-018-0521-7
- Jonkman et al. (2003)
S.N. Jonkman, P.H.A.J.M. Van Gelder, J.K. Vrijling. An overview of quantitative risk measures for loss of life and economic damage. *J of Hazardous Mats A99* (2003) 1–30.
- Jonkman (2007)
S.N. Jonkman. Loss of life estimation in flood risk assessment Theory and applications. Delft U of Tech.
- Jonkman & Penning-Rowse (2008)
S.N. Jonkman, E. Penning-Rowse. Human Instability in Flood Flows. *J of the American Water Resources Association (JAWRA)* 44(4):1-11 DOI: 10.1111/1752-1688200800217x.
- Jurevicius et al. (2015)
D. Jurevicius, M. Stead, G. Barry. A Case Study Of Damage Effects To Residential Buildings Caused By Vibratory Compaction Equipment. *Acoustics Hunter Valley*.
- Jurina et al. (2019)
L. Jurina, G. Mantegazza, E.O. Radaelli. FRM - Strengthening of masonry vaults: the “Duomo di Colorno” and “Braidense Library” cases in Italy. *Key Eng Mats Vol 624*.
- Kallioras et al. (2018a)
S. Kallioras, G. Guerrini, U. Tomassetti, B. Marchesi, A. Penna, F. Graziotti, G. Magenes. Experimental seismic performance of a full-scale unreinforced clay-masonry building with flexible timber diaphragms. *Eng Structs* 161 (2018) 231–249.
- Kallioras et al. (2018b)
S. Kallioras, F. Graziotti, A. Penna. Numerical assessment of the dynamic response of a URM terraced house exposed to induced seismicity. *Bull Earthq Eng* 2018. doi.org/10.1007/s10518-018-0495-5
- Kanit et al. (2010)
R. Kanit, M. Erdal, Ö. Can. Assessing the experimental behaviour of load bearing masonry walls subjected to out-of-plane loading. *Scientific Research and Essays Vol 5(21)*, pp 3336-3344, 4 November, 2010 Available online at <http://www.academicjournals.org/SRE> ISSN 1992-2248 ©2010 Academic Js.
- Kanit & Atimtay (2006)
R. Kanit, E. Atimtay. Experimental Assessment of the Seismic Behavior of Load-Bearing Masonry Walls Loaded Out-of-Plane. *Turkish J Eng Env Sci* 30 (2006) , 101 – 113.
- Kashyap (2014)
J. Kashyap. Out-of-plane Strengthening Of Unreinforced Masonry Walls Using Frp. *School Of Civil, Environmental and Mining Eng, U Of Adelaide*.
- Kaushik et al. (2007)
H.B. Kaushik, D.C. Rai, S.K. Jain. Stress-Strain Characteristics of Clay Brick Masonry under Uniaxial Compression. *J Mater Civ Eng* 200719:728-739.
- Kelman (2002)
I. Kelman. Physical Flood Vulnerability of Residential Properties in Coastal, Eastern England. *U of Cambridge, UK*.
- Kelman & Spence (2004)
I. Kelman, R. Spence. An overview of flood actions on buildings. *Eng Geology* 73 (2004) 297–309.
- Khalaf (2005)
F.M. Khalaf. New Test for Determination of Masonry Tensile Bond Strength. *JOURNAL OF MATERIALS IN CIVIL ENGINEERING © ASCE / NOVEMBER/DECEMBER 2005*.
- Kim & J.Y. Kim (2014)
D.H. Kim, J.Y. Kim. Assessment on Natural Frequencies of Structures using Field Measurement and FE Analysis. *Intl J of High-Rise Bldgs* December 2014, Vol 3, No 4, 305-310.
- Kim & Lee (1999)
D.H. Kim, J.S. Lee. Propagation and attenuation characteristics of various ground vibrations. *Soil Dyns and Earthq Eng*.
- Kita et al. (2020)
A. Kita, N. Cavalagli, M.G. Masciotta, P.B. Lourenço, F. Ubertini. Rapid post-earthquake damage localization and quantification in masonry structures through multidimensional non-linear seismic IDA. *Eng Structs* 219 (2020) 11084.
- Kooi et al. (2021)
H. Kooi, J.C. Landwehr, R.J. Stuurman, J.J. van Meerten, O. Levelt, M. Korff. Indirecte schade-effecten van diepe bodemdaling en -stijging bij het Groningen gasveld en gasopslag Norg. *Deltares*, 11207096-002-BGS-0001, 30 augustus 2021.

- Korff (2009)
M. Korff. Deformations and damage to buildings adjacent to deep excavations in soft soils. COB, Delft Cluster - Deltares.
- Korff et al. (2013)
M. Korff, H.M.G. Kruse, T.P. Stoutjesdijk, J. Breedevelde, G.A. van den Ham, P. Holscher, G. de Lange, P. Meijers, E. Vastenburg, T. Vermaas, M.A.T. Visschedijk. Effecten geïnduceerde aardbevingen op kritische infrastructuur Groningen. Deltares.
- Kowalewski & Gajewski (2015)
Ł. Kowalewski, M. Gajewski. Determination of failure modes in brick walls using cohesive elements approach. *Procedia Eng* 111 (2015) 454 – 461.
- Kralj et al. (1990)
B. Kralj, G.N. Pande, J. Middleton. On the mechanics of frost damage to masonry. *Computers and Struc*, Vol 41, no 1, pp 53-66, 1991.
- Kruiver et al. (2017a)
P.P. Kruiver, E. van Dedem, R. Romijn, G. de Lange, M. Korff, J. Stafleu, J.L. Gunnink, A. Rodriguez-Marek, J.J. Bommer, J. van Elk, D. Doornhof. An integrated shear-wave velocity model for the Groningen gas field, The Netherlands. *Bull Earthq Eng* (2017) 15:3555–3580 - DOI. doi.org/10.1007/s10518-017-0105-y
- Kruiver et al. (2017b)
P.P. Kruiver, A. Wiersma, F.H. Kloosterman, G. de Lange, M. Korff, J. Stafleu, F.S. Busschers, R. Harting, J.L. Gunnink, R.A. Green, J. van Elk, D. Doornhof. Characterisation of the Groningen subsurface for seismic hazard and risk modelling. *Netherlands J of Geosciences — Geologie en Mijnbouw* 196 – 5 | s215–s233 | 2017.
- Kumar et al. (2019)
S.L. Kumar, H.B. Aravind, N. Hossiney. Digital image correlation (DIC) for measuring strain in brick masonry specimen using Ncorr open source 2D MATLAB program. *Results in Eng* 4 (2019) 100061.
- Lagomarsino et al. (2013)
S. Lagomarsino, A. Penna, A. Galasco, S. Cattari. TREMURI program: An equivalent frame model for the nonlinear seismic analysis of masonry buildings. *Eng Struc* 56 (2013) 1787–1799.
- Lam et al. (2002)
N.T.K. Lam, M. Griffith, J. Wilson, K. Doherty. Time-history analysis of URM walls in out-of-plane flexure. *Eng Struc* 25 (2003) 743–754.
- Langroudi et al. (2011)
J.R. Langroudi, M.M. Ranjbar, S.J. Hashemi, A.S. Moghadam. Evaluation of Roof Diaphragm Effect on Seismic Behavior of Masonry Buildings. *Procdngs of the 8th Intl Conf on Struct Dyns, EURODYN 2011* 453 Leuven, Belgium, 4-6 July 2011.
- Larby (2004)
J.A. Larby. Microscopy applied to the diagnosis of the deterioration of brick masonry. *Construction and Bldg Mats* 18 (2004) 299–307.
- Laurin et al. (2012)
F. Laurin, J.S. Charrier, D. Lévêque, J.F. Maire, A. Mavel, P. Nuñez. Determination of the properties of composite materials thanks to digital image correlation measurements. *Procedia IUTAM* 4 (2012) 106 – 115.
- Lava (2015)
P. Lava. Practical considerations in DIC measurements. 10th international conference on Advcs in Experimental Mechs.
- Lawrence & Marshall (2000)
S. Lawrence, R. Marshall. Virtual Work Design Method For Masonry Panels Under Lateral Load. 12Th Intl Brick/Block Masonry Conf.
- Lee & Lopez (2014)
J. Lee, M.M. Lopez. An Experimental Study on Fracture Energy of Plain Concrete. *Intl J of Conc Struc* and Mats Vol8, No2, pp129–139, June 2014 DOI. doi.org/10.1007/s40069-014-0068-1 ISSN 1976-0485 / eISSN 2234-1315
- Leiva (1991)
G.H. Leiva. Seismic Resistance of Two-Storey Masonry Walls. U of Texas at Austin.
- Lendering et al. (2015)
K.T. Lendering, S.N. Jonkman, M. Kok. Flood risk of regional flood defences. Delft U of Tech.
- Li et al. (2024)
X. Li, F. Messali, R. Esposito. Mechanical Characterisation of Multi-Wythe Masonry Bridge in the City of Amsterdam. *SAHC 2023, RILEM Bookseries* 47, pp 527–540. 10.1007/978-3-031-39603-8_43
- Licciardello et al. (2020)
L. Licciardello, J.G. Rots, R. Esposito.

- Performance Of Unreinforced Masonry Strengthened With Bed Joint Reinforced Repointing. 12th Intl Conf on Struct Analysis of Historical Constrcs, SAHC. doi
- Likas et al. (2003)
A. Likas, N. Vlassis, J.J. Verbeek. The global k-means clustering algorithm. *Pattern Recognition* 36 (2003) 451 – 461. doi.org/10.1016/S0031-3203(02)00060-2
- Liu & Xu (2022)
X. Liu, L. Xu. Soil-Building Interaction under Surface Horizontal Strain Induced by Underground Mining. *Advcs in Civil Eng* Volume 2022, Article ID 2425936. doi.org/10.1155/2022/2425936
- Lourenço et al. (1995)
P.B. Lourenço, J.G. Rots, J. Blaauwendraad. Two approaches for the analysis of masonry structures: micro and macro-modeling. *HERON* Vol 40 No4 ISSN 0046-7316.
- Lourenço (1996)
P.B. Lourenço. Computational strategies for masonry structures. PhD Dissertation, TU Delft.
- Lourenço & Rots (1997)
P.B. Lourenço, J.G. Rots. Multisurface interface model for analysis of masonry structures. *J of Eng Mechs*, 123 (7), pp 660-668.
- Lubelli et al. (2004)
B. Lubelli, R.P.J. van Hees, C.J.W.P. Groot. The role of sea salts in the occurrence of different damage mechanisms and decay patterns on brick masonry. *Construction and Bldg Mats* 18 (2004) 119–124. 10.1016/j.conbuildmat.2003.08.017
- Magenes et al. (1995)
G. Magenes, G.M. Calvi, G.R. Kingsley. Seismic Testing of a Full-Scale, Two-Story Masonry Building: Test Procedure and Measured Experimental Response. *Experimental and Numerical Investigation on a brick Masonry Bldg Prototype - Numerical Prediction of the Experiment*, Report 30 - GNDT, U of Pavia, Department of Struct Mechs.
- Magenes (2006)
G. Magenes. Masonry Building Design in Seismic Areas: Recent Experiences and Prospects From a European Standpoint. *First European Conf on Earthq Eng and Seismology*.
- Magenes et al. (2008)
G. Magenes, P. Morandi, A. Penna. Experimental In-plane Cyclic Response Of Masonry Walls With Clay Units. *The 14th World Conf on Earthq Eng* October 12-17, 2008, Beijing, China.
- Magenes (2010)
G. Magenes. Earthquake resistant design of masonry structures: rules, backgrounds, latest findings. *8th Intl Masonry Conf 2010 in Dresden*.
- Magenes et al. (2010)
G. Magenes, A. Penna, A. Galasco, M.D. Paré. In-plane cyclic shear tests of undressed double-leaf stone masonry panels. *8th Intl Masonry Conf 2010 in Dresden*.
- Magenes et al. (2012)
G. Magenes, P. Morandi, A. Penna. In-plane Cyclic Tests Of Calcium Silicate Masonry Walls. *14th Intl Brick and Block Masonry Conf*, Sydney, Australia.
- Magenes & Calvi (1992)
G. Magenes, G.M. Calvi. Cyclic behaviour of brick masonry walls. *Earthq Eng*, Tenth World conference.
- Magenes & Calvi (1997)
G. Magenes, G.M. Calvi. In-plane Seismic Response Of Brick Masonry Walls. *Earthq Eng and Struct Dyns*, Vol 26, 1091–1112 (1997).
- Maheri & Najafgholipour (2012)
M.R. Maheri, M.A. Najafgholipour. In-plane Shear and Out-of-plane Bending Capacity Interaction in Brick Masonry Walls. *15 WCEE*.
- Mair (2003)
R.J. Mair. Research on tunnelling-induced ground movements and their effects on buildings – Lessons from the Jubilee Line extension. In: *Bldg response to tunnelling: Case studies from construction of the Jubilee Line extension*, Eds Burland JB, Standing JR and Jardine FM CIRIA SP199 and Thomas Telford, London.
- Malomo et al. (2018)
D. Malomo, M.J. DeJong, A. Penna. Distinct Element Modelling Of The In-Plane Failure Mechanisms Of Urm Walls. *10th IMC*, Milan 2018.
- Mariani et al. (2017)
V. Mariani, F. Messali, M.A.N. Hendriks, J.G. Rots. Numerical Modelling And Seismic Analysis Of Dutch Masonry Structural Components And Buildings. *16th World Conf on Earthq*, 16WCEE 2017.

- Masia et al. (2004)
M.J. Masia, Y. Han, S.J. Lawrence, A.W. Page. An Experimental Study Of Brick Masonry Specimens Subjected To Biaxial Bending. 13th Intl Brick and Block Masonry Conf Amsterdam, July 4-7, 2004.
- Masia et al. (2007)
M.J. Masia, Y. Han, C.J. Player, M.R.S. Correa, A.W. Page. Torsion Shear Test for Mortar Joints in Masonry: Preliminary Experimental Results. 10th NAMC, Missouri.
- Masia et al. (2009)
M.J. Masia, R.B. Petersen, Y. Han, M.R.S. Correa. Torsion Shear Test For Mortar Joints in Masonry: Specimen Preparation and Experimental Results. 11th Canadian Masonry Symp, Toronto, Ontario, May 31- June 3, 2009.
- Mason et al. (2019)
M.S. Mason, E. Phillips, T. Okada, J. O'Brien. Analysis of damage to buildings following the 2010–11 Eastern Australia floods. National Climate Change Adaptation Research Facility, Gold Coast.
- Massarsch (2002)
K.R. Massarsch. Effects of Vibratory Compaction. Geo Eng AB, Stockholm, Sweden.
- Matteis et al. (2014)
G.D. Matteis, E. Ciber, G. Brando. Seismic Vulnerability Assessment Of Masonry Churches Through the Application Of Probabilistic Methods. SAHC2014 – 9th Intl Conf on Struct Analysis of Historical Constrcs.
- Mazzorana et al. (2014)
B. Mazzorana, S. Simoni, C. Scherer, B. Gems, S. Fuchs, M. Keiler. A physical approach on flood risk vulnerability of buildings. Hydrol Earth Syst Sci, 18, 3817–3836, 2014
www.hydrol-earth-syst-sci.net/18/3817/2014/.
doi.org/10.5194/hess-18-3817-2014
- Meillyta (2012)
Meillyta. Finite Element Modelling of Unreinforced Masonry (URM) Wall with Openings: Studies in Australia. The Procdngs of 2nd Annual Intl Conf Syiah Kuala U 2012 & 8th IMT-GT Uninet Biosciences Conf Banda Aceh, 22-24 November 2012.
- Melis (2002)
G. Melis. Displacement-based Seismic Analysis For Out Of Plane Bending Of Unreinforced Masonry Walls. European School Of Advanced Studies in Reduction Of Seismic Risk Rose School.
- Mendes & Lourenço (2010)
N. Mendes, P.B. Lourenço. Seismic Assessment of Masonry “Gaioleiro” Buildings in Lisbon, Portugal. J of Earthq Eng, 14:80–101, 2010.
- Mergos & Beyer (2014)
P. Mergos, K. Beyer. Loading protocols for European regions of low to moderate seismicity. Bull Earthq Eng (2014) 12:2507–2530 - DOI. doi.org/10.1007/s10518-014-9603-3
- Mergos & Beyer (2015)
P. Mergos, K. Beyer. Loading Protocols For Structures Designed For Different Behaviour Factors. SECED 2015 Conf: Earthq Risk and Eng towards a Resilient World 9-10 July 2015, Cambridge UK.
- Messali et al. (2017)
F. Messali, G.J.P. Ravenshorst, R. Esposito, J.G. Rots. Large-scale testing program for the seismic characterization of Dutch masonry walls. 16th World Conf on Earthq, WCEE 2017, 9-13 Jan 2017, Santiago, Chile.
- Messali et al. (2018)
F. Messali, M. Pari, R. Esposito, J. Rots, D. Den Hertog. Blind Predictions Of A Cyclic Pushover Test On A Two- Storey Masonry Assemblage: A Comparative Study. 16th European Conf on Earthq Eng, Thessaloniki 2018.
- Messali & Rots (2018)
F. Messali, J.G. Rots. In-plane drift capacity at near collapse of rocking unreinforced calcium silicate and clay masonry piers. Eng Struct 164 (2018) 183–194.
- Meyer & Caballero-González (2019)
U. Meyer, A. Caballero-González. Esecmase – Shaking Table Tests At the National Technical University in Athens. U of Athens.
- Michel et al. (2010)
C. Michel, B. Zapico, P. Lestuzzi, F.J. Molina, F. Weber. Quantification of fundamental frequency drop for unreinforced masonry buildings from dynamic tests. Earthq Eng Struct Dyn 2011; 40:1283–1296.
- Mignan et al. (2015)
A. Mignan, D. Landtwing, P. Kästli, B. Mena, S. Wiemer. Induced seismicity risk analysis of the 2006 Basel, Switzerland, Enhanced Geothermal System project: Influence of uncertainties on

- risk mitigation. *Geothermics* 53 (2015) 133–146.
- Milosevic et al. (2018)
J. Milosevic, R. Bento, S. Cattari. Development Of Seismic Fragility Curves For Mixed Masonry-Rc Buildings In Lisbon. 10th IMC, Milan 2018.
- Miraglia et al. (2015)
S. Miraglia, W. Courage, P. Meijers. Fragility Functions for Pipeline in Liquefiable Sand: a Case Study on the Groningen Gas-Network. 12th Intl Conf on Applications of Statistics and Probability in Civil Eng, ICASP12 Vancouver, Canada, July 12-15, 2015.
- Modena et al. (2013)
C. Modena, F.d. Porto, M.R. Valluzzi, M. Munari. Criteria and Technologies For the Structural Repair and Strengthening Of Architectural Heritage. Intl Conf, Chennai, India, 13th – 16th February 2013.
- Mohammed et al. (2009)
B.S. Mohammed, B.H.A. Bakar, K.K. Choong. The Effects of Opening on the Structural Behavior of Masonry Wall Subjected to Compressive Loading - Strain Variation. *The Open Civil Eng J*, 2009, 3, 62-73.
- Mojsilovic et al. (2019)
N. Mojsilovic, G. Simundic, A. Page. Static-Cyclic Shear Tests on Masonry Wallettes with a Damp-Proof Course Membrane. J or hosting entity.
- Mojsilović & Salmanpour (2016)
N. Mojsilović, A.H. Salmanpour. Masonry walls subjected to in-plane cyclic loading: Application of Digital Image Correlation for deformation field measurement. Institute of Struct Eng, Department of Civil, Environmental and Geomatic Eng, ETH Zurich, 8093, Switzerland.
- Moon (2004)
F.L. Moon. Seismic Strengthening Of Low-rise Unreinforced Masonry Structures With Flexible Diaphragms. Georgia Institute of Tech May.
- Moon et al. (2006)
F.L. Moon, Y. Tianyi, R.T. Leon, L.F. Kahn. Recommendations for Seismic Evaluation and Retrofit of Low-Rise URM Structures. *J Struct Eng*, 2006, 132(5): 663-672.
- Morandi et al. (2018)
P. Morandi, L. Albanesi, F. Graziotti, T. Li Piani, A. Penna, G. Magenes. Development of a dataset on the in-plane experimental response of URM piers with bricks and blocks. *Construction and Bldg Mats* 190 (2018) 593–611.
- Moreira et al. (2012)
S. Moreira, D.V. Oliveira, L.F. Ramos, P.B. Lourenço, R.P. Fernandes, J. Guerreiro. Experimental study on the seismic behavior of masonry wall-to-floor connections. 15 Wcee.
- Mors & Jonkers (2013)
R.M. Mors, H.M. Jonkers. Reduction of water permeation through cracks in mortar by addition of bacteria based healing agent. Faculty of Civil Eng and Geosciences, Mats & Environment section, Delft U of Tech.
- Mosalam et al. (2009)
K. Mosalam, L. Glascoe, J. Bernier. Mechanical Properties of Unreinforced Brick Masonry, Section 1. Lawrence Livermore National Laboratory LLNL-TR-417646.
- Mosallam (2007)
A.S. Mosallam. Out-of-plane flexural behavior of unreinforced red brick walls strengthened with FRP composites. *Composites: Part B* 38 (2007) 559–574.
- Muir et al. (2017)
C.A. Muir, P.L. Beazley, R.D. Jury, W.Y. Kam, P.D. Den Hertog. Terraced House – Practical application of NZSEE principles in the Netherlands. NZSEE Conf.
- Mulder et al. (2018)
M. Mulder, P. Perey, B. Scholtens, G. de Kam, G. Perlaviciute. Gas production and earthquakes in Groningen - reflection on economic and social consequences. Centre for Energy Economics Research - CEER - Policy Papers I no 3 | June 2018.
- Mylonakis et al. (2006)
G. Mylonakis, S. Nikolaou, G. Gazetas. Footings under seismic loading: Analysis and design issues with emphasis on bridge foundations. *Soil Dyns and Earthq Eng* 26 (2006) 824–853.
- NAM et al. (2015)
NAM, M. Pickering, J. van Elk, D. Doornhof. An estimate of the earthquake hypocenter locations in the Groningen Gas Field. NAM.
- NAM (2017)
NAM. Trillingsschade aan gebouwen. NAM 170822-HA.
- NEN (2015)
NEN. NPR 9998. NEN.

- NZSEE et al. (2006)
NZSEE, SESOC, NZGS, MBIE, EQC.
Assessment and Improvement of the Structural Performance of Buildings in Earthquakes - Section 10 Revision Seismic Assessment of Unreinforced Masonry Buildings. New Zealand Soc For Earthq Eng, ISBN 978-0-473-32278-6, Update 2015.
- Nam (2018)
Nam. Field Test and Analysis of Everyday Train-induced Ground Motions. Nam.
- Narassiguin et al. (2016)
A. Narassiguin, M. Bibimoune, H. Elghazel, A. Aussem. An extensive empirical comparison of ensemble learning methods for binary classification. *Pattern Anal Applic* (2016) 19:1093–1128. 10.1007/s10044-016-0553-z
- Nateghi & Alemi (2008)
F. Nateghi, F. Alemi. Experimental study of seismic behaviour of typical Iranian URM brick walls. 14th world conference on earthquake engineering, October 12-17, 2008, Beijing, China.
- Negulescu et al. (2014)
C. Negulescu, T. Ulrich, A. Baills, D.M. Seyed. Fragility curves for masonry structures submitted to permanent ground displacements and earthquakes. *Nat Hrzds* (2014) 74:1461–1474 -DOI. doi.org/10.1007/s11069-014-1253-x
- Nehrp (2012)
Nehrp. Soil-Structure Interaction for Building Structures. NIST GCR 12-917-21 US Department of Commerce National Institute of Standards and Tech.
- Nen (2005)
Nen. NEN 6790 - Technische grondslagen voor bouwconstructies - TGB 1990 - Staanconstructies - Basiseisen en bepalingmethoden. NEN - Nederlands Normalisatie-instituut.
- Nen (2018)
Nen. Nederlandse Praktijkrichtlijn (NPR) 9998 - Dutch guideline of practice. Nen.
- Nepveu et al. (2016)
M. Nepveu, K. van Thienen-Visser, D. Sijacic. Statistics of seismic events at the Groningen field. *Bull Earthq Eng* (2016) 14:3343–3362 DOI. doi.org/10.1007/s10518-016-0007-4
- Nguyen & Lallemand (2022)
M. Nguyen, D. Lallemand. Order Matters: The Benefits of Ordinal Fragility Curves for Damage and Loss Estimation. *Risk Analysis*, Vol 42, No 5, 2022. doi.org/10.1111/risa.13815
- Noorlandt et al. (2018)
R. Noorlandt, P.P. Kruiver, M.P.E. de Kleine, M. Karaoulis, G. de Lange, A. di Matteo, J. von Kettlehodt, E. Ruigrok, B. Edwards, A. Rodriguez-Marek, J.J. Bommer, J. van Elk, D. Doornhof. Characterisation of ground motion recording stations in the Groningen gas field. *J Seismol* (2018) 22:605–623. doi.org/10.1007/s10950-017-9725-6
- Noortman (2019)
F.J. Noortman. Applicability Of the Pushover Method For the Seismic Assessment Of Urm Structures in Groningen. Delft U of Tech.
- Ntinalexis et al. (2022)
M. Ntinalexis, P.P. Kruiver, J.J. Bommer, E. Ruigrok, A. Rodriguez-Marek, B. Edwards, R. Pinho, J. Spetzler, E.O. Hernandez, M. Pefkos, M. Bahrapouri, E.P. van Onselen, B. Dost, J. van Elk. A database of ground motion recordings, site profiles, and amplification factors from the Groningen gas field in the Netherlands. *Earthq Spectra* 2023, Vol 39(1) 687–701. 10.1177/87552930221140926
- Okada & Takai (2000)
S. Okada, N. Takai. Classifications of Structural Types and Damage Patterns of Buildings for Earthquake field Investigation. *Struct and Construction Eng* (Transactions of AIJ). doi.org/10.3130/aijs.64.65_5
- Oktiovan et al. (2023)
Y.P. Oktiovan, F. Messali, J.G. Rots. Detailed distinct element modeling of a Utrecht wharf cellar for the assessment of the load-bearing capacity and failure mechanism. *Procndgs of the Seventeenth Intl Conf on Civil, Struct and Environmental Eng Computing* (Vol 6) Civil-Comp Press. doi.org/10.4203/ccc.6.6.2
- Oliveira et al. (2003)
J.T. Oliveira, J.O. Barros, P.B. Lourenço, E. Bonaldo. Flexural behavior of reinforced masonry panels. GROW-1999-70420 "ISO-BRICK" from the European Commission.
- Olivito & Stumpo (2001)
R.S. Olivito, P. Stumpo. Fracture mechanics in the characterisation of brick masonry structures. *Mats and Structs/Matériaux et Constcrs*, Vol 34, May 2001, pp 217-223.

- Oses et al. (2014)
N. Oses, F. Dornaika, A. Moujahid. Image-Based Delineation and Classification of Built Heritage Masonry. *Remote Sens* 2014, 6, 1863-1889. 10.3390/rs6031863
- Osterberg (1935)
G. Osterberg. Topography of the layer of rods and cones in the human retina. *Acta Ophthalmol [Suppl]* 13:6,1-102.
- Page (1995)
A.W. Page. Unreinforced Masonry Structures - an australian overview. Pacific conference on earthquake engineering (PCEE 95), Melbourne.
- Palmisano et al. (2016)
F. Palmisano, C. Vitone, F. Cotecchia. Methodology for Landslide Damage Assessment. ScienceDirect.
- Palomo-Velez et al. (2023)
G. Palomo-Velez, N. Contzen, G. Perlaviciute, L. Steg. Trust in institutions and public acceptability of risky energy production: Testing the causal relationships in the context of Groningen earthquakes. *Energy Research & Social Science* 96 (2023) 102927. doi.org/10.1016/j.erss.2022.102927
- Paparo & Beyer (2014)
A. Paparo, K. Beyer. Quasi-static cyclic tests of two mixed reinforced concrete-unreinforced masonry wall structures. *Eng Struct* 71 (2014) 201-211.
- Pari et al. (2017)
M. Pari, M.A.N. Hendriks, J.G. Rots. Sequentially Linear Analysis On Masonry Walls – New Crack Closure Algorithm. 13Th Canadian Masonry Symp Halifax, Canada June 4Th – June 7Th 2017.
- Pari et al. (2018)
M. Pari, J.G. Rots, M.A.N. Hendriks. Non-proportional loading for 3-D stress situations in Sequentially Linear Analysis. EuroC 2018.
- Pavía & Hanley (2010)
S. Pavía, R. Hanley. Flexural bond strength of natural hydraulic lime mortar and clay brick. *Mats and Structs* (2010) 43:913-922 DOI. doi.org/10.1617/s11527-009-9555-2
- Pelà et al. (2014)
L. Pelà, M. Cervera, S. Oller, M. Chiumenti. A localized mapped damage model for orthotropic materials. *Eng Fracture Mech* 124-125 (2014) 196-216.
- Pereira et al. (2008)
E.B. Pereira, G. Fischer, J.A.O. Barros. Image-based detection and analysis of crack propagation in cementitious composites. U of Minho, Guimaraes, Portugal.
- Petry & Beyer (2015a)
S. Petry, K. Beyer. Limit states of modern unreinforced clay brick masonry walls subjected to in-plane loading. *Bull Earthq Eng* (2015) 13:1073-1095 DOI. doi.org/10.1007/s10518-014-9695-9
- Petry & Beyer (2015b)
S. Petry, K. Beyer. Cyclic test data of six unreinforced masonry walls with different boundary conditions. *Earthq Spectra* November 2015, Vol 31, No 4, pp 2459-2484.
- Pina-Henriques et al. (2004)
J. Pina-Henriques, P.B. Lourenço, L. Binda, A. Anzani. Testing and modelling of multiple-leaf masonry walls under shear and compression. U of Minho, Department of Civil Eng.
- Pitilakis (2006)
D. Pitilakis. Soil-structure Interaction Modeling Using Equivalent Linear Soil Behavior in the Substructure Method. École Centrale Des Arts Et Manufactures.
- Van Der Pluijm (1997)
R. Van Der Pluijm. Non-Linear Behaviour of Masonry under Tension. *Heron*, Vol 42 No 1 ISSN 0046-7316.
- Van Der Pluijm (1999)
R. Van Der Pluijm. Out-of-plane Bending Of Masonry Behaviour and Strength. TU Eindhoven.
- Van Der Pluijm (2001)
R. Van Der Pluijm. Laterally Loaded Masonry Panels made with Thin Layer Mortar. TNO-report 2001-CON-BM-R5015.
- Van Der Pluijm (2019)
R. Van Der Pluijm. Tests on Laterally Loaded Clay Brick Panels. EINDHOVEN UNIVERSITY of TECHNOLOGY TUE/BCO/9903.
- Popal (2013)
R. Popal. A New Shear Test Method for Mortar Bed Joints. Department Of Civil Eng Calgary, Alberta.
- Portioli et al. (2018)
F. Portioli, R. Gagliardo, L. Landolfo. Evaluation Of Collapse Displacements In Dry-Jointed Masonry Structures Subjected To Settlements:

- Experimental Tests And Rigid Block Modelling. 10th IMC, Milan 2018.
- Portioli & Cascini (2015)
F. Portioli, L. Cascini. Assessment of masonry structures subjected to foundation settlements using rigid block limit analysis. *Eng Struct* 113 (2016) 347–361.
- Portioli & Cascini (2016)
F. Portioli, L. Cascini. Contact Dynamics of Masonry Block Structures Using Mathematical Programming. *J of Earthq Eng*, 22:94–125, 2018.
- Portioli & Cascini (2017)
F. Portioli, L. Cascini. Large displacement analysis of dry-jointed masonry structures subjected to settlements using rigid block modelling. *Eng Struct* 148 (2017) 485–496.
- da Porto et al. (2010)
F. da Porto, G. Guidi, E. Garbin, C. Modena. In-Plane Behavior of Clay Masonry Walls: Experimental Testing and Finite-Element Modeling. *J Struct Eng* 2010136:1379-1392.
- Potts & Addenbrooke (1997)
D.M. Potts, T.I. Addenbrooke. A structure's influence on tunnelling-induced ground movements. *Procngs of the Institution of Civil Engineers, Geotechnical Eng* 1997, 125, April, 109-125.
- Price (2013)
A.D. Price. Multi-GPU Computing with Abaqus: Benchmarking and scaling for multiphysics applications in mechatronics. 2013 SIMULIA Community Conf.
- Puente et al. (2018)
I. Puente, R. Lindenbergh, A. Van Natijs, R. Esposito, R. Schipper. Monitoring Of Progressive Damage In Buildings Using Laser Scan Data. *Isprs*.
- Raaijmakers (1994)
B.H.J. Raaijmakers. Modelling van Constructies bij een Dynamische Excitatie via de fundering. TNO.
- Ramos et al. (2015)
T. Ramos, A. Furtado, S. Eslami, S. Alves, H. Rodrigues, A. Arêde, P. Tavares, P. Moreira. 2D and 3D Digital Image Correlation in Civil Engineering – Measurements in a Masonry Wall. *Procedia Eng* 114 (2015) 215 – 222.
- Rapone et al. (2020)
D. Rapone, G. Brando, E. Spacone. A Discontinuum Finite Element Modelling Approach For Reproducing the Structural Behaviour Of Masonry Walls. 14th World Congress in Comput Mechs (WCCM).
- United Nations Office for Disaster Risk Reduction (2022)
United Nations Office for Disaster Risk Reduction. Global Assessment Report on Disaster Risk Reduction 2022 - Our World at Risk: Transforming Governance for a Resilient Future.. Geneva ISBN: 9789212320281.
- Ren et al. (1987)
G. Ren, D.J. Reddish, B.N. Whittaker. Mining Subsidence and Displacement Prediction Using Influence Function Methods. *Mining Science and Tech*, 5 (1987) 89-104. doi
- Reneckis & LaFave (2010)
D. Reneckis, J.M. LaFave. Out-of-Plane Seismic Performance and Detailing of Brick Veneer Walls. *J Struct Eng* 2010136:781-794.
- Reyes et al. (2008)
E. Reyes, M.J. Casati, J.C. Gálvez. Cohesive crack model for mixed mode fracture of brick masonry. *Int J Fract* (2008) 151:29–55.
- Ritter (2017)
S. Ritter. Experiments in tunnel–soil–structure interaction. Department of Eng, U of Cambridge.
- Ritter et al. (2017)
S. Ritter, G. Giardina, M.J. Dejong, R.J. Mair. Influence of building characteristics on tunnelling-induced ground movements. *Géotechnique* 67, No 10, 926–937. doi.org/10.1680/jgeot.SIP17.P.138
- Ritter et al. (2020)
S. Ritter, G. Giardina, A. Franza, M.J. DeJong. Building Deformation Caused by Tunneling: Centrifuge Modeling. *J of Geotechnical and Geoenvironmental Eng*. 10.1061/%28ASCE%29GT.1943-5606.0002223
- Robertson & Wride (1998)
P.K. Robertson, C.E. Wride. Evaluating cyclic liquefaction potential using the cone penetration test. *Can Geotech J* 35: 442–459.
- Rodríguez et al. (2013)
J. Rodríguez, F. Martínez, J. Martí. Concrete Constitutive Model, Calibration and Applications. 2013 SIMULIA Community Conf.
- Romao et al. (2008)
X. Romao, J. Guedes, A. Costa, R. Delgado. Adequacy Of the Ec8-part 3 Proposed Confidence Factors For the Assessment Of

- Existing Rc Structures. 14th World Conf Earthq Eng, Beijing, China.
- Romijn et al. (2017)
R. Romijn, J. van Elk, D. Doornhof. Groningen Velocity Model 2017 - Groningen full elastic velocity model September 2017. NAM.
- de Roo & Straman (1991)
de Roo, Straman. Numerieke Analyse van de Schijfwerking in Geprefabriceerde Vloeren. Cement nr 11, p76-80.
- Rota et al. (2010)
M. Rota, A. Penna, G. Magenes. A methodology for deriving analytical fragility curves for masonry buildings based on stochastic nonlinear analyses. Eng Structs 32 (2010) 1312–1323.
- Rots et al. (1985)
J.G. Rots, P. Nauta, G.M.A. Kusters, J. Blaauwendraad. Smeared Crack Approach and Fracture Localization in Concrete. Heron Vol 30, No 1.
- Rots (1988)
J.G. Rots. Computational Modeling of Concrete Fracture. Delft U of Tech.
- Rots et al. (1994)
J.G. Rots, R. Van Der Pluijm, A.T. Vermeltoort. Structural Masonry - An Experimental/ Numerical Basis for Practical Design Rules. CUR Report 171, CUR, Gouda (Dutch version) See Rots et al. (1997) for english translation.
- Rots et al. (1997)
J.G. Rots, R. Van Der Pluijm, A.T. Vermeltoort. Structural Masonry - An Experimental/ Numerical Basis for Practical Design Rules. Balkema - ISBN 90 5410 680 8.
- Rots (2000)
J.G. Rots. Computational Modelling Of Cracking And Settlement Damage In Masonry Structures. Faculty of Architecture, Delft U of Tech.
- Rots et al. (2016)
J.G. Rots, F. Messali, R. Esposito, S. Jafari, V. Mariani. Computational Modelling of Masonry with a view to Groningen induced Seismicity. 10th SAHC Struct Analysis of Historical Construction, Leuven.
- Rots et al. (2017)
J.G. Rots, F. Messali, R. Esposito, V. Mariani, S. Jafari. Multi-Scale Approach towards Groningen Masonry and Induced Seismicity. Key Eng Mats, 747, 653-661.
- Rots et al. (2019)
J.G. Rots, S. Invernizzi, B. Belletti, M.A.N. Hendriks. Circumventing bifurcations in structural softening. Comput Modeling Workshop on Conc, Masonry and on Fiber-reinforced Composites.
- Rots & Blaauwendraad (1989)
J.G. Rots, J. Blaauwendraad. Crack models for concrete- Discrete, smeared, fixed, multi-directional or rotating. Heron, vol 34 ISSN 0046-7316.
- Rots & De Borst (1989)
J.G. Rots, R. De Borst. Analysis Of Concrete Fracture in "direct" Tension. Inl J Solids Structs Vol 25 No 12 pp 1381-1394 1989.
- Rots & Van Staalduinen (2016)
J.G. Rots, P.C. Van Staalduinen. Plan of approach NAM/TU Delft Program "Damage Sensitivity of Groningen Masonry Structures - Computational and Experimental Studies". TU Delft.
- Roy (2019)
A. Roy. Efficient Reliability Analysis Of Concrete Structures On the Basis Of Non-linear Finite Element Analysis Under Numerical Noise. TU Delft.
- Rutqvist et al. (2014)
J. Rutqvist, F. Cappa, A.P. Rinaldi, M. Godano. Modeling of induced seismicity and ground vibrations associated with geologic CO2 storage, and assessing their effects on surface structures and human perception. Intl J of Greenhouse Gas Control 24 (2014) 64–77.
- SBR (2010)
SBR. Schade aan gebouwen. SBR.
- SBR (2017)
SBR. Trillingsrichtlijn Deel A (2017). SBR.
- van der Salm et al. (2012)
R. van der Salm, P. Hölscher, A.J. Snethlage. SBR-A richtlijn niet eenduidig voor trillinggevoelige funderingen. Geotechniek.
- Salmanpour (2017)
A.H. Salmanpour. Displacement Capacity of Structural Masonry. ETH Zürich, PhD Dissertation, 2017.
- Salmanpour & Schwartz (2015)
A.H. Salmanpour, N.M.J. Schwartz. Displacement capacity of contemporary unreinforced masonry walls: An experimental study. Eng Structs 89 (2015) 1–16.

- Saloustros et al. (2018)
S. Saloustros, L. Pelà, M. Cervera, P. Roca. An enhanced finite element macro-model for the realistic simulation of localized cracks in masonry structures: A large-scale application. *Intl J of Architectural Heritage*, 12:3, 432-447. doi.org/10.1080/15583058.2017.1323245
- San-Bartolomé & Castro-Morán (2009)
A. San-Bartolomé, A. Castro-Morán. Reparación de un Muro de Albañilería confinada. Pontificia Universidad Católica del Perú.
- De Santis et al. (2018)
S. De Santis, F. Roscini, G. de Felice. Full-scale tests on masonry vaults strengthened with Steel Reinforced Grout. *Composites Part B* 141 (2018) 20–36.
- De Santis et al. (2019)
S. De Santis, G. de Felice, F. Roscini. Retrofitting of Masonry Vaults by Basalt Textile-Reinforced Mortar Overlays. *INTERNATIONAL JOURNAL OF ARCHITECTURAL HERITAGE*. doi.org/10.1080/15583058.2019.1597947
- Sarhosis et al. (2014)
V. Sarhosis, S.W. Garrity, Y. Sheng. Influence of brick–mortar interface on the mechanical behaviour of low bond strength masonry brickwork lintels. *Eng Struct* 88 (2015) 1–11.
- Sarhosis et al. (2019)
V. Sarhosis, D. Dais, E. Smyrou, I.E. Bal. Evaluation of modelling strategies for estimating cumulative damage on Groningen masonry buildings due to recursive induced earthquakes. *Bull of Earthq Eng*. doi.org/10.1007/s10518-018-00549-1
- Satti (1972)
K.M.H. Satti. Model Brickwork Walls Panels under Lateral Loading. U of Edinburgh.
- Schauer & Rodriguez (2019)
M. Schauer, G.R. Rodriguez. A coupled FEM-SBFEM approach for soil-structure-interaction analysis using non-matching meshes at the near-field far-field interface. *Soil Dyns and Earthq Eng* 121 (2019) 466–479.
- Scherer (2006)
G.W. Scherer. Internal Stress and Cracking in Stone and Masonry. MS Konsta-Gdoutos, (ed), *Measuring, Monitoring and Modeling Conc Properties*, 633–641. doi
- Scheufler et al. (2008)
W. Scheufler, Habil, E.h.K. Zilch, W. Finckh, S. Grabowski, D. Schermer. Test results on the behaviour of masonry under static cyclic in plane lateral loads. *Esecmase*.
- Schneemayer et al. (2014)
A. Schneemayer, C. Schranz, A. Kolbitsch, E.K. Tschegg. Fracture Mechanical Properties of Mortar to Brick Interfaces. *J Mater Civ Eng*, 2014, 26(9): -1–1, ASCE.
- Schreppers et al. (2016)
G.M.A. Schreppers, A. Garofano, F. Messali, J.G. Rots. DIANA validation report for masonry modelling. DIANA FEA report 2016-DIANA-R1601 TU Delft Struct Mechs Report CM-2016-17, 143 pp.
- Schultz & Mueffelman (2013)
A.E. Schultz, J.G. Mueffelman. Elastic Stability of URM Walls Under Transverse Loading. *TMS J* September.
- Schwarz & Maiwald (2012)
J. Schwarz, H. Maiwald. Empirical vulnerability assessment and damage for description natural hazards following the principles of modern macroseismic scales. 15 WCEE Lisboa, 2012.
- Seible et al. (1994)
F. Seible, M.J.N. Priestley, G.R. Kingsley, A.G. Kürkschübasche. Seismic Response Of Full-scale Five-story Reinforced-masonry Building. *J Struct Eng* 1994120:925-946.
- Shafiei et al. (2016)
S. Shafiei, B.W. Melville, A.Y. Shamseldin. Experimental investigation of tsunami bore impact force and pressure on a square prism. *Coastal Eng* 110 (2016) 1–16.
- Sharafati et al. (2021)
A. Sharafati, S.B.H.S. Asadollah, N. Al-Ansari. Application of bagging ensemble model for predicting compressive strength of hollow concrete masonry prism. *Ain Shams Eng J* 12 (2021) 3521–3530. doi.org/10.1016/j.asej.2021.03.028
- Sharma et al. (2018)
S. Sharma, U. Tomassetti, F. Graziotti. Commentary On Annex H Of Npr 9998 (2018). EUCENTRE, Pavia, Italy.
- Sharma et al. (2023)
S. Sharma, M. Longo, F. Messali. A novel tier-based numerical analysis procedure for the structural assessment of masonry quay walls under traffic loads. *Front Built Environ* 9:1194658. 10.3389/fbuil.2023.1194658

- Sierra-Beltran & Jonkers (2012)
M.G. Sierra-Beltran, H.M. Jonkers. Bio-Based Mortar For Concrete Repair. 14th Intl Conf Struct Faults and Repair, Edinburgh, Scotland, UK, 3-5 July 2012.
- Simpson & Grose (1996)
B. Simpson, W.J. Grose. Discussion: The effect of ground movements on rigid masonry facades. *Geotechnical Aspects of Underground Construction in Soft Ground*, Mair & Taylor (eds).
- Singh (1999)
M.M. Singh. *Mining Engineering Book*, Mine Subsidence, Chapter 10.6. Book. doi
- Skroumpelou et al. (2018)
G. Skroumpelou, F. Messali, R. Esposito, J.G. Rots. Mechanical Characterization Of Wall Tie Connection In Cavity Walls. *Australasian Masonry Conf*, Sydney Australia.
- Slobbe et al. (2013)
A.T. Slobbe, M.A.N. Hendriks, J.G. Rots. Systematic assessment of directional mesh bias with periodic boundary conditions: Applied to the crack band model. *Eng Fracture Mech*, 109, pp 186-208.
- Smrkić et al. (2018)
M.F. Smrkić, J. Koščak, D. Damjanović. Application of 2D digital image correlation for displacement and crack width measurement on RC elements. *Građevinar* 70 (2018) 9, 771-781.
- Smyrou et al. (2011)
E. Smyrou, P. Tasiopoulou, I.E. Bal, G. Gazetas. Ground Motions versus Geotechnical and Structural Damage in the February 2011 Christchurch Earthquake. *Seismological Research Letters* Volume 82, Number 6 November/December 2011.
- Sousamli (2024)
M. Sousamli. Orthotropic Cyclic Continuum Constitutive Model For Masonry Structures and Comparative Studies. TU Delft.
- Son et al. (2014)
H. Son, C. Kim, N. Hwang, C. Kim, Y. Kang. Classification of major construction materials in construction environments using ensemble classifiers. *Advanced Eng Informatics* 28 (2014) 1–10. doi.org/10.1016/j.aei.2013.10.001
- Son & Cording (2005)
M. Son, E.J. Cording. Estimation of Building Damage Due to Excavation-Induced Ground Movements. *J Of Geotechnical and Geoenvironmental Eng*.
- Son & Cording (2007)
M. Son, E.J. Cording. Evaluation of Building Stiffness for Building Response Analysis to Excavation-Induced Ground Movements. *J of Geotechnical and Geoenvironmental Eng* 133(8).
- Soysal & Arici (2023)
B.F. Soysal, Y. Arici. Crack Width - Seismic Intensity Relationships for Concrete Gravity Dams. *J of Earthq Eng*. 10.1080/13632469.2023.2220048
- Spence et al. (1999)
R.J.S. Spence, A. Pomonis, P.J. Baxter, A.W. Coburn, M. White, M. Dayrit. Building Damage Caused by the Mount Pinatubo Eruption of June 15, 1991. Department of Architecture, U of Cambridge.
- Spetzler & Dost (2017)
J. Spetzler, B. Dost. Probabilistic Seismic Hazard Analysis for Induced Earthquakes in Groningen - Update. KNMI report - PSHA Groningen, 2017 update.
- Spyrakos & Xu (2003)
C.C. Spyrakos, C. Xu. Seismic soil–structure interaction of massive flexible strip-foundations embedded in layered soils by hybrid BEM–FEM. *Soil Dyns and Earthq Eng* 23 (2003) 383–389.
- Van Staalduinen et al. (2018)
P.C. Van Staalduinen, K. Terwel, J.G. Rots. Onderzoek naar de oorzaken van bouwkundige schade in Groningen Methodologie en case studies ter duiding van de oorzaken.. Delft U of Tech Report number CM-2018-01, 11 July 2018 - Downloadable from www.NationaalCoördinatorGroningen.nl.
- Van Staalduinen & Smits (1993)
P.C. Van Staalduinen, M.T.J.H. Smits. Trillingscriteria voor schade aan gebouwen. TNO.
- Stafford et al. (2019)
P.J. Stafford, B.D. Zurek, M. Ntinalexis, J.J. Bommer. Extensions to the Groningen ground-motion model for seismic risk calculations: component-to-component variability and spatial correlation. *Bull of Earthq Eng* (2019) 17:4417–4439. doi.org/10.1007/s10518-018-0425-6

- Stagg et al. (1984)
M.S. Stagg, D.E. Siskind, M.G. Stevens, C.H. Dowding. Effects of Repeated Blasting on a Wood-Frame House. US Department of Interior - Office of Surface Mining.
- Steenbergen et al. (2015)
R.D.J.M. Steenbergen, A.C.W.M. Vrouwenvelder, N.P.M. Scholten. Veiligheidsbeschouwing aardbevingen Groningen t.b.v. NPR 9998. TNO.
- Steenbergen et al. (2017)
R.D.J.M. Steenbergen, R.D.J.M. Steenbergen, I. van Straalen, A.C.W.M. Vrouwenvelder. Background Report Draft NPR 9998:2017 Part A: Terminology and Safety Philosophy. NEN.
- Steenbergen & Geurts (2016)
R.D.J.M. Steenbergen, C.P.W. Geurts. Relatie tussen PGA waarden en kans op schade voor geïnduceerde aardbevingen in Groningen. TNO.
- Stryszewska & Kanka (2019)
T. Stryszewska, S. Kanka. Forms of Damage of Bricks Subjected to Cyclic Freezing and Thawing in Actual Conditions. *Mats* 2019, 12, 1165. 10.3390/ma12071165
- Sucuoglu (2013)
H. Sucuoglu. Implications of Masonry Infill and Partition Damage in Performance Perception in Residential Buildings after a Moderate Earthquake. *Earthq Spectra*, Volume 29, No 2, pages 661–667, May 2013. 10.1193/1.4000147
- Suhairy (2000)
S.A. Suhairy. Prediction of Ground Vibration from Railways. SP Swedish National Testing and Research Institute.
- Sullivan et al. (2004)
T.J. Sullivan, R. Pinho, A. Pavese. An Introduction to Structural Testing Techniques in Earthquake Engineering. ROSE School Collegio Alessandro Volta.
- Sullivan et al. (2013)
T.J. Sullivan, P.M. Calvi, R. Nascimbene. Towards improved floor spectra estimates for seismic design. *Earthqs and Structs*, Vol 4, No 1 (2013) 109-132.
- Suppasri et al. (2013)
A. Suppasri, E. Mas, I. Charvet, R. Gunasekera, K. Imai, Y. Fukutani, Y. Abe, F. Imamura. Building damage characteristics based on surveyed data and fragility curves of the 2011 Great East Japan tsunami. *Nat Hzdts* (2013) 66:319–341 DOI. doi.org/10.1007/s11069-012-0487-8
- Svinkin (1999)
M.R. Svinkin. Prediction and Calculation of Construction Vibrations. Deep Foundations Institute.
- Svinkin (2013)
M.R. Svinkin. Forensic engineering of construction vibrations. *Forensic Eng.*
- Sweeney et al. (2005)
S.C. Sweeney, M.A. Horney, S.L. Orton. Seismic Response of a Half-Scale Masonry Building with Flexible Diaphragms. *Erdc/cerl Tr-05-25*.
- Tarbotton et al. (2015)
C. Tarbotton, F. Dall'Osso, D. Dominey-Howes, J. Goff. The use of empirical vulnerability functions to assess the response of buildings to tsunami impact: Comparative review and summary of best practice. *Earth-Science Reviews* 142 (2015) 120–134.
- Tedesco et al. (2016)
F. Tedesco, A. Bilotta, E. Turcoa. Multiscale 3D mixed FEM analysis of historical masonry constructions. *European J of Environmental and Civil Eng*, 2016 dx. doi.org/10.1080/19648189.2015.1134676
- Tena-Colunga et al. (2015)
A. Tena-Colunga, K.L. Chinchilla-Portillo, G. Juárez-Luna. Assessment of the diaphragm condition for floor systems used in urban buildings. *Eng Structs*, 93, p70-84.
- Thamboo et al. (2013)
J.A. Thamboo, M. Dhanasekar, C. Yan. Flexural and shear bond characteristics of thin layer polymer cement mortared concrete masonry. *Construction and Bldg Mats* 46 (2013) 104–113.
- Thamboo & Dhanasekar (2015)
J.A. Thamboo, M. Dhanasekar. Characterisation of thin layer polymer cement mortared concrete masonry bond. *Construction and Bldg Mats* 82 (2015) 71–80.
- Theodossopoulos et al. (2014)
D. Theodossopoulos, J. Sanderson, M. Scott. Strengthening masonry cross vaults damaged by geometric instability. *Key Eng Mats* ISSN: 1662-9795, Vol 624, pp 635-643.
- van Thienen-Visser & Breunese (2015)
K. van Thienen-Visser, J.N. Breunese. Induced seismicity of the Groningen gas field: History and recent developments. *THE LEADING*

- EDGE June 2015 Special Section: Injection-induced seismicity dx. doi.org/10.1190/tle34060664.1.
- Thijssen (1999)
C.C.F. Thijssen. *Bouwconstructieve Analyse Van Naoor- Logse Eengezinsbui- Zen in De Non-profit Huursector 1946-1980*. Delft U of Tech Press.
- Tiel et al. (2022)
B.v. Tiel, U. Sauerland, M. Franke. Meaning and Use in the Expression of Estimative Probability. *Open Mind: Discoveries in Cognitive Science*, 6, 250–263. doi.org/10.1162/opmi_a_00066
- Tomassetti et al. (2017a)
U. Tomassetti, S. Kallioras, F. Graziotti, A.A. Correia. Preliminary report on the construction of the building prototype at the LNEC laboratory. Lisbon, March 2017.
- Tomassetti (2017)
U. Tomassetti. Selection of Vertical Acceleration Time-Series for Shake Table Testing of Groningen Masonry Building at LNEC. EUCENTRE.
- Tomassetti et al. (2017b)
U. Tomassetti, A.A. Correia, F. Graziotti, A.I. Marques, M. Mandirola, P.X. Candeias. Collapse Shaking Table Test On A Urm Cavity Wall Structure Representative Of A Dutch Terraced House. EUCENTRE.
- Tomassetti et al. (2017c)
U. Tomassetti, A.A. Correia, A. Marques, F. Graziotti, A. Penna, G. Magenes. Dynamic collapse testing of a full-scale URM cavity-wall structure. Anidis 2017, Pistoia.
- Tomassetti et al. (2018)
U. Tomassetti, A.A. Correia, P.X. Candeias, F. Graziotti, A.C. Costa. Two-way bending out-of-plane collapse of a full-scale URM building tested on a shake table. *Bull of Earthq Eng*. doi.org/10.1007/s10518-018-0507-5
- Tomazevic (2007)
M. Tomazevic. Damage as a measure for earthquake-resistant design of masonry structures: Slovenian experience. *Can J Civ Eng* 34: 1403–1412 (2007).
- Tondelli et al. (2013)
M. Tondelli, S. Petry, S. Peloso, K. Beyer. Shake-table test on a four-storey structure with reinforced concrete and unreinforced masonry walls. Vienna Congress on Recent Advcs in Earthq Eng and Struct Dyns 2013 (VEESD 2013).
- Trifunac (1971)
M.D. Trifunac. Zero Baseline Correction Of Strong-Motion Accelerograms. *Bull of the Seismological Soc of America* Vol 61, No 5, pp 1201-1211 October, 1971.
- Tung et al. (2008)
S. Tung, M. Shih, W. Sung. Development of digital image correlation method to analyse crack variations of masonry wall. *Sadhana* Vol 33, Part 6, December 2008, pp 767–779.
- Turner et al. (2012)
F. Turner, K. Elwood, M. Griffith, J. Ingham, J. Marshall. Performance of Retrofitted Unreinforced Masonry Buildings during the Christchurch Earthquake Sequence. *Asces*.
- Tziviloglou et al. (2017)
E. Tziviloglou, Z. Pan, H.M. Jonkers, E. Schlangen. Bio-based Self-healing Mortar: An Experimental and Numerical Study. *J of Advanced Conc Tech* Vol 15, 536-543, September 2017.
- Uva et al. (2012)
G. Uva, F. Porco, A. Fiore. Appraisal of masonry infill walls effect in the seismic response of RC framed buildings: A case study. *Eng Struct* 34 (2012) 514–526.
- Vaculik & Griffith (2016)
J. Vaculik, M. Griffith. Shaketable Tests on Masonry Walls in Two-Way Bending. Dept of Civil and Environmental Eng, U of Adelaide.
- Vaculik & Griffith (2017a)
J. Vaculik, M.C. Griffith. Out-of-plane load–displacement model for two-way spanning masonry walls. *Eng Struct* 141 (2017) 328–343.
- Vaculik & Griffith (2017b)
J. Vaculik, M.C. Griffith. Out-of-plane shaketable testing of unreinforced masonry walls in two-way bending. *Bull Earthq Eng*. doi.org/10.1007/s10518-017-0282-8
- Vandoren et al. (2012)
B. Vandoren, K. de Proft, A. Simone, B. Sluys. Modelling of Crack Initiation and Propagation using the Partition of Unity Method. VIII Intl Conf on Fracture Mechs of Conc and Conc Structs FraMCoS-8.
- Vasconcelos & Lourenço (2006)
G. Vasconcelos, P.B. Lourenço. Assessment of the in-plane shear strength of stone masonry

- walls by simplified models. *Struct Analysis of Historical Constrcs*, New Delhi 2006.
- Vasconcelos & Lourenço (2009)
G. Vasconcelos, P.B. Lourenço. In-Plane Experimental Behavior of Stone Masonry Walls under Cyclic Loading. *J Struct Eng* 2009;135:1269-1277.
- Vecchio & Collins (1986)
F.J. Vecchio, M.P. Collins. The modified compression field theory for reinforced concrete elements subjected to shear. *ACI J* 83, 22 (1986), 219-231.
- de Vent et al. (2011)
I. de Vent, J.G. Rots, R.P.J. van Hees. Structural Damage in Masonry - Developing diagnostic decision support. TU Delft.
- de Vent (2011)
I. de Vent. Prototype of a diagnostic decision support tool for Structural damage in masonry. Delft U of Tech, Faculty of Architecture ISBN: 978-90-8570-760-8.
- Vermeltfoort (2005)
A.T. Vermeltfoort. Brick-mortar interaction in masonry under compression. Eindhoven: Technische Universiteit Eindhoven. doi.org/10.6100/IR589402
- Van Verseveld et al. (2015)
H.C.W. Van Verseveld, A.R. Van Dongeren, N.G. Plant, W.S.J.C. Den Heijer. Modelling multi-hazard hurricane damages on an urbanized coast with a Bayesian Network approach. *Coastal Eng* 103 (2015) 1–14.
- Verstrynge et al. (2016)
E. Verstrynge, K. De Wilder, L. Bejarano-Urrego, E. Voet, K. Van Balen. Advanced techniques for monitoring of settlement-induced deformations and crack growth in historical masonry. *Struct Analysis of Historical Constrcs – Anamnesis, diagnosis, therapy, controls – Van Balen & Verstrynge (Eds) © 2016 Taylor & Francis Group, London, ISBN978-1-138-02951-4.*
- Verstrynge et al. (2020)
E. Verstrynge, G. Lacidogna, F. Accornero, A. Tomor. A review on acoustic emission monitoring for damage detection in masonry structures. *Construction and Bldg Mats*.
- Vlachakis (2017)
G. Vlachakis. Out-of-plane simulation of masonry structures using novel finite element techniques. *Erasmus Mundus*.
- Vlek (2018)
C. Vlek. Induced Earthquakes from Long-Term Gas Extraction in Groningen, the Netherlands: Statistical Analysis and Prognosis for Acceptable-Risk Regulation. *Risk Analysis*, Vol 38, No 7, 2018.
- Van Vliet (2004)
M.R.A. Van Vliet. Shear tests on masonry panels; Literature survey and proposal for experiments. TNO report 2004-CI-R0171.
- Voigt et al. (2016)
S. Voigt, F. Giulio-Tonolo, J. Lyons, J. Kučera, B. Jones, T. Schneiderhan, G. Platzcek, K. Kaku, M.K. Hazarika, L. Czarán, S. Li, W. Pedersen, G.K. James, C. Proy, D.M. Muthike, J. Bequignon, D. Guha-Sapir. Global trends in satellite-based emergency mapping. *Science Magazine* VOL 353 ISSUE 6296. doi
- van der Voort & Vancly (2014)
N. van der Voort, F. Vancly. Social impacts of earthquakes caused by gas extraction in the Province of Groningen, The Netherlands. *Environmental Impact Assessment Review* 50 (2015) 1–15. doi.org/10.1016/j.eiar.2014.08.008
- de Waal et al. (2015)
J.A. de Waal, A.G. Muntendam-Bos, J.P.A. Roest. Production induced subsidence and seismicity in the Groningen gas field – can it be managed?. *Proc IAHS*, 372, 129–139, 2015
proc-iahsnet/372/129/2015. doi.org/10.5194/piahs-372-129-2015
- Waarts (1997)
P. Waarts. Kans op schade aan bouwwerken door trillingen. TNO.
- Wald et al. (1999)
D.J. Wald, V. Quitoriano, T.H. Heaton, H. Kanamori. Relationships between Peak Ground Acceleration, Peak Ground Velocity and Modified Mercalli Intensity in California. *Earthq Spectra*, Volume 15, No 3, August 1999.
- Walsh et al. (2014)
K. Walsh, D. Dizhur, J. Shafaei, H. Derakhshan, J. Ingham. Out-of-Plane In-Situ Testing of Masonry Cavity Walls in As-Built and Improved Conditions. *Australian Earthq Eng Soc* 2014 Conf, Nov 21-23, Lorne, Victoria.
- Walsh et al. (2015)
K.Q. Walsh, D.Y. Dizhur, J. Shafaei, H. Derakhshan, J.M. Ingham. In Situ Out-of-Plane Testing of Unreinforced Masonry Cavity Walls in

- as-Built and Improved Conditions. *Structs* 3 (2015) 187–199.
- Walsh et al. (2016)
K.Q. Walsh, D.Y. Dizhur, J.M. Ingham. Estimating Thrust Forces Resulting from Arching Action of Clay Brick Masonry Infill. *J Struct Eng*, 06016003.
- Walsh et al. (2017a)
K. Walsh, D. Dizhur, I. Giongo, H. Derakhshan, J. Ingham. Comparison Between Predicted Urm Wall Out-of-plane Strength- Based Capacity and in Situ Proof Test Results. 13th Canadian Masonry Symp Halifax, Canada.
- Walsh et al. (2017b)
K.Q. Walsh, D.Y. Dizhur, I. Giongo, H. Derakhshan, J.M. Ingham. Effect Of Boundary Conditions and Other Factors On Urm Wall Out-of-plane Behaviour: Design Demands, Predicted Capacity, and in Situ Proof Test Results. *SESOC J Volume 30 No1 April 2017*.
- Wang et al. (2012a)
S.Y. Wang, S.W. Sloan, A.J. Abbo, M.J. Masia, C.A. Tang. Numerical simulation of the failure process of unreinforced masonry walls due to concentrated static and dynamic loading. *Intl J of Solids and Structs* 49 (2012) 377–394.
- Wang et al. (2012b)
T. Wang, X. Chen, W. Li, Q. Miao. Seismic Performance of Masonry Buildings Retrofitted by Pre-Cast RC Panels. *Applied Mechs and Mats*. doi.org/10.4028/www.scientific.net/AMM.166-169.1811
- Wassing & Dost (2012)
B.B.T. Wassing, B. Dost. Seismisch hazard van geïnduceerde aardbevingen - Integratie van deelstudies. TNO/KNMI.
- Wijanto (2007)
L.S. Wijanto. Seismic Assessment of Unreinforced Masonry Walls. Department of Civil Eng U of Canterbury Christchurch, New Zealand.
- Van Wijnbergen (2015)
E. Van Wijnbergen. Seismic retrofit - an architectural approach for the situation in Groningen. Delft U of Tech.
- Willis (2004)
C.R. Willis. Design of Unreinforced Masonry Walls for Out-of-plane Loading. School of Civil and Environmental Eng, The U of Adelaide.
- Willis et al. (2004)
C.R. Willis, M.C. Griffith, S.J. Lawrence. Horizontal Bending of Unreinforced Clay Brick Masonry. *Masonry Intl Vol 17, No 3*.
- Willis et al. (2010)
C.R. Willis, R. Seracino, M.C. Griffith. Out-of-plane strength of brick masonry retrofitted with horizontal NSM CFRP strips. *Eng Structs* 32 (2010) 547–555.
- Wilson et al. (2011)
A. Wilson, P. Quenneville, J. Ingham. Assessment of timber floor diaphragms in historic unreinforced masonry buildings. Department of Civil and Environmental Eng, The U of Auckland.
- Wilson et al. (2014)
A. Wilson, P.J.H. Quenneville, J.M. Ingham. In-Plane Orthotropic Behavior of Timber Floor Diaphragms in Unreinforced Masonry Buildings. *J Struct Eng*, 2014, 140(1): 04013038.
- Wojciechowska et al. (2015)
K. Wojciechowska, G. Pleijter, M. Zethof, F.J. Havinga, D.H. Van Haaren, W.L.A. Ter-Horst. Application of Fragility Curves in Operational Flood Risk Assessment. *Geotechnical Safety and Risk V T Schweckendiek et al (Eds)*. doi.org/10.3233/978-1-61499-580-7-528
- Xu & Zhu (2009)
S. Xu, Y. Zhu. Experimental determination of fracture parameters for crack propagation in hardening cement paste and mortar. *Int J Fract* (2009) 157:33–43 DOI. doi.org/10.1007/s10704-009-9315-x
- Yang et al. (2017)
T.Y. Yang, K. Li, J. Lin, Y. Yi, D.P. Tung, J. Fawcett. Advanced shake table controler design using model predictive strategy. 16th World Conf on Earthq Eng, 16WCEE 2017.
- Yi (2004)
T. Yi. Experimental Investigation and Numerical Simulation Of an Unreinforced Masonry Structure With Flexible Diaphragms. Georgia Institute of Tech.
- Yi et al. (2006a)
T. Yi, F.L. Moon, R.T. Leon, L.F. Kahn. Analyses of a Two-Story Unreinforced Masonry Building. *J Struct Eng* 2006132:653-662.
- Yi et al. (2006b)
T. Yi, F.L. Moon, R.T. Leon, L.F. Kahn. Lateral Load Tests on a Two-Story Unreinforced Masonry Building. *J Struct Eng* 2006132:643-652.

- Younis et al. (2020)
A. Younis, A.S. Ramadan, L.S. Wong, M.L. Nehdi. New rational test for reinforced-concrete pipe eliminating subjective crack-width criteria. *Structs* 28 (2020) 2507–2522. doi.org/10.1016/j.istruc.2020.10.076
- Zhai et al. (2016)
C. Zhai, J. Kong, X. Wang, Z. Chen. Experimental and finite element analytical investigation of seismic behavior of full-scale masonry infilled RC frames. *J of Earthq Eng.* doi.org/10.1080/13632469.2016.1138171
- Zhu (2006)
Y. Zhu. Breach Growth in Clay-Dikes. Delft U of Tech.
- van Zijl et al. (2001)
G.P.A.G. van Zijl, R. de Borst, J.G. Rots. The Physical Role of Crack Rate Dependence in the Long-Term Behaviour of Cementitious Materials. *Intl J Solids & Structs* 38, pp 5063-5079.
- Zuccaro et al. (2010)
G. Zuccaro, F. Cacace, M. Rauci. A Multimedia and didactic handbook for seismic Damage evaluation. *Urban Habitat Constrcs under Catastrophic Events.*
- Zucchini & Lourenço (2006)
A. Zucchini, P.B. Lourenço. Homogenization of Masonry Using a Micro-mechanical Model Compressive Behaviour. *III European Conf on Comput Mechs Solids, Structs and Coupled Problems in Eng CA.*
- Červenka et al. (1998)
J. Červenka, J.M.C. Kishen, V.E. Saouma. Mixed Mode Fracture of Cementitious Bimaterial Interfaces. *Eng Fracture Mechs Vol* 60, No 1, pp 95±107.

List of Authors

The following is a list containing all the authors consulted in the referenced publications. The entry for each author includes their last name, initials, publication year or range of years of the consulted works, and number of consulted works (in parenthesis).

- | | | |
|-------------------------------|------------------------------|----------------------------|
| Abbati, S.D. 2015 (1) | Almeida, J.C. 1999,2012 (2) | Aussem, A. 2016 (1) |
| Abbiati, G. 2017,2018 (2) | Alves, S. 2015 (1) | Badalà, A. 2014 (1) |
| Abbo, A.J. 2012 (1) | Anania, L. 2012-2014 (3) | Badoux, M. 2005-2016 (3) |
| Abo-El-Ezz, A. 2013 (1) | Anthoine, A. 1995,2008 (2) | Bahrampouri, M. 2022 (1) |
| Abrams, D.P. 1996 (1) | Antonaci, P. 2011 (1) | Baills, A. 2014 (1) |
| Accornero, F. 2020 (1) | Antoniou, A. 2015 (1) | Bakar, B.H.A. 2009 (1) |
| Acikgoz, S. 2023 (1) | Anzani, A. 2004 (1) | Bakema, M.M. 2018 (1) |
| Acosta, D.Y. 2016 (1) | Aravind, H.B. 2019 (1) | Baker, J.W. 2019 (1) |
| Adair, B. 2015 (1) | Aref, A.J. 2011,2015 (2) | Bal, I.E. 2011-2021 (4) |
| Adam, J.M. 2016 (1) | Argiento, L.U. 2016 (2) | Van Balen, K. 2016 (1) |
| Addenbrooke, T.I. 1997 (1) | Arias, A. 1970 (1) | Banting, B.R. 2013 (1) |
| AeDES, 2007 (1) | Arici, Y. 2023 (1) | Barros, J.A. 2003-2012 (3) |
| Aguilar, V. 2016 (1) | Arnesen, A. 1998 (1) | Barry, G. 2015 (1) |
| Akhavissy, A.H. 2012,2013 (2) | Arup, 2013-2018 (7) | Basilio, I. 2014 (1) |
| Al-Ansari, N. 2021 (1) | Arya, A.S. 2013 (1) | Baxter, P.J. 1999 (1) |
| Albanesi, L. 2018 (1) | Arède, A. 2007-2015 (4) | Beattie, G. 2007 (1) |
| Albert, V. 2010 (1) | Asadollah, S.B.H.S. 2021 (1) | Beazley, P.L. 2017 (1) |
| Alberto, A. 2011 (1) | Astroza, M. 2012 (1) | Beck, 2008 (1) |
| Aldemir, A. 2015 (1) | Atimtay, E. 2006 (1) | Behnamfar, F. 2015 (1) |
| Alemi, F. 2008 (1) | Atkinson, G.M. 2015 (1) | Benedetti, D. 1998 (1) |
| Allen, C. 2015 (1) | Attard, M.M. 2009 (1) | Bibimoune, M. 2016 (1) |

- Bilotta, A. 2016 (1)
 Binda, L. 2004 (2)
 Bindiganavile-Ramadas, S. 2018 (1)
 Binici, B. 2015 (1)
 Bird, J.F. 2006 (1)
 Blaauwendraad, J. 1985-1995 (3)
 Blaber, J. 2015 (1)
 Blong, R. 2003 (1)
 Boen, T. 2013 (1)
 de Boer, S.J. 2016 (1)
 de Boer, A. 2014 (1)
 Bommer, J.J. 1998-2022 (23)
 Bonaldo, D. 2016 (1)
 Bonaldo, E. 2003 (1)
 Boonpichetvong, M. 2004 (1)
 de Borst, R. 1989,2001 (2)
 Borzi, B. 2001,2008 (2)
 van den Bos, A. 2016 (1)
 Boscardin, M.D. 1989 (1)
 Bosiljkov, V. 2008,2015 (2)
 Boulanger, R.W. 2014 (1)
 Bourne, S.J. 2015-2020 (5)
 BouwenmetStaal, 2015 (1)
 Boyd, S.W. 2013 (1)
 Brando, G. 2014,2020 (2)
 Bray, 2008 (1)
 Bredevelde, J. 2013 (1)
 Breunese, J.N. 2015 (1)
 Broccardo, M. 2017,2018 (2)
 Broms, B.B. 1977 (1)
 Bunyan, J. 2015 (1)
 Burd, H. 2023 (1)
 Burland, J.B. 1974-2001 (3)
 Burnett, S. 2007 (1)
 Busschers, F.S. 2017 (1)
 CUR, 1990 (1)
 Caballero-González, A. 2019 (1)
 Cacace, F. 2010 (1)
 Caccavale, M. 2013 (1)
 Calderini, C. 2008,2015 (2)
 Calduran, 2004 (1)
 Calvi, G.M. 1992-2006 (6)
 Calvi, P.M. 2013 (1)
 Camp, W.M. 2013 (1)
 Campos-Costa, A. 2008,2018 (2)
 Can, Ö. 2010 (1)
 Canbay, E. 2015 (1)
 Candeias, P.X. 2008-2018 (3)
 Cappa, F. 2014 (1)
 Carydis, P. 1998 (1)
 Casadei, P. 2016 (1)
 Casati, M.J. 2008 (1)
 Cascini, L. 2015-2017 (3)
 Castellani, A. 1986,1988 (2)
 Castellazzi, G. 2017 (2)
 Castro-Morán, A. 2009 (1)
 Cattari, S. 2008-2024 (4)
 Caudron, M. 2008 (1)
 Causevic, M. 2010 (1)
 Cavalagli, N. 2020 (1)
 Cavalieri, F. 2019 (1)
 Cenja, E. 2015 (1)
 Centeno, J. 2011 (1)
 Ceran, H.B. 2013 (1)
 Cervera, M. 2014,2018 (2)
 Chacko, J. 2018,2019 (2)
 Chaimoon, K. 2009 (1)
 Charrier, J.S. 2012 (1)
 Charvet, I. 2013 (1)
 Chen, Z. 2016 (1)
 Chen, X. 2012 (1)
 Chinchilla-Portillo, K.L. 2015 (1)
 Chiozzi, A. 2017 (1)
 Chiumenti, M. 2014 (1)
 Chong, V.L. 1993 (1)
 Choong, K.K. 2009 (1)
 Chopra, A.K. 1999 (1)
 Chuang, S. 2004 (1)
 Chummar, A.V. 1984 (1)
 Chung, L. 2016 (1)
 Coburn, A.W. 1999 (1)
 Coelho, E. 2008 (1)
 Colangelo, F. 2015 (1)
 Collins, M.P. 1986 (1)
 Contzen, N. 2023 (1)
 Cording, E.J. 1989-2007 (3)
 Cornelissen, H.A.W. 1986 (1)
 Correa, M.R.S. 2007,2009 (2)
 Correia, A.A. 2017-2018 (5)
 Costa, A.A. 2007-2018 (10)
 Costley, A.C. 1996 (1)
 Cotecchia, F. 2016 (1)
 Cotič, P. 2015 (1)
 Courage, W. 2015 (1)
 Crammond, G. 2013 (1)
 Criber, E. 2014 (1)
 Crowley, H. 2004-2019 (11)
 Curtin, 2008 (1)
 Custer, R. 2015 (1)
 Czarán, L. 2016 (1)
 D'Agata, G. 2012 (1)
 Dainotti, S. 2017 (1)
 Dais, D. 2018-2021 (3)
 Dalgic, K.D. 2023 (1)
 Dall'Osso, F. 2015 (1)
 Damiola, M. 2018 (1)
 Damjanović, D. 2018 (1)
 Damoni, C. 2014 (1)
 Danciu, L. 2017 (1)
 Datoussaid, S. 2012 (1)
 Dayrit, M. 1999 (1)
 DeCanio, G. 2016 (1)
 DeJong, M.J. 2009-2020 (5)
 DeSantis, S. 2016 (1)
 Debailleux, L. 2019 (1)
 Deckner, F. 2013 (1)
 van Dedem, E. 2017-2019 (3)
 Degede, H. 2008 (1)
 Dehghan-Niri, E. 2013 (1)
 Delgado, R. 2008 (1)
 Dempsey, D. 2017 (1)
 Denoel, V. 2008 (1)
 Derakhshan, H. 2011-2018 (11)
 Dhanasekar, M. 2013-2019 (3)
 Dickie, J. 2011 (1)
 Didier, M. 2017,2018 (2)
 Dizhur, D. 2010-2019 (17)
 Doherty, K. 2000-2004 (4)
 Dolan, C.W. 1998 (1)
 Dolatshahi, K.M. 2011,2015 (2)
 Dolšek, M. 2008 (1)
 Dominey-Howes, D. 2015 (1)
 Van Dongeren, A.R. 2015 (1)
 Dorji, J. 2019 (1)
 Dornaika, F. 2014 (1)
 Dost, B. 2012-2022 (10)
 Douglas, J. 2013 (1)
 Dowding, C.H. 1984 (1)
 Drosos, V. 2018,2019 (2)
 Dudine, A. 2016 (1)
 Dulieu-Barton, J.M. 2013 (1)
 Dungca, J.R. 2016 (1)
 D'Agata, G. 2014 (2)
 D'Altri, A.M. 2017 (3)
 EQC, 2006 (1)
 Easterbrook, 2008 (1)
 van Eck, T. 2013 (1)
 Edward, B. 2020 (1)
 Edwards, B. 2015-2022 (8)
 El-Dakhkhni, W.W. 2013 (1)

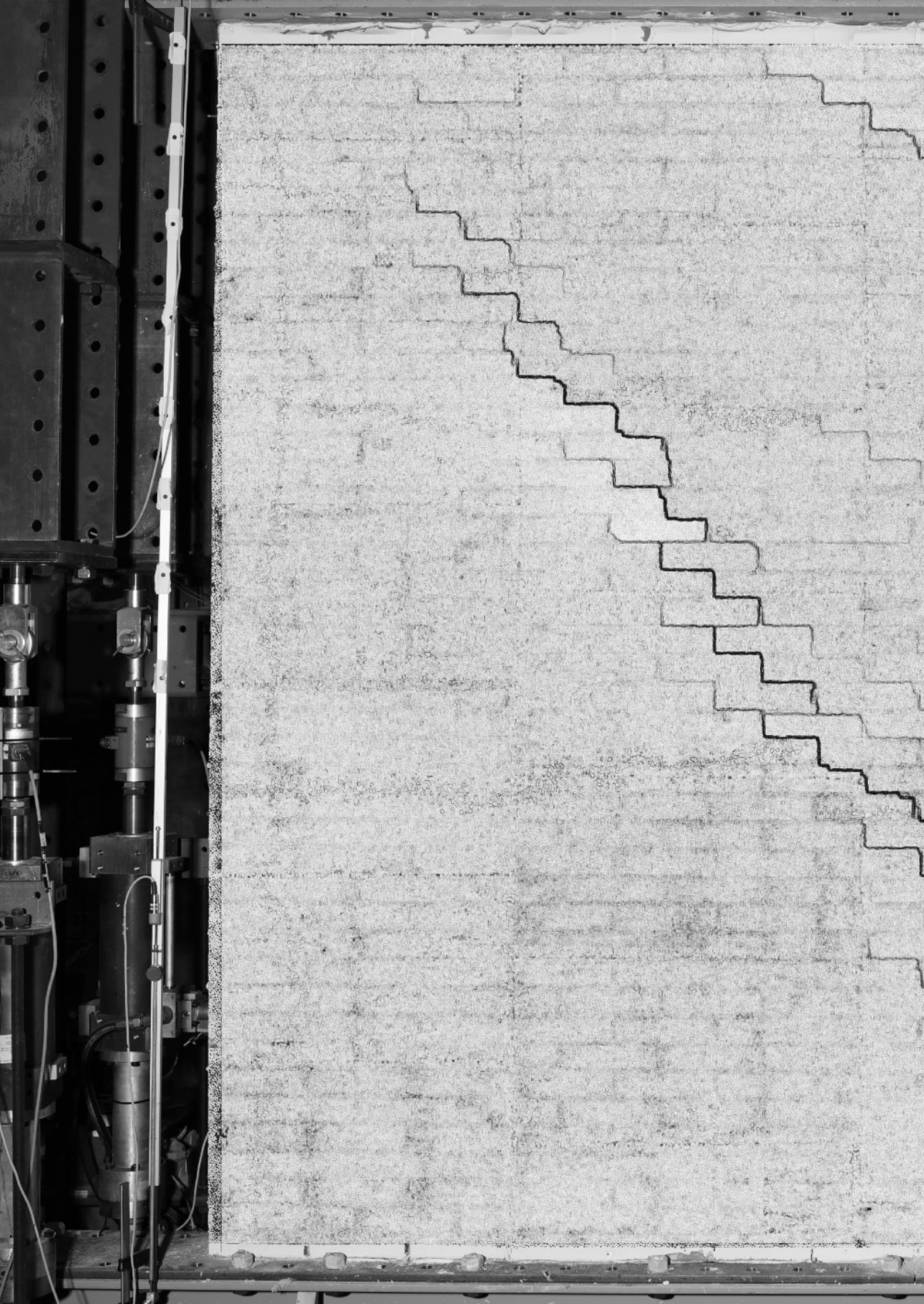
- ElGawady, M.A. 2005-2016 (3)
 Elefante, L. 2009 (1)
 Elghazel, H. 2016 (1)
 van Elk, J. 2015-2022 (24)
 Ellsworth, W.L. 2016 (1)
 Elmenshawi, A.E. 2010 (1)
 Elwood, K. 2012 (1)
 Emeriault, F. 2008 (1)
 Emeriault, 2013 (1)
 Erberik, M.A. 2013 (1)
 Erdal, M. 2010 (2)
 van Es, J. 2016 (1)
 Eslami, S. 2015 (1)
 Esposito, R. 2016-2024 (22)
 Eucentre, 2015 (1)
 Evangeliou, P. 2016 (1)
 Ewing, B.D. 2004 (1)
 Fabrice, 2013 (1)
 Faccioli, E. 2001 (1)
 Fajfar, P. 2008 (1)
 Farhidzadeh, A. 2013 (1)
 Farrell, R. 2014 (1)
 Fathy, A.M. 2008 (1)
 Fawcett, J. 2017 (1)
 Fedele, R. 2014 (1)
 Feenstra, P.H. 1998 (1)
 de Felice, G. 2018,2019 (2)
 Fema, 2000-2020 (4)
 Fernandes, R.P. 2012 (1)
 Fernandez, R. 2010 (1)
 Ferreira, T.M. 2015 (1)
 Ferretti, F. 2018 (2)
 Ferris, M.C. 2001 (1)
 Finckh, W. 2008 (1)
 Fiore, A. 2012-2014 (3)
 Fischer, G. 2008 (1)
 Foraboschi, P. 2009 (1)
 Forbes, R.H. 2013 (1)
 Forrest, J.A. 1999 (1)
 Fragomeli, A. 2016 (1)
 Franchin, P. 2009 (1)
 Franke, M. 2022 (1)
 Franza, A. 2020 (1)
 Friedland, C.J. 2009 (1)
 Fuchs, S. 2014 (1)
 Fuente, J.V. 2010 (1)
 Fukutani, Y. 2013 (1)
 Furtado, A. 2015 (1)
 Gad, E.F. 2008 (1)
 Gagliardo, R. 2018 (1)
 Gajewski, M. 2015 (1)
 Galasco, A. 2010,2013 (2)
 Gams, M. 2014 (1)
 Garbin, E. 2010 (1)
 Garcia, F. 2012 (1)
 García-Macías, E. 2019 (1)
 Garofano, A. 2016 (1)
 Garrity, S.W. 2014 (1)
 Garzón-Roca, J. 2016 (1)
 Gattesco, N. 2016 (1)
 Del Gaudio, C. 2017 (1)
 Gazetas, G. 1991-2011 (3)
 Gehl, P. 2013 (1)
 Gehri, N. 2020 (1)
 Van Gelder, P.H.A.J.M. 2003 (1)
 Gems, B. 2014 (1)
 Geurts, C.P.W. 2016 (1)
 Ghandil, M. 2015 (1)
 Ghobarah, A. 2004 (1)
 Ghorbani, R. 2015 (1)
 Giannakou, A. 2018,2019 (2)
 Giaquinta, C. 2012,2014 (2)
 Giardina, G. 2008-2020 (8)
 Giaretton, M. 2015-2017 (5)
 Gil, L. 2014 (1)
 Gilbert, M. 2002,2007 (2)
 Gill, J.C. 2014 (1)
 Gilstrap, J.M. 1998 (1)
 Giongo, I. 2014-2019 (5)
 Giulio-Tonolo, F. 2016 (1)
 Giuriani, G. 2012 (1)
 Giusto, S. 2024 (1)
 Glascoe, L. 2009 (1)
 Godano, M. 2014 (1)
 Godio, M. 2019 (1)
 Goel, R.K. 1999 (1)
 Goff, J. 2015 (1)
 Goldsworthy, H. 2018 (1)
 van de Graaf, A.V. 2011,2013 (2)
 Grabowski, S. 2008 (1)
 Grant, D. 2015 (1)
 Graziotti, F. 2015-2019 (19)
 Green, R.A. 2017-2020 (3)
 Griffith, M.C. 2000-2018 (24)
 Groot, C.J.W.P. 2004 (1)
 de Groot, A. 2019 (1)
 Grose, W.J. 1996 (1)
 Grottoli, L. 2017-2019 (3)
 Grünberg, J. 2005 (1)
 Grünthal, G. 1998 (1)
 Guedes, J. 2008 (1)
 Guerreiro, J. 2012 (1)
 Guerini, G. 2016-2018 (4)
 Guha-Sapir, D. 2016 (1)
 Guidi, G. 2010 (1)
 Gulen, B. 2023 (1)
 Gunasekera, R. 2013 (1)
 Gunnink, J.L. 2017 (2)
 Gupta, A. 2019 (1)
 Gálvez, J.C. 2008 (1)
 Gálvez, F. 2017 (1)
 De Haan, F.S. 2016 (1)
 Van Haaren, D.H. 2015 (1)
 Habil, 2008 (1)
 Hadzima-Nyarko, M. 2020 (1)
 Hak, S. 2017 (1)
 van den Ham, G.A. 2013 (1)
 Hamed, E. 2010 (1)
 Han, Y. 2004-2009 (3)
 Hancock, J. 2004,2006 (2)
 Hanley, R. 2010 (1)
 Harting, R. 2017 (1)
 Hashemi, S.J. 2011 (1)
 Hatzigeorgiou, G.D. 2010 (1)
 Hazarika, M.K. 2016 (1)
 Heath, D.J. 2008 (1)
 Heaton, T.H. 1999 (1)
 van Hees, R.P.J. 2004-2011 (3)
 Hefti, F. 2018 (1)
 Al Heib, M. 2008,2013 (2)
 Den Heijer, W.S.J.C. 2015 (1)
 Hendriks, M.A.N. 1995-2019 (15)
 Hendry, E.A.W. 2001 (1)
 Hernandez, E.O. 2022 (1)
 Den Hertog, D. 2018 (1)
 Den Hertog, P.D. 2017 (1)
 Hildebrand, R. 2008 (1)
 Hillerborg, A. 1985 (1)
 Hobbs, B. 2002,2007 (2)
 Hoiseth, K.V. 1998 (1)
 Hojdys, Ł. 2014 (1)
 Holscher, P. 2013 (1)
 Hordijk, D.A. 1986 (1)
 Horney, M.A. 2005 (1)
 Hossiney, N. 2019 (1)
 Huissoon, H. 2019 (1)
 Hwang, N. 2014 (1)
 Hölscher, P. 2012 (1)
 Idriss, I.M. 2014 (1)
 Iervolino, I. 2009 (1)
 Ilki, A. 2023 (1)

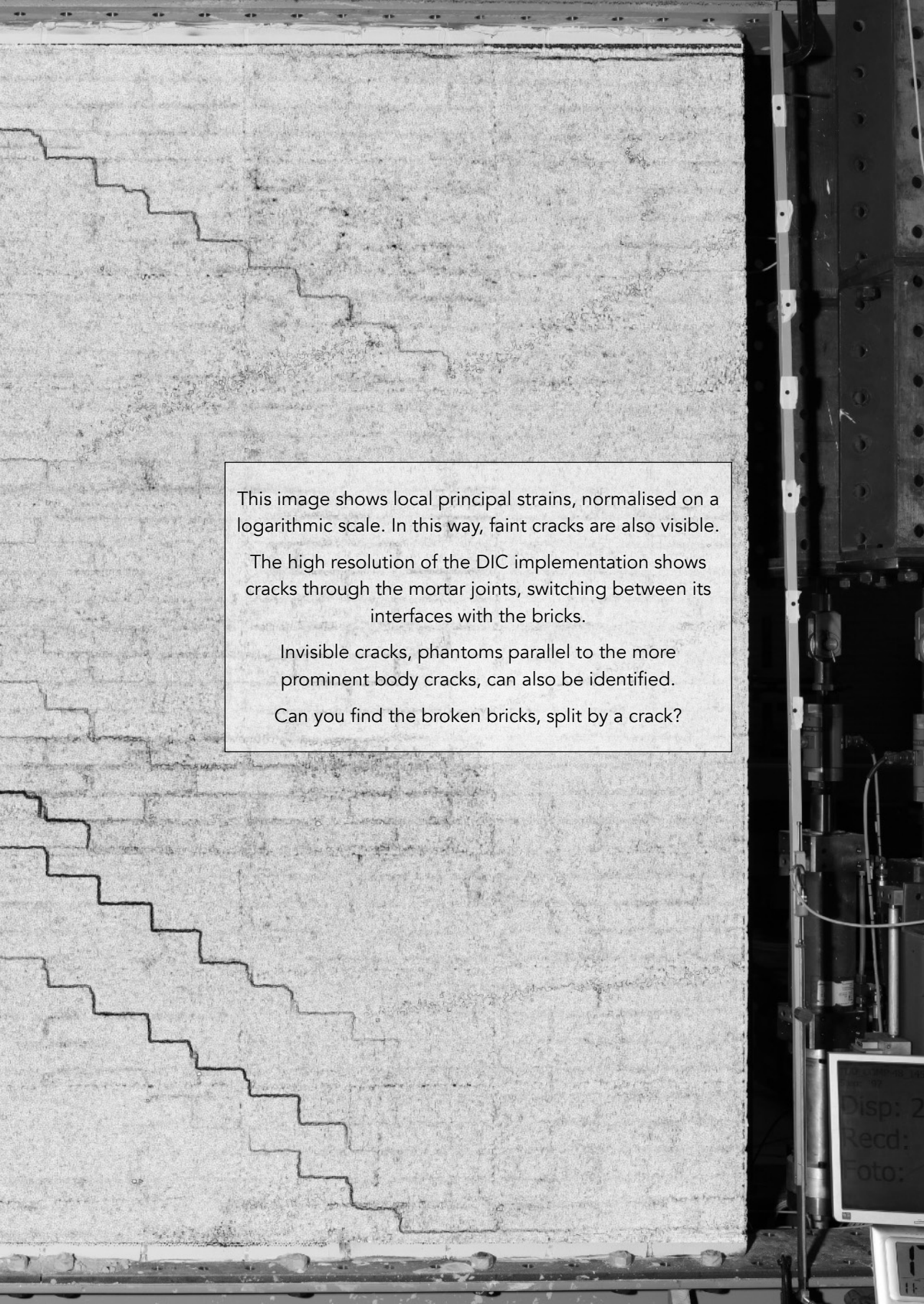
- Imai, K. 2013 (1)
 Imamura, F. 2013 (1)
 Ingham, J. 2010-2019 (24)
 Invernizzi, S. 2011,2019 (2)
 Ip, K. 2017 (1)
 Ishiyama, Y. 2013 (1)
 Ismail, N. 2010 (1)
 J.Y. Kim, 2014 (1)
 Jaeger, L.G. 2010 (1)
 Jafari, S. 2015-2019 (11)
 Jain, S.K. 2007 (1)
 Jalayer, F. 2009 (1)
 James, G.K. 2016 (1)
 Jansen, 1990 (1)
 Jardine, F.M. 2001 (1)
 Jeary, A.P. 2015 (1)
 Jonaitis, B. 2009 (1)
 Jones, B. 2016 (1)
 Jongejan, R. 2019 (1)
 Jonkers, H.M. 2012-2017 (3)
 Jonkman, S.N. 2003-2015 (4)
 Juego, M.B. 2016 (1)
 Jurevicius, D. 2015 (1)
 Jurina, L. 2019 (1)
 Jury, R.D. 2017 (1)
 Juárez-Luna, G. 2015 (1)
 Kahn, L.F. 2006 (3)
 Kaku, K. 2016 (1)
 Kallioras, S. 2015-2019 (7)
 Kam, W.Y. 2017 (1)
 de Kam, G. 2018 (1)
 Kanamori, H. 1999 (1)
 Kang, Y. 2014 (1)
 Kanit, R. 2006,2010 (2)
 Kanka, S. 2019 (1)
 Karaoulis, M. 2018 (1)
 Kashyap, J. 2014 (1)
 Kaufmann, W. 2020 (1)
 Kaushik, H.B. 2007 (1)
 Keiler, M. 2014 (1)
 Kelman, I. 2002,2004 (2)
 Keskinen, E. 2008 (1)
 von Kettlehodt, J. 2018 (1)
 Khalaf, F.M. 2005 (1)
 Kim, D.H. 1999,2014 (2)
 Kim, C. 2014 (2)
 Kingsley, G.R. 1994-1996 (3)
 Kishen, J.M.C. 1998 (1)
 Kita, A. 2020 (1)
 de Kleine, M.P.E. 2018 (1)
 Kloosterman, F.H. 2017 (1)
 Knox, C. 2010 (1)
 Kok, M. 2015 (1)
 Kolbitsch, A. 2014 (1)
 Kong, J. 2016 (1)
 Kooi, H. 2021 (1)
 Korff, M. 2009-2021 (5)
 Korswagen, P. 2019 (1)
 Kostense, N. 2016 (1)
 Kowalewski, Ł. 2015 (1)
 Kowalsky, M.J. 2004 (1)
 Koščak, J. 2018 (1)
 Kraaijpoel, D. 2012,2013 (2)
 Krajewski, P. 2014 (1)
 Kralj, B. 1990 (1)
 Krijgsman, H. 2016 (1)
 Kruiver, P.P. 2015-2022 (9)
 Kruse, H.M.G. 2013 (1)
 Kržan, M. 2015 (1)
 Kumar, S.L. 2019 (1)
 Kusters, G.M.A. 1985 (1)
 Kučera, J. 2016 (1)
 Kwiecien, A. 2014 (1)
 Kästli, P. 2015 (1)
 Kürschbasche, A.G. 1994 (1)
 LaFave, J.M. 2010 (1)
 Lacidogna, G. 2020 (1)
 Lagomarsino, S. 2008-2024 (3)
 Lallemand, D. 2022 (1)
 Lam, N. 2002-2007 (4)
 Landolfo, L. 2018 (1)
 Landtwing, D. 2015 (1)
 Landwehr, J.C. 2021 (1)
 de Lange, G. 2013-2020 (6)
 Langroudi, J.R. 2011 (1)
 Larby, J.A. 2004 (1)
 Laucelli, D. 2014 (1)
 Laurin, F. 2012 (1)
 Lava, P. 2015 (1)
 Lawrence, S.J. 2000-2005 (4)
 Lee, J.S. 1999,2014 (2)
 Leite, J. 2011 (1)
 Leiva, G.H. 1991 (1)
 Lendering, K.T. 2015 (1)
 Leon, R.T. 2006 (3)
 Lestuzzi, P. 2005-2016 (4)
 Levelt, O. 2021 (1)
 Li, K. 2017 (1)
 Li, W. 2012 (1)
 Li, S. 2016 (1)
 Li, X. 2024 (1)
 Licciardello, L. 2020 (1)
 Likas, A. 2003 (1)
 Longo, M. 2023 (1)
 Lopez, M.M. 2014 (1)
 Lourenco, P. 2011 (1)
 Lourenço, P.B. 1995-2020 (13)
 Lubelli, B. 2004 (1)
 Lucas, W. 2018 (1)
 Lumantarna, R. 2010 (1)
 Lumantarna, E. 2007 (1)
 Lyons, J. 2016 (1)
 Lévêque, D. 2012 (1)
 MBIE, 2006 (1)
 Macorini, L. 2016 (1)
 Magenes, G. 1992-2018 (28)
 Magonette, G. 1995 (1)
 Maheri, M.R. 2012 (1)
 Mair, R.J. 2003-2017 (4)
 Maire, J.F. 2012 (1)
 Maiwald, H. 2012 (1)
 Malamud, B.D. 2014 (1)
 Malena, M. 2016 (1)
 Malomo, D. 2018 (1)
 Mandirola, M. 2015-2017 (4)
 Mandooh-Galal, K.E. 2004 (1)
 Manfredi, G. 2009 (1)
 Manie, J. 2016 (1)
 Mantegazza, G. 2019 (1)
 Marano, G.C. 2014 (1)
 Marasli, M. 2023 (1)
 Marchesi, B. 2016,2018 (2)
 Marciukaitis, G. 2009 (1)
 Mariani, V. 2016-2017 (3)
 Marini, A. 2012,2013 (2)
 Marques, A.I. 2017 (2)
 Marshall, R. 2000 (1)
 Marshall, J. 2012 (1)
 Martinez, F. 2013 (1)
 MartinezPereira, A. 1998 (1)
 Martí, J. 2013 (1)
 Mas, E. 2013 (1)
 Masciotta, M.G. 2020 (1)
 Masia, M.J. 2004-2015 (5)
 Mason, M.S. 2019 (1)
 Massarsch, K.R. 2002 (1)
 Mata-Falcón, J. 2020 (1)
 Matta, F. 2015 (1)
 Matteis, G.D. 2014 (1)
 di Matteo, A. 2018 (1)
 Maurer, B.W. 2019,2020 (2)
 Mavel, A. 2012 (1)
 Mazzorana, B. 2014 (1)

- Mazzotti, C. 2018 (2)
 McBean, P.C. 2004 (1)
 McCann, P. 2018 (1)
 McGarr, A.F. 2016 (1)
 van Meerten, J.J. 2021 (1)
 Meijers, P. 2013-2016 (4)
 Meilyta, 2012 (1)
 Meincke, S. 2005 (1)
 Melis, G. 2002,2003 (2)
 Mellia, E. 2016 (1)
 Mello, V.F.B.D. 1977 (1)
 Melville, B.W. 2016 (1)
 Mena, B. 2015 (1)
 Mendes, N. 2010 (1)
 Mergos, P. 2014-2015 (3)
 Messali, F. 2016-2024 (16)
 Meyer, U. 2019 (1)
 Miao, Q. 2012 (1)
 Michel, C. 2010 (1)
 Middleton, J. 1990 (1)
 Mignan, A. 2015 (1)
 Milani, G. 2013,2014 (2)
 Miller, S.C. 2013 (1)
 Milosevic, J. 2018 (1)
 Miraglia, S. 2015 (1)
 de Miranda, S. 2017 (2)
 Mitrovic, S. 2010 (1)
 Modena, C. 2010,2013 (2)
 Moghadam, A.S. 2011 (1)
 Mohammed, B.S. 2009 (1)
 Mojsilovic, N. 2019 (1)
 Mojsilović, N. 2016,2017 (2)
 Molina, F.J. 2008,2010 (2)
 Molyneaux, T. 2002,2007 (2)
 Monaco, P. 2012,2014 (2)
 Monteiro, S.N. 1999 (1)
 Moon, L. 2011 (1)
 Moon, F.L. 2004-2006 (4)
 Morandi, P. 2008-2018 (4)
 Moreira, P. 2015 (1)
 Moreira, S. 2012 (1)
 Moroni, O. 2012 (1)
 Mors, R.M. 2013 (1)
 Mosalam, K. 2009 (1)
 Mosallam, A.S. 2007 (1)
 Mosayk, 2015 (1)
 Moujahid, A. 2014 (1)
 Moustafa, A. 2013 (1)
 Mueffelman, J.G. 2013 (1)
 Mufti, A. 2010 (1)
 Muir, C.A. 2017 (1)
 Mulder, M. 2018 (1)
 Munari, M. 2013 (1)
 Muntendam-Bos, A.G. 2015 (1)
 Musson, R.M.W. 1998 (1)
 Muthike, D.M. 2016 (1)
 Mylonakis, G. 2006 (1)
 NZGS, 2006 (1)
 NZSEE, 2006 (1)
 Najafgholipour, M.A. 2012 (1)
 Nakamura, Y. 2018 (1)
 Nam, 2015-2018 (3)
 Narassiguin, A. 2016 (1)
 Nascimbene, R. 2013 (1)
 Nastev, M. 2013 (1)
 Nateghi, F. 2008 (1)
 Van Natijne, A. 2018 (1)
 Nauta, P. 1985 (1)
 Negulescu, C. 2014 (1)
 Nehdi, M.L. 2020 (1)
 NEHRP, 2012 (1)
 Nen, 2005-2018 (3)
 Nepveu, M. 2016 (1)
 Netti, A. 2012 (1)
 Netzel, H. 2004 (1)
 Nghiem, H.L. 2013 (1)
 Nguyen, M. 2022 (1)
 Nikolaou, S. 2006 (1)
 Nollet, M. 2013 (1)
 Noorlandt, R. 2018 (1)
 Noortman, F.J. 2019 (1)
 Ntinalexis, M. 2015-2022 (8)
 Nuñez, P. 2012 (1)
 Oates, S.J. 2015-2020 (6)
 Okada, S. 2000 (1)
 Okada, T. 2019 (1)
 Oktiovan, Y.P. 2023 (1)
 Oliveira, C.S. 2012 (1)
 Oliveira, D.V. 2012 (1)
 Oliveira, J.T. 2003 (1)
 Olivito, R.S. 2001 (1)
 Oller, S. 2014 (1)
 Omid, P. 2020 (1)
 van Onselen, E.P. 2022 (1)
 Orton, S.L. 2005 (1)
 Oses, N. 2014 (1)
 Osterberg, G. 1935 (1)
 O'Brien, J. 2019 (1)
 Page, A.W. 1995-2019 (6)
 Palmisano, F. 2016 (1)
 Palomo-Velez, G. 2023 (1)
 Pan, Z. 2017 (1)
 Pande, G.N. 1990 (1)
 Paparo, A. 2014 (1)
 Papayianni, I. 2004 (1)
 Pari, M. 2017-2018 (3)
 Park, T. 2016 (1)
 Parra, C. 2018 (1)
 Parys, L.V. 2012 (1)
 Paré, M.D. 2010 (1)
 Pavese, A. 2004 (1)
 Pavia, S. 2010 (1)
 Pedersen, W. 2016 (1)
 Pefkos, M. 2022 (1)
 Peloso, S. 2013,2016 (2)
 Pelà, L. 2014,2018 (2)
 Penna, A. 2008-2018 (20)
 Penning-Rowse, E. 2008 (1)
 Pereira, E.B. 2008 (1)
 Perey, P. 2018 (1)
 Perlaviciute, G. 2018,2023 (2)
 Petersen, R.B. 2009 (1)
 Petrović, M. 2017 (1)
 Petry, S. 2013-2015 (3)
 Pezzoli, P. 1998 (1)
 Phillips, E. 2019 (1)
 Li Piani, T. 2018 (1)
 Picchi, L. 2003 (1)
 Pickering, M. 2015 (1)
 Pigorini, A. 2014 (1)
 Pina-Henriques, J. 2004 (1)
 Pinho, R. 2004-2022 (13)
 Pinto, P.E. 2009 (1)
 Pitolakis, D. 2006 (1)
 Planas, J. 2008 (1)
 Plant, N.G. 2015 (1)
 Platzcek, G. 2016 (1)
 Player, C.J. 2007 (1)
 Pleijter, G. 2015 (1)
 Van Der Pluijm, R. 1994-2019 (6)
 Polidoro, B. 2015-2017 (3)
 Pomonis, A. 1999 (1)
 Popal, R. 2013 (1)
 Porco, F. 2012 (1)
 Portioli, F. 2015-2018 (5)
 Porto, F.d. 2013-2016 (3)
 da Porto, F. 2010 (1)
 Potts, D.M. 1997 (1)
 Prasad, P. 2019 (1)
 Price, A.D. 2013 (1)
 Priestley, M.J.N. 1994 (1)
 de Proft, K. 2012 (1)

- Proy, C. 2016 (1)
 Puente, I. 2018 (1)
 Qian, C. 2015 (1)
 Quintela, C. 2012 (1)
 Quitariorio, V. 1999 (1)
 Raaijmakers, B.H.J. 1994 (1)
 Rabinovitch, O. 2010 (1)
 Radaelli, E.O. 2019 (1)
 Radtke, F. 2005 (1)
 Rai, D.C. 2007 (1)
 Rajeev, P. 2009 (1)
 Ramadan, A.S. 2020 (1)
 Ramos, T. 2015 (1)
 Ramos, L.F. 2012 (1)
 Ranjbar, M.M. 2011 (1)
 Rapone, D. 2020 (1)
 Rauci, M. 2010 (1)
 Ravenshorst, G.J.P. 2017-2019 (5)
 Reddish, D.J. 1987 (1)
 Reinhardt, H.W. 1986 (1)
 Ren, G. 1987 (1)
 Reneckis, D. 2010 (1)
 Restrepo-Vélez, L.F. 2006 (1)
 Reyes, E. 2008 (1)
 Ricci, P. 2017 (1)
 Rinaldi, A.P. 2014 (1)
 Ringers, R. 2016 (1)
 De Risi, M.T. 2017 (1)
 Ritter, S. 2017-2020 (3)
 Rizzardini, F. 2012 (1)
 Robertson, P.K. 1998 (1)
 Roca, P. 2014,2018 (2)
 Rodriguez-Marek, A. 2015-2022 (7)
 Rodriguez-Marek, A. 2019 (1)
 Roest, J.P.A. 2015 (1)
 Roijackers, R. 2016 (1)
 Romao, X. 2008 (1)
 Romero Navarrete, J.A. 2008 (1)
 Romijn, R. 2017 (2)
 de Roo, 1991 (1)
 Roscini, F. 2018,2019 (2)
 Roselli, I. 2016 (1)
 Rossi, A. 2015-2016 (3)
 Rota, M. 2010 (1)
 Rots, J.G. 1985-2023 (51)
 Ruigrok, E. 2018,2022 (2)
 Rutqvist, J. 2014 (1)
 SBR, 2010,2017 (2)
 SESOC, 2006 (1)
 Salamone, S. 2013 (1)
 van der Salm, R. 2012 (1)
 Salmanpour, A.H. 2015-2017 (3)
 Saloustros, S. 2018 (1)
 San-Bartolomé, A. 2009 (1)
 Sanches H., 2016 (1)
 Sanches I., 2016 (1)
 Sancho, J.M. 2008 (1)
 Sanderson, J. 2014 (1)
 Sandoval, C. 2016 (1)
 De Santis, S. 2018,2019 (2)
 Saouma, V.E. 1998 (1)
 Sarhosis, V. 2014-2021 (3)
 Satti, K.M.H. 1972 (1)
 Sauerland, U. 2022 (1)
 Schauer, M. 2019 (1)
 Scherer, C. 2014 (1)
 Scherer, G.W. 2006 (1)
 Schermer, D. 2008 (1)
 Scheufler, W. 2008 (1)
 Schipper, H.R. 2017-2019 (3)
 Schipper, R. 2018 (1)
 Schlangen, E. 2017 (1)
 Schneemayer, A. 2014 (1)
 Schneiderhan, T. 2016 (1)
 Scholten, N.P.M. 2015 (1)
 Scholtens, B. 2018 (1)
 Schranz, C. 2014 (1)
 Schreppers, G.M.A. 2016 (1)
 Schultz, A. 2011,2013 (2)
 Schwartz, N.M.J. 2015 (1)
 Schwarz, J. 1998,2012 (2)
 Sciotti, A. 2014 (1)
 Scott, M. 2014 (1)
 Seible, F. 1994 (1)
 Senaldi, I. 2011 (1)
 Seracino, R. 2010 (1)
 Seyedi, D.M. 2013,2014 (2)
 Shafaei, J. 2014,2015 (2)
 Shafiei, S. 2016 (1)
 Shamseldin, A.Y. 2016 (1)
 Sharafati, A. 2021 (1)
 Sharma, S. 2018,2023 (2)
 Shaw, 2008 (1)
 Sheng, Y. 2014 (1)
 Shih, M. 2008 (1)
 Shrive, N. 2010 (1)
 Sierra-Beltran, M.G. 2012 (1)
 Sijacic, D. 2016 (1)
 Simone, A. 2012 (1)
 Simoni, S. 2014 (1)
 Simpson, B. 1996 (1)
 Simundic, G. 2019 (1)
 Singh, M.M. 1999 (1)
 Siskind, D.E. 1984 (1)
 Skroumpelou, G. 2018 (1)
 Sloan, S.W. 2012 (1)
 Slobbe, A.T. 2013 (1)
 Sluys, B. 2012 (1)
 Smits, M.T.J.H. 1993 (1)
 Smrkić, M.F. 2018 (1)
 Smyrou, E. 2011-2021 (4)
 Snethlage, A.J. 2012 (1)
 Son, M. 2005,2007 (2)
 Son, H. 2014 (1)
 Sorour, M. 2010 (1)
 Sorrentino, L. 2017 (1)
 Sousa-Oliveira, C. 2012 (1)
 Sousamli, M. 2024 (1)
 Soysal, B.F. 2023 (1)
 Spacone, E. 2020 (1)
 Spence, R. 1999,2004 (2)
 Spetzler, J. 2017,2022 (2)
 Spyrakos, C.C. 2003 (1)
 Van Staaldunin, P.C. 1993-2018 (4)
 Stafford, P.J. 2015-2020 (11)
 Stafleu, J. 2017 (2)
 Stagg, M.S. 1984 (1)
 Standing, J.R. 2001 (1)
 Stead, M. 2015 (1)
 Steenbergen, R.D.J.M. 2015-2017 (4)
 Steg, L. 2023 (1)
 Stevens, M.G. 1984 (1)
 Stojadinovic, B. 2018 (1)
 Stojadinović, B. 2017 (1)
 Storck, T. 2020 (1)
 Stoutjesdijk, T.P. 2013 (1)
 van Straalen, I. 2017 (1)
 Straman, 1991 (1)
 Stryszewska, T. 2019 (1)
 Stucchi, M. 1998 (1)
 Stumpo, P. 2001 (1)
 Stuurman, R.J. 2021 (1)
 Suckale, J. 2017 (1)
 Sucuoglu, H. 2013 (1)
 Suhairy, S.A. 2000 (1)
 Sullivan, T.J. 2004,2013 (2)
 Sung, W. 2008 (1)
 Suppasri, A. 2013 (1)
 Sutton, M.A. 2015 (1)

- Svinkin, M.R. 1999,2013 (2)
 Sweeney, S.C. 2005 (1)
 TUDelft, 2015 (1)
 Takai, N. 2000 (1)
 Tang, C.A. 2012 (1)
 Tanner, J. 2012 (1)
 Tarbotton, C. 2015 (1)
 Tasiopoulou, P. 2011-2019 (3)
 Tavares, P. 2015 (1)
 Tedesco, F. 2016 (1)
 Teigen, J.G. 1998 (1)
 Tena-Colunga, A. 2015 (1)
 Ter-Horst, W.L.A. 2015 (1)
 Terwel, K. 2017,2018 (2)
 Thamboo, J.A. 2013,2015 (2)
 Theodossopoulos, D. 2014 (1)
 van Thienen-Visser, K.
 2015,2016 (2)
 Thijsen, C.C.F. 1999 (1)
 Thürlimann, B. 1984 (1)
 Tianyi, Y. 2006 (1)
 Tin-Loi, F. 2001 (1)
 Tomasi, R. 2014,2019 (2)
 Tomassetti, U. 2015-2018 (14)
 Tomazevic, M. 2007,2014 (2)
 Tomor, A. 2020 (1)
 Tondelli, M. 2013 (1)
 Toumbakari, E. 2004 (1)
 Tralli, A. 2017 (2)
 Trifunac, M.D. 1971 (1)
 Trovato, D. 2011 (1)
 Tschegg, E.K. 2014 (1)
 Tung, D.P. 2017 (1)
 Tung, S. 2008 (1)
 Turcoa, E. 2016 (1)
 Turner, F. 2012 (1)
 Tziviloglou, E. 2017 (1)
 Ubertini, F. 2019,2020 (2)
 Uilenreef, J. 2017,2018 (2)
 Ulrich, T. 2014 (1)
 Uva, G. 2012 (1)
 Vaculik, J. 2007-2017 (6)
 Valdebenito, G. 2016 (1)
 Valente, S. 2011 (1)
 Valivonis, J. 2009 (1)
 Valluzzi, M.R. 2013 (1)
 Vanclay, F. 2014 (1)
 Vandoren, B. 2012 (1)
 Vecchio, F.J. 1986 (1)
 de Vent, I. 2011 (2)
 Ventura, C. 2011 (1)
 Verbeek, J.J. 2003 (1)
 Verderame, G.M. 2017 (1)
 Vermaas, T. 2013 (1)
 Vermeltfoort, A.T. 1994-2005 (3)
 Van Verseveld, H.C.W. 2015 (1)
 Verstrynge, E. 2016,2020 (2)
 Verweij, A. 2016 (1)
 Visintin, P. 2018 (1)
 Visschedijk, M.A.T. 2013 (1)
 Vitone, C. 2016 (1)
 Vlachakis, G. 2017 (1)
 Vlassis, N. 2003 (1)
 Vlek, C. 2018 (1)
 van der Vliet, C. 2016 (1)
 Van Vliet, M.R.A. 2004 (1)
 Voet, E. 2016 (1)
 Voigt, S. 2016 (1)
 Vonk, R. 2016 (1)
 van der Voort, N. 2014 (1)
 Vrijling, J.K. 2003 (1)
 Vrouwenvelder, A.C.W.M.
 2015,2017 (2)
 Vázquez Gutiérrez, P.A. 2016
 (1)
 de Waal, J.A. 2015 (1)
 Waarts, P. 1997 (1)
 Wald, D.J. 1999 (1)
 Walraven, 1990 (1)
 Walsh, K.Q. 2014-2018 (7)
 Wang, S.Y. 2012 (1)
 Wang, X. 2016 (1)
 Wang, T. 2012 (1)
 Wassing, B.B.T. 2012 (1)
 Weber, F. 2010 (1)
 White, M. 1999 (1)
 Whittaker, A.S. 2013,2015 (2)
 Whittaker, B.N. 1987 (1)
 Wiemer, S. 2015 (1)
 Wiersma, A. 2017 (1)
 Wijanto, L.S. 2007 (1)
 Van Wijnbergen, E. 2015 (1)
 De Wilder, K. 2016 (1)
 Willis, C.R. 2004-2010 (4)
 Wilson, J. 2002-2008 (5)
 Wilson, A. 2011-2014 (3)
 Winant, T. 2015 (1)
 de Wit, S. 2019 (1)
 Wojciechowska, K. 2015 (1)
 Wong, L.S. 2020 (1)
 Wride, C.E. 1998 (1)
 Wroth, C.P. 1974 (1)
 Xu, S. 2009 (1)
 Xu, C. 2003 (1)
 Xu, L. 2022 (1)
 Yakut, A. 2015 (1)
 Yan, C. 2013 (1)
 Yang, T.Y. 2017 (1)
 Yi, Y. 2017 (1)
 Yi, T. 2004-2006 (3)
 Younis, A. 2020 (1)
 Zahra, T. 2019 (1)
 Zapico, B. 2010 (1)
 Zarnić, R. 2008 (1)
 Zethof, M. 2015 (1)
 Zhai, C. 2016 (1)
 Zhang, S. 2019 (1)
 Zhu, Y. 2006,2009 (2)
 Zhuge, Y. 2004 (1)
 van Zijl, G.P.A.G. 2001 (1)
 Zilch, E.h.K. 2008 (1)
 Zuccaro, G. 2010 (1)
 Zucchini, A. 2006 (1)
 Zuideveld-Venema, N. 2019 (1)
 Zurek, B. 2019 (2)
 daPorto, F. 2016 (2)
 deFelice, G. 2016 (1)
 deMartin, B. 2019 (1)
 Červenka, J. 1998 (1)
 Šipoš, T.K. 2020 (1)





This image shows local principal strains, normalised on a logarithmic scale. In this way, faint cracks are also visible.

The high resolution of the DIC implementation shows cracks through the mortar joints, switching between its interfaces with the bricks.

Invisible cracks, phantoms parallel to the more prominent body cracks, can also be identified.

Can you find the broken bricks, split by a crack?

Disp: 2
Recd:
Foto:

Appendices

Appendix A

Overview of Related Work.....i

Appendix B

Ψ Damage Parameterxxix

Appendix C

Supervised MSc Projectsxxxv

Appendix D

Glossaryxxxix

Appendix E

Loppersum Visitxliii

Appendix F

Dataset.....xlix

Appendix G

Tool for Crack Trackingli

Curriculum Vitæ.....lxvii

Propositionslxix

Acknowledgementslxxi

Extended Table of Contents.....lxxvi

Appendix A

Overview of Related Work

During the time in which this work was conceived, several related, and sometimes less-related, projects and activities were undertaken.

This appendix summarises the various topics into up to four pages for each section. These summaries serve as quick references from the main text and link to other works where the topics are further elaborated. Wherever possible, every section provides references to further reading.

A.1. Laboratory High-Resolution Monitoring with DIC	ii
A.2. Geometry Statistics from 3D-BAG	iv
A.3. Experiments and Models of NeHoBo Floors	vii
A.4. SLAMA-based, parametric computational models for pushover ADRS analyses of masonry typologies	ix
A.5. Strengthening: Structural Glass.....	xii
A.6. Repair: Self-Healing Mortar.....	xiii
A.7. Out-of-Plane of Masonry Walls during Hydrostatic Loading.....	xiv
A.8. The Action of Debris during the German Flood of 2021	xvi
A.9. Strategy for Safety Assessment of Historical Quay Walls	xviii
A.10. Experiments during course 'Masonry Bend & Break'	xxi
A.11. Analysis of Waarts' Probabilistic Estimation of Damage	xxii
A.12. InSAR Analysis of Cyclic Soil Movements in Norg.....	xxiii
A.13. The Effect of Deep Subsidence on Masonry Façades.....	xxiv
A.14. The Effect of Combined Horizontal Strain and Curvature on Masonry Façades from Soil Movements	xxv
A.15. The Effect of Truck Vibrations in Comparison to Earthquakes'	xxvii

A.1. Laboratory High-Resolution Monitoring with DIC

Processing images with Digital Image Correlation to measure displacements is a photogrammetry technique that was developed almost along side digital cameras. However, increased computational processing capacity, storage capabilities, and camera resolutions have shaped DIC into a versatile and popular tool in recent years. Yet, DIC was, so far, focused on measuring strains over small surfaces. For this study, discrete cracks over large surfaces needed to be captured.

For this purpose, a considerable amount of work was conducted to develop a DIC system capable of accurately tracking invisible cracks on a masonry wall. For the large surface of a full-scale masonry wall, instead of using several cameras, typically associated with issues when composing the images or processed results together, a single camera with 51 Mpx was employed. This yielded a theoretical resolution of $20\mu\text{m}$. To achieve this, however, the surface of the masonry had to produce an optimal pattern suited for the apparent pixel size of the camera. Given the distance of the camera to capture the full wall, the surface of the masonry was too fine and a marker per brick, as used in previous tests, was too coarse. Similarly, spraying the masonry with a speckle pattern could not guarantee the required resolution over the entire wall. Consequently, a flexible acrylic stencil was designed and laser-cut to produce a speckle pattern that would be optional for the camera settings.

On the processing side, the software (commercially) available in 2017 was not optimised for detecting discrete cracks. Therefore, a solution was developed which could detect discrete discontinuities in the displacement field, recognise the concept of individual cracks, and track their progress, in width and length, over an entire experiment. This software solution, coded in Matlab and deployed as a stand-alone program, was optimised to run in multiple processors and allowed processing images, with about one million measuring points each, in about one minute per image. Moreover, the process is largely automatised and specific for the types of masonry walls studied in the laboratory.

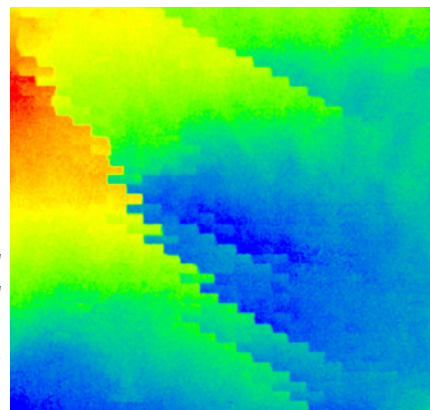


Figure A.1a A portion of a shear masonry wall of fired-clay brick showing zigzag diagonal and vertical cracking smeared around the centre of the wall just before it consolidates into a single crack.

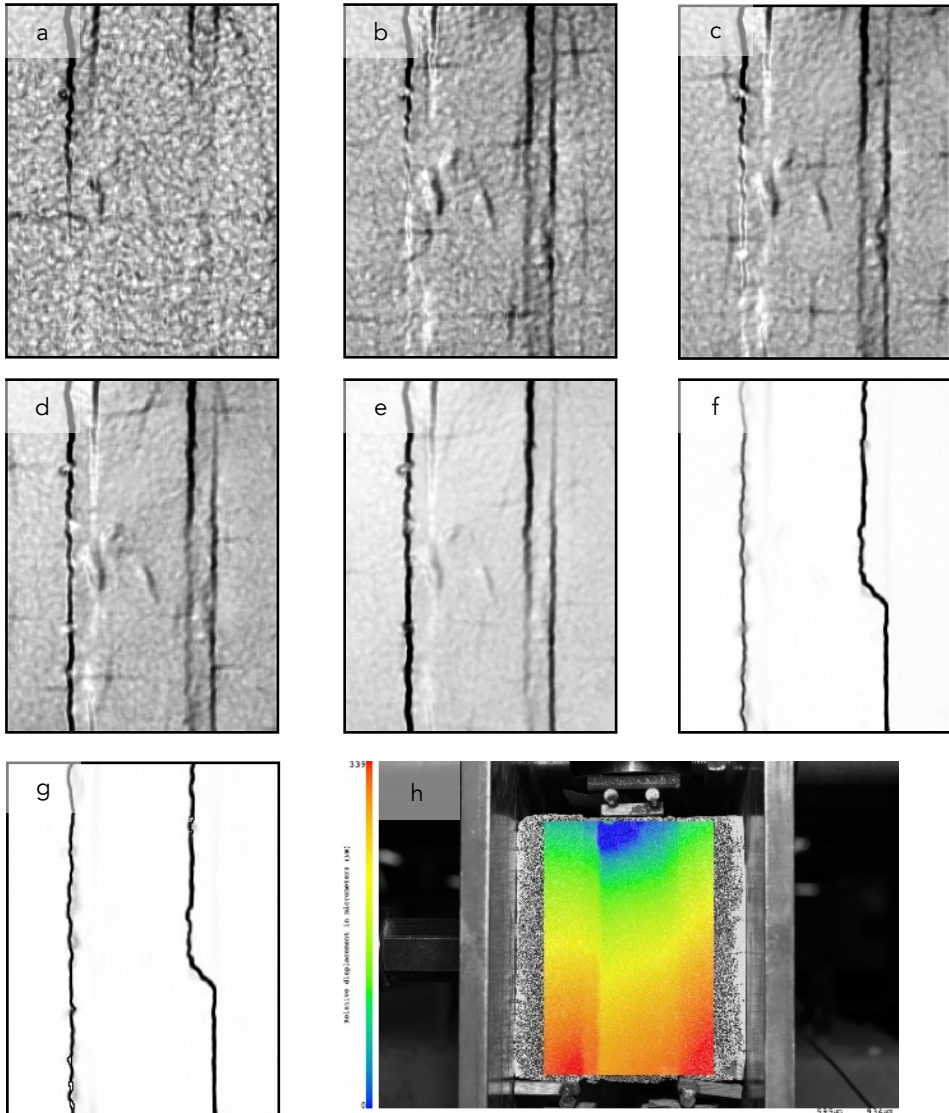


Figure A.1.2. Normalised principal strain plots of a section of a shear-triplet test sample (h) towards the end of the test starting at the last zero position (a), followed by the last peak displacement (b) and throughout the monotonic phase until total failure (g). Notice how initially incipient strains are localised at the top of the four potential failure planes. Then, the strains grow towards the bottom and also start to reach up from the bottom (c and d). In the case of the right mortar joint, the potential cracks grow from the top at the face of the middle brick and from the bottom at the face of the right brick (e). This results in the crack that crosses the mortar joint diagonally (f).

See [24], sections J and H.

A.2. Geometry Statistics from 3D-BAG

The 3D BAG project is an adaptation of the Netherlands' Basisregistraties Adressen en Gebouwen (BAG), enhanced by the 3D geoinformation research group at Delft University of Technology to include building height information. This project transforms the BAG dataset, incorporating aerial laser measurements to provide detailed geometries and is freely accessible for public use.

The comprehensive database has been meticulously post-processed, yielding statistics on various architectural features such as wall shapes and roof types from about 10 million buildings dating from 1770 to 2022, covering approximately 45GB of data. A significant portion of the analysis focuses on examining building façades by "unfolding" the 3D geometries to better understand wall dimensions and configurations across different construction periods. This effort has unearthed patterns in wall length and height, identifying common dimensions that correlate with typical Dutch architectural styles and construction practices. Further analysis delves into the distribution of these dimensions across the nation, with special attention to areas surrounding the Groningen gasfield and regions defined by PGA contours related to seismic activity risks.



Figure A.2.1. 3D view of the faculty of Civil Engineering and Geosciences on the campus of the TU Delft projected onto an aerial view of the ground. From the website of 3dbag.nl [3].

The study categorises wall shapes into several typologies, including flat, gable, single-sloped, and variant gables, among others, based on the geometric data derived from the unfolding algorithm. This classification aids in identifying prevalent architectural features and assessing potential vulnerabilities, especially in areas prone to earthquakes.

Despite the valuable insights provided, the report acknowledges limitations due to uncertainties in data accuracy, measurement interpretations, and post-processing methodologies. The reliance on aerial measurements and database records, both subject to errors and inconsistencies, introduces potential for inaccuracies in the final geometric representations and the derived statistics.

In conclusion, the "3D BAG" project offers a groundbreaking perspective on the Netherlands' built environment, presenting a rich dataset for architectural, urban planning, and seismic vulnerability analyses. While acknowledging the challenges and uncertainties inherent in such a comprehensive dataset, the project illustrates the potential of integrating aerial measurements with traditional building registries to enhance our understanding of building characteristics and vulnerabilities at a national scale.

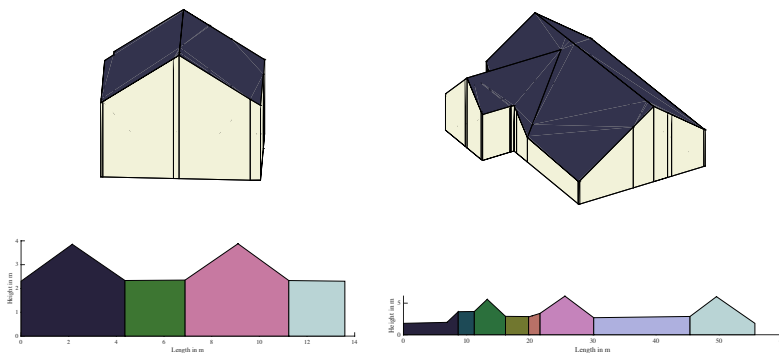


Figure A.2.2. Two examples of the unfolded geometry of two buildings showing the individual walls' length and height.

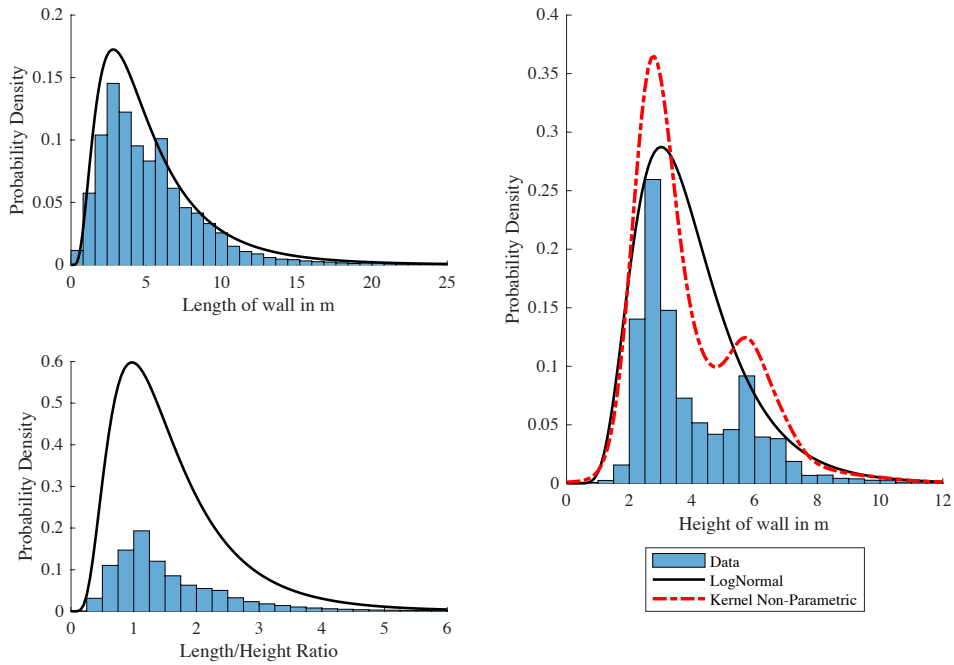


Figure A.2.3. Distribution fit to length and height properties.

References

- <https://docs.3dbag.nl/en/>
- <https://tudelft3d.github.io/bag3d/intro.html>
- <https://3dbag.nl/en/viewer>

A.3. Experiments and Models of NeHoBo Floors

NeHoBo floors were pre-fabricated masonry floor panels used in the Netherlands in the 50s-70s. Unlike modern concrete floors where masonry units are employed as lost formwork to make the floor lighter, NeHoBo floors were actual masonry wallets that would be constructed vertically as a regular wall and then placed horizontally to form a floor. In the bed joints, steel rebar would be embedded in between masonry units of a special shape. In most cases, the floors would be finished with a top concrete layer.

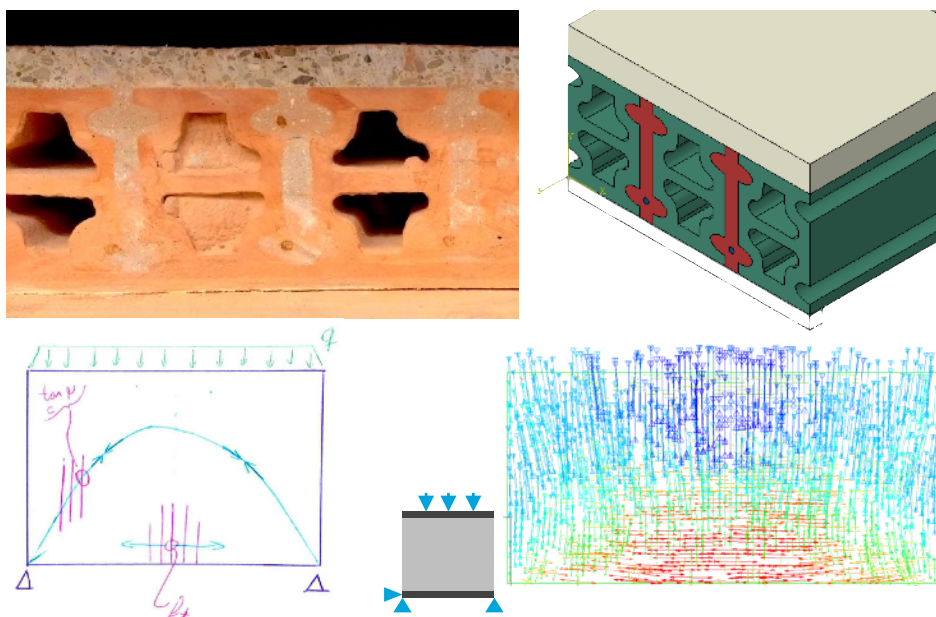


Figure A.3a. Top: a crosscut of a NeHoBo floor panel in horizontal position, left; and its 3D model, right. The bed joints (with rebar) appear vertical in between units. The panel is topped by a concrete layer. Bottom: deep beam action of a floor diaphragm (view from the top). Left, the required material properties to determine the capacity of the deep beam.

The goal of this project, officiated by NAM, was to determine whether NHB floors could provide sufficient diaphragm action between masonry walls during lateral loading of a structure. To answer this question two aspects needed to be understood. First, what were the relevant mechanical properties for the behaviour of this floor and to characterise these experimentally - floor samples from existing structures were available. Secondly, whether the actual strength from the floors was sufficient for a typical masonry structure. The study was thus a mix of experimental characterisation and (numerical) modelling.

In the first step, the diaphragm action from the floor in a masonry structure was likened to a deep beam (Figure A.3.b) where a tensile strut and a compression arch appear in the floor. For this tension strut, the tensile strength of the masonry perpendicular to the joints had to be obtained. For the compressive zone, shear parallel to the joints had to be evaluated. For the latter, a modified triplet shear test was used, while for the former, a 3 or 4-point bending test, where flexure leads to tensile stresses, was employed to determine the tensile capacity of the joints.

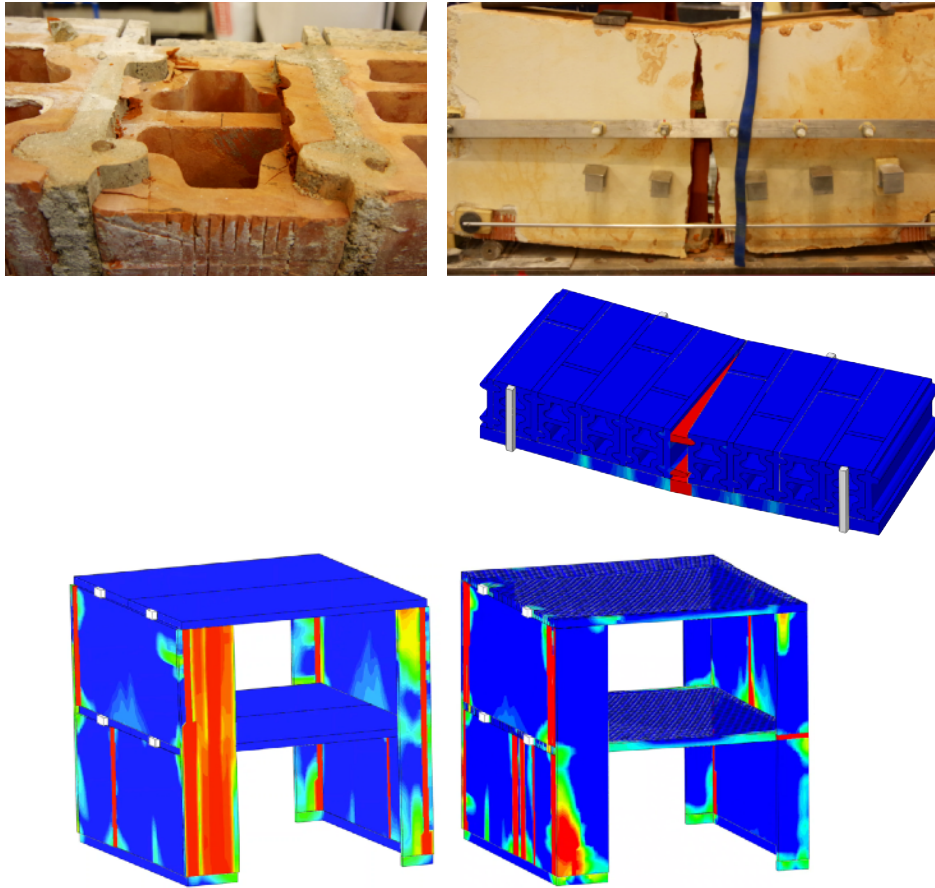


Figure A.3.b. Top left, shear triplet specimen after failure. Top right, 4-point bending test with flexural crack. Middle; reproduction with an Abaqus detailed model showing failure at the mortar and mortar-unit interface. Bottom, comparison of a masonry assemblage with concrete (left) or NeHoBo floors.

The characterisation experiments were reproduced with detailed finite-element-method models and virtual tests were subsequently performed to evaluate the behaviour of the floor panels in other situations such as out-of-

plane flexure in the parallel and perpendicular directions. Moreover, the influence of the concrete layer could be quantified and subtracted to account for the conservative situation when this layer was damaged or not present. Finally, a quasi-static test of a masonry house, tested at the TU Delft, was reproduced. Then, the original concrete floor plates were replaced with NeHoBo floor panels in the models to assess their effect and observe if they would behave non-linearly.

The study concluded that the strength of the NeHoBo floors was not negligible and that it was sufficient to provide the diaphragm action associated with stiff floors. See [25].

A.4. SLaMA-based, parametric computational models for pushover ADRS analyses of masonry typologies

Analytical models were used to evaluate structures subjected to lateral loading, as recommended by numerous codes and guidelines worldwide. A programmatic approach to these analyses enabled a probabilistic and iterative assessment of different typologies, structural parameters, connections, and even strengthening interventions. This method also provided insights into failure mechanisms, damage, and consequences. Unlike FE models, which are hard to parametrise and expensive to run, programmatic analytical models allowed for quick quantification of a typologies' features or modifications.

The program, dubbed CLaRA, was developed for analytically assessing structures against seismic demands. It performs all the aforementioned tasks but is initially limited to a set of sub-typologies. These include rigid concrete floors, single-wythe calcium-silicate walls, and the absence of spandrels between piers. Plans for future enhancements aim to cover most unreinforced masonry typologies found in the province of Groningen by incorporating features like timber or flexible floors, spandrels, and double-wythe walls.

Clara's assessment included analysing the in-plane direction behaviour through lateral pushover analysis, contrasted with the acceleration and displacement demands from response spectra. Out-of-plane evaluations were conducted independently for each component, yet linked to the in-plane behaviour, highlighting the importance of true boundary conditions for accurate predictions.

Probabilistic analyses, where each model represented a sample from material, geometric, and model parameter distributions, were coupled with the probabilistic hazard. The demand for each location and sub-typology could be directly defined, allowing for quick reassessment with changes in demand. The

program could evaluate 35,000 non-linear models per hour on a single desktop computer, a capability beyond that of FEM modelling for complete non-linear structures. The inclusion of a consequence model enabled outputting individual risk per typology, with preliminary values around $6 \cdot 10^{-6}$ for the implemented sub-typologies.

The core methodology involved a SLaMA-type approach for computing the global pushover curve for in-plane analysis, combining the behaviour of individual walls and piers per storey through an adaptive, mass-proportional pushover analysis. Iterative evaluations against non-linear response spectra determined the capacity/demand ratio, demonstrating the program's capability for detailed failure rate assessments under varying assumptions. In a sense, Clara's approach follows a simplified Sequentially Linear Analysis (SLA), where failure of individual components triggers a re-evaluation of the lateral stiffness of the structure. In this manner, a pushover capacity curve could be generated including the possibility of snap-back where the force and drift unload.

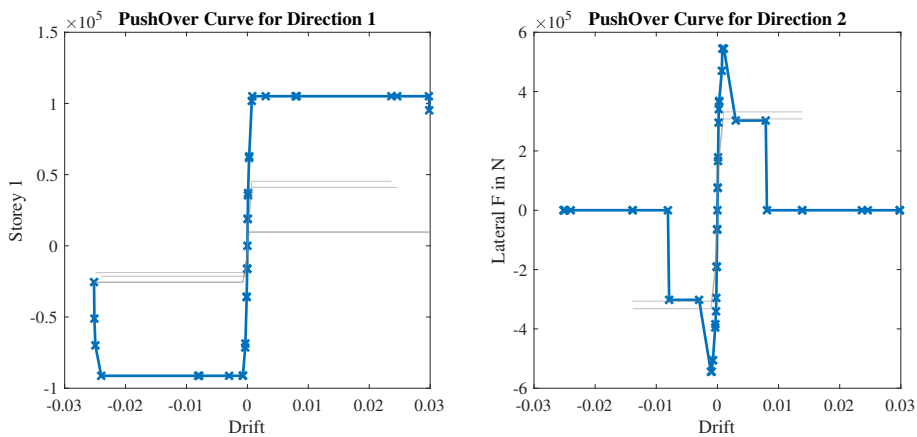


Figure A.4.1. The pushover curve of an example building. Every point marks an event in one of the structural components.

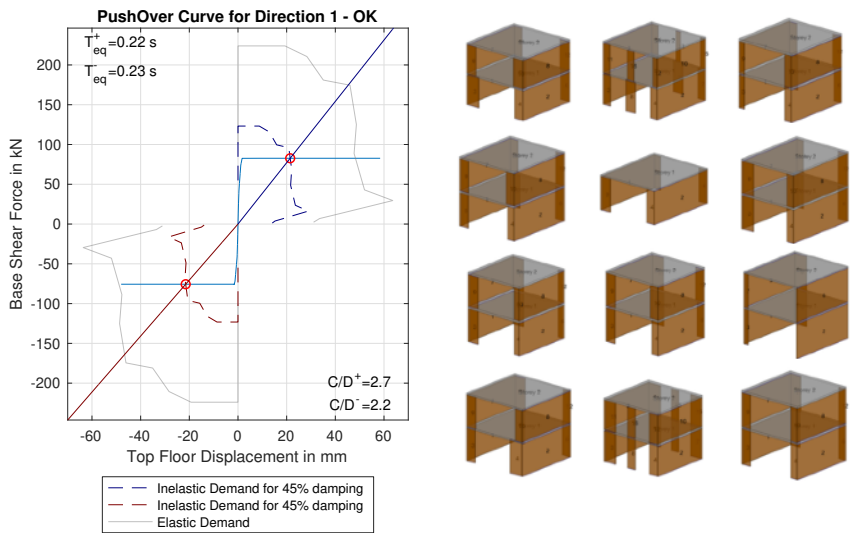


Figure A.4.2. Left, the intersection of a pushover curve and the ADRS. Damping is iteratively calculated. Right, examples of the geometry of buildings following a parametrisation via probabilistic distributions for the number, location, size, etc of the structural components.

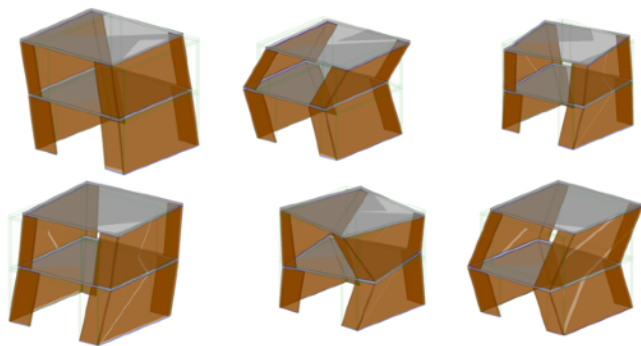


Figure A.4.3. Modal modes (and periods) for the building. 3D modes are also computed. The modal behaviour can be iteratively re-computed based on yielding or failure of structural components.

A.5. Strengthening: Structural Glass

Gaggero et al. [19] investigated using structural glass to strengthen or retrofit masonry structures. Preliminary numerical studies were conducted by de Groot (2019). The solution consisted of timber-framed laminated glass. In the experimental campaign, the windows were tested separately first and then inside the opening of a masonry wall.

The goal of the timber-glass design was to provide increased in-plane stiffness during small values of drift. This would reduce light damage during vibrations as the stiffer structure would develop smaller inter-storey drift. The glass was attached to the timber frame with a thin, semi-flexible adhesive. At larger values of drift, the adhesive would tear. The relative sliding between timber and glass, together with crushing of the timber, lead to an extremely high capacity for the release of hysteretic energy. Hence, for larger values of drift associated with the near-collapse stage, the masonry structure would acquire significant dampening capacity, which significantly decreases the spectral demand. In this manner, the strengthening solution does not lead to increased forces on the foundation or other structural elements, a typical ailing of many strengthening methods. Hence, both light damage and near-collapse states are addressed.



Figure A.5.1. Experimental masonry wall with window of timber-glass design. The glass is painted for DIC purposes.

In subsequent iterations, improvements were made in the installation of the window by injecting with grout the tolerance between masonry and timber frame. Moreover, an anchoring system, that allowed pushing the frame from the front of the wall, guaranteed that failure would never occur at the masonry-

timber interface, but focus instead on the timber-adhesive-glass interface. Because of the relatively soft timber in comparison to the laminated glass, the glass panels never failed during any of the experiments.

A.6. Repair: Self-Healing Mortar

The project delves into the innovative application of a bacteria-based self-healing mortar, initially designed for concrete structures, to masonry work. This initiative is driven by the need to address the prevalent issue of cracks in masonry, which not only diminish the visual appeal of buildings but also undermine their structural integrity and weather/water resistance. The goals of the project are twofold. First, it seeks to confirm whether the self-healing mortar can effectively repair masonry structures, ensuring compatibility and efficiency in real-world applications. This involved a comprehensive series of experimental tests to assess the mortar's healing capabilities, including its strength restoration and aesthetic recovery post-damage. Second, the project aims to evaluate the feasibility of incorporating self-healing mortar into new construction projects, offering a proactive approach to enhancing the durability and resilience of masonry structures.

Several key advantages of using self-healing mortar in masonry have been identified. One of the most significant benefits is the mortar's capacity for automatic crack repair, which activates upon the occurrence of damage, thereby reducing the need for manual repair work and potentially lowering long-term maintenance costs. Additionally, the self-healing process is designed to restore the masonry's original properties, including its structural strength and aesthetic appearance, following damage. This contributes to the overall durability of the structure, extending its lifespan and improving its resistance to environmental factors.

The project's experimental findings highlight the mortar's effectiveness across various types of bricks, including calcium-silicate and clay bricks, indicating its versatility for different masonry applications. Moreover, the research underscores the importance of tailoring the healing conditions—such as humidity levels—to match the specific requirements of the masonry material, ensuring optimal healing outcomes.

Gaggero et al. [21] performed initial tests as a proof-of-concept. These demonstrated the effectiveness of the self-healing for cement-based mortar. Additional tests, focused on historical masonry, explore the compatibility with older bricks and lime-based mortars.

A.7. Out-of-Plane of Masonry Walls during Hydrostatic Loading

In a pragmatic experiment conducted at Flood Proof Holland, we sought to determine the ability of fired-clay-brick masonry walls to withstand hydrostatic water pressures and impacts from debris, providing experimental data for the calibration of structural models. These models were intended for the development of fragility models to evaluate economic and life loss from Dutch flood scenarios.

The experiment involved constructing a 2.7x2.7 meter square wall, 100 mm thick, on a steel rig designed to simulate real-world conditions as closely as possible. The wall faced hydrostatic loads by subjecting it to a water level difference of up to 125 cm on one side, while maintaining the opposite side at 0 cm, effectively mimicking conditions where the interior of a structure remains dry during a flood. This setup aimed to assess the wall's structural integrity under varying water pressures, particularly looking for the onset of cracking and the overall deformation of the wall under stress.

The wall was restrained on all four sides to simulate the constraints buildings typically place on such walls. This restraint was achieved through adhesion to top and bottom steel beams and lateral steel columns of the rig. During the tests, the most challenging scenarios involved different combinations of water levels, resulting in minor cracking and an out-of-plane deformation of approximately 2 mm when subjected to a hydrostatic pressure equivalent to 95 cm of water. This deformation reflected two-way bending behaviour due to the horizontal supports preventing lateral movement. Further complexity was added to the experiment by considering the vertical overburden imposed by the steel rig, which simulated the gravitational loads buildings impose on their walls. This addition aimed to provide a more accurate representation of real-world stresses.

Non-linear, finite element models, calibrated using the experimental data, offered deeper insights into the wall's behaviour under varying conditions. Initial observations showed linear-elastic behaviour up to a water level of approximately 90 cm. Beyond this point, significant deformation and the initiation of cracking were noted. The models attributed this to a redistribution of bending stresses, moving from the vertical axis, where the wall is stiffer but weaker, to the horizontal axis, which could better support the stress. At a water level of 125 cm, the wall's deformation escalated to 5 mm, signalling a progression towards failure, which was projected to occur around a depth of 150 cm, a threshold not experimentally tested but inferred from the data and model predictions.

The research also incorporated the effect of debris impact in conjunction with hydrostatic pressure. Simulating scenarios where the wall was hit by a floating tree log and a suspended steel cube represented soft and hard debris, respectively. Soft debris impacts up to 1.8 m/s (90 Joules) did not significantly alter the wall's deformation. However, impacts from the steel cube, especially in combination with water depth nearing 90 cm, caused noticeable out-of-plane deformations, diagonal cracking, water leakage through cracks, and localised masonry failure.



Figure A.7. Collage detailing the construction and context of the tested wall.

This detailed analysis concluded that traditional, single-wythe masonry walls could safely withstand up to 90 cm of water depth when the interior remains dry. However, it also revealed that such walls are considerably more vulnerable

without lateral support, emphasising the need for adequate structural constraints in building designs to mitigate flood damage.

Future research directions were outlined to further explore the differences in wall behaviour under one-way versus two-way bending conditions, the effects of water leakage through openings, and the performance of cavity walls common in Dutch construction. These studies aim to enhance the understanding of flood resilience in buildings, contributing to more effective flood prevention and mitigation strategies. See [5] and {C.13}.

A.8. The Action of Debris during the German Flood of 2021

The July 2021 flood in Germany, particularly in the Ahr Valley, exemplifies the destructive potential of extreme weather events exacerbated by climate change. This disaster not only claimed lives and inflicted injuries but also caused significant damage to buildings, critical infrastructure, and the environment, highlighting the urgent need for comprehensive flood risk management and resilient infrastructure design. Conducted by a team of hydraulic and structural engineers, including the author, a field survey in the aftermath of the flood sought to understand the mechanisms behind the widespread structural failures. In hindsight, one of the critical aspects of this survey was to assess the impact of floating and water-borne debris on buildings and infrastructure. Debris, consisting of natural materials like wood and man-made objects, played a significant role in exacerbating the damage by colliding with structures and forming "debris dams" that increased the hydrostatic pressure on buildings. This summary focuses on the actions of debris during the flood, revealing the challenges in managing such dynamic and destructive forces and the importance of incorporating debris impact considerations into flood protection and infrastructure design strategies.

The floating and water-borne debris consisted mainly of tree trunks, branches, construction materials, and household items. It inflicted damage in two main ways: by colliding with structures due to the momentum of the floodwaters and by gathering around buildings to form "debris dams." These dams increased hydrostatic pressures on structures, reduced flow areas around buildings, and, in many cases, led to structural failures due to the additional load imposed by the accumulation of debris.



Figure A.8.1. Left, marks induced on buildings by debris impact, and right, debris damming around building openings.

Debris impacts were noted to occur mostly at the corners of buildings or around openings, suggesting that the collisions were partly responsible for structural failures. Debris dams formed upstream of buildings, blocking openings and contributing to backwater effects, which magnified the flood's impact by increasing the depth and extent of water around the buildings. The debris also posed a significant challenge by filling up space inside buildings, reducing the capacity for floodwaters to flow through, thereby increasing the pressure on the buildings' walls and foundations.



Figure A.8.2. Example of a façade where the flow of water and floating/trapped debris removed windows and knocked out a pier.

The survey conducted in the aftermath of the flood provided evidence of the damage caused by debris, including marks and structural failures induced by debris impact. The type of debris varied widely but was primarily composed of natural materials like wood, as well as man-made objects and materials dislodged from buildings and infrastructure. This wide variety of debris types contributed to the complex nature of the damage and highlighted the importance of considering debris management in flood risk analysis and mitigation strategies.

In summary, the action of debris during the 2021 German flood significantly contributed to the damage observed in the Ahr Valley. The findings underscore the importance of incorporating the potential impact of debris into flood protection measures and the design of flood-resistant buildings and infrastructure.

See [26] and D. Wüthrich, P.A. Korswagen, H. Selvam, J. Oetjen, J. Bricker, H. Schüttrumpf (2024). *Field survey assessment of flood loads and related building damage from the July 2021 event in the Ahr Valley (Germany)*. *Journal of Flood Risk Management*.

A.9. Strategy for Safety Assessment of Historical Quay Walls

Dutch cities are known for their masonry infrastructure such as bridges and quay-walls along the city canals. Many of the centenarian quay walls have been insufficiently maintained or are unprepared for today's (traffic) loads. A comprehensive strategy was devised to assess the vulnerability of these structures with a focus on the masonry aspect. The approach integrates three main phases: Insight, Deepening, and Synthesis, across four distinct topic lines, providing a holistic view of the project's progression from initial analysis to the development of actionable guidelines. While only portions of the original strategy are currently being addressed at the TU Delft, several advances have been made in the characterisation of quay walls (Li et.al, 2023), and modelling of quay walls (Sharma et.al, 2023) and wharf cellars (Oktiovan et.al, 2023). The municipality of Amsterdam has investigated several of the topics, too.

A brief description of each topic line and phase is gathered next.

Characterisation of Masonry Material begins with the Insight phase, focusing on gathering existing material data, conducting initial material tests, and developing small scale brick-to-brick models. These steps establish a foundational understanding of masonry materials observed in aged multi-wythed masonry, documented in successive versions of a Material's Abacus. The Deepening phase continues with additional material tests and

investigations into non-destructive tests, size, shape, boundary effects, and tests on deterioration and connections, aiming to refine and expand the material's database. Finally, in the Synthesis phase, further material testing solidifies the data, offering a comprehensive characterisation of masonry materials for use in subsequent analyses and model developments.

Computational Modelling & Structural Analysis transitions from the creation of integral models, which encompass structures and their surroundings, to zoomed-in models of masonry structures and analytical models in its initial phase. These efforts produce a first version of the modelling report. As the project deepens, improvements to material models for multi-wythe masonry are made, alongside the development of models to replicate damage patterns and parametric structural models, leading to a second modelling report. The Synthesis phase validates these models and simplifies them for practical application, generating a final modelling report. This progression encapsulates the project's evolving understanding and simulation capabilities regarding masonry structure behaviours and their analysis.

Framework for Causality/Attributability is primarily developed in the Synthesis phase. It involves consolidating the project's findings into a comprehensive report that addresses failure, fragility, and reliability. This framework supports the creation of guidelines for diagnosis and assessment, aiming to provide a systematic approach to understanding and addressing the vulnerabilities and failure mechanisms in masonry structures. By establishing clear connections between causes and observed conditions, the project lays the groundwork for effective structural assessment and the development of targeted interventions.

Inventory Masonry Structures and Validation Tests commence with a review of existing data and the definition of typologies, progressing through novel techniques for data acquisition and the preparation of large-scale laboratory and in-situ testing. The overview report summarises these initial findings and methodologies. The phase continues with the execution of these tests, which serve to validate the project's earlier findings and hypotheses. This line culminates in a preliminary investigation into strengthening techniques, aiming to enhance the resilience and durability of masonry structures based on the insights gained throughout the project. The focus on typologies and the incorporation of both laboratory and real-world testing ensure a robust and applicable framework for future masonry structure analysis and reinforcement.

Across these four topics, the proposal's phased approach—beginning with foundational insights, moving through detailed analysis and model development, and culminating in actionable frameworks and validation tests—

illustrates a comprehensive strategy for understanding, analysing, and enhancing masonry city infrastructure. Each topic line contributes to the project's overall goal of improving the assessment, maintenance, and preservation of masonry constructions.



Figure 1. Old city-canal in Delft with masonry quay walls and a masonry overpassing with abutments.

A.10. Experiments during course 'Masonry Bend & Break'

The masonry course, part of the BSc minor "Bend and Break", has two parts: theory and practice. In the practical, the students begin by constructing small samples: masonry couplets for bond-wrench tests, to look at the tensile strength of the bond, and square towers, for a compressive test to determine the strength of their masonry. Often, both fired-clay and calcium-silicate masonry are compared and, sometimes, the effect of dry or wetted bricks is investigated. These small tests give the students the practice and the insight to design their larger experiment.

Indeed, during the rest of the practical, the students have a choice of building a wall or an arch. For the latter, the students submit a plan and only the two most feasible arches are selected - the entire class should be able to see examples of walls and arches. The single-wythe wall has one-brick buttresses at the edges which triggers a more interesting failure with two-way bending. A point load is applied on the centre of the wall and the arch is loaded by gravity using sandbags.



Figure A.10. Various experiments from the course, featuring a compressive test on masonry, a wall tested out-of-plane, with vertical and horizontal cracking, and an arch.

A.11. Analysis of Waarts' Probabilistic Estimation of Damage

Waarts' framework, originally developed in 1997 to predict damage initiation in masonry structures exposed to dynamic soil vibrations, was re-evaluated in detail using contemporary computational techniques. The study introduced updated material properties derived from recent laboratory tests on pre-1950s clay-brick and calcium-silicate brick masonry conducted at TU Delft. By employing Monte Carlo simulations, the updated analysis refines the framework's ability to estimate the probability of damage under varied dynamic conditions, making it more statistically robust and reflective of real-world variability.

The framework of Waarts (1997) is a simple, yet powerful method for assessing the probability for the initiation of damage in masonry structures subjected to predominantly vertical vibrations from nearby sources. Due to its age and the way it was conceived, it would seem to be limited in the nature of the vibrations and its quantification of damage.

While the intent of Waarts framework was to determine a probability of damage, its linear-elastic approach makes it actually determine the very initiation of damage, when the first tensile strength is reached. However, it uses the flexural strength of masonry instead of its tensile strength. If the input values are replaced with tensile strength, the framework can be used to determine the initiation of damage.

Limitations notwithstanding, when reproducing the framework, the results obtained are similar to the original curves but differ slightly, presumably due to differences in the reported input values.

The input values are modified with current knowledge about the material parameters of vulnerable structures in the area to produce "updated" curves. These curves are then approximated to log-normal distributions revealing a good fit in the interval of PGV of 0 to 20 mm/s, in particular for the case of baked-clay masonry with parameters $\mu=3.11$ and $\sigma=1.21$ for an estimation of slight damage.

Consequently, the probability for the initiation of damage based on the framework of Waarts (1997) using updated material properties for clay-brick masonry can be computed directly with a spreadsheet application by invoking a log-normal distribution and specifying PPV, logarithmic mean, and scale parameters in a way similar to LN(PPV in mm/s, $\mu=3.11$, $\sigma=1.21$).

A.12. InSAR Analysis of Cyclic Soil Movements in Norg

InSAR satellite data measuring the elevation of the ground surface from the combination of four satellite datasets can be used to estimate the effect of (cyclic) deep soil actions caused by extraction and injection of gas in the field of Norg. The satellite data is post-processed to produce a time lapse of elevation contours lines; these, in turn, are used to determine the relative vertical displacements and surface curvatures over select cross-sections across the 6 km buffer-zone of the gas field. The post-processed data is compared against GPS measurements and analytical model results for gas reservoir depletion and storage, revealing no stark dissimilarities and good compatibility overall. Furthermore, in contrast to thresholds for building damage, the values of curvature and derived horizontal strains from the satellite elevation data, appear lower even when considering individual satellite datasets which present a higher variability and uncertainty. This analysis concludes therefore that analytical models can well represent ground surface deformations in the context of deep-soil effects and that observed soil deformations appear below set thresholds for building damage parameters.

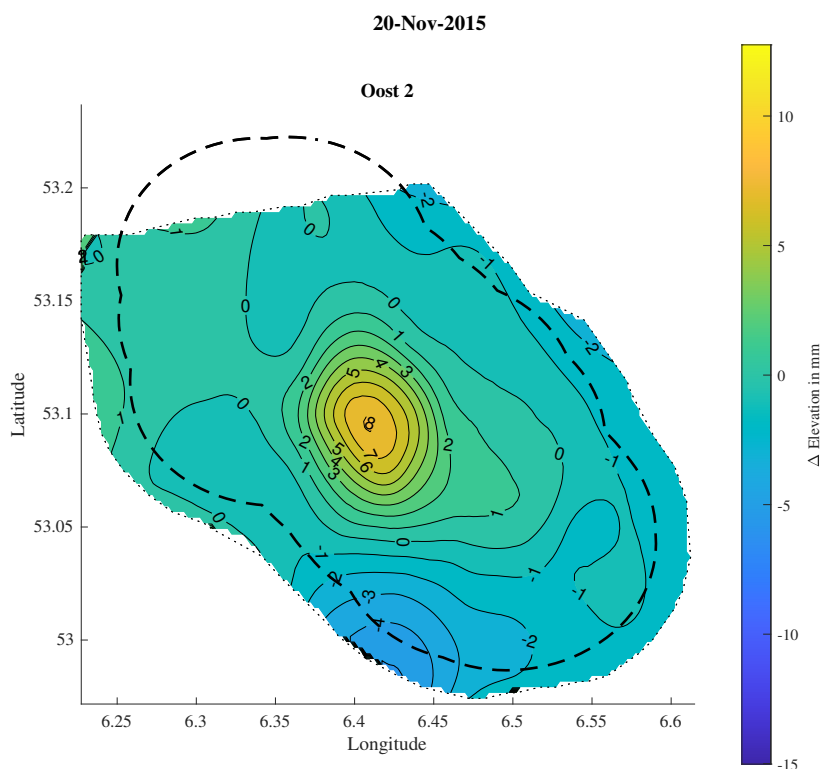


Figure A.12.1. The buffer zone at Norg overlaid with vertical displacement contours.

A.13. The Effect of Deep Subsidence on Masonry Façades

The Instituut Mijnbouwschade Groningen (IMG) was interested in determining whether subsidence caused by gas extraction could also be responsible for building damage, especially over the gas field of Norg which is also used for storage of gas. This leads to a seasonal subsidence in late winter and heave in late summer. The curvatures at the soil surface that occur because of the subsidence are negligible. Subsidence also leads to horizontal strains, however; and, while these are small, they have the potential to cause damage since masonry is sensitive to tensile strains.

To investigate this potential, a series of worst-case scenarios were conceived and analysed with FEM models of masonry façades. For instance, the worst locations along the subsidence trough were selected, masonry was assumed to be weak but stiff, and a high transfer of the horizontal soil strains via the foundation was selected. For the façade geometries, large openings and long façades were modelled.

The study concluded that the current and anticipated levels of ground deformation due to deep subsidence from gas storage operations at Norg do not cause visible masonry damage. It suggested that similar findings could likely apply to the Groningen field, assuming comparable conditions of ground deformation. There were large margins (from 6x to 10x) between the horizontal strains expected in Norg and the horizontal strains required to cause visible damage, $\Psi=1$, in the masonry façades.

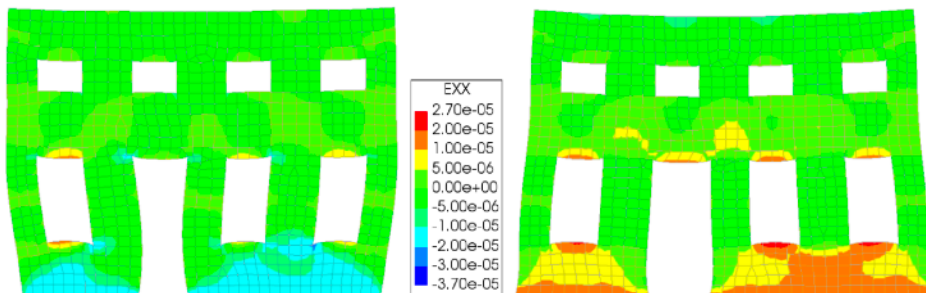


Figure A.13.1. One of the façades subjected to horizontal strain at the foundation. Left, in contraction, caused by subsidence at the centre of the Norg region; and right, in extension, caused by heave at the centre or by subsidence at the perimeter of the region.

See Rots, J.G., Korswagen, P.A., Longo, M. (2021). Computational modelling checks of masonry building damage due to deep subsidence. Delft University of Technology. Report number 01, Version 05, February 18, 2021. Including Appendices H to J to initial report, version 6, 8 September 2022.

A.14. The Effect of Combined Horizontal Strain and Curvature on Masonry Façades from Soil Movements

Another study for IMG looked at the combination of soil horizontal strain, soil curvature and earthquake vibrations for causing damage to masonry façades. The first is related to the effects of gas extraction or soil mining, the second could come from local effects like lowering of the ground water table inducing changes in the soil, and the third is caused by seismicity. What happens when façades are subjected to a combination of all three loads?

To investigate this, a two-tiered strategy was used. A block of layered soil, 45 m long and 12.5 m deep, was used to determine the boundary inputs required to produce a certain combination of strain and curvature seen at the soil surface. These are the so-called 'Greenfield' strain and curvature, typically obtained from geotechnical calculations for the deformation expected from tunnelling and mining. These boundary inputs are then used in an identical soil block with a masonry façade on top. In this manner, the soil-structure interaction is included. The models are complex, including non-linear soil modelled with a small-strain soil hardening model, and with 3D buildings comprising a façade and its transversal walls. The models are axisymmetric parallel to the façade.

The models reveal for example, that only a portion of the horizontal soil strain of the soil gets transferred to the façade. However, as the façade develops cracks and becomes more flexible, more of the strain is transferred.

Thousands of façade geometries and soil combinations were modelled at increasing values of strain and curvature for cases of pure horizontal strain, pure curvature and everything in between. Ψ thresholds for the combination of strain and curvature were drawn and adjusted when a vibration characterised with its PGV was included. These results are compared against known limits from literature proposed by Boscardin and Cording. The figure next focuses on the soil deformations: for distortions below $8 \cdot 10^{-4}$ coupled with strains below $1 \cdot 10^{-4}$, no visible damage is expected.

See Korswagen P.A., Longo M., Rots J.G. (2024). *Research into the combined effects of soil strains, soil curvatures and earthquakes from multiple mining activities on damage to masonry*. Delft University of Technology. Report number 01, First draft version 01, April 9, 2024.

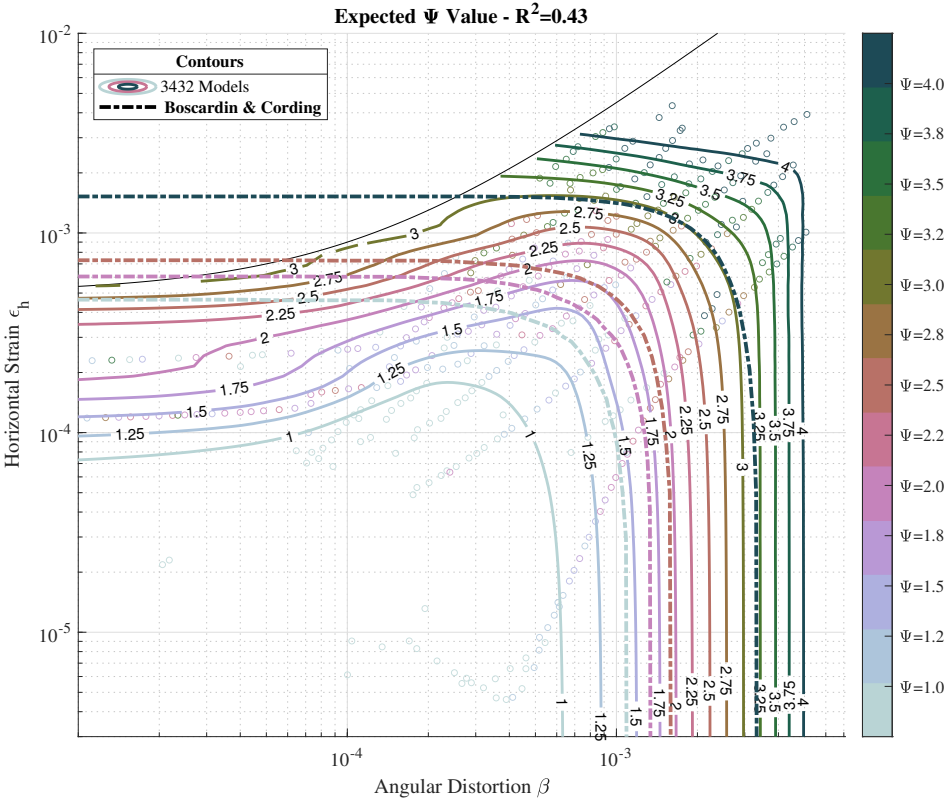


Figure A.14.1. Thresholds for Ψ given a combination of Greenfield tensile horizontal strain and soil curvature.

A.15. The Effect of Truck Vibrations in Comparison to Earthquakes'

A paper presented at the conference of seismic analysis of historical masonry constructions (SAHC), used FEM models similar to those used in Chapter 5, to analyse not only the effect of earthquake vibrations but also those of truck passages. TNO provided the records or acceleration time series for the passages. To adapt the models to the context of the conference, a historical masonry façade, with matching material properties were selected. The models are employed to replicate the geometry of (historical) masonry facades to determine their sensitivity to light damage as a consequence of the two damaging processes observed to be most common for this type of façade, namely (differential) settlements and (earthquake) vibrations.

The masonry façades were first pre-damaged via settlement distortions which generate just-visible cracks in the order of 0.1 mm to 1 mm in width. Then, an acceleration time history corresponding to two different Dutch earthquake events and two recordings of traffic-induced building vibrations were separately applied at the base of the models. In this manner, the effect of existing damage could be assessed in regard to the aggravation generated by vibrations.

The settlement part of the study revealed that long façades were more vulnerable to applied soil distortions, for instance. Then, subsequent vibrations further increased damage for intensities measured with a peak ground velocity (PGV) larger than 2 mm/s while the control set of virgin or uncracked façades remained undamaged at this PGV. At 32 mm/s, many pre-damaged façades also exceeded the light damage range. At equal PGV, the traffic vibrations, with a larger number of effective cycles, resulted in increased damage aggravation in comparison to the earthquake recordings.

The study evaluated two geometrical variations of a double-wythe, fired-clay brick masonry façade subjected to varying settlement shapes and subsequently, to seismic and traffic vibrations. The goal is to establish a relationship between these processes, several façade properties, such as their length and material strength, and the development of light, crack-based damage on the façades. We have observed that:

- At low values of damage, only a small amount of the soil distortion underneath the façade foundations is transferred to the masonry leading to cracks.
- Longer façades required a smaller applied soil distortion to develop visible damage in comparison to shorter façades. Similarly, these façade geometries

were more vulnerable to sagging settlement shapes than hogging shapes. The settlement shape did not affect the damage increase caused by subsequent vibrations.

- Vibrations, even with low PGV values of 2 mm/s, increased visible damage in most cases, while seldom initiated cracks in undamaged façades. In particular, traffic vibrations lead to increased damage in all pre-damaged cases investigated.
- At low values of PGV, traffic vibrations lead to twice as much damage as earthquake vibrations, and to about 30% more damage at high values of PGV; though these high PGVs are not expected for traffic vibrations.
- Horizontal drift values of 0.4‰ are associated with the upper boundary of light damage for these historical façades; much lower than comparable drift limits established for DS1 of regular masonry buildings.
- In fact, when compared against simple masonry walls from an earlier study [2], seismic vibrations were about 40% more damaging to the historical façades, and even more severe in the range of 2-4 mm/s.

These observations warrant future, more in-depth analyses looking at important effects such as the transfer of soil deformations to the shallow foundations, typical of historical heritage, 3D building effects so far neglected, so as interlocking with transversal walls, the participation of the floors and their potential restraining effect, additional vibration sources and more measurements of traffic vibrations on actual buildings, and more complex structural typologies and variations. See [20].

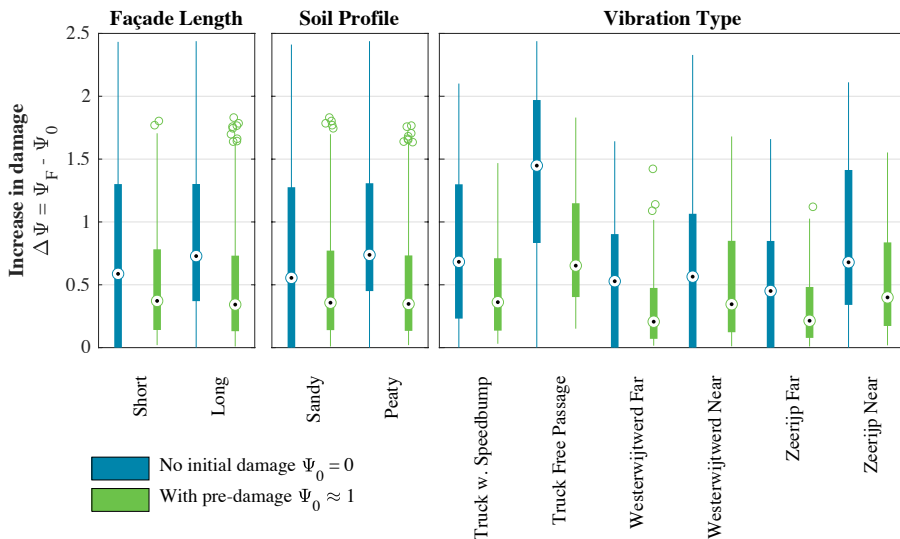


Figure A.15.1. Influence of a few parameters on the increase in damage, $\Delta\Psi$, in particular, the various types of vibrations are compared.

Appendix B

Ψ Damage Parameter

B.1. Equations and Definition of Ψ

See also Section 2.2.

$$\Psi = 2 \cdot n^{0.15} \cdot c_w^{0.3} \quad \text{Definition of } \Psi: \text{Equation 2.4}$$

To determine Ψ on a single type of masonry wall or building with multiple cracks, the weighted crack width needs to be computed.

$$c_w = \frac{\sum_{i=1}^n c_i^2 \cdot L_i}{\sum_{i=1}^n c_i \cdot L_i} \quad \text{Weighted crack width: Equation 2.3}$$

$$c_i = \sqrt{c_o^2 + c_s^2} \quad \text{Squared Sum. Equation 2.3b}$$

Where c_i is the maximum crack width of crack i , and L_i is the length. The crack width is composed by both the opening (c_o) and sliding (c_s) components.

Table 2.2.2. Comparison Damage States and damage levels with approximate values of Ψ.

State	DS0		DS1		DS2
Level	DL0	DL1	DL2	DL3	DL4
Ψ	Ψ < 1	1 < Ψ < 1.4	1.5 < Ψ < 2.4	2.5 < Ψ < 3.4	Ψ > 3.5
Aproximate Crack Width	Imperceptible cracks	up to 0.1mm	up to 1mm	up to 5mm	5 to 15mm

Table 2.2.3. Overview of the scalar value of Ψ for SLS (black) and ULS (grey).

Values of ψ	Description	Representative Crack Width	Damage State	
$\psi = 0$	No damage	N.A.	DS0	L i g h t
$\psi \approx 0.5$	Invisible damage	< 0.1 mm		
$\psi \geq 1.0$	Just-visible light damage	> 0.1 mm	DS1	
$\psi \geq 2.0$	Easily-observable light damage	> 1 mm		
$\psi \geq 2.5$	Costly light damage	> 2 mm	DS1 or DS2	D a m a g e
$\psi \geq 3.0$	End of light damage	> 4 mm	DS2	
	Severe.			S t a b i l i t y
$\psi \geq 4.5$	No longer light damage, usage of a different damage metric is recommended.	> 10 mm	DS3	
$\psi \geq 6.0$	Very Severe	> 25 mm	DS4	
$\psi \geq 8$	Near Collapse	> 50 mm	DS4 or DS5	

Damage Increase

The increase in damage can be measured with Ψ by determining $\Delta\Psi$.

$$\Delta\Psi = \Psi - \Psi_0 \quad \text{Damage Increase: Equation 2.5.}$$

Where Ψ_0 is the initial damage condition. Because of the power law of Equation 2.4, the importance of the absolute damage increase remains constant within the light damage range ($\Psi_0 < 3$); this means that an increase of $\Delta\Psi$ of 0.2 for instance, will be equally noticeable and affect the cost of repair in a similar manner for a case of $\Psi_0=1$ or $\Psi_0=2$. In both situations a $\Delta\Psi$ of 0.2 represents a measurable increase in damage and is used as the lower threshold for quantifying an aggravation in crack-based damage.

Relative Increase in Damage: $r\Delta\Psi$

The relative increase, $\Delta\Psi / \Psi$ or $\Delta\Psi / \Psi_0$, can also be used to characterise damage aggravation. However, because Ψ is based on a power law, the importance of relative increases are dependent on the starting value of Ψ . For example, an increase of 50% when $\Psi_0=0.5$ doesn't reach visible damage; but, if $\Psi_0=2$, the increase of $\Delta\Psi=1$ is significant. For this reason, the $r\Delta\Psi$ is only

sporadically used, with a preference instead to the absolute $\Delta\Psi$ as presented in Table 2.2.4.

Table 2.2.4. Overview and thresholds for $\Delta\Psi$ when $\Psi_0 \geq 1.0$.

Values of $\Delta\Psi$	Description
$\Delta\Psi < 0.1$	Imperceptible
$0.2 > \Delta\Psi \geq 0.1$	Only noticeable in comparison photographs
$0.5 > \Delta\Psi \geq 0.2$	Above 0.2 an increase in damage becomes visible for recurrent observers
$1 > \Delta\Psi \geq 0.5$	Evident damage increase, significant influence in the cost of repair
$\Delta\Psi \geq 1$	Increase in damage contributes most to repair cost and detectability; fully attributable damage

Comparison Ψ

The Ψ parameter has been mainly developed to assess the progression of damage on a certain specimen or between identical specimens. However, sometimes different walls or structures would like to be compared to each other to determine which presents lower or higher damage. In this case, it is convenient to express a relative version of Ψ based on the surface area of the masonry:

$$\Psi'_i = \Psi_i \cdot \frac{A_i \cdot \zeta_i}{\bar{A}} \quad \text{Equation 2.6.}$$

Where A_i is the surface area of the wall i , \bar{A} is the mean area of the walls considered and Ψ' is the relative Ψ . Additionally, if the walls are of different masonry material, the unitary cost of repair ζ can be included in the comparison.

Furthermore, if a structure where each wall is monitored separately wants to be characterised with a single value of Ψ , the damage in the N walls can be accounted as:

$$\bar{\Psi} = \frac{1}{A_T} \sum_{i=1}^N \Psi_i \cdot A_i \quad \text{Equation 2.7.}$$

Where $\bar{\Psi}$ is the mean Ψ value and A_T is the sum of the surface areas. However, Ψ can be directly determined as the sum of all cracks in the structure. If the unitary cost to repair all walls is similar, this approach is preferred.

B.2. Table with Practical examples of Ψ and $\Delta\Psi$

Table B.1 (left side).

Before				After			
n	cw	L	Ψ	n	cw	L	Ψ
1	0.2 mm	NA	1.23	3	0.2 mm + 2x 0.1 mm	NA	1.33
1	0.1 mm	NA	1.0	2	0.1 mm	NA	1.11
3	0.1 mm	NA	1.18	3	0.15 mm	NA	1.33
2	0.5 mm + 1 mm	0.5 m	2.1	2	0.5 mm + 1.2 mm	0.5 m + 1 m	2.27
1	0.5 mm	NA	1.62	2	0.5 mm	NA	1.8
1	0.5 mm	NA	1.62	1	0.7 mm	NA	1.8
1	1 mm	NA	2	2	1 mm	NA	2.22
1	0.1 mm	NA	1	1	0.2 mm	NA	1.23
1	1 mm	NA	2.0	1	1.5 mm	NA	2.26
1	0.1 mm	NA	1	5	0.1 mm	NA	1.28
2	0.5 mm + 0.5 mm	NA	1.8	2	0.5 mm + 1 mm	NA	2.1
3	0.5 mm	NA	1.91	3	1 mm	NA	2.36
1	1 mm	NA	2	1	2 mm	NA	2.46
1	1 mm	NA	2	4	1 mm	NA	2.46
1	0.1 mm	NA	1	15	0.1 mm	NA	1.5
3	0.5 mm	NA	1.92	11	1 mm	NA	2.87

Table B.1. (right side, continued). Practical examples of Ψ and $\Delta\Psi$.

$\Delta\Psi$	$r\Delta\Psi$	Observation
0.1	8.1%	An existing crack of 0.2 mm is joined by two new cracks that become visible.
0.11	11.0%	A second crack of identical width appears, the first crack is unchanged. Both cracks are narrow.
0.15	12.7%	Three cracks of 0.1 mm all increase in width by 50%.
0.17	8.1%	Two existing cracks, where the wider one increases in width and length
0.18	11.1%	A second crack of identical width appears, the first crack is unchanged.
0.18	11.1%	A crack of 0.5 mm increases by 0.2 mm.
0.22	11.0%	A second crack of 1 mm appears
0.23	23.0%	1 barely visible crack doubles in width
0.26	13.0%	A 1 mm crack increases in width by 50%.
0.28	28.0%	Four new cracks become detectable when only one was before.
0.3	16.7%	Two existing cracks where one doubles in width
0.45	23.6%	Three cracks of 0.5 mm all double in width
0.46	23.0%	A 1 mm crack doubles in width.
0.46	23.0%	Four new cracks of 1 mm appear
0.5	50.0%	Where only one crack was visible, 14 more cracks become visible
0.95	49.5%	Three cracks of 0.5 mm widen and 8 new cracks of 1 mm appear

B.3. Perception of Damage

Table B.2. Influence values for various non-structural aspects influential in damage perception. Empiric exemplary values.

1 - Reduces the perception of damage significantly; 2 - Reduces the perception of damage; 3 - Does not influence; 4 - Increases the perception of damage; 5 - Increases the perception of damage significantly.

Category	Subcategories	Influence Value (k)	Description
Age	very old	2	older than 1970
	older	3	between 1970 and 2000
	new	4	newer than 2000
Material	fired-clay brick	3	often exposed
	calcium silicate br.	4	sharper crack edges
Wall type	slender	4	less than 120mm
	thick	3	greater than 120mm
	double	2	more than one layer of bricks
Cavity	without cavity	3	one single leaf
	cavity and	4	two leaves, where only one is structural
	cavity and	3	two leaves, both structural
Brick Type	regular bricks	3	units with a height smaller than 150mm
	large blocks	4	units with a height larger than 150mm
	hollow units	3	units that are not solid
Mortar	thin	4	the joints are around 3mm according to EC
	free verticals	2	vertical joints between the bricks are not
	normal	3	all joints are filled and greater than 3mm
Finish	exposed	2	the bricks and joints can be seen
	plaster + paint	3	the wall is covered with plaster and painted
	mortar + paint	4	the wall is covered with mortar and painted
	elastomeric paint	2	wall is (covered and) painted with flexible
	wall paper	1	the wall is plastered and covered with paper

Appendix C

Supervised MSc Projects

In the extensive period that I was busy with this study, I had the opportunity to supervise many MSc graduation projects. Some topics were conceived directly by this work and I was thus the main supervisor of the graduating student. In other situations, the topic was related to my interests but I didn't act as the daily supervisor. And, for yet another portion of the projects, my involvement, as committee member, was strictly limited to the official progress meetings. These topics were then related to my knowledge of masonry and/or structural mechanics.

In this appendix, I present an overview of the MSc projects with which I was involved. The complete reports can be found at the university website repository.tudelft.nl under the section for "education".

Table C.1. Summary of supervised MSs projects.

#	Title	Student
1	Non-linear Time History Modelling Of Damage Initiation and Development in an Unreinforced Masonry Cavity Wall Under Out-of-plane Loading	Amey Joshi
2	Structural Window Design For In-plane Seismic Strengthening: Numerical Predictions Of Strengthening Unreinforced Masonry Structures in Groningen	Arthur de Groot
3	Hydrodynamic Loading Of Dutch Terraced Houses Due To Flood Actions Using Computational Fluid Dynamics	Benedikt Bratz
4	From the Sea Into the Sky	Boris
5	Recognizing Critically Damaged Quay Wall Structures Using a Three-dimensional Numerical Model	Chris van Hulten
6	Het Effect Van Ontwerpmaatregelen Bij Trein-geïnduceerde Trillingen in Woongebouwen	Daan Westerink
7	Simulation Of the Overall Performance Of Glazed Unitised Curtain Walls Under Seismic Action Through Finite Element Modelling and Validation Via Full-scale Experimental Testing	Evdokia Stavridou
8	Multiaxial Compressive Stress States Within a Concrete Onshore Wind Turbine Foundation	Jelle de Groot
9	Nonlinear Modelling Of Non-structural Masonry Walls under a Low-intensity Earthquake Motion: Calibration through a Parametric Study	Laura Masini
10	Structural Damage To Dutch Terraced Houses Due To Flood Actions	Lise Jansen
11	Experimental Research On the Factors Which Influence the Fleeing Time and Rescue Time Of People Evacuating Flooded Areas	Marion van den Bulk
12	Experimental Validation Of a Structural Glass Window Design For In-plane Seismic Strengthening	Mehmet Kisa
13	Flood Fragility Of a Cavity Wall	Mick van Haren
14	Finite Element Analysis Of Building Deformations Due To Deep Excavations	Mohammed Harrouni

#	Title	Student
15	Dynamic Modelling Of Crack Damage At the Interface Of Non-structural Masonry walls and the Structure Due To earthquake Motion	Nikita Cattini
16	Stabilising Buildings With Glass	Parviz Azamy
17	Probability Of Damage Of Masonry Structures Due To External Ground Vibrations	Pieter Potuijt
18	Validation Of a Thermo-mechanical Fe Model Of Onshore Wind Turbine Foundation	Pragya Mukherjee
19	The Historic Quay Walls Of Amsterdam: a Study Into the Hidden Structural Capacity Of Masonry Quay Walls Under the Condition Of a Partly Failing Foundation	Rick Voortman
20	Developing a Diagnostic Assessment Tool To Evaluate Damage in Buildings	Rick Willems
21	A Hyperbolic Model For Degradation in Tension Mode-i Fracture Of Masonry	Srinidhi Bindiganavile -Ramadas
22	Photogrammetric Deformation Analysis Of a Quay Wall	Stijn Lodder
23	Rocking Revisited Analysis Of Rocking-induced Stresses For Concrete Breakwater Armour Units	Thomas Goud

Appendix D

Glossary

Various terms and concepts employed throughout this work are gathered and defined in this section. Some concepts vary in definition depending on the field of engineering and the authors. The list presented here and the definitions as used in this work.

Aggravation, Accumulation. These terms are almost synonyms; they refer to an increase in damage. The first is employed to describe a worsening of the damage: damage is aggravated. The second conveys a worsening over repeated actions: damage accumulates due to the effect of various actions or events. "Cumulation" is also a related term, it means to gather several effects. "Accumulate" is similar but progressive.

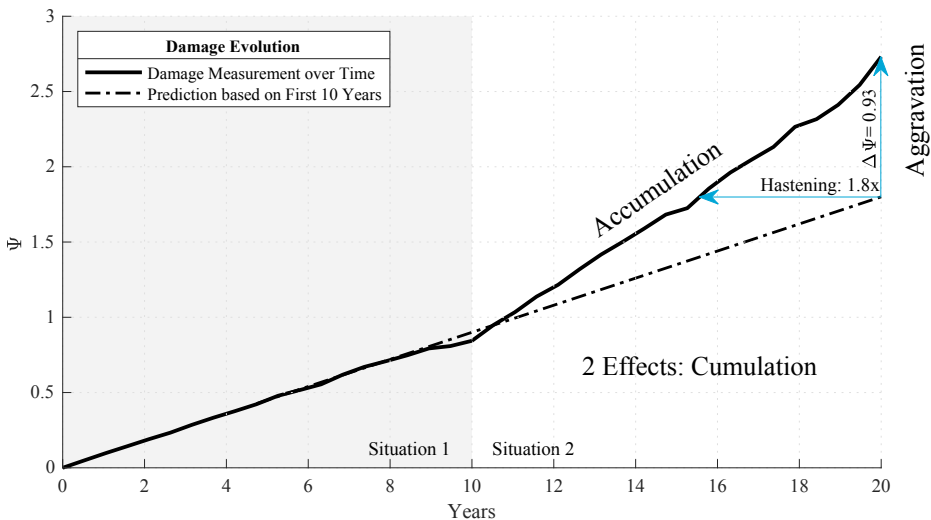


Figure D.1. Aggravation and accumulation of damage.

Action/loading. The action of a hazard is essentially how the hazard affects structures. It is the direct impact or the mechanism through which a hazard imposes stress or damage on a structure. For example, while a storm itself is the hazard, the wind pressure it generates against the side of a building is

considered its action. The modelling or presentation of the action is a load or loading. Similarly, in the case of a fire, the hazard is the fire itself, while the increase in temperature or temperature gradient it causes on structural elements represents the action; the load, in this case, is an internal strain on the material.

Calibration, validation. The modelling strategy and the parameters employed in models are adjusted and contrasted against another source, typically experimental results.

Cracks, cracking, fracture. When (quasi-)brittle materials reach their tensile strength, the material fractures. The fracture opens into a crack. This is called cracking.

Damage scale, damage state, grade. In a scale used to assess the intensity of damage, the several steps are called grades or states. Each state or grade in the scale is based on descriptions of the damage or is classified in combination with a measurement or indicator.

Degradation. It refers to the decrease or worsening of a measure. The strength of masonry can degrade over time, or, its capacity can degrade because of a particular action.

DIC. Digital Image Correlation is a photogrammetry technique where digital photographs are using to measure the displacements or deformations of an object.

Drift. It is the ratio of the lateral, horizontal displacement and the inter-storey height. In this study, the applied displacement at the top of the wall divided by the height of the wall gives the drift. While unitless, it is usually expressed in mm/m.

Extrapolation, exploration. An extrapolation is the conducted when, based on known parameters, new situations are concluded. In this work, models calibrated against specific loads are used to explore the effects or other loads.

Façade, Wall. A façade is one of the outer walls of a building, typically the architecturally most important wall. In this study, 'façade' is used to convey a geometrically more complex wall, typically with a larger area. A 'wall' is thus a simpler façade. Walls are used as a proxy for façades and buildings in this study.

FEM. The finite-element-method subdivides a structural problem in a large but finite number of small pieces or elements that can be analysed independently.

Fragility, vulnerability. The response of a structure or component to a certain hazard, expressed in terms of probability, represents its fragility. At increasing hazard intensity, the probability of failure increases. This relationship is called a fragility or vulnerability curve.

Hastening. The earlier arrival to a certain damage condition because of the contribution of a particular hazard. The damage evolution is accelerated. This concept is central to Chapter 6.

Hazard. A hazard, in structural engineering, refers to any condition, event, or factor that has the potential to cause harm to structures, infrastructure, or the occupants of buildings. Hazards can be natural, like storms, floods, or earthquakes, or anthropogenic, such as terrorist attacks, fires, or traffic. These hazards represent the various risks that can impact the integrity and safety of built environments and the people within them. A hazard is a danger; a multi-hazard involves several hazards. 'Normal' loads, like the design live load for a housing building, consisting of people and furniture, are also hazards; a small probability of overloading by the weight of people exists.

Propagation, initiation. The beginning of cracking in masonry is referred to as the initiation of damage. When cracks lengthen and widen (damage is aggravated), a propagation of the crack is taking place.

Metric, measure. A parameter used to indicate or quantify damage. The width or the extend of cracks, for example, can be a measure of damage. Drift, is often employed as an indirect metric of structural capacity.

NLTHA. Is an acronym for Non Linear Time History Analysis. It is a numerical procedure involving a model with a non-linear material. The load steps become time steps in a dynamic analysis. Usually, a history of a load or acceleration over time is applied to the model. In earthquake engineering, a NLTHA refers to an analysis of an earthquake vibration.

Psi (Ψ). The greek letter Ψ , pronounced /psi/ in greek and not (p)sai in English is used as a continuous damage scale comprising the width, length and number of cracks in a masonry construction. See Chapter 2.

Repetition. A recurrence of an action or an event. The effect of repetition is used to describe the contribution (in terms of damage increase) or a repeating action.

Shear-wall, Pier. In a structural context, when the design of an element is governed by shear, one can speak of a shear element. In buildings with columns and walls, against high lateral loads, walls quickly become shear-walls.

In this study, the wall without openings acts as a shear-wall. The wall with an opening in turn, has two piers next to its opening which fail in flexion.

Shrinkage. The contraction of masonry due to hardening effects of the mortar soon after construction. This is not to be confused with the contraction occurring from temperature changes.

Transitory, transient damage. Refers to temporary damage a structure experiences during specific events, such as earthquakes, which may not reflect its permanent condition. Unlike residual damage, which is long-lasting, transitory damage can change or become less noticeable after the event. Since damage aggravates based on previous damage, using the maximum transitory damage is required.

Wythe. Pronounced exactly as width - is the thickness of a masonry wall. A single-wythe wall has the thickness of a brick. A double-wythe wall has the thickness of two bricks, usually one brick length. In Dutch this can be confusing, because the length of a brick is used as the measure of the thickness of a wall. So, a double-wythe wall is actually a 'full-brick-long'.

Appendix E

Loppersum Visit

On the first of November of 2022 I was in Loppersum for a small conference. The day after I wrote a small note. This is it.



Figure E.1. A street sign with guidance to neighbouring towns. I visited several of these towns over the years.

Memoir uit Loppersum

2 November 2022

Paul Korswagen - TU Delft

I arrived late the night before the first of november and went to sleep in the only hotel I had found listed in Loppersum. That I could see "Ons Dorphuis", the location of the kennistafel that would take place at noon the next day, was both a nice coincidence and an unavoidable circumstance in such a small village.

Because Loppersum is a small town, as I would find out the next morning when I took a two-hour stroll through most of its streets. In the time I was walking around, sometimes checking a map that I didn't need anymore after the first hour, I must have managed to see all the old houses. That is also what makes Loppersum so charismatic. The free-standing houses are all different, some older, some with gables or turtle roofs, almost none with a rectangular footprint. These houses were not built in series and it seems each must have its own stories.

"Do you find the houses so nice?" said an old lady who had been sweeping away the fallen leaves of autumn and had seen me make a few pictures with my phone. It was quite windy, so I'm not sure sweeping the leaves made much sense.

"Yes, they are all different and with character." I replied.

"They give Loppersum the real feeling of a town" she added.

"Yes, you can walk across the town in a few minutes and at the edges you see large green fields" I complemented.

The exchange was in dutch but she didn't ask me where I came from.

"It's really nice despite all our misery" she commented. I didn't reply but looked a bit worried. Did a topic about houses always led to talking about earthquakes?

"With the earthquakes, they created lots of problems. At the end of this street you will see a neighbourhood with new houses. It was needed because our houses are not safe." She explained.

"Oh."

"But now they are starting to strengthen the houses" She pointed at the house across the street. "They will also start with my house. They will keep only the façade and the rest will be replaced. Just like a few houses you will see further ahead if you keep walking".

"Is this your house, it's quite beautiful; I like it". I said

"They will start soon, they have promised."

"But I think that is really a good solution. They are keeping the nice and characteristic part of the houses while making them safe then." I said.

She didn't want to agree. "We started in 2016. It's been a long time until something is happening. I'm 75; I don't think I will be back in that house."

"Oh, you think so?" I didn't know what to say as the conversation turned dark. "I hope that is not the case."

"Well, I have to head back inside. Enjoy Loppersum." The old lady said.

"Thank you and have a nice day." I finished the conversation.

On the same street I saw three houses in scaffolds. Other houses were getting new roof insulation, new bricks, or even solar panels. As I walked around town, I was actually surprised to find at least one container for debris in every street; there were many vans of construction companies.



Figure E.2. Scaffolding on the street.

I didn't see much damage, but I was also not inspecting the masonry from up close. There were cracks around windows, on the piers, above the foundation, and at the corners. In most cases, the cracks were more visible because they

had been repaired and the mortar looked new. They were the same sort of cracks you see when walking around the centre of Delft.

I only saw one case that really pulled my attention. It was a house with lime mortar. It had clearly settled over time but there were no cracks. Below the window, a bedjoint went up to the level of the next bedjoint and then back down; the deformation was plastic and maybe took place over a long time but - no cracks.

The church and its large tower were also being remodelled with safety as a priority. Some houses had windows filled-in with masonry. Is that for strengthening?

Loppersum has a train station that tangentially touches the town. There were houses on both sides with only one street crossing the tracks. I saw a few houses for sale but there were no "sold" stickers attached to the signs.

By the time I circled back to that street in the centre, the old lady was gone and so were the leaves.



Figure E.3. At close inspection, the bed joints appear plastically deformed.

Kennistafel

I had seen the Dorphuis already as I had walked past it a few times. “I saw you go by half an hour ago” said Chris Geurts. Apparently they had come earlier and had been having lunch inside. “Yes, I was walking around and looking at the houses.” I replied.

The kennistafel included two interesting presentations and a round of discussions where everyone present got to tell a bit about what they were doing or where they work and what questions they could add to the topic about preventing damage. Please see the agenda and my technical notes attached to this text.

Two contributions stood out from inhabitants of the region that also worked in related subjects. The first criticised that IMG was thinking about preventing damage when they hadn’t yet addressed the other problems, and added that IMG and NCG should work together more. The second doubted that the strengthening did anything, added that it wasn’t necessary. Both men appeared frustrated with the situation and wanted the topic of earthquakes to be out of their lives. A lady working at a different gemeente was actually quite happy with the strengthening projects.

During the “borrel” at the end of the afternoon, I talked with Jacob Mink from a company that specialises in adding micropiles to houses with foundation problems. I asked about whether they had “bed joint measures” which they did with a total-station instead of water hoses. They also had damage reports and promised to fix the damage by lifting up the settled foundations in specific places. They also always conducted CPTs at the locations.

I explained that we would be very interested to find relationships between deformations in the houses, the soil beneath them, and the damage observed. We exchanged emails but I’m not sure what we could offer them.



Figure E.4. The location of the village hall or community centre.



Figure E.5. Some additional examples of buildings in the town of Loppersum.

Appendix F

Dataset

<https://doi.org/10.4121/58d1f5e6-5db3-4a74-a3d1-6e88a3bd8bce>

PhD dissertations at the TU Delft must provide background research data. Typically, much of the data has been published along side core publications. In this case, experiments have continued and so, earlier data may be segmented or incomplete. For this purpose, a summative dataset is provided.

The data is referenced by the above doi and can also be accessed via this link:



edu.nl/jfe8w

The repository gathers essentially three packages:

1) **ExperimentalData.mat**

Containing measurements from the wall experiments for all masonry wall tests. Including Force, Drift, and Ψ .

2) **Zip files with DIC processed data**

Compressed .csv files with the horizontal (X) and vertical (Z) displacement fields as determined with DIC. Refer to ExperimentalData.mat for folder and file names associated with the experimental data.

3) **ComputationalData.mat**

With the results of the extrapolation models. Tabular Diana output files and processed Ψ values are collected.

A ReadMe file included in the repository details additional metadata.

Appendix G

Tool for Crack Tracking

In the experimental context, crack tracking refers to the technique where an individual crack is detected and recognised as such on a (masonry) sample, and tracked throughout the test. This requires the following:

- Detecting local opening and sliding,
- Gathering neighbouring cracked points into the notion of a single crack,
- Computing the properties of the crack in terms of width and length,
- Recognising the same crack over multiple measurement instances, even as the crack propagates or remains closed at certain instances.

This appendix presents an overview of the Digital Image Correlation technique adapted for this purpose. The validation against 'traditional' sensors is also included.

G.1. Application of DIC for Monitoring of Masonry Test Samples in the Laboratory

Digital Image Correlation (DIC) is a non-contact measurement technique widely utilised in laboratory settings to monitor displacements and deformations in masonry test samples. This method employs digital imaging to capture displacement fields across a specimen by comparing differences between two sequentially captured images. The process identifies differential displacements which are crucial for detecting and analysing the progression of cracks in masonry structures. DIC offers two primary advantages over traditional displacement measurement techniques:

- Non-contact Measurement: Reduces the risk of damaging sensitive equipment and minimises interference with the specimen under test, such as obscuring potential cracks.
- Capable of tracking a large number of points simultaneously on the sample's surface, providing a comprehensive view of displacements and facilitating detailed analysis of crack propagation.

This technique is adaptable to various scales and complexities of structural testing, from small components to large masonry walls, and can be implemented in both two-dimensional and three-dimensional formats. DIC's flexibility and precision make it particularly useful for the challenges posed by masonry testing where traditional sensors may fail to capture unforeseen crack locations and behaviours. In this work, DIC has been used only on planar surface to monitor in-plane displacements.

Implementation and Optimisation in the Laboratory

Developed in-house, this specific DIC system aims to maximise the resolution of displacement fields. This development focuses on enhancing the clarity of detected discontinuities, such as cracks, while maintaining reasonable computation times and utilising straightforward photographic equipment.

In a structural mechanics lab environment, where the accurate measurement of forces and displacements is essential, DIC proves invaluable. Traditional sensors, such as Linear Variable Differential Transformers (LVDTs), are effective for monitoring specific crack movements but are limited by their need for direct contact and fixed placement. DIC overcomes these limitations by using photogrammetry to evaluate the entire specimen, enabling the detection of crack initiation and progress over a large area and at numerous points.

Technical Advantages and Laboratory Application

DIC has been successfully applied to various masonry tests to detect and monitor cracks (Tung et al. 2008; Ghorbani et al. 2015). Its application ranges from detecting small-scale discontinuities to tracking large-scale deformations across the entire specimen. Optimisations specific to our laboratory's needs include refining the correlation algorithms and speckle patterns—the latter being crucial for accurately capturing the displacements. Gehri et al. (2020) worked on similar improvements.

Further, the system's design ensures that it can capture a dense array of displacement points, allowing for the detailed mapping of cracks as they develop. Such comprehensive monitoring is crucial to understanding the behaviour of masonry under test conditions, particularly in assessing the material's response to stress and identifying potential failure points.

The following sections will discuss the specific capabilities of DIC in producing various types of plots and visual representations, the theoretical foundation of the technique, and the practical implementations of the hardware and software systems supporting it. Each of these aspects plays a critical role in harnessing the full potential of DIC for structural analysis and research.

G.2. Theory and Programming of DIC

Basic Concepts

Digital Image Correlation involves capturing digital photos of the sample at specific intervals. These images are used in the correlation process to determine the displacement field of the sample. Depending on the desired accuracy and scale of the test, one or more cameras may be required, and a special pattern might need to be applied to the sample to facilitate accurate tracking.

Subsets and Gridpoints

The correlation process starts with an initial or 'base' image that serves as the reference to which subsequent images are compared. The base image is divided into smaller sections called 'subsets', which are then located in the subsequent images. If the subsets remain unchanged, they are found in the same positions; if not, their movements indicate displacements.

Four assumptions can be made when tracking subsets:

- The subsets have displaced without rotating and deforming.
- The subsets have displaced and rotated.
- The subsets have displaced, rotated, and deformed.
- Alternatively, the subsets are destroyed and cannot reasonably be found.

For masonry testing in our laboratory, the assumption typically holds that subsets undergo minimal rotation and no deformation, reflecting the brittle nature of masonry and the small-scale displacements observed. In in-plane tests, where only horizontal and vertical movements are relevant, the problem simplifies further, requiring potentially only one camera and treating the situation as two-dimensional.

Search Zone and Grid Size

The 'search zone' limits where the subsets are expected to be found, speeding up the computation by reducing the area of search. This is useful when dealing with small displacements typically seen in masonry tests.

The output of the DIC process is not continuous across the specimen but instead focuses on specific 'gridpoints' within the defined 'area of interest'. The accuracy and resolution of the correlation depend on the size of the subsets and the density of the gridpoints, which in turn are influenced by the quality and resolution of the images used. See Figure G.2.1 for an overview of these terms.

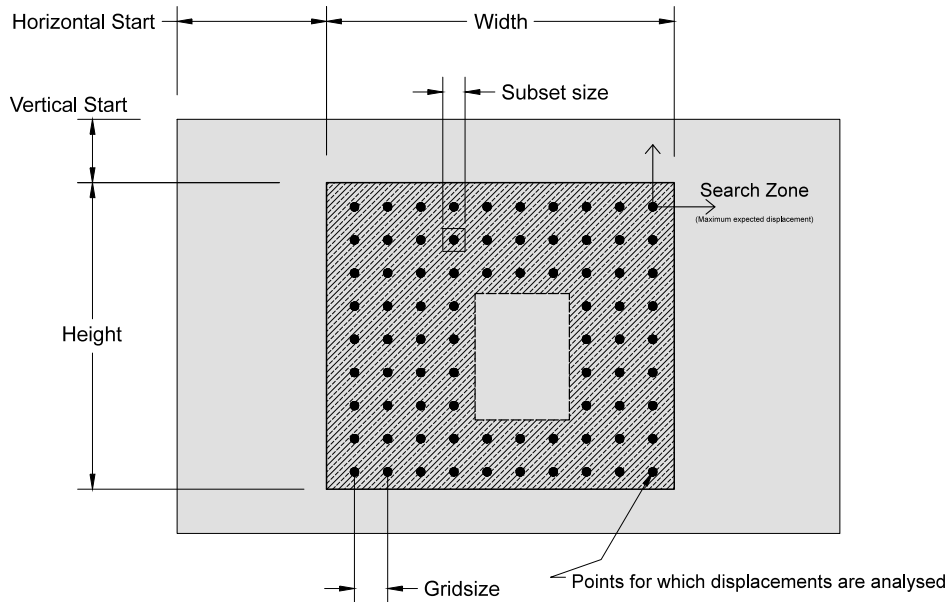


Figure G.2.1. Scheme of main parameters. Area of interest (with an opening) within the image.

Solution Algorithm

Image correlation in DIC can be approached in various ways, but the most straightforward and effective method for detecting cracks in masonry involves treating each subset independently. This discrete method compares potential positions of a subset in sequential images, selecting the position that maximises the Pearson correlation coefficient.

To achieve sub-pixel accuracy, necessary for detecting minute displacements, interpolation techniques are used. This allows DIC to precisely determine how much a subset has moved, even if the displacement is less than the size of a pixel.

Moreover, since the correlation of each point is independent of any other point in the image, multiple points can be solved simultaneously. On multi-processor or multi-core systems the correlation of a single image can be significantly sped up. This is particularly advantageous when using DIC to assist in laboratory testing where the processing of a single image must occur as fast as possible.

Crack Detection

1. Initial Detection of Discontinuities

The DIC algorithm begins with the detection of discontinuities in the displacement fields generated from the series of images captured during

testing. This step is crucial for identifying potential cracks before more detailed analysis takes place.

- Subsets Analysis: Each image is divided into subsets. The algorithm compares these subsets between successive images to detect shifts that indicate displacements both vertically and horizontally.
- Gradient Thresholding: By calculating the gradients of displacement between these subsets, the algorithm can highlight areas with abrupt changes, which often signify the edges of cracks.
- Noise Reduction: To distinguish genuine cracks from noise, a filtering process is applied, often utilising morphological operations that enhance the features of interest while suppressing irrelevant variations.

If the results are imported directly from computational exports, a third input matrix is expected already containing the discontinuities (crack width) per cell. From here on, both experimental (laboratory) and computational (FEM) cases are treated equally by the program.

2. Grouping of Discontinuities

Once potential cracks are identified, the next step involves grouping these discontinuities to form coherent crack patterns. This phase is critical for mapping the entire crack trajectory across the specimen.

- Spatial Clustering: Discontinuities that are spatially close to each other and align in a pattern suggestive of a crack are grouped together.
- Connectivity Analysis: The algorithm employs connectivity criteria, where adjacent pixels showing similar displacement anomalies are linked to form continuous lines or curves, reflecting the crack path.

Neighbouring cells with discontinuities are assigned a crack number. The grouping algorithm executes a line scan in two directions and checks whether a cell with a discontinuity value neighbours other "cracked" cells. If it does, then it receives the crack number of neighbouring cells, if the neighbouring cells do not have a crack number yet, a new crack number is created. The coordinates of every cell with the same crack number is registered in a matrix for this crack number.

Because the line scan moves forward, it may fail to group cracks in a certain pattern. It is thus necessary to iteratively look for and merge neighbouring groups. The algorithm compares a random coordinate of crack 1 with a random coordinate of crack 2. If they are found to be relatively close, all coordinates of crack 1 are compared to every coordinate of crack 2; if any are found to be

neighbouring (the comparison stops here), the matrices of coordinates are merged, crack 2 is removed from the list of valid crack numbers, and the matrix with crack numbers per cell is overwritten for all coordinates of crack 2. This is done for all valid crack numbers without repeating any crack number combinations. After all cracks have been compared, the process is run again to further merge nearby groups of discontinuities. The merge iterations continue until no more groups can be merged, or up to a customisable limit number of runs.

The final output of this module are: a few matrices containing the coordinates of all the cells that belong to each group, the main matrix with the crack number of each cell, and a list with all valid crack numbers.

3. Removal of crack noise

The following groups of cells (cracks) are considered noise and eliminated from the list with valid crack numbers:

- Groups with a few cells (customisable, the minimum is 1).
- Groups forming a crack with a length shorter than specified (default 100mm).
- Groups forming a shape resembling a circle, spot, or cloud.
- Cracks appearing in less than 1% of the number of images (when multiple cases are analysed).

4. Refinement and Characterisation of Cracks

After initial grouping, further refinement is necessary to accurately characterise each crack, determining its width, length, and orientation.

- Width Calculation: The width of each detected crack is estimated by measuring the gap between the displacement fields on either side of the crack. This measurement considers the highest displacement gradients to define the crack.
- Length and Orientation: The overall length of the crack and its orientation are determined by tracking the grouped discontinuities from one end to the other. Advanced algorithms calculate the geometric centre-line of the crack and use it to define these parameters.
- Ψ based on number, width and length of cracks.

5. Validation and Tracking

For dynamic tests where images are captured over time under varying loads, the algorithm tracks the development of each crack across the image series.

This involves identifying and linking the same crack across different images, observing changes in its length, width, and direction.

If multiple cases are evaluated, it is possible to unify the results by uniquely identifying cracks throughout the cases. This is done by comparing the coordinates of each crack and merging of the crack data in time. The process is retroactive, meaning that if two cracks eventually extend into one, they are identified as a single crack from the beginning.

The crack progression data is exported as a spreadsheet and as graphs. Width, length, and damage progression graphs can also be exported. Additionally, a spreadsheet file with multiple sheets (one for general properties and one for each crack), and a graph showing the nomenclature of cracks is exported. Furthermore, "trail plots" will be computed and exported. These plots show the width of the crack along its entire length and reveal progression by the darkening of colour. It is possible that individual lines in these plots are outliers, but the general behaviour can be quite interesting.

Moreover, crack surfaces and all the data above are exported into a "crack output" file that can be read with a separate application. This small application allows the visualisation and animation of crack data in 3D.

6. Quantitative Analysis and Reporting

The final phase involves quantitative analysis and the generation of reports that provide detailed information about the detected cracks.

- Quantitative Metrics: Detailed metrics such as crack width, total crack length, and average width are computed, providing valuable insights into the overall integrity and deterioration of the specimen.
- Visualisation: Visual reports are generated, often overlaying detected cracks on the original images or providing schematic representations of the cracks. These visualisations are crucial for both technical assessments and presentations to non-specialist stakeholders.
- Data Export: For further analysis or archival purposes, the crack data, along with associated metrics, are exported in formats compatible with other engineering analysis tools.

Software and Tools

The DIC software developed for our laboratory applications is capable of running multi-processor or multi-core systems to expedite the analysis of large image files. It includes functionalities for loading images, defining coordinates,

and exporting results in various formats, including graphical plots and data files.

FemPsi

In parallel with the custom DIC solution, a program to import FEM results and process cracking was also formulated. The program is called FemPsi. Since finite-element-model results already include crack width information at the integration point level, collected at every load step. Adapting the DIC code, which consolidates cracked points into the notion of a crack and tracks each crack over time, was trivial. The aforementioned steps, from 2 to 6, are virtually unchanged.

G.3. Optimisation and Calibration of DIC

Optimisation of the DIC Setup

Optimising the DIC setup is critical for achieving precise and reliable measurements. This section covers the integral components of the setup, from the pattern applied on the specimens to the camera configurations used for capturing images.

Pattern Layout

The clarity and uniqueness of the speckle pattern on the test specimen are essential for accurate DIC analysis. The pattern must provide sufficient contrast and sharpness for the DIC software to track movements accurately.

- For Small Samples: When working with smaller specimens, a finely detailed pattern can be created using sponges or foam rollers with viscous paint. In scenarios where masonry joints are recessed, techniques like sandblasting with fresh paint or applying matte glue are used to achieve a controllable pattern granularity. A spray gun with an adjustable nozzle can also produce an adequate pattern.

- For Larger Specimens: Techniques suitable for smaller samples do not scale well to larger specimens such as full masonry walls. Here, larger, more distinct patterns applied via positive or negative moulds are necessary. These patterns must be sizeable enough to be trackable from a distance but small enough to ensure small subsets and enable high-resolution data capture. The ideal pattern involves shapes spaced 4 to 6 pixels apart, with each subset comprising at least 10x10 pixels to ensure a trackable and unique pattern.

Example: Figure G.3.1 presents a portion of a masonry wall featuring a coarse pattern using a positive mould at the top and a finer pattern with a negative mould at the bottom. The coarse pattern requires larger subsets (25x25 pixels), whereas the finer pattern allows for smaller subsets (12x12 pixels), enhancing the resolution of the displacement field.

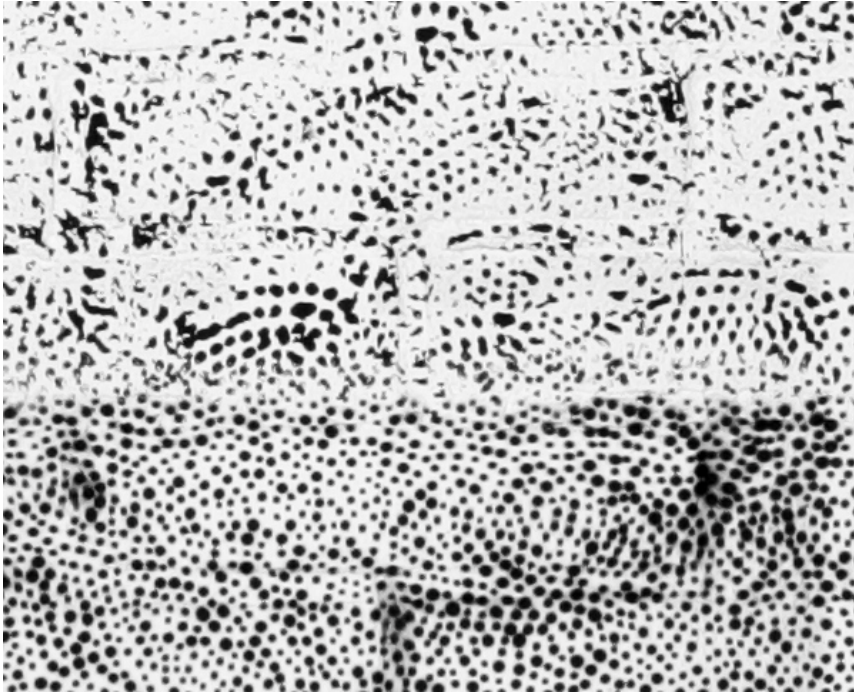


Figure G.3.1. Comparison between two speckle patterns.

Camera Setup

Optimal camera setup is paramount for capturing clear and usable images for DIC processing.

- The specimen should be centrally framed in the camera's viewfinder to ensure consistent imaging and minimise lens distortion.
- Alignment is critical, especially for in-plane displacement analysis. The camera's sensor plane must be parallel to the specimen's plane. For vertical walls, this might involve using a tripod with a level. A small mirror placed on the specimen can help verify this alignment by reflecting the camera lens when perfectly parallel.
- Uniform lighting is crucial to minimise shadows and reflections. This can be achieved using flashes, DC lamps, screens, or reflectors. Proper lighting ensures consistent image quality unaffected by natural light variations.
- A high-resolution camera with a sharp prime lens is recommended. Natural focal lengths (50mm for 35mm equivalent) are ideal, though slightly wider lenses (35mm) may be necessary for large specimens.
- The camera should be mounted on a tripod and operated either with a timer or remotely to prevent shaking.

- Manual camera settings are crucial:
 - ISO: Set as low as possible to reduce noise.
 - Focus: Manually adjusted and locked.
 - Aperture: Around f/8.0 to optimise depth of field and sharpness.
 - Exposure: Adjusted via flash or shutter settings to maximise pattern contrast.

Additional settings such as mirror lockup, JPEG compression settings, and black-and-white modes can further enhance image quality.

Understanding Noise and Error

Noise and error can significantly affect the quality of DIC results. These can arise from various sources, such as camera sensor issues, environmental factors like dust or temperature changes, and inherent limitations in the image processing algorithms. Systematic calibration and the use of sophisticated noise-reduction algorithms are essential for minimising these effects and ensuring the integrity of the displacement data obtained from DIC.

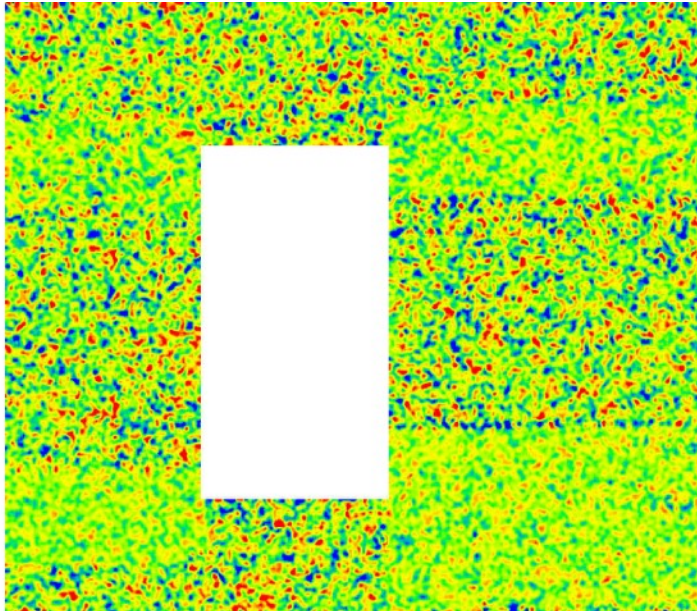


Figure G.3.2. Random noise with a maximum error of 0.025 pixels when analysing two images of zero displacement. Areas with a good pattern result in significantly less noise (around 0.01 pixels).

Calibration is crucial in ensuring that the Digital Image Correlation system provides accurate and reliable measurements. This process involves comparing

DIC results with known standards or other validated measurement techniques under controlled test conditions. Here, we detail the types of calibration tests performed, the methodologies applied, and the key considerations for each.

Test Configurations and Methodology

Calibration tests are designed to closely mimic expected real-experiment conditions but within a controlled environment to precisely evaluate the performance of the DIC system. Each test aims to validate different aspects of the DIC system—from its ability to detect small displacements to its precision in tracking complex deformations.

1. Sliding Test (Linear Displacement)

Objective: To assess the system's accuracy in detecting linear displacements.

Setup: Two plates, each painted with a high-contrast DIC pattern, are arranged in parallel. One plate remains fixed while the other slides linearly along a track, simulating straightforward, controlled displacement.

Measurement: Displacement between the plates is measured using both DIC and traditional linear displacement sensors (e.g., LVDTs) attached to the back of the moving plate.

Analysis: Comparisons are made between the sensor readings and DIC measurements to determine the system's accuracy. The consistency of these measurements across multiple trials helps identify any systematic errors or biases in the DIC setup.

On the back of the plates are sensors that measure the rotation of the upper plate with respect to the lower one. The first step is to perform the test keeping the steel plates against which the sensors react perfectly parallel to the opening. During the test a picture is taken every 0.1 mm, then a comparison between the sensor reading and the DIC is performed. Also during this test, it can be observed that the overlapping between the two curves is very good with an error of $\pm 0.01\text{mm}$ and a standard deviation equal to 0.01.

2. Rotation Test (Angular Displacement)

Objective: To evaluate the DIC system's capacity to measure angular displacements. **Setup:** Similar to the sliding test but with the moving plate able to rotate around a hinge. **Measurement:** Angular displacement is quantified using linear sensors fixed relative to the hinge point, alongside DIC measurements.

Sensor 1 is the closest to the hinge thus showing the lowest displacement, while sensor 3 is the one subjected to the biggest opening.

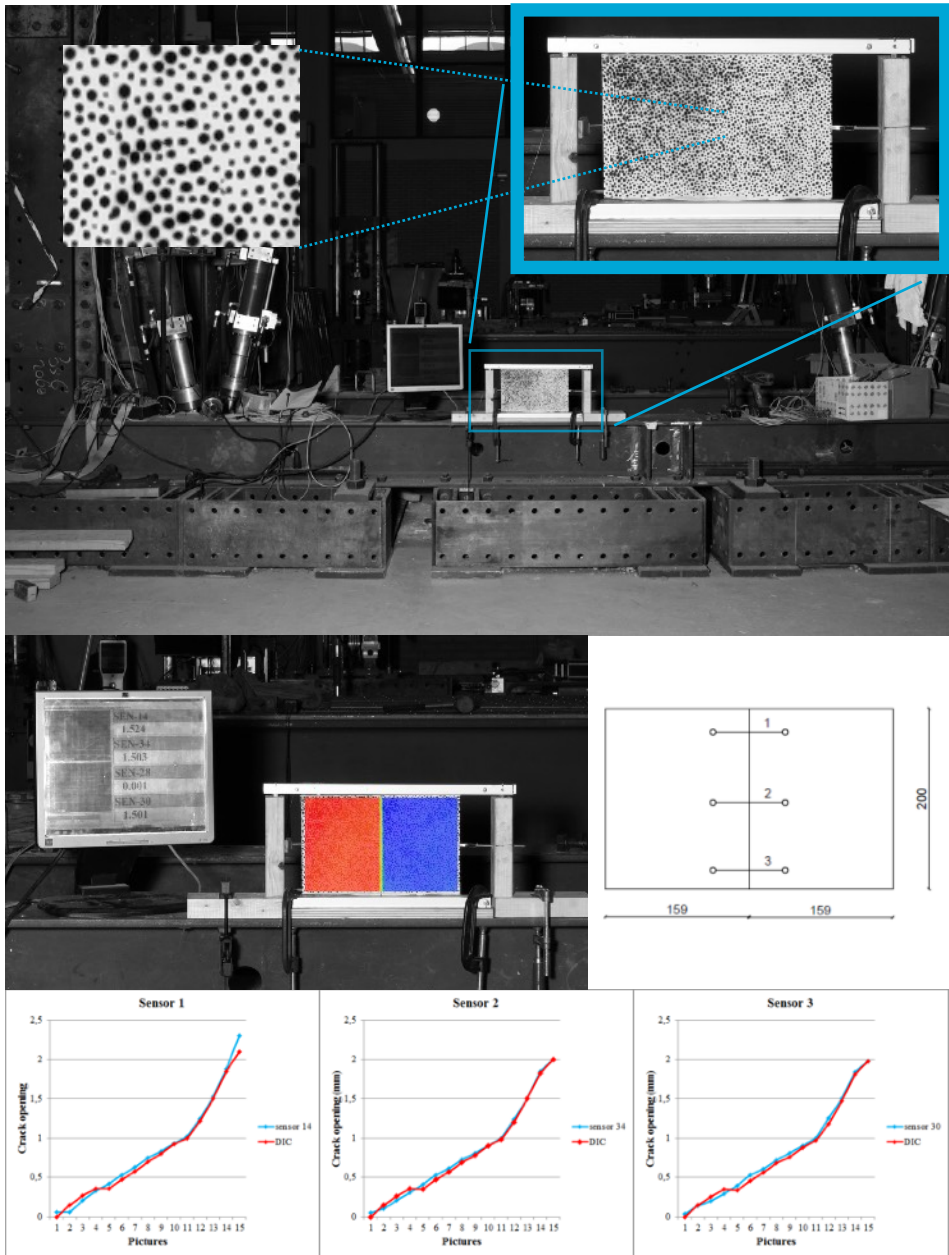


Figure G.3.3. Setup and results of the sliding test. Note the size of the pattern relative to the photo frame and the actual resolution of the image. The camera was placed at the same distance as during the tests on masonry walls. The picture appears dark but lightning is optimised for the portion with the pattern.

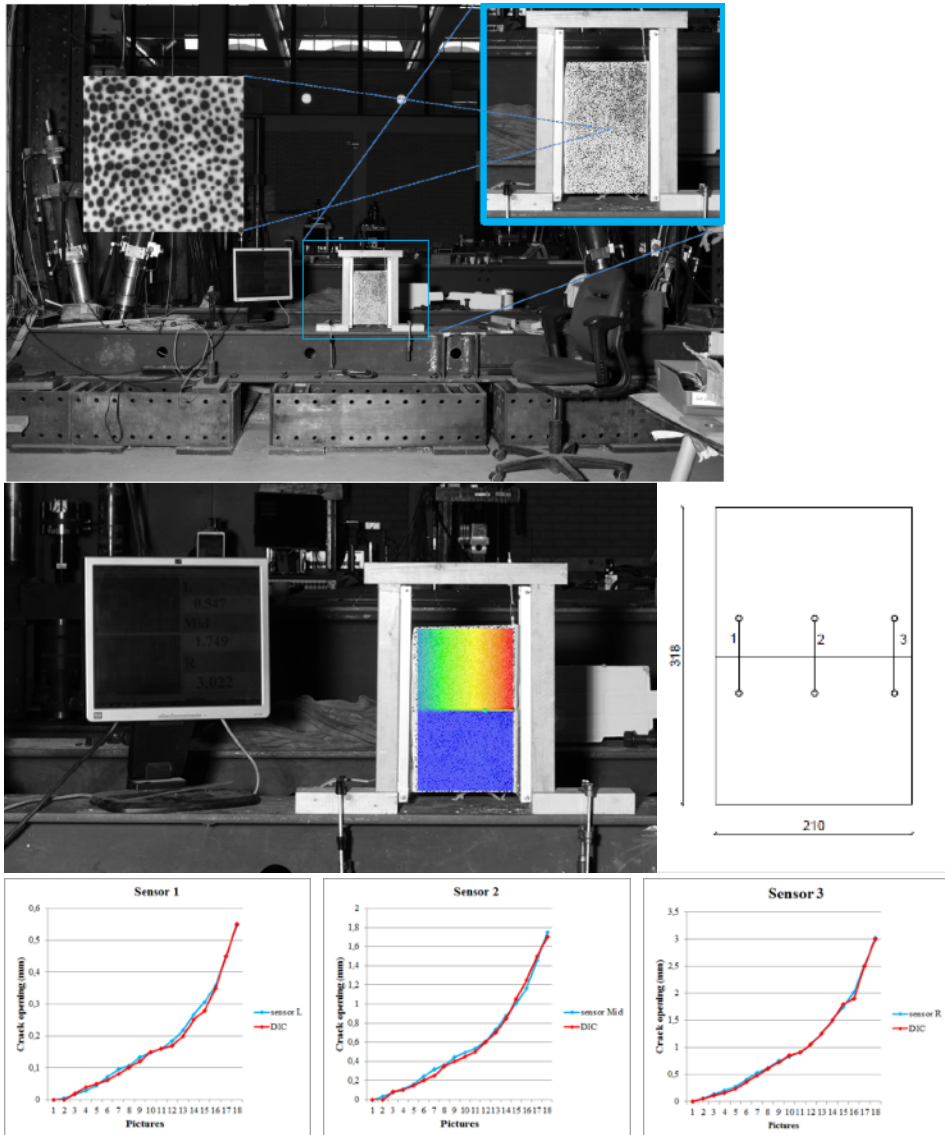


Figure G.3.4. Rotation test.

Calibration Outcomes and Adjustments

The results from these calibration tests are critical for fine-tuning the DIC system:

- Direct comparisons between DIC readings and sensor data allow for adjustments in software algorithms and imaging techniques, ensuring that DIC can offer reliable measurements across a range of conditions.

- Findings from calibration tests can lead to improvements in hardware setups, such as adjustments in camera angles, lighting configurations, or changes in the speckle pattern to enhance measurement precision.
- Calibration helps in identifying and quantifying potential sources of error, such as optical distortions, environmental influences on sensors, or algorithmic biases in image processing.

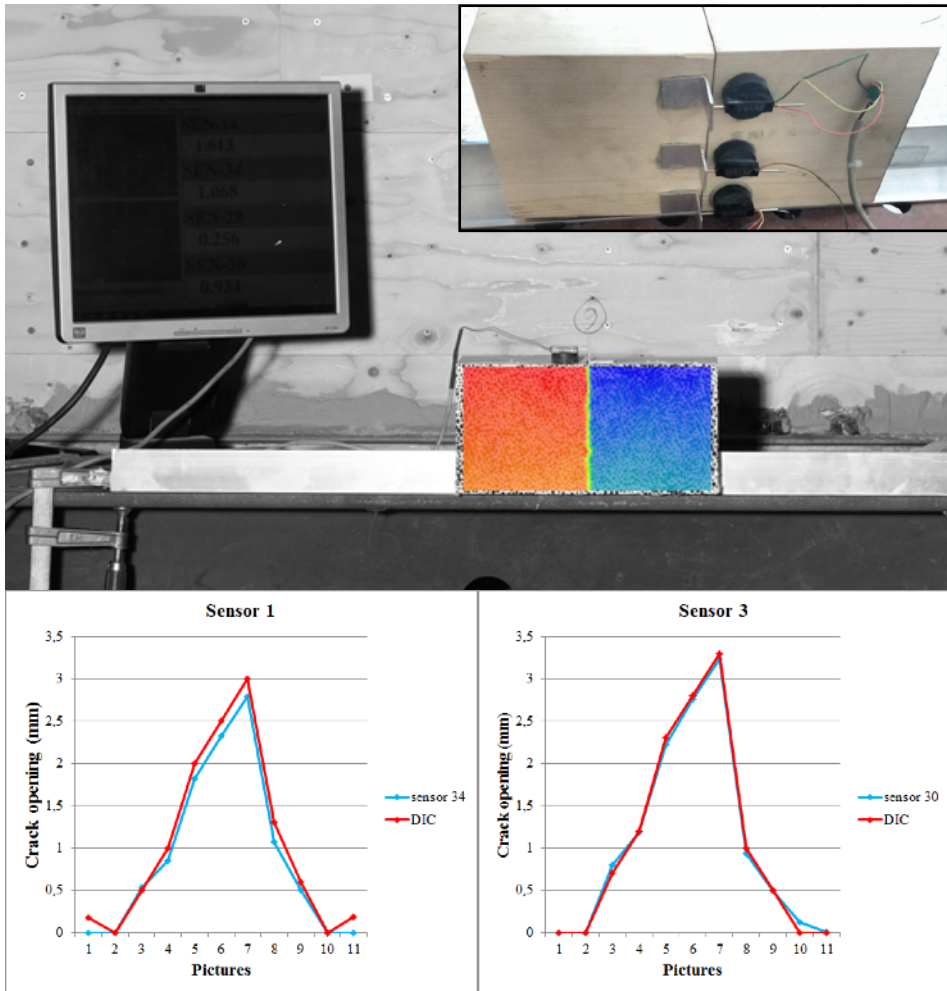


Figure G.3.5. Free sliding and rotation test on a thicker timber block.

Future Directions

Ongoing calibration is essential as the DIC system evolves with technological advancements and as new applications emerge. Enhanced calibration routines, possibly incorporating machine learning algorithms for error correction and

adaptive thresholding, could further improve the reliability and accuracy of DIC measurements. Moreover, extending calibration protocols to include three-dimensional analysis will broaden the applicability of DIC in complex structural assessments and dynamic testing environments.

In conclusion, meticulous calibration is integral to leveraging the full capabilities of DIC technology in structural engineering, ensuring that the data obtained is both accurate and actionable for diagnostic and research purposes.

Curriculum Vitæ

- 13 May 1988 Born in Lima, Perú
Parents: Dr. Liliana M.I. Eguren Corso
 Prof.dr. Richard P. Korswagen Edery
- 2007 — 2012 Bachelor of Science (BSc)
 mention in Civil Engineering
 Pontificia Universidad Católica del Perú (PUCP), Lima, Perú
- 2012 Title Civil Engineer (Ing.)
 Pontificia Universidad Católica del Perú (PUCP), Lima, Perú
Thesis: Seismic Isolation of Buildings
- 2012 — 2014 Structural Design Engineer
 Antonio Blanco Blasco Ingenieros EIRL, Lima, Perú
- 2014 — 2016 Master of Science (MSc) in Civil Engineering
 Specialisation: Structural Engineering / Hydraulic Structures
 Delft University of Technology (TU Delft), The Netherlands
Thesis: Structural Damage to Masonry Housing due to
 Earthquake-Flood Multi-hazards
- 2017 — 2024 PhD in Structural Mechanics
 Delft University of Technology (TU Delft), The Netherlands
Thesis: Quantifying the probability of light damage to
 masonry structures
Promotors: Prof.dr.ir. Jan G.Rots
 Dr. ir. Karel C. Terwel

PROPOSITIONS

accompanying this dissertation

1. The probability of visible damage or noticeable damage aggravation at the perimeter of the Groningen buffer zone due to earthquake vibrations does not exceed 1% even for masonry walls with pre-existing cracks. (*)
2. Repetition of light vibrations, as in the Groningen field, can lead to a damage increase of up to 10%. (*)
3. Damage that is not defined, cannot be measured. (*)
4. Light damage only matters if someone else is responsible.
5. Heating buildings is an archaic practice. With modern insulation and conscious design, buildings wouldn't need any active heating.
6. The only way to solve a housing crisis is to create more housing: adapt existing buildings into housing and build more and affordable houses, too.
7. Without understanding and quantifying the risk to buildings, new technologies, like geothermal energy, should not be deployed.
8. Masonry can be the most sustainable of building materials.
9. It is more important to formulate a clear path and skip some steps than to stop at each step exhaustively and not reach the end.
10. When life doesn't let you pursue your hobbies, like photography, then adapt them, like photogrammetry.

() These propositions pertain to the dissertation.*

These propositions are regarded as opposable and defensible, and have been approved as such by the promotor **Prof.dr.ir Jan G. Rots** and the co-promotor **Dr.ir. Karel C. Terwel**.

Acknowledgements

This research was performed as part of several projects. It began as a study for NAM and NCG. Later, a PhD project was conceived from this research. It was mainly funded by NAM, in management by **Jan van Elk** and **Jeroen Uilendreef**. Their feedback and confirmation during spaced progress meetings I still value today. In this part of the project, guidance was provided also by **Beatriz Zapico Blanco** and **Michele Palmieri** from ARUP, who helped simplify difficult choices. A parallel project from NAM, focused on analysing the structural capacity of NeHoBo floors, was helpful in advancing modelling strategies and characterising experiments in the lab; for their feedback and guidance, I am thankful to **Dick den Hertog** and **Reza Sarkhosh**, and for her collaboration, to **Valentina Mariani**.

Later, my PhD benefited greatly from our collaboration with IMG in the project *Advies Schadebeoordeling IMG*. Several people from IMG must be acknowledged: **Bas Schultze** for his leadership role, **Thijs Franssen** for his legal perspective, and **Herke Stuit** for his guidance and supervision. This part of the project was also conducted in collaboration with TNO; the interaction with TNO is extensive. I must thank **Chris Geurts** for his ideas about my work, **Davide Moretti** for some interesting questions, and **Huibert Borsje** for his lectures on the practical side of damage assessment. Some of his lectures were part of the Kennistafels organised by BuildinG, to which I was also invited to speak by **Jelle Pama**. The feedback by **Arie Koot**, from Zonneveld, supervising projects with IMG, is also appreciated.

Similarly, **Piet van Staalduinen** has been continuously involved with the project in one way or another, initially via his supervisory role in the NAM project, then with a small collaboration (from my side) into the project *Onderzoek naar de oorzaken van bouwkundige schade* in Groningen, funded by NCG. Later, we worked together while defining a strategy for soil-structure interaction, and he was present even during my Go/NoGo meeting. In his involvement with the Commissie Mijnbouwschade and advisor for IMG, he has kept track of most of my work. Piet's critical feedback and recurrent praise for my work is greatly appreciated. Thanks are also given to **Pieter van Gelder** for the useful feedback at my Go/NoGo.

Foremost, great thanks must go to **Michele Longo**. It is not without reason that he is co-author in the majority of my papers; the *Maestro* Michele has been the driving force behind most of the FE models I've used in this work. While we discussed together much of the conceptualising work to define the models,

Michele took to himself the actual implementation of them, struggling with DIANA and our limited computational resources. The capability to run batches of models automatically was only possible due to his efforts. Without his contribution, the results needed to understand damage, would be missing. Much of the calibration of models against the experiments is thanks to Michele; hereby my deep appreciation.

The early experiments could only have been realised thanks to the organising and execution work of **Edwin Meulman**. The initial interpretation of these experiments was conducted by him. Much of what I learned about working in the lab is thanks to Edwin. Our collaboration in the NeHoBo project was also enriching for me and is much appreciated.

Of course, several people are to be thanked for my possibility to follow a PhD. Principally, **Jan Rots**, who has been a leading figure since the beginning. Jan's feedback, brainstorming, and teachings have been a constant motivation for me. Especially his insightful questions, to which he often already knew the answers, have been helpful to me. His role as promotor, trust in my work, praise of my writing, and alignment with my vision, have made sure this project became a success.

Similarly, **Karel Terwel**, who also supervised my MSc graduation project, is to be thanked for my decision to proceed with research. Without his encouragement, I would be doing something else. During the research, Karel provided expert judgment on damage forensics; in the later stages of my PhD, his quick feedback helped shape my results and conclusions in meaningful ways.

Also **Bas Jonkman** had a hand in steering me towards research and ultimately a PhD; this is greatly appreciated. Moreover, during my work at the university, I have been involved in other projects, specifically at the hydraulic section. Here I also looked at the behaviour of masonry buildings during floods. The collaboration with **Jeremy Bricker**, and **M. Andres Diaz-Loaiza** was rewarding for me. For the experiments at Flood Proof Holland I must also thank **Jean-Paul de Garde** and **Lindsey Schwidder**. Moreover, the cooperation with **Karin de Bruijn**, from Deltares, is well appreciated.

During my involvement with the hydraulic section, I also worked with **Davide Wüthrich**. We traveled to Germany to look at building damage. This also resulted in a collaboration with **Jan Oetjen** and **Harish Selvam** from the Rheinisch Westfälische Technische Hochschule Aachen. Their perspective in building damage and hydraulics is valued.

Furthermore, much of the late experimental work wouldn't have been possible without **Maria Belen Gaggero**. Belen took over my ideas about self-healing mortar and structural strengthening with glass, and, for the self-healing process, she made them her own. For assessing the effect of the glass-timber window, she conducted tests on masonry walls, which have been invaluable for my research, too. Coordinating laboratory work without her help would have been much more demanding. Moreover, she participated in my course in the Bend & Break minor, where she taught the students about bond-wrench tests. Belen's presence in our office was always uplifting. Her organisation skills were also inspiring for me. For all of this, I am very grateful.

Similarly, **Alfonso Prosperi** is to be thanked for many a brainstorming session, for his review/testing of my code and critical observations about some of my results. Our off-topic discussions were always a welcome distraction on our way to the coffee machine. I also thank Alfonso for giving me the challenge of guidance; this has helped me become a better supervisor. In a similar way, I am thankful to the many **MSc students** that have allowed me to coach them during their projects.

Naturally, laboratory experiments wouldn't have been possible without the support of the **Lab Staff**. In particular, **Georgios Stamoulis** and **Kees van Beek** have been instrumental in conducting the tests and providing advice over important choices. **John Hermesen**, with his dry humour and expertise in metal fabrication, and **Ruben Kunz**, with his invaluable timber skills, are also acknowledged. Management by **Peter de Vries**, who also provided useful ideas and suggestions, is appreciated, too. Early experiments were also possible only due to the help of **Lucia Licciardello**, **Carlijn van Hoogdalem**, and **Jakub Pawlowicz**. Finally, the professional mason, **Oscar Storm**, responsible for much of our replicated masonry samples, is also thanked. Student assistants **Andrea Gena**, **Tu Martin**, **Qingpeng Li**, **Sneha Kasturi**, and **Robin Straathof** are also acknowledged. Experimental work also benefitted from interactions with **Michele Mirra** and **Geert Ravenshorst**, from whom I learned about timber structures and its connections to masonry.

Some collaborations were also international. I was invited by the **EUCENTRE** to use DIC on one of their specimens. I am thankful to the team at the time, and especially to **Francesco Graziotti** for some small discussions. Moreover, with the University of Bologna, we have had several visiting MSc students; I am thankful to **Giovanni Castellazzi** for the joint supervision of these students, together with **Anjali Mehrotra**, who was a member of our group as of recently.

Indeed, I am thankful to the group of **Structural Mechanics** for having been my professional family during this period. I cannot mention everyone individually

but will emphasise instead the many fruitful discussions and collaborations: **Rita Esposito**, for her committed suggestions and ideas on material characterisation; **Francesco Messali**, for his interest in the project and for other discussions on typology approaches for NEN; **Manimaran Pari**, for his work on SLA and on recent CaSi models; and, **Marianthi Sousamli**, for our collaboration in the soil-structure interaction interface and the various conversations about modelling. In particular, the work of **Samira Jafari** has been exceedingly useful.

Similarly, thanks are given to the **entire department** of Materials, Mechanics, Management and Design (3MD) for the many spontaneous conversations in our hallways, the department dinners, and the team-building activities at the beach or in the city. Thanks go to **Jaap Meijer**, for always being available with knowledge about the logistics of the university, to **Iris Nederhof**, for much administrative work, and to the other support and secretary staff for all their help. I'm also thankful to **Bert Sluijs** for his leadership of the department during most of the time I was busy with this project.

Furthermore, thanks are due to many colleagues, with whom I also collaborated or consulted within the group, the department or the faculty: **Marteen Bakker**, for the coordination of the B&B minor; **Karel van Dalen**, for his advice about dynamics; **Giorgia Giardina**, for her previous work into masonry cracking; **Max Hendriks**, for his help in supervising students and involving me in concrete topics; **Pierre Hoogenboom**, for his expertise with the graphical method for forces; **Mandy Korff**, for her mastery of geotechnics and supervision; **Roderik Lindenbergh**, for including me in the graduation projects of geoscience students; **Sander Pasterkamp**, for his knowledge about building codes and building practice; and, **Roel Schipper**, for his insight about damage and supervising students.

In addition, I would like to thank the **Graduate School** for its role in my doctoral education. The programme and courses it organised have been a constructive contribution to my schooling. Similarly, the **support staff** at the university, including the ICT section, financial division, and facility management, are thanked.

I am also thankful to the many **academics and professionals** I have met at several international **conferences**. They are too many to mention without forgetting someone, so I will refrain to specify. Instead, I would like to highlight the many interesting presentations, our discussions about the state-of-the-art or about life around the globe, our joint travels and visits to new places; these have all been extremely enriching.

Further, I would like to thank my partner, **Luka**, who has been supportive throughout my entire PhD trajectory. Likewise, my **friends and family**, who have provided a necessary respite when it was due. Finally, I would like to thank my **parents**, who were the main inspiration for my commitment to a PhD, especially my **mother**, who I am sure would be proud today.

Extended Table of Contents

For quick searching in the physical version of this book, this extended table of contents is provided at the end.

Abstract	I
Table of Contents	II
Summary	VII
English	
Samenvatting	XXI
Dutch	
Chapter 1	1
Introduction	
1.1. Relevance.....	2
1.1.1. Societal Relevance	2
1.1.2. Scientific Relevance	2
1.2. State of the Art and Knowledge Gaps.....	4
1.2.1. Literature and its Limitations	4
1.2.2. Knowledge Gaps	6
1.3. Research Objective	8
1.4. Research Methodology.....	9
Chapter 2	13
Damage Metric for Masonry Cracking	
2.1. Background and Introduction	15
2.1.1. Necessity for Objective Measurement	16
2.1.2. Damage in Masonry	16
2.1.3. Fracture Mechanics and Cracks-based Damage	19
2.1.4. Visible Cracks and Visibly Aggravated Cracks	22
2.1.5. Limitations of Existing Approaches	24
2.2. The Ψ Damage Parameter.....	28
2.2.1. Damage Classification Based on Visibility and Ease of Repair	28
2.2.2. Cost of Repair	29
2.2.3. Proposal for Ψ Damage Intensity Parameter	32

2.2.4. Thresholds for Ψ , $\Delta\Psi$, and Their Meaning	35
2.2.5. Agglomeration of Ψ	39
2.2.6. Perception of Damage and Ψ	39
2.3. Utilisation: Examples of Application of Ψ	41
2.3.1. Ψ in Experiments surveyed with Digital Image Correlation	41
2.3.2. Damage Aggravation by $\Delta\Psi$ in Finite Element Models	44
2.3.3. Predictions with Ψ	46
2.4. Discussion	47
2.4.1. Transitory and Residual Damage	47
2.4.2. Summary of Advantages, Disadvantages and Limitations	48
2.4.3. Potential Future Improvements	49
2.4.4. Relevance of Ψ for Modelling and for Real Life Uses	51
2.5. Conclusions about Ψ , $\Delta\Psi$, Ψ_0	51
Chapter 3	53
Experiments to Characterise Cracks	
3.1. Definition of Experiments to Investigate Light Damage.....	55
3.1.1. Loading Protocol for Light Damage and Evaluating Repetition	56
3.1.2. DIC Monitoring System for Experimental Crack-Based Damage	63
3.1.3. Overview of the Tests Performed from 2017 to 2024	68
3.2. Results from Experiments on Walls and Spandrels	73
3.2.1. Summary of Results on Wall Tests	73
3.2.2. Summary of Results on Spandrel Tests	79
3.2.3. Lessons about Crack Propagation	84
3.2.4. Conclusions about Crack Propagation	91
3.2.5. Four Ways to Utilise the Experimental Results	92
3.3. Crack-Based Drift Limits from Experimental Results.....	93
3.3.1. Drift Limits for Light Damage Lacking in Literature	93
3.3.2. Repetition in the Loading Protocol of Experiments	95
3.3.3. Relationship between Crack-based Damage and in-plane Drift	96
3.3.4. Discussion and Comparison to Other Drift Limits	102
3.3.5. Summary of Drift Limits for Light Damage	104
3.4. Conclusions: Experiments to Understand Crack Behaviour.....	105
Chapter 4	107
Damaging (Multi)Hazards and Modelling their Effects	
4.1. Hazards and Multi-hazards.....	109
4.1.1. Hazards	110
4.1.2. Multi-hazards	111

4.2. Overview of Actions causing Damage to Masonry Buildings	113
4.2.1. Vibrations	114
4.2.2. Restrained Deformations	115
4.2.3. Imposed Deformations	115
4.2.4. Out of Plane Loading	115
4.2.5. Gravity Overloading	116
4.3. Calibrating Crack Behaviour from Experiments into FEM Models	117
4.3.1. Background on Validation Experiments	118
4.3.2. Overview of Calibration Models	119
4.3.3. Model Properties and Boundaries	120
4.3.4. Calibration of Spandrels and Walls with Openings	125
4.3.5. Additional Model for Walls with Pre-Damage	130
4.3.6. FEM Model for Shear Walls	133
4.3.7. Conclusions from the Calibration Process	137
4.4. Modelling Damage: Shrinkage, Settlements, and Vibrations	139
4.4.1. Modelling Restrained Deformations: Shrinkage	139
4.4.2. Modelling Imposed Deformations: Settlements	141
4.4.3. Dynamic, Non-Linear Time History Analysis: Vibrations	143
4.4.4. Modelling Multi-hazards	146
4.5. Conclusions: Modelling and Calibration.....	147

Chapter 5 **149**

Fragility

5.1. Introduction	150
5.2. Extrapolation to Non-Linear Dynamic Analyses	152
5.2.1. Background on Experiments and Calibration	152
5.2.2. Setup of Extrapolation Models (Based on Field Cases)	153
5.2.3. Results from Extrapolation Models	161
5.3. Regression of Damage Function from FEM Results.....	167
5.3.1. Reasoned Regression Model Considering Ψ_0	167
5.3.2. Model Uncertainty	173
5.3.3. Surrogate Model with Machine Learning	175
5.4. Fragility Curves for Seismic Vibrations.....	178
5.4.1. Probabilistic distributions and Parameters	178
5.4.2. Results of Monte Carlo Simulation	180
5.4.3. Comparisons to other Studies	184
5.4.4. Fragility Maps	187
5.5. Fragility Curves for Settlements from Soil Curvatures	191
5.5.1. Overview of Semi-Coupled Models of Masonry Façades	191
5.5.2. Fragility Curves for Soil Angular Distortion: β vs. Ψ	198

5.6. Conclusions: Probability of Damage and Aggravation.....	206
Chapter 6	209
Hastening: Damage Accumulation Function	
6.1. Analysis of Repetition Effect in Experiments	212
6.2. Damage Accumulation due to Repetition in FEM Models	218
6.2.1. Methodology: Brief Description of the FE Models	218
6.2.2. Variations investigated with the FE Models	221
6.2.3. Model Results: Effect of Repetition	223
6.2.3. Summary of Observations from Repetitions Models	228
6.3. Damage Accumulation Function (DAF)	229
6.3.1. Function for Ψ from Variable PGV Sequences	229
6.3.2. Comparison of DAF against Model Results	235
6.3.3. Comparison of DAF against Experimental Results	241
6.3.4. Application: Probability Maps for Accumulated Damage	244
6.4. Concept of Damage Hastening	248
6.4.1. Definition of 'Hastening' in the Context of Damage	249
6.4.2. Time as the Hazard	252
Chapter 7	257
Conclusions and Outlook	
7.1. Answers and Conclusions	258
7.1.1. Objective, Continuous Scale for Damage and its Aggravation	258
7.1.2. Monitoring Crack-Based Damage Aggravation from Experiments	260
7.1.3. Damage Aggravation by Subsequent Actions	261
7.1.4. The Effect of Repetition on Damage Accumulation	263
7.1.5. Answer to the Main Objective	264
7.2. Relevance and Contributions.....	265
7.2.1. Scientific Relevance	265
7.2.2. Societal Relevance	265
7.2.3. Utilisation	267
7.3. Limitations - Restrictions of the Scope	268
7.3.1. One Parameter to Describe it All	268
7.3.2. Single-Wythe Brick Walls and In-Plane Damage	269
7.3.3. Quasi-static Extrapolation to Dynamic Actions	270
7.3.4. Repetition at the Material Model	271
7.4. Recommendations for Further Study	271
7.4.1. Crack-Based Damage in Modern Masonry	271
7.4.2. Mixed-Mode Fracture and Degradation	272
7.4.3. Monitoring Damage in the Field	273

7.4.4. Strategies for Repair, Mitigation, and Adaptation	273
7.5. Outlook.....	275
7.5.1. Climate Change and Building Fragility	275
7.5.2. Cracking and the Energy Transition	275
7.5.3. Risk Reluctance, Acceptance and Damage Policy	276
List of Publications	277
Journal Papers	277
Conference Papers	278
Scientific Reports	280
Bibliography	281
List of Authors.....	310
Appendix A	i
Overview of Related Work	
A.1. Laboratory High-Resolution Monitoring with DIC	ii
A.2. Geometry Statistics from 3D-BAG	iv
A.3. Experiments and Models of NeHoBo Floors	vii
A.4. SLaMA-based, parametric computational models for pushover ADRS analyses of masonry typologies	ix
A.5. Strengthening: Structural Glass	xii
A.6. Repair: Self-Healing Mortar.....	xiii
A.7. Out-of-Plane of Masonry Walls during Hydrostatic Loading.....	xiv
A.8. The Action of Debris during the German Flood of 2021	xvi
A.9. Strategy for Safety Assessment of Historical Quay Walls.....	xviii
A.10. Experiments during course 'Masonry Bend & Break'	xxi
A.11. Analysis of Waarts' Probabilistic Estimation of Damage	xxii
A.12. InSAR Analysis of Cyclic Soil Movements in Norg	xxiii
A.13. The Effect of Deep Subsidence on Masonry Façades.....	xxiv
A.14. The Effect of Combined Horizontal Strain and Curvature on Masonry Façades from Soil Movements	xxv
A.15. The Effect of Truck Vibrations in Comparison to Earthquakes'	xxvii
Appendix B	xxix
Ψ Damage Parameter	
B.1. Equations and Definition of Ψ	xxix

Table of Contents	lxxxi
B.2. Table with Practical examples of Ψ and $\Delta\Psi$	xxxii
B.3. Perception of Damage.....	xxxiv
Appendix C	xxxv
Supervised MSc Projects	
Appendix D	xxxix
Glossary	
Appendix E	xliii
Loppersum Visit	
Appendix F	xlix
Dataset	
Appendix G	li
Tool for Crack Tracking	
G.1. Application of DIC for Monitoring of Masonry Test Samples in the Laboratory.....	li
G.2. Theory and Programming of DIC	liiii
G.3. Optimisation and Calibration of DIC.....	lix
Curriculum Vitæ	lxvii
Propositions	lxix
Acknowledgements	lxxi
Extended Table of Contents	lxxvi